Dark Matter on the Galactic Scale: From Particle Physics and Cosmology to Local Properties

Martin Stref

THÈSE POUR OBTENIR LE GRADE DE DOCTEUR
DE L'UNIVERSITÉ DE MONTPELLIER

En physique théorique

École doctorale : Information, Structures, Systèmes

Unité de recherche Laboratoire Univers et Particules de Montpellier

Dark Matter on the Galactic Scale: From Particle Physics and Cosmology to Local Properties

Présentée par Martin Stref

Le 11 septembre 2018

Sous la direction de Julien Lavalle

Devant le jury composé de

Pierre Salati, Professeur, Laboratoire de physique théorique d'Annecy-Le-Vieux	Président du jury
Julien Lavalle, Chargé de recherche, Laboratoire Univers et Particules de Montpellier	Directeur de thèse
Anne Green, Professor, University of Nottingham	Rapporteuse
Torsten Bringmann, Professor, University of Oslo	Rapporteur
Malcolm Fairbairn, Professor, King's College London	Examinateur
Joseph Silk, Professeur, Institut d'Astrophysique de Paris	Examinateur
Benoit Famaey, Chargé de recherche, Observatoire Astronomique de Strasbourg	Examinateur
Emmanuel Nezri, Chargé de recherche, Laboratoire d'Astrophysique de Marseille	Examinateur

UNIVERSITÉ DE MONTPELLIER

"If I have seen further it is by standing in between the shoulders of dwarfs"
Sidney Coleman

Remerciements

Je tiens à remercier Julien Lavalle pour avoir été mon directeur de thèse. Tu m'as appris de très nombreuses choses au cours de ces trois années de travail, tant sur le plan scientifique que sur le plan humain. Tu m'as transmis un modèle du chercheur qui me donne aujourd'hui envie de faire de la recherche un métier. Merci de m'avoir communiqué tes connaissances et ton enthousiasme, tu es la principale raison pour laquelle je garderai un excellent souvenir de cette thèse. J'espère que nous continuerons à travailler ensemble à l'avenir!

Je remercie également Thomas Lacroix. J'ai beaucoup apprécié travailler avec toi au cours de ces deux années passées ensemble. Merci d'avoir relu mon manuscrit! J'en profite pour remercier tous les jeunes du LUPM et du L2C avec qui j'ai passé beaucoup de bons moments. Merci donc à Ronan, Justine, Michelle, Rupert, Valentin, Camille, Thibault, Duncan, Julien, Grazia, Quentin, Loann, Nishita, Manal et Marco!

Merci aux "marseillais" Emmanuel et Arturo pour le bon temps passé ensemble, au travail et en dehors!

Je remercie tous les membres permanents du LUPM, en particulier Denis Puy et Agnès Lèbre pour leur aide et leur soutient. Je remercie tous les permanents de l'équipe IFAC avec qui j'ai pu intéragir: Michele, Nicolas, Félix, Karsten, Cyril, Gilbert, Jean-Loïc et Sacha.

Merci aux responsables des enseignements que j'ai effectué au cours de ma thèse: Bertrand Plez, Coralie Weigel, Jérôme Dorignac, Simon Modeste et Didier Laux.

Merci au Labex OCEVU pour avoir financé ma thèse et m'avoir permis de voyager à travers le monde!

I thank Professor Anne Green and Professor Torsten Bringmann for accepting to review this manuscript and be part of my defence committee. I would also like to thank the other members of the committee: Professor Silk, Professor Fairbairn, Professeur Salati and Benoît Famaey.

Enfin merci papa, maman et soeurette pour votre soutien et votre amour. And thank you Lisa. I told you these caramels you sent me would earn you a spot here, so there you go! I am really glad I met you, you have changed my life these past few months.

Contents

Chapter 1

Introduction

Physicists today are confronted with a wealth of astrophysical and cosmological evidence that a large fraction of the mass content of the Universe is invisible. Though theorists have come up with numerous possible explanations for that missing mass, there is at the moment no experimental data supporting one explanation over the others. This missing mass problem has been resisting investigations for decades and is considered one of the most important problem of modern physics. For a historical review on the missing mass problem, we refer to Bertone & Hooper (2016).

Interestingly, this is not the first time physicists have faced an observational missing mass problem. Back in 1846, French astronomer Le Verrier and English astronomer John Couch Adams were trying to explain some anomalies observed in the trajectory of Uranus [see *e.g.*, Weinberg (1972)]. The trajectory seemed to be in contradiction with the Universal law of gravitation and Newtonian dynamics. To account for this discrepancy, Le Verrier and Adams assumed, independently, that the trajectory is perturbed by another orbiting body. They computed the theoretical position this object should have to explain the anomaly and Le Verrier sent his result to astronomer Johann Gottfried Galle in Berlin. Galle, upon receiving Le Verrier's letter, immediately looked for the object and discovered Neptune. This discovery remains one of the most astonishing successes of Newton's theory. In that particular case, the missing mass problem was really a missing *matter* problem since theory and observations were reconciled thanks to an object unseen at the time. A few years later, another missing problem appeared in astronomy. It was Le Verrier, again, who showed that the rate of precession of the perihelion of Mercury's orbit was anomalous with respect to Newton's theory. In light of its past success with Uranus, Le Verrier suggested that Mercury's anomaly could be explained by another yet undiscovered planet he called Vulcan. However, this time, all observational efforts to observe the hypothetical planet failed. Mercury's anomaly remained unexplained for decades before being finally accounted for by the general theory of relativity of Albert Einstein (1915). This new theory of gravity perfectly accounts for the effect without introducing any unobserved matter, hence in that case, the missing mass problem was an indication that the theory had to be revised in depth. These historical examples point toward two ways of solving the current missing mass problem. Either we have to revise the established theory of gravity (*i.e.* general relativity), or the Universe is filled with a new form of matter whose properties are unknown.

We begin by reviewing the astrophysical and cosmological evidence for the missing mass problem. We then discuss the theoretical approaches currently under investigation, and finally we present the experimental searches for particle dark matter.

1.1 The missing mass problem on the scale of individual structure

In this section, we present the astrophysical evidence for a missing mass. We discuss observations of galaxies and galaxy clusters.

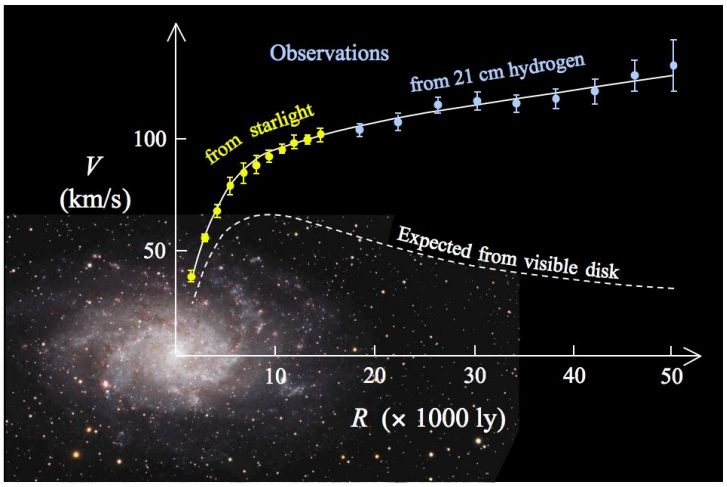

Figure 1.1 – Rotation curve for the M33 galaxy, by Stefania Deluca for *Wikipedia*. The data are taken from Corbelli & Salucci (2000).

1.1.1 Galactic rotation curves

Perhaps the most striking observation leading to the missing mass problem is the rotation curves of galaxies, *i.e.* the circular velocity profile of stars as a function of their distance to the centre of galaxies. The first measurements of rotation curves were performed in the 1930s and the 1940s but were limited to the innermost regions of galaxies. The birth of radio astronomy with the first observation of the 21 cm line of neutral hydrogen (Ewen & Purcell, 1951; van de Hulst, 1951) allowed astronomers to explore the outer parts of galaxies. The realization that rotation curve data were in apparent disagreement with the observed distribution of matter took place in the 1970s. Observations showed that the rotation curve of most spiral galaxies flatten at high radius (Freeman, 1970; Rogstad & Shostak, 1972; Roberts & Rots, 1973; Bosma, 1978; Rubin et al., 1978). A modern measurement of the rotation curve of M33 is shown in Fig. 1.1. If the luminosity is a good tracer of the mass density of matter in galaxies, we expect the disc density to be exponentially falling with radius. We show in Fig. 1.1 the rotation curve of the galaxy M33. One can see by eye that the luminous matter does not extend much beyond 10^4 ly. Such a distribution leads to a prediction for the rotation curve which is shown as a dashed line. This curve strongly differs from the measured rotation curve, shown by the data points. These anomalies motivated authors to suggest the presence of a large quantity of unobserved matter in galaxies (Einasto et al., 1974; Ostriker et al., 1974).

While rotation curves are a spectacular observational proof of the missing mass problem, this problem is not limited to spiral galaxies. The measured velocity dispersion of stars combined with the virial theorem allows one to predict the mass of any type of galaxy. It is found that *all* types of galaxies, irrespective of their morphology (spiral or elliptical) or their size, contain a large amount of missing mass. Our own galaxy, the Milky Way, is no exception.

The rotation curves of the Milky Way point toward an invisible mass [see *e.g.*, Fich et al. (1989); Dehnen & Binney (1998); Catena & Ullio (2010); McMillan (2011); Binney & Piffl (2015)]. Measures of the velocity dispersion of nearby stars also lead to a non-zero invisible matter density [see for instance the pioneering work of Oort (1932) and the review of Read (2014)].

1.1.2 Galaxy clusters

Though galactic rotation curves provide the most striking astrophysical evidence for a missing mass, it was not in galaxies that the problem first became quantitatively worrying. The first evidence for an invisible mass on extragalactic scales came from the analysis of the observations

of the Coma Cluster by Zwicky (1933). Zwicky found an unusually large velocity dispersion for several galaxies within the galaxy cluster. He applied the virial theorem to the structure in order to estimate its mass, assuming an average mass of $10^9\,M_\odot$ for galaxies, and found that the large velocity scatter led to a total mass far above the "luminous" mass. He concluded that most of the mass in the Coma Cluster had to be made of dark matter. He later returned to his analysis of the Coma Cluster, this time with the aim of estimating the average mass of galaxies within the cluster (Zwicky, 1937). This led him to find an average mass-to-light ratio of order 500 for galaxies. It later turned out that this estimate was based on a poorly measured Hubble parameter. More modern measurements lead to a mass-to-light ratio roughly ten times lower. This does not change Zwicky's conclusion that most of the mass in galaxies is dark. Several methods exist to measure the mass of galaxy clusters. Apart from the measure of the velocity dispersion of galaxies and the use of the virial theorem, one can study the large amount of gas which is observable in X-ray. Assuming hydrostatic equilibrium, one can link the gas temperature profile to its mass profile. Temperatures inferred through this method are approximately an order of magnitude lower than the temperature measured in X-ray. Theory and observations can be reconciled if a large fraction of the mass is dark. Finally, a third probe of the mass in galaxy clusters is gravitational lensing (already suggested by Zwicky (1937), see Massey et al. (2010) for a review). This method relies on the deflection of light by massive bodies as predicted by the general theory of relativity. Two distinct regimes are used to study galaxy clusters. In the *strong gravitational lensing* regime, photons are significantly deflected and the presence of a massive object in the foreground (a "lens") leads to multiple images of background light sources (like galaxies or quasars). Many strong lensing arcs have been detected by the *Hubble* space telescope such as those observed in the Abell 2218 galaxy cluster, see Fig. 1.2. The study of these arcs allows one to estimate the total mass within the cluster and again a large discrepancy is found with respect to the luminous mass. Another interesting regime is *weak gravitational lensing* which occurs when light rays pass too far from the lens for the distorsion and magnification of the individual background objects to be detectable. However, two nearby sources are approximately distorted by the same amount, which enables a statistical treatment of background sources [see *e.g.*, Hoekstra et al. (2013)]. Strong lensing probes the inner parts of a cluster, while weak lensing probes the more external parts (also better suited to study). These methods allow one to reconstruct the mass distribution in galaxy clusters and lead to results consistent with the previous methods. By combining with spectrometric/photometric-redshift measurements, one can also use weak lensing to make a tomography of structures in the universe.

1.2 The missing mass problem on cosmological scales

This section focuses on the missing mass problem on cosmological scales. Two pillars of modern cosmology, the Cosmic Microwave Background (CMB) and Big Bang Nucleosynthesis (BBN), are briefly reviewed. We also say a few words about the use of large-scale structures (LSS).

1.2.1 The Cosmic Microwave Background

The CMB is fossil radiation emitted approximately 300,000 years after the Big Bang. Its existence was predicted in the 1940s (Gamow, 1948a,b; Alpher & Herman, 1948a,b). It was discovered accidentally by Penzias & Wilson (1965) and immediately interpreted as the primordial background radiation (Dicke et al., 1965). In the hot Big Bang model, this radiation is interpreted as a remnant of the time of recombination, when the first hydrogen atoms were formed and the photon temperature decreased below their binding energy. It is of paramount importance for cosmology because the matter perturbations that later gave rise to cosmological structures left an imprint on the radiation (Zeldovich & Sunyaev, 1969; Peebles, 1982a,b). These imprints manifest themselves as small temperature anisotropies on an otherwise perfectly isotropic background

Figure 1.2 – Lensing arcs in the Abell 2218 galaxy cluster as observed by the *Hubble* space telescope. Credit: NASA, ESA, and Johan Richard (Caltech, USA).

radiation. The CMB anisotropies were first observed by the COBE satellite (Smoot et al., 1992) and found to be in agreement with theoretical predictions. The discovery of the CMB, the observed low degree of anisotropy and the measured spectrum all provided strong arguments in favour of the hot Big Bang model (Peebles, 1965; Peebles & Dicke, 1966; Peebles et al., 1991).

A variety of effects contribute to shape the CMB as we observe it today. Reviews on the subject are for instance Hu (1995); Durrer (2001). The most striking feature found in the anisotropies is the presence of acoustic peaks, which were predicted long before their discovery in the 1990s (Silk, 1968; Peebles & Yu, 1970; Sunyaev & Zeldovich, 1970). These peaks appear because baryons fall into the potential wells created by the primordial perturbations. Because baryons are tightly coupled to photons, they experience a radiation pressure which drives these baryons outward from the perturbation. At recombination, baryons stop interacting with photons and are therefore frozen in a shell surrounding the dark matter perturbation. The radius of this shell is given by the sound horizon at the time of recombination and leads to a characteristic angular scale in the CMB. The temperature fluctuation correlation function measured by *Planck* is shown in Fig. 1.3 as a function of the multipole l (a multipole is related to an inverse angular size on the CMB). Acoustic peaks are clearly visible in the figure. The existence of baryonic acoustic oscillations in the CMB is a robust indication that the Universe contains a form of non-interacting matter. Without this dark matter, perturbations would be washed out by radiation pressure. This effect is called Silk damping (Silk, 1968) or diffusion damping. It occurs because of the departure of the baryon-photon plasma from a perfect fluid. This departure takes place because photons have a non-zero free-streaming length which allows them to escape potential wells. Their subsequent collisions with baryons damp the baryon perturbations below a given scale. If all matter were interacting with photons, high-l peaks in the CMB would be completely suppressed. Since these peaks are observed, we conclude that a fraction of matter does not interact with photons.

Baryonic acoustic oscillations and Silk damping are the two main effects shaping primordial perturbations in the CMB. Also contributing to anisotropies are late-time effects such as the interaction of CMB photons with electrons in galaxy clusters (Sunyaev & Zeldovich, 1970), or the blueshifting/redshifting of photons due to the presence of potential wells along the line-of-sight (Sachs & Wolfe, 1967).

Taking into account all these effects allows one to fit the CMB data to an exquisite precision. Only six independent parameters are needed to account for all CMB-related observations. These

parameters constitute the basis of the ΛCDM standard model of cosmology, and include the baryons abundance relative to the critical density $\Omega_{\rm b}h^2$ (the factor h^2 allows one to factorize the uncertainty associated to the Hubble parameter $H_0 = 100\,h\,\mathrm{km/s/Mpc}$), the cold dark matter abundance $\Omega_{\rm c}h^2$, the optical depth τ, the amplitude of primordial perturbations ($A_{\rm s}$ or σ_8), the primordial spectral index $n_{\rm s}$ and the value of the cosmological constant.[1] The parameters obtained with Planck are shown in Table. 1.1. One sees that the fraction of ordinary matter in the model is

$$\frac{\Omega_{\rm b}h^2}{\Omega_{\rm b}h^2 + \Omega_{\rm c}h^2} = 15.8\%\,, \tag{1.1}$$

hence a bit more than 84% of all matter in the Universe is non-interacting around the time of recombination. The properties of dark matter in the ΛCDM model are the following: it is a non-interacting (pressureless), non-relativistic fluid (hence the word "cold") characterized by its abundance only.

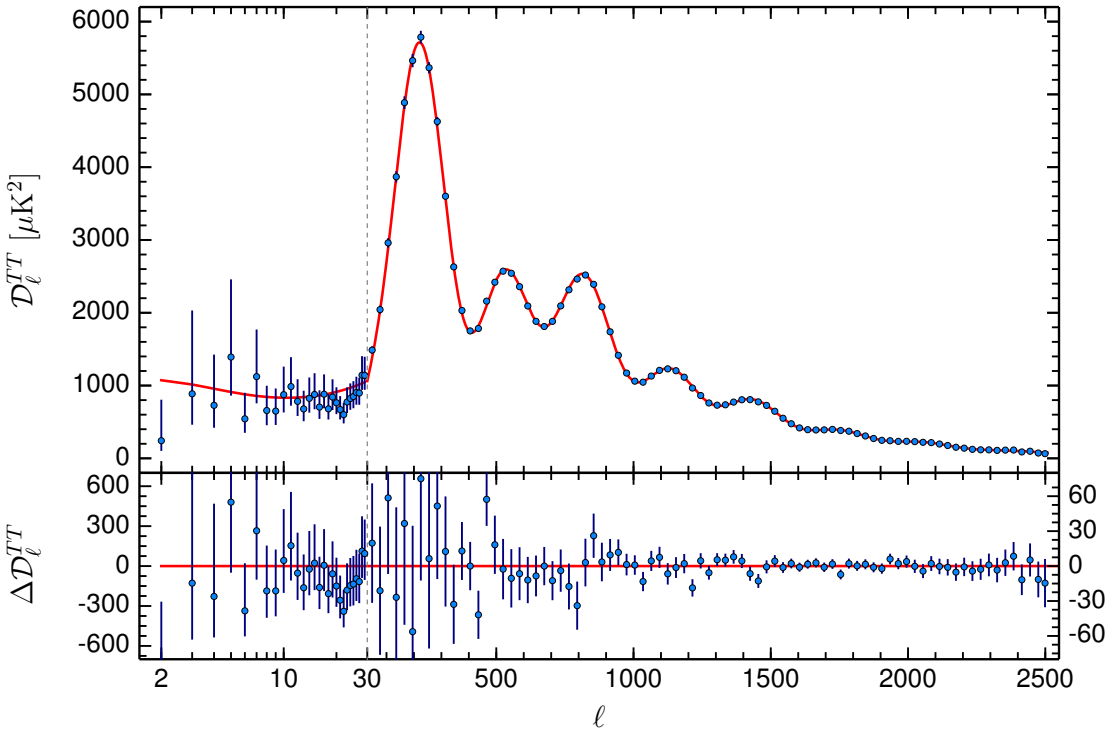

Figure 1.3 – Temperature power spectrum of the CMB as obtained by Ade et al. (2016).

	$\Omega_{\rm b}h^2$	$\Omega_{\rm c}h^2$	τ	σ_8	$n_{\rm s}$	h	
Planck 2015	0.02226	0.1186	0.066	0.8149	0.9677	0.6781	
Planck 2018	0.02237	0.1200	0.0544	0.8111	0.9649	0.6736	

Table 1.1 – Parameters of the ΛCDM model as measured by Ade et al. (2016) and Aghanim et al. (2018).

[1] It is also implicitly assumed that the Standard Model of particle physics is valid at all times.

1.2.2 The Big Bang Nucleosynthesis

Another major part of the current standard model of cosmology is Big Bang Nucleosynthesis (BBN). This is the theory that describes the formation of light elements (D, ^{3}He, ^{4}He, ^{7}Li). The foundations of the theory were laid down in the 1940s and 1950s (Gamow, 1946; Alpher et al., 1948, 1953). Reviews can be found in Sarkar (1996); Olive et al. (2000). Though initially designed as a theory explaining the formation of all elements, it was soon realized that BBN could not account for elements heavier than lithium. This is because these elements are produced through 3-body and 4-body processes which are very unlikely at the time of BBN due to the small baryon-to-photon ratio. Heavier elements are actually formed much later inside stars, see Fig. 1.4. As stated, predictions of BBN for the abundances of ^{3}He and ^{4}He depend on the baryon-to-photon ratio (Peebles, 1966; Wagoner et al., 1967; Reeves et al., 1973). This ratio can be independently measured from the CMB, and this value leads to good agreement between predictions of BBN and observations. Hence the primordial formation of elements also points toward a Universe dominated by a form of non-interacting matter.

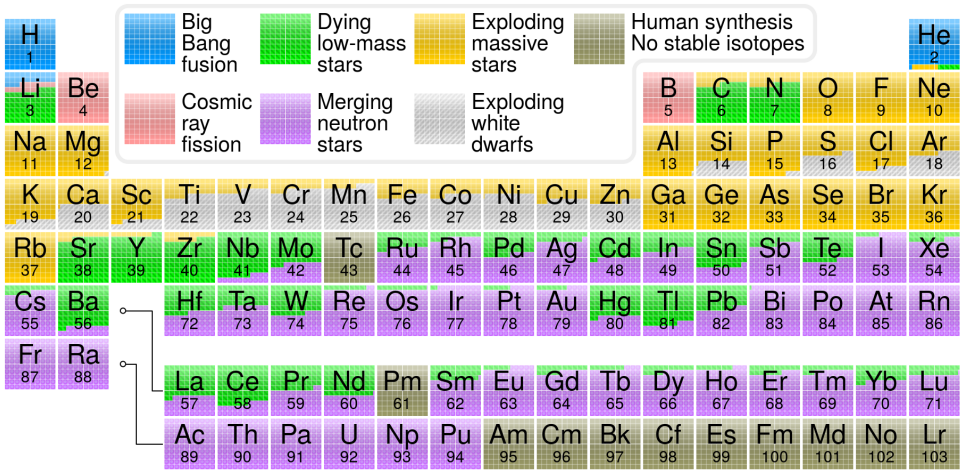

Figure 1.4 – The periodic table of elements with their cosmological or astrophysical origin. By Cmglee for *Wikipedia*, based on work by Jennifer Johnson at Ohio University.

1.2.3 Large-scale structures

After recombination, the growth and formation of large-scale structures is dominated by dark matter (Blumenthal et al., 1984). Galaxy surveys such as CfA (de Lapparent et al., 1986; Geller & Huchra, 1989), 2dFGRS (Colless et al., 2001), SDSS (York et al., 2000) and BOSS (Anderson et al., 2014) also lead to results in full agreement with the primordial probes that are the CMB and BBN. In particular, observations of large-scale structure are recovered in numerical simulations starting with CMB-like initial conditions (see *e.g.*Springel et al. (2005); Klypin et al. (2011)). The observation of baryonic acoustic oscillations in the matter power spectrum is another strong argument in favour of dark matter (Percival et al., 2010). The consistency of large-scale structures with CMB and BBN data shows that ΛCDM is a robust cosmological model, at least for all times in between BBN and today and on super-galactic scales.

We would like to mention a tension that appears when the value of the Hubble parameter H_0 as inferred from the CMB is compared to the value obtained from local, low redshift measurements (Bernal et al., 2016). Using Cepheid variables as distance rulers, Riess et al. (2016); Riess et al. (2018); Riess et al. (2018) measured the Hubble parameter to a value $H_0 = 73.48 \pm 1.66\,\mathrm{km/s/Mpc}$, which is in disagreement at the 3.6σ level with the CMB value $H_0 = 67.4 \pm 0.5\,\mathrm{km/s/Mpc}$. Minimal extensions of ΛCDM are not able to resolve the tension on H_0 without introducing new tensions on other cosmological parameters (Ade et al., 2016; Aghanim et al., 2018). Alternatively, the

discrepancy could be due to a systematic uncertainty on the local measurement as proposed by Rigault et al. (2015). A clear solution to this issue is yet to be found.

1.3 Theoretical approaches to the missing mass problem

We have presented the astrophysical and cosmological evidence for missing mass in the Universe. We have discussed how the ΛCDM model accounts for observations by introducing a non-interacting, non-relativistic matter fluid that makes up most of the mass in the Universe. We now turn to theories attempting to describe the physics of the dark matter itself. We first discuss theories of modified gravity and then turn to particle dark matter which is the main focus of this work.

1.3.1 Modification of the theory of gravity

The general theory of relativity is very well tested on scales from a few centimeters to the size of the solar system, essentially in the weak-field regime (Will, 2014). A wide variety of phenomena predicted by the theory have been observed, such as gravitational lensing (Dyson et al., 1920) or gravitational waves (Hulse & Taylor, 1975; LIGO Scientific Collaboration & Virgo Collaboration, 2016). However, the overwhelming amount of anomalous observations, to which we can add the discovery of the accelerated expansion (Riess et al., 1998; Perlmutter et al., 1999), might cast some doubts on the validity of the theory on large scales. This motivates the search for an alternative theory of gravity which could explain these anomalies while still accounting for observations consistent with general relativity, just like Einstein's theory explains Mercury's anomaly and reproduces Newton's gravity in the non-relativistic weak-scale regime. We note that there are other reasons that might motivate revisions of general relativity, whether it is on rather philosophical grounds (Brans & Dicke, 1961) or in the perspective of building a theory of quantum gravity [see *e.g.*, Rovelli (1998)].

In the context of the galactic rotation curve issue, an empirical formulation of modified gravity was developed by Milgrom (1983) as an alternative to Newtonian gravity, that would provide an explanation to the flatness of rotation curves without resorting to dark matter. This theory is known as Modified Newtonian Dynamics (MOND). We refer to Famaey & McGaugh (2012) for a review. In MOND, the Newtonian acceleration is given by

$$\vec{a}_{\mathrm{N}} = \mu\left(\frac{a}{a_0}\right)\vec{a}\,, \tag{1.2}$$

where a_0 is a constant acceleration and μ is an interpolating function which satisfies

$$\mu(x) \to \begin{cases} 1 \text{ for } x \gg 1 \\ x \text{ for } x \ll 1\,. \end{cases} \tag{1.3}$$

This modification of Newton's law is motivated by the flattening of galactic rotation curves. A test particle on a circular orbit, in the deep-MOND regime $a \ll a_0$, around a point-mass M has a velocity solution of

$$\frac{(v^2/r)^2}{a_0} = \frac{G_{\mathrm{N}}M}{r^2}\,, \tag{1.4}$$

which leads

$$v = (G_{\mathrm{N}}\,M\,a_0)^{1/4}\,, \tag{1.5}$$

therefore the speed is independent of the radius, in agreement with the observation of flat rotation curves. MOND is very successful at explaining galactic dynamics without relying on any invisible

form of matter. In particular, as seen in Eq. (1.5) where M is the baryonic mass, it naturally accounts for correlations between dark matter and baryons such as the baryonic Tully-Fisher relation (Tully & Fisher, 1977) or the mass discrepancy-acceleration relation (McGaugh et al., 2016), while explaining these relations in the framework of ΛCDM is challenging. However, MOND has difficulties accounting for the dynamics observed on larger scales. For instance, in its simplest version, it is not compatible with the inner dynamics of galaxy clusters (The & White, 1988; Sanders, 1999, 2003; Pointecouteau & Silk, 2005). MOND has also difficulties with cosmology. In order to get cosmological predictions for MOND, one must first construct a relativistic extension of MOND. There is no generic way of constructing such a theory, therefore several examples exist *e.g.*, Bekenstein & Milgrom (1984); Bekenstein (2004); Zlosnik et al. (2007); Blanchet (2007); Skordis (2008); Milgrom (2009). Since there is no unique theory, there is no unique prediction for cosmology. It seems difficult for known theories of modified gravity to account for all observations, especially CMB anisotropies (McGaugh, 1999; Slosar et al., 2005). This obviously does not rule out modified gravity as an idea.

We would like to mention an interesting observation put forward as a strong case in favour of particle dark matter over modified gravity. This is the observation of the so-called Bullet cluster (Clowe et al., 2006). The name actually refers to a pair of clusters having experienced a collision. Combined lensing and X-ray observations show that the mass distributions and the gas are not overlapping, see Fig. 1.5. This observation is easy to interpret in the ΛCDM framework. As the two clusters collided, the dark matter halos passed through each other thanks to the collisionless nature of the dark matter fluid. In contrast, the two gas clouds originally sitting at the centres of the two clusters did collide and remained where the collision took place. Note however that such a high-speed collision might actually be quite rare in a ΛCDM universe (Kraljic & Sarkar, 2015). The situation is more surprising in a modified gravity context since one has to explain why the centre of mass is not overlapping with the gas cloud. A detailed study of the Bullet cluster (Angus et al., 2007) showed that to reproduce the observations, MOND typically needs an amount of collisionless, invisible matter *e.g.*, in the form of neutrinos with mass 2 eV. One of the biggest challenges of the MOND class of approaches is to come up with predictions that can help distinguish them from the particle dark matter scenarios.

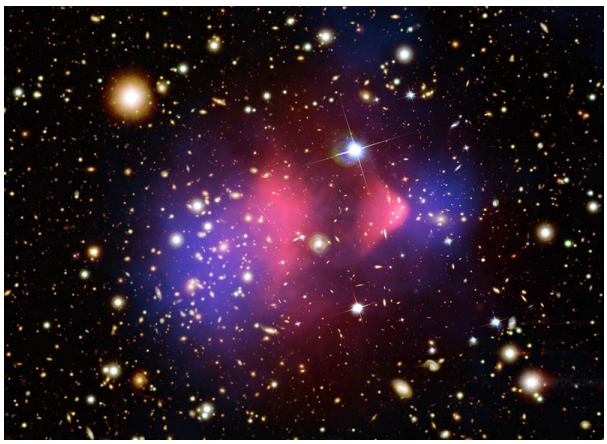

Figure 1.5 – Segregation of the centres of mass and gas in the Bullet Cluster, as observed by the *Hubble* space telescope (the coloration has been added artificially). Credit: X-ray: NASA/CXC/CfA/M.Markevitch, Optical and lensing map: NASA/STScI, Magellan/U.Arizona/D.Clowe, Lensing map: ESO WFI .

1.3.2 Particle dark matter

We now turn to the Uranus-like approach to the missing mass problem, *i.e.* particle dark matter. In contrast to modified gravity, particle dark matter provides a consistent picture for the dark

matter from the early universe to the local universe, and is the pillar of our understanding of structure formation which copes with almost all observed phenomena: CMB, Ly-α, large-scale structures, rotation curves, galaxy properties (pending ongoing work on baryonic effects). It is somewhat impressive that starting from initial conditions set by the CMB, we can get the Universe we observe simply by assuming an extra pressureless cold dark matter component. We quickly present the main particle candidates and refer to Bertone et al. (2005) and Bergstrom (2009) for detailed reviews on the subject.

1.3.2.1 Baryonic dark matter

Let us first examine the possibility that dark matter is actually made of ordinary matter. The requirement that dark matter particles be neutral and stable rules out all known particles with the exception of neutrinos. Neutrinos are also excluded because of their mass ($\sum m_\nu \leqslant 0.23\,\mathrm{eV}$ (Ade et al., 2016)) which implies these particles decoupled while they were relativistic, hence neutrinos are hot dark matter. Hot dark matter particles have too large a free-streaming scale to form galaxies at early times, instead they form first much larger structures like super-clusters. Forming galaxies in that scenario is only possible through fragmentation of large structures, however this is not compatible with observations which show that older structures are smaller on average.

An alternative scenario where dark matter is made of ordinary matter is Massive Astrophysical Compact Halo Objects (MACHOs) such as planets, neutron stars, brown dwarfs or black holes (Petrou, 1981; Paczynski, 1986). The amount of observed baryonic matter in galaxies only makes up a fraction of the total baryonic abundance constrained by BBN and the CMB. Therefore there is room for a large fraction of invisible baryonic matter in galaxies. However, MACHOs have been ruled out as the main components of the Milky Way halo through microlensing studies (Tisserand et al., 2007). Black holes are still alive as dark matter candidates if they are primordial *i.e.* they formed during the radiation era (Hawking, 1971) and are consequently seen as part of the dark matter at the time of the CMB (see Carr et al. (2016) for a review). Numerous bounds from cosmology and astrophysics are currently available (from lensing, dynamics, gravitational waves, etc.) yet a couple of mass windows are still open for primordial black holes to make up nearly all of dark matter. The recent discovery of black hole binaries through their gravitational radiation (LIGO Scientific Collaboration & Virgo Collaboration, 2016) has renewed interest in few-solar-mass black holes as dark matter (Bird et al., 2016; Clesse & García-Bellido, 2017).

1.3.2.2 Weakly Interacting Massive Particles

The most popular class of beyond-the-Standard-Model dark matter candidates are Weakly Interacting Massive Particles (WIMPs). This term refers to particles being neutral, stable (or at least very long-lived), interacting weakly (though not necessarily through the SM weak interaction) and having a mass in the GeV-TeV range (the MeV range is also accessible to scalars (Boehm & Fayet, 2004)). The main motivation for these particles to be the dark matter is their very simple production mechanism in the early Universe (Lee & Weinberg, 1977) and the fact that they are *cold* dark matter candidates. The next chapter is devoted to the presentation of the WIMP's thermal history, therefore we do not enter into these details here. The GeV-TeV mass range is currently being deeply probed by observations and experiments. The sub-GeV and multi-TeV ranges are still to be explored.

Supersymmetry Supersymmetry was developed in the early 1970s as an extension of gauge theories for a variety of reasons, including purely aesthetic ones (Ramond, 1971; Neveu & Schwarz, 1971; Gervais & Sakita, 1971; Golfand & Likhtman, 1971; Wess & Zumino, 1974; Volkov & Akulov, 1973). It was soon realized however that this framework offers a solution to the gauge hierarchy problem (Gildener, 1976; 't Hooft, 1980). Supersymmetry also helps unifying all gauge

interactions into a grand unified theory (Marciano & Senjanovic, 1982). Moreover, promoting supersymmetry to a gauge symmetry (*i.e.* a local one) rather than a global one leads to the theory of supergravity (Nath & Arnowitt, 1975; Freedman et al., 1976) which can be interpreted as a low-energy effective theory of superstrings, thus linking supersymmetry to the unification of all interactions including gravity. On top of this, supersymmetry provides a number of dark matter candidates (Ellis et al., 1984). The most promising one is the neutralino, which is a mixing of the superpartners of the gauge and Higgs fields. If the neutralino is the lightest supersymmetric particle, R-parity ensures its stability. The neutralino is by far the most studied dark matter candidate in the literature. We refer to Jungman et al. (1996) for a classic review on supersymmetric dark matter and to Martin (1997) for a review on supersymmetry and the associated formalism.

Extra dimensions Extra dimensions of space were first considered in the 1920s (Kaluza, 1921; Klein, 1926) in the context of unification of electromagnetism and gravity. They regained attention in the 1980s when it was demonstrated that string theory is not viable with only three dimensions of space. Since then, a number of models with extra dimensions has been proposed, such as new dimensions at a millimetre (Arkani-Hamed et al., 1998; Antoniadis et al., 1998; Arkani-Hamed et al., 1999), Randall-Sundrum models (Randall & Sundrum, 1999) and Universal Extra Dimensions (UED). UED provide a dark matter candidate in the form of the lightest Kaluza-Klein particle, whose stability is protected by the conservation of momentum in the extra-dimensions (Servant & Tait, 2003; Agashe & Servant, 2004). The most promising dark matter candidate is the Kaluza-Klein photon $B^{(1)}$, see Hooper & Profumo (2007) for a review.

Simple models Supersymmetry and extra-dimensions are consistent frameworks that are primarily motivated as solutions to problems other than dark matter, like the hierarchy problem, but provide a dark matter candidate as a bonus. The absence of discovery of a dark matter particle (or any new particle) at LEP and LHC renders these framework more and more contrived. Supersymmetry, for instance, is now less and less favoured as a solution to the hierarchy problem, due to the lack of "naturalness" ('t Hooft, 1980) of the supersymmetric models that have not been excluded yet [although the measure of naturalness and its meaning are still under debate (Anderson & Castaño, 1995; Wells, 2018)]. In light of this situation, physicists have started paying attention to simpler models aiming only at providing a dark matter candidate. To study simple models while still being relevant to more sophisticated theories, one can work on simplified dark matter models (Abdallah et al., 2015). The dark matter is then assumed to be a fermion or a scalar interacting with Standard-Model-particles through a single mediator (scalar or vector). This considerably simplifies the phenomenology and allows one to study a wide variety of constraints, from theoretical consistency (Kahlhoefer et al., 2016) to experimental searches. Another guiding principle that can be used to build a dark matter model is minimality, *i.e.* the requirement that dark matter be explained with a minimum number of extra particles added to the Standard Model. This leads to the minimal dark matter model (Chardonnet et al., 1993; Cirelli et al., 2006, 2007, 2015) where dark matter is part of a $SU(2)$ multiplet and has a mass at the TeV scale.

1.3.2.3 Axions and axion-like particles

QCD axion The axion is a light boson first introduced to solve the CP problem of strong interactions (Peccei & Quinn, 1977; Weinberg, 1978; Wilczek, 1978). The original "Standard Model" axion was very quickly excluded but alternative models of a so-called "invisible" axion were built. Two main axion models are currently considered: the KSVZ axion (Kim, 1979; Shifman et al., 1980) and the DFSZ axion (Zhitnitsky, 1980; Dine et al., 1981), which both rely on new physics above some very high energy scale. It was quickly realised that axions are dark matter candidates, which can be produced non-thermally in the early Universe (Preskill et al.,

1983). The QCD axion has a mass in the range $10^{-12}\,\mathrm{eV} \leqslant m_\mathrm{a} \leqslant 10^{-3}\,\mathrm{eV}$ (Abbott & Sikivie, 1983) and very feeble interactions with ordinary matter. Its mechanism of production makes it extremely cold, hence it behaves like any other cold dark matter candidate on cosmological scales. For a review on the cosmology of axions, we refer to Marsh (2016). The QCD axion as dark matter is being looked for in resonant microwave cavities (Sikivie, 1983) such as the one used in the ADMX experiment.

Axion-like-particles One can study light bosons without trying to solve the strong-CP problem. Such particles are referred to as axion-like particles (ALPs). These particles have an interesting phenomenology on cosmological and astrophysical scales due to their large de Broglie wavelength, see Hui et al. (2017) for a review. If ALPs have a mass of order $10^{-22}\,\mathrm{eV}$, their de Broglie wavelength is $\lambda \sim 1\,\mathrm{kpc}$ and such particles can solve the small-scale issues discussed in Sec. 1.4 (Hu et al., 2000). However, such a low mass may be in conflict with observations of the Lyman-α forest (Iršič et al., 2017; Armengaud et al., 2017).

1.3.2.4 Other candidates

There are many dark matter candidates other than WIMPs and axions. We very briefly mention some of them.

Sterile neutrinos Sterile neutrinos are right-handed neutrinos that are not charged under SU(2) and have therefore suppressed couplings to other SM particles.. They are very well motivated as explanations for such phenomena as neutrino oscillations and the matter-antimatter asymmetry. Their feeble interactions make sterile neutrinos with a mass of a few keV viable dark matter candidates. Unlike WIMPs and axions, sterile neutrinos are unstable particles but their lifetime can be longer than the age of the Universe, see *e.g.*Dodelson & Widrow (1994). Their dominant decay channel is through a photon and an active neutrino, giving rise to a very nice astrophysical signature: an X-ray line at half the sterile neutrino mass (for a decay at rest). Another major difference is that sterile neutrinos behave as warm dark matter *i.e.* their free-streaming scale is near the scale of observed dwarf galaxies. For a review on sterile neutrinos as dark matter, we refer to Boyarsky et al. (2009); Drewes et al. (2017).

Asymmetric dark matter Asymmetric dark matter is motivated by the observation that dark matter and baryons have similar cosmological abundances $\Omega_\mathrm{c} \simeq 5\,\Omega_\mathrm{b}$. Since the observed abundance of baryons is due to a baryon-antibaryon asymmetry in the early Universe, it is natural to assume a similar asymmetry in the dark sector. Therefore, asymmetric models assume that dark matter is not its own antiparticle (while this is the case in most WIMPs models). The value of the dark matter relic abundance sets its mass to a few GeV (Gu et al., 2011). There are many different models of asymmetric dark matter, all with a very rich phenomenology. For a detailed discussion of these models, we refer to Petraki & Volkas (2013).

1.4 ΛCDM on small scales

The ΛCDM model is extremely successful at describing all cosmological observations on large-scale and at any redshift currently accessible to observation. It predicts the statistical properties of galaxies and galaxy clusters starting from the initial conditions given by the CMB. On sub-galactic scales however, it is not clear yet if ΛCDM gives a good description of observations. A series of apparent mismatches between observations and ΛCDM numerical simulations have been identified. We refer to Bullock & Boylan-Kolchin (2017) for a review on these small-scale challenges.

1.4.1 Issues

Core versus cusp The absence of pressure in the dark matter fluid leads to the formation of dark matter halos with very cuspy density profiles in numerical simulations (Navarro et al., 1996; Navarro et al., 1997; Diemand et al., 2008; Springel et al., 2008). However, many observations point toward the presence of a central core in DM halos across all scales, from galaxy clusters to dwarf spheroidal galaxies, see *e.g.*, Flores & Primack (1994); Moore (1994); de Blok et al. (2001); Oh et al. (2011). This difference between CDM numerical simulations and observations is called the core-cusp problem and it has been a source of much debate ever since its identification. It is not clear that observations unambiguously imply the existence of dark matter cores. The only way to infer the shape of the dark matter profile at the centres of galaxies is to study the dynamics of luminous matter. However, the central gravitational potential of Milky-Way-like galaxies is dominated by baryons hence it is difficult to make robust statements about the dark matter distribution at the centres of galaxies. An alternative is to study dark-matter-dominated systems such as dwarf galaxies, however these systems contain few stars and analyses are limited by statistics. The core-cusp problem is actually divided into two different problems: there is an apparent discrepancy between the density slopes found in simulations and the slopes inferred from observations, but there is also an excess of dark matter mass at the centres of galaxies *i.e.* a problem of normalisation (Bullock & Boylan-Kolchin, 2017). Another related issue is the so-called "diversity problem", the fact that galaxies with the same halo mass can have widely different rotation curves (Oman et al., 2015).

Missing satellites Another issue concerns the number count of satellite galaxies in the Milky Way. While we observe a handful of galaxies orbiting the Milky Way (Drlica-Wagner et al., 2015), cold dark matter numerical simulations predict thousands of objects with similar mass (Moore et al., 1999). However, dozens of dwarfs are now discovered every year thanks to new surveys and the discrepancy is getting smaller and smaller.

Too big to fail A third issue, related to the missing satellites problem, is the "too big to fail" problem (Boylan-Kolchin et al., 2011, 2012). Not only does our Galaxy seem to be missing satellites, it seems to be missing the most massive ones. Another way of stating the problem is that the observed satellites are not as massive as we expect them to be on the basis of cold dark matter simulations. A mismatch appears when comparing the rotation curves of dwarfs to the rotation curves of the most massive satellites in simulations, the former being generically lower than the latter. Note that this issue is not restricted to satellite galaxies, as it is also observed in field dwarfs.

1.4.2 Possible solutions

The small-scale issues have been identified for a long time now (nearly twenty years for the cusp-core and missing satellites problems) but there is still no consensus on the solution. Two different approaches are currently explored.

Baryonic physics A possible solution to the small-scale problem might be baryonic feedback, which should anyway be at play whatever the dark matter scenario. The idea is that a strong episode of star formation can lead to supernovae-driven winds that expel baryonic matter from potential wells at the centres of galaxies. This decreases the depth of the potential wells and removes dark matter from the centre (Navarro et al., 1996). Also, ultraviolet pressure in the early Universe prevents baryons from cooling in the smallest objects. It has be shown on the basis of numerical simulations that this process is efficient at depleting the central regions of CDM halos and turning their initial cusp into cores (Mashchenko et al., 2008; Pontzen & Governato, 2012; Mollitor et al., 2015; Oñorbe et al., 2015; Read et al., 2016). It is also efficient at removing

baryons and dark matter out of satellites which helps solving the too big to fail and missing satellites problems. However, one has to keep in mind that baryonic physics is not fully under control in cosmological simulations. Since the numerical resolution is far too limited to resolve the scales relevant to star formation, baryonic feedback is modelled using simplified recipes. There is no consensus yet on which recipe is the most accurate to describe baryonic processes, hence the resolution of the small-scale problems through baryonic physics is still a matter of debate (Renaud et al., 2013; Rosdahl et al., 2017). However, this solution is rather elegant since it only involves interactions that are known to exist and does not require an extension of the unknown dark matter sector. Moreover, the state of the art has been very successful in reproducing most of the observed properties of galaxies and galaxy clusters (Pillepich et al., 2018; Springel et al., 2018).

Departure from ΛCDM One can assume these problems point toward a failure of the CDM paradigm on small scales, and require a revision of the properties of the dark matter sector. A way to address these issues from the dark matter sector is to modify the behaviour of dark matter on small scales, to keep the virtue of CDM on large scales while suppressing some power on small scales. Two mechanisms are used to suppress formation below a given scale: either dark matter particles have a free-streaming length much larger than CDM candidates, or a pressure is introduced to offset gravity.

A way of suppressing power on small scales is to depart from the "cold" regime and assume the dark matter particle is close to relativistic when structures start to form efficiently. This is the so-called Warm Dark Matter (WDM) scenario. We refer to Colombi et al. (1996); Bode et al. (2001); Schneider (2015); Vogelsberger et al. (2016) for numerical studies and *e.g.*, Bond et al. (1982); Peebles (1982a); Dodelson & Widrow (1994) for analytical studies and models. If produced thermally, the dark matter particle must have a mass in the keV range to lead to a suppression scale right below the scale of dwarf galaxies. WDM has become popular with the advent of a scenario where a sterile neutrino is a viable dark matter candidate, allowing to incorporate several issues (*e.g.*, neutrino masses, leptogenesis, etc.) in the same framework. Reviews on particle-physics models can be found in Boyarsky et al. (2009) and in Drewes et al. (2017). The WDM scenario is constrained by cosmological observations of the Lyman-α forest and the CMB anisotropies (Viel et al., 2005). The observed number of DM dominated satellite of the Milky Way also leads to a lower bound on the WDM mass (Polisensky & Ricotti, 2011; Lovell et al., 2014). In fact, it has been shown that the WDM scenario cannot solve both the core-cusp and missing satellites problem (Maccio et al., 2012). All these constraints push the WDM scenario to colder and colder regions of the parameter space, making it less and less appealing solution per se of the small-scale problems (while still an appealing realization of particle physics scenarios in the form of sterile neutrinos, bearing in mind that these small-scale issues could be solved by baryonic physics).

Among the second class of solutions, we find self-interacting dark matter (SIDM) as originally proposed in the context of dark matter by Carlson et al. (1992) and put forward by Spergel & Steinhardt (2000) as a solution to the small-scale issues. We refer to Tulin & Yu (2018) for a review on the subject. In SIDM, dark matter particles are assumed to have a sizeable self-scattering cross-section. This naturally induces a pressure in high-density regions and turns cusps into cores. The lower concentration of SIDM halos with respect to CDM halos also helps to address the too big to fail issue as well as the missing satellite problem (subhalos are more sensitive to tidal stripping and subject to evaporation). On large scales, SIDM behaves just like cold dark matter (van den Aarssen et al., 2012). Observations of the Bullet Cluster (Markevitch et al., 2004) give an upper limit of $\sigma/m \lesssim 1\,\mathrm{cm}^2/\mathrm{g}$ on the scattering cross-section divided by the dark matter mass. Another interesting scenario is fuzzy dark matter (Sin, 1994; Hu et al., 2000; Arbey et al., 2001). In this case, the DM particle is a boson with an extremely small mass $m \sim 10^{-22}\,\mathrm{eV}$. Such a small mass implies a de Broglie wavelength $\lambda \sim 1\,\mathrm{kpc}$ which has observable

consequences on the small-scale structuring of dark matter, see Marsh (2016); Hui et al. (2017) for reviews. A lower bound on the fuzzy dark matter mass can be set using Lyman-α data (Iršič et al., 2017; Armengaud et al., 2017) which make this scenario a very contrived solution to the small-scale issues.

1.5 Experimental searches for particle dark matter

In this section, we review searches for particle dark matter, with an emphasis on WIMP searches.

1.5.1 Particle colliders

Dark matter can be searched for in particle colliders such as the Large Hadron Collider (LHC), see *e.g.*, Fairbairn et al. (2007). The overwhelming amount of data recorded by the ATLAS (Aad et al., 2008) and CMS (Chatrchyan et al., 2008) experiments at CERN makes it a necessity to look into specific directions in order to obtain any valuable information. Three main approaches are currently used to look for dark matter at the LHC: effective field theories, simplified models and complete theories (Abercrombie et al., 2015). Since dark matter is stable and very weakly interacting, it escapes the detector if produced. The creation of a dark matter particle in a collision manifests itself through missing transverse energy $\not{E}_{\mathrm{T}}$ and missing transverse momentum $\not{p}_{\mathrm{T}}$. Since the LHC is a proton collider, the typical event being looked for is $pp \to \chi\chi X$, where χ is the dark matter particle and X is a Standard Model contribution (jets from quarks or gluons, electroweak bosons, Higgs, etc.). LHC constraints on dark matter models can be found in Goodman et al. (2010, 2011); Askew et al. (2014). It is standard to translate constraints from the LHC into direct-detection-like constraints in order to compare the two approaches, generally in terms of effective operators (Fitzpatrick et al., 2013). Collider constraints exhibits more model-dependence than direct searches in general, which induces the need for specific analyses. Other older colliders such as the Large Electron-Positron (LEP) collider can also be used to put complementary constraints on dark matter (Fox et al., 2011). For an overview of collider searches, we refer to Kahlhoefer (2017); Penning (2018).

1.5.2 Direct searches

1.5.2.1 WIMPs

Direct dark matter searches are based on the assumption that the dark matter particle can interact with atomic nuclei. Direct detection experiments are designed to observe the nuclear recoil caused by interactions with dark matter particles from the Galactic halo. This idea was first proposed for the detection of neutrinos (Drukier & Stodolsky, 1984) then applied to dark matter (Goodman & Witten, 1985). It was then extended by taking into account the dark matter distribution in the Galaxy as well as the rotation of the Earth around the Sun which lead to the very distinct feature of annual modulation (Drukier et al., 1986). A review on annual modulation can be found in Freese et al. (2013). General reviews on direct searches can be found in Jungman et al. (1996); Lewin & Smith (1996); Cerdeno & Green (2010); Baudis (2012). There are a number of direct detection experiments currently probing the WIMP parameter space. Since no recoil signal unambiguously attributed to dark matter has been detected yet (at the notable exception of the modulated signal observed in the DAMA experiment, see Bernabei et al. (2018)), experimental efforts are summarized through upper bounds on the WIMP-nucleon scattering cross-section. A compilation of exclusion limits is shown in Fig. 1.6.

The main ingredient necessary to make predictions for direct searches is the expected event rate

$$R = \frac{n_\odot}{m_{\mathrm{A}}} \langle v' \sigma(v') \rangle \ , \tag{1.6}$$

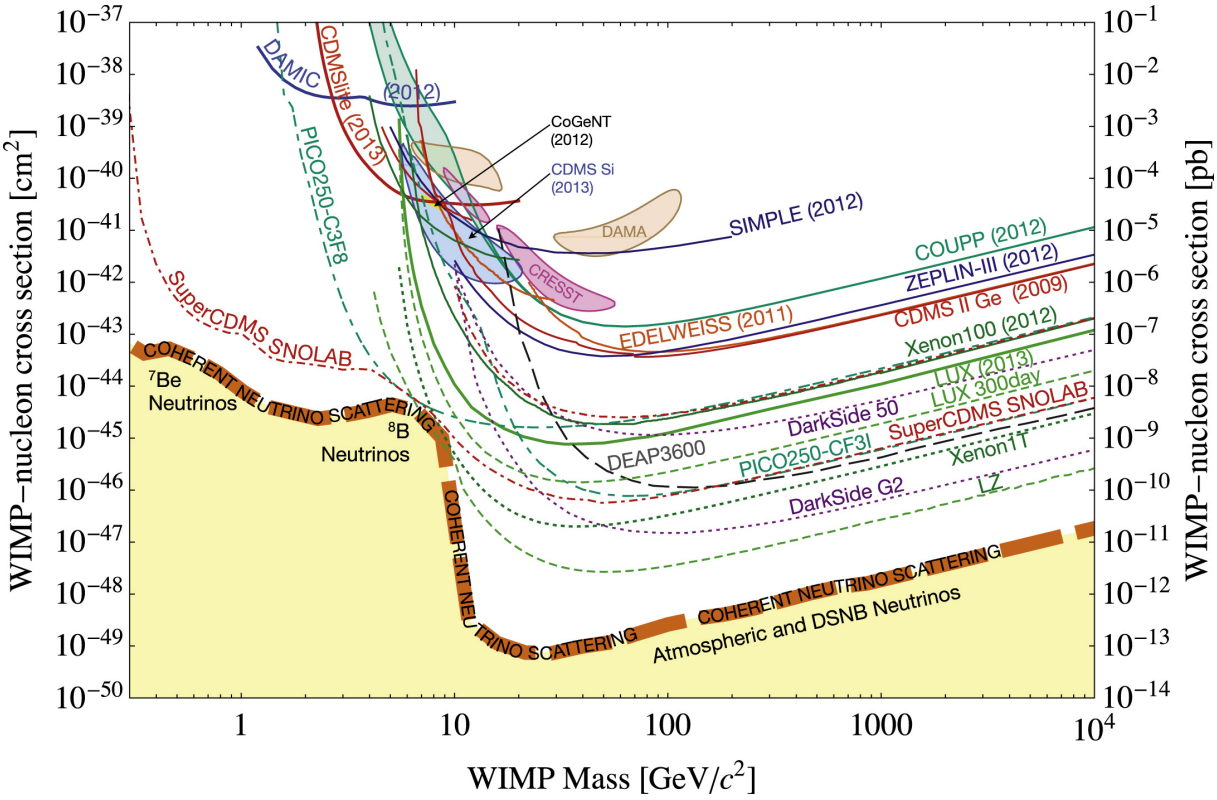

Figure 1.6 – Compilation of direct detection limits taken from various experiments. Also shown is the expected background from coherent neutrino scattering. This figure was taken from Cooley (2014).

where $n_\odot$ is the local dark matter number density, m_A is the mass of the atomic nucleus used in the experiment, σ is the WIMP-nucleus scattering cross-section and the average is over the local WIMP velocity distribution. The event rate can also be written

$$R = \frac{n_\odot}{m_\mathrm{A}} \left\langle v' \int_{E_\mathrm{T}}^{E_\mathrm{max}(v')} \mathrm{d}E_\mathrm{r} \, \frac{\mathrm{d}\sigma}{\mathrm{d}E_\mathrm{r}}(E_\mathrm{r}, v') \right\rangle , \tag{1.7}$$

where the integral is performed over the recoil energy E_r. The lower bound on the integral is the threshold energy E_T of the detector. The upper bound is the maximal recoil energy, which depends on the WIMP velocity. This expression can be transformed into

$$R = \int_{E_\mathrm{T}}^{\infty} \mathrm{d}E_\mathrm{r} \, \frac{\mathrm{d}R}{\mathrm{d}E_\mathrm{r}}(E_\mathrm{r}) , \tag{1.8}$$

with the differential event rate

$$\frac{\mathrm{d}R}{\mathrm{d}E_\mathrm{r}}(E_\mathrm{r}) = \frac{n_\odot}{m_\mathrm{A}} \int_{v' > v_\mathrm{min}(E_\mathrm{r})} \mathrm{d}^3\vec{v'} \, v' \, f_{\vec{v'}}(\vec{v'}) \, \frac{\mathrm{d}\sigma}{\mathrm{d}E_\mathrm{r}}(E_\mathrm{r}, v') , \tag{1.9}$$

where $v_\mathrm{min}(E_\mathrm{r})$ is the minimal speed needed for a WIMP to create a recoil E_r. The function $f_{\vec{v'}}$ is the WIMP velocity distribution in the rest frame of the Earth. The expression in Eq. (1.9) is very intricate as it mixes elements from particle physics (masses and cross-section) with elements from astrophysics (number density and velocity distribution). For elastic scattering, the expression can be simplified by writing the differential cross-section as

$$\frac{\mathrm{d}\sigma}{\mathrm{d}E_\mathrm{r}}(E_\mathrm{r}, v) = \frac{\sigma_0 m_\mathrm{A}}{2\,\mu^2 v^2} \, F^2(E_\mathrm{r}) , \tag{1.10}$$

where σ_0 is a standard cross-section at zero momentum transfer, μ is the reduced dark matter-nucleus mass

$$\mu \equiv \frac{m\, m_{\rm A}}{m + m_{\rm A}}\,, \tag{1.11}$$

and F is a form factor associated to the nucleus. More precisely, the cross-section can be divided into a spin-independent (relevant for scalar interactions) and a spin-dependent (relevant for axial-vector interactions) part

$$\frac{{\rm d}\sigma}{{\rm d}E_{\rm r}}(E_{\rm r}, v) = \frac{m_{\rm A}}{2\,\mu^2 v^2}\left[\sigma_{\rm SI}\, F_{\rm SI}^2(E_{\rm r}) + \sigma_{\rm SD}\, F_{\rm SD}^2(E_{\rm r})\right]\,. \tag{1.12}$$

These two possibilities are usually considered separately. Note that a more general expression can be written in the language of effective field theories (Fitzpatrick et al., 2013). For a given channel channel (spin-independent or spin-dependent), the differential event rate can be written as

$$\frac{{\rm d}R}{{\rm d}E_{\rm r}}(E_{\rm r}) = \frac{\rho_\odot \sigma_0}{2\, m_\chi \mu^2}\, F^2(E_{\rm r})\, \eta(E_{\rm r})\,, \tag{1.13}$$

with $\sigma_0 = \sigma_{\rm SI}$ or $\sigma_0 = \sigma_{\rm SD}$ depending on the channel, and

$$\eta(E_{\rm r}) \equiv \int_{v' > v_{\rm min}(E_{\rm r})} {\rm d}^3\vec{v'}\, \frac{1}{v'}\, f_{\vec{v'}}(\vec{v'})\,. \tag{1.14}$$

This shows that the particle physics and astrophysics contributions can be completely factorized and therefore treated independently. This is not true if the mediator has a mass $m \ll q$, where q is the exchanged momentum, see *e.g.*, Schwetz & Zupan (2011).

1.5.2.2 Axions

Axions are also being looked for through direct detection techniques. Most experiments looking directly for axions rely on the Primakoff effect (Primakoff, 1951) which predicts a conversion of axions into photons in a magnetic field. For instance, the Axion Dark Matter Experiment (ADMX) (Du et al., 2018) uses a microwave cavity placed in strong magnets to probe the axion parameter space. For a review on microwave cavity searches, we refer to Shokair et al. (2014). For a general review on the experimental searches for axions, we refer to Graham et al. (2015).

1.5.3 Indirect searches

Indirect searches rely on the assumption that dark matter can annihilate or decay into Standard Model particles. One could also include other classes of signatures in this category, for instance: gravitational signals (dynamics of stellar systems, lensing, or waves), impact on stellar evolution, etc. In this section, we will focus on the indirect searches for WIMPs. Particles originating for WIMP annihilation or decay, after having propagated through the Galactic or extra-galactic medium, could be detected in the Solar System. The main difficulty of these types of searches is to disentangle a potential dark matter signature from an "ordinary" astrophysical contribution. For reviews on the subject, we refer to Profumo & Ullio (2010); Lavalle & Salati (2012); Cirelli (2015).

1.5.3.1 Gamma rays

Indirect detection of annihilating dark matter through gamma rays has been investigated for a long time (Gunn et al., 1978; Stecker, 1978; Silk & Bloemen, 1987; Bergstrom & Snellman, 1988; Bouquet et al., 1989; Jungman & Kamionkowski, 1995; Bergstrom et al., 1998). We refer

to Bringmann & Weniger (2012) for a review on this topic. There are several reasons why gamma rays are extremely appealing for dark matter searches. First of all, photons propagate in straight lines, which is a considerable advantage with respect to charged cosmic rays. Second, photons are a generically expected product of dark matter annihilation into Standard Model particles, irrespective of the annihilation final state (leptons, quarks, gauge bosons,etc).[2] The γ-ray emission from these processes is called prompt emission and it has the very nice feature of directly tracing the morphology of the underlying dark matter density profile in addition to providing information on the WIMP mass and its self-annihilation branching ratio. Hence an unambiguous detection of dark matter annihilation through gamma rays would allow one to reconstruct the dark matter distribution in our Galaxy (and possibly in others galaxies as well). Finally, gamma-ray emission from dark matter annihilation may present spectral features that could enable one to distinguish it from conventional astrophysical sources. In particular, the detection of a gamma-ray line in the GeV-TeV range would be extremely hard to explain in terms of known astrophysical phenomena (atomic lines are X-rays and nuclear lines are in the MeV range).

A number of experiments are currently probing gamma-rays in a range relevant for WIMP searches, including satellite-based experiments like *Fermi*-LAT (Atwood et al., 2009) and ground-based experiments like the High Energy Stereoscopic System (H.E.S.S.), the Major Atmospheric Gamma-ray Imaging Cherenkov (MAGIC) and the Very Energetic Radiation Imaging Telescope Array System (VERITAS). For a review of the history and techniques of ground-based telescopes, we refer to Hillas (2013).

Privileged targets for dark matter annihilation are regions of high density, and ideally of low signal-to-noise ratio. These include the Galactic centre (see the discussion below) and satellites like dwarf spheroidal galaxies (Ackermann et al., 2015; Albert et al., 2017). Dark matter contributions can also be searched for in the diffuse emission (Ackermann et al., 2012b) which leads to very competitive constraints, see Chang et al. (2018) for a recent study. Finally, extragalactic contributions are also expected (Ullio et al., 2002; Serpico et al., 2012; Sefusatti et al., 2014; Hütten et al., 2018). While we have only discussed WIMP annihilation, all the searches actually extend to any dark matter candidate which can annihilate into gamma rays. These searches also apply to decaying dark matter (Cirelli et al., 2012).

GeV gamma-ray emission at the Galactic centre Let us briefly discuss a gamma-ray observation which has been put forward as a potential signature of annihilating dark matter. A number of studies have found that the gamma-ray emission at the centre of the Galaxy as measured with *Fermi* exceeds expectations from supposedly known astrophysical backgrounds (Goodenough & Hooper, 2009; Vitale et al., 2009; Hooper & Goodenough, 2011; Hooper & Linden, 2011; Abazajian & Kaplinghat, 2012; Macias & Gordon, 2014; Abazajian et al., 2014; Calore et al., 2015; Daylan et al., 2016; Calore et al., 2015; Ajello et al., 2016). The Galactic centre has always been a prime target because the dark matter density is expected to be very high there (Silk & Bloemen, 1987; Stecker, 1988; Bouquet et al., 1989; Berezinsky et al., 1992; Berezinsky et al., 1994; Bergstrom et al., 1998). The observation of a gamma-ray emission, which, after subtraction of a background strongly extrapolated from observations in the disc (where cosmic-ray models are constrained), points to a morphology that resembles that expected from dark matter annihilation (Daylan et al., 2016) and the fact that it can be explained by a WIMP with a thermal cross-section has raised a lot of excitement in the community. It has been realized however that less exotic interpretations of the gamma-ray excess are possible, such as injection of cosmic rays (Carlson & Profumo, 2014; Petrović et al., 2014; Gaggero et al., 2015) or a population of unresolved millisecond pulsars (Abazajian, 2011; Abazajian et al., 2014; Mirabal, 2013). Evidence for a large contribution from unresolved point-sources (Bartels et al., 2016; Lee et al., 2016) seems to disfavour the dark matter interpretation (Clark et al., 2016) and favour

[2] A notable exception is the annihilation into neutrino pairs.

instead the pulsar scenario, but the debate remains open. However, it should not come as a surprise that unexpected emissions are found in regions where the astrophysical background is very difficult to predict. The Galactic center is indeed a region expected to host a plethora of high-energy phenomena and sources (some of them yet to be discovered), which will take a lot of time to be fully understood. In such difficult regions, clean signals like gamma-ray lines are likely to be the most reliable smoking gun of dark matter annihilation or decay (a previous tentative identification in Weniger (2012) looked promising from this perspective, even though it turned out to be a statistical fluke).

1.5.3.2 Neutrinos

Neutrinos share with photons the appealing property of propagating in straight lines through the Galactic and intergalactic medium. This makes them an interesting probe of annihilating and decaying dark matter. Their very feeble interaction with matter also makes them very difficult to detect. Experiments rely on the Čerenkov light emitted as neutrinos pass though a medium to infer there momentum and trajectory. Examples of such experiments are IceCube (Ahrens et al., 2003), Super-Kamiokande (Fukuda et al., 2003) and ANTARES (Aslanides et al., 1999). Apart from the targets also interesting for gamma-ray searches such as the dark matter halo and the Galactic centre, neutrino telescopes also look for WIMP annihilation inside the Sun and the Earth. Indeed, WIMPs can in principle be gravitationally captured by the Sun (Press & Spergel, 1985; Silk et al., 1985; Hagelin et al., 1986; Srednicki et al., 1987; Bouquet et al., 1987) or the Earth (Krauss et al., 1986; Sivertsson & Edsjö, 2012) and subsequently annihilate at their core.

1.5.3.3 Cosmic rays

The last main detection channel often considered is antimatter charged cosmic rays. A major difference between cosmic rays and gamma rays or neutrinos is their propagation in the Galaxy. While photons and neutrinos propagate in straight lines, charged particles are scattered off the inhomogeneities of the interstellar magnetic field. Therefore, their trajectory is a random walk and the detection of a charged particle on Earth does not allow one to infer their spatial origin in general. We leave the details of the propagation of cosmic rays aside for now, it will be reviewed in Chap. 4. Dark matter being neutral, its annihilation should create an equal number of particles and antiparticles. Since the overwhelming majority of cosmic rays received on Earth are particles owing to the matter-antimatter asymmetry of the universe, dark matter contributions are being looked for in antiparticle channels, for which the background is expected to be not only much smaller, but also predictable.

Antiprotons Antiprotons are particularly interesting as a probe of dark matter (Silk & Srednicki, 1984; Stecker et al., 1985; Hagelin & Kane, 1986; Jungman & Kamionkowski, 1994; Bergström et al., 1999). Antiprotons are appealing because there are no known sources of primary antiprotons (in contrast to positrons). Their propagation is a bit simpler than that of positrons because energy losses are negligible in the GeV-TeV range, which makes them having a larger diffusion horizon with respect to positrons with the same energy (Maurin et al., 2002; Donato et al., 2004; Barrau et al., 2005; Bringmann & Salati, 2007; Lavalle et al., 2008; Lavalle, 2010; Cerdeño et al., 2012; Boudaud et al., 2015). This makes them a good probe of the dark matter halo and its substructures, as we will see in Chap. 4. Recently, features above idealized background models have been reported in the latest antiprotons flux measurements performed by the AMS-02 collaboration (Aguilar et al., 2016). It has been suggested that this excess could be due to dark matter annihilation (Cuoco et al., 2017; Cui et al., 2017, 2018) though an improvement of background models significantly reduces the excess (Giesen et al., 2015; Winkler, 2017; Reinert & Winkler, 2018).

Positrons Another interesting channel is cosmic-ray positrons. Unlike antiprotons and other nuclei, the propagation of positrons at high energies is dominated by energy losses. This makes 0.1-1 TeV positrons a very local probe, complementary to antiprotons. An excess in the positron fraction $e^+/(e^+ + e^-)$, first hinted by Barwick et al. (1997), has been reported by the PAMELA collaboration (Aguilar et al., 2007; Adriani et al., 2009, 2013) and then confirmed by the *Fermi* (Ackermann et al., 2012a) and AMS-02 collaborations (Aguilar et al., 2013). While an interpretation of the excess in terms of dark matter is possible in principle (Bergstrom et al., 2008), it requires a clumpiness enhancement which is very unlikely in the ΛCDM model (Lavalle et al., 2007; Lavalle et al., 2008; Pieri et al., 2011). An alternative explanation would be a contribution from nearby pulsars (Hooper et al., 2009; Delahaye et al., 2010; Profumo, 2011; Linden & Profumo, 2013) which have been known for a long time to be able to efficiently produce electron-positron pairs and accelerate them to GeV-TeV energies in the surrounding nebulae (Rees & Gunn, 1974; Gaensler & Slane, 2006). It has been claimed, on the basis of gamma-ray observations of nearby pulsars by the HAWC collaboration, that these objects cannot account for the observed excess (Abeysekara et al., 2017) though this conclusion has been contested (Hooper & Linden, 2017). Questions regarding the origin of the positron excess are still very much open today, though it is likely that these positrons originate from conventional astrophysical processes.

Cosmic-ray positrons actually turn out to be an excellent probe of MeV WIMPs thanks to the satellite experiment Voyager I. The latter, launched in 1977, has crossed the heliopause in the early 2010's (today at a distance of 140 AU from the Earth) and makes it possible to detect cosmic rays which are no longer deflected by solar modulation. Voyager I can detect electrons and positrons in the 10-50 MeV range, the flux of which provides a very strong constraint on MeV DM annihilation (slightly below the CMB constraints for s-wave annihilation, but much more stringent for p-wave annihilation), see Boudaud et al. (2017) and Boudaud et al., 2018 (in preparation).

1.5.3.4 Cosmological probes

While all the probes we have discussed so far are based on the detection of dark matter annihilation products today, it is actually possible to use cosmology to probe annihilation in the past. In particular, the CMB is a cosmological probe that is very sensitive to energy injections, which can affect temperature anisotropies, distort the CMB spectrum and change its polarization. This allows one to constrain annihilation and decay at the time of recombination but also during the dark ages (Salati, 1985; Hu & Silk, 1993; Chen & Kamionkowski, 2004; Padmanabhan & Finkbeiner, 2005; Slatyer et al., 2009; Slatyer, 2016a,b; Slatyer & Wu, 2017; Poulin et al., 2016). Complementary to CMB constraints, BBN can also be used to place constraints on earlier decay or annihilation (Jedamzik, 2004, 2006). Finally, the absorption of 21 cm CMB photons by hydrogen atoms right before the formation of the first stars can be used as a probe of dark matter at redshifts unexplored so far (Loeb & Zaldarriaga, 2004; Lopez-Honorez et al., 2016).

Chapter 2

Thermal history of weakly interacting massive particles

This chapter presents a class of particle dark matter candidates known as WIMPs, which stands for Weakly Interacting Massive Particles. WIMPs are among the most studied and well-motivated explanations of the missing mass problem, and they offer a very rich phenomenology which can be tested through collider experiments as well as direct and indirect dark matter searches. In Sec. 2.1, we introduce the Friedmann-Lemaitre-Robertson-Walker (FLRW) cosmological model which is the basis of the current Standard Model of Cosmology, and discuss the laws of thermodynamics in an expanding Universe. In Sec. 2.2, we introduce a simplified WIMP model which is used as an illustration of the processes experienced by WIMPs in general. Sec. 2.3 focuses on the process of chemical decoupling which fixes the abundance of dark matter particles in the Universe, while Sec. 2.4 is centred on kinetic decoupling and the birth of the first dark matter structures.

2.1 Thermodynamics in an expanding universe

2.1.1 Friedmann-Lemaitre-Robertson-Walker cosmological model

The Standard Model of Cosmology, also called Λ-Cold Dark Matter (ΛCDM in short), belongs to the class of Friedmann-Lemaitre-Robertson-Walker (FLRW) models named after Friedmann (1922); Lemaître (1927); Robertson (1935); Walker (1935).[1] These models rest on the *Cosmological Principle* which states that space-time is statistically homogeneous and isotropic, which is experimentally verified on the largest observable scales by CMB experiments and large-scale structure surveys. The most general homogeneous and isotropic metric one can write is the FLRW metric where the space-time interval reads

$$\begin{aligned} \mathrm{d}s^2 &= g_{\mu\nu}\,\mathrm{d}X^\mu\,\mathrm{d}X^\nu \\ &= c^2\mathrm{d}t^2 - a^2(t)\gamma_{ij}\,\mathrm{d}x^i\,\mathrm{d}x^j \\ &= c^2\mathrm{d}t^2 - a^2(t)\left(\frac{\mathrm{d}r^2}{1-K\,r^2} + r^2\mathrm{d}\theta^2 + r^2\sin^2(\theta)\mathrm{d}\phi^2\right), \end{aligned} \tag{2.1}$$

where $g_{\mu\nu}$ is the metric tensor, γ_{ij} is the spatial metric, a is the dimensionless *scale factor* and K is the spatial curvature. The coordinates X^μ are called *comoving coordinates*. Observations of the CMB are compatible with a flat Universe $K = 0$, in which case the interval is simply

$$\mathrm{d}s^2 = c^2\mathrm{d}t^2 - a^2(t)\,\mathrm{d}\vec{x}^2\,. \tag{2.2}$$

[1] The first homogeneous and isotropic cosmological models were considered by Friedmann, then independently by Lemaitre. Later, Robertson and Walker found the most general form of a homogeneous and isotropic metric.

It is standard to introduce the *physical coordinates* Y^μ which follow the space-time dynamics and are related to the comoving coordinates through $Y^0 = X^0$ and $\vec{y} = a(t)\,\vec{x}$. The metric measured by a physical observer is simply the Minkowski metric

$$\begin{aligned} \mathrm{d}s^2 &= c^2\mathrm{d}t^2 - \mathrm{d}\vec{y}^2 \\ &= \eta_{\mu\nu}\,\mathrm{d}Y^\mu\,\mathrm{d}Y^\nu\,. \end{aligned} \tag{2.3}$$

The energy-momentum tensor $T^{\mu\nu}$ is severely constrained by the symmetries of the metric tensor $g_{\mu\nu}$. It can be shown, see *e.g.* Weinberg (1972), that the most general energy-momentum tensor compatible with the cosmological principle is

$$T_{\mu\nu} = \left(\rho + \frac{p}{c^2}\right) U_\mu U_\nu - p\, g_{\mu\nu}\,, \tag{2.4}$$

where U is a 4-velocity. This is the energy-momentum tensor of an ideal fluid with energy density $\rho(t)$ and pressure $p(t)$. This is also the energy-momentum tensor of a collection of ideal fluids such that

$$\begin{aligned} \rho &= \sum \rho_i \\ p &= \sum p_i\,. \end{aligned} \tag{2.5}$$

The space-time dynamics is related to the matter content through Einstein's equations

$$G_{\mu\nu} + \Lambda g_{\mu\nu} = \frac{8\pi G_\mathrm{N}}{3}\,T_{\mu\nu}\,, \tag{2.6}$$

where $G_{\mu\nu}$ is the Einstein tensor and Λ is the cosmological constant. The $\binom{\mu=0}{\nu=0}$ and $\binom{\mu=i}{\nu=i}$ components lead to

$$\left(\frac{\dot{a}}{a}\right)^2 = \frac{8\pi G_\mathrm{N}}{3}\,\rho + \frac{\Lambda c^2}{3} - \frac{K\,c^2}{a^2} \tag{2.7}$$

$$\frac{\ddot{a}}{a} = -\frac{4\pi G_\mathrm{N}}{3}\left(\rho + 3\,\frac{p}{c^2}\right) + \frac{\Lambda c^2}{3}\,, \tag{2.8}$$

which are called the *Friedmann equations*. The *Hubble parameter* is defined as $H \equiv \dot{a}/a$ and its value today $H_0 \equiv H(t_0)$ is the Hubble constant. It is conventional to fix the value of the scale factor today $a(t_0) = 1$. Another set of useful equations is given by the covariant conservation of $T^{\mu\nu}$:

$$\nabla_\mu T^{\mu\nu} = 0\,, \tag{2.9}$$

which leads to

$$\dot{\rho} = -3H\left(\rho + \frac{p}{c^2}\right)\,. \tag{2.10}$$

This last equation actually holds separately for each ideal fluid, under the assumption these fluids are not interacting with each other.

2.1.2 Matter content and time evolution

For a given fluid, it is standard to defined its *equation of state* as

$$w(t) = \frac{p(t)}{\rho(t)c^2}\,. \tag{2.11}$$

Studies of the CMB point toward a Universe containing radiation (photons), pressureless matter (cold dark matter, and baryons after recombination) and a cosmological constant, see Ade et al. (2016). The equation of state of each of these components can be computed, see *e.g.* Weinberg (1972), and we get

$$w_{\rm rad} = \frac{1}{3} \tag{2.12}$$
$$w_{\rm mat} = 0 \tag{2.13}$$
$$w_{\Lambda} = -1\,, \tag{2.14}$$

hence all the equations of state of the known components of the Universe are time-independent in first approximation. Note that the radiation pressure is purely relativistic in origin and does not stem from interactions within the radiation fluid. The cosmological constant has its energy density defined through Eq. (2.7) which leads to $\rho_\Lambda = \Lambda c^2/(8\pi G_{\rm N})$, hence ρ_Λ is positive and the cosmological constant has a negative pressure. In General Relativity, the cosmological constant is often interpreted as a property of space-time itself rather than a fluid. It could also be interpreted as a new dark energy component with its own dynamics, which the subject of intense research in cosmology. For more details on the cosmological constant, we refer to the classic review by Weinberg (1989) and to Martin (2012). For a time-independent equation of state, Eq. (2.10) leads to

$$\rho(t) = \rho_0\, a(t)^{-3(1+w)}\,, \tag{2.15}$$

where we set $a(t_0) = 1$ for the value of the scale factor today (with t_0 the age of the Universe). Consequently, we have

$$\rho_{\rm rad}(t) = \rho_{\rm rad,0}\, a(t)^{-4} \tag{2.16}$$
$$\rho_{\rm mat}(t) = \rho_{\rm mat,0}\, a(t)^{-3} \tag{2.17}$$
$$\rho_{\Lambda}(t) = \rho_{\Lambda,0}\,, \tag{2.18}$$

From these equations, we can already identify three main epochs in an expanding universe where a goes from zero to one. The universe is initially dominated by the radiation component, hence the qualification of "hot Big Bang". What happens next depends on the relative abundance between the three species. If $\rho_\Lambda \geqslant \rho_{m,0}^4 \rho_{r,0}^{-3}$, the universe switches from a radiation-dominated epoch to an epoch dominated by the cosmological constant. Alternatively, if $\rho_\Lambda < \rho_{m,0}^4 \rho_{r,0}^{-3}$ which is effectively the case in our Universe, the radiation epoch is followed by a period of matter domination before eventually entering the cosmological constant epoch.

We would like to derive the evolution of the scale factor as a function of the cosmic time. Using the first Friedmann equation (2.7), and assuming the Universe is flat ($K = 0$) and dominated by a single component with equation of state $w > -1$, we can derive an expression for $a(t)$

$$a(t) = \left[1 - \frac{3(1+w)}{2}\sqrt{\frac{8\pi G_{\rm N}}{3}\,\rho_0}(t_0 - t)\right]^{\frac{2}{3(1+w)}}\,. \tag{2.19}$$

This solution describes an expanding Universe. Note that Eq. (2.7) has an alternative, contracting, solution which we reject on the basis of observations. If we set the origin of time through $a(t = 0) = 0$, we get the age of the universe

$$t_0 = \frac{1}{1+w}\sqrt{\frac{1}{6\pi G_{\rm N}\rho_0}}\,, \tag{2.20}$$

and a very simple expression for the scale factor

$$a(t) = \left(\frac{t}{t_0}\right)^{\frac{2}{3(1+w)}}\,. \tag{2.21}$$

We see that the FLRW models predict a power-law dilation of space in the absence of a cosmological constant. The Hubble parameter is then

$$H(t) = \frac{2}{3(1+w)t}\,. \tag{2.22}$$

From this last equality, the age of the Universe can be estimated using the value of the Hubble constant since we have $t_0 \simeq H_0^{-1}$ up to a factor of order unity. This leads to $t_0 \simeq 14.4\,\mathrm{Gyr}$, not too far from the CMB estimate of 13.8 Gyr. The previous time evolutions were derived assuming $w > -1$, it is worth doing the analysis for $w = -1$ *i.e.* when the Universe is dominated by a cosmological constant. In that case, the first Friedmann equation leads to the expanding solution

$$a(t) = \exp\left[H(t - t_0)\right]\,, \tag{2.23}$$

with $H = c\sqrt{\Lambda/3}$ the Hubble parameter which is time-independent. In this case, the Universe undergoes an exponential growth.

In cosmology, it is standard to use the *cosmological redshift* rather than the cosmic time. Let us consider a photon emitted at time t with frequency ν_{em} and observed by a comoving observer at time t_0, then we have

$$\frac{\nu_{\mathrm{em}}}{\nu_{\mathrm{obs}}} = \frac{1}{a(t)} \equiv 1 + z\,, \tag{2.24}$$

where z is the redshift. The abundance of a given species in the Universe is usually expressed as

$$\Omega_i = \frac{\rho_i}{\rho_{\mathrm{c}}}\,, \tag{2.25}$$

where ρ_{c} is the critical density, defined as the total density of a FLRW Universe without curvature ($K = 0$). According to Eq. (2.7), we have

$$\rho_{\mathrm{c}} = \frac{3\,H^2}{8\pi G_{\mathrm{N}}}\,, \tag{2.26}$$

and Eq. (2.7) can be written in the very simple form

$$1 = \Omega_K(t) + \sum_i \Omega_i(t)\,, \tag{2.27}$$

where Ω_K is the curvature density. The curvature abundance today is compatible with $\Omega_K = 0$, see Ade et al. (2016), therefore our Universe is flat and the total energy density is equal to the critical density. The Hubble parameter can be expressed as a function of the cosmic abundances and the redshift as

$$H(z) = H_0\sqrt{\Omega_{\mathrm{m},0}(1+z)^3 + \Omega_{\mathrm{r},0}(1+z)^4 + \Omega_{\Lambda,0}}\,, \tag{2.28}$$

where $\Omega_{\mathrm{m},0}$, $\Omega_{\mathrm{r},0}$ and $\Omega_{\Lambda,0}$ are today's matter, radiation and cosmological constant abundances. The values inferred from the CMB are $\Omega_{\mathrm{m},0} \simeq 0.3$ with a small baryonic fraction $\Omega_{\mathrm{bar},0} \simeq 0.05$, and $\Omega_\Lambda \simeq 0.7$. Hence the energetic content of the Universe is essentially made of CDM and Λ, with ordinary matter only contributing 5%.

The redshift dependency of each cosmic abundance is

$$\Omega_{\mathrm{m}}(z) = \Omega_{\mathrm{m},0}(1+z)^3 \left(\frac{H_0}{H(z)}\right)^2 \tag{2.29}$$

$$\Omega_{\mathrm{r}}(z) = \Omega_{\mathrm{r},0}(1+z)^4 \left(\frac{H_0}{H(z)}\right)^2 \tag{2.30}$$

$$\Omega_\Lambda(z) = \Omega_{\Lambda,0} \left(\frac{H_0}{H(z)}\right)^2\,. \tag{2.31}$$

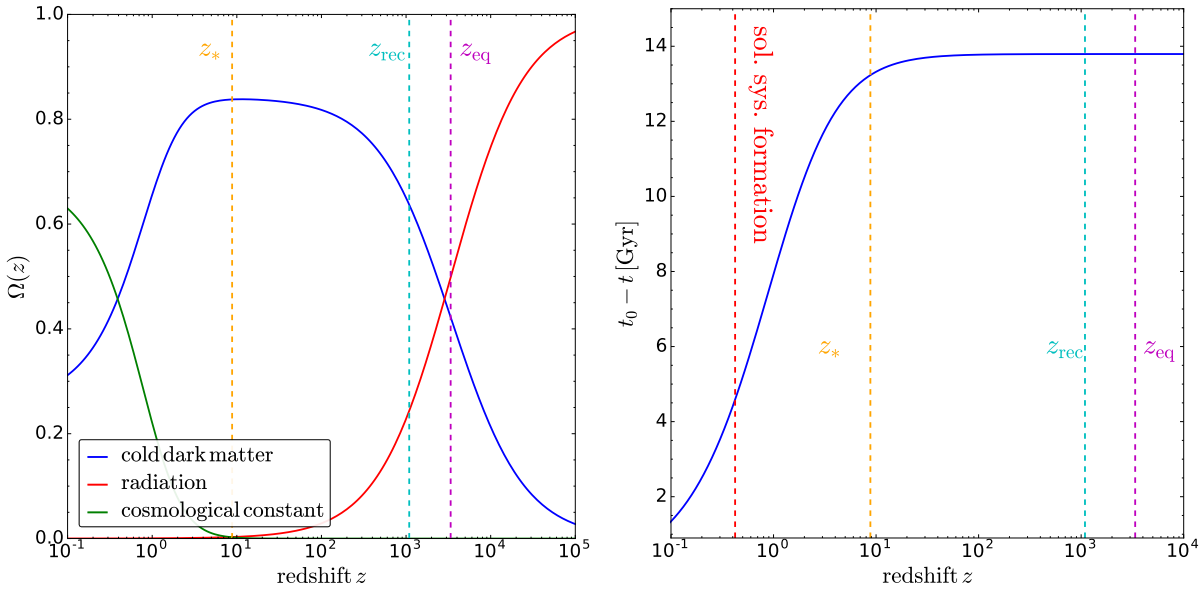

Figure 2.1 – Left panel: Redshift evolution of the cosmic abundances of cold dark matter (blue), radiation (red) and cosmological constant (green). The epochs of matter-radiation equality (dashed purple), recombination (dashed cyan) and reionization (dashed orange) are also shown. **Right panel:** cosmic time as a function of the redshift.

The evolution of the abundances as a function of z is shown on the left panel in Fig. 2.1. One notices that the radiation-to-matter ratio is $(1+z)\,\Omega_{\rm r,0}/\Omega_{\rm m,0}$ so, even though today's ratio $\Omega_{\rm r,0}/\Omega_{\rm m,0}$ is very small, there is a redshift $z_{\rm eq}$ at which this ratio is equal to one. This transition, when the Universe leaves the radiation-dominated era and enters the matter-dominated era, is called the matter-radiation equality and is a crucial epoch for structure formation, as we will see in Sec. 3.1. CMB studies point toward a value for the redshift at equality $z_{\rm eq} = 3365$. Since cosmic time is a more intuitive quantity than redshift, it is useful to relate t to z. We have

$$\begin{aligned} {\rm d}t &= \frac{{\rm d}a}{\dot{a}} \\ &= -\frac{{\rm d}z}{(1+z)H(z)}\,, \end{aligned} \tag{2.32}$$

hence

$$t_0 - t = \frac{1}{H_0}\int_0^z \frac{{\rm d}z'}{(1+z')\sqrt{\Omega_{\rm m}(1+z')^3 + \Omega_{\rm r}(1+z')^4 + \Omega_\Lambda}}\,. \tag{2.33}$$

The quantity $t_0 - t$ is shown on the right panel in Fig. 2.1. As one can see, $t_0 - t$ saturates for $z \geqslant 10$ and most of the major events of the cosmological history such as the matter-radiation equality, the formation of the first hydrogen atoms and the formation of the first stars happens at least 13 billion years ago.

2.1.3 Statistical mechanics in an expanding universe

We now focus on the radiation-dominated era and assume some species were in thermodynamic equilibrium. This must be true for photons, electrons and positrons at least, since the interaction rate of photons with charged particles was much larger than the Hubble rate. The number of particles in an elementary phase-space volume is

$$\begin{aligned} {\rm d}N &= f(\vec{x},\vec{p},t)\,{\rm d}^3\vec{x}\,{\rm d}^3\vec{p} \\ &= f(\vec{x},\vec{p},t)\,{\rm d}x^1{\rm d}x^2{\rm d}x^3{\rm d}p_1{\rm d}p_2{\rm d}p_3\,. \end{aligned} \tag{2.34}$$

We have, from the i component of the geodesic equation (B.55), $p^i \propto a^{-2}$ and the modulus of the momentum is given by $p = \sqrt{-a^2 \delta_{ij} p^i p^j}$ hence $p \propto 1/a$. The elementary phase-space volume $\mathrm{d}^3\vec{x}\,\mathrm{d}^3\vec{p}$ is invariant under the expansion. This implies that the phase-space distribution is a scalar under coordinate transformations, which means we do not have to worry about the choice of coordinates (comoving or physical for instance) when giving the expression of the phase-space distribution. The equilibrium phase-space occupation number of particles of species A is

$$f_{\rm A}^{\rm eq}(\vec{p}) = \frac{1}{\exp\left[\frac{E}{k_{\rm B}T}\right] + \epsilon}\,, \tag{2.35}$$

where $\epsilon = +1/-1$ if A is a fermion/boson (Fermi-Dirac/Bose-Einstein statistics). For simplicity, we use from now on the natural units $\hbar = c = k_{\rm B} = 1$. The number density, energy density and pressure are defined by

$$n_{\rm A}(t) = g_{\rm A} \int \frac{\mathrm{d}^3\vec{p}}{(2\pi)^3}\, f_{\rm A}(\vec{p},t) \tag{2.36}$$

$$\rho_{\rm A}(t) = g_{\rm A} \int \frac{\mathrm{d}^3\vec{p}}{(2\pi)^3}\, f_{\rm A}(\vec{p},t)\, E \tag{2.37}$$

$$p_{\rm A}(t) = g_{\rm A} \int \frac{\mathrm{d}^3\vec{p}}{(2\pi)^3}\, f_{\rm A}(\vec{p},t)\, \frac{\vec{p}.\vec{v}}{3}\,, \tag{2.38}$$

where $g_{\rm A}$ is the number of spin/helicity degrees of freedom of A. These definitions are also valid out of equilibrium. Alternatively, these quantities can be computed directly from the energy-momentum tensor $T_{\mu\nu}$. Note that in the convention we adopt henceforth, the integration is over the *physical momentum* such that $n_{\rm A}$, $\rho_{\rm A}$ and $p_{\rm A}$ decrease as the Universe expands. Equilibrium quantities can be expressed in term of the temperature T rather than time. We have the explicit expressions

$$n_{\rm A}^{\rm eq}(T) = \frac{g_{\rm A}}{2\pi^2}\, T^3 \int_0^\infty \frac{u^2}{e^{\sqrt{u^2+x^2}} + \epsilon}\,\mathrm{d}u \tag{2.39}$$

$$\rho_{\rm A}^{\rm eq}(T) = \frac{g_{\rm A}}{2\pi^2}\, T^4 \int_0^\infty \frac{u^2}{e^{\sqrt{u^2+x^2}} + \epsilon}\,\sqrt{u^2+x^2}\,\mathrm{d}u \tag{2.40}$$

$$p_{\rm A}^{\rm eq}(T) = \frac{g_{\rm A}}{2\pi^2}\, T^4 \int_0^\infty \frac{u^2}{e^{\sqrt{u^2+x^2}} + \epsilon}\,\frac{u^2}{3\sqrt{u^2+x^2}}\,\mathrm{d}u\,, \tag{2.41}$$

where

$$x \equiv m_{\rm A}/T \tag{2.42}$$

and $m_{\rm A}$ is the mass of the species under consideration. In the relativistic limit $x \ll 1$, we immediately get $\rho_{\rm A} = 3\,p_{\rm A}$ hence the equation of state of radiation is $w = 1/3$. Using the integral expression of the Riemann zeta function in Appendix A.3, the number density and energy density in the relativistic limit can be expressed as

$$n_{\rm A}^{\rm eq}(T) = \frac{\zeta(3)}{\pi^2}\, g_{\rm A}\, T^3 \left\{ \begin{array}{ll} 1 & \text{if A is a boson} \\ 3/4 & \text{if A is a fermion} \end{array} \right. \tag{2.43}$$

$$\rho_{\rm A}^{\rm eq}(T) = \frac{\pi^2}{30}\, g_{\rm A}\, T^4 \left\{ \begin{array}{ll} 1 & \text{if A is a boson} \\ 7/8 & \text{if A is a fermion} \end{array} \right. \tag{2.44}$$

$$p_{\rm A}^{\rm eq}(T) = \frac{\pi^2}{90}\, g_{\rm A}\, T^4 \left\{ \begin{array}{ll} 1 & \text{if A is a boson} \\ 7/8 & \text{if A is a fermion} \end{array} \right. \tag{2.45}$$

In the non-relativistic limit $x \gg 1$, if the energy is approximated with $E \simeq m + p^2/(2m)$ there is no distinction between bosons and fermions any more (the statistics follows the Maxwell-Boltzmann law) and we have

$$n_{\rm A}^{\rm eq}(T) = \frac{g_{\rm A}\, m_{\rm A}^3}{(2\pi\, m_{\rm A}/T)^{3/2}}\, e^{-m_{\rm A}/T} \tag{2.46}$$

$$\rho_{\rm A}^{\rm eq}(T) = m_{\rm A}\, n_{\rm A}(T) = \frac{g_{\rm A}\, m_{\rm A}^4}{(2\pi\, m_{\rm A}/T)^{3/2}}\, e^{-m_{\rm A}/T} \tag{2.47}$$

$$p_{\rm A}^{\rm eq}(T) = \rho_{\rm A}^{\rm eq}(T)/x\,. \tag{2.48}$$

The equation of state of non-relativistic matter is then $w = 1/x \simeq 0$.

Entropy Assuming adiabatic expansion and no entropy production, the entropy in a comoving volume is conserved therefore we have

$$s(T)\, a^3(t) = \text{cst} \tag{2.49}$$

where s is the entropy density. The second law of thermodynamics reads

$$\mathrm{d}(\rho a^3) = T\, \mathrm{d}(s a^3) - p\, \mathrm{d}(a^3)\,, \tag{2.50}$$

which gives the relation

$$s(T) = \frac{\rho + p}{T}\,. \tag{2.51}$$

In the relativistic limit, we can use $p = \rho/3$ and Eq. (2.44) to get

$$s_{\rm A}^{\rm eq}(T) = \frac{2\pi^2}{45}\, g_{\rm A}\, T^3 \begin{cases} 1 & \text{if A is a boson} \\ 7/8 & \text{if A is a fermion} \end{cases} \tag{2.52}$$

Therefore, the entropy density goes like T^3. Since the entropy is conserved in a comoving volume, it immediately follows that the temperature of a relativistic component goes like

$$T \propto \frac{1}{a(t)}\,, \tag{2.53}$$

i.e. the temperature decreases like the inverse of the scale factor as the Universe expands. This makes the temperature of the photon bath yet another alternative time variable along with the scale factor and the redshift. Note that the relation between the temperature and the scale factor depends on the species at equilibrium in the thermal bath.

Effective degrees of freedom Since photons are always part of the thermal bath, it is conventional to express the total energy and entropy densities in units of the photon energy and entropy densities by introducing the effective degrees of freedom $g_{\rm eff}$ and $h_{\rm eff}$ defined by

$$\begin{aligned} \rho(T) &= \frac{\pi^2}{30}\, g_{\rm eff}(T)\, T^4 \\ s(T) &= \frac{2\pi^2}{45}\, h_{\rm eff}(T)\, T^3\,. \end{aligned} \tag{2.54}$$

Another more formal definition can be extracted from the equation above

$$g_{\rm eff} \equiv \sum_i g_\gamma\, \frac{\rho_i(T_i)}{\rho_\gamma(T)} \tag{2.55}$$

$$h_{\rm eff} \equiv \sum_i g_\gamma\, \frac{s_i(T_i)}{s_\gamma(T)} \tag{2.56}$$

For relativistic species, the effective degrees of freedom can be written explicitly

$$g_{\rm eff}(T) \equiv \sum_{\text{boson } i} g_i \left(\frac{T_i}{T}\right)^4 + \frac{7}{8} \sum_{\text{fermion } j} g_j \left(\frac{T_j}{T}\right)^4 \tag{2.57}$$

$$h_{\rm eff}(T) \equiv \sum_{\text{boson } i} g_i \left(\frac{T_i}{T}\right)^3 + \frac{7}{8} \sum_{\text{fermion } j} g_j \left(\frac{T_j}{T}\right)^3 . \tag{2.58}$$

We introduced specific temperatures T_i and T_j to account for species which are not in thermal equilibrium with the thermal bath.[2] For particles in equilibrium with the bath, we have $g_{\rm eff} = h_{\rm eff}$. The effective degrees of freedom of a particular species A can be expressed using Eqs. (2.40) and (2.41). We find

$$g_{\rm eff,A}(T) = g_{\rm A} \frac{15}{\pi^4} \int_0^\infty \frac{u^2}{e^{\sqrt{u^2+x^2}} + \epsilon} \sqrt{u^2+x^2}\, {\rm d}u \tag{2.59}$$

$$h_{\rm eff,A}(T) = g_{\rm A} \frac{45}{4\pi^4} \int_0^\infty \frac{u^2}{e^{\sqrt{u^2+x^2}} + \epsilon} \left(\sqrt{u^2+x^2} + \frac{u^2}{3\sqrt{u^2+x^2}}\right) {\rm d}u\,. \tag{2.60}$$

Using the definition and recurrence property of the modified Bessel functions, one can express $g_{\rm eff,A}$ and $h_{\rm eff,A}$ in term of rapidly converging series

$$g_{\rm eff,A}(T) = g_{\rm A} \frac{15}{\pi^4} \sum_{n=1}^{\infty} (-\epsilon)^{n+1} \left\{ \left(\frac{6x}{n^3} + \frac{x^3}{n}\right) K_1(nx) + \frac{3x^2}{n^2} K_0(nx) \right\} \tag{2.61}$$

$$h_{\rm eff,A}(T) = g_{\rm A} \frac{45}{4\pi^4} \sum_{n=1}^{\infty} (-\epsilon)^{n+1} \left\{ \left(\frac{8x}{n^3} + \frac{x^3}{n}\right) K_1(nx) + \frac{4x^2}{n^2} K_0(nx) \right\} \tag{2.62}$$

These expressions are established in App. B.1. The quantity $g_{\rm eff}$ is shown in Fig. 2.2. One notices an important decrease of $g_{\rm eff}$ around $T \simeq 150\,{\rm MeV}$: this is the QCD phase transition, when the temperature is low enough so that quarks are confined into hadrons (see *e.g.*, Borsanyi et al. (2016) for a detailed study of the transition using lattice simulations).

2.2 A simplified WIMP model

2.2.1 Lagrangian

We introduce a very simple model of WIMP dark matter. Our goal is to use this model as illustration of the typical thermal history of WIMPs. In this spirit, we do not try to address any potential issues, *e.g.*consistency with respect to quantum field theory, that this model might have. We will not try to address questions related to the generation of the dark mass or the impact on the hierarchy problem. We are considering a simplified model, in the sense of Abdallah et al. (2015) rather than a fully consistent theory like supersymmetry. We consider a fermion χ as the dark matter particle. This fermion can be either a Dirac or a Majorana fermion. Dark matter can interact with SM fermions through a real scalar field ϕ or a real pseudo-scalar field a. The scalar/pseudo-scalar particle is massive and the scalar particle is assumed to be different from the Higgs field. Our working Lagrangian is the following

$$\mathcal{L} = \mathcal{L}_{\rm SM} + \mathcal{L}_{\rm kin} + \mathcal{L}_{\rm int}\,, \tag{2.63}$$

where $\mathcal{L}_{\rm sm}$ is the SM Lagrangian, $\mathcal{L}_{\rm kin}$ contains the kinetic terms for χ, ϕ and a, and $\mathcal{L}_{\rm int}$ contains the mass terms and the interactions terms. The interaction part in the case of Majorana dark

[2] In the standard cosmological evolution, species that decouple from the thermal bath never maintain thermal equilibrium on their own and the temperature is not rigorously defined, therefore T_i and T_j should be thought of as effective temperature instead.

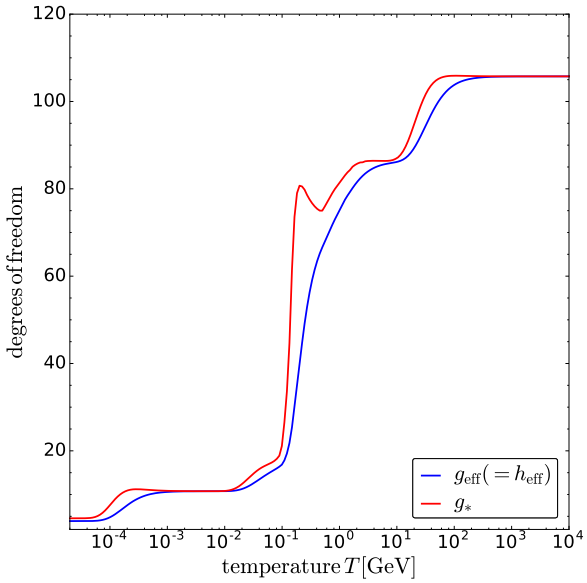

Figure 2.2 – Effective degrees of freedom $g_{\rm eff}$ (blue) and g_* (red) as functions of the temperature.

matter can be written

$$\begin{aligned}\mathcal{L}_{\rm int} = &-\frac{1}{2}\,m_\chi\,\overline{\chi}\chi - \frac{1}{2}m_\phi^2\,\phi^2 - \frac{1}{2}m_a\,a^2 \\ &-\frac{\lambda_\phi}{2}\,\overline{\chi}\chi\,\phi - \frac{\lambda_a}{2}\,\overline{\chi}\,\gamma^5\,\chi\,a \\ &-\lambda'_\phi\,\overline{f}f\,\phi - \lambda'_a\,\overline{f}\,\gamma^5\,f\,a\,.\end{aligned} \tag{2.64}$$

If dark matter is a Dirac field, there is no 1/2 factor in front of the dark matter mass term and coupling term. In Eq. (2.64), f refers to a SM fermion. The scalar and pseudo-scalar particles can in principle interact with several SM fermions, in which case there are couplings λ'_ϕ and λ'_a for each fermion. Free parameters in our model are the masses m_χ, m_ϕ, m_a, and the couplings λ_ϕ, λ_a, λ'_ϕ, λ'_a. Note that such a simplified model is already constrained by several experiments (*e.g.*, LHC, Xenon, indirect searches).

2.2.2 Tree-level amplitude

Two types of reactions are especially relevant during the thermal history of our dark matter candidate: annihilation and elastic scattering. The tree-level Feynman diagrams for the annihilation are shown in Fig. 2.3. The dark matter particle, whether a Majorana or a Dirac fermion, can annihilate through the scalar or the pseudo-scalar into a pair of SM fermions. Note that these diagrams, up to a time-reversal transformation, also control the production of dark matter from the annihilation of SM fermions. The squared amplitude for the annihilation processes, averaged over initial spins and summed over final spins, is given by

$$\overline{|\mathcal{M}_{\rm ann}|^2} = N_{\rm c}\,\frac{(\lambda_{\rm med}\lambda'_{\rm med})^2}{\left(s - m_{\rm med}^2\right)^2}\begin{cases}\left(s - 4\,m_\chi^2\right)\left(s - 4\,m_{\rm f}^2\right) & \text{scalar} \\ s^2 & \text{pseudoscalar}\end{cases} \tag{2.65}$$

This result is demonstrated in App. B. In Eq. (2.65), $N_{\rm c}$ is the number of non-spin degrees of freedom of the SM fermion (for instance the number of colors if f is a quark). If p_1 and p_2 are the 4-momenta of the incoming dark matter particles, and k_3 and k_4 the 4-momenta of the outgoing SM fermions, s is the Lorentz-invariant Mandelstam variable accounting for centre-of-mass energy $s = (p_1 + p_2)^2 = (k_3 + k_4)^2$.

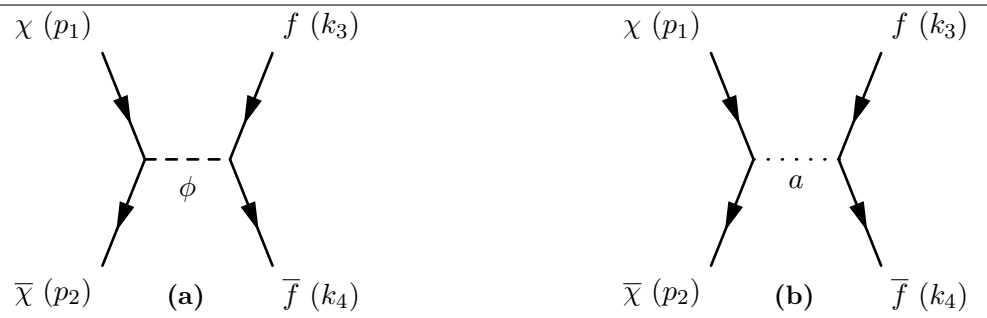

Figure 2.3 – Pair annihilation of the dark matter particle into SM fermions through the scalar portal (a) or the pseudo-scalar portal (b).

Tree-level diagrams for the elastic scattering of a dark matter particle off a SM fermion are shown in Fig. 2.4. These diagrams are simply obtained by rotating the annihilation diagrams in Fig. 2.3. For the amplitude, this translates into a change $s \to t$, where $t = (p_1 - p_2)^2 = (k_3 - k_4)^2$ and this time p_1 (p_2) is the 4-momentum of the incoming (outgoing) dark matter particle and k_3 (k_4) is the 4-momentum of the incoming (outgoing) SM fermion. The amplitude for the process is

$$\overline{|\mathcal{M}_{\rm scat}|^2} = N_{\rm c}\,\frac{\left(\lambda_{\rm med}\lambda'_{\rm med}\right)^2}{\left(t - m^2_{\rm med}\right)^2}\begin{cases}\left(t - 4\,m^2_\chi\right)\left(t - 4\,m^2_{\rm f}\right) & \text{scalar}\\ t^2 & \text{pseudoscalar}\end{cases} \tag{2.66}$$

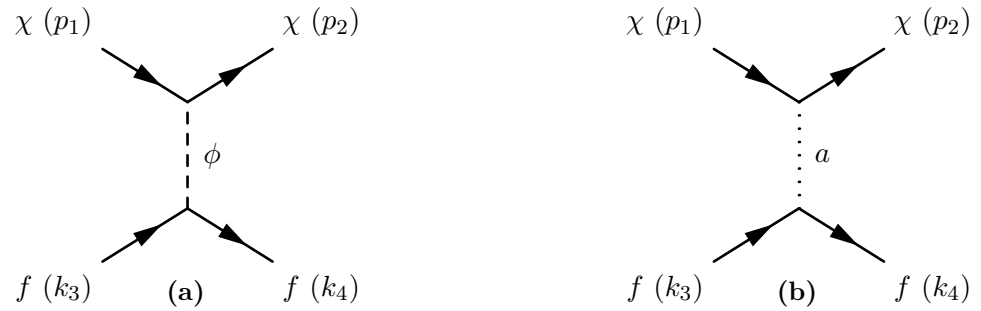

Figure 2.4 – Elastic scattering of a dark matter particle off a SM fermion through the exchange of a scalar (a) or a pseudo-scalar (b).

2.2.3 Cross-sections

As shown in the appendix, the Lorentz-invariant annihilation cross-section is given by

$$\sigma_{\rm ann} = \frac{1}{16\pi}\,\frac{\left(\lambda_{\rm med}\lambda'_{\rm med}\right)^2}{\left(s - m^2_{\rm med}\right)^2 + m^2_{\rm med}\Gamma^2_{\rm med}}\begin{cases}(s - 4\,m^2)^{1/2}(s - 4\,m^2_{\rm f})^{3/2}\,s^{-1} & \text{scalar}\\ \left(\frac{s-4\,m^2_{\rm f}}{s-4\,m^2}\right)^{1/2} s & \text{pseudoscalar}\end{cases} \tag{2.67}$$

The cross-sections are shown for both mediators in Fig. 2.5. As one can see, the two cross-sections have a similar behaviour at high energies. A difference appears at low energies: while the scalar cross-section is suppressed when the WIMPs annihilate at rest ($\sqrt{s} = 2\,m$), the pseudoscalar cross-section diverges.

2.3 Chemical decoupling

A fundamental element for any dark matter candidate is its production mechanism in the early Universe. The case of the WIMP was first discussed by Lee & Weinberg (1977) (see also Vysotsky et al. (1977); Sato & Kobayashi (1977); Hut (1977); Dicus et al. (1977)). In this seminal paper, Lee and Weinberg established the evolution equation for the number density of a weakly interacting particle (having in mind a heavy neutrino) and set a lower bound on its mass by

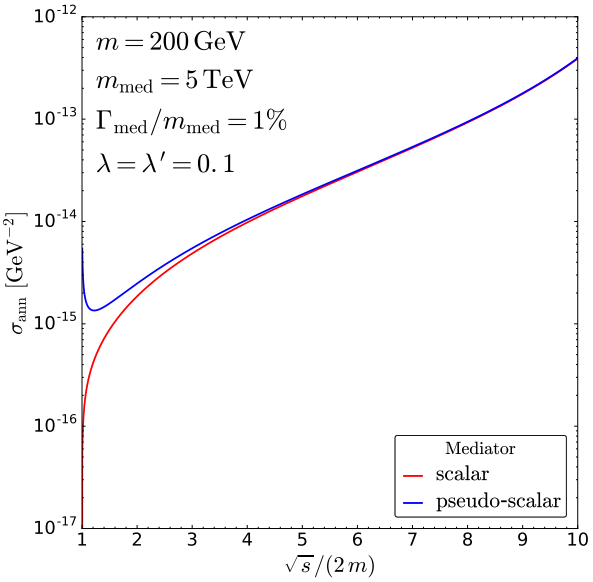

Figure 2.5 – Annihilation cross-sections as functions of the centre-of-mass energy $\sqrt{s}$ (normalized to the sum of the masses of the incoming particles).

requiring that its energy density does not overclose the Universe. This original calculation has since then been revisited many times, see for instance Bernstein et al. (1985); Kolb & Olive (1986); Srednicki et al. (1988); Griest & Seckel (1991); Gondolo & Gelmini (1991); Edsjo & Gondolo (1997); Steigman et al. (2012), and the astrophysical and cosmological phenomenology of WIMPs have been investigated in details (Gunn et al., 1978; Tremaine & Gunn, 1979).

In this section, we review the standard calculation of the WIMP relic density. We show that the number density of WIMPs today is set by the chemical decoupling of the dark matter particle. Using our toy model, we illustrate the freeze-out and freeze-in scenarios.

2.3.1 The Boltzmann equation

Evolution of the number density In this section, we establish the master equation for the time evolution of the WIMP number density, following the standard treatment of Gondolo & Gelmini (1991). We assume that dark matter particles can annihilate into SM particles through a reaction

$$1 + 2 \to 3 + 4\,, \tag{2.68}$$

where 1 and 2 are dark matter particles, and 3 and 4 are SM particles. In our simplified model, these SM particles are fermions, however the following treatment holds regardless of the nature of the outgoing particles. The phase-space number density of 1 obeys the Boltzmann equation

$$\hat{L}[f_1] = \hat{C}[f_1] \tag{2.69}$$

where $\hat{L}$ and $\hat{C}$ are the Liouville and collision operators, respectively. As shown in App. B.3, taking the zeroth-order moment of the Boltzmann equation leads to the evolution equation of the number density

$$\frac{\mathrm{d}n_1}{\mathrm{d}t} + 3\,H\,n_1 = -\,\langle\sigma_{\mathrm{ann}} v\rangle\,(n_1 n_2 - n_{1,\mathrm{eq}} n_{2,\mathrm{eq}})\,. \tag{2.70}$$

Note the equilibrium number densities n_1^{eq} and n_2^{eq} actually represent the plasma production term. It can be conveniently expressed in terms of the WIMPs equilibrium density thanks to the

principle of detailed balance. In this equation, $\langle \sigma_{\rm ann} v \rangle$ is the thermally-averaged cross-section defined as

$$\langle \sigma_{\rm ann} v \rangle \equiv \frac{\int \mathrm{d}^3\vec{p}_1\, \mathrm{d}^3\vec{p}_2\, f_1(\vec{p}_1)\, f_2(\vec{p}_2)\, \sigma_{\rm ann}\, v_{\rm m}}{\int \mathrm{d}^3\vec{p}_1\, \mathrm{d}^3\vec{p}_2\, f_1(\vec{p}_1)\, f_2(\vec{p}_2)}\,, \tag{2.71}$$

where f_i is the phase-space number density of i, $\sigma_{\rm ann}$ is the cross-section of the reaction in Eq. (2.68), and $v_{\rm m}$ is the Møller velocity

$$\begin{aligned} v_{\rm m} &\equiv \frac{\sqrt{(p_1.p_2)^2 - m_1^2 m_2^2}}{E_1\, E_2} && (2.72)\\ &= \sqrt{|\vec{v}_1 - \vec{v}_2|^2 - |\vec{v}_1 \times \vec{v}_2|^2}\,. && (2.73) \end{aligned}$$

The Moller velocity is such that $v_{\rm m}\, n_1\, n_2$ is Lorentz-invariant. Note that the averaged cross-section depends on the temperature in the dark matter bath through the phase-space distribution function (DF).

The standard treatment of chemical decoupling assumes thermal equilibrium between dark matter particles and the thermal bath is maintained during decoupling. For a study of the full out-of-equilibrium decoupling, see Binder et al. (2017). Two cases are usually considered for 1 and 2: either these particles are identical and the dark matter number density is $n = n_1 = n_2$ (which is the case if dark matter is a Majorana fermion), or 1 and 2 are different (which is the case if dark matter is a Dirac fermion) and we further assume $n_1 = n_2$ to get $n = n_1 + n_2 = 2\, n_1$. In the following, we focus on the case of identical particles where the Boltzmann equation is

$$\frac{\mathrm{d}n}{\mathrm{d}t} + 3\, H\, n = -\langle \sigma_{\rm ann} v \rangle \left(n^2 - n_{\rm eq}^2 \right)\,. \tag{2.74}$$

For non-identical particles, the evolution equation for n is the same with the replacement $\langle \sigma_{\rm ann} v \rangle \to \langle \sigma_{\rm ann} v \rangle / 2$. In Eq. (2.74), the first term on the right-hand side accounts for the depletion of the dark matter density by annihilation of dark matter particles. The second term accounts for the creation of dark matter particles by annihilation of particles in the thermal bath. The second term on the left-hand side of the equation is a friction term accounting for the expansion of the Universe. We know that a constant number of dark matter particles inside a comoving volume yields a number density $n(t) \propto a^{-3}(t)$, hence it is useful to introduce a quantity that remains constant during the expansion. If the total entropy of the Universe is conserved, the entropy density verifies $s \propto a^{-3}(t)$ (see Eq. (2.49)), therefore we define a *comoving number density*[3]

$$Y \equiv \frac{n}{s}\,. \tag{2.75}$$

Plugging the definition of the comoving density in Boltzmann equation (2.74), we get

$$\frac{\mathrm{d}Y}{\mathrm{d}t} = -s\, \langle \sigma_{\rm ann} v \rangle \left(Y^2 - Y_{\rm eq}^2 \right)\,. \tag{2.76}$$

Note that the Hubble friction term is gone, as expected. We make use of $x = m/T$ as a time variable, where m is the dark matter mass and T is the temperature of the thermal bath. With the substitution

$$\begin{aligned} \frac{\mathrm{d}}{\mathrm{d}t} &= \frac{\mathrm{d}s}{\mathrm{d}t}\frac{\mathrm{d}x}{\mathrm{d}s}\frac{\mathrm{d}}{\mathrm{d}x}\\ &= -3Hs\,\frac{\mathrm{d}x}{\mathrm{d}s}\frac{\mathrm{d}}{\mathrm{d}x}\,, \end{aligned} \tag{2.77}$$

[3]Note that the term comoving density is abusive since Y has units of inverse entropy.

we get

$$\frac{\mathrm{d}Y}{\mathrm{d}x} = \frac{1}{3H}\frac{\mathrm{d}s}{\mathrm{d}x}\langle\sigma_{\rm ann}v\rangle\left(Y^2 - Y_{\rm eq}^2\right) . \tag{2.78}$$

We can go further by using the effective degrees of freedom introduced in Eq. (2.54) and the expression of the Hubble parameter $H^2 = 8\pi G_{\rm N}\rho/3$. We finally get

$$\frac{\mathrm{d}Y}{\mathrm{d}x} = -\left(\frac{\pi}{45\,G_{\rm N}}\right)^{1/2}\frac{m\,g_*^{1/2}}{x^2}\langle\sigma_{\rm ann}v\rangle\left(Y^2 - Y_{\rm eq}^2\right) , \tag{2.79}$$

with

$$g_*^{1/2} \equiv \frac{h_{\rm eff}}{g_{\rm eff}^{1/2}}\left(1 + \frac{1}{3}\frac{\mathrm{d}\ln h_{\rm eff}}{\mathrm{d}\ln T}\right) . \tag{2.80}$$

The behaviour of g_* with the temperature closely follows that of $g_{\rm eff}$, as shown on the left panel in Fig. (2.2). Equation (2.79) is the most practical form of the Boltzmann equation when it comes to numerical calculations.

Thermally-averaged annihilation cross-section Let us comment on the averaged cross-section defined in Eq. (2.71). If the WIMP has a Maxwell-Boltzmann phase-space distribution, Gondolo & Gelmini (1991) showed that it can be expressed as a single integral

$$\langle\sigma_{\rm ann}v\rangle = \frac{1}{8m^4TK_2^2(m/T)}\int_{4m^2}^{\infty}\sigma_{\rm ann}(s)\left(s - 4m^2\right)\sqrt{s}K_1(\sqrt{s}/T)\,\mathrm{d}s\,. \tag{2.81}$$

This result is exact and valid if the temperature is low enough for the Maxwell-Boltzmann approximation to hold. Numerically, it is a very good approximation if $T < 3m$.

As the temperature gets lower and $x \gg 1$, $\langle\sigma_{\rm ann}v\rangle$ can be expanded in powers of x^{-1}

$$\langle\sigma_{\rm ann}v\rangle \simeq a + \frac{b}{x} + \frac{c}{x^2} + \frac{d}{x^3} + \dots \tag{2.82}$$

The first, temperature-independent term is referred to as the s-wave contribution, while the second term is referred to as p-wave. The relation between the cross-section $\sigma_{\rm ann}$ and coefficients a, b, c and d is explicitly given by Srednicki et al. (1988). The coefficients are expressed in terms of the Lorentz-invariant function

$$\begin{aligned} w(s) &\equiv E_1E_2\,\sigma_{\rm ann}\,v_{\rm m} \\ &= \sigma_{\rm ann}(s)\sqrt{(p_1.p_2)^2 - m_1^2m_2^2} \\ &= \sigma_{\rm ann}(s)\,\frac{\sqrt{s}}{2}\sqrt{s + \frac{(m_1^2 - m_2^2)^2}{s} - 2(m_1^2 + m_2^2)}\,, \end{aligned} \tag{2.83}$$

and its derivatives. Expressions for a and b in our simplified model are given in App. B.2.4. The thermal cross-sections are shown in Fig. (2.6). The behaviour as a function of the temperature is very different depending on the nature of the mediator: while the pseudo-scalar cross-section keeps a constant value at low temperature, the scalar one is falling like T.

2.3.2 Freeze-out and freeze-in

Freeze-out The Boltzmann equation (2.79) cannot be solved analytically but we can guess the qualitative behaviour of the solution. Let us suppose the WIMP is in thermal and chemical equilibrium with the plasma at a given x. When the temperature of the plasma drops well below

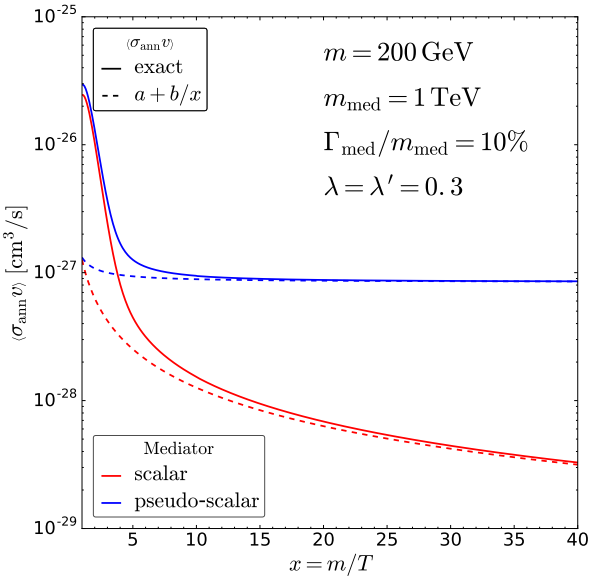

Figure 2.6 – Thermally-averaged annihilation cross-sections as functions of the temperature. We show the scalar (red) and pseudo-scalar (blue) channels, for both the exact solution (solid) and the $1/x$ expansion (dashed).

the WIMP mass, *i.e.* when $x \gg 1$, conservation of energy forbids the creation of WIMPs from collisions in the plasma. The Boltzmann equation then reduces to

$$\frac{\mathrm{d}Y}{\mathrm{d}x} = -\left(\frac{\pi}{45\,G_{\rm N}}\right)^{1/2} \frac{m\,g_*^{1/2}}{x^2}\,\langle\sigma_{\rm ann}v\rangle\;Y^2\,, \tag{2.84}$$

which shows that dark matter self-annihilation depletes the comoving density. At some point, as the number of dark matter particles drops and the Universe expands, self-annihilation becomes inefficient and the comoving density remains roughly constant. At this point the dark matter is chemically decoupled from the thermal bath. Chemical decoupling happens when the annihilation rate drops below the expansion rate

$$\Gamma_{\rm ann}(x_{\rm cd}) \simeq H(x_{\rm cd})\,, \tag{2.85}$$

where $\Gamma_{\rm ann} = n\,\langle\sigma_{\rm ann}v\rangle$. We assume the decoupling occurs when WIMPs are well into the non-relativistic regime, hence we can use Eq. (2.46) for the WIMP number density. The annihilation and Hubble rates are shown on the left panel in Fig. 2.7. The value of $x_{\rm cd}$ at the intersection between the two rates is solution of

$$x_{\rm cd}^{1/2} e^{-x_{\rm cd}} \simeq \left(\frac{\pi^5}{45}\,g_{\rm eff}\right)^{1/2} \frac{1}{m_{\rm p}\,m\,\langle\sigma_{\rm ann}v\rangle}\,, \tag{2.86}$$

where $m_{\rm p} \equiv (8\pi G_{\rm N})^{-1/2}$ is the reduced Planck mass. For a WIMP with mass $m = 100\,\mathrm{GeV}$ and a cross-section at the electroweak scale $\langle\sigma_{\rm ann}v\rangle \sim 10^{-8}\,\mathrm{GeV}^{-2}$, we get $x_{\rm cd} \simeq 30$. Note that $x_{\rm cd}$ depends only logarithmically on the mass and the cross-section. We evaluate $x_{\rm cd}$ in our toy model using the Boltzmann equation as done by Gondolo & Gelmini (1991). The result is shown in the right panel on Fig. 2.7. The value of $x_{\rm cd}$ changes by ten units over two decades in dark matter mass. Note that this change is partly due to resonant annihilation at $2\,m = m_{\phi/a}$, which is clearly visible in the figure.

We now integrate Eq. (2.84) between $x_{\rm cd}$ and x_0 (T_0 is the temperature of the photon bath today) to get

$$\frac{1}{Y_0} - \frac{1}{Y_{\rm cd}} = \left(\frac{\pi}{45\,G_{\rm N}}\right)^{1/2} m \int_{x_{\rm cd}}^{x_0} \frac{g_*^{1/2}}{x^2}\,\langle\sigma_{\rm ann}v\rangle\;\mathrm{d}x\,. \tag{2.87}$$

If enough particles annihilate right after $x_{\rm cd}$, we can neglect $1/Y_{\rm cd}$ in Eq. (2.87). If we further assume $\langle\sigma_{\rm ann}v\rangle$ to be temperature-independent and take an average value for $g_*^{1/2}$, we get an expression for today's relic abundance

$$\Omega_{\rm cdm} = \frac{m\, s_0\, Y_0}{\rho_{\rm c}}\,. \tag{2.88}$$

Using

$$\begin{aligned}\rho_{\rm c} &= \frac{3}{8\pi G_{\rm N}}\, H_0^2 \\ &= \frac{3}{8\pi G_{\rm N}}\, (100\, h\,{\rm km/s/Mpc})^2\,,\end{aligned} \tag{2.89}$$

we get

$$\Omega_{\rm cdm}h^2 = \left(5\pi G_{\rm N}^3\right)^{1/2} \frac{s_0}{g_*^{1/2}} \frac{x_{\rm cd}}{\langle\sigma_{\rm ann}v\rangle}\, (100\,{\rm km/s/Mpc})^{-2}\,. \tag{2.90}$$

The dark matter abundance does not depend explicitly on the dark matter mass. There is actually a hidden dependency in $x_{\rm cd}$ but as we have seen before, it is very weak. The evolution of the dark matter density is shown in the left panel of Fig. 2.8 for a constant annihilation cross-section. An important feature of the freeze-out scenario is the dependence of the relic abundance on the *inverse* of the cross-section: the higher the cross-section, the later the decoupling and the lower the abundance. In a given model, the cross-section obviously depends on the dark matter mass. We show the evolution of the dark matter density in our toy model in the right panel on Fig. 2.8 for different values of the dark matter mass.

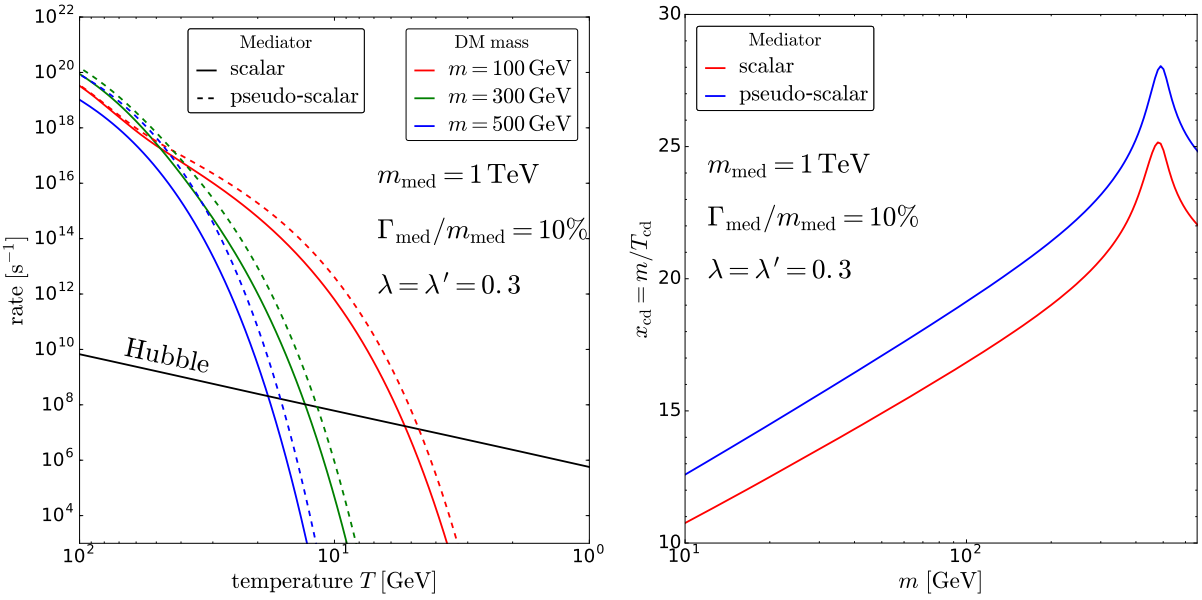

Figure 2.7 – Left panel: Hubble rate (black curve) compared to the annihilation rate for a scalar (solid curve) or a pseudoscalar channel (dashed curve) with a dark matter mass $m = 100/300/500\,$GeV (red/green/blue). **Right panel:** $x_{\rm cd} = m/T_{\rm cd}$ with $T_{\rm cd}$ the temperature of chemical decoupling, as a function of the dark matter mass. Are shown the scalar (red) and pseudoscalar channels (blue).

The dark matter relic abundance is almost entirely fixed by the annihilation cross-section. We can turn the expression around and compute the cross-section that leads to the observed dark matter abundance. We get

$$\langle\sigma_{\rm ann}v\rangle \simeq 3\times10^{-26}\,{\rm cm^3 s^{-1}} \simeq 10^{-8}\,{\rm GeV^{-2}}\,, \tag{2.91}$$

which turns out to be the order of magnitude of an electroweak cross-section. The fact that a massive particle with electroweak scale interactions leads to the correct order of magnitude for the dark matter relic abundance is dubbed the "WIMP miracle" and is one of the main reasons why WIMP models have been extensively studied in the literature. The value of the constant/s-wave annihilation cross-section that leads to the correct relic abundance is shown in the left panel on Fig. 2.9. The cross-section varies from $4.5 \times 10^{-26}\,\mathrm{cm}^3/\mathrm{s}$ to $2 \times 10^{-26}\,\mathrm{cm}^3/\mathrm{s}$ over four orders of magnitude of the dark matter mass. This dependence on the dark matter mass is also shown in Steigman et al. (2012). The dark matter relic abundance today is shown as a function of the dark matter mass in the right panel in Fig. 2.9. We can constrain our model by fixing, for a given dark matter and mediator mass, the product of the coupling constants $\lambda\lambda'$ by requiring that the relic abundance matches the value measured by Ade et al. (2016).

Our very simple WIMP model captures the essential features of the freeze-out mechanism. In more complicated models, such as those coming from supersymmetric theories, the phenomenology of freeze-out can be significantly modified by the presence of other non-standard particles in the spectrum. A typical example is coannihilation (Binétruy et al., 1984; Edsjo & Gondolo, 1997). This occurs when a particle has a mass right above the dark matter mass. In that case, the dark matter particle can coannihilate with that particle, which opens a new channel changing the dark matter relic abundance. Interestingly, the Boltzmann equation governing the number density of non-standard particles in the presence of coannihilation can be written

$$\frac{\mathrm{d}n}{\mathrm{d}t} + 3\,H\,n = -\,\langle\sigma_{\mathrm{eff}} v\rangle \left(n^2 - n_{\mathrm{eq}}^2\right)\,, \tag{2.92}$$

i.e. it is exactly the same equation as Eq. (2.74) with an effective annihilation cross-section $\langle\sigma_{\mathrm{eff}} v\rangle$ whose expression is given in Edsjo & Gondolo (1997). This equation is valid if all the non-standard particles are in equilibrium. Note that in the non-relativistic limit, we have

$$\frac{n_2^{\mathrm{eq}}}{n_1^{\mathrm{eq}}} = \frac{g_2}{g_1}\left(\frac{m_2}{m_1}\right)^{3/2} e^{-\Delta m/T}\,, \tag{2.93}$$

with $\Delta m = m_2 - m_1$. Consequently, the impact of coannihilation of 1 with 2 on the calculation of the relic density crucially depends on $\Delta m > 0$, and is more important for a small mass difference.

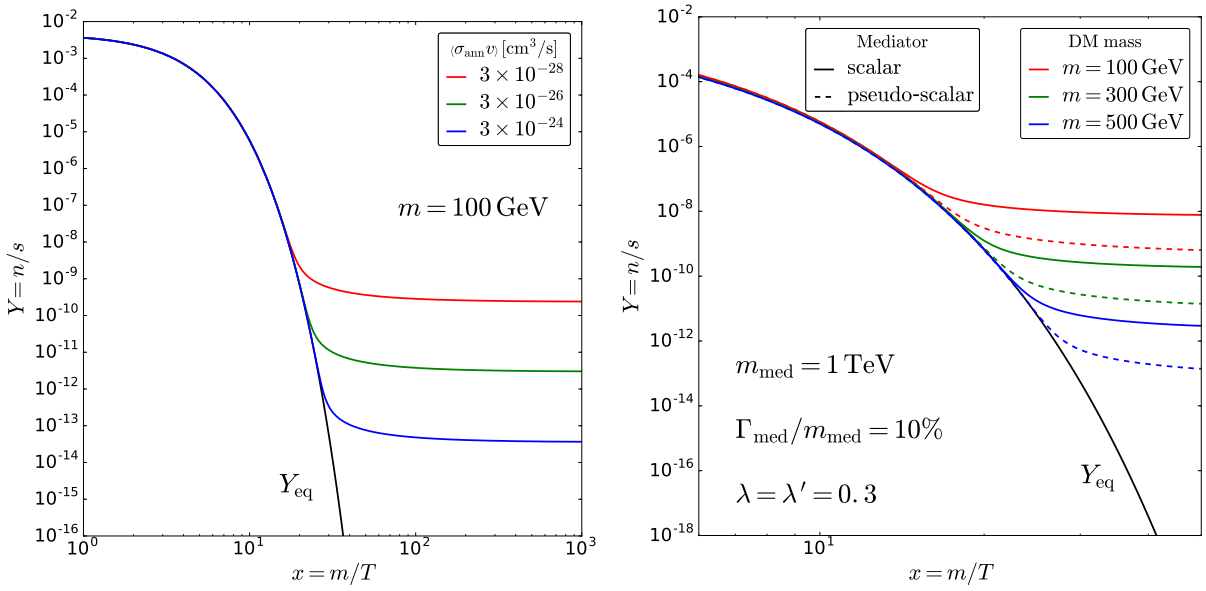

Figure 2.8 – Left panel: chemical decoupling in the freeze-out regime, in the case of a constant annihilation cross-section (s-wave) $\langle\sigma_{\mathrm{ann}} v\rangle$. **Right panel:** chemical decoupling for the scalar (solid curve) and pseudoscalar channel (dashed curve), for a dark matter mass $m = 100/300/500\,\mathrm{GeV}$ (red/green/blue).

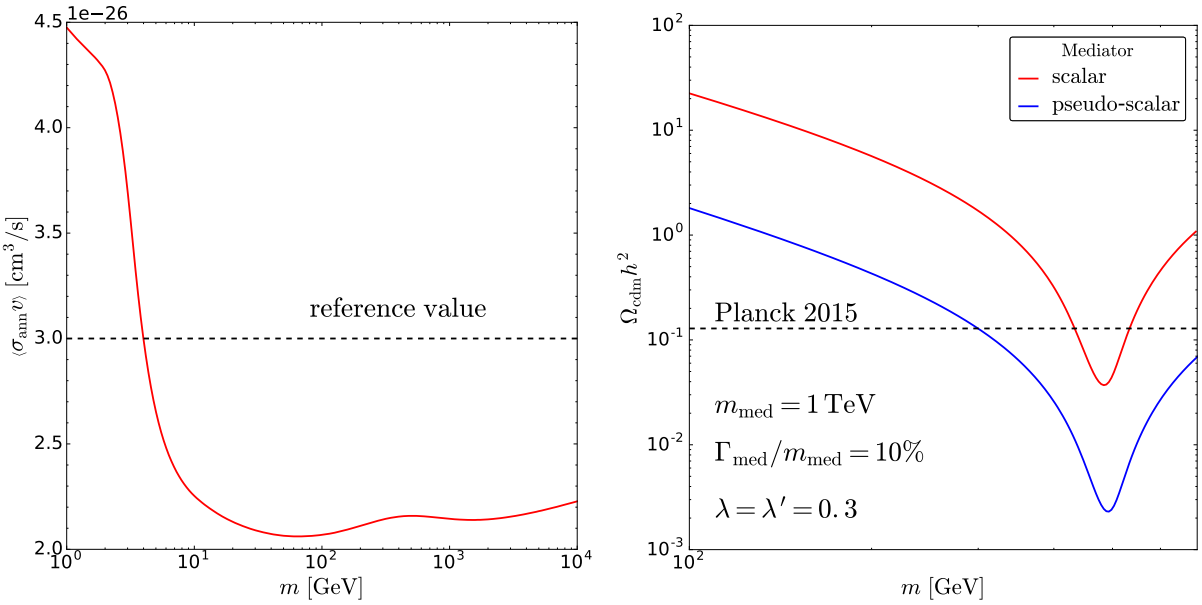

Figure 2.9 – Left panel: s-wave value of the annihilation cross-section to get the observed relic abundance (red), compared to the "canonical" value (dashed black). **Right panel:** Final relic abundance for the scalar (red) and pseudoscalar channel (blue), compared to the observed abundance from the Planck collaboration (dashed black).

Freeze-in The main assumption behind the freeze-out scenario is that dark matter has reached chemical and thermal equilibrium at some temperature $T > m$. This assumption can be relaxed. We can instead assume that dark matter is produced by collisions within the plasma through a continuous process. This can happen in the inflationary scenario: after inflation, the inflaton decays into Standard Model particles during what is called the reheating epoch (Turner, 1983; Traschen & Brandenberger, 1990; Kofman et al., 1997). If we assume dark matter is not directly produced by the inflaton or in negligible proportions, then our initial condition is $n(T_{\rm rh}) = 0$ where $T_{\rm rh}$ is the reheating temperature. Dark matter is then produced by annihilation of Standard Model particles and its comoving density follows Eq. (2.79). There are then two possibilities. Either the production/annihilation cross-section is large enough for the dark matter to reach chemical and thermal equilibrium before decoupling, in which case we are back to the freeze-out scenario, or the cross-section is too small for dark matter to ever reach equilibrium. The latter case is an example of freeze-in scenario, when dark matter chemical decoupling occurs out-of-equilibrium. Hall et al. (2010) showed that the freeze-in scenario leads to predictions that are independent of the reheating temperature so long as $T_{\rm rh} \gg T_{\rm cd}$, so the freeze-in scenario is independent of the high-energy physics just like the freeze-out scenario. Hall et al. (2010) considered dark matter produced through the decay of some heavier particle, however their conclusions also holds for dark matter produced through annihilation. We show the chemical decoupling in the freeze-in regime in Fig. 2.10 for different value of the s-wave cross-section (note the very low values $\langle\sigma_{\rm ann}v\rangle$ with respect to the freeze-out scenario). A major difference between freeze-out and freeze-in is visible in the figure: while the asymptotic value at $x \gg x_{\rm cd}$ is roughly proportional to $1/\langle\sigma_{\rm ann}v\rangle$ in the freeze-out case, it goes like $\langle\sigma_{\rm ann}v\rangle$ in the freeze-in scenario. This can bee seen from the Boltzmann equation (2.79) where we can assume $Y \ll Y_{\rm eq}$. The Boltzmann equation is then simply

$$\frac{{\rm d}Y}{{\rm d}x} = \left(\frac{\pi}{45\,G_{\rm N}}\right)^{1/2} \frac{m\,g_*^{1/2}}{x^2}\,\langle\sigma_{\rm ann}v\rangle\,Y_{\rm eq}^2\,, \tag{2.94}$$

which can be directly integrated between $x_{\rm rh}$ and x_0 to get

$$Y_0 = \left(\frac{\pi}{45\,G_{\rm N}}\right)^{1/2} m\,\langle\sigma_{\rm ann}v\rangle \int_{x_{\rm rh}}^{x_0} g_*^{1/2}\,\frac{Y_{\rm eq}^2}{x^2}\,{\rm d}x\,. \tag{2.95}$$

This shows that the relic abundance in the freeze-in scenario is indeed proportional to the s-wave annihilation cross-section. Note that the integral in Eq. (2.95) diverges if $x_{\rm rh} \to 0$ therefore it strongly depends on $x_{\rm rh}$, which seems to be in contradiction with what we have stated earlier. This is because we assumed temperature independent cross-section, which cannot be the case at low x. In a simple scenario where dark matter is linked to the Standard Model through a single mediator with mass $m_{\rm med}$, the cross-section is suppressed for $x \ll m/m_{\rm med}$, which regularises the integral if the reheating temperature is such that $T_{\rm rh} \gg m_{\rm med}$. WIMPs which experience a freeze-in are sometimes referred to as FIMPs for Feebly Interacting Massive Particles *i.e.* very weakly interacting massive particles.

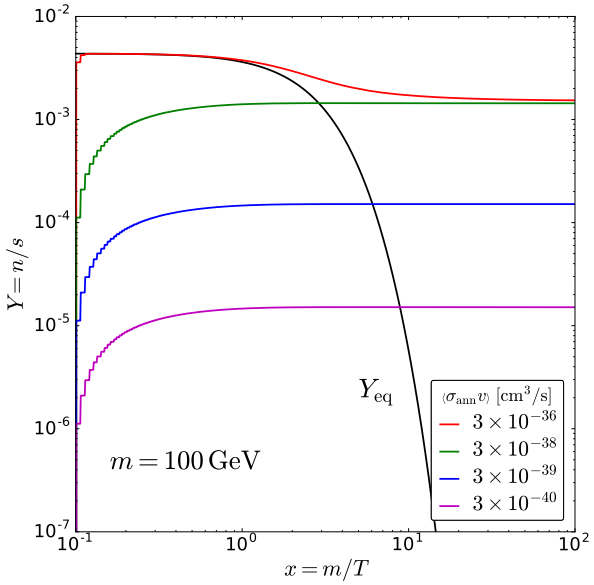

Figure 2.10 – Chemical decoupling in the freeze-in regime. The initial condition is $Y(x_{\rm rh}) = 0$ with $x_{\rm rh} = 0.1$. The "step" features at low x are due to numerical issues.

2.4 Kinetic decoupling and primordial structures

Immediately after dark matter annihilation stops being efficient, elastic scattering between dark matter and Standard Model particles maintains the two in kinetic equilibrium. Let us show that kinetic decoupling generically happens after chemical decoupling. We recall that freeze-out happens roughly when the annihilation rate becomes lower than the Hubble rate

$$\Gamma_{\rm ann} = n\,\langle\sigma_{\rm ann}v\rangle < H\,. \tag{2.96}$$

and we typically get $x_{\rm cd} = m/T_{\rm cd} \simeq 25$ as seen in the previous section. To obtain a precise estimate of the kinetic decoupling temperature, one must solve the Boltzmann equation

$$L_0[f] = C_0[f]\,. \tag{2.97}$$

with

$$L_0[f] = \frac{\partial f}{\partial t} - \frac{H|\vec{p}|^2}{E}\frac{\partial f}{\partial E}\,. \tag{2.98}$$

Let us first try to find a simple estimate. A naive approach would be to compare the scattering rate to the Hubble rate

$$\Gamma_{\rm scat} = \sum_i n_i^{\rm eq} \langle \sigma_{\chi i} v \rangle < H \,, \tag{2.99}$$

where the sum is over the different targets the dark matter particle can scatter off. We can assume these targets to be in thermal equilibrium with the photon bath. Comparing the scattering rate to the Hubble rate is not correct however. Many interactions are actually needed to maintain local thermal equilibrium. When the WIMP is in equilibrium with the thermal bath, it has an average momentum $p = \sqrt{3mT}$ while the momentum exchange during a single encounter with a particle from the bath is $\delta p \simeq T$ hence

$$\frac{\delta p}{p} = \sqrt{\frac{T}{3\,m}} \ll 1 \,, \tag{2.100}$$

since the WIMP is non-relativistic. What should really be compared to the typical expansion time is the relaxation time (Hofmann et al., 2001; Bringmann & Hofmann, 2007), *i.e.* the time needed to maintain local equilibrium. We assume $N_{\rm coll}$ collisions are needed for the change in momentum to be comparable to the momentum of the dark matter particle. Since scattering is a random process, this leads to

$$p = \delta p \sqrt{N_{\rm coll}} \,, \tag{2.101}$$

i.e.

$$N_{\rm coll} = \left(\frac{p}{\delta p}\right)^2 = \frac{3\,m}{T} \,. \tag{2.102}$$

The relaxation time can be written

$$\tau_{\rm rel} = \frac{N_{\rm coll}}{\Gamma_{\rm scat}} \simeq \frac{N_{\rm coll}}{n^{\rm eq} \langle \sigma_{\rm scat} v \rangle} \,. \tag{2.103}$$

Assuming the Standard Model scattering partners are relativistic and the scattering cross-section is $\sigma_{\rm scat} = G_{\rm F}^2 T^2$ with $G_{\rm F}$ the Fermi constant, we get by comparing $\tau_{\rm rel}$ to H^{-1}

$$T_{\rm kd} \simeq 10\,{\rm MeV} \left(\frac{m}{100\,{\rm GeV}}\right)^{1/4} \,. \tag{2.104}$$

This is indeed lower than the typical freeze-out temperature

$$T_{\rm fo} \simeq 4\,{\rm GeV} \left(\frac{m}{100\,{\rm GeV}}\right) \,. \tag{2.105}$$

While chemical decoupling takes place at temperatures in the GeV range for a dark matter mass of $10 - 100$ GeV, $T_{\rm kd}$ is in the MeV range (Schmid et al., 1999; Boehm et al., 2001; Chen et al., 2001). The scaling of $T_{\rm kd}$ with respect to the dark matter mass is not necessarily in $m^{1/4}$ as it depends on the mass scaling of the scattering cross-section. Note that in some models, kinetic decoupling happens close enough to chemical decoupling to affect the prediction of the relic density (Binder et al., 2017).

2.4.1 Boltzmann equation and decoupling temperature

Let us now go back to the Boltzmann equation. In practice, the evolution of the full phase-space density is not needed if we are only interested in the evolution of the temperature. It is enough

for our purpose to compute the second-order moment of the Boltzmann equation. Following Bringmann & Hofmann (2007), we define a dark matter temperature parameter as

$$T_{\rm dm} \equiv \frac{2}{3}\frac{1}{n}\int \frac{{\rm d}^3\vec{p}}{(2\pi)^3}\,\frac{\vec{p}^2}{2\,m}\,f(\vec{p})\,. \tag{2.106}$$

Note that $T_{\rm dm}$ is strictly speaking a temperature only when dark matter is still in equilibrium with the thermal bath (and we have $T_{\rm dm} = T$). After kinetic decoupling, local thermal equilibrium cannot be maintained and the temperature is ill-defined. The average kinetic energy in Eq. (2.106) is however well defined at any time, hence we can use it to define a temperature-like parameter for the out-of-equilibrium WIMP bath. Taking the second moment of the Boltzmann equation leads to (Bertschinger, 2006; Bringmann & Hofmann, 2007; Bringmann, 2009; Gondolo et al., 2012)

$$a\,\frac{{\rm d}T_{\rm dm}}{{\rm d}a} + 2\,T_{\rm dm} = -2\,\frac{\gamma(T)}{H(T)}(T_{\rm dm} - T)\,, \tag{2.107}$$

where

$$\gamma(T) = \sum_i \frac{g_i}{6\,m\,T}\int_0^\infty \frac{{\rm d}^3\vec{p}}{(2\pi)^3}\,f_i(1\pm f_i)\,\frac{p}{\sqrt{p^2+m_i^2}}\int_{-4\,p^2}^0 {\rm d}t\,(-t)\,\frac{{\rm d}\sigma_{\chi i}}{{\rm d}t} \tag{2.108}$$

is the momentum relaxation rate as given in Gondolo et al. (2012). This equation has the following boundary conditions: at early times, the dark matter is in thermal equilibrium with the photon bath and we have $T_{\rm dm} \propto a^{-1}$. Inserting this into Eq. (2.107) leads to

$$T - T_{\rm dm} = \frac{T_{\rm dm}}{2}\frac{H}{\gamma}\,, \tag{2.109}$$

and since at high temperature $\gamma \gg H$, we have $T_{\rm dm} \simeq T$. At late times, after kinetic decoupling, the momenta of dark matter particles redshift as $p \propto a^{-1}$ and according to the definition of the temperature parameter in Eq. (2.106), we have $T_{\rm dm} \propto a^{-2}$. Solving the Boltzmann equation in the general case requires numerical integration, however analytical expressions are available in some cases (Bertschinger, 2006; Bringmann & Hofmann, 2007; Visinelli & Gondolo, 2015). The kinetic decoupling temperature can be defined at the intersection between these two asymptotic regimes (Bringmann & Hofmann, 2007). Alternatively, it can be defined through $\gamma(T_{\rm kd}) = H(T_{\rm kd})$ (Visinelli & Gondolo, 2015). Using the former definition and using a zero-momentum transfer approximation for the collision term leads to a very simple expression for the kinetic decoupling temperature (Bringmann & Hofmann, 2007)

$$\frac{m}{T_{\rm kd}} = \left(\frac{a}{n+2}\right)^{1/(n+2)}\Gamma\left[\frac{n+1}{n+2}\right] \tag{2.110}$$

The expressions of n and a are given in App. B.3.5. The derivation of this expression relies on the zero-momentum transfer approximation which cannot be applied to the case of the pseudoscalar portal (this is because in that particular case $a = 0$ according to the expression given in the appendix). We limit our analysis to the scalar channel and therefore to the p-wave annihilation case, assuming the dark matter couples to the three generations of leptons. The resulting decoupling temperature is shown in the left panel in Fig. 2.11.

2.4.2 Minimal mass of dark matter halos

Kinetic decoupling is of great importance for WIMPs as it sets the size of the first dark matter structures to be formed in the Universe (Boehm et al., 2001; Hofmann et al., 2001; Berezinsky et al., 2003; Green et al., 2004; Boehm & Schaeffer, 2005; Loeb & Zaldarriaga, 2005; Green et al.,

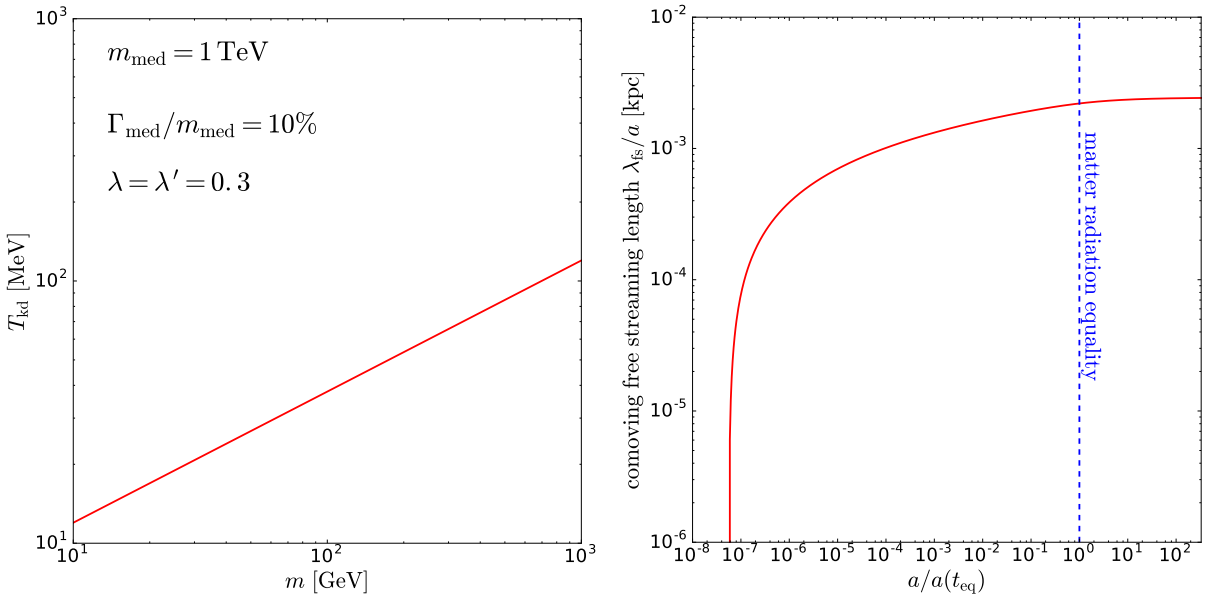

Figure 2.11 – Left panel: kinetic decoupling temperature as a function of the dark matter mass m, assuming the dark matter-SM mediator is a scalar particle. **Right panel:** comoving free-streaming length as a function of the scale factor.

2005; Profumo et al., 2006; Bertschinger, 2006; Bringmann & Hofmann, 2007; Bringmann, 2009). These primordial structures are the smallest bound dark matter structures and their mass is of great importance for dark matter searches. The damping scale in the CDM power spectrum is set by several mechanisms. Before kinetic decoupling, collisions between plasma particles and dark matter induce a pressure that counteracts the effect of gravity. During kinetic decoupling, a remaining viscous coupling between baryons and dark matter also suppresses power below some scale. Finally, once dark matter is kinetically decoupled it enters the free-streaming regime which further damps matter perturbations. The collisional and free-streaming damping mechanisms are discussed below.

2.4.2.1 Collisional damping

In the next chapter, we establish the evolution equation for the overdensity $\hat{\delta}(t,k)$ of a given mode k

$$\frac{\partial^2\hat{\delta}}{\partial t^2} + 2H\,\frac{\partial\hat{\delta}}{\partial t} + \left(c_{\rm s}^2\,\frac{k^2}{a^2} - 4\pi G_{\rm N}\overline{\rho}\right)\hat{\delta} = 0\,. \tag{2.111}$$

In this equation, $c_{\rm s}^2 = {\rm d}p/{\rm d}\rho$ is the sound speed in the plasma and $\overline{\rho}$ the average matter density of the Universe. Solutions of this equation have a very different behaviour depending on the sign of the term between brackets. If this term is positive, solutions have an oscillatory behaviour damped by the Hubble expansion. If this term is negative, solutions are growing like the scale factor. The transition between these two regimes sets the Jeans scale

$$k_{\rm J} \equiv \frac{2\pi a}{c_{\rm s}}\sqrt{\frac{G_{\rm N}\overline{\rho}}{\pi}}\,, \tag{2.112}$$

which can also be expressed as a length

$$\lambda_{\rm J} \equiv \frac{2\pi a}{k_{\rm J}} = c_{\rm s}\sqrt{\frac{\pi}{G_{\rm N}\overline{\rho}}}\,. \tag{2.113}$$

This length defines the scale at which pressure and gravity compensate each other, and below which the overdensity is damped because of pressure. In the radiation era, the sound speed is $c/\sqrt{3}$, such that the Jeans scale is almost equal to the horizon scale. The pressure term characterized by the sound speed is only relevant when WIMPs are kinetically coupled to the plasma, therefore this damping mechanism is collisional in nature. The minimal mass needed for a dark matter perturbation to overcome pressure forces is

$$M_{\rm ao} \equiv \frac{4}{3}\,\pi\,\rho_{\rm cdm}(t_{\rm kd})\left(\frac{\lambda_{\rm J}}{2}\right)^3 . \tag{2.114}$$

In this expression, "ao" stands for acoustic oscillations. In a relativistic fluid $\overline{\rho}$ is given in Eq. (2.54). Conservation of number density and entropy yields the dark matter mass density as a function of the photon bath temperature:

$$\rho_{\rm cdm}(T) = \rho_{\rm cdm}(T_0)\frac{s(T)}{s(T_0)} = \rho_{\rm c}\,\Omega_{\rm cdm}\frac{h_{\rm eff}(T)}{h_{\rm eff}(T_0)}\left(\frac{T}{T_0}\right)^3 , \tag{2.115}$$

where T_0 is the CMB temperature today. Putting this together, we get $M_{\rm ao} \propto T^{-3}$. We show $M_{\rm ao}$ as function of the kinetic decoupling temperature in the left panel in Fig. 2.12. We obtain very small masses, ranging from $10^{-11}\,{\rm M}_\odot$ to $10^{-5}\,{\rm M}_\odot$. Note that $M_{\rm ao}$ only depends on the dark matter mass through the decoupling temperature $T_{\rm kd}$.

2.4.2.2 Collisionless damping

After dark matter gets kinetically decoupled, it enters the free-streaming regime, which induces an additional damping of perturbations. This damping occurs because structures only start growing efficiently after matter-radiation equality. Before equality, the growth is suppressed by the Meszaros effect (Meszaros, 1974). Between the time of decoupling and the time when structures start growing, dark matter particles can free-stream away from perturbations and thus wash out the small-scale power spectrum. Unlike the previous damping mechanism we discussed, this damping is collisionless in nature. The physical distance travelled by a dark matter particle from the time of decoupling $t_{\rm kd}$ to some later time t is (see *e.g.*, Berezinsky et al. (2003))

$$\lambda_{\rm fs}(t) = a(t)\int_{t_{\rm kd}}^{t}\frac{v_{\rm cdm}(t')}{a(t')}\,{\rm d}t' , \tag{2.116}$$

where $v_{\rm dm}$ is the dark matter particle speed. This speed can be estimated from the pseudo-temperature of the dark matter bath. We have, after decoupling

$$T_{\rm cdm}(t) = T_{\rm kd}\left(\frac{a(t_{\rm kd})}{a(t)}\right)^2 , \tag{2.117}$$

and

$$v_{\rm cdm}(t) \simeq \sqrt{\langle v^2\rangle} = \sqrt{\frac{3\,T_{\rm cdm}(t)}{m}} . \tag{2.118}$$

Changing variable from t to $a(t)$ in Eq. (2.116) and using the expression of the Hubble rate in Eq. (2.28) we get

$$\lambda_{\rm fs}(t) = \frac{a(t)\,a(t_{\rm kd})}{H_0}\sqrt{\frac{3\,T_{\rm kd}}{m}}\int_{a(t_{\rm kd})}^{a(t)}\frac{{\rm d}a}{a^3\sqrt{\Omega_{\rm m}\,a^{-3}+\Omega_{\rm r}\,a^{-4}+\Omega_\Lambda}} . \tag{2.119}$$

It is not very clear at what time t this free-streaming length should be evaluated. In principle, we should take $t = t_0$ but after matter-radiation equality structures start to grow efficiently

and WIMPs can get captured by the potential wells and stop free-streaming. Fortunately, the comoving length $\lambda_{\rm fs}(t)/a(t)$ saturates at matter-radiation equality, see right panel in Fig. 2.11, therefore we evaluate it there. The free-streaming mass at equality is then defined as

$$M_{\rm fs} \equiv \frac{4}{3}\,\pi\,\rho_{\rm cdm}(t_{\rm eq})\left(\frac{\lambda_{\rm fs}}{2}\right)^3 . \tag{2.120}$$

This quantity is shown in the left panel in Fig. 2.12. Unlike the acoustic oscillation mass, it depends explicitly on the dark matter mass and it gets lower as the mass gets higher. This is because, at a given $T_{\rm kd}$, the speed of high-mass dark matter particles is lower at matter-radiation equality. Also, for a given $x_{\rm kd}$, heavier particles have more time to decrease their speed before equality. Since the smallest dark matter objects observed in the Universe are dwarf spheroidal galaxies with masses around $10^7 - 10^8\,{\rm M}_\odot$, a lower limit can be set on the dark matter mass by requiring $M_{\rm fs} \lesssim 10^7\,{\rm M}_\odot$. This leads to a limit $m \gtrsim$ keV, which corresponds to the typical mass of warm dark matter candidates. Note that this bound only applies to thermally produced dark matter.

The mass under which all perturbations are erased is given by the maximum of $M_{\rm ao}$ and $M_{\rm fs}$

$$M_{\rm min} \equiv {\rm Max}[M_{\rm ao}, M_{\rm fs}]\,. \tag{2.121}$$

It is the typical mass of the first dark matter structures to form and, since structure formation is a hierarchical process, the core mass of the smallest dark matter halos. Using the mass dependence of the decoupling temperature given in Eq. (2.110), we can express the minimal mass $M_{\rm min}$ as a function of the dark matter mass m. This is shown in the right panel in Fig. 2.12. We see that the minimal mass is a decreasing function of the dark matter mass: heavier dark matter candidates lead to smaller structures. This correlation is also recovered in more complicated model such as supersymmetry (Bringmann, 2009). This provides a direct link between astrophysics and the microscopic properties of the dark matter particle. This allows one to put generic constraints on the dark matter interaction properties using structure formation (Boehm & Schaeffer, 2005; Cyr-Racine et al., 2016).

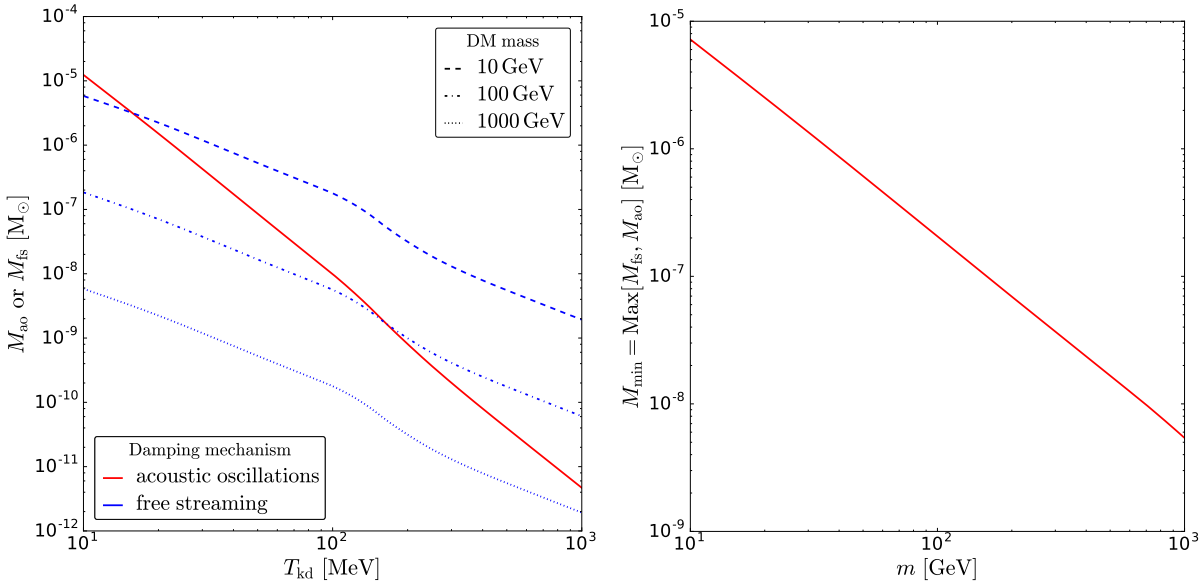

Figure 2.12 – Left panel: cut-off mass as a function of the kinetic decoupling temperature, for collisional damping (red curve) and collisionless damping (blue curve). **Right panel:** minimal halo mass as a function of the dark matter mass.

As stated above, the smallest dark matter structures observed today are dwarf spheroidal galaxies with masses $10^7 - 10^8\,{\rm M}_\odot$. This mass range is orders of magnitude higher than the

masses we have just computed. There is no contradiction here because halos with masses smaller than those of ultra-faint dwarf galaxies are too light to efficiently accrete baryons and form stars, therefore they remain dark and not directly observable. This does not mean these small structures are impossible to probe. In particular, the presence of such structures in our Galaxy could impact on dark matter searches. In the next chapter, we explore the formation of dark matter halos and study their distribution in our Galaxy.

Chapter 3

Dark matter halos and subhalos in the Universe

This chapter is devoted to the study of dark matter structures in the Universe. The first section focuses on the formation of dark matter halos, starting from the theory of cosmological perturbations in a Newtonian framework. We investigate the statistics of the perturbations and use the Press-Schechter theory to derive the halo mass function. The internal structure of CDM halos is discussed based on the results of numerical simulations and theoretical arguments. The second section focuses on halos within halos, which are called subhalos. The interactions of these subhalos with their host is studied in details, including the effect of baryonic matter on these substructures. Finally, we elaborate a semi-analytical model to predict the distribution of subhalos in our own Galaxy, and we obtain the first kinematically consistent Milky Way halo model including a self-consistent subhalo population.

3.1 The formation of dark matter structures

3.1.1 Evolution of cosmological perturbations

3.1.1.1 Newtonian perturbation theory

We wish to give a brief description of the theory of cosmological structure formation, following Mo et al. (2010) and Knobel (2012). We study a non-relativistic ideal fluid with density $\rho(\vec{r},t)$, pressure $p(\vec{r},t)$ and velocity field $\vec{v}(\vec{r},t)$ where t is the cosmic time and $\vec{r}$ the physical position vector. We restrict ourselves to a Newtonian analysis, which is a valid approximation for modes much smaller than the horizon. The fundamental hydrodynamical equations of Newtonian gravity are:

$$\begin{cases} \partial_{\mathrm{t}}\rho + \vec{\nabla}.(\rho\vec{v}) = 0 \quad \text{(continuity)} \\ \partial_{\mathrm{t}}\vec{v} + (\vec{v}.\vec{\nabla})\vec{v} = -(\vec{\nabla}p)/\rho - \vec{\nabla}\phi \quad \text{(Euler)} \\ \Delta\phi = 4\pi G_{\mathrm{N}}\rho \quad \text{(Poisson)}\,, \end{cases} \tag{3.1}$$

where ϕ is the gravitational potential. This is not a closed system since we have five equations for six unknowns (ρ, p, $\vec{v}$ and ϕ). We must add an equation of state for the fluid

$$p = p(\rho, s) \quad \text{(state)}\,, \tag{3.2}$$

where s is the entropy per unit mass of the fluid. Finally, we add a conservation equation for the entropy

$$\frac{\partial s}{\partial t} + \vec{\nabla}.(s\vec{v}) = 0 \quad \text{(entropy conservation)}\,. \tag{3.3}$$

Since we only consider the case of a single fluid, entropy is indeed conserved. The hydrodynamical treatment is valid if the mean free path of the particles constituting the fluid is much smaller than the scale of interest. In the case of a collisionless fluid like dark matter, the treatment holds as long as we are considering scales larger than the free streaming scale (which means dissipative processes can be neglected). A fully consistent treatment of the growth of perturbations must rely on the relativistic Boltzmann equation, which we do not discuss here. The generic effect of free streaming is the damping of perturbations below the free streaming scale, as discussed in the previous chapter (see *e.g.*, Bertschinger (2006) for a fully consistent treatment of dark matter perturbations). Note that we only wish to describe the evolution of a non-relativistic fluid ($v \ll c$ and $p \ll \rho c^2$) and we ignore the effect of relativistic components (like neutrinos) and the cosmological constant. The inclusion of such components would introduce relativistic pressure and also affect the expansion rate. The modern formalism of relativistic perturbation theory was developed by Bardeen (1980).

We wish to study the growth of perturbations under the effect of gravity, therefore we perturb our system of equation by defining

$$\begin{aligned} \rho(\vec{r},t) &= \overline{\rho}(t) + \delta\rho(\vec{r},t) && (3.4)\\ p(\vec{r},t) &= \overline{p}(t) + \delta p(\vec{r},t) && (3.5)\\ \vec{v}(\vec{r},t) &= \overline{\vec{v}}(t,\vec{r}) + \delta\vec{v}(\vec{r},t) && (3.6)\\ \phi(\vec{r},t) &= \overline{\phi}(t,\vec{r}) + \delta\phi(\vec{r},t) && (3.7) \end{aligned}$$

The over-lined symbols refer to the (homogeneous and isotropic) background quantities. The perturbation of the velocity field $\delta\vec{v}$ is called the *peculiar* velocity field. Note that we do not perturb the entropy, *i.e.* we are only considering *isentropic* perturbations (also called *curvature* perturbations in a relativistic context). Again, this is because we only consider a single fluid at all times. Using Eq. (3.2), we express the pressure perturbation as

$$\delta p = \left(\frac{\partial p}{\partial \rho}\right)_S \delta\rho \equiv c_\mathrm{s}^2 \delta\rho\,, \tag{3.8}$$

where c_s is the speed of sound in the fluid (assumed independent of the density in the following). It is convenient to perform calculations in comoving coordinates $\vec{x} = \vec{r}/a(t)$ where $\vec{x}$ is time-independent in a FRW background. The average velocity field is then

$$\vec{\overline{v}}(t) \equiv \dot{\vec{r}} = H(t)\,\vec{r}\,, \tag{3.9}$$

where $H = \dot{a}/a$ is the Hubble parameter and Eq. (3.9) is simply the Hubble law. Derivatives transform as

$$\begin{aligned} \vec{\nabla}_r &= \frac{1}{a}\vec{\nabla}_x \\ \left.\frac{\partial}{\partial t}\right|_r &= \left.\frac{\partial}{\partial t}\right|_x - H\vec{x}.\vec{\nabla}_x \end{aligned} \tag{3.10}$$

The hydrodynamical equations can be written, at first order in perturbation theory, as

$$\begin{cases} \partial_t \delta\rho|_x + 3H\delta\rho + \overline{\rho}(\vec{\nabla}_x.\delta\vec{v})/a = 0 \\ \partial_t \delta\vec{v}|_x + H\delta\vec{v} = -c_\mathrm{s}^2(\vec{\nabla}_x\,\delta\rho)/(a\overline{\rho}) - (\vec{\nabla}_x)/a\,\delta\phi \\ \Delta_x\,\delta\phi = 4\pi G_\mathrm{N} a^2 \delta\rho\,. \end{cases} \tag{3.11}$$

Since the equations above are all linear in the perturbed quantities, it is convenient to move to Fourier space by defining

$$\begin{aligned} \delta\hat{\rho}(\vec{k},t) &\equiv \frac{1}{V}\int \delta\rho(\vec{x},t)\,e^{-i\vec{k}.\vec{x}}\,\mathrm{d}^3\vec{x} \\ \delta\rho(\vec{x},t) &\equiv \frac{V}{(2\pi)^3}\int \delta\hat{\rho}(\vec{k},t)\,e^{i\vec{k}.\vec{x}}\,\mathrm{d}^3\vec{k} \end{aligned} \tag{3.12}$$

where $\vec{k}$ is the comoving wave vector. The volume V in Eq. (3.12) is introduced to ensure that $\delta\rho(\vec{x})$ and $\delta\hat{\rho}(\vec{k})$ have the same dimensions. We similarly define $\delta\hat{\vec{v}}(\vec{k},t)$. Note that the spatial integral is performed over a large volume $V \propto L^3$ with L larger than any scale under study here. In Fourier space, we now get

$$\begin{cases} \partial_\mathrm{t}\delta\hat{\rho}|_k + 3H\delta\hat{\rho} + \overline{\rho}\, i\vec{k}.\delta\vec{v}/a = 0 \\ \partial_\mathrm{t}\delta\hat{\vec{v}}\Big|_k + H\delta\hat{\vec{v}} = -c_\mathrm{s}^2\, i\vec{k}\,\delta\hat{\rho}/(a\overline{\rho}) - i\vec{k}\,\delta\hat{\phi}/a \\ -k^2\delta\hat{\phi} = 4\pi G_\mathrm{N} a^2 \delta\hat{\rho}\,. \end{cases} \tag{3.13}$$

We introduce the relative density perturbation, or overdensity, as

$$\hat{\delta}(\vec{k},t) \equiv \frac{\hat{\rho}(\vec{k},t) - \overline{\rho}(t)}{\overline{\rho}(t)} = \frac{\delta\hat{\rho}}{\overline{\rho}}\,. \tag{3.14}$$

Combining Eqs. (3.13) leads to

$$\left.\frac{\partial^2\hat{\delta}}{\partial t^2}\right|_k + 2H\left.\frac{\partial\hat{\delta}}{\partial t}\right|_k + \left(c_\mathrm{s}^2\frac{k^2}{a^2} - 4\pi G_\mathrm{N}\overline{\rho}\right)\hat{\delta} = 0\,. \tag{3.15}$$

This is the evolution equation for the fluid overdensity $\delta(\vec{k},t)$ in an expanding Universe. It is a second-order differential equation, thereby it has two independent solutions for each Fourier mode $\vec{k}$.

3.1.1.2 Jeans instability

To understand the behaviour of the overdensity, we first consider the case of a static Universe. We have $H = 0$ and $\overline{\rho}$ is a constant, Eq. (3.15) then simply becomes

$$\left.\frac{\partial^2\hat{\delta}}{\partial t^2}\right|_k + \left(c_\mathrm{s}^2\frac{k^2}{a^2} - 4\pi G_\mathrm{N}\overline{\rho}\right)\hat{\delta} = 0\,. \tag{3.16}$$

The form of the solution depends on the sign of the quantity in front of δ. If this quantity is negative, then there is an exponentially growing solution and an exponentially decaying one. If the quantity is positive, we get two independent oscillating solutions. This behaviour is the result of a competition between pressure and gravity. Thus the time evolution of a perturbation depends critically on its size, which must be compared to the *Jeans length*

$$\lambda_\mathrm{J} \equiv \frac{2\pi a}{k_\mathrm{J}} = c_\mathrm{s}\sqrt{\frac{\pi}{G_\mathrm{N}\overline{\rho}}}\,. \tag{3.17}$$

A perturbation at a (physical) scale larger than λ_J either grows and enters the non-linear regime $\delta \geqslant 1$, or decays (depending on the initial condition on δ). Smaller perturbations however are not able to overcome the pressure and keep oscillating. The criterion is often expressed in terms of mass rather than length, by defining the *Jeans mass*

$$M_\mathrm{J} \equiv \frac{4}{3}\pi\overline{\rho}\left(\frac{\lambda_\mathrm{J}}{2}\right)^3 = \frac{c_\mathrm{s}^3}{6}\sqrt{\frac{\pi^5}{G_\mathrm{N}^3\overline{\rho}}}\,. \tag{3.18}$$

This is simply the mass within a sphere of diameter λ_J. We can estimate the Jeans length in the baryonic matter fluid right after recombination. The fluid is then made of hydrogen atoms which are decoupled from radiation. If the fluid is modelled as an ideal monoatomic gas, the speed of sound is

$$c_\mathrm{s} = \left(\gamma\frac{k_\mathrm{B}T_\mathrm{rec}}{m_\mathrm{p}}\right)^{1/2}\,, \tag{3.19}$$

with γ the adiabatic index ($\gamma = 5/3$ for a monoatomic gas), $T_{\rm rec} \simeq 2.7 \times (1+1100)\,{\rm K}$ is the temperature at recombination and $m_{\rm p}$ is the proton mass. We get $c_{\rm s} \simeq 193\,{\rm m/s}$ and this leads to the *comoving* Jeans Length

$$\tilde{\lambda}_{\rm J} \simeq 0.01 \left(\Omega_{\rm b,0} h^2\right)^{-1/2} {\rm Mpc}\,, \tag{3.20}$$

and the corresponding Jeans mass

$$M_{\rm J} \simeq 1.5 \times 10^5 \left(\Omega_{\rm b,0} h^2\right)^{-1/2} M_\odot\,. \tag{3.21}$$

This is roughly the mass of a globular cluster, therefore after recombination all baryons start falling efficiently into perturbations the size of globular clusters and beyond. Before recombination, the tight coupling between matter and radiation induces a large pressure and increases the Jeans mass by roughly ten orders of magnitude (Mo et al., 2010) which corresponds to the scale of a super-cluster. The formation of baryonic structures therefore begins only at the end of recombination.

We neglected the effect of the expansion in the analysis above. The expansion enters through a friction term in Eq. (3.15). This friction damps the oscillatory modes and slows down the growth (decay) of the growing (decaying) modes. We can still find solutions in some special cases. A useful example is a matter-dominated Universe, which is a valid approximation when $z \ll z_{\rm eq}$ and the cosmological constant is still negligible. We focus on modes much larger than the Jeans length, in which case the overdensity is solution of

$$\left.\frac{\partial^2\delta}{\partial t^2}\right|_k + 2H \left.\frac{\partial\delta}{\partial t}\right|_k - 4\pi G_{\rm N}\bar{\rho}\,\delta = 0\,. \tag{3.22}$$

This equation is also valid for all modes of perturbations in the CDM fluid since it is pressureless (and therefore has a vanishing speed of sound). In the case of a pressureless fluid, the solutions of Eq. (3.22) can be found, see *e.g.*, Mo et al. (2010), and they read

$$\begin{aligned} \delta_{\rm decay}(t) &\propto H(t)\,, \\ \delta_{\rm growth}(t) &\propto H(t) \int_0^t \frac{{\rm d}t'}{a^2(t')H^2(t')}\,. \end{aligned} \tag{3.23}$$

In the case of a matter-dominated universe, it is straightforward to show $\delta_{\rm decay} \propto t^{-1}$ (also valid in a radiation-dominated universe) and $\delta_{\rm growth} \propto t^{2/3}$. While perturbations grow exponentially fast in a static Universe, the growth follows a power law in the case of an expanding Universe. Note that the growing mode has the same time evolution as the scale factor, *i.e.* $\delta_{\rm growth} \propto a$, in the matter dominated case. The general solution of Eq. (3.22) can be written

$$\delta(\vec{k},t) = \delta_-(\vec{k}) D_-(t) + \delta_+(\vec{k}) D_+(t)\,. \tag{3.24}$$

where δ_- and δ_+ are set by the initial conditions. We only focus on the growing part. We simply have $\delta(\vec{k},t) = \delta_+(\vec{k}) D_+(t)$ with D_+ the *linear growth function*, or *linear growth factor* (Heath, 1977). An approximate formula for the growth function is given by Carroll et al. (1992); Hamilton (2001)

$$D_+(z) = \frac{1}{1+z}\frac{g(z)}{g(0)}\,, \tag{3.25}$$

where

$$g(z) = \frac{\Omega_{\rm m}(z)}{\Omega_{\rm m}^{4/7}(z) - \Omega_\Lambda(z) + \left(1 + \frac{\Omega_{\rm m}(z)}{2}\right)\left(1 + \frac{\Omega_\Lambda(z)}{70}\right)}\,. \tag{3.26}$$

The growth function is shown in Fig. 3.1.

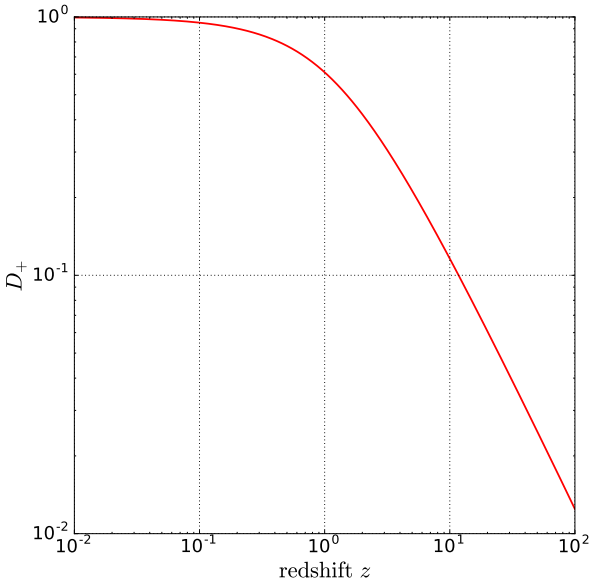

Figure 3.1 – Linear growth factor as given in Eq. (3.25), for the cosmology of Ade et al. (2016).

3.1.1.3 Non-linear evolution: the spherical collapse case

Derivation We would like to gain further insights on the evolution of overdensities in the non-linear regime. Unfortunately, there are no known solutions of the hydrodynamical equation in the general case. The standard way of investigating the non-linear growth of structures is to rely on cosmological numerical simulations. It is possible however to derive useful analytical results by considering simple, highly symmetric cases. Here we focus on the growth of an isolated, *spherical* perturbation over a homogeneous and isotropic background, following the treatment given in Knobel (2012). We consider the matter as being homogeneously distributed in the spherical perturbed region, with a density $\rho = \overline{\rho} + \delta\rho$ where $\overline{\rho}$ is the background density and $\delta\rho > 0$. By virtue of the Birkhoff theorem (Weinberg, 1972), the background and the perturbation evolve independently. The scale factor $a(t)$ of the background obeys the Friedmann equation with zero curvature (we further assume no cosmological constant)

$$\left(\frac{\dot{a}}{a}\right)^2 = \frac{8\pi G_\mathrm{N}}{3}\,\overline{\rho}\,. \tag{3.27}$$

The background density evolves as

$$\overline{\rho}(t) = \frac{1}{6\pi G_\mathrm{N} t^2}\,. \tag{3.28}$$

The "universe" defined by the perturbation, however, has a curvature $K = 1$ since it is a collapsing, closed region. The corresponding scale factor $\mathcal{A} \equiv R(t)/R_0$ then obeys

$$\left(\frac{\dot{\mathcal{A}}}{\mathcal{A}}\right)^2 = \frac{8\pi G_\mathrm{N}}{3}\,\rho - \frac{c^2}{R_0^2}\,, \tag{3.29}$$

where $R_0 = R(t_0)$ is the radius of the perturbation at the present day. We perform the following change of variable

$$\mathrm{d}t = \frac{\mathcal{A} R_0}{c}\,\mathrm{d}\tau = \frac{R}{c}\,\mathrm{d}\tau\,, \tag{3.30}$$

where τ is a (dimensionless) conformal time. Introducing the (constant) mass within the perturbation $M = 4/3\,\pi\rho_0 R_0^3$, Eq. (3.29) can be written

$$\left(\frac{\mathrm{d}\mathcal{A}}{\mathrm{d}\tau}\right)^2 = 2\,\frac{G_\mathrm{N} M}{c^2 R_0}\mathcal{A} - \mathcal{A}^2\,. \tag{3.31}$$

This equation has the following solution for the growing mode

$$\mathcal{A}(\tau) = \frac{G_{\rm N} M}{c^2 R_0}(1 - \cos(\tau)) \tag{3.32}$$

We can now express the cosmic time as a function of the conformal time by using Eq. (3.30)

$$t(\tau) = \frac{G_{\rm N} M}{c^3}\left(\tau - \sin(\tau)\right), \tag{3.33}$$

and inject this into the expression of the background density in Eq. (3.28) to get

$$\overline{\rho}(\tau) = \frac{1}{6\pi G_{\rm N}}\left[\frac{G_{\rm N} M}{c^3}(\tau - \sin(\tau))\right]^{-2}. \tag{3.34}$$

The time evolution of the overdensity is then

$$\delta(\tau) = \frac{\rho}{\overline{\rho}} - 1 = \frac{9}{2}\frac{(\tau - \sin(\tau))^2}{(1 - \cos(\tau))^3} - 1\,. \tag{3.35}$$

This expression is valid for the entire lifetime of the overdensity, even when it enters the non-linear regime. Note that it does not explicitly depend on the mass of the perturbation.

Time evolution Let us analyse in detail the evolution of the overdensity. At early times we have $\tau \ll 1$ and

$$\delta(\tau) = \frac{3}{20}\tau^2 = \frac{3}{20}\left(\frac{6\,c^3}{G_{\rm N} M}t\right)^{2/3}, \tag{3.36}$$

which is obtained by using Eq. (3.33). The $\delta \propto t^{2/3}$ behaviour is precisely the one predicted by linear theory for a matter-dominated universe. The evolution quickly departs from the prediction of linear theory however, as can be seen on the left panel in Fig. 3.2. While the linear overdensity remains finite at all times, the spherical model prediction diverges as $\tau \to 2\pi$. On the right panel in Fig. 3.2, we show the evolution of the scale factor $\mathcal{A}$. At first, $\mathcal{A}$ follows the evolution of the background $\mathcal{A} \propto \tau^2$ then quickly decouples and starts collapsing at $\tau = \pi$.

Virialization The spherical model predicts a collapse of the overdense region to a singularity. However, a realistic perturbation is not perfectly spherical and the system is expected to reach a steady state. The equilibrium of a self-gravitating structure can be characterized via the *scalar virial theorem*, see *e.g.*, Binney & Tremaine (1987), which states that a system in a steady state satisfies

$$2K + W = 0\,. \tag{3.37}$$

In this equation, K is the total kinetic energy and W the potential energy of the system. We can ask what is the radius at which the spherical perturbation reaches its virial equilibrium. First, let us compute the potential energy of a homogeneous sphere of mass M and radius R. We consider a radial shell of thickness $\mathrm{d}r$ at radius r, its potential energy is

$$\mathrm{d}W = -\frac{G_{\rm N}\, m_{\rm shell}\,(4/3\,\pi\, r^3\rho)}{r}, \tag{3.38}$$

where $m_{\rm shell} = 4\pi r^2 \mathrm{d}r$. Integrating over all radial shells, we get

$$W = -\frac{3}{5}\frac{G_{\rm N} M^2}{R}\,. \tag{3.39}$$

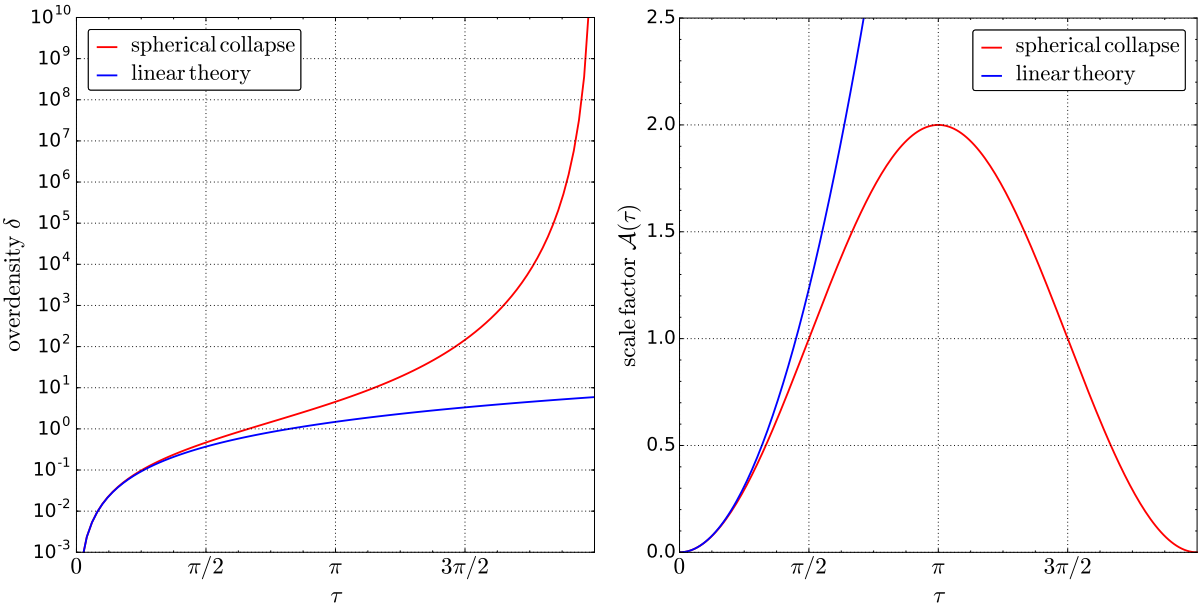

Figure 3.2 – Left panel: Evolution of the overdensity δ as a function of the dimensionless conformal time τ. Are shown the prediction of the spherical collapse model (red curve) and the linear theory (blue curve) **Right panel:** Evolution of the scale factor (with arbitrary normalization) within the perturbation as a function of the conformal time.

The radius of the spherical density has no choice but to follow the evolution of the scale factor, as displayed on the right panel of Fig. 3.2. Consequently the scale factor, and therefore the radius, reaches its maximum at $\tau = \pi$. At this point we have $\mathrm{d}R/\mathrm{d}\tau = 0$ and therefore the kinetic energy is $K = 0$. Consequently the total energy of the structure is $E_{\rm tot}(R_{\rm max}) = W(R_{\rm max})$. Now let us compute the kinetic energy when the radius is $R = R_{\rm max}/2$:

$$\begin{aligned} K(R_{\rm max}/2) &= E_{\rm tot} - W(R_{\rm max}/2) \\ &= W(R_{\rm max}) - W(R_{\rm max}/2) \\ &= -\frac{1}{2}\, W(R_{\rm max}/2)\,, \end{aligned} \tag{3.40}$$

which gives the virial relation in Eq. (3.37). Therefore we can assume the structure reaches equilibrium when its radius has decreased to a value equal to half its maximum $R_{\rm vir} = R_{\rm max}/2$. This corresponds to a conformal time $\tau_{\rm vir} = 3\pi/2$. However, simulations show that virial equilibrium is reached later so $\tau_{\rm vir} = 2\pi$ is usually assumed. The corresponding cosmic time is computed using Eq. (3.33)

$$t_{\rm vir} = 2\pi\, \frac{G_{\rm N} M}{c^3}\,. \tag{3.41}$$

The spherical collapse model predicts an infinite density at this time, which is not of great use. The prediction of the linear theory, however, remains finite. If the linear overdensity $\delta_{\rm lin}(t)$ is defined using Eq. (3.36), we get at the time of virial equilibrium

$$\delta_{\rm lin}(t_{\rm vir}) = \frac{3}{20}\left(\frac{6\,c^3}{G_{\rm N} M} t_{\rm vir}\right)^{2/3} = \frac{3}{20}\,(12\pi)^{2/3} \simeq 1.686\,. \tag{3.42}$$

This value is independent of the perturbation's mass or its time of collapse and is therefore universal. Note this value does not reflect in any way the actual overdensity of the structure since it has fully entered the non-linear regime by then. It is a very useful result nonetheless because it allows to define a threshold for the virialization of a non-linear structure through *linear* theory. This remarkable result is the starting point to compute the mass function of dark matter halos.

3.1.2 The halo mass function

The previous section dealt with the time evolution of small perturbations. In this section, we investigate the statistics of these perturbations and compute the Press & Schechter mass function of dark matter halos.

3.1.2.1 Power spectrum and transfer function

We previously defined the overdensity field $\delta(\vec{x})$. It is standard, when studying the statistics of cosmological structures, to consider δ as being a *random field*. This is meaningful if the initial conditions on the density field are set by a stochastic process. This is the case in the standard inflationary paradigm where the density fluctuations are seeded by the quantum fluctuations of a scalar field called the inflaton (Guth & Pi, 1982; Hawking, 1982; Starobinsky, 1982; Bardeen et al., 1983). When dealing with a random field, it is convenient to introduce its moments, which characterize the distribution function of the field. By definition of the overdensity field, the first moment is $\langle\delta(\vec{x})\rangle = 0$. The two-point correlation function is a priori less trivial and reads

$$\xi(\vec{x}_1, \vec{x}_2) \equiv \langle\delta(\vec{x}_1)\delta(\vec{x}_2)\rangle \ , \tag{3.43}$$

where the average is taken over different *initial* configurations of the overdensity field. In agreement with the Cosmological Principle, the overdensity field is assumed statistically homogeneous and isotropic, therefore $\xi(\vec{x}_1, \vec{x}_2) = \xi(|\vec{x}_1 - \vec{x}_2|)$. Consequently we can write

$$\xi(r) = \langle\delta(\vec{x} + \vec{r})\,\delta(\vec{x})\rangle \ . \tag{3.44}$$

The variance of the field is simply $\sigma^2 = \xi(0)$. Using our definition of the Fourier transform in Eq. (3.12), we can show

$$\xi(r) = \frac{1}{(2\pi)^3}\int P_{\rm m}(k)\, e^{i\vec{k}.\vec{r}}\,\mathrm{d}^3\vec{k}\,, \tag{3.45}$$

where

$$P_{\rm m}(k) \equiv V\,\left\langle|\delta(\vec{k})|^2\right\rangle \tag{3.46}$$

is the *matter power spectrum*. Note that the power spectrum has dimensions of a volume. A dimensionless power spectrum is often introduced

$$\Delta^2_{\rm m}(k) = \frac{k^3 P_{\rm m}(k)}{2\pi^2}\,, \tag{3.47}$$

so that integration of a quantity $A(k)$ over momentum $\vec{k}$ can be written

$$\int\frac{\mathrm{d}^3\vec{k}}{(2\pi)^3}\,P_{\rm m}(k)\,A(k) = \int\mathrm{d}\ln k\,\Delta^2_{\rm m}(k)\,A(k)\,. \tag{3.48}$$

For the correlation function, integration over the angles gives the simple expression

$$\xi(r) = \int_0^\infty \Delta^2_{\rm m}(k)\,\frac{\sin(kr)}{kr}\,\mathrm{d}\ln k\,. \tag{3.49}$$

To compute the distribution of cosmological structures, we have to make an assumption on the distribution function of the overdensity field. The simplest case is to assume the field follows a Gaussian distribution at each point $\vec{x}$

$$\mathcal{P}_x(\delta)\,\mathrm{d}\delta = \frac{1}{\sqrt{2\pi\sigma^2}}\exp\left[-\frac{\delta^2}{2\sigma^2}\right]\,\mathrm{d}\delta\,. \tag{3.50}$$

Since the variance is independent of $\vec{x}$, so is the distribution. The real and imaginary part of $\delta(\vec{k})$ are also distributed according to a Gaussian distribution. Additionally, all modes $\vec{k}$ are independent of each other. A Gaussian distribution is conveniently entirely determined by its second moment, therefore the power spectrum alone is enough to characterize the whole distribution. This is a very nice and practical feature, and it is standard to assume a Gaussian distribution for the overdensity field for this reason. This simple case is also a standard prediction of many models of inflation (Martin et al., 2014). Furthermore, observations so far do not show any sign of non-gaussianity. We do not expect the Gaussian assumption to hold in the non-linear $\delta \gtrsim 1$ regime however. One reason is that the non-linear evolution mixes the modes, it is therefore unlikely that their distribution remain independent. Another simpler reason is that by definition of the overdensity in Eq. (3.14) we have $\delta \geqslant -1$, while the Gaussian distribution is even and extends to arbitrary low values of δ.

Inflationary models predict the power spectrum of primordial fluctuations, which is usually called the *primordial power spectrum*. What is needed to compute the mass function of dark matter halos is the power spectrum today. Perturbation modes today are related to their initial condition through the *transfer function* $T(k)$. Parametric fitting formulas for $T(k)$ are given by Eisenstein & Hu (1998); Eisenstein & Hu (1999). The transfer function is shown on the left panel in Fig. 3.3. We show $T(k)$ when only CDM is taken into account (blue curve) and when baryonic features are included (red curve). There is little difference between the two, though one notes the presence of wiggles in the transfer function accounting for baryonic effects. This is a signature of baryonic acoustic oscillations. The asymptotic behaviour of the transfer function is the following:

$$T(k) = \begin{cases} 1 \text{ for } k \ll k_{\rm eq} \\ \frac{\ln(k)}{k^2} \text{ for } k \gg k_{\rm eq} \end{cases} \tag{3.51}$$

where $k_{\rm eq}$ is the mode entering the horizon at equivalence. The suppression of power on small scales in due to the suppression of growth during the radiative era [the Meszaros effect (Meszaros, 1974)]: small-scale modes entering the horizon before matter-radiation equality grow logarithmically until equality, while mode entering during the matter-dominated era grow efficiently right away.

The power spectrum today is related to the primordial spectrum $P_{\rm m,0}$ through

$$P_{\rm m}(k) = |T(k)|^2 \, P_{\rm m,0}(k) \, . \tag{3.52}$$

The primordial power spectrum inferred from observations of the Cosmic Microwave Background has a power-law behaviour $P_{\rm i}(k) \propto k^{n_{\rm s}}$ with $n_{\rm s} = 0.9677 \pm 0.0060$ according to Ade et al. (2016). A spectrum with index $n_{\rm s} = 1$ is called scale-invariant or Harrison-Zel'dovich spectrum (Harrison, 1970; Zel'dovich & Novikov, 1970; Peebles & Yu, 1970), therefore the power spectrum of the CMB is nearly scale-invariant. The term scale-invariant can be understood by looking at the *gravitational potential power spectrum* $P_\phi \propto \langle |\delta\phi|^2 \rangle$. The potential fluctuation is related to the density fluctuation through Poisson's equation (3.13) which gives

$$\delta\phi(k) = -\frac{3}{2} \frac{H_0^2 \Omega_{\rm m,0}}{k^2 \, a} \, \delta(k) \, . \tag{3.53}$$

Consequently, we have $P_\phi \propto k^{-4} \, P_{\rm m}(k) \propto k^{n_{\rm s}-4}$ and the dimensionless power spectrum $\Delta^2_\phi \propto k^3 \, P_\phi \propto k^{n_{\rm s}-1}$. For a value $n_{\rm s} = 1$, we see that the dimensionless gravitational potential power spectrum is independent of k. This is not true for the dimensionless *matter* power spectrum however, which has the scaling $\Delta^2_{\rm m} \propto k^{n_{\rm s}+3}$.

The ΛCDM transfer function as shown in the left panel on Fig. 3.3 assumes a perfectly cold dark matter fluid. If the dark matter particle is a WIMP, the collisional and collisionless damping mechanisms discussed in Sec. 2.4 leave an imprint on the dark matter transfer function. This translates into a strongly suppressed transfer function above a comoving mode given by the

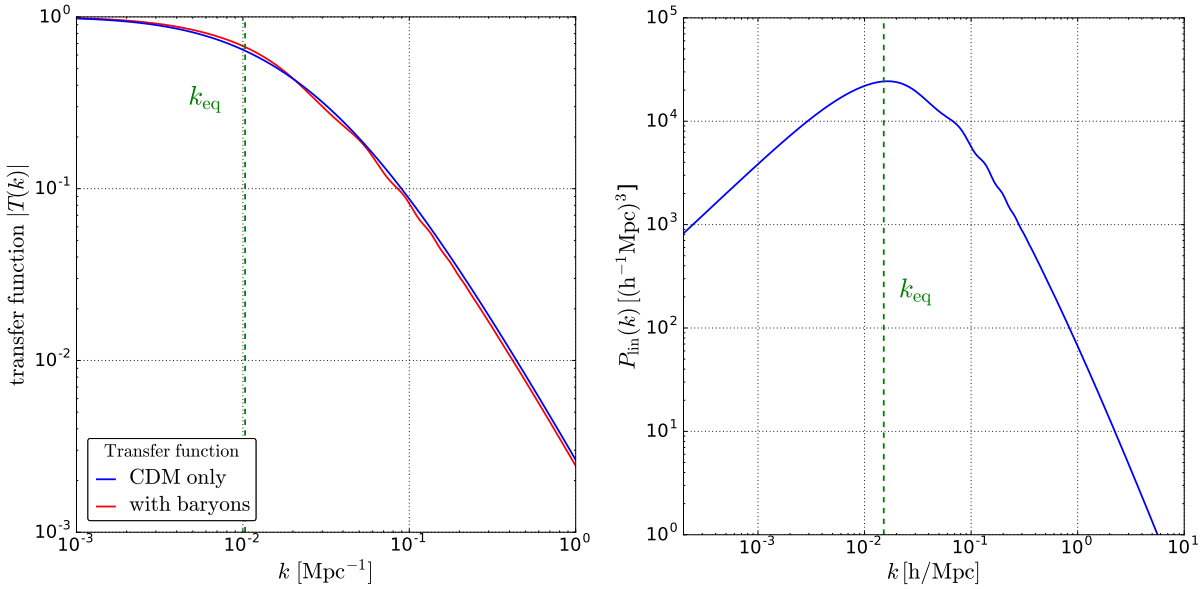

Figure 3.3 – Left panel: CDM transfer function (blue) and matter transfer function (red) from Eisenstein & Hu (1998). **Right panel:** linear matter power spectrum in the cosmology of Ade et al. (2016).

kinetic decoupling of the dark matter particle (Loeb & Zaldarriaga, 2005). Consequently, the dark matter power spectrum is also suppressed below that scale and strongly departs from the scale-invariant spectrum (Green et al., 2005).

3.1.2.2 Filtering

Our goal is to derive the halo mass function, that is the number density of dark matter halos per unit of mass. In order to do this, we need to assign a mass M, or a scale length R, to a region of space from the overdensity field $\delta(\vec{x})$. This is achieved by defining a *smoothed* density field

$$\delta_R(\vec{x}) = \int \delta(\vec{x}')\, W(\vec{x}-\vec{x}', R)\, \mathrm{d}^3\vec{x}'\,, \tag{3.54}$$

where W is a window function (with units of inverse volume). In Fourier space, we have simply

$$\hat{\delta}_R(\vec{k}) = \tilde{W}(kR)\, \hat{\delta}(\vec{k})\,. \tag{3.55}$$

A common choice for the window function is the real-space top-hat

$$W(\vec{x}-\vec{x}', R) = \begin{cases} 3/(4\pi R^3) & \text{if } |\vec{x}-\vec{x}'| \leqslant R \\ 0 & \text{if } |\vec{x}-\vec{x}'| > R\,. \end{cases} \tag{3.56}$$

The associated Fourier transform is

$$\hat{W}(kR) = \frac{3}{(kR)^3}\left[\sin(kR) - kR\cos(kR)\right]\,. \tag{3.57}$$

Another popular choice is the Gaussian window function

$$W(\vec{x}-\vec{x}', R) = \left(\frac{1}{2\pi R^2}\right)^{3/2} \exp\left[-\frac{|\vec{x}-\vec{x}'|^2}{2\,R^2}\right]\,, \tag{3.58}$$

with Fourier transform

$$\hat{W}(kR) = \exp\left[-\frac{(kR)^2}{2}\right]\,. \tag{3.59}$$

A third useful choice is the Fourier-space top-hat window

$$\hat{W}(kR) = \Theta(1 - kR)\,, \tag{3.60}$$

where Θ is the Heaviside step function. This window does not have a well-defined volume in real space. A volume can be assigned in a formal way by requiring that $W(0,R)V(R) = 1$, which leads $V(R) = 6\pi^2 R^3$. Note that the windows are all normalized

$$\int W(\vec{x},R)\,\mathrm{d}^3\vec{x} = 1\,. \tag{3.61}$$

Furthermore, their Fourier transform is defined through

$$\hat{W}(kR) = \int W(\vec{x},R)\,e^{-i\vec{k}.\vec{x}}\,\mathrm{d}^3\vec{x}\,, \tag{3.62}$$

which differs by a factor $1/V$ from our definition of the Fourier transform given in Eq. (3.12) (this factor is actually included in the definition of W). A variance can be straightforwardly defined for the smoothed density field

$$\begin{aligned}\sigma_R^2 \equiv \left\langle \delta_R^2(\vec{x}) \right\rangle &= \frac{1}{(2\pi)^3}\int P_\mathrm{m}(k)\,|\hat{W}(kR)|^2\,\mathrm{d}^3\vec{k} \\ &= \int \Delta_\mathrm{m}^2(k)\,|\hat{W}(kR)|^2\,\mathrm{d}\ln k\,.\end{aligned} \tag{3.63}$$

The smoothing on a length scale R can be translated into a smoothing on a mass scale M through the volume of the window in real space. This volume can be generically written $V(R) = \gamma\,R^3$, with γ a constant equal to $4\pi/3$ for the top-hat filter, $(2\pi)^{3/2}$ for the Gaussian filter and $6\pi^2$ for the k-space top-hat. The mass is then

$$M = \overline{\rho}\,V(R)\,. \tag{3.64}$$

with $\overline{\rho}$ the background density (which is time-dependent in general). For a power-law spectrum $P(k) \propto k^n$, we get the scaling of the variance $\sigma_R^2 \propto R^{-(3+n)} \propto M^{-(3+n)/3}$. Since the smoothed density field δ_R is linearly related to the density field, it also follows a Gaussian statistics, and its variance is simply σ_R^2. The mass root mean square σ_M is shown in the left panel on Fig. 3.4.

3.1.2.3 The Press-Schechter mass function

We now arrive at the actual computation of the mass function. The original derivation was performed by Press & Schechter (1974). Though the derivation has some important shortcomings, which we briefly discuss later on, it leads to a very simple and powerful expression for the mass function. A nice review on the Press-Schechter mass function and its extensions can be found in Zentner (2007). The main assumption of Press and Schechter relies on the spherical collapse model. The idea is that a smoothed fluctuation $\delta_M(t)$ equating some critical overdensity δ_c collapses into a halo of mass M. If a region of scale R (mass M) has a density fluctuation $\delta > \delta_\mathrm{c}$, then we can reasonably conceive that a more extended region of scale $R' > R$ (mass $M' > M$) would be less contrasted with $\delta' < \delta$, while still with $\delta' \geqslant \delta_\mathrm{c}$. This leads to the *assumtion* that if $\delta_R > \delta_\mathrm{c}$, there is a region of size $R' > R$ that crosses the threshold $\delta_{R'} = \delta_\mathrm{c}$. This means that for a given scale R (M), probing $\delta > \delta_\mathrm{c}$ upward translates into probing more and more massive collapsed objects of mass $M' > M$. The value of δ_c is usually set to be $\delta_\mathrm{c} = 1.69$, as predicted by the spherical collapse model in Eq. (3.42). If we assume the probability distribution of δ_M is the Gaussian distribution with variance σ_M^2, the fraction of dark matter collapsed into halos of mass M or higher is

$$\begin{aligned}F(M) &= \int_{\delta_\mathrm{c}}^{\infty}\left(\frac{1}{2\pi\sigma_M^2}\right)^{1/2}\exp\left[-\frac{\delta^2}{2\sigma_M^2}\right]\mathrm{d}\delta \\ &= \frac{1}{2}\,\mathrm{erfc}\left(\frac{\nu}{\sqrt{2}}\right)\,.\end{aligned} \tag{3.65}$$

Here erfc is the complementary error function and $\nu \equiv \delta_c/\sigma_M$ is the peak height. The number density of objects with mass between M and $M + \mathrm{d}M$ is then

$$\begin{aligned}\frac{\mathrm{d}n}{\mathrm{d}M}\,\mathrm{d}M &= \frac{\overline{\rho}}{M}\left|\frac{\mathrm{d}F}{\mathrm{d}M}\right|\mathrm{d}M \\ &= \frac{\overline{\rho}}{M^2}\left|\frac{\mathrm{d}\ln\sigma_M}{\mathrm{d}\ln M}\right|\nu\sqrt{\frac{2}{\pi}}\exp\left[-\frac{\nu^2}{2}\right]\mathrm{d}M\,.\end{aligned} \tag{3.66}$$

A factor of two has been added by hand to the formula to get the correct estimate. This is related to the cloud-in-cloud problem which we discuss below. Note that if σ_M has a weak dependence with respect to M, which is the case if the power spectrum is scale-invariant, then the mass function has a power-law behaviour $\mathrm{d}n/\mathrm{d}M \propto M^{-2}$ at small masses and is exponentially cut off at large masses. The typical mass M_* at which the transition happens is set by $\sigma(M_*) = \delta_c$. The Press-Schechter mass function multiplied by M^2 is shown in the right panel in Fig. 3.4. The quantity $M^2\,\mathrm{d}n/\mathrm{d}M$ spans less than two orders of magnitude over 23 orders of magnitude in M, which shows the goodness of the approximation $\mathrm{d}n/\mathrm{d}M \propto M^{-2}$ below the galactic scale $M \sim 10^{12}\,\mathrm{M}_\odot$. The mass function falls sharply above $M \sim 10^{14}\,\mathrm{M}_\odot$.

3.1.2.4 Beyond the Press-Schechter theory

The Press-Schechter mass function is surprisingly successful at capturing the behaviour of dark matter halos found in cosmological simulations. The derivation of the formula suffers however from the multiplication by a factor of two with little justification. There is actually already a problem in the expression of the halo fraction in Eq. (3.65). This can be understood from the scaling $\sigma^2 \propto M^{-(3+n)/3}$, which implies that $\sigma \overset{M\to 0}{\longrightarrow} \infty$, and hence that $\nu \overset{M\to 0}{\longrightarrow} 0$. Hence the fraction of mass contained in collapsed objects of arbitrary small mass is $F(0) = 1/2$, *i.e.* the model predicts that only half of the dark matter can collapse into halos. This issue was already noted by the original authors who argued that the discrepant factor of two is linked to the cloud-in-cloud problem. The idea is that an under-dense region $\delta_M(\vec{x}) < \delta_c$ can be embedded in an over-dense region $\delta_{M'}(\vec{x}) = \delta_c$ and will eventually collapse into a halo of mass M', therefore under-dense regions should also be included in the halo fraction (3.65). Including these clouds-in-cloud certainly increases $F(M)$, however it is not clear that this leads to an exact factor of two.

The cloud-in-cloud problem was solved by Bond et al. (1991) who used the *excursion set theory* to consistently derive the mass function. Amazingly, they recovered the Press-Schechter mass function in Eq. (3.66) with the factor of two lacking in the original derivation. The formalism they used is therefore often referred to as the *extended Press-Schechter formalism*. This technique is not only a tool to derive mass functions, it can also be used to study the formation history of dark matter halos. In particular, it can be used to simulate merger trees as it was first shown by Lacey & Cole (1993). The extended Press-Schechter theory motivates the study of generalized mass functions of the form

$$\frac{\mathrm{d}n}{\mathrm{d}M} = \frac{\overline{\rho}}{M^2}\left|\frac{\mathrm{d}\ln\sigma_M}{\mathrm{d}\ln M}\right|\nu\,f(\nu)\,, \tag{3.67}$$

where $f(\nu) = \mathrm{d}F/\mathrm{d}\nu$, and for the Press-Schechter mass function $f(\nu) = \sqrt{2/\pi}\exp(-\nu^2/2)$. The derivation of Bond et al. (1991) was extended beyond the spherical collapse approximation by Sheth & Tormen (1999), see also Sheth et al. (2001), to include ellipsoidal collapse. This leads to a simple form of the mass function

$$\nu\,f(\nu) = 2A\left(1 + \frac{1}{\nu'^{2q}}\right)\left(\frac{\nu'^2}{2\pi}\right)^{1/2}\exp\left(-\frac{\nu'^2}{2}\right)\,, \tag{3.68}$$

where $\nu' = \sqrt{a}\nu$, $a = 0.707$, $q = 0.3$, and $A \simeq 0.322$. The original Press-Schechter mass function in Eq. (3.66) is recovered with $a = 1$, $q = 0$ and $A = 1/2$. The Sheth-Tormen mass function is compared to the Press-Schechter mass function in the right panel on Fig. 3.4. The Sheth-Tormen mass function predicts more structures at very high masses where the function is sharply falling, less structures below down to $M \sim 10^6\,\mathrm{M}_\odot$, and more structures even below. The latter regime is not probed by observations nor cosmological simulations, hence the robustness of the Seth-Tormen and Press-Schechter mass functions in that region is unknown.

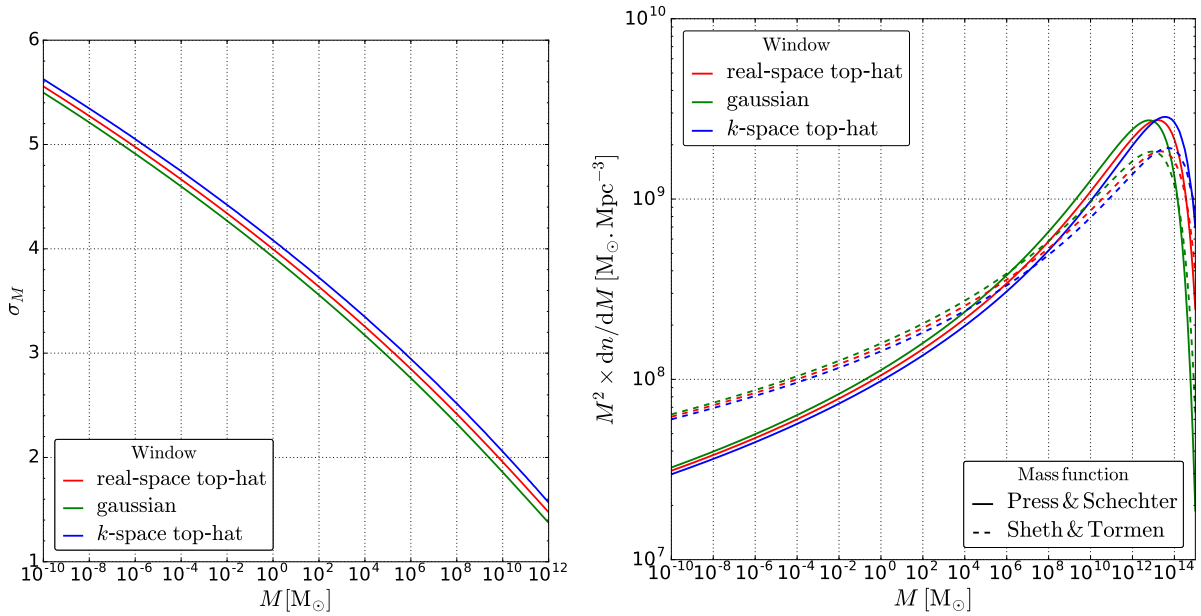

Figure 3.4 – Left panel: Root mean square of the smoothed overdensity field as a function of the mass. **Right panel:** Press-Schechter mass function (solid line) and Seth-Tormen mass function (dashed line). We used the cosmology of Planck 2015 (Ade et al., 2016).

3.1.3 The internal structure of dark matter halos

In this section, we describe the internal structure of dark matter halos. Since the evolution of a virialized dark matter structure is a non-linear process, the prime tool to study it is numerical simulation. The shape of the density profile of dark matter structure is the result of several physical processes. Some, such as phase-mixing and violent relaxation (Lynden-Bell, 1967; Binney & Tremaine, 1987), are internal to the structure and may drive it to its equilibrium state. Others come from the interaction of the halo with its environment, such as accretion and mergers. A naive expectation would be that the internal shape of a halo depends on its particular history and its environment. Quite remarkably, N-body cosmological simulations where all these effects are accounted for have shown that this is not the case. Indeed, if the effect of baryonic matter is ignored, virialized dark matter halos have a *universal shape*. This fundamental result was first established by Navarro et al. (1996); Navarro et al. (1997) and recently probed further down to the origin of the first peaks by Angulo et al. (2016). Another investigation based on simulations was done here Ogiya & Hahn (2018). It was shown by Navarro et al. (1996); Navarro et al. (1997) that CDM halos are spherical and their density profile is very well fitted by what is now called the Navarro-Frenk-White (NFW) profile

$$\rho(r) = \rho_\mathrm{s} \frac{1}{x} \frac{1}{(1+x)^2} \tag{3.69}$$

$$x \equiv \frac{r}{r_\mathrm{s}} \tag{3.70}$$

Fitting parameters ρ_s and r_s are called scale density and scale radius, respectively, and they depend on the mass and the size of the dark matter halo. The NFW profile exhibits a steep r^{-1} diverging behaviour as $r \ll r_s$ and a steeper r^{-3} tail when $r \gg r_s$. However, if dark matter self-annihilates, then a core should appear at the very center of a halo around the radius at which the dynamical time exceeds the annihilation time

$$t_{\rm dyn} \simeq [G_{\rm N}\rho(r_{\rm core})]^{-1/2} > t_{\rm ann} \simeq \frac{m}{\langle\sigma_{\rm ann}v\rangle\ \rho(r_{\rm core})}\,. \tag{3.71}$$

While the emergence of this profile is reproduced by most simulations, it is still not clear what are the physical mechanisms setting this power-law scaling. The mass can be expressed analytically

$$\begin{aligned} m(r) &= 4\pi \int_0^r {\rm d}r'\, r'^2\, \rho(r') \\ &= 4\pi\rho_s r_s^3 \left[\ln(1+x) - \frac{x}{x+1}\right], \end{aligned} \tag{3.72}$$

hence it has a logarithmic divergence at large radii. This is not an issue in practice since one can always associate to a halo a virial radius and compute a finite mass within that radius. A generalized version of the NFW profile is often used in the literature

$$\rho(r) = \rho_s\, x^{-\gamma}\, [1 + x^\alpha]^{(\gamma-\beta)/\alpha} \tag{3.73}$$

The index γ measures the inner slope of the dark matter profile while β controls the outer slope, and α sets the transition between the two regimes. The NFW profile is recovered for $(\alpha, \beta, \gamma) = (1, 3, 1)$. Since the original work of Navarro, Frenk and White, it has been found that the Einasto profile (Einasto, 1965, 1968) actually provides a better fit to CDM halos found in simulations (Navarro et al., 2004; Merritt et al., 2005; Graham et al., 2006; Gao et al., 2008; Springel et al., 2008). The Einasto profile takes the following form

$$\rho(r) = \rho_s\, \exp\left\{-\frac{2}{\alpha}\left[x^\alpha - 1\right]\right\}. \tag{3.74}$$

While the NFW profile has a central cusp, the Einasto profile has a core.[1] It involves a free parameter α which sets the transition between the inner core and the exponential behaviour in the outskirts, hence it takes the same role as the α parameter in Eq. (3.73). The α parameter in the Einasto profile is found in simulations to be very small, typically of order $\alpha \sim 0.1$, hence the core is very small. This is a general property of CDM halos: they present little to no core and exhibit instead a cuspy behaviour in their central regions. Some (α, β, γ) and Einasto profiles are shown in the left panel of Fig. 3.5, normalised to their scale density ρ_s.

It has been found in dedicated simulations that near the free-streaming scale, the profile of halos is significantly cuspier than the NFW profile, exhibiting instead a $\rho \propto r^{-1.5}$ behaviour (Ishiyama et al., 2010; Anderhalden & Diemand, 2013; Ishiyama, 2014; Ogiya & Hahn, 2018). We do not account for this effect in the following but note that it might have interesting consequences on indirect searches for instance.

3.1.3.1 The concentration parameter

The shape of a dark matter halo with a given virial mass $m_{\rm vir}$ is often described with a single parameter called the *concentration*

$$c_{\rm vir} = \frac{r_{\rm vir}}{r_{-2}}\,, \tag{3.75}$$

[1] Note however that the central region of dark matter halos in simulations suffer from resolution loss, hence the observation of a core might not reflect the true physical behaviour of the profile.

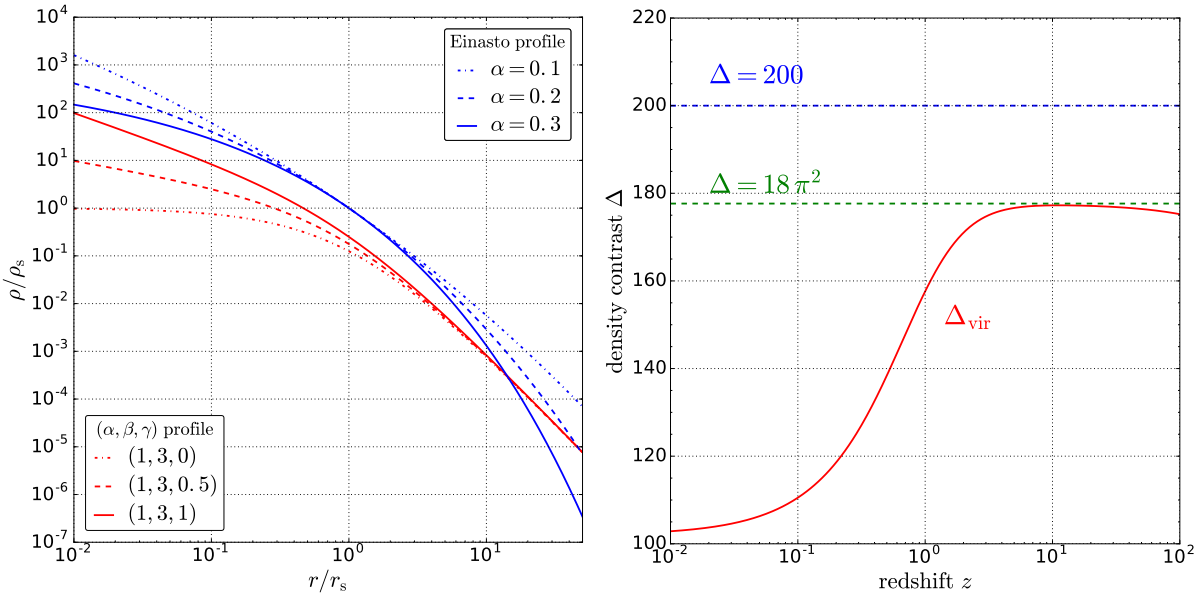

Figure 3.5 – Left panel: a variety of density profiles often used to describe CDM halos, including the NFW profile $(\alpha, \beta, \gamma) = (1, 3, 1)$ and several Einasto profiles. **Right panel:** density contrast Δ for the parametrisation of Bryan & Norman (1998) (red), the value in a matter dominated universe (green) and $\Delta = 200$ (blue).

where $r_{\rm vir}$ is the virial radius of the halo and r_{-2} is defined as

$$\left.\frac{\mathrm{d}\ln\rho}{\mathrm{d}\ln r}\right|_{r=r_{-2}} = -2\,. \tag{3.76}$$

The virial radius is set through the relation

$$\frac{m(r_{\rm vir})}{\frac{4}{3}\,\pi\,r_{\rm vir}^3} \equiv \Delta_{\rm vir}\,\rho_{\rm c}\,, \tag{3.77}$$

where $\rho_{\rm c}$ is the critical density and $\Delta_{\rm vir}$ is the density contrast defined by

$$\Delta_{\rm vir} \equiv \delta_{\rm vir} + 1\,, \tag{3.78}$$

with $\delta_{\rm vir}$ the overdensity at the epoch of virialization. This density contrast can be evaluated through the spherical collapse model, see Sec. 3.1.1.3, and it depends on redshift and cosmology. Fitting formulae are provided by Bryan & Norman (1998) in terms of the parameter $x = \Omega_{\rm m}(z) - 1$ where $\Omega_{\rm m}(z)$ is the matter abundance given in Eq. (2.29). The formulae in the absence of curvature $(\Omega_K = 0)$ is

$$\Delta_{\rm vir} = 18\pi^2 + 82\,x - 39\,x^2\,. \tag{3.79}$$

Note that $\Delta = 18\pi^2$ is the value of the density contrast in a matter dominated universe. To avoid the dependence over the cosmological parameters, it is conventional to fix the value of the density contrast to $\Delta = 200$. This is a conservative choice in that it underestimates the virial radius, as one can see on the right panel in Fig. 3.5. From now on, we fix the virial contrast to $\Delta = 200$ and consider the virial quantities r_{200}, m_{200} and c_{200}. The radius r_{-2} is proportional to the scale radius $r_{\rm s}$ up to a numerical factor that depends on the profile. For the $\alpha\beta\gamma$ profile in Eq. (3.73), we have

$$r_{-2} = r_{\rm s}\left(\frac{2-\gamma}{\beta-2}\right)^{1/\alpha}\,. \tag{3.80}$$

hence $r_{-2} = r_\mathrm{s}$ for the NFW profile. Similarly, we also have $r_{-2} = r_\mathrm{s}$ for the Einasto profile. Note that r_{-2} is ill-defined for $\beta = 2$, which happens in the case of the cored isothermal sphere $(\alpha, \beta, \gamma) = (2, 2, 0)$ for instance

$$\rho(r) = \frac{\rho_\mathrm{s}}{1 + \frac{r^2}{r_\mathrm{s}^2}} \,. \tag{3.81}$$

In that case, one can simply choose $r_{-2} \equiv r_\mathrm{s}$.

The concentration parameter is directly related to the scale density ρ_s. Given the virial mass and concentration m_{200} and c_{200}, one can compute the scale parameters ρ_s and r_s. As shown before, we have

$$\frac{m(r_{200})}{\frac{4}{3}\,\pi\, r_{200}^3} = 200\,\rho_\mathrm{c} \,. \tag{3.82}$$

For a given density profile, we introduce a dimensionless mass profile $\tilde{m}$ such that

$$m(r) = 4\pi\rho_\mathrm{s}\, r_\mathrm{s}^3\, \tilde{m}\left(\frac{r}{r_\mathrm{s}}\right) \,, \tag{3.83}$$

hence Eq. (3.82) becomes

$$\frac{4\pi\rho_\mathrm{s}\, \tilde{m}\left(\frac{r_{200}}{r_\mathrm{s}}\right)}{\frac{4}{3}\,\pi\,\left(\frac{r_{200}}{r_\mathrm{s}}\right)^3} = 200\,\rho_\mathrm{c} \,. \tag{3.84}$$

The ratio r_{200}/r_s is related to the concentration up to profile-dependent numerical factor therefore we write

$$\frac{r_{200}}{r_\mathrm{s}} = \eta\, c_{200} \,, \tag{3.85}$$

with $\eta = [(\beta - 2)/(2 - \gamma)]^{1/\alpha}$ for $\alpha\beta\gamma$ profiles according to Eq. (3.80). We get the scale density as a function of the concentration *only*

$$\rho_\mathrm{s} = \frac{200\,\rho_\mathrm{c}}{3}\,\frac{(\eta\, c_{200})^3}{\tilde{m}\,(\eta\, c_{200})} \,. \tag{3.86}$$

The virial mass is simply

$$\begin{aligned} m_{200} \equiv m(r_{200}) &= \frac{4}{3}\,\pi\, r_{200}^3\, 200\,\rho_\mathrm{c} \\ &= \frac{4}{3}\,\pi\,(\eta\, c_{200}\, r_\mathrm{s})^3\, 200\,\rho_\mathrm{c} \end{aligned} \tag{3.87}$$

therefore

$$r_\mathrm{s} = \frac{1}{\eta\, c_{200}}\left(\frac{3\, m_{200}}{4\pi\, 200\,\rho_\mathrm{c}}\right)^{1/3} \,. \tag{3.88}$$

This shows that the mass and the concentration together completely determine the density profile of a dark matter halo.

3.1.3.2 The mass-concentration relation

Though mass and concentration are independent parameters, a correlation between the two is found in cosmological simulations as already noticed by Navarro et al. (1996). This is quite natural in the context of hierarchical clustering since smaller structures are more likely to collapse earlier, when the Universe was denser. A variety of studies have proposed semi-analytical models of this mass-concentration relation, see *e.g.*, Navarro et al. (1996); Bullock et al. (2001); Macciò et al. (2008); Prada et al. (2012); Dutton & Macciò (2014); Ludlow et al. (2014); Diemer & Kravtsov (2015); Ludlow et al. (2016); Diemer & Joyce (2018). A fit of the relation for field halos is provided by Sánchez-Conde & Prada (2014), and by Moliné et al. (2017) for subhalos in simulated Milky-Way-like galaxies – we will further investigate the later case based on theoretical grounds.

We review the model of Bullock et al. (2001) as modified by Macciò et al. (2008) that helps understand and predict this relation. The first step is to relate the mass of a halo at the redshift of collapse $z_{\rm c}$ to its virial mass at redshift $z < z_{\rm c}$

$$m_*(z_{\rm c}) = F\, m_{200}(z)\,, \tag{3.89}$$

where F is a free parameter to be determined, assumed to be independent of the redshift of collapse, and m_{200} is the virial mass

$$m_{200} = \frac{4}{3}\,\pi\, r_{200}^3\, 200\,\rho_{\rm c}(z)\,. \tag{3.90}$$

The spherical collapse model prediction in Eq. (3.42) defines the characteristic mass as the one crossing the non-linear threshold at the collapse redshift $z_{\rm c}$

$$\sigma(m_*, z_{\rm c}) = 1.686\,. \tag{3.91}$$

Note that

$$\sigma(m_*, z) = \sigma(m_*, 0)\, D_+(z)\,, \tag{3.92}$$

where D_+ is the linear growth factor already introduced in Eq. (3.25). The redshift of collapse is shown as a function of the mass in the left panel on Fig. 3.6. The redshift is a decreasing function of the mass *i.e.* more massive halos collapse later as expected in the hierarchical scenario of structure formation. All structures collapse at a much lower redshift than matter-radiation equality which takes place at $z_{\rm eq} \simeq 3300$ (Ade et al., 2016). The choice of the window function defining $\sigma(M)$ introduces a small uncertainty on the redshift. In the right panel, we compare the redshift of collapse to the redshift when structures enter the non-linear regime, defined for a given mass m by

$$\sigma(m, z_{\rm nl}) = 1\,. \tag{3.93}$$

Obviously, this redshift is always superior to the redshift of collapse $z_{\rm c}$. We note that the redshifts of collapse we obtain are significantly smaller than those found in other studies (Diemand et al., 2005; Green et al., 2005). This might be due to differences in the cosmological parameters since we used the cosmology of Ade et al. (2016) while older studies relied on the results from WMAP.

Let us go back to the concentration model. We introduce a characteristic density $\tilde{\rho}_{\rm s}$ defined as

$$\begin{aligned}
\tilde{\rho}_{\rm s}(z) &= \frac{m_{200}(z)}{\frac{4}{3}\,\pi\, r_{\rm s}^3(z)} \\
&= \left(\frac{r_{200}(z)}{r_{\rm s}(z)}\right)^3\, 200\,\rho_{\rm c}(z) \\
&= \left[\eta\, c_{200}(z)\right]^3\, 200\,\rho_{\rm c}(z)\,,
\end{aligned} \tag{3.94}$$

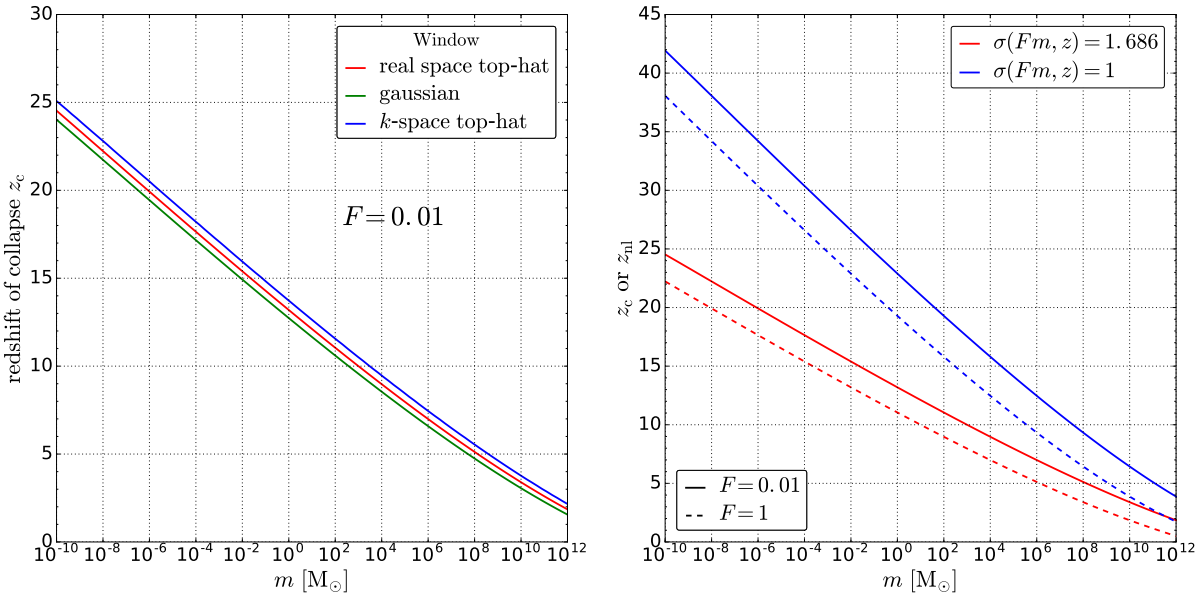

Figure 3.6 – Left panel: redshift of collapse as defined by $\sigma(F\,m_{200}, z_c) = 1.686$, with $F = 0.01$ and for various choices of the window function. **Right panel:** redshift of collapse and redshift of non-linear evolution, defined by $\sigma(F\,m_{200}, z_c) = 1.686$ and $\sigma(F\,m_{200}, z_{nl}) = 1$ respectively. We used the real space top-hat window function, and show the results for two values of the F parameter: $F = 0.01$ (solid line) and $F = 1$ (dashed line).

with the η parameter introduced in Eq. (3.85). Note that $\tilde{\rho}_s$ is a priori different from the scale density ρ_s. In the model of Macciò et al. (2008), the characteristic density is assumed to be *independent of the redshift*, which implicitly entails that further evolution of the halo after virialization does not strongly affect its very internal structure. If we further assume that the density contrast $\tilde{\rho}_s/(200\,\rho_c)$ is universal at any collapse redshift z_c, and set to a constant K^3 to be determined, then we get[2]

$$c_{200}(z) = K\left[\frac{\rho_c(z_c)}{\rho_c(z)}\right]^{1/3} = K\left[\frac{H(z_c)}{H(z)}\right]^{2/3}. \tag{3.95}$$

The concentration is therefore related to the mass m_{200} through the redshift of collapse z_c. The model has two independent free parameters F and K that must be calibrated on cosmological simulations. For the cosmology of Planck 2013 (Ade et al., 2014), it is found by Dutton & Macciò (2014) that $F = 0.01$ and $K = 4.2$ provide a good fit to their simulations. Even though this model is tested over five decades of mass from dwarf galaxies to galaxy clusters, it is shown by Sánchez-Conde & Prada (2014) that it also agrees with simulations of Earth-mass halos with $m_{200} \sim 10^{-6}\,\mathrm{M}_\odot$ (Diemand et al., 2005; Ishiyama et al., 2010). We show the mass-concentration relation in the Planck cosmology in the left panel on Fig. 3.7. We show the model of Prada et al. (2012), using the fitting function provided by Sánchez-Conde & Prada (2014) (P12 in the legend), as well as the concentration from the Bullock et al. (2001); Macciò et al. (2008) model we discussed above (P01/B08 in the legend). Both models give a close prediction over eighteen decades in mass, with a predicted concentration of around 10 for Milky-Way-like halos and around 60 for Earth-mass halos. Since the scale density of a halo is uniquely determined by its concentration, we can compute ρ_s as a function of the mass using a model for the concentration. The result is shown in the right panel on Fig. 3.7. Unlike the concentration, the scale density depends on the functional form of the density profile. This leads to large differences as we show by comparing ρ_s for an NFW and an Einasto profile.

[2]This assumes that halos are isolated, or do not experience major mergers after their formation (accretion of much smaller objects only).

In the following, we use the fitting formulae for $c_{200}(m_{200})$ provided by Sánchez-Conde & Prada (2014) of the model of Prada et al. (2012) and do not consider the Bullock et al. (2001); Macciò et al. (2008) model.

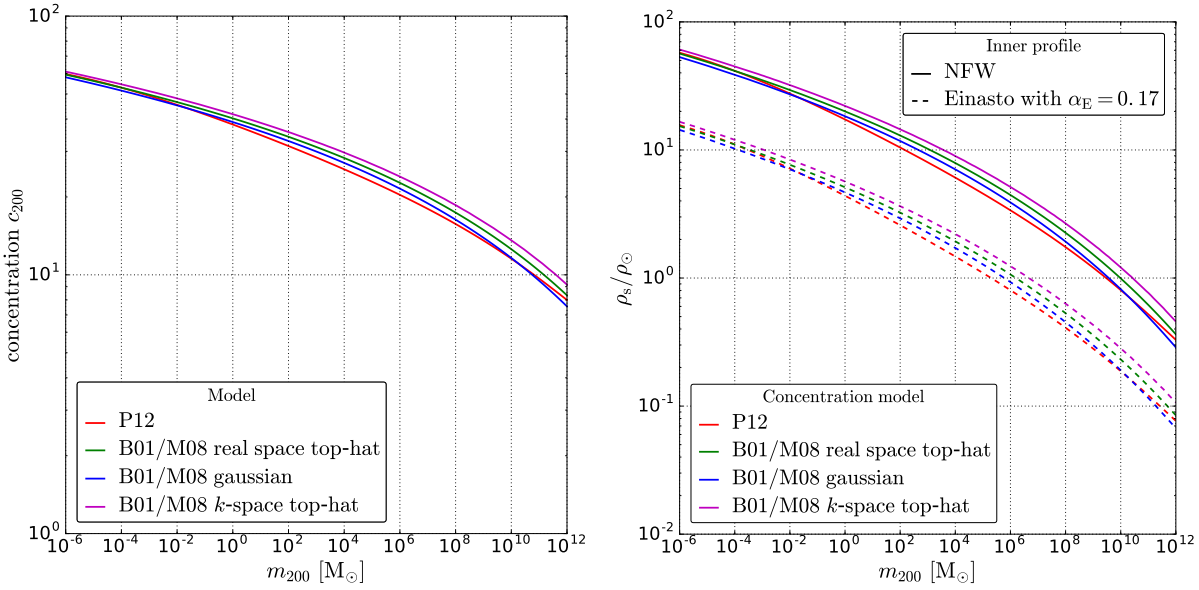

Figure 3.7 – Left panel: concentration $\bar{c}_{200}$ at $z = 0$ for the model of Prada et al. (2012) with the fitting function given in Sánchez-Conde & Prada (2014) (red line), and the model of Bullock et al. (2001) revised by Macciò et al. (2008); Dutton & Macciò (2014) (green, blue and magenta lines). **Right panel:** scale density ρ_s in units of the local density, for the concentration models shown in the left panel, and two inner profiles (NFW and Einasto).

3.2 Subhalos and their evolution

The previous section describes the formation of dark matter halos and their statistics from a cosmological point of view. The hierarchical scenario of structure formation predicts that large dark matter halos are formed by the collapse of a collection of smaller, already formed halos. We can wonder whether these small objects survive the collapse of their larger host structure and are still present in galactic halos today. This is a crucial question for particle dark matter searches as these subhalos can strongly impact predictions for direct and indirect searches as well as gravitational searches, as discussed in Chap. 4. The evolution of a subhalo inside a galactic halo is a priori very complex as it experiences a variety of gravitational effects from the host galaxy: tidal stripping, shocking, heating, dynamical friction, interactions with baryons (shocking by the disc, encounter with stars), etc. To account for all these effects in a self-consistent way, study of subhalos often rely on numerical cosmological simulations like Via Lactea II Diemand et al. (2008) or Aquarius Springel et al. (2008) for dark matter-only simulations. For numerical studies of subhalos in simulations including baryons, see *e.g.*, Zhu et al. (2015); Garrison-Kimmel et al. (2017); Rodriguez-Puebla et al. (2016). These simulations allow to self-consistently follow the evolution of subhalos from their collapse to $z = 0$. A major drawback is the very high computational cost of numerical simulations, which strongly limits their resolution. As an example, the best mass resolution achieved in the Aquarius simulation is $M_{\rm res} \simeq 10^3\,{\rm M}_\odot$ which is orders of magnitude higher than the lowest mass achievable in typical WIMP models $m_{\rm min} \simeq 10^{-6}\,{\rm M}_\odot$, see Sec. 2.4. Some simulations focus on the smallest scales, see *e.g.*, Diemand et al. (2005); Ishiyama et al. (2010); Anderhalden & Diemand (2013); Ishiyama (2014), but can only do so at very high redshifts and therefore cannot investigate subhalos in galactic halos today. Moreover, it has recently be pointed out that cosmological simulations

are very likely to strongly overestimate the tidal disruption of subhalos due to resolution limit (van den Bosch et al., 2018; van den Bosch & Ogiya, 2018). It is therefore important to question this survival issue on first-principle grounds.

An alternative approach to the subhalo problem is semi-analytic modelling, see *e.g.*, Berezinsky et al. (2003); Green & Goodwin (2007); Kamionkowski et al. (2010); Gan et al. (2010); Bartels & Ando (2015); Han et al. (2016); Stref & Lavalle (2017); Hiroshima et al. (2018), see also Berezinsky et al. (2014) for a review. Given the complexity of the issue, analytic calculations are possible only at the cost of approximations and therefore partial loss of consistency. A major benefit of this approach is the possibility of investigating all scales at play in one unified framework. It also provides ways to account for known cosmological and dynamical constraints. This is especially appealing for dark matter searches which is why we focus on this approach in the following. We still keep an eye on the results of numerical simulations to qualitatively check the validity of our calculations.

In what follows we present semi-analytic methods to model tidal effects, including the contribution of the host halo, the galactic disc and the stars. Before going into the details, let us give a rough estimate of the typical number of subhalos in a Milky-Way-like galaxy. An estimation of this number can be obtained from cosmological simulations. For instance, in the Aquarius simulation of Springel et al. (2008) the number of subhalos found in the best resolved Milky-Way-sized halo is $\sim 300\,000$, with the mass resolution $M_{\rm res} \simeq 10^5\,{\rm M}_\odot$. Extrapolating the M^{-2} behaviour of the halo mass function to subhalo masses down to $m_{\rm min} = 10^{-6}\,{\rm M}_\odot$, we get a total number of subhalos $N_{\rm sub} \simeq 3 \times 10^{16}$! Such a gigantic number suggests that subhalos do not "see" the clumpy nature of the galactic halo and essentially behave as if they were moving through a smooth potential. This simplifies our study of tidal effects.

3.2.1 Tidal stripping

The first effect we investigate is tidal stripping. When a subhalo orbits a host potential, part of its material is stripped away by the host galaxy. This effect has long been known to be relevant in Galactic dynamics as it explains for instance the observed finite extensions of globular clusters (King, 1962).

3.2.1.1 Tidal radius for point masses

Let us consider two point masses m and M orbiting each other at a fixed separation R, with $M \gg m$, such that the rotation angular frequency about the center of mass is given by

$$\omega = \sqrt{\frac{G_{\rm N}(m+M)}{R^3}}\,. \tag{3.96}$$

Placing ourselves in the co-rotating frame, we now investigate the motion of a vanishingly light test-mass particle in the joint potential induced by the two bodies, assuming it is initially positioned at a distance $x \ll R$ from the lightest one. This can be thought of as a WIMP orbiting a point-like subhalo embedded in the potential generated by a point-like host halo. This is called the restricted three-body problem (Spitzer, 1987; Binney & Tremaine, 1987). We consider a massless test particle confined to the axis linking the masses m and M, and call x its distance to the mass m. The equations of motion for the test particle are

$$\ddot{x} = \frac{G_{\rm N}\,m}{x^2} - \frac{G_{\rm N}\,M}{(R-x)^2} + \frac{G_{\rm N}(M+m)}{R^3}\left(\frac{M}{M+m}\,R - x\right)\,, \tag{3.97}$$

where the last term accounts for the centrifugal force in the co-rotating frame. We look for a stationary point $\ddot{x} = 0$. To get a close expression for x, we assume $M \gg m$, hence M represents a galactic halo and m a satellite subhalo. This implies $x \ll R$ and we get the solution

$$x \simeq R\left(\frac{m}{3M}\right)^{1/3}\,. \tag{3.98}$$

This stationary solution is actually the approximate position of a Lagrange point. It also defines the radius of the Hill sphere, or Roche sphere (named after astronomers George William Hill and Édouard Roche) which is the region of influence of a celestial body. More precisely, it is the region inside which a particle is bound to the satellite rather than the host halo, therefore it gives the maximal spatial extent of the satellite. This spatial boundary is referred to as the *tidal radius*.

A very rough estimation of the tidal radius is obtained by assuming a point-like structure for the Galaxy. Using Eq. (3.98), we get

$$r_{\rm t,point1} \equiv R \left(\frac{m_{\rm int}(r_{\rm t,point1})}{3\, M_{\rm tot}} \right)^{1/3} , \tag{3.99}$$

where $M_{\rm tot} = M_{\rm dm} + M_{\rm bar}$ is the total mass of the Galaxy, including both dark matter and baryons. From now on, we refer to this definition as the *first point-like Jacobi radius*. This is an implicit definition since the tidal radius appears on both sides of the equation. In practice we solve this equation numerically to get the radius.

Assuming the Galaxy has a point-like structure is of course a very bad approximation, except for subhalos orbiting in the outskirts of the dark halo. For a subhalo on a circular orbit of radius R, we can instead define its tidal radius by replacing the total mass $M_{\rm tot}$ in Eq. (3.99) with the mass $M(R)$ within the orbit. We refer to this new definition as the *second point-like Jacobi radius*

$$r_{\rm t,point2} \equiv R \left(\frac{m_{\rm int}(r_{\rm t,point2})}{3\, M(R)} \right)^{1/3} . \tag{3.100}$$

Note that $M(R)$ also includes both dark matter and baryons. As we go to very large radii, we expect the value of $r_{\rm t,point1}$ and $r_{\rm t,point2}$ to coincide. We can rewrite Eq. (3.100) as

$$\frac{3\, m_{\rm int}(r_{\rm t,point2})}{4\pi\, r_{\rm t,point2}^3} = 3 \times \frac{3\, M(R)}{4\pi\, R^3} , \tag{3.101}$$

which is

$$\overline{\rho}_{\rm sub}(r_{\rm t,point2}) = 3\, \overline{\rho}_{\rm host}(R) , \tag{3.102}$$

where $\overline{\rho}_{\rm sub}$ and $\overline{\rho}_{\rm host}(R)$ are the mean density of the subhalo and the host, respectively. Note that the definition of the tidal radius in Eq. (3.100) is not considered in Stref & Lavalle (2017).

What is the mass and concentration dependence of the Jacobi radii? We saw in Sec. 3.1.3 that the scale density $\rho_{\rm s}$ is determined by the concentration parameter c_{200} alone, $\rho_{\rm s} = \rho_{\rm s}(c_{200})$, and is independent of the cosmological mass m_{200}. The mass profile can be expressed

$$m_{\rm int}(r) = 4\pi \int_0^r r'^2\, \rho(r')\, {\rm d}r' = 4\pi \rho_{\rm s} r_{\rm s}^3\, \tilde{m}_{\rm int}(r/r_{\rm s}) , \tag{3.103}$$

with $\tilde{m}_{\rm int}$ a dimensionless function. For both point-like radii, we have

$$\frac{\tilde{m}_{\rm int}(r_{\rm t,point}/r_{\rm s})}{(r_{\rm t,point}/r_{\rm s})^3} = \frac{3}{4\pi\, \rho_{\rm s}(c_{200})} \frac{M}{R^3} , \tag{3.104}$$

where $\rho_{\rm s}$ and $r_{\rm s}$ are the scale density and radius of the subhalo, and M refers to $M_{\rm tot}$ or $M(R)$ depending on the definition of the tidal radius. This shows that the ratio $r_{\rm t,point}/r_{\rm s}$ only depends on the concentration c_{200} and the radius of the orbit R, and is independent of the cosmological mass m_{200}. Consequently, $r_{\rm t,point}$ depends on m_{200} like $r_{\rm s}$ does, so $r_{\rm t,point} \propto m_{200}^{1/3}$.

3.2.1.2 Tidal radius for a smooth mass distribution

The case where the host has an extended mass distribution can be treated in a consistent way, although the computation is more involved (Binney & Tremaine, 1987; Tollet et al., 2017). It can be shown that the Jacobi radius is modified to

$$r_{\rm t,smooth} \equiv R \left\{ \frac{m_{\rm int}(r_{\rm t,smooth})}{3M(R)\left(1-\frac{1}{3}\frac{{\rm d}\ln M}{{\rm d}\ln R}(R)\right)} \right\}^{1/3} . \tag{3.105}$$

We refer to this definition as the *smooth Jacobi radius*. As for the point-like case, the ratio $r_{\rm t,smooth}/r_{\rm s}$ is independent of m_{200}. Indeed the ratio is solution of the equation

$$\frac{\tilde{m}_{\rm int}(r_{\rm t,smooth}/r_{\rm s})}{(r_{\rm t,smooth}/r_{\rm s})^3} = \frac{3}{4\pi\,\rho_{\rm s}(c_{200})}\frac{M(R)}{R^3}\left(1-\frac{1}{3}\frac{{\rm d}\ln M}{{\rm d}\ln R}(R)\right) , \tag{3.106}$$

It has therefore the scaling with the cosmological mass $r_{\rm t,smooth} \propto m_{200}^{1/3}$, similar to the point-like radius. We note that if the host halo has a constant density ${\rm d}\ln M/{\rm d}\ln R = 3$, the right-hand side of Eq. (3.105) diverges and the definition of the tidal radius breaks down. This is because a subhalo evolving in a constant-density field experiences tidal compression which prevents its mass from being transferred to its host, see Dekel et al. (2003) for a detailed discussion.

For the sake of comparison, we introduce another tidal radius $r_{\rm t,dens}$ based on a simple criterion involving only the density of the satellite and the host:

$$\rho_{\rm int}(r_{\rm t,dens}) \equiv \rho_{\rm host}(R) . \tag{3.107}$$

Unlike the Jacobi radii, this radius is not motivated by first principles. It is a rather phenomenological definition, as the radial boundary of a halo is defined as the point where its density reaches the background density. Like in the case of the Jacobi radii, the ratio $r_{\rm t,dens}/r_{\rm s}$ is independent of m_{200} since the mass density profile is $\rho_{\rm int}(r) = \rho_{\rm s}\,\tilde{\rho}_{\rm int}(r/r_{\rm s})$ with $\tilde{\rho}_{\rm int}$ a dimensionless function. Consequently, $r_{\rm t,dens}/r_{\rm s}$ is solution of

$$\tilde{\rho}_{\rm int}\left(\frac{r_{\rm t,dens}}{r_{\rm s}}\right) = \frac{\rho(R)}{\rho_{\rm s}(c_{200})} , \tag{3.108}$$

and only depends on c_{200} and R.

The tidal radii defined above assume a circular orbit for the satellite. However, we do not expect subhalos to have circular orbits in general. A more realistic description should involve elliptical orbits. Despite this approximation, it is found that a simple prescription such as Eq. (3.105) gives a radius which is tightly correlated to the observed radius of subhalos in N-body simulations, see *e.g.*, Fig. 15 in Springel et al. (2008).

The different definitions of the tidal stripping radius $r_{\rm t}$ are compared in Fig. 3.8. The position dependence of the ratio $r_{\rm t}/r_{\rm s}$ is shown for two Milky Way mass models from McMillan (2017): the NFW model (left panel) and the $(\alpha,\beta,\gamma) = (1,3,0)$ model (right panel). Irrespective of the definition, the tidal radius gets smaller and smaller as the subhalo orbits closer and closer to the center of the Galaxy. The only exception is the smooth Jacobi radius in the cored dark matter-only mass model, but as we discussed above, this definition of the tidal radius breaks down when the density is too flat. This potential problem disappears when the baryons are added to the mass model, hence it does not have any consequences in a realistic framework. We observe that the point-like approximation leads to the strongest tides, while the smooth and density-based models give rather close predictions. Interestingly, the exact shape of the Galactic dark matter profile has no impact on the calculation when baryons are also included. This can be seen by comparing the left and right panels of Fig. 3.8. The red curves (NFW+baryons) and green curves (core+baryons) are nearly identical, hence the calculation of the tidal radius

is robust and insensitive to the largely unknown inner shape of the dark halo profile. Fig. 3.9 shows the concentration dependence of the tidal radius for subhalos at the position of the Sun ($R_\odot = 8.21\,\mathrm{kpc}$ for the mass model considered here). This shows that tides have a stronger effect on less concentrated structures. We compare subhalos with two different density profiles: either an NFW profile, or an Einasto profile with $\alpha_\mathrm{E} = 0.17$, see Eq. (3.74). The difference between the two profiles is small over most of the relevant concentration range.

Both Fig. 3.8 and Fig. 3.9 show that the first Jacobi radius is smaller than all the other radii, at all position in the host Galaxy and for all concentrations. The other radii, *i.e.* the second and smooth Jacobi radii as well as the density-based radius, lead to comparable values. This is an indication that the first Jacobi radius probably overestimates the effect of tides on subhalos. Consequently, we do not consider this tidal radius in the following. From now on, each time a tidal radius is referred to as "point-like", it actually refers to the second Jacobi radius defined in Eq. (3.100). We stress that this is different from Stref & Lavalle (2017), where the only point-like radius considered was the one defined in Eq. (3.99).

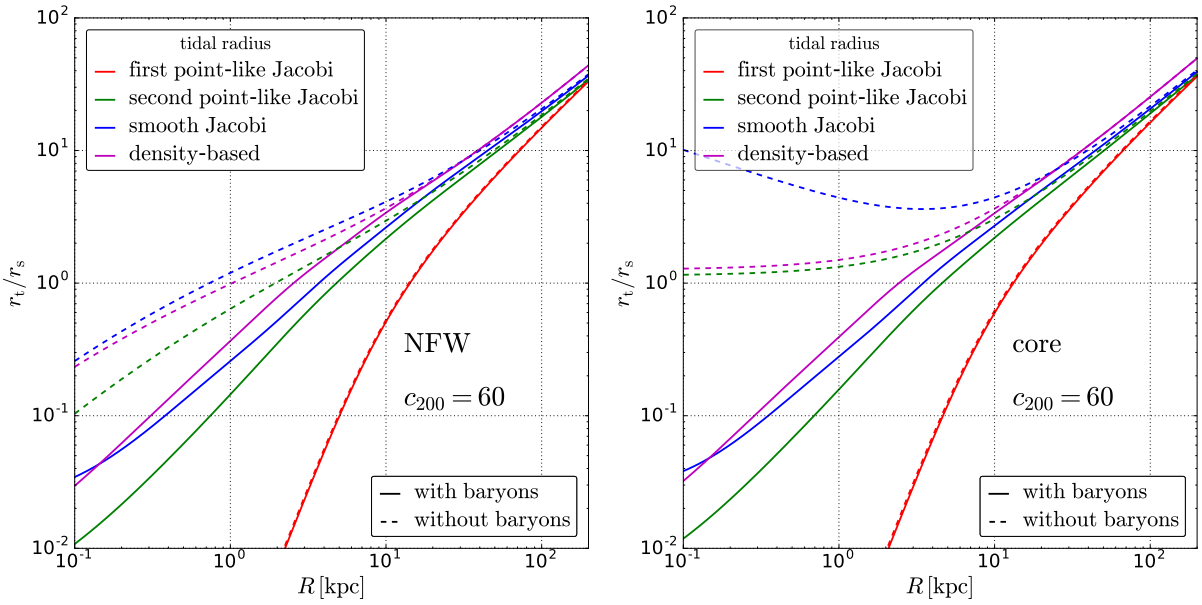

Figure 3.8 – Left panel: tidal radius to scale radius ratio as a function of the position inside the Galaxy, for the NFW mass model of McMillan (2017). The subhalo internal profile is an NFW with concentration $c_{200} = 60$. **Right panel:** same as left panel for the cored mass model of McMillan (2017).

3.2.2 Tidal shocking

We described tidal stripping which is the effect on a satellite of a constant or slowly-varying gravitational potential. We now discuss the opposite situation where the gravitational potential rapidly varies in time: this is called tidal shocking. The physical effect is very simple to understand: as a subhalo passes by or passes trough a dense object (a dark matter cusp, a stellar disc, a star,etc.), it experiences a strong gravitational field which strips away some particles previously bounded to the subhalo. In the following, we investigate in details the shocking effect induced by the Galactic disc.

3.2.2.1 Shocking by the Galactic disc

A very important effect is the shocking induced by the Galactic disc. This effect was first discussed, in the context of star clusters affected by the passing of a nearby cloud, by Spitzer (1958). This paper makes use of the *impulsive approximation* which consists in ignoring the

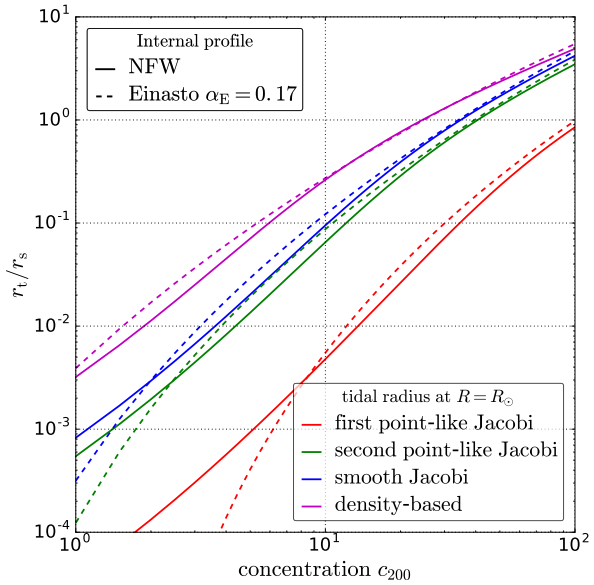

Figure 3.9 – Tidal radius to scale radius ratio as a function of the concentration, at the position of the Sun $R_\odot = 8.21\,\mathrm{kpc}$. We show the ratio for the first Jacobi radius (red), the second Jacobi radius (green), the smooth Jacobi radius (blue) and the density-based radius (magenta). We compare the prediction for two different internal density profiles: NFW (solid lines) and Einasto (dashed lines).

inner dynamics of the cluster when evaluating the effect of the shock. Tidal shocking was then investigated by Ostriker et al. (1972) to evaluate the impact of the Galactic disc on globular clusters, again using the impulsive approximation. The importance of adiabatic invariance was pointed out by Weinberg (1994b,a) and the shocking calculation was revised and generalized by Gnedin et al. (1999); Gnedin & Ostriker (1999). The impact of disc shocking on subhalos has been numerically studied in a cosmological context by D'Onghia et al. (2010); Yurin & Springel (2015); Errani et al. (2017) and generically found to be a major source of stripping in the inner part of the host halo. Here we provide several semi-analytic methods to evaluate the impact of the disc on subhalos.

First, we reproduce the original computation of Ostriker et al. (1972). We consider an object (subhalo, globular cluster) crossing the galactic disc. We work in the rest frame of the disc and define the z-axis as perpendicular to the disc. The object is on a circular orbit of radius R. Let z_c and z_p be the z-coordinate of the object's center and of a particle orbiting in the object, respectively. We define $\Delta z \equiv z_\mathrm{p} - z_\mathrm{c}$, $v_z \equiv \mathrm{d}\Delta z/\mathrm{d}t$ and the equation of motion is

$$\begin{aligned} \frac{\mathrm{d}v_z}{\mathrm{d}t} &= g_\mathrm{d}(R, z_\mathrm{p}) - g_\mathrm{d}(R, z_\mathrm{c}) \\ &\simeq \Delta z \, \frac{\partial g_\mathrm{d}}{\partial z}\,(R, z_\mathrm{c}) \ , \end{aligned} \tag{3.109}$$

where g_d is the gravitational acceleration caused by the disc. If the disc has a mass density ρ_d, the modulus of the acceleration is given by

$$|g_\mathrm{d}(R, z)| = 4\pi G_\mathrm{N}\, z_\mathrm{d}\, \rho_\mathrm{d}(R, z)\,. \tag{3.110}$$

Integrating Eq. (3.109) over time, we get the net velocity change

$$\Delta v_z = \int \mathrm{d}t\, \Delta z(t)\, \frac{\partial g_\mathrm{d}}{\partial z}\,[z_\mathrm{c}(t)]\ . \tag{3.111}$$

We now make the impulsive approximation: the dynamics within the object is considered very slow compared to the crossing of the disc, hence Δz is roughly time-independent. Changing the

integration variable from t to z_c we get

$$\Delta v_z = \frac{\Delta z}{V_z}\, 2\, g_\mathrm{d}(R,0)\,, \tag{3.112}$$

where V_z is the z-velocity of the object's center and the factor of two comes from the odd-parity of g_d. Consequently, the kinetic-energy gain per unit of particle mass in the rest frame of the object is

$$\begin{aligned}\delta\epsilon &= \frac{1}{2}\,(\Delta v_z)^2 = \frac{2\,g_\mathrm{d}^2}{V_z^2}\,(\Delta z)^2 \\ &= \frac{2\,g_\mathrm{d}^2}{V_z^2}\,r^2\cos^2(\theta)\,,\end{aligned} \tag{3.113}$$

where r is the distance between the particle and the object's center, and θ is the angle between the radial and vertical directions. This result holds if $T_\mathrm{cross}(R) \ll \tau_\mathrm{sub}(r)$ where T_cross is the object crossing time and $\tau_\mathrm{sub}(r)$ the orbital period of the particle within the object. This is the content of the impulsive approximation. This approximation might break down for particles near the center of the object which have a very short period. These particles are then protected by adiabatic invariance, which can be accounted for by multiplying the right-hand side of Eq. (3.113) by a corrective factor $A(\eta)$ (Weinberg, 1994b,a). Using analytical and numerical studies, Gnedin et al. (1999); Gnedin & Ostriker (1999) proposed a parametric form for this factor

$$A(\eta) = (1+\eta^2)^{-3/2}\,, \tag{3.114}$$

where η is the *adiabatic parameter* defined as

$$\eta \equiv \omega_\mathrm{int}(r) T_\mathrm{cross}\,, \tag{3.115}$$

with ω_int the orbital frequency of particles within the clump. The energy gain is modified to

$$\delta\epsilon(r,\theta) = \frac{2\,g_\mathrm{d}^2}{V_z^2}\,r^2\cos^2(\theta)\,A(\eta)\,. \tag{3.116}$$

If $\eta \gg 1$ *i.e.* the orbital time of a test particle in the subhalo is much smaller than the disk-crossing time, then the impulsive approximation breaks down and $A(\eta) \to 0$: particles are adiabatically protected against tidal shocking. Let us estimate the importance of adiabatic invariance in subhalos. With z_d the length scale of the disk along the z-axis, the typical crossing-time is $T_\mathrm{cross}(R) = z_\mathrm{d}/V_z(R)$. The z-component of the velocity should be close to the velocity dispersion along z, *i.e.* $V_z \simeq \sigma_z$. Assuming an isotropic velocity distribution of subhalos, we have $\sigma_z^2 = \sigma^2/3$ where σ is the total velocity dispersion. To evaluate this velocity dispersion, we may assume a Maxwell-Boltzmann velocity distribution for subhalos in the Galaxy. As we will see in Chap. 5, this is equivalent to assuming a singular isothermal sphere for the subhalo spatial distribution. In that case, the velocity dispersion is simply related to the circular velocity

$$\sigma^2(R) = \frac{1}{2}\,v_\mathrm{c}^2(R)\,, \tag{3.117}$$

where

$$v_\mathrm{c}(R) = \sqrt{\frac{G_\mathrm{N}\,m(R)}{R}} \tag{3.118}$$

with $m(R)$ the Galactic mass within R. This should give the right order of magnitude of V_z even if the subhalo distribution does not strictly follow the isothermal profile. The crossing time is

then

$$T_{\rm cross}(R) = \sqrt{2}\frac{z_{\rm d}}{v_{\rm c}(R)} = z_{\rm d}\sqrt{\frac{2R}{G_{\rm N}\, m(R)}} \\ \simeq 0.45\,{\rm Myr}\left(\frac{z_{\rm d}}{100\,{\rm pc}}\right)\left(\frac{200\,{\rm km/s}}{V_z}\right) . \tag{3.119}$$

Assuming the internal density profile of subhalos is also not too far from the singular isothermal sphere, we can express the internal velocity dispersion as

$$\sigma_{\rm int}^2 = \frac{3}{2}\frac{G_{\rm N}\, m_{\rm int}(r)}{r} \tag{3.120}$$

and the orbital frequency

$$\begin{aligned}\omega_{\rm int}(r) &= \frac{\sigma_{\rm int}}{r} \\ &= \sqrt{\frac{3\, G_{\rm N}\, m_{\rm int}(r)}{2\, r^3}} \\ &= 2.4\times 10^{-2}\,{\rm Myr}^{-1}\left(\frac{m_{\rm int}(r)}{10^{-6}\,{\rm M}_\odot}\right)^{1/2}\left(\frac{3.5\times 10^{-3}\,{\rm pc}}{r}\right)^{3/2}\end{aligned} \tag{3.121}$$

Note that $\omega_{\rm int}$, expressed as a function of $r/r_{\rm s}$, depends only on the concentration c_{200} and not on the mass m_{200}. We find that the adiabatic correction becomes relevant only when $r < 10^{-3}\, r_{\rm s}$ *i.e.* subhalos are stripped down to their very center. This only happens for the most extreme stripping and shocking models discussed in this section [like the first point-like Jacobi radius in Eq. (3.99)], and only in the inner parts of the Galaxy. This means that the impulsive approximation is a good approximation in most cases. Nevertheless, we performed our calculations including the corrective factor regardless of the modelling of tidal effects.

Shocking radius: differential method What is the tidal radius induced by disc shocking? There is no prescription available in the literature to compute this radius, therefore we propose several definitions. One way to identify a maximal radius is to compare the kinetic energy gain in Eq. (3.116) to the potential energy of a dark matter particle in the subhalo. Let us consider a subhalo with pre-crossing radial extension r_0, and a dark matter particle on a circular orbit at $r < r_0$ in that subhalo. Assuming a hard truncation of the subhalo at radius r_0, the potential energy (per unit of particle mass) is given by

$$\phi_{\rm int}(r) - \phi_{\rm int}(r_0) \tag{3.122}$$

where

$$\phi_{\rm int}(r) = -G_{\rm N}\int_r^\infty \frac{m_{\rm int}(r')}{r'^2}\,{\rm d}r' , \tag{3.123}$$

is the solution of Poisson's equation cancelling at infinity. If the kinetic energy gain by a particle inside a subhalo during the crossing of the disc exceeds its potential energy, this particle becomes unbound to the subhalo. The new radius r_1 after a single crossing of the disc can be evaluated by equating the kinetic energy gain and the potential energy:

$$\delta\epsilon(r_1) \equiv \phi_{\rm int}(r_0) - \phi_{\rm int}(r_1) . \tag{3.124}$$

This definition is meaningful because $|\phi_{\rm int}(r) - \phi_{\rm int}(r_0)|$ is a decreasing function of r, hence the dark matter particles removed by that procedure are in the outskirts of the clump, see the left

panel in Fig. 3.10. Note that the energy gain given in Eq. (3.116) has an angular dependence, hence we use instead the energy gain averaged on the sphere of radius r:

$$\begin{aligned}\langle\delta\epsilon\rangle(r) &\equiv \frac{1}{4\pi}\int_0^{2\pi}\mathrm{d}\phi\int_0^{\pi}\mathrm{d}(\cos\theta)\delta\epsilon(r,\theta)\\ &= \frac{2\,g_\mathrm{d}^2}{3\,V_z^2}\,r^2\,A(\eta)\,,\end{aligned} \tag{3.125}$$

and the radius r_1 after disc shocking is really defined by

$$\langle\delta\epsilon\rangle(r_1) \equiv \phi_\mathrm{int}(r_0) - \phi_\mathrm{int}(r_1)\,. \tag{3.126}$$

This definition of the tidal shocking radius depends on the radial extension r_0 before crossing. This means that the radius of the clump has to be computed after each crossing of the stellar disc. We call the final radius obtained via this procedure the *differential radius* $r_{\mathrm{t,diff}}$. The ratio $r_{\mathrm{t,diff}}/r_\mathrm{s}$ is independent of m_{200}. Indeed the adiabatic correction $A(\eta)$ only depends on $\rho_\mathrm{s}(c_{200})$, the energy gain scales like r_s^2 and the potential energy like $\rho_\mathrm{s}r_\mathrm{s}^2$ hence the ratio only depends on the scale density $\rho_\mathrm{s}(c_{200})$, the position of the subhalo R and its radius before crossing r_0. The angle-averaged energy gain and the potential energy for a single crossing, for a clump at the position of the Solar System $R = R_\odot$, are shown on the left panel in Fig. 3.10. The ratio $r_{\mathrm{t,diff}}/r_\mathrm{s}$ is the x-axis value of the intersection between the red curve (energy gain) and the blue curve (potential). The radius before crossing is chosen to be the cosmological radius r_{200} such that $r_{200}/r_\mathrm{s} = c_{200}$.

Shocking radius: integral method We consider an alternative definition of the shocking radius based on integrated quantities. The idea is to compute the total energy gain of a subhalo and compare it to its binding energy. The total energy gain is computed from Eq. (3.116)

$$\begin{aligned}\Delta E(<r_0) &= \int\delta\epsilon\,\rho_\mathrm{int}(\vec{r})\,\mathrm{d}^3\vec{r}\\ &= 2\pi\int_0^{r_0}\mathrm{d}r\,r^2\int_{-1}^{1}\mathrm{d}\cos\theta\,\delta\epsilon(r,\theta)\,\rho_\mathrm{int}(r)\end{aligned} \tag{3.127}$$

If the adiabatic correction is neglected and the subhalo has an NFW profile, the total energy gain is analytical

$$\Delta E(<r_0) \simeq \frac{8\pi}{3}\,\frac{g_\mathrm{d}^2}{V_z^2}\,\rho_\mathrm{s}r_\mathrm{s}^5\left[\frac{(x_0-3)x_0^2-6x_0}{2(x_0+1)} + 3\ln(1+x_0)\right], \tag{3.128}$$

where $x_0 = r_0/r_\mathrm{s}$. This energy has to be compared with the binding energy of the subhalo, which is defined by

$$U(<r_0) = G_\mathrm{N}\int\frac{m_\mathrm{int}(\vec{r})}{|\vec{r}|}\,\rho_\mathrm{int}(\vec{r})\,\mathrm{d}^3\vec{r}. \tag{3.129}$$

This is also an analytical function for the NFW profile

$$U(<r_0) = 16\pi^2 G_\mathrm{N}\rho_\mathrm{s}^2 r_\mathrm{s}^5\left[\frac{1}{2}\left(1-\frac{1}{(1+x_0)^2}\right) - \frac{\ln(1+x_0)}{1+x_0}\right]. \tag{3.130}$$

Having computed the total energy gain and the total binding energy of a subhalo, we can define its extension $r_{\mathrm{t,int}}$ after disc shocking as follow

$$\Delta E(<r_{\mathrm{t,int}}) = U(<r_{\mathrm{t,int}})\,. \tag{3.131}$$

Beyond $r_{\rm t,int}$, the total energy gain is larger than the binding energy of the clump as shown in the right panel on Fig. 3.10. This gives the shocking radius after one single crossing. For the radius after $N_{\rm cross}$ crossing, we prescribe

$$N_{\rm cross}\Delta E(< r_{\rm t,int}) = U(< r_{\rm t,int})\,. \tag{3.132}$$

The ratio $r_{\rm t,int}/r_{\rm s}$ is, again, independent of m_{200} which can be seen from Eqs. (3.128)(3.130). We have $\Delta E \propto \rho_{\rm s} r_{\rm s}^5$ and $U \propto \rho_{\rm s}^2 r_{\rm s}^5$ therefore $r_{\rm t,int}/r_{\rm s}$ only depends on $\rho_{\rm s}(c_{200})$ and R. The total energy gain for a single crossing, at the position of the Sun $R = R_\odot$, is compared to the binding energy and the total potential energy on the right panel in Fig. 3.10. The ratio $r_{\rm t,int}/r_{\rm s}$ is defined by the x-axis value of the intersection between the green curve and the blue curve. Fixing the integral radius with the potential energy (red curve) rather than the binding energy leads to a similar, though slightly lower, numerical value.

Shocking radius: simulation-based estimate We finally consider a third definition of the shocking radius based on a numerical study by D'Onghia et al. (2010). This study focuses on the effect of a Galactic disc on subhalos and shows that it is very efficient at disrupting these structures. The authors propose an empirical criterion to model the effect of disc shocking. They propose an expression for the total energy gain in units of the binding energy

$$\frac{\Delta\tilde{E}}{U} = \frac{(1.84\, r_{1/2})^2 g_{\rm d}^2}{3\,\tilde{\sigma}^2 V_z^2}\,, \tag{3.133}$$

where $r_{1/2}$ is the radius containing half the subhalo's mass and $\tilde{\sigma}$ is an estimate of the internal velocity dispersion of the clump

$$\tilde{\sigma}^2 = 0.4\,\frac{G_{\rm N} m_{\rm sub}^{\rm tot}}{r_{1/2}}\,, \tag{3.134}$$

where $m_{\rm sub}^{\rm tot}$ is the total subhalo mass. The dynamical grounds for this expression are taken from Binney & Tremaine (1987). The authors argue that a subhalo is destroyed when the total energy after $N_{\rm cross}$ crossing of the galactic disc is comparable to the binding energy. Whether clumps are actually destroyed in numerical simulations or disappear due to limited resolution is a difficult question which has very likely not fully been addressed in the past. Indeed, recent work has shown that criteria based on the binding energy strongly overestimate the disruption efficiency (van den Bosch et al., 2018; van den Bosch & Ogiya, 2018). This can be understood from the adiabatic invariance argument stated before, which makes the dense cores of subhalos very resilient to tidal effects. For the sake of comparison, we define a disc shocking radius through

$$N_{\rm cross}\,\frac{\Delta\tilde{E}}{U}(r_{\rm t,sim}) = 1\,, \tag{3.135}$$

This radius is similar to our integral definition, with a different expression for the total energy gain. This simulation-based definition also leads to a ratio $r_{\rm t,sim}/r_{\rm s}$ independent of m_{200} because the total energy gain has the scaling $\Delta\tilde{E} \propto \rho_{\rm s} r_{\rm s}^5$ just like our integral definition. The energy $\Delta\tilde{E}$ is shown on the right panel in Fig. 3.10. We see that for $c_{200} < 10$, we have $\Delta\tilde{E} > \Delta E$ hence the simulation-based estimate is more efficient at stripping subhalos. Note that the simulations of D'Onghia et al. (2010) focuses on massive subhalos $m \gtrsim 10^6\,{\rm M}_\odot$ hence their results might not apply to smaller, more concentrated structures.

3.2.2.2 Encounter with stars

Another effect quite similar to disc shocking is the effect of individual stars on subhalos passing close by. This effect has been investigated in several studies (Berezinsky et al., 2006; Angus

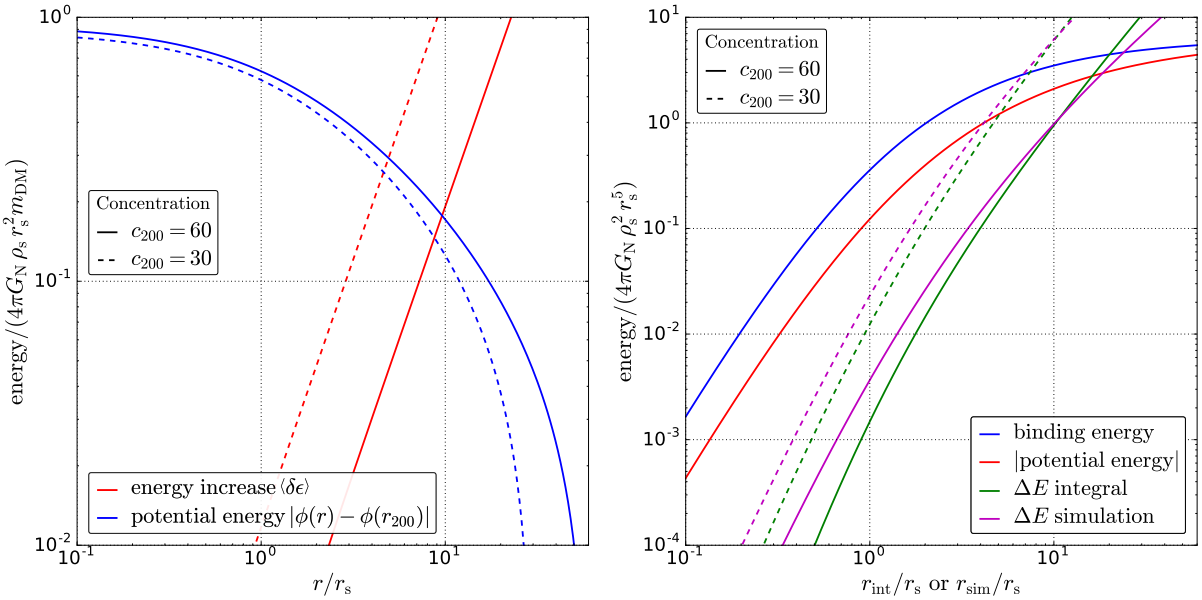

Figure 3.10 – Left panel: angle-averaged energy gain (red) compared to the potential energy (blue) of a dark matter particle at a radius r within a subhalo orbiting at $R = R_\odot$. Two possible values of the concentration are shown $c_{200} = 60$ and $c_{200} = 30$. **Right panel:** integrated energy gain following the definition in Eq. (3.127) (green) and in Eq. (3.133) (purple), for $c_{200} = 60$ and $c_{200} = 30$. Are shown the binding energy (blue) and the total potential energy (red).

& Zhao, 2007; Zhao et al., 2007; Green & Goodwin, 2007; Schneider et al., 2010), using both analytical and numerical estimates. It can be shown that for subhalos, the effect of disc shocking dominates over the shocking from each star (Berezinsky et al., 2014). Encounters with stars might be more important for ultracompact minihalos which are halos having collapsed during the radiation-dominated era (Berezinsky et al., 2010). These structures are dense enough to be practically immune against regular tidal effects, in which case stellar encounters might be the only potential source of disruption.

3.2.3 Disruption of subhalos

All the tidal radii we have introduced to model the effects of halo stripping and disc shocking are compared in Fig. 3.11. The ratio r_t/r_s where r_t is the tidal radius is shown for a particular concentration c_{200} (we recall that this ratio is independent of the subhalo's mass). The coloured curves show the tidal radii for the stripping methods discussed in Sec. 3.2.1 and the black curves show the tidal radii for the disc shocking methods discussed in Sec. 3.2.2. Irrespective of the particular methods chosen for stripping and shocking, the effect of disc shocking is sub-dominant at large radius $R \gg 10\,\mathrm{kpc}$ with respect to halo stripping. This is not a surprise since the Galactic disc extends to $R_{\mathrm{disc}} \sim 15\,\mathrm{kpc}$ and we assumed subhalos are on circular orbits. For subhalos on radial orbits, we expect disc shocking to play a role even at distances $R > R_{\mathrm{disc}}$ but we do not take this possibility into account. More interesting is the hierarchy below 10 kpc: disc shocking is generically more important than halo stripping in that region. However, the choice of the shocking radius definition leads to important differences in that region: while the differential and integral methods lead to similar results, the simulation-based method is much more efficient at stripping subhalos. We recall however that this criterion has only been probed on massive subhalos which tend to be less concentrated due to their late collapse, see Sec. 3.1.3.

We now discuss the possible disruption of subhalos by tidal effects. We have seen that tidal effects are very efficient at stripping subhalos down to their scale radius and below, the question is then: can a structure survive after having lost most of its mass? This is crucial for indirect

dark matter searches for instance, as the impact of a clump on these searches depends on its luminosity $\propto \int \rho^2 \mathrm{d}^3\vec{r}$ rather than its mass, and most of the luminosity comes from the structure's core, see *e.g.*, Berezinsky et al. (2008). The question of survival under tidal effects also concerns luminous structures. Star clusters in particular have been under investigation for a long time, see *e.g.*, Spitzer (1958). However these stellar systems are subject to phenomena like relaxation and evaporation which facilitate their disruption but are not relevant for the particle dark matter scenario (at the notable exception of primordial black hole dark matter). The question of the survival of dark matter subhalos is a more recent one. It has been investigated numerically, in dedicated studies Tormen et al. (1998); Hayashi et al. (2003) or within general studies on subhalos Diemand et al. (2004, 2008); Springel et al. (2008); van den Bosch (2017). Cosmological simulations seem to agree on the fact that subhalos are very efficiently disrupted by the tidal field of the host galaxy. Hayashi et al. (2003) find that subhalos are disrupted when their tidal radii become similar to their scale radii $r_\mathrm{t} \sim r_\mathrm{s}$. The numerical study of disruption is unfortunately complicated by the resolution limit inherent to simulations. A recent detailed analytical and numerical investigation van den Bosch et al. (2018); van den Bosch & Ogiya (2018) point toward a resilience of subhalos against tidal effects. It is shown by the authors that the disruption observed in simulations could be almost entirely explained by numerical artefacts and therefore vastly overestimated. This very recent result needs confirmation and calls for more dedicated studies of artificial disruption in simulations.

In order to account for all possible scenarios (disruption when $r_\mathrm{t} \sim r_\mathrm{s}$, complete resilience, and everything in between) we model subhalo disruption in a flexible way. Concretely, we assume a subhalo is fully disrupted if its tidal radius verifies

$$\frac{r_\mathrm{t}}{r_\mathrm{s}} \leqslant \epsilon_\mathrm{t} \,, \tag{3.136}$$

where ϵ_t is a free parameter we refer to as the *disruption parameter*. To get results in agreement with Hayashi et al. (2003), we can fix $\epsilon_\mathrm{t} = 1$ while a value compatible with van den Bosch et al. (2018) would be much lower, for instance $\epsilon_\mathrm{t} = 10^{-2}$. We recall that, incidentally, the ratio $r_\mathrm{t}/r_\mathrm{s}$ is mass-independent for all the tidal radius definitions considered here, and only depends on c_{200} and R. Hence Eq. (3.136) can be rewritten as a condition on the concentration c_{200}

$$c_{200} \geqslant c_\mathrm{min}(R) \,, \tag{3.137}$$

where $c_\mathrm{min}(R)$ is the minimal concentration a subhalo needs to survive tidal effects at a position R. This concentration is the solution of

$$\frac{r_\mathrm{t}}{r_\mathrm{s}}(c_\mathrm{min}, R) \equiv \epsilon_\mathrm{t} \,. \tag{3.138}$$

and therefore it is a function of the position R only. The minimal concentration is shown in Fig. 3.12 for $\epsilon_\mathrm{t} = 1$ (left panel) and $\epsilon_\mathrm{t} = 10^{-2}$ (right panel). The value of $c_\mathrm{min}(R)$ is very roughly ten times lower in the $\epsilon_\mathrm{t} = 10^{-2}$ case compared to the $\epsilon_\mathrm{t} = 1$ case. The hierarchy between the different definitions of the tidal radius is left essentially unaffected by the choice of ϵ_t. The relative position of the coloured and black curves shows, again, that disc shocking dominates in the inner parts of the Galaxy ($R < 10\,\mathrm{kpc}$) while halo stripping dominates outside. Note that, unlike Fig. 3.11 which shows $r_\mathrm{t}/r_\mathrm{s}(R)$ for only one particular value of the concentration c_{200}, the entire information on $r_\mathrm{t}/r_\mathrm{s}$ is contained in Fig. 3.12. Hence the minimal concentration is a very convenient tool to compare the different definitions of the tidal radius, irrespective of the survival of subhalos under tidal effects and the realistic value of ϵ_t.

3.3 A constrained model of Galactic subhalos

In this section, we use our knowledge of tidal effects to build a semi-analytic model of Galactic subhalos. This is essentially the content of Stref & Lavalle (2017), though we also discuss

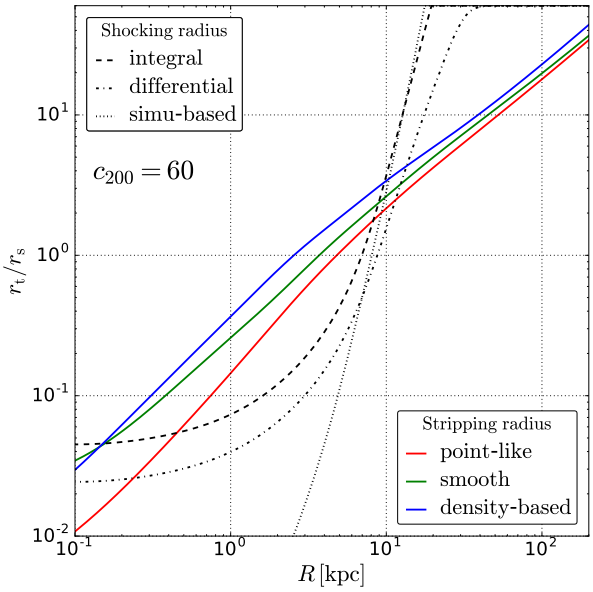

Figure 3.11 – Tidal-to-scale radius ratio r_t/r_s as a function of the position R in the Galaxy, for the different definitions of the stripping and shocking radii given in Secs. 3.2.1 and 3.2.2. The concentration is fixed to $c_{200} = 60$.

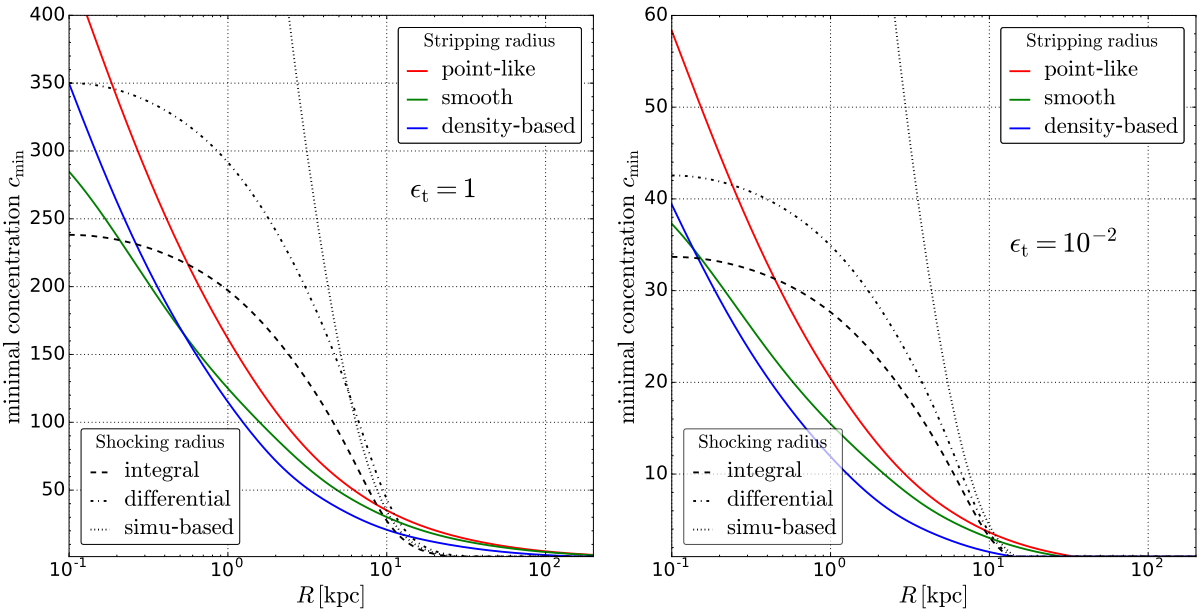

Figure 3.12 – Minimal concentration $c_{\rm min}$ for the survival of a subhalo as a function of the position R in the Galaxy, for two values of the disruption parameter: $\epsilon_t = 1$ (left panel) and $\epsilon_t = 10^{-2}$ (right panel).

here cases that are not considered in the original paper. Let us first discuss the other subhalo models available in the literature. The small-scale structuring of CDM is of great interest for essentially two distinct communities: cosmologists working on structure formation, and astroparticle physicists interested in dark matter searches. Models built by cosmologists tend to focus on a consistent modelling of the formation, mergers and evolution of dark matter structures with redshift, see *e.g.*, Taylor & Babul (2004); Penarrubia & Benson (2005); van den Bosch et al. (2005); Zentner et al. (2005); Gan et al. (2010); Pullen et al. (2014); Han et al. (2016). Astroparticle physicists, on the other hand, are, for instance, interested in computing the boost factor for indirect searches for annihilating dark matter. Hence all is needed is the subhalo

distribution today and the full modelling of the redshift evolution is not required. Semi-analytic models are in general calibrated on N-body simulations, see *e.g.*, Lavalle et al. (2007); Lavalle et al. (2008); Kamionkowski et al. (2010); Pieri et al. (2011); Bartels & Ando (2015); Hiroshima et al. (2018) though some rely only on first principles *e.g.*, Berezinsky et al. (2003). Our model belongs to the dark matter-searches-oriented category. Its originality with respect to other models resides in the implementation of *dynamical constraints*: the model is built in such a way that it is, by construction, consistent with existing observations of our own Galaxy. This is of crucial importance for dark matter searches as observations of the Milky Way have become more and more precise, peaking with the recent results of the Gaia mission, see Gaia Collaboration et al. (2018).

3.3.1 Outline of the model

Before going into the details of the modelling, we give a general outline of the method. A subhalo in our Galaxy is characterized by three quantities: its mass m, its concentration c and its position within the Galaxy $\vec{r}$ – we further assume spherical symmetry, so we will consider the radial position $|\vec{r}| = R$. We have knowledge of the cosmological mass and concentration PDFs of *isolated* dark matter halos, as we have seen in Secs. 3.1.2 and 3.1.3. The main assumption of our model is that the mass, concentration and position PDFs of subhalos is only affected by the tidal effects experienced by these subhalos. The construction of the model is as follows. We start from a virtual configuration where the dark matter halo of the Galaxy is made of smoothly distributed dark matter and non-interacting subhalos. By non-interacting, we mean that subhalos in this initial configuration do not "feel" the tides from the host. The subhalos are considered as test particles and initially follow the dark matter distribution as inferred by studies of the Galactic dynamics, for instance the dynamically constrained NFW profile constructed by McMillan (2017). Their mass and concentration PDFs are the cosmological ones. We then plug in tidal effects, considering stripping by the Galactic potential and shocking by the Galactic disc. Tidal effects remove matter from subhalos, which is transferred to the smooth dark matter component. Since tides affect subhalos according to their mass, concentration and position, the initial (cosmological) PDFs are all modified by stripping and shocking. The posterior PDFs are computable and constitute outputs of our model. These modified PDFs completely determine the subhalo population in the Galaxy today and therefore allow us to compute all the quantities relevant for dark matter searches such as the boost factor, the subhalo number density, etc.

3.3.2 Initial subhalo PDFs

Mass function Let us start by describing the initial (pre-tides) PDFs. We assume the mass PDF to be the cosmological mass function given by the Press-Schechter theory in Eq. (3.66). On scales far smaller than that of galaxy clusters, the Press-Schechter mass function behaves as a power law

$$\frac{\mathrm{d}P}{\mathrm{d}m_{200}}(m_{200}) = \frac{1}{K_\mathrm{m}} \left(\frac{m_{200}}{M_\odot}\right)^{-\alpha_\mathrm{m}} , \tag{3.139}$$

with $\alpha_\mathrm{m} \simeq 2$. The factor K_m is set by requiring that the mass PDF be normalized to one over the range of mass m_{200} explored by subhalos. If we impose $m_{200} \in [m_\mathrm{min}, m_\mathrm{max}]$, the factor is given by

$$K_\mathrm{m} = \int_{m_\mathrm{min}}^{m_\mathrm{max}} \left(\frac{m}{M_\odot}\right)^{-\alpha_\mathrm{m}} \mathrm{d}m = \frac{M_\odot}{\alpha_\mathrm{m} - 1} \left[\left(\frac{m_\mathrm{min}}{M_\odot}\right)^{1-\alpha_\mathrm{m}} - \left(\frac{m_\mathrm{max}}{M_\odot}\right)^{1-\alpha_\mathrm{m}}\right] . \tag{3.140}$$

The minimal cosmological mass m_min is set by the free-streaming scale of the dark matter particle, see Sec. 2.4 for details. Assuming dark matter is thermally produced in the early Universe, the

epoch of free streaming follows kinetic decoupling and therefore depends on the microscopic interactions of the dark matter particle. To be as general as possible, we take $m_{\rm min}$ as a free parameter, keeping in mind its very low value in typical WIMPs models $m_{\rm min} \sim 10^{-6}\,{\rm M}_\odot$, see *e.g.*, Green et al. (2004, 2005); Bringmann & Hofmann (2007); Bringmann (2009). The maximal mass is set to $m_{\rm max} = 10^{-2}\,{\rm M}_{\rm halo}$ where $M_{\rm halo}$ is the total (virial) mass of the Galactic dark matter halo. This value of the maximal mass is set by the pre-infall mass scale of satellite galaxies like Draco (Read et al., 2018). Note the smallness of $m_{\rm min}$ implies

$$K_{\rm m} \simeq \frac{M_\odot}{\alpha_{\rm m}-1}\left(\frac{m_{\rm min}}{M_\odot}\right)^{1-\alpha_{\rm m}}, \tag{3.141}$$

hence the normalization is not sensitive to the value of $m_{\rm max}$. Note that we account for the suppression of power below the free-streaming scale through a sharp cutoff in the mass function. A more realistic description could be obtained by multiplying the power law by a factor $1-\exp\left(-(m_{200}/m_{\rm min})^n\right)$ with an index n controlling the sharpness of the mass cutoff. Finally, a fully consistent treatment would require the computation of the power spectrum including the free-streaming (and collisional) damping, and the computation of the mass function using the Press-Schechter formalism as done in *e.g.*, Schneider et al. (2013).

Concentration PDF The cosmological concentration PDF is given by a log-normal distribution

$$\frac{{\rm d}P}{{\rm d}c_{200}}(c_{200}, m_{200}) = \frac{1}{K_{\rm c}}\frac{1}{c_{200}\sqrt{2\pi}\,\sigma_{\rm c}}\,\exp\left[-\left(\frac{\ln c_{200}-\ln\bar{c}(m_{200})}{\sqrt{2}\sigma_{\rm c}}\right)^2\right], \tag{3.142}$$

with a scatter $\sigma_{\rm c}$, and a mass-dependent median concentration $\bar{c}(m_{200})$. This mass dependence induces a correlation between c_{200} and m_{200}. We recall that this correlation has a cosmological origin: dark matter halos of low mass are more likely to collapse earlier, in a denser Universe, and are therefore more concentrated on average. For the median mass-concentration relation, we use the relation given by Sánchez-Conde & Prada (2014), which is obtained by fitting the relation found in CDM numerical simulations

$$\bar{c}(m_{200}) = \sum_{n=0}^{5} c_n \left[\ln\left(\frac{m_{200}}{h^{-1}M_\odot}\right)\right]^n, \tag{3.143}$$

where h is the scaled Hubble parameter and $c_{\rm n} = [37.5153, -1.5093, 1.636\times10^{-2}, 3.66\times10^{-4}, -2.89237\times10^{-5}, 5.32\times10^{-7}]$. The scatter $\sigma_{\rm c}$ is found to be mass independent in CDM numerical simulations, see Macciò et al. (2008). We fix its value to $\sigma_{\rm c} = 0.14\,{\rm dex} = 0.14\,\ln(10)$, as in Macciò et al. (2008); Sánchez-Conde & Prada (2014); Dutton & Macciò (2014). Note that the concentration PDF differs from the usual log-normal PDF by a factor $1/K_{\rm c}$. This is because $c_{200} \geqslant 1$ by definition, hence we have

$$\begin{aligned} K_{\rm c} &= \int_1^{+\infty} {\rm d}c\,\frac{1}{\sqrt{2\pi}\sigma_{\rm c}c}\,\exp\left[-\left(\frac{\ln c-\ln\bar{c}}{\sqrt{2}\sigma_{\rm c}}\right)^2\right] \\ &= \frac{1}{2}\,{\rm erfc}\left(-\frac{\ln\bar{c}}{\sqrt{2}\sigma_{\rm c}}\right). \end{aligned} \tag{3.144}$$

In practice however, we find that $K_{\rm c}$ is equal to one over the entire range of m_{200}. The n-th moment of the concentration PDF takes the following form

$$\langle c^n\rangle = \frac{\bar{c}^n}{2K_{\rm c}}\,e^{n^2\sigma_{\rm c}^2/2}\,{\rm erfc}\left[-\frac{1}{\sqrt{2}}\left(n\sigma_{\rm c}+\frac{\ln\bar{c}}{\sigma_{\rm c}}\right)\right]. \tag{3.145}$$

The average concentration $\langle c_{200}\rangle$ is compared to the median concentration $\bar{c}$ on the left panel in Fig. 3.13. The average is close to the median for all masses though it is systematically higher. The concentration PDF is shown on the right panel in Fig. 3.13 for three subhalo masses $m_{200} = 10^{-6}/10^{0}/10^{6}\,{\rm M}_\odot$.

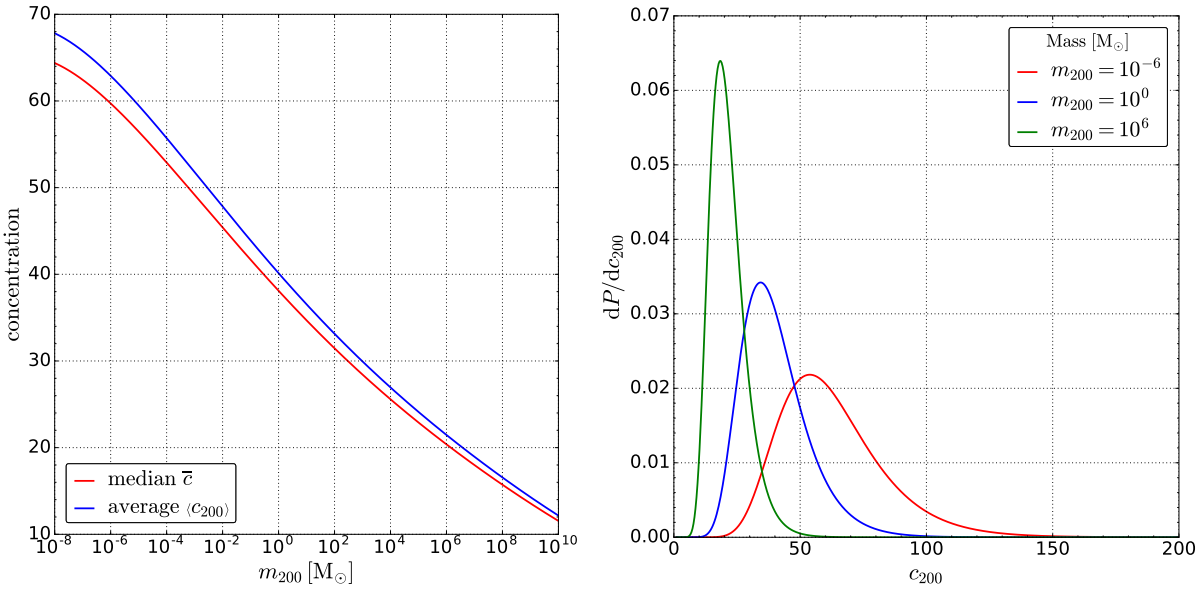

Figure 3.13 – Left panel: median concentration (red curve) and average concentration (blue curve) as functions of the mass m_{200}. **Right panel:** concentration PDF for $m_{200} = 10^{-6}/10^{0}/10^{6}\,\mathrm{M}_\odot$ (red/blue/green curve, respectively).

Spatial distribution In our initial, virtual set-up, subhalos are test particles thus their spatial distribution is given by the global dark matter density profile

$$\frac{\mathrm{d}P}{\mathrm{d}V}(R) = \frac{\rho_{\mathrm{DM}}(R)}{M_{\mathrm{DM}}}\,, \tag{3.146}$$

where M_{DM} is the virial mass of the dark matter halo, so that the spatial distribution is normalized to one over the virialized halo. As a reference, we use the dynamically constrained NFW profile of McMillan (2017) for ρ_{DM}. We insist on the fact that this spatial distribution corresponds to a *virtual* configuration since tides are ignored. Indeed, while the NFW profile is in general a good fit to the global dark matter profiles (smooth dark matter *and* subhalos together) found in N-body simulations, it is not a good description of the subhalo spatial distribution. While galactic halos have a cuspy profile, the subhalo distribution is in general cored, which means most of the dark matter at the center of galaxies is smooth. We will see that this feature can be entirely explained in our model, even when starting from test particles spatially tracing the smooth potential. Once these effects are plugged in, the initial spatial PDF in Eq. (3.146) is strongly modified and a core naturally emerges, as we show in the following.

Phase-space number density Having characterized the PDFs of our three parameters c_{200}, m_{200} and R, we can define a subhalo phase-space number density $\mathrm{d}^3N/\mathrm{d}w^3$ where $\mathrm{d}w^3 = 4\pi R^2 \mathrm{d}R\,\mathrm{d}c_{200}\,\mathrm{d}m_{200}$.[3] To slightly simplify the notation, we introduce

$$\mathcal{F}_0(c_{200}, m_{200}, R) \equiv \frac{\mathrm{d}^3N}{\mathrm{d}w^3}\,, \tag{3.147}$$

and we have

$$\mathcal{F}_0(c_{200}, m_{200}, R) = \frac{N_{\mathrm{sub},0}}{K_0}\,\frac{\mathrm{d}P}{\mathrm{d}c_{200}}(c_{200}, m_{200}) \times \frac{\mathrm{d}P}{\mathrm{d}m_{200}}(m_{200}) \times \frac{\mathrm{d}P}{\mathrm{d}V}(R)\,. \tag{3.148}$$

[3] What is referred to as the phase space here is the parameter space with coordinates (c_{200}, m_{200}, R). In chapters 5 and 6, the notion of phase space is also used but it refers to the usual statistical-physics space with coordinates $(\vec{r}, \vec{v})$ where $\vec{r}$ is the position and $\vec{v}$ is the velocity.

The quantity $N_{\rm sub,0}$ is the total number of subhalos in the absence of tidal effects, which is *not* the real number of subhalos in the Galaxy. The factor K_0 ensures the normalization of $\mathcal{F}_0$ to $N_{\rm sub,0}$ over the entire phase-space. Since all the individual PDFs are normalized to one, we immediately have

$$K_0 = \int \mathrm{d}V \, \frac{\mathrm{d}P}{\mathrm{d}V} \int \mathrm{d}m_{200} \, \frac{\mathrm{d}P}{\mathrm{d}m_{200}} \int \mathrm{d}c_{200} \, \frac{\mathrm{d}P}{\mathrm{d}c_{200}} = 1 \,. \tag{3.149}$$

We stress here that in the initial, virtual configuration all the PDFs factorize. This will *not* be the case when we will plug in tidal effects. Note that in many subhalo models, this separability of the PDFs is often assumed [see *e.g.*, Charbonnier et al. (2012)].

We would like to define a mass density profile $\rho_{\rm sub}(R)$ associated with the subhalo population. This density profile has to verify

$$4\pi \int_0^{R_{200}} \mathrm{d}R \, R^2 \, \rho_{\rm sub}(R) = M_{\rm sub} \,, \tag{3.150}$$

where $M_{\rm sub}$ is total dark matter mass within subhalos in the virialized Galactic halo. This mass is also given by

$$M_{\rm sub} = 4\pi \int_0^{R_{200}} \mathrm{d}R \, R^2 \int \mathrm{d}m_{200} \int \mathrm{d}c_{200} \, \mathcal{F}_0(c_{200}, m_{200}, R) \, m_{200} \,, \tag{3.151}$$

hence the definition of the subhalo mass density

$$\rho_{\rm sub}(R) \equiv \int \mathrm{d}m_{200} \int \mathrm{d}c_{200} \, \mathcal{F}_0(c_{200}, m_{200}, R) \, m_{200} \,. \tag{3.152}$$

Without tidal effect, the integration over c_{200} is trivial and the subhalo mass density simplifies to

$$\begin{aligned} \rho_{\rm sub}(R) &= N_{\rm sub,0} \, \frac{\mathrm{d}P}{\mathrm{d}V}(R) \int_{m_{\rm min}}^{m_{\rm max}} \mathrm{d}m_{200} \, \frac{\mathrm{d}P}{\mathrm{d}m_{200}} \, m_{200} \\ &= \frac{N_{\rm sub,0} \, \langle m_{200} \rangle}{M_{\rm DM}} \, \rho_{\rm DM}(R) \end{aligned} \tag{3.153}$$

We introduce the subhalo mass fraction

$$f_{\rm sub,200} \equiv \frac{N_{\rm sub,0} \, \langle m_{200} \rangle}{M_{\rm DM}} = \frac{M_{\rm sub}}{M_{\rm DM}} \tag{3.154}$$

which is the proportion of dark matter mass inside subhalos. If the dark halo of the Galaxy was initially entirely made of subhalos, *i.e.* there was no smooth component, we would have $f_{\rm sub,200} = 1$ and consequently $\rho_{\rm sub} = f_{\rm sub,200} \rho_{\rm DM} = \rho_{\rm DM}$. The number of subhalos would then be

$$N_{\rm sub,0} = \frac{M_{\rm DM}}{\langle m_{200} \rangle} \,. \tag{3.155}$$

For a mass index $\alpha_{\rm m} = 2$, and using the approximation in Eq. (3.141), we get

$$N_{\rm sub,0} = \frac{M_{\rm DM}}{m_{\rm min} \, \ln(m_{\rm max}/m_{\rm min})} \simeq 3.5 \times 10^{16} \,, \tag{3.156}$$

for $M_{\rm DM} = 1.3 \times 10^{12} \, \mathrm{M}_\odot$, $m_{\rm max} = 10^{-2} M_{\rm DM}$ and $m_{\rm min} = 10^{-6} \, \mathrm{M}_\odot$. Note that this is a rough approximation since we expect some dark matter to be smoothly accreted to the Galactic halo during its lifetime.

In general, we assume that the Galactic halo is partly made of subhalos and partly made of smoothly distributed dark matter. The consistency with respect to dynamical constraints is ensured by the definition of the smooth density:

$$\rho_{\rm smooth}(R) = \rho_{\rm DM}(R) - \rho_{\rm sub}(R) \,. \tag{3.157}$$

In words, the constrained profile $\rho_{\rm DM}$ constitutes our Galactic dark matter "budget" and we assume that all the dark matter that is not in clumps in necessarily smoothly distributed. Note that this is a consistent picture only if $\rho_{\rm smooth}(R) \geqslant 0$ at all R *i.e.* we do not predict a subhalo mass distribution in disagreement with observations. Nothing in our model ensures this to be true in general, however we did not find any configuration where the smooth density becomes negative at some radii.

We now plug-in tidal effects. We know that the general consequence of tides is to remove dark matter from subhalos, hence adding a smooth dark matter component to the Galaxy. This smooth component must satisfy Eq. (3.157). To compute $\rho_{\rm sub}$, we need to find the subhalo phase-space number density *with* tidal effects. The subhalo number density is only modified if tides change the number of subhalos. This happens if some subhalos are disrupted. According to the disruption criterion in Eq. (3.136), a subhalo with phase-space coordinates (c_{200}, m_{200}, R) is disrupted if

$$\frac{r_{\rm t}}{r_{\rm s}}(c_{200}, R) \leqslant \epsilon_{\rm t} \,. \tag{3.158}$$

Taking into account this disruption, the phase-space number density becomes

$$\begin{aligned}\mathcal{F}_{\rm t}(c_{200}, m_{200}, R) = \frac{N_{\rm sub}}{K_{\rm t}} \times \frac{{\rm d}P}{{\rm d}c_{200}}(c_{200}, m_{200}) \times \frac{{\rm d}P}{{\rm d}m_{200}}(m_{200}) \times \frac{{\rm d}P}{{\rm d}V}(R) \\ \times \Theta\left[\frac{r_{\rm t}}{r_{\rm s}}(c_{200}, R) - \epsilon_{\rm t}\right] \,,\end{aligned} \tag{3.159}$$

where Θ is the Heaviside step-function and $K_{\rm t}$ is an overall normalization factor given by

$$\begin{aligned}K_{\rm t} = 4\pi \int {\rm d}R\, R^2 \frac{{\rm d}P}{{\rm d}V}(R) \int {\rm d}m_{200} \frac{{\rm d}P}{{\rm d}m_{200}}(m_{200}) \\ \times \int {\rm d}c_{200} \frac{{\rm d}P}{{\rm d}c_{200}}(c_{200}, m_{200})\, \Theta\left[\frac{r_{\rm t}}{r_{\rm s}}(c_{200}, R) - \epsilon_{\rm t}\right] \,.\end{aligned} \tag{3.160}$$

The tidal-to-scale-radius ratio $r_{\rm t}/r_{\rm s}$ can be computed as a function of c_{200}, m_{200} and R using the stripping and shocking methods discussed in Sec. 3.2. We recall that for all the definitions we have considered, the ratio $r_{\rm t}/r_{\rm s}$ is independent of m_{200}. The dependence of $r_{\rm t}/r_{\rm s}$ on c_{200} *and* R makes the new phase-space number density a very intricate function of all the initial PDFs. In particular, the property of separability of the PDFs is not valid any more. In our initial configuration, the mass and concentration parts of the phase-space are independent of the position part, but tidal effects introduce a correlation between the concentration and the position. Since the mass and the concentration are already correlated through the median mass-concentration relation, the phase-space is now completely entangled.

Note that the number of subhalos $N_{\rm sub}$ is different a priori from the initial number $N_{\rm sub,0}$. We need an additional constraint to compute this number.

3.3.3 Calibrating the subhalo mass fraction

We choose to calibrate the subhalo mass fraction on a dark matter-only cosmological simulation, where tidal effects are consistently accounted for. We use a numerical calibration out of convenience rather than necessity since the mass fraction can be computed from first principles, though the calculation is involved and requires several approximations, see Berezinsky et al. (2014).

Using a dark-matter-only N-body simulation presents a couple of advantages with respect to a hydrodynamical run including baryons. First, the high-resolution N-body simulations available like *Via Lactea II* (Diemand et al., 2008) and Aquarius (Springel et al., 2008) have a spatial resolution comparable to or better than any other cosmological simulation performed since then

[see *e.g.*, Springel et al. (2018)].[4] Second, the properties of baryons in simulations differ from the observed properties of baryons in the Milky Way. The point is that galaxies in simulations are identified as "Milky-Way-like" on the criteria such as the dark matter mass, the baryonic mass, the dark-matter-to-baryons mass ratio, the presence of a disc, etc. However the detailed kinematics of the Milky Way is in general not recovered by simulated Milky-Way-like galaxies. Since we want our model to be predictive regarding the effect of tides in general, and the impact of the disc in particular, we calibrate on a CDM simulation.

We calibrate on the VL2 simulation of Diemand et al. (2008). One has to keep in mind that a cosmological simulation is run for a particular set of cosmological parameters. Three parameters are especially important for the formation and evolution of dark matter halos: the matter abundance Ω_m, the normalization of the power spectrum σ_8 and the spectral index n_s. The most recent estimates for these parameters are provided by Ade et al. (2016) who find $\Omega_\mathrm{m} \simeq 0.31$, $\sigma_8 \simeq 0.82$ and $n_\mathrm{s} \simeq 0.97$. The matter abundance Ω_m and the normalization σ_8 impact the concentrations of halos on all scales with larger values leading to more concentrated structures, while n_s controls the amount of power on small scales, see Guo et al. (2013). The cosmological parameters used in VL2 are $\Omega_\mathrm{m} = 0.24$, $\sigma_8 = 0.74$ and $n_\mathrm{s} = 0.951$, based on the WMAP-3 cosmology Spergel et al. (2007). This makes VL2 a rather conservative simulation in terms of subhalo abundance and concentration. For comparison, the *Aquarius* simulation of Springel et al. (2008) was run with $\Omega_\mathrm{m} = 0.25$, $\sigma_8 = 0.9$ and $n_\mathrm{s} = 1$ with a spatial resolution similar to VL2.

The authors of VL2 provide the cumulative number of subhalos above a given maximal velocity $N_\mathrm{VL2}(> v_\mathrm{max})$, see Fig. 3 in Diemand et al. (2008). The velocity v_max is the peak height of the subhalo circular velocity

$$v_\mathrm{max} = \mathrm{Max}\left(\sqrt{\frac{G_\mathrm{N}\, m_\mathrm{int}(r)}{r}}\right) = \sqrt{\frac{G_\mathrm{N}\, m_\mathrm{int}(r_{v_\mathrm{max}})}{r_{v_\mathrm{max}}}}\,. \tag{3.161}$$

Assuming subhalos have an NFW profile and they follow the mass-concentration relation given in Eq. (11) of Pieri et al. (2011) (which is fitted over the VL2 subhalos) we can associate, in a unique way, a value of m_{200} to a maximal velocity v_max. This association is possible if the subhalo internal profiles are not strongly modified by tidal effects, *i.e.* their scale parameters ρ_s and r_s remain roughly unchanged. The subhalo mass fraction between $v_{\mathrm{max},1}$ and $v_{\mathrm{max},2}$ is given by

$$f^\mathrm{VL2}_{\mathrm{sub},200} = \frac{1}{M_{200,\mathrm{VL2}}} \int_{v_{\mathrm{max},1}}^{v_{\mathrm{max},2}} \mathrm{d}v_\mathrm{max}\, \frac{\mathrm{d}N_\mathrm{VL2}}{\mathrm{d}v_\mathrm{max}}\, m_{200}(v_\mathrm{max})\,. \tag{3.162}$$

Note that $f_{\mathrm{sub},200}$ is an effective mass fraction in terms of m_{200} rather than the actual mass fraction f_sub. The latter cannot be estimated however since we do not know the actual mass of stripped subhalos in VL2. A fit of N_VL2 is provided in Diemand et al. (2008)

$$N_\mathrm{VL2}(> v_\mathrm{max}) = 0.036 \left(\frac{v_\mathrm{max}}{201\,\mathrm{km/s}}\right)^{-3}\,, \tag{3.163}$$

which is very accurate for $v_\mathrm{max} \in [3\,\mathrm{km/s}, 20\,\mathrm{km/s}]$. Using this fit and the virial mass of the galactic halo in VL2 $M_{200,\mathrm{VL2}} = 1.42 \times 10^{12}\,\mathrm{M}_\odot$, we get the subhalo mass fraction

$$f^\mathrm{VL2}_{\mathrm{sub},200} = 0.116 \text{ for } v_\mathrm{max} \in [3\,\mathrm{km/s}, 20\,\mathrm{km/s}]\,. \tag{3.164}$$

[4] The reason why simulations performed ten years ago have a resolution comparable to simulations being performed now is a change of focus in the numerical simulation community. Now that CDM physics is under control on sub-galactic scales and the small-scale issues have been clearly identified, the challenge is to incorporate realistic baryonic physics in the picture or explore departures from ΛCDM (Bullock & Boylan-Kolchin, 2017).

Using the relation between $v_{\rm max}$ and m_{200}, we convert it into a fraction on a mass interval

$$f_{\rm sub,200}^{\rm VL2} = 0.116 \text{ for } m_{200} \in [3.14 \times 10^6\,{\rm M}_\odot, 1.25 \times 10^9\,{\rm M}_\odot]\,. \tag{3.165}$$

Dividing by the total dark matter mass, we get

$$f_{\rm sub,200}^{\rm VL2} \simeq 11\% \text{ for } \frac{m_{200}}{M_{200}} \in [2.2 \times 10^{-6}, 8.8 \times 10^{-4}]\,. \tag{3.166}$$

We use this last equation to calibrate the mass fraction in our subhalo model, replacing M_{200} by the total dark matter mass in the particular mass model we use. We note that the use of a different N-body simulation like Aquarius leads to a similar mass fraction.

Having estimated the mass fraction in VL2, we must now express the same mass fraction in our subhalo model. By definition, the mass fraction in subhalos with cosmological masses between m_1 and m_2 is

$$f_{\rm sub,200} = \frac{1}{M_{\rm DM}} \int {\rm d}V \int_{m_1}^{m_2} {\rm d}m_{200} \int_1^\infty {\rm d}c_{200}\, \mathcal{F}_{\rm t}^{\rm sim}(c_{200}, m_{200}, R)\, m_{200}\,, \tag{3.167}$$

where $\mathcal{F}_{\rm t}^{\rm sim}$ is the subhalo phase-space density as defined in Eq. (3.159). There are some subtleties associated with the computation of tidal effects while doing the calibration. The calibration is done on a dark matter-only simulation, hence the baryonic effects (stripping by the baryonic potential and shocking by the Galactic disc) should not be included in $\mathcal{F}_{\rm t}^{\rm sim}$. The only effect that should be included when doing the calibration is tidal stripping by the dark matter halo. Another important point concerns the relevant value of the disruption parameter $\epsilon_{\rm t}$. As discussed in Sec. 3.2.3, the value of this parameter has been found in simulation to be $\epsilon_{\rm t}^{\rm sim} \simeq 1$ (Hayashi et al., 2003). However, subhalo disruption in simulations might be entirely explained by numerical artefacts as argued by van den Bosch et al. (2018), hence the realistic value of this parameter might be much lower, possibly $\epsilon_{\rm t} \simeq 0$ if subhalos are never completely disrupted (they should be strongly resilient to tidal shocks in the regime of very large inner density and when the inner orbital timescale is small with respect to the timescale of gravitational encounter).

Irrespective of the realistic value of $\epsilon_{\rm t}$, the artificial disruption discussed by van den Bosch et al. should be present in VL2 or any other N-body simulation used for the calibration. Therefore, when computing the mass fraction in Eq. (3.167) to perform the calibration, one should fix the disruption parameter to $\epsilon_{\rm t} = \epsilon_{\rm t}^{\rm sim} = 1$ for consistency. The masses m_1 and m_2 in Eq. (3.167) are set to the VL2 values in Eq. (3.166)

$$\begin{aligned} m_1 &= 2.2 \times 10^{-6}\, M_{\rm DM} \\ m_2 &= 8.8 \times 10^{-4}\, M_{\rm DM}\,. \end{aligned} \tag{3.168}$$

Using the definition of the minimal concentration (3.138), we have

$$\begin{aligned} f_{\rm sub,200} = {} & \frac{4\pi N_{\rm sub}^{\rm sim}}{M_{\rm DM} K_{\rm t}^{\rm sim}} \\ & \times \int_0^{R_{200}} {\rm d}R\, R^2\, \frac{{\rm d}P}{{\rm d}V}(R) \int_{m_1}^{m_2} {\rm d}m\, \frac{{\rm d}P}{{\rm d}m_{200}}(m)\, m \int_{c_{\rm min}^{\rm sim}(R)}^\infty {\rm d}c\, \frac{{\rm d}P}{{\rm d}c_{200}}(c, m)\,. \end{aligned} \tag{3.169}$$

Equating the mass fraction in Eq. (3.169) with the value found for VL2, we can deduce the number of subhalos $N_{\rm sub}^{\rm sim}$ in our model. We stress that this is the number of subhalos in the simulation-like configuration, *i.e.* without baryons and with $\epsilon_{\rm t} = \epsilon_{\rm t}^{\rm sim} = 1$.

Since the calibration is only performed on the CDM part only, our model is *predictive* regarding the effect of the baryonic distribution on subhalos. However, before doing predictions we must compute the total number of subhalo $N_{\rm sub}$ beyond the simulation-like configuration. Starting from $N_{\rm sub}^{\rm sim}$, we want to add the effects of tidal stripping by the full baryonic potential

and disc shocking. We also want to investigate situations where the disruption parameter is much smaller than the simulation value. A simple way to compute the number of subhalos in these cases is to assume the subhalo density profile $\rho_{\rm sub}$ *in the outer region of the dark halo* is left unchanged compared to the simulation-like case (dark-matter-only and $\epsilon_{\rm t} = 1$). This is a reasonable assumption since subhalos near the virial radius of the Galactic halo experience nearly no tidal effects and behave as field halos. The asymptotic preservation of $\rho_{\rm sub}$ at $R \simeq R_{200}$ can be written using Eq. (3.152)

$$\frac{N_{\rm sub}^{\rm sim}}{K_{\rm t}^{\rm sim}} \int_{m_{\rm min}}^{m_{\rm max}} {\rm d}m_{200} \int_{c_{\rm min}^{\rm sim}(R)}^{+\infty} {\rm d}c_{200}\, \mathcal{F}_{\rm t}\, m_{200} = \frac{N_{\rm sub}}{K_{\rm t}} \int_{m_{\rm min}}^{m_{\rm max}} {\rm d}m_{200} \int_{c_{\rm min}(R)}^{+\infty} {\rm d}c_{200}\, \mathcal{F}_{\rm t}\, m_{200}\,, \tag{3.170}$$

where $N_{\rm sub}^{\rm sim}$ ($N_{\rm sub}$) and $K_{\rm t}^{\rm sim}$ ($K_{\rm t}$) are the number of subhalos and normalization factor in the simulation-like case ("realistic" case, respectively). According to Fig. 3.12, the minimal concentration in the outer region of the halo is $c_{\rm min} \simeq 1$, irrespective of the value of $\epsilon_{\rm t}$ or the inclusion of baryonic effects. This just means subhalos are not affected by tidal effects when they orbit far from the Galactic center. We have $c_{\rm min}(R_{200}) \simeq c_{\rm min}^{\rm sim}(R) = 1$, hence the simple relation

$$\frac{N_{\rm sub}^{\rm sim}}{K_{\rm t}^{\rm sim}} = \frac{N_{\rm sub}}{K_{\rm t}}\,. \tag{3.171}$$

This relation allows us to compute $N_{\rm sub}$ regardless of the presence of baryons or the value of $\epsilon_{\rm t}$. We computed the number of subhalos for several values of $\alpha_{\rm m}$ and $m_{\rm min}$, the results are featured in Tab. 3.1. The upper (lower) panel shows values obtained for $\epsilon_{\rm t} = 1$ ($\epsilon_{\rm t} = 0$). We first note the high sensitivity of $N_{\rm sub}$ to the mass index $\alpha_{\rm m}$. Going from an index of $\alpha_{\rm m} = 2$ to $\alpha_{\rm m} = 1.9$, $N_{\rm sub}$ drops by a factor of more than fifty for $M_{\rm min} = 10^{-10}\,{\rm M}_\odot$ and more than twenty for $M_{\rm min} = 10^{-6}\,{\rm M}_\odot$. This points toward the crucial importance of the small-scale power spectrum when dealing with subhalos. The fact that this spectrum is almost completely unprobed at these scales (see however constraints from ultracompact mini-halos considerations Bringmann et al. (2012); Aslanyan et al. (2015)) makes the actual number of subhalos greatly uncertain. The value of the mass cutoff is also crucial, as it changes the number of subhalos by orders of magnitude. The impact of $M_{\rm min}$ is more important for high values of the mass index $\alpha_{\rm m}$. Note however that the mass cutoff can be determined in principle from the interaction properties of the dark matter particle (Green et al., 2005; Bringmann & Hofmann, 2007; Bringmann, 2009), hence it is calculable in the framework of a specific dark matter model. The disruption parameter has a much smaller impact than the mass functions parameters, as a change from $\epsilon_{\rm t} = 0$ to $\epsilon_{\rm t} = 1$ only increases $N_{\rm sub}$ by roughly 3%. The main reason why this number is not very sensitive to $\epsilon_{\rm t}$ is that most subhalos reside in the outer regions of the Galaxy, where tidal effects are ineffective. Another reason is that the subhalos most exposed to disruption are the less concentrated ones. Since subhalos with low concentration are among the most massive on average, their number is low and their survival does not impact the total number of structures.

$N_{\rm sub}$ ($\epsilon_{\rm t} = 1$)	$M_{\rm min} = 10^{-10}\,{\rm M}_\odot$	$M_{\rm min} = 10^{-6}\,{\rm M}_\odot$
$\alpha_{\rm m} = 1.9$	4.79×10^{18}	1.20×10^{15}
$\alpha_{\rm m} = 2$	2.60×10^{20}	2.59×10^{16}
$N_{\rm sub}$ ($\epsilon_{\rm t} = 0$)	$M_{\rm min} = 10^{-10}\,{\rm M}_\odot$	$M_{\rm min} = 10^{-6}\,{\rm M}_\odot$
$\alpha_{\rm m} = 1.9$	4.97×10^{18}	1.25×10^{15}
$\alpha_{\rm m} = 2$	2.70×10^{20}	2.70×10^{16}

Table 3.1 – Number of subhalos for several value of $\alpha_{\rm m}$ and $m_{\rm min}$, and two values of the disruption parameter: $\epsilon_{\rm t} = 1$ (Upper panel) and $\epsilon_{\rm t} = 0$ (Lower panel). The computation is done for the NFW mass model of McMillan (2017), with the smooth stripping radius and the differential shocking method introduced in Sec. 3.2

3.3.4 Post-tides parameter space

3.3.4.1 Mass density profiles

In the previous section, we showed how to compute the number of subhalos $N_{\rm sub}$ for all types of tidal effects and for any value of the disruption parameter $\epsilon_{\rm t}$. We can now evaluate any subhalo-related quantity, starting with the global mass density profile of the subhalo population

$$\rho_{\rm sub}(R) = \frac{N_{\rm sub}}{K_{\rm t}} \int_{m_{\rm min}}^{m_{\rm max}} {\rm d}m_{200} \int_{c_{\rm min}(R)}^{\infty} {\rm d}c_{200}\, \mathcal{F}_{\rm t}(c_{200}, m_{200}, R)\, m_{\rm t}\,. \tag{3.172}$$

Note that we integrate the *tidal mass* $m_{\rm t}$, and not the cosmological mass m_{200}, to get the true subhalo population mass density profile. For a subhalo with internal mass density $\rho_{\rm int}$, the tidal mass is simply defined through

$$m_{\rm t}(c_{200}, m_{200}, R) \equiv 4\pi \int_0^{r_{\rm t}(c_{200}, m_{200}, R)} {\rm d}r\, r^2\, \rho_{\rm int}(r)\,, \tag{3.173}$$

where $r_{\rm t}(c_{200}, m_{200}, R)$ is the tidal radius. Hence the tidal mass depends on all our parameters in a non-trivial way. We can exploit the m_{200}-independence of $r_{\rm t}/r_{\rm s}$ to rewrite the tidal mass

$$m_{\rm t} = 4\pi\rho_{\rm s} r_{\rm s}^3 \int_0^{r_{\rm t}/r_{\rm s}} {\rm d}x\, x^2\, \tilde{\rho}_{\rm int}(x)\,. \tag{3.174}$$

Moreover $\rho_{\rm s}$ only depends on c_{200}, and $r_{\rm s}^3 \propto m_{200}$, hence $m_{\rm t}/m_{200}$ only depends on c_{200} and R. The tidal mass $m_{\rm t}$ is simply proportional to the cosmological mass m_{200}.

We investigate the impact of tidal effects on the subhalo mass density profile. We compare the different tidal radius recipes introduced in Sec. 3.2 on the left panel in Fig. 3.14. The results are consistent with the hierarchy observed through the minimal concentration in Fig. 3.12: the point-like stripping method is the most destructive while the smooth and density-based ones lead to similar results. Disc shocking has a dramatic impact on the subhalo distribution regardless of the method used, although the simulation-based one is by far the most destructive. Note that here disc shocking is added on top of halo stripping, which was not the case when we discussed the minimal concentration for instance. This is done by computing the stripping radius first and then using it as the initial radius before subhalos experience disc shocking. The impact of the disruption parameter is shown on the right panel in Fig. 3.14. The value of this parameter has very important consequences on the subhalo distribution. Lowering its value from $\epsilon_{\rm t} = 1$ to $\epsilon_{\rm t} = 0.1$ increases the subhalo density at $R = 0.1\,{\rm kpc}$ by more than five orders of magnitude! Further dividing $\epsilon_{\rm t}$ by ten only increases $\rho_{\rm sub}$ by less than an order of magnitude though.

Another source of uncertainty on the subhalo mass distribution is the global dark matter distribution in our Galaxy. For instance, McMillan (2017) fits a set of kinematic data with an NFW dark matter profile and a cored profile $(\alpha, \beta, \gamma) = (1, 3, 0)$. Both these models are in agreement with the data used by McMillan though they lead to a very different dark matter abundance in the inner region of the Milky Way. The subhalo mass density profile for these two mass models is shown on the left panel of Fig. 3.15. Note that assuming as we did at the beginning that subhalos initially behave as test particles in a global potential allows us to remain agnostic as for the possible origin of a cored halo profile, which should affect identically the smooth and subhalo components. The subhalo density in the cored model (red dashed line) is lower than in the NFW model (red solid line) by roughly the same factor as the total dark matter density (black lines). Note that a lower total density implies a lower subhalo number density because we define the *initial* spatial distribution as

$$\frac{{\rm d}P}{{\rm d}V}(R) = \frac{\rho_{\rm DM}(R)}{M_{\rm DM}}\,. \tag{3.175}$$

Note that a lower total dark matter density also leads to weaker tidal effects, however tides from dark matter are subdominant compared to baryonic contributions in the inner region of the

Galaxy. This leads to a prediction for the local mass fraction inside subhalos which is *independent* of the global dark matter density profile in the Galaxy. This has strong consequences on dark matter searches with cosmic rays, as we will see in the next chapter. We look at the impact of the mass function parameters α_m and m_min on the right panel in Fig. 3.15. Changing the mass cutoff from $m_\mathrm{min} = 10^{-6}\,\mathrm{M}_\odot$ to $m_\mathrm{min} = 10^{-10}\,\mathrm{M}_\odot$ increases the subhalo central density by roughly an order of magnitude, while changing from $\alpha_\mathrm{m} = 1.9$ to $\alpha_\mathrm{m} = 2$ leads to a comparable, somewhat bigger increase.

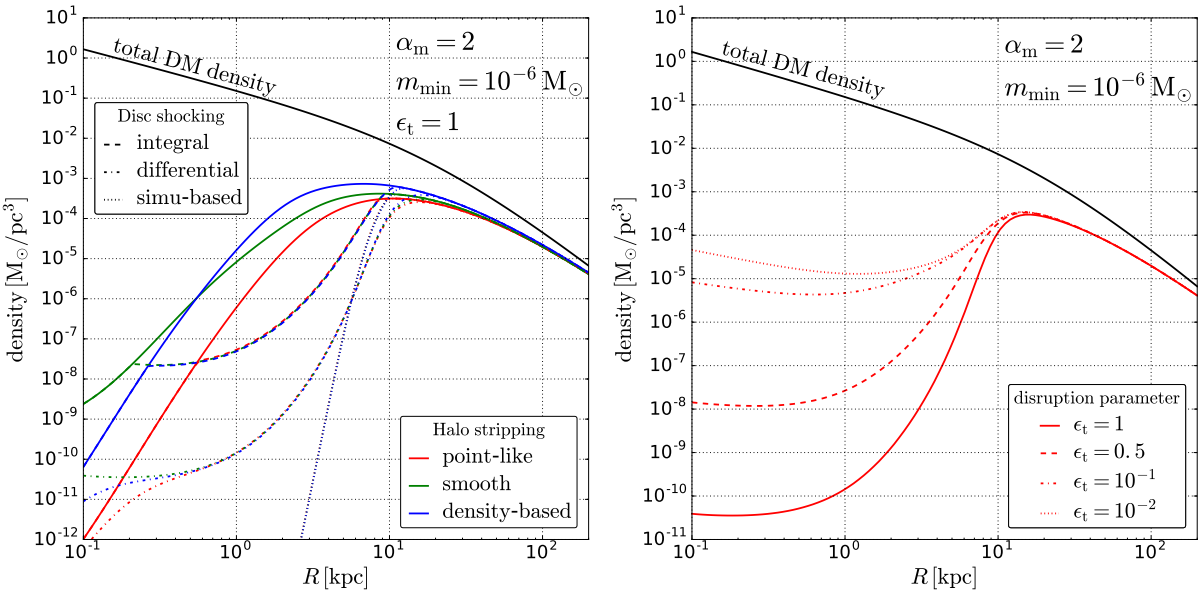

Figure 3.14 – For both panels, we use the NFW model of McMillan (2017) and the mass function parameters $\alpha_\mathrm{m} = 2$ and $m_\mathrm{min} = 10^{-6}\,\mathrm{M}_\odot$. **Left panel:** subhalo mass density profile for the different tidal effect recipes discussed in Sec. 3.2. Are shown the stripping by the total potential through the point-like (red), smooth (green) and density-based (blue) methods. Disc shocking is added to tidal stripping with the integral (dashed), differential (dotted-dashed) and simulation-based (dotted) methods. **Right panel:**. For the smooth halo stripping and differential disc shocking, we show the subhalo mass density for different value of the disruption parameter $\epsilon_\mathrm{t} = 1/0.5/10^{-1}/10^{-2}$ (solid/dashed/dotted-dashed/dotted line, respectively).

3.3.4.2 Number density profiles

A quantity complementary to the mass density is the subhalo number density profile, defined as

$$\begin{aligned} n_\mathrm{sub}(R) &= \int_{m_\mathrm{min}}^{m_\mathrm{max}} \mathrm{d}m_{200} \int_1^\infty \mathrm{d}c_{200}\, \mathcal{F}_\mathrm{t}(c_{200}, m_{200}, R) \\ &= \frac{N_\mathrm{sub}}{K_\mathrm{t}} \frac{\mathrm{d}P}{\mathrm{d}V} \int_{m_\mathrm{min}}^{m_\mathrm{max}} \mathrm{d}m_{200}\, \frac{\mathrm{d}P}{\mathrm{d}m_{200}} \int_{c_\mathrm{min}(R)}^\infty \mathrm{d}c_{200}\, \frac{\mathrm{d}P}{\mathrm{d}c_{200}} \,. \end{aligned} \tag{3.176}$$

Note that the number density is related to the spatial distribution through

$$n_\mathrm{sub}(R) = N_\mathrm{sub}\, \left.\frac{\mathrm{d}P}{\mathrm{d}V}\right|_\mathrm{t} (R) \,. \tag{3.177}$$

The function $\mathrm{d}P/\mathrm{d}V|_\mathrm{t}$ is the subhalo spatial distribution when tidal effects are accounted for. According to Eq. (3.176), it is given by

$$\left.\frac{\mathrm{d}P}{\mathrm{d}V}\right|_\mathrm{t} (R) = \frac{1}{K_\mathrm{t}} \frac{\mathrm{d}P}{\mathrm{d}V} \int_{m_\mathrm{min}}^{m_\mathrm{max}} \mathrm{d}m_{200} \int_{c_\mathrm{min}(R)}^\infty \mathrm{d}c_{200}\, \frac{\mathrm{d}P}{\mathrm{d}m_{200}} \frac{\mathrm{d}P}{\mathrm{d}c_{200}} \tag{3.178}$$

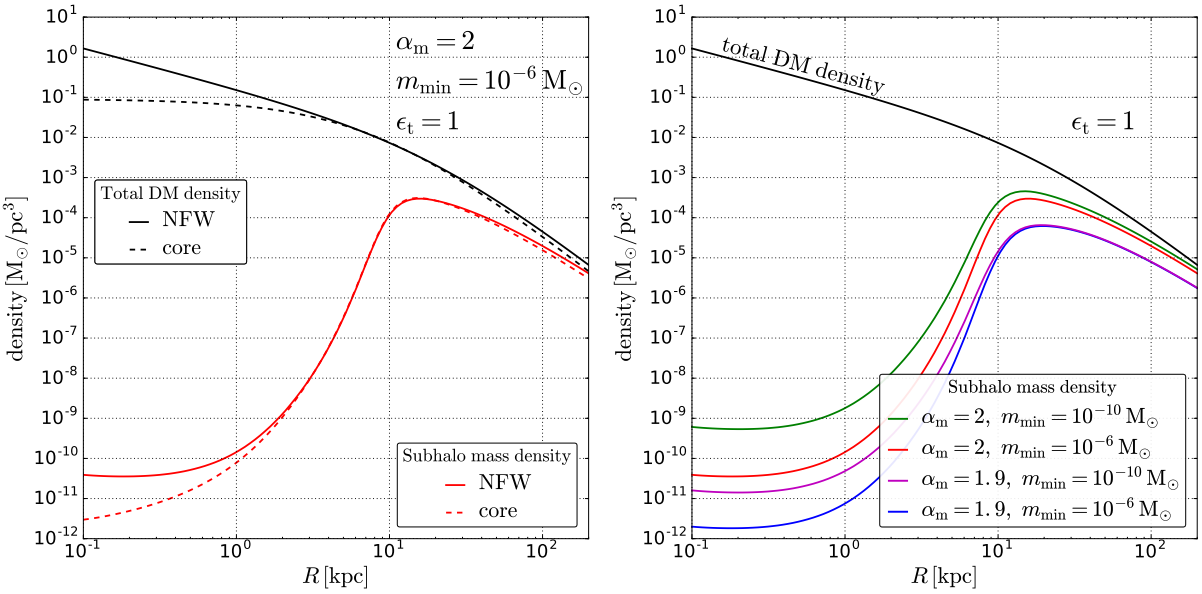

Figure 3.15 – For both panels, we use the smooth halo stripping and differential disc shocking, and the disruption parameter is fixed to $\epsilon_t = 1$ **Left panel:** total dark matter (black) and subhalo (red) mass density profiles for the NFW (solid line) and cored (dashed line) models of McMillan (2017). **Right panel:** subhalo mass density profile in the NFW model of McMillan (2017), for different values of the mass function power index α_m and mass cutoff m_{min}.

It is a priori different from the initial subhalo distribution $\mathrm{d}P/\mathrm{d}V$. The number density is shown on the left panel in Fig. 3.16 for different values of α_m and m_{min}. As for the mass density profile, tidal effects strongly impact the number density in the central region of the Galaxy. When all effects are included, the number density is depleted for radii smaller than $R \simeq 10\,\mathrm{kpc}$. Depending on the values of α_m and m_{min}, $n_{sub}(10\,\mathrm{kpc})$ varies between $8\,\mathrm{pc}^{-3}$ (for $\alpha_m = 1.9$ and $m_{min} = 10^{-6}\,\mathrm{M}_\odot$) and $2 \times 10^6\,\mathrm{pc}^{-3}$ (for $\alpha_m = 2$ and $m_{min} = 10^{-10}\,\mathrm{M}_\odot$). The number of subhalos at the position of the Sun $R \simeq 8.2\,\mathrm{kpc}$ depends crucially on the careful modelling of disc shocking. Indeed, if the only effect considered is stripping by the Galactic potential the subhalo number density peaks at $R \simeq 4\,\mathrm{kpc}$ instead of 10 kpc. The disruption parameter ϵ_t has also a strong influence on n_{sub} as shown on the right panel in Fig. 3.16. The lower ϵ_t, the closer n_{sub} is to the number density without tidal effects (dashed black line). For a parameter $\epsilon_t = 10^{-2}$, the number density profiles with and without tides are almost indistinguishable, which means $\epsilon_t = 10^{-2}$ is low enough for nearly all subhalos to survive tidal effects. These subhalos still lose most of their mass, which can be seen by looking at the subhalo mass density on Fig. 3.14. For $\epsilon_t = 10^{-2}$, the mass density is significantly depleted at the center of the Galaxy and strongly differs from the overall dark matter profile.

3.3.4.3 Concentration

In our initial set-up, there is no correlation between concentration and position in the halo. If subhalo can be disrupted by tidal effects, this introduces a correlation. Indeed, low-concentration halos are more susceptible to tides than more concentrated ones, consequently they are more likely to be disrupted. By a selection effect, the tidally-stripped subhalo population is more concentrated than the same population without tides. This can be seen by computing the average cosmological concentration at a position R, for a given cosmological mass m_{200}

$$\langle c_{200} \rangle (m_{200}, R) = \frac{\int_{c_{min}(R)}^{+\infty} \mathrm{d}c_{200}\, \frac{\mathrm{d}P}{\mathrm{d}c_{200}}\, c_{200}}{\int_{c_{min}(R)}^{+\infty} \mathrm{d}c_{200}\, \frac{\mathrm{d}P}{\mathrm{d}c_{200}}} \,. \tag{3.179}$$

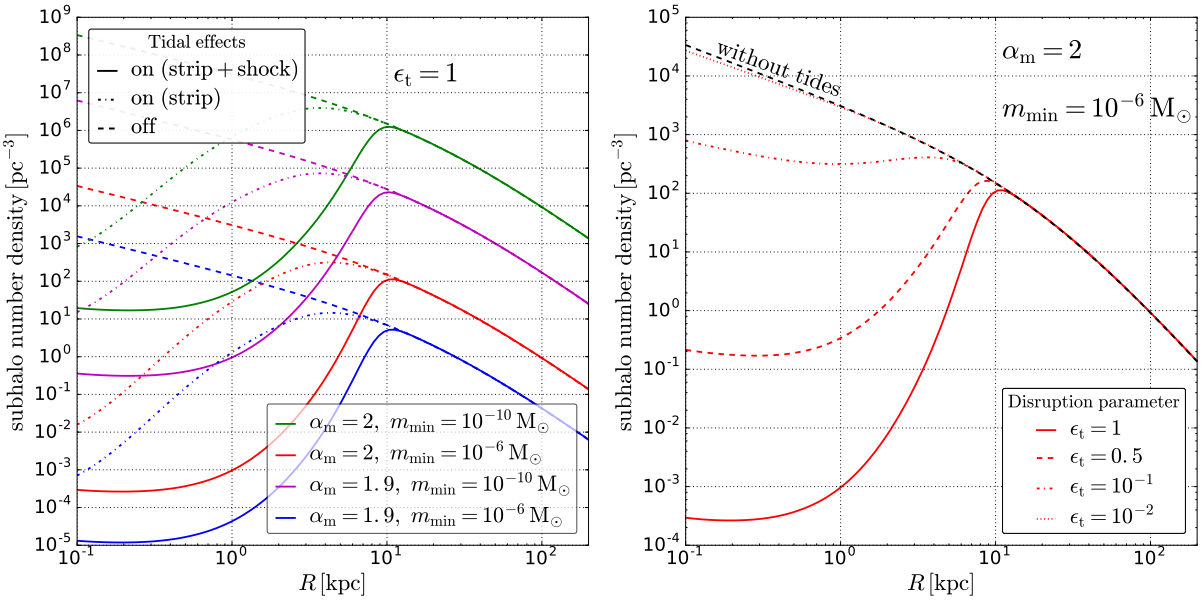

Figure 3.16 – The NFW mass model of McMillan (2017) is used for both panels. **Left panel:** subhalo number density without tides (dashed lines), with stripping (dotted-dashed lines) and with stripping and shocking (solid lines). The number density is shown for different values of α_m and m_{min}. **Right panel:** subhalo number density for different values of the disruption parameter $\epsilon_t = 1/0.5/10^{-1}/10^{-2}$ (solid/dashed/dotted-dashed/dotted lines, respectively).

We recall that the mass dependence is coming from the cosmological correlation between c_{200} and m_{200} which is implemented in $\mathrm{d}P/\mathrm{d}c_{200}$. The average concentration in Eq. (3.179) should be compared to the average for field halos given in Eq. (3.145). Both are shown on Fig. 3.17. One can see that in the presence of tides, $\langle c_{200} \rangle$ rises at the center of the Galaxy. The lower the disruption parameter gets, the closer the average concentration is from the cosmological, radius-independent value. When $\epsilon_t = 0$, the minimal concentration is $c_{min} = 1$ everywhere and there is no selection any more, hence the average concentration is given by Eq. (3.145).

We recall that we assume the internal profile of subhalos is not modified by tidal effects, in particular the scale parameters ρ_s and r_s remain constant. In principle, these parameters can change as the dark matter rearranges within the subhalo after part of it has been stripped. It was shown by Penarrubia et al. (2008), based on a numerical study, that the maximal velocity v_{max} and the associated radius r_{max} change as functions of the mass stripped from the subhalo only. The radius r_{max} decreases as the subhalo lose mass, hence the structure gets artificially more concentrated as some of its mass is stripped away. This increase in concentration is artificial in the sense that is does not mean the subhalo gets denser as some of the matter is stripped away. In fact, the density in the inner parts of the subhalo decreases with the mass loss. Scaling laws for the evolution of v_{max} and r_{max} are given by Penarrubia et al. (2008); Errani et al. (2018), although it is not completely clear whether the numerical artefacts pointed out by van den Bosch et al. could also be at play here. An analytic study of the phase space of tidally stripped halos leads to similar conclusions, see Drakos et al. (2017); Lacroix et al. (2018).

3.3.4.4 Mass function modification

The mass function is also affected by tides. To see how tides affect the mass function, it is more meaningful to look at the physical mass m_t rather than the cosmological mass m_{200}. Therefore we would like to compute a mass function $\mathrm{d}n/\mathrm{d}m_t$ with respect to the physical mass. We noted earlier that the tidal mass is related to the cosmological mass through a scaling relation

$$m_t = m_{200}\,\Delta(c_{200}, R)\,, \tag{3.180}$$

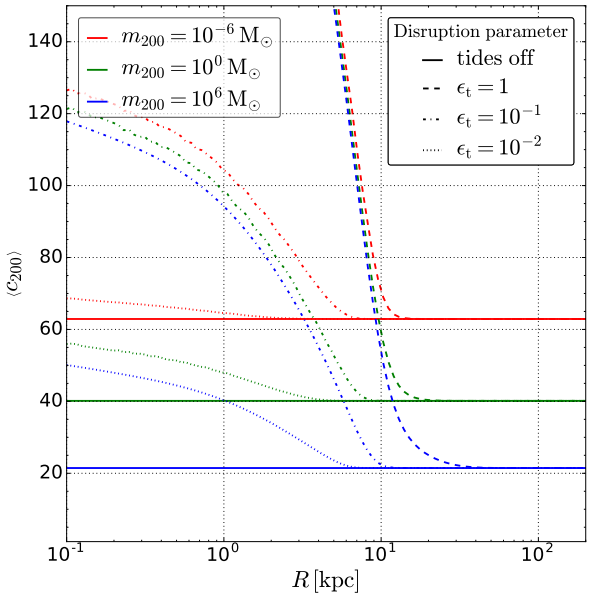

Figure 3.17 – Average cosmological concentration as a function of the position in the Galaxy, for different values of ϵ_t.

where Δ is an integral depending on the tidal radius. We can define a new phase-space number density where m_{200} is replaced by m_t by performing the following operation

$$\tilde{\mathcal{F}}_\mathrm{t}(c_{200}, m_{200}, R) = \int_{m_\mathrm{min}}^{m_\mathrm{max}} \mathrm{d}m_{200}\, \mathcal{F}_\mathrm{t}(c_{200}, m_{200}, R)\, \delta\left[m_\mathrm{t} - m_{200}\Delta(c_{200}, R)\right] \quad (3.181)$$

$$= \int_{m_\mathrm{min}}^{m_\mathrm{max}} \frac{\mathrm{d}m_{200}}{m_{200}}\, \mathcal{F}_\mathrm{t}(c_{200}, m_{200}, R)\, \delta\left[\frac{m_\mathrm{t}}{m_{200}} - \Delta(c_{200}, R)\right], \quad (3.182)$$

Further integration over the cosmological concentration c_{200} leads to the number density $\mathrm{d}n/\mathrm{d}m_\mathrm{t}$ per unit of physical mass

$$\frac{\mathrm{d}n}{\mathrm{d}m_\mathrm{t}}(m_\mathrm{t}, R) = \frac{N_\mathrm{sub}}{K_\mathrm{t}} \frac{\mathrm{d}P}{\mathrm{d}V} \int_{m_\mathrm{min}}^{m_\mathrm{max}} \frac{\mathrm{d}m_{200}}{m_{200}} \frac{\mathrm{d}P}{\mathrm{d}m_{200}} \int_{c_\mathrm{min}(R)}^{\infty} \mathrm{d}c_{200}\, \frac{\mathrm{d}P}{\mathrm{d}c_{200}}\, \delta\left[\frac{m_\mathrm{t}}{m_{200}} - \Delta(c_{200}, R)\right] \quad (3.183)$$

This quantity, multiplied by the mass squared, is shown in Fig. 3.18. We show the mass function inside the disc ($R = 8$ kpc), at the very end of the disc ($R = 20$ kpc) and far from the disc ($R = 100$ kpc). The initial mass function, when tides are unplugged, is shown as the dotted curves. It is perfectly flat *i.e.* it goes like m_{200}^2. The mass function with respect to the cosmological mass m_{200} when tides are plugged in is shown as the dashed curves. There is a significant departure from the m_{200}^2 regime, especially at high masses. The departure is stronger in the central region of the halo. This is easily understood in terms of stripping: the most massive halos are also the less concentrated and therefore the most likely to be disrupted by tidal effects. If the disruption parameter was set to zero, the slope would not be affected because all subhalos would survive tidal effects. Finally, we look at the "true" mass function $\mathrm{d}n/\mathrm{d}m_\mathrm{t}$, defined with respect to the physical mass as in Eq. (3.183). The slope of the mass function is also modified, in more or less the same way as it was for $\mathrm{d}n/\mathrm{d}m_{200}$. The normalization of the mass function is much different however, with $\mathrm{d}n/\mathrm{d}m_\mathrm{t}$ being much lower than $\mathrm{d}n/\mathrm{d}m_{200}$ at a value of the mass $m = m_\mathrm{t} = m_{200} > m_\mathrm{min}$. Below the cosmological mass cutoff m_min, the situation is reversed. While $\mathrm{d}n/\mathrm{d}m_{200}$ is zero, we have $\mathrm{d}n/\mathrm{d}m_\mathrm{t} \neq 0$. This happens because some subhalos with a cosmological mass $m_{200} \geqslant m_\mathrm{min}$ get stripped to a mass $m_\mathrm{t} < m_\mathrm{min}$ hence the power spectrum extends below the cutoff scale. This analysis shows the cosmological information imprinted in the mass function is partly lost in the local Galaxy due to tidal effects. The mass index α_m differs significantly from the Press-Schechter prediction of $\alpha_\mathrm{m} \simeq 2$ and the mass cutoff m_min, related to the kinetic decoupling of the dark matter particle, is significantly lowered.

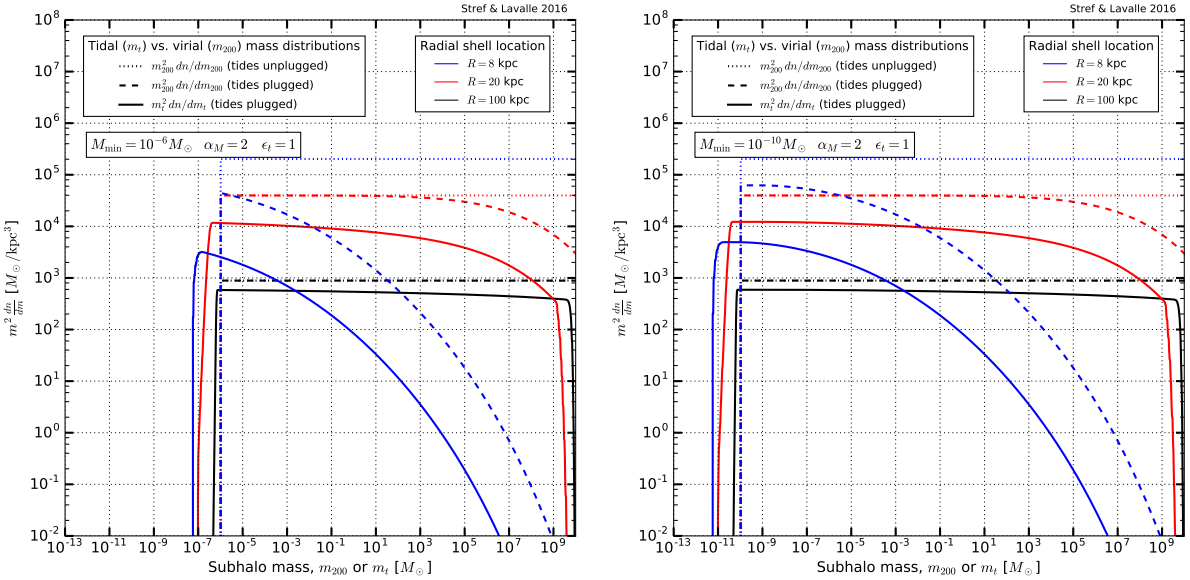

Figure 3.18 – Left panel: mass-differential number density $\mathrm{d}n/\mathrm{d}m$ in terms of both the cosmological mass (dotted/dashed curves for tidal effects unplugged/plugged) and the real tidal mass (solid curves), assuming a cutoff mass $m_{\rm min} = 10^{-6}\,\mathrm{M}_\odot$, and calculated at 3 positions ($R = 8/20/100\,\mathrm{kpc}$ in blue/red/black), as a function of the relevant mass (a scaling of m^2 is applied as $\alpha_{\rm m} = 2$ is chosen here). **Right panel:** same as in the left panel but with $m_{\rm min} = 10^{-10}\,\mathrm{M}_\odot$.

Chapter 4

Impact of dark matter subhalos on indirect searches

The WIMP miracle has motivated several avenues of research based on the interaction between dark and ordinary matter through means other than gravitation. These include particle accelerator searches, direct and indirect searches. The latter are the focus of this chapter. Indirect searches aim at identifying the dark matter particle(s) by detecting the products of its annihilation or decay, assuming these interactions are possible. Dark matter is being looked for in a number of channels, including gamma rays, neutrinos and charged cosmic rays such as antiprotons and positrons. The observability of dark matter through its annihilation or decay depends on its detailed microscopic interactions and on its clustering properties. In this chapter, we aim at evaluating the uncertainty coming from the sub-galactic scale clustering, focusing on the case of annihilating dark matter. We first work out the generic impact of subhalos on indirect searches in Sec. 4.1. We investigate two detection channels to illustrate the effect of clustering. We first look at gamma rays in Sec. 4.2. After describing the propagation of charged cosmic rays in the Galaxy in Sec. 4.3, we investigate the case of cosmic-ray antiprotons in Sec. 4.3.

4.1 Boost factor

The impact of clustering on indirect searches for annihilating dark matter was first pointed out by Silk & Stebbins (1993). The idea is quite simple: since subhalos are overdense regions with respect to the smooth dark matter distribution, the annihilation rate is locally enhanced in subhalos. This means that a clustered dark matter halo should yield a higher overall annihilation rate than a perfectly smooth one. Since we expect CDM to structure on small-scales, the size of this effect should be estimated and its impact on indirect searches evaluated.

Given a halo with internal mass density profile $\rho_{\rm int}$ and radial extension $r_{\rm t}$, we define its luminosity as

$$L_{\rm t} \equiv 4\pi \int_0^{r_{\rm t}} {\rm d}r\, r^2\, \rho_{\rm int}^2(r)\,. \tag{4.1}$$

The luminosity of a structure is directly related to its average annihilation rate

$$\Gamma_{\rm ann} = \frac{\langle \sigma_{\rm ann} v \rangle}{2\, m^2}\, L_t\,. \tag{4.2}$$

The luminosity is a function of the cosmological mass m_{200} and concentration c_{200} through the internal profile, and a function of the spatial extension $r_{\rm t}$. Using the links between m_{200}, c_{200}, $\rho_{\rm s}$ and $r_{\rm s}$, one can show that

$$L_{\rm t} = \frac{200\,\rho_{\rm c}}{3}\, m_{200} (\eta\, c_{200})^3 \frac{\int_0^{x_{\rm t}} {\rm d}x\, x^2\, \tilde{\rho}^2(x)}{\left[\int_0^{\eta\, c_{200}} {\rm d}x\, x^2\, \tilde{\rho}(x)\right]^2}\,, \tag{4.3}$$

with $x_\mathrm{t} = r_\mathrm{t}/r_\mathrm{s}$ and $\tilde{\rho} = \rho/\rho_\mathrm{s}$ as already introduced in Eq. (3.108). This shows that the luminosity is proportional to the cosmological mass and goes roughly like c_{200}^3. As shown in Fig. 4.1, most of the luminosity of a dark matter halo comes from its inner region: more than 80% of the luminosity originates from the core of the structure ($r < r_\mathrm{s}$), regardless of its density profile.

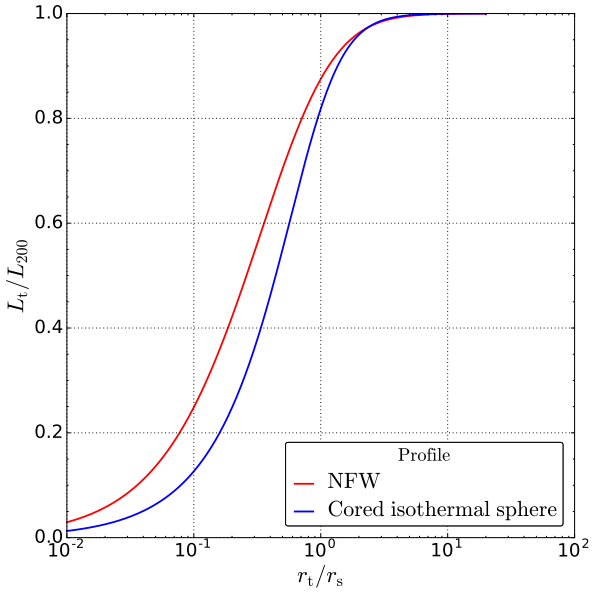

Figure 4.1 – Ratio of the truncated luminosity to the cosmological luminosity as a function of the truncation radius, for the NFW profile (red) and the cored isothermal sphere (blue).

For a tidally stripped subhalo, the radial extension is given by the tidal radius $r_\mathrm{t} = r_\mathrm{t}(c_{200}, m_{200}, R)$ where R is the distance from the Galactic centre. This makes L_t a function of c_{200}, m_{200} and R. The luminosity of the whole Galactic subhalo population is obtained by summing the contribution from each individual subhalo

$$L_\mathrm{sub} = \sum_{\text{subhalo } i} L_\mathrm{t}(c_{200,i}, m_{200,i}, R_i)\,. \tag{4.4}$$

In our statistical description of the subhalo population in the previous chapter, we introduced and computed the parameter-space subhalo number density $\mathcal{F}_\mathrm{t}(c_{200}, m_{200}, R)$ (see Sec. 3.3.2). Using this density, the luminosity can be written as

$$L_\mathrm{sub} = \int \mathrm{d}V \int \mathrm{d}m_{200} \int \mathrm{d}c_{200}\, \mathcal{F}_\mathrm{t}(c_{200}, m_{200}, R)\, L_\mathrm{t}(c_{200}, m_{200}, R)\,. \tag{4.5}$$

The luminosity L_sub is a single number characterising the entire subhalo population. It is convenient to introduce a luminosity density $\mathcal{L}_\mathrm{sub}(R)$ such that

$$L_\mathrm{sub} \equiv \int \mathrm{d}V\, \mathcal{L}_\mathrm{sub}\,. \tag{4.6}$$

With Eq. (4.5), the subhalo luminosity density can be written

$$\begin{aligned}\mathcal{L}_\mathrm{sub}(R) &= \int \mathrm{d}m_{200} \int \mathrm{d}c_{200}\, \mathcal{F}_\mathrm{t}(c_{200}, m_{200}, R)\, L_\mathrm{t}(c_{200}, m_{200}, R) \\ &= \frac{N_\mathrm{sub}}{K_\mathrm{t}} \frac{\mathrm{d}P}{\mathrm{d}V} \int_{m_\mathrm{min}}^{m_\mathrm{max}} \mathrm{d}m_{200} \int_{c_\mathrm{min}(R)}^{\infty} \mathrm{d}c_{200}\, \frac{\mathrm{d}P}{\mathrm{d}m_{200}} \frac{\mathrm{d}P}{\mathrm{d}c_{200}}\, L_\mathrm{t}(c_{200}, m_{200}, R)\,.\end{aligned} \tag{4.7}$$

Of course, annihilation in the Galaxy is not sourced only by subhalos. Two other contributions should be taken into account: annihilation between dark matter particles in the smooth halo,

and annihilation of subhalo particles onto dark matter particles in the smooth halo. Let us work out all these contributions in a consistent way. The luminosity of the whole Galaxy, including the subhalo and the smooth contribution, is given by

$$L_{\rm tot} = \int {\rm d}V \left[\rho_{\rm smooth}(\vec{R}) + \sum_i \rho_{{\rm int},i}\left(\left|\vec{R}-\vec{r}_i\right|\right)\right]^2 , \tag{4.8}$$

where we used the exact contribution of subhalos by summing over all the objects. The development of $L_{\rm tot}$ leads to three terms

$$L_{\rm tot} = \int {\rm d}V\, \rho^2_{\rm smooth} + 2\int {\rm d}V \left[\rho_{\rm smooth}\sum_i \rho_{{\rm int},i}\right] + \int {\rm d}V \left[\sum_i \rho_{{\rm int},i}\right]^2 , \tag{4.9}$$

namely the smooth, cross (subhalo particles on smooth particles) and subhalo contributions. We neglect the possible overlap between subhalos which simplifies the subhalo contribution into

$$\begin{aligned}\int {\rm d}V \left[\sum_i \rho_{{\rm int},i}\right]^2 &\simeq \sum_i \int_{\rm vol.\,sub.} {\rm d}V\, \rho^2_{{\rm int},i} \\ &= \sum_i L_{{\rm t},i}\,.\end{aligned} \tag{4.10}$$

Using our statistical description of the subhalo population, the average value of this sum leads precisely to the expression of $L_{\rm sub}$ in Eq. (4.5). Likewise, the cross term simplifies to

$$2\int {\rm d}V \left[\rho_{\rm smooth}\sum_i \rho_{{\rm int},i}\right] = 2\sum_i \int_{\rm vol.\,sub.} {\rm d}V\, \rho_{\rm smooth}\, \rho_{{\rm int},i}\,. \tag{4.11}$$

Assuming the smooth background is constant within the volume of a subhalo, we get the luminosity of the "cross" contribution

$$L_{\rm cross} \simeq 2\sum_i \rho_{{\rm smooth},i}\, m_{{\rm t},i}\,. \tag{4.12}$$

where $\rho_{{\rm smooth},i}$ is the value of the smooth density in subhalo i and $m_{{\rm t},i}$ the mass of that subhalo. In our statistical description, this is

$$\begin{aligned}L_{\rm cross} &= 2\int {\rm d}V\, \rho_{\rm smooth}\int {\rm d}m_{200}\int {\rm d}c_{200}\, \mathcal{F}_{\rm t}\, m_{\rm t} \\ &= 2\int {\rm d}V\, \rho_{\rm smooth}\, \rho_{\rm sub}\,,\end{aligned} \tag{4.13}$$

where we used the definition of $\rho_{\rm sub}$ in Eq. (3.152). Putting everything together, we get

$$\begin{aligned}L_{\rm tot} &= L_{\rm smooth} + L_{\rm cross} + L_{\rm sub} \\ &= \int {\rm d}V\, \left(\mathcal{L}_{\rm smooth} + \mathcal{L}_{\rm cross} + \mathcal{L}_{\rm sub}\right)\,,\end{aligned} \tag{4.14}$$

with the expressions of the luminosity densities:

$$\mathcal{L}_{\rm smooth} = \rho^2_{\rm smooth} \tag{4.15}$$

$$\mathcal{L}_{\rm cross} = 2\,\rho_{\rm smooth}\,\rho_{\rm sub} \tag{4.16}$$

$$\mathcal{L}_{\rm sub} = \int {\rm d}m_{200}\int {\rm d}c_{200}\, \mathcal{F}_{\rm t}\, L_{\rm t}\,. \tag{4.17}$$

These luminosity density profiles serve as the basis to compute the annihilation signal in indirect searches, irrespective of the particular messenger used (gamma rays, antiprotons, positrons, etc.).

As realized by Silk & Stebbins (1993), a clumpy halo generically leads to a stronger annihilation signal than a smooth halo. A convenient way to quantify this enhancement is through a *boost factor*. The integrated boost factor is defined as the ratio of the luminosity of a clumpy halo to the luminosity of the same halo if all the dark matter was smoothly distributed. In other words, the boost factor is

$$B \equiv \frac{\int \mathrm{d}V \ (\mathcal{L}_{\rm smooth} + \mathcal{L}_{\rm cross} + \mathcal{L}_{\rm sub})}{\int \mathrm{d}V \ \rho^2_{\rm DM}} \,, \tag{4.18}$$

where $\mathcal{L}_{\rm smooth}$, $\mathcal{L}_{\rm cross}$ and $\mathcal{L}_{\rm sub}$ are given in Eqs. (4.15) to (4.17). By definition, the boost factor is an annihilation signal multiplier equal to 1 in the absence of small-scale clustering.[1] The integrated boost factor is a single number characterizing the clumpiness enhancement within a given volume. A local information on the impact of clumps on the annihilation rate can be obtained with the differential boost factor

$$\mathcal{B}(R) \equiv \frac{\mathcal{L}_{\rm smooth}(R) + \mathcal{L}_{\rm cross}(R) + \mathcal{L}_{\rm sub}(R)}{\rho^2_{\rm DM}(R)} \,. \tag{4.19}$$

Using the luminosity density rather than the integrated luminosity allows us to identify regions in the host halo where the enhancement is stronger and thus point toward potentially interesting targets for indirect searches. So far, our definitions are not specific to any detection channel. We will see in the following that our definition of the boost has to be modified when looking at a particular channel. For now, our definition in Eq. (4.19) is enough to find the regions in the Galaxy most affected by the clustering of CDM.

The luminosity densities are shown in Fig. 4.2. The left panel shows the impact of the minimal mass $m_{\rm min}$ and the right panel shows the impact of the mass index $\alpha_{\rm m}$. The bottom panels show the associated differential boost. We see that the boost is 1 for radii smaller than $R \sim 5$ kpc and it grows to very high values at large radii. This difference is entirely due to tidal effects which, as we have seen in the previous chapter, deplete of subhalos the central region of the Galaxy while leaving the outer part unchanged. Both $m_{\rm min}$ and $\alpha_{\rm m}$ have a high impact on the luminosity and the boost. The impact of the disruption parameter is shown in Fig. 4.3. While the luminosity of the subhalo contribution alone is strongly affected by the value of $\epsilon_{\rm t}$, especially within $R \lesssim 10$ kpc, the overall luminosity is not very sensitive to this value. The reason is that enough dark matter in the inner region ($R < 4$ kpc) is in the smooth component of the halo for this contribution to dominate the luminosity. The subhalo contribution dominates at large radii but the value of $\epsilon_{\rm t}$ is unimportant there because tides have little effects in that region. On the bottom panel in Fig. 4.3, we see that a small difference appears in the transition region 4 kpc$< R <$10 kpc. This surely is of interest because this is precisely where the Solar system is located.

4.2 Indirect searches with gamma rays

The impact of dark matter clumpiness on gamma-ray searches has been investigated in numerous studies, see *e.g.* Bergstrom et al. (1999); Ullio et al. (2002); Berezinsky et al. (2003); Kamionkowski et al. (2010); Pieri et al. (2011); Blanchet & Lavalle (2012); Serpico et al. (2012); Bartels & Ando (2015); Hiroshima et al. (2018). Subhalos could affect gamma-ray searches in a number of ways. The individual detection of subhalos is a possibility (Tasitsiomi & Olinto, 2002; Koushiappas, 2006; Moore et al., 2005; Pieri et al., 2008; Ando et al., 2008; Kuhlen et al., 2008; Hütten et al., 2016; Calore et al., 2017). Observed satellites like dwarf spheroidal galaxies constitute privileged targets in this context (Ackermann et al., 2015; Albert et al., 2017). The vast majority of subhalos have masses much too small to allow their individual detection unless they are very close to

[1] Note that an alternative definition can be found in the literature where the boost is shifted by one so that it is zero if there is no enhancement. We will not use this definition in the following.

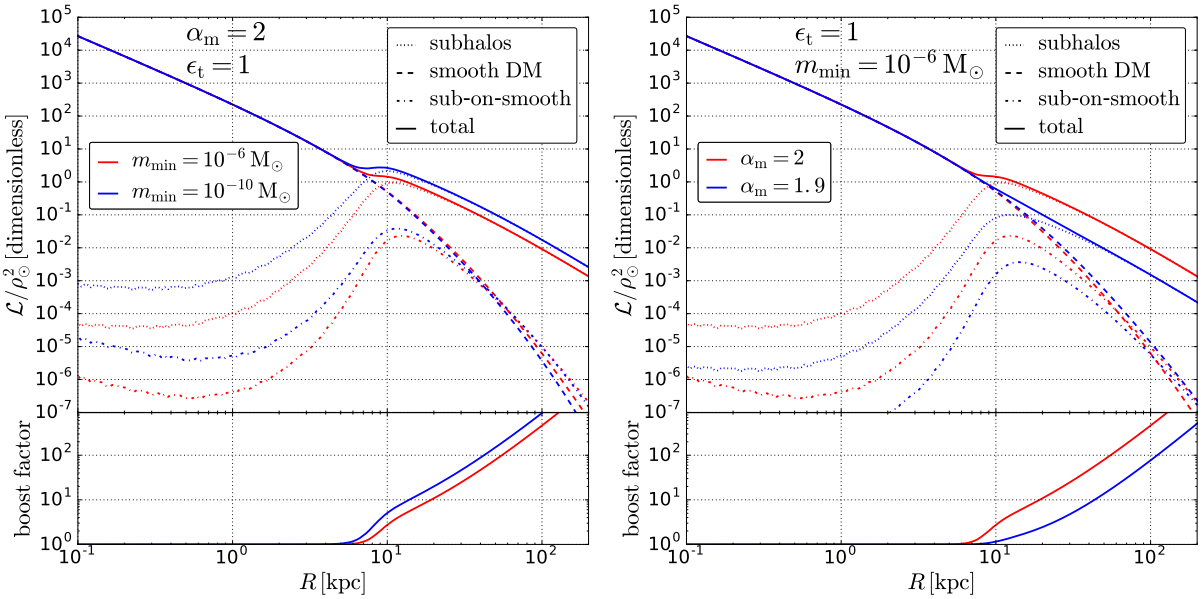

Figure 4.2 – **Left, upper panel:** luminosity density profile for subhalos (dotted lines), smooth dark matter (dashed lines) and the cross contribution (dotted-dashed lines), as well as the sum of all contributions (solid lines), for two values of the minimal mass $m_{\rm min}$. **Left, lower panel:** differential boost factor, as defined in Eq. (4.19). **Right panel:** same as left panel, with $m_{\rm min} = 10^{-6}\,{\rm M}_\odot$ and $\alpha_{\rm m} = 2$ or $\alpha_{\rm m} = 1.9$.

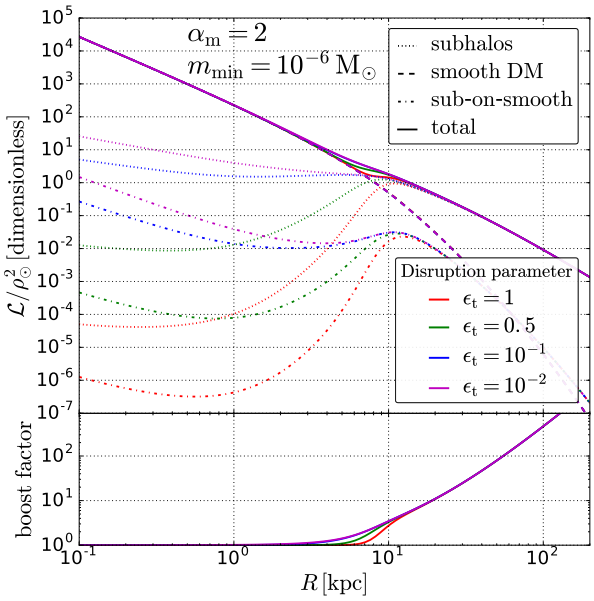

Figure 4.3 – **Upper panel:** luminosity density profile for subhalos (dotted lines), smooth dark matter (dashed lines) and the cross contribution (dotted-dashed lines), as well as the sum of all contributions (solid lines), for different values of the disruption parameter $\epsilon_{\rm t}$. **Lower panel:** differential boost factor, as defined in Eq. (4.19).

the Earth. However, these structures should contribute significantly to the diffuse gamma-ray background (Ackermann et al., 2012b).

In order to estimate the contribution of dark matter clumps to the annihilation signal, let us first express the gamma-ray flux for a smooth galactic halo. The energy-differential flux per unit

of solid angle is given by

$$\left.\frac{\mathrm{d}\phi}{\mathrm{d}E\,\mathrm{d}\Omega}\right|_{\mathrm{l.o.s.}} = \frac{1}{4\pi}\frac{\langle\sigma_{\mathrm{ann}}v\rangle}{2\,m^2}\frac{\mathrm{d}N_\gamma}{\mathrm{d}E}\int_{\mathrm{l.o.s.}}\mathrm{d}s\,\rho^2(s)\,, \tag{4.20}$$

where $\mathrm{d}N_\gamma/\mathrm{d}E$ is the gamma-ray spectrum emitted at annihilation.[2] Interpolation functions for all possible spectra are given in Cirelli et al. (2011). In this expression, l.o.s. stands for line of sight. The line of sight is usually characterized by two angles: the latitude b and the longitude l, with $-90^\circ \leqslant b \leqslant 90^\circ$ and $0 \leqslant l \leqslant 360^\circ$. Relations between these coordinates and Cartesian coordinates are given in App. C. The differential flux is obtained by integrating over the solid angle (defined by the region of interest or the angular resolution of the detector)

$$\left.\frac{\mathrm{d}\phi}{\mathrm{d}E}\right|_{\mathrm{l.o.s.}} = \frac{1}{4\pi}\frac{\langle\sigma_{\mathrm{ann}}v\rangle}{2\,m^2}\frac{\mathrm{d}N_\gamma}{\mathrm{d}E}\int_{\Delta\Omega}\mathrm{d}\Omega\int_{\mathrm{l.o.s.}}\mathrm{d}s\,\rho^2(s)\,. \tag{4.21}$$

Much like the expression of the event rate in direct detection experiments, the particle physics and astrophysical of the expression can be factorized. The astrophysical part is referred to as the J-factor

$$J(\Delta\Omega) \equiv \int_{\Delta\Omega}\mathrm{d}\Omega\int_{\mathrm{l.o.s.}}\mathrm{d}s\,\rho^2(s)\,. \tag{4.22}$$

When looking at targets within the Milky Way, a different definition of the J-factor is sometimes used

$$J_\odot(\Delta\Omega) \equiv \int_{\Delta\Omega}\mathrm{d}\Omega\int_{\mathrm{l.o.s.}}\mathrm{d}s\,\left(\frac{\rho(s)}{\rho_\odot}\right)^2\,, \tag{4.23}$$

where $\rho_\odot$ is the local dark matter density. The J-factor is highly sensitive to the shape of the dark matter density profile. Since the profile is poorly known at the centre of the Galaxy, this is a major source of uncertainty for gamma-ray searches. This uncertainty is illustrated in the right panel on Fig. 4.4 where we show the J-factor as a function of the longitude, for a latitude $b = 0^\circ$ (so that for $l = 0^\circ$, the line of sight points toward the Galactic centre). While there is little difference above $l = 60^\circ$, predictions at the centre varies by several orders of magnitude depending on the central slope.

It is straightforward to express the J-factor including the contribution from substructures given our discussion in the previous section. One simply has to replace in Eq. (4.22) or Eq. (4.23) the density ρ^2 by the luminosity densities defined in Eqs. (4.15) to (4.17). Hence the J-factor along any line of sight can be separated into three contributions: annihilation in subhalos, in the smooth halo and the "cross" contribution

$$J(\Delta\Omega) = \int_{\Delta\Omega}\mathrm{d}\Omega\int_{\mathrm{l.o.s.}}\mathrm{d}s\,\left[\mathcal{L}_{\mathrm{sub}} + \mathcal{L}_{\mathrm{smooth}} + \mathcal{L}_{\mathrm{cross}}\right]\,. \tag{4.24}$$

These contributions are shown in the right panel on Fig. 4.4, for the mass function parameters $\alpha_{\mathrm{m}} = 2$ and $m_{\mathrm{min}} = 10^{-6}\,\mathrm{M}_\odot$ and a disruption parameter $\epsilon_{\mathrm{t}} = 1$. The inclusion of substructures significantly affects the J-factor, which is increased by a factor of more than two with respect to the no-subhalo configuration for longitudes $l > 50^\circ$. We note that the contribution from subhalos is nearly independent of the latitude, which is a consequence of their spatial distribution which is mainly shaped by tidal effects. The cross contribution is always at least an order of magnitude below the other contributions, which is why it is often neglected in the literature.

Since subhalos can have a sizeable contribution to the gamma-ray flux, it is worth defining a boost factor. Its definition is straightforward given our discussion in the previous section:

$$\mathcal{B}_{\mathrm{J}} = \frac{\int_{\Delta\Omega}\mathrm{d}\Omega\int_{\mathrm{l.o.s.}}\mathrm{d}s\,\left[\mathcal{L}_{\mathrm{sub}} + \mathcal{L}_{\mathrm{smooth}} + \mathcal{L}_{\mathrm{cross}}\right]}{\int_{\Delta\Omega}\mathrm{d}\Omega\int_{\mathrm{l.o.s.}}\mathrm{d}s\,\rho^2(s)}\,, \tag{4.25}$$

[2] This expression is valid for dark matter particles which are there own antiparticle. If that is not the case, the flux should be multiplied by a factor of 1/2.

i.e. it is simply the ratio between the J-factor including subhalos to the J-factor assuming all the dark matter is smoothly distributed. Unlike our definition of the differential boost in the previous section, see Eq. (4.19), this boost factor depends on the direction of the line of sight and not on the distance to the Galactic centre. The "J-factor boost factor" is very sensitive to the parameters characterizing the clump distribution. In particular, the disruption parameter ϵ_t can significantly affect the boost, as shown in Fig. 4.5. For $\alpha_m = 2$ and $m_{min} = 10^{-6}\,M_\odot$ (top left panel), and for very low values of ϵ_t, motivated by the recent results of van den Bosch et al. (2018), we get a boost of $\mathcal{B}_J = 2$ at $l = 40°$ and more than $\mathcal{B}_J = 4$ at $l = 90°$, to nearly 6 at the anti-centre at $l = 180°$. Such high values should strongly impact dark matter searches using the diffusive gamma-ray background, see for instance the recent analysis of Chang et al. (2018). However, the impact of subhalos is strongly sensitive to the mass index α_m and the mass cutoff m_{min}, as shown in the top right panel and the bottom panel in Fig. 4.5. For a value of $\alpha_m = 1.9$, as found in the simulation of Springel et al. (2008), the boost is greatly suppressed and stays below 2 at all longitudes.

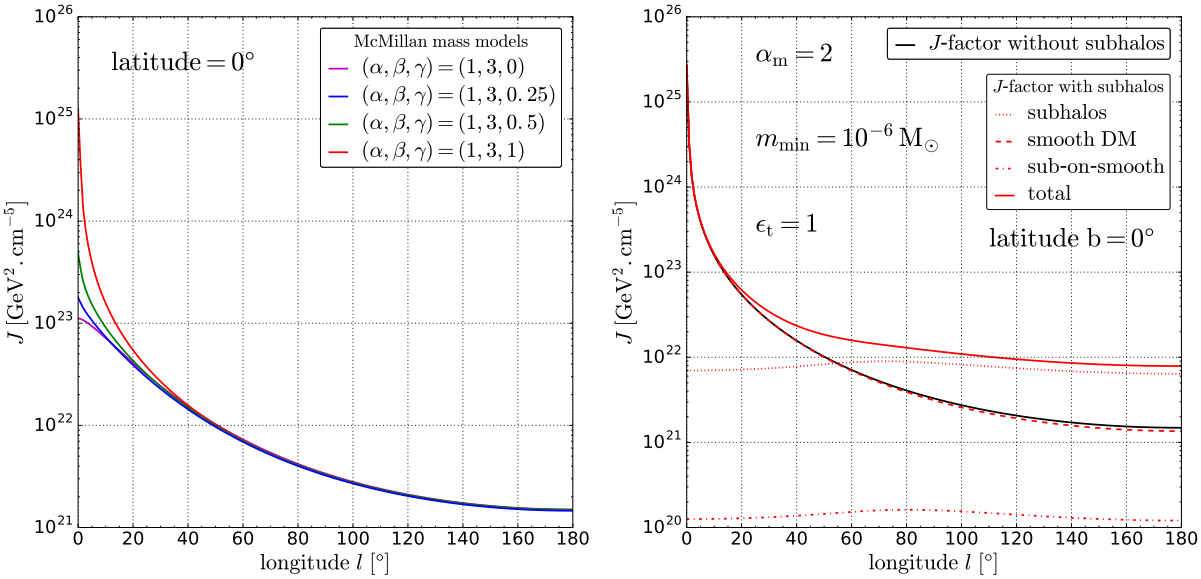

Figure 4.4 – Left panel: J-factor has defined in Eq. (4.22) as a function of the longitude, for a latitude $l = 0°$. We used the mass models of McMillan (2017) and the angular resolution is 0.5°. **Right panel:** J-factor including the contribution of substructures (red) compared to the no-subhalos case (black). The mass function parameters are $\alpha_m = 2$ and $m_{min} = 10^{-6}\,M_\odot$, and the disruption parameter is $\epsilon_t = 1$.

4.3 Indirect searches with antimatter cosmic rays

Since their discovery by Hess in 1912 (F. Hess, 1912), cosmic rays have been collected by a wide variety of ground-based and spatial experiments. Cosmic rays are relativistic charged particles wandering in the interstellar medium. They are composed primarily of nuclei (99%) and leptons (1%). Among the nuclei, around 90% are protons, 9% are helium nuclei and 1% heavier nuclei. Leptons are composed essentially of electrons 90% and positrons 10%. The cosmic-ray spectrum is measured over several decades in energy and behaves approximately as a power-law, see Fig. 4.6 (Blasi, 2013; Aloisio et al., 2018). Measurements are precise enough to show features in the spectrum, which depart from a perfect power-law. Below 10 GeV, cosmic rays received at the Earth are affected by solar modulation which we discuss below. Between 10 GeV and 3 PeV, the data are well-fitted by a power law with an index of $\gamma \simeq 2.7$. At 3 PeV, there is a first breaking of the power-law called the "first knee". Between 3 PeV and 300 PeV, the spectrum softens to $\gamma \simeq 3.1$. At 300 PeV, another feature called the "second knee" marks the transition between an

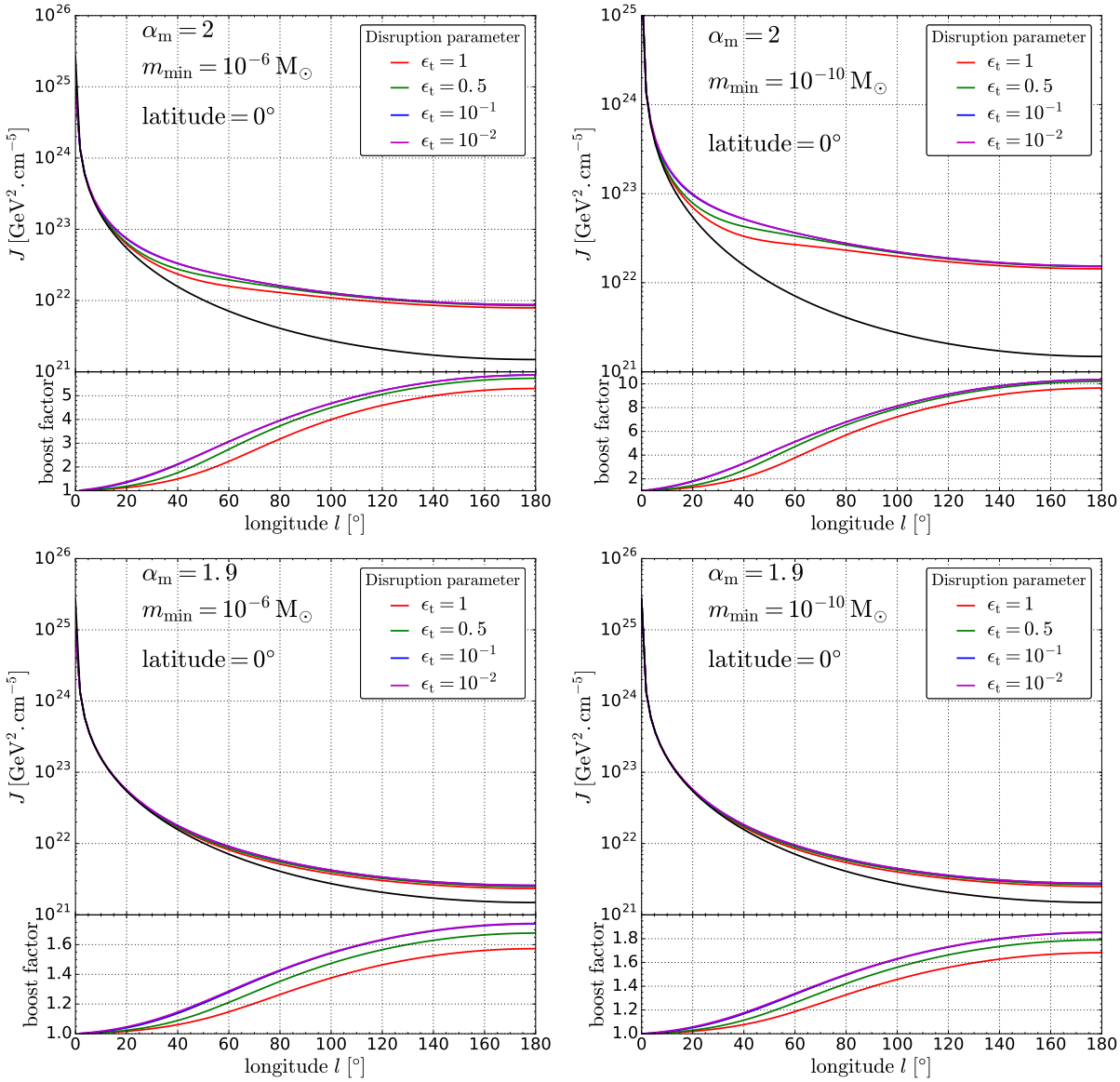

Figure 4.5 – Top panel: J-factor has a function of the longitude for different values of the disruption parameter ϵ_t (coloured lines). We also show the J-factor for a smooth halo (black line). The bottom panel shows the boost factor for each ϵ_t. The mass function index is $\alpha_m = 2$ and the mass cutoff is $m_{min} = 10^{-6}\,M_\odot$ (left panel) or $m_{min} = 10^{-10}\,M_\odot$ (right panel). **Bottom panel:** same figure as the top panel, for $\alpha_m = 1.9$.

index $\gamma \simeq 3.1$ and $\gamma \simeq 3.3$. This regime holds up to the "ankle" at 1 EeV ($= 10^{18}$ eV), where it hardens to $\gamma \simeq 2.6$. At 50 EeV, cosmic rays have enough energy to efficiently interact with CMB photons which strongly limit their propagation in the intergalactic medium. The effect is referred to as the GZK effect after Greizen, Zatsepin and Kuzmin (Greisen, 1966; Zatsepin & Kuz'min, 1966).[3]

The two knees in the cosmic-ray spectrum are thought to mark the transition between Galactic cosmic rays and extragalactic cosmic rays. The radius of gyration of a charged species with momentum p and charge number Z, interacting with a constant magnetic field $\vec{B}$ is

$$r_g \simeq 1\,\mathrm{pc}\left(\frac{p}{\mathrm{PeV}}\right)\left(\frac{B}{\mu\mathrm{G}}\right)^{-1} Z^{-1}\,, \tag{4.26}$$

[3]Note that the limit of 50 EeV is only valid for protons. Heavier elements can violate this limit, which explains why some cosmic rays have been detected at much higher energies.

therefore in the 1-100 PeV range the radius is comparable to the size of the Milky Way. Below this energy range, we expect cosmic rays to have mainly a Galactic origin, while cosmic rays with higher energies are expected to come from extragalactic sources.

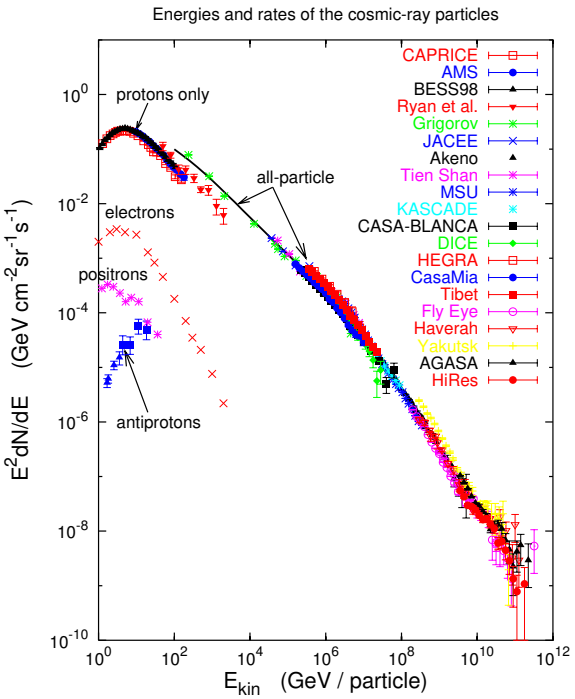

Figure 4.6 – Observed cosmic-ray spectrum as a function of the kinetic energy. Figure taken from Hillas (2006).

4.3.1 Origin and acceleration of cosmic rays

4.3.1.1 Acceleration mechanisms

To accelerate a charged particle, one needs a non-zero electric field. Large scale electric fields are rare in astrophysics because astrophysical plasmas are highly conductive. However, stochastic acceleration can be achieved by small-scale electric fields. We very briefly present the two main mechanisms of acceleration of cosmic rays. For reviews, we refer to Drury (1983); Blandford & Eichler (1987); Malkov & Drury (2001).

Second-order Fermi acceleration A mechanism to accelerate cosmic rays was originally proposed by Fermi (1949). The idea is that cosmic rays can be deflected by molecular clouds, which contain magnetic fields stronger than those found in the interstellar medium. The random motion of molecular clouds in the Galaxy tend to increase the average energy of cosmic rays. A

calculation shows that the average relative energy gain is given by

$$\left\langle \frac{\Delta E}{E} \right\rangle \simeq \frac{4}{3}\beta^2 \,, \tag{4.27}$$

where $\beta = V/c$ and V is the average speed of molecular clouds in the Galactic referential (typically a few hundred of km/s). The dependence on the square of β justifies the designation of second-order for this acceleration mechanism. Though this mechanism does play a role in accelerating cosmic rays, its suppression in β^2 limits its importance.

First-order Fermi acceleration The dominant process in the acceleration of cosmic rays is believed to be the so-called first-order Fermi mechanism (Axford et al., 1977; Bell, 1978a,b). The principle is the same as the second-order mechanism except the interaction is between a cosmic ray and a shock wave rather than a molecular cloud. A shock can be described as a frontier between two mediums with different thermodynamic variables (temperature, pressure, density): the upstream medium (interstellar medium) and the downstream medium (the inside of the shell). Charged particles can diffuse on magnetic inhomogeneities and cross the shock front back and forth, as represented in the lower right bubble in Fig. 4.9. The average relative energy gain can be computed to get

$$\left\langle \frac{\Delta E}{E} \right\rangle = \frac{4}{3}\frac{\Delta v}{c} = \frac{4}{3}\beta \,, \tag{4.28}$$

where $\Delta v = v_2 - v_1$ is the difference between the upstream medium velocity and the downstream medium velocity (typically more than a thousand km/s). Unlike the previous acceleration mechanism, here the relative energy gain is linear in β hence it is referred to as a first-order Fermi acceleration mechanism. It is much more efficient at accelerating cosmic rays than the second-order mechanism and is actually thought to be the dominant acceleration mechanism up to the ankle.

4.3.1.2 Interactions with the interstellar medium

Energy losses Cosmic rays lose energy by interacting with the interstellar medium. These interactions are the following:

- ionization of the interstellar atomic gas
- Coulomb interaction with electrons and protons in an ionized plasma
- Bremmsstrahlung: photon emission from interactions between electrons and the gas nuclei
- inverse Compton: scattering of a relativistic electrons on a photon
- synchrotron: photon emission when an electron propagates in a magnetic field

These interactions are relevant for all charged species. However, the relative importance of the loss mechanism depends on the particle's mass. Consequently, nuclei are mostly affected by the first two processes, while all interactions are important for leptons. As a result, the propagation of high-energy leptons is dominated by energy losses, while losses can often be neglected for high-energy nuclei.

Destruction Cosmic-ray nuclei can be destroyed by inelastic interactions with other atoms or ions in the interstellar gas. Nuclear reactions of spallation split nuclei into smaller products. For a nucleus N interacting with a nucleus C from the gas to create a product P, the interaction rate can be expressed

$$\Gamma_{N+C\to P} = n_{\rm C}\, v_{\rm N}\, \sigma_{N+C\to P} \,, \tag{4.29}$$

where n_C is the number density of C, v_N is the speed of N and $\sigma_{N+C\to P}$ the cross-section.

Destruction is also relevant for antimatter which can annihilate with the interstellar matter (this concerns positrons and antiprotons, but is relevant mostly close to or in the non-relativistic regime).

4.3.1.3 Sources of cosmic rays

Cosmic rays below a few tens of MeV come from the Solar wind while ultra-high energy ones ($T > 10^{18}$ eV) have an extragalactic origin. In between, cosmic rays must have a Galactic origin. We will focus on Galactic cosmic rays below.

Galactic primary cosmic rays A primary cosmic ray is a cosmic ray directly accelerated at its source. Major contributors to the injection and acceleration of cosmic rays in the Galaxy are supernovae. A supernova is the explosion of a star at the end of its life. As the star explodes, all the elements synthesized in its core are injected into the interstellar medium (Baade & Zwicky, 1934; Sekido et al., 1951). A shock wave is also created which expands at high speed away from the supernova. The most famous and spectacular example of supernova remnant (SNR) is the Crab nebula, see Fig. 4.7. Supernovae explosions occur at a rate of three per century in our Galaxy. While supernovae inject heavy nuclei in the interstellar medium, they also accelerate particles with their shock wave through the first-order Fermi mechanism. This acceleration is powerful enough to explain cosmic rays with energies up to the ankle and it is therefore thought to be the main source of acceleration in the Galaxy. Another major source of primary cosmic rays are Pulsar Wind Nebulae (PWNe) which are the by-products of core-collapse supernovae (ending with a rotating and magnetized neutron star). Each PWN is in principle associated to a SNR but contributes to the acceleration of cosmic rays at relativistic shocks (a large fraction of cosmic rays accelerated by PWNe are electron/positron pairs).

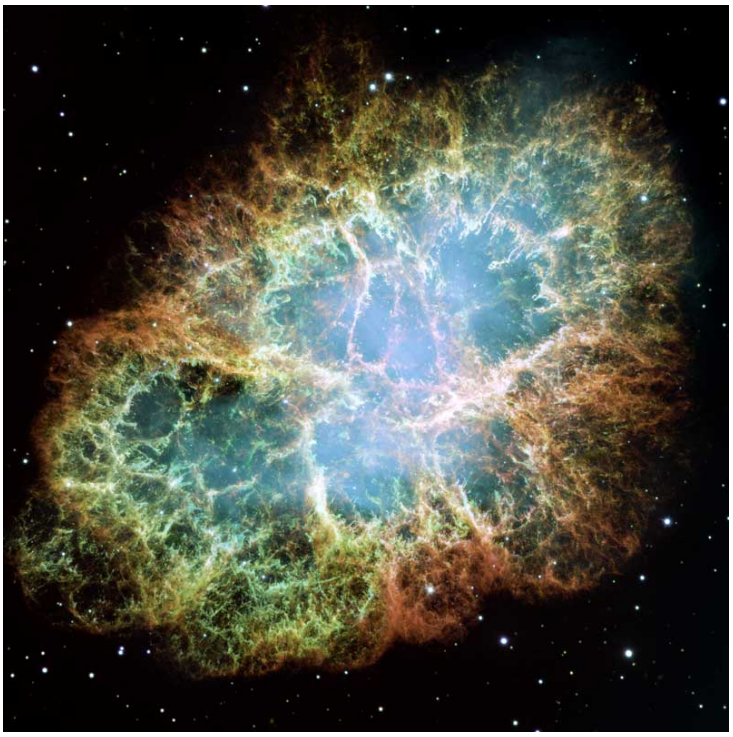

Figure 4.7 – The Crab nebula. The associated supernova exploded in 1024 and was observed at the time by Chinese and Japanese astronomers. Picture taken by the *Hubble* space telescope.

Galactic secondary cosmic rays In opposition to primary sources, a secondary origin for cosmic rays is spallation. Spallation is a nuclear process where a nucleus is hit by another particle or a gamma-ray and subsequently split into a lighter nucleus and other particles (neutrons, protons, antiprotons, etc.). The process occurs when cosmic rays interact with atoms in the interstellar medium, mostly hydrogen and helium but also carbon, nitrogen and oxygen. Thus, spallation is a process that converts primary cosmic rays into secondary cosmic rays (Berezhko et al., 2003). Light nuclei like beryllium and boron are entirely created by spallation, see Fig. 1.4. Secondary cosmic rays provide a powerful test of the cosmic-ray transport properties, since the source acceleration properties may somewhat factorize in the ratio of secondary-to-primary cosmic-ray fluxes. Note that secondaries, if produced in the acceleration zone at a source, may also be accelerated themselves, gaining the status of primaries. Finally, note that secondaries can also experience inelastic processes, and be either destroyed or inelastically driven to lower energies: in the latter case, we talk about "tertiaries" (this happens for instance to antiprotons at low energy).

4.3.1.4 Solar modulation

For cosmic rays to reach the Earth, they have to enter the zone of magnetic influence of the Sun (Potgieter, 2013). This zone is called the heliosphere and is created by the Solar wind, a flow of magnetized plasma ejected from the Sun. The heliosphere ends at the heliopause which is determined by the equilibrium between the pressure from the Solar wind and the pressure of the interstellar medium. The properties of the Solar wind strongly depend on the Solar activity which is known to have periodicity of 11 years. This period corresponds to the time between two inversions of the Sun's magnetic poles.

Cosmic rays lose energy due to their interaction with the Solar wind. This strongly affects the cosmic-ray flux below 10-20 GeV, with a periodicity of 11 years. The equation governing the propagation of cosmic rays in the heliosphere is complex and getting solutions requires numerical calculations. An alternative is to use the effective descrition of Gleeson & Axford (1968) in terms of force-field. Let $\Phi_{\rm IS}$ and $\Phi_{\rm TOA}$ be the interstellar and top-of-atmosphere fluxes, respectively. We consider a nucleus with atomic number A and Z, then the top-of-atmosphere flux is given by

$$\Phi_{\rm TOA}(T_{\rm TOA}) = \Phi_{\rm IS}(T_{\rm IS}) \frac{p_{\rm TOA}^2}{p_{\rm IS}^2} \tag{4.30}$$

$$T_{\rm IS} = T_{\rm TOA} + \frac{Z\,e\,\phi_{\rm F}}{A} \tag{4.31}$$

where $p_{\rm TOA}$ and $p_{\rm IS}$ are the top-of-atmosphere and interstellar momentum *per nucleon*, *i.e.*

$$p_{\rm TOA}^2 = (T_{\rm TOA} + m_{\rm p})^2 - m_{\rm p}^2 \tag{4.32}$$

$$p_{\rm IS}^2 = (T_{\rm IS} + m_{\rm p})^2 - m_{\rm p}^2\,, \tag{4.33}$$

where $m_{\rm p}$ is the proton mass. The parameter $\phi_{\rm F}$ is called the Fisk potential and it has to be inferred from experimental measurements. This parameter depends on time, it is periodic with a period of 11 years. The effect of solar modulation in this simple parametric model is shown for a primary antiproton flux in Fig. 4.8.

4.3.2 The master equation

Let us know introduce the phenomenological model of cosmic-ray propagation. For classic textbooks on cosmic rays, we refer to Ginzburg & Syrovatskii (1964); Berezinsky et al. (1990). The magnetic halo is approximated to a cylinder of radius $R_{\rm gal} = 20\,{\rm kpc}$ and half-height L between 1 and 15 kpc. All the matter is concentrated in the Galactic disc, which is itself identified to a cylinder with radius $R_{\rm gal}$ and half-height $h \sim 100\,{\rm pc}$. This model is referred to as a 2D

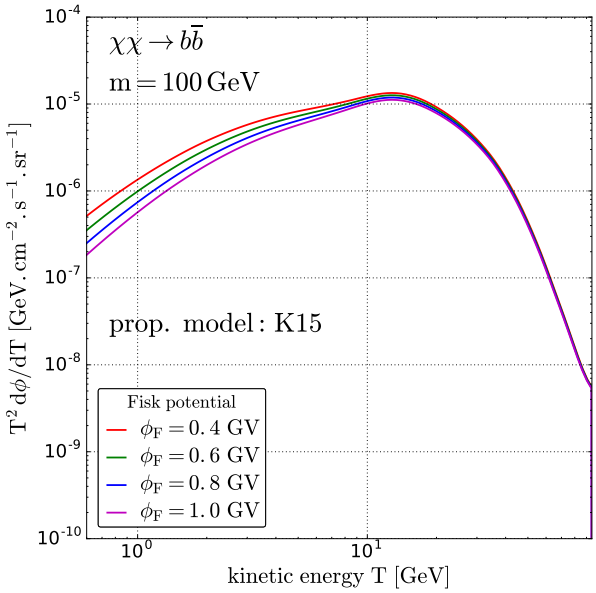

Figure 4.8 – Effect of solar modulation of the antiproton flux using the Fisk potential. We show the flux for a smooth NFW profile and a thermal annihilation cross-section $\langle\sigma_{\rm ann}v\rangle = 3.10^{-26}\,{\rm cm}^3/{\rm s}$. We used the propagation model of Kappl et al. (2015), see Tab. 4.1.

model because the cosmic-ray density only depends on the cylindrical radius R and the altitude z.

We denote Ψ the cosmic-ray density per unit energy

$$\Psi(E,t,\vec{x}) \equiv \frac{{\rm d}n}{{\rm d}E}\,. \tag{4.34}$$

The evolution of Ψ follows a Fokker-Planck equation (Blandford & Eichler, 1987). Instead of deriving the transport equation from first principles, we simply sketch the main physical processes coming into play. For a detailed review on cosmic-ray propagation, we refer to Strong et al. (2007). The cosmic-ray density obeys a continuity equation

$$\partial_{\rm t}\Psi + \vec{\nabla}.\vec{J} + \partial_E J_E = Q - S\,, \tag{4.35}$$

where Q and S are the source and sink term, respectively. The spatial current can be written

$$\vec{J} = \vec{V}_{\rm c}\,\Psi - K\vec{\nabla}\Psi\,, \tag{4.36}$$

where $\vec{V}_{\rm c}$ encodes the convection due to the Galactic wind and K is the coefficient of spatial diffusion. The structure of the Galactic wind is widely unknown (Cox, 2005). From now on, we make the very simplistic assumption that the wind is perpendicular to the disc and goes away from it *i.e.*

$$\vec{V}_{\rm c} = {\rm sign}(z)\,V_{\rm c}\,\vec{e}_z\,. \tag{4.37}$$

The diffusion coefficient is assumed homogeneous and isotropic. The non-linear diffusion theory (Shalchi, 2009) and numerical simulations (Casse et al., 2002) show that it has a power-law dependence on the rigidity

$$K(E) = K_0\,\beta\,\left(\frac{\mathcal{R}}{1\,{\rm GV}}\right)^{\delta}\,, \tag{4.38}$$

where $\beta = v/c$ and $\mathcal{R} = p/q$ is the rigidity. In the particular case of Kolmogorov magnetic turbulence, we have $\delta = 1/3$ (Kolmogorov, 1941). Note that since we expect different sources of

turbulence on different scales, the diffusion coefficient should somewhat reflect these features. This is actually observed as breaks in the spectra of nuclei and in the B/C ratio, and can be interpreted as breaks in the diffusion coefficient (Panov et al., 2009; Ahn et al., 2010; Adriani et al., 2011; Aguilar et al., 2015b,a; Aguilar et al., 2016). For theoretical studies, we refer to Génolini et al. (2017); Evoli et al. (2018).

The energy current is given by

$$J_E = -b\,\Psi - D\,\partial_E\Psi\,, \tag{4.39}$$

where $b = b_{\rm loss} + b_{\rm adia}$ with

$$b_{\rm loss} = -\left\langle \frac{{\rm d}E}{{\rm d}t} \right\rangle \tag{4.40}$$

is the average energy loss rate (from synchrotron, inverse Compton, etc...) and

$$b_{\rm adia} = -\frac{\vec{\nabla}.\vec{V}_{\rm c}}{3}\,T\,\left(\frac{2\,m\,c^2+T}{m\,c^2+T}\right) \tag{4.41}$$

is the adiabatic loss rate due to the convective wind (Maurin et al., 2001). Cosmic rays diffuse on the inhomogeneities of the magnetic halo which themselves are moving at the Alfvén speed $V_{\rm a}$. At the encounter with inhomogeneities, cosmic rays are reaccelerated following the second-order Fermi mechanism. The energy diffusion coefficient is linked to the Alfvén speed and the spatial diffusion through

$$D(E) = \frac{2}{9}\,V_{\rm a}^2\,\frac{E^2\beta^2}{K}\,. \tag{4.42}$$

If reacceleration is intimately linked to spatial diffusion, it should occur all over the magnetic halo. However, we could think about cases where reacceleration is more efficient where sources are confined, in the disc. This assumption notably helps in solving the transport equation analytically. Formally, the reacceleration region can however be rescaled to an arbitrary size by rescaling the Alfvén speed $V_{\rm a}$, which should be thought about as an effective speed.

A term of energy gain should in principle be added to the transport equation as in Strong & Moskalenko (1998), however it is not necessary to account for experimental results hence we do not consider it in the following. To summarize, the transport equation is

$$\partial_{\rm t}\Psi + \vec{\nabla}.\left[\vec{V}_{\rm c}\Psi - K\vec{\nabla}\Psi\right] + \partial_E\left[b\,\Psi - D\partial_E\Psi\right] = Q - S\,. \tag{4.43}$$

The sink term can in general be written

$$S = \Gamma_{\rm tot}\Psi\,, \tag{4.44}$$

where $\Gamma_{\rm tot}$ is the total destruction rate taking into account all processes that can remove the species under study, at a given position, time, and/or energy. (including decay if the species is unstable). Since the half-height of the disc is much smaller than the half-height of the magnetic halo in most propagation models, we can assume the disc to be infinitely thin. In that case, all processes that occur only in the disc come with a pre-factor $2h\delta(z)$, hence we get

$$\partial_{\rm t}\Psi + \vec{\nabla}.\left[\vec{V}_{\rm c}\Psi - K\vec{\nabla}\Psi\right] + \partial_E\left[b\,\Psi - 2h\delta(z)\,D\partial_E\Psi\right] + \Gamma_{\rm tot}\Psi = Q\,. \tag{4.45}$$

All processes of acceleration and diffusion included in the equation are schematically represented in Fig. 4.9.

A cosmic-ray proton spends millions of years diffusing in the Galactic disc, and hundreds of millions of years diffusing in the whole halo, while the rate of supernovae explosions is a few

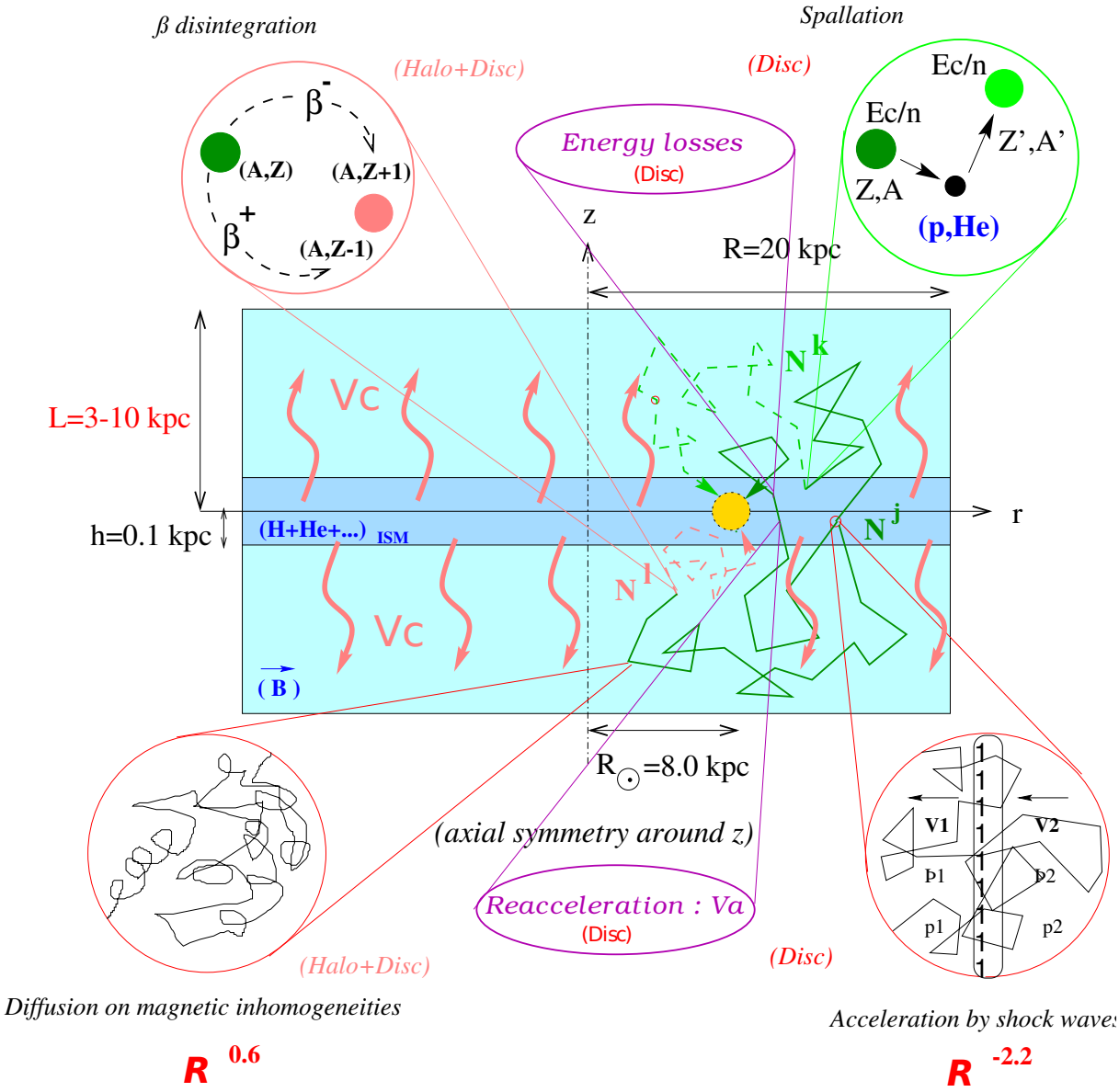

Figure 4.9 – Schematic edge-on view of the Milky Way diffusive halo. The stellar and gaseous disk is sandwiched between two thick layers which contain turbulent magnetic fields. After having been accelerated by supernova driven shock waves or produced by dark matter species annihilating in the Galactic halo, cosmic rays diffuse on magnetic inhomogeneities and are wiped away by a Galactic wind with velocity V_c. They can lose energy and are also mildly subject to diffusive reacceleration. The former process is by far the dominant one in the case of electrons and positrons. This figure is taken from Maurin et al. (2002).

per century. Since supernovae are likely to be the main source of injection and acceleration of cosmic rays, it is natural to look for a steady-state solution of the transport equation. Eq. (4.43) is usually solved numerically. Public codes are available for this purpose. Some codes use a fully numerical approach to solve the equation in a general context, *e.g.* GALPROP (Strong & Moskalenko, 1998), DRAGON (Maccione et al., 2011) and PICARD (Kissmann, 2014; Kissmann et al., 2015). These codes allow one to explore more realistic, full 3D configurations. The code USINE (Maurin, 2016) relies instead on semi-analytic solutions, valid under some restrictive assumptions. The transport equation can slightly differ from code to code, a fact that must be kept in mind when comparing results.

The propagation equation has essentially two types of solutions: full solutions, and solutions

based on Green functions. The latter are most suited for the study of subhalos because they allow us to compute the moments of the subhalo flux distribution, and study the associated statistical variance.

4.3.3 Propagation parameters and dark matter searches

Free parameters in the propagation model are δ, K_0, L, V_c and V_a. While in principle these parameters could be derived from the microscopic properties of the interstellar plasma, the lack of knowledge on the interstellar medium limits this approach. Instead, this parameters are constrained using measurements of cosmic-ray fluxes at the Earth. The ratio of secondary to primary species is particularly interesting because it is sensitive to the propagation parameters and mostly independent of the primaries injection spectrum. The boron-to-carbon ratio B/C is used because the boron is entirely secondary in origin. The high precision of the data on B/C also makes this ratio the most interesting to derive the propagation parameters.

Using the USINE code, Donato et al. (2004) derived sets of parameters compatible with the B/C data available at the time. They classified the sets of parameter in terms of their contribution to the expected flux of antiprotons from dark matter annihilation. The propagation parameters for these models (MIN/MED/MAX) are given in Tab. 4.1. The MIN model gives the smallest antiproton flux while the MAX model gives the largest flux. A parameter especially important for dark matter annihilation is the half-height of the magnetic halo L, because it determines the part of the dark matter halo which is actually probed by cosmic rays. This is the main reason why the MIN model, which has a half-height of 1 kpc, leads to a smaller flux than the MAX model which has $L = 13.5$ kpc. The effect of L on the primary antiproton flux is illustrated in the left panel on Fig. 4.10. We also show the effect of the normalization K_0 of the diffusion coefficient in the right panel. The effect of δ and V_c are also shown in the appendix on Fig. C.2. Note that the MIN and MED models have since then been excluded by low-energy positron data (Lavalle et al., 2014; Boudaud et al., 2017).

Recently, very accurate measurements of B/C by the AMS collaboration (Aguilar et al., 2016) have allowed the best-fitting parameters to be recomputed. This exercise was done by Kappl et al. (2015) on preliminary data from 2015, with the resulting model (hereafter K15) shown in Tab. 4.1. For a more recent analysis, we refer to Reinert & Winkler (2018). The recent data point toward a break in the diffusion coefficient at high rigidity (Génolini et al., 2017). The recent B/C data favour a large diffusive halo, comparable in size to the one found in the MAX model. Unlike the MAX model however, a low convective wind (V_c) and diffusive reacceleration (V_a) is preferred which will actually improve the quality of our predictions as for the effect of dark matter subhalos (the Green function method that we use cannot account for diffusive reacceleration).

	δ	K_0 [kpc^2/Myr]	L [kpc]	V_c [km/s]	V_a [km/s]
K15	0.408	0.0967	13.7	0.2	31.9
MIN	0.85	0.0016	1	13.5	22.4
MED	0.70	0.0112	4	12	52.9
MAX	0.46	0.0765	13.5	5	117.6

Table 4.1 – Propagation parameters for the model of Kappl et al. (2015) (K15) and the MIN/MED/MAX models (Maurin et al., 2002; Donato et al., 2004).

4.3.4 Boost factor for cosmic-rays

The computation of the boost factor for indirect searches with cosmic rays has first been performed in a consistent way by Lavalle et al. (2007). It has been subsequently shown that the enhancement had been greatly overestimated in the past and that it is in fact limited to a factor of a few (Lavalle et al., 2008; Pieri et al., 2011). The most convenient way to compute the boost factor is

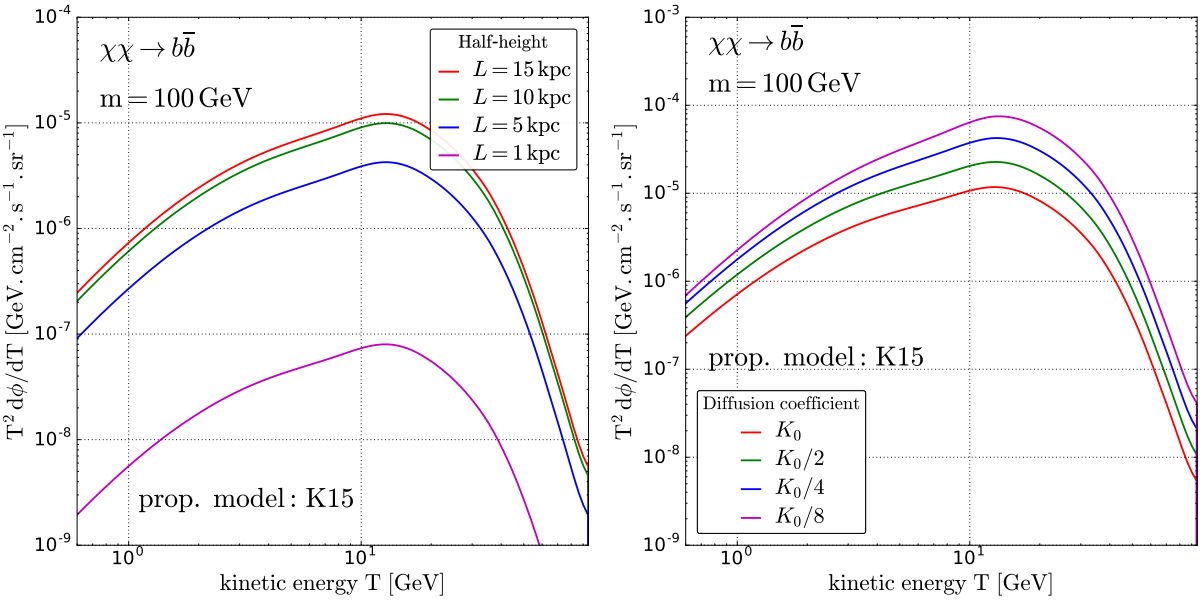

Figure 4.10 – Left panel: effect of the half-height L on the primary antiproton flux from dark matter annihilation. We used a smooth NFW profile and a thermal cross-section $\langle\sigma_{\rm ann}v\rangle = 3.10^{-26}\,{\rm cm}^3/{\rm s}$. The propagation model is K15 (see table below) apart from the value of K_0. **Right panel:** same as left panel, but varying the normalization K_0 of the diffusion coefficient.

through the Green's function formalism. The source term in the propagation equation for dark matter annihilation is

$$Q(\vec{x}, E) = \frac{\langle\sigma_{\rm ann}v\rangle}{2}\left(\frac{\rho(\vec{x})}{m}\right)^2 \frac{{\rm d}N_{\overline{p}}}{{\rm d}E}\,, \tag{4.46}$$

As for the gamma-ray flux, ${\rm d}N_{\overline{p}}/{\rm d}E$ is the antiproton spectrum generated at annihilation, see Cirelli et al. (2011).[4] The cosmic-ray density can be written

$$\Psi(\vec{x}, E) = \frac{\langle\sigma_{\rm ann}v\rangle}{2\,m^2}\int {\rm d}E_{\rm s}\int {\rm d}^3\vec{x}_{\rm s}\,G(\vec{x}_{\rm s}, E_{\rm s}\to\vec{x}, E)\,\frac{{\rm d}N_{\overline{p}}}{{\rm d}E}(E_{\rm s})\,\rho^2(\vec{x}_{\rm s})\,. \tag{4.47}$$

To get the flux per unit of solid angle, one simply has to multiply the density by $v_{\overline{p}}/(4\pi)$ where $v_{\overline{p}}$ is the antiproton speed at energy E. Since we neglected all the terms inducing a change in energy during the transport, the integral over $E_{\rm s}$ is trivial and we get the (differential) flux

$$\frac{{\rm d}\phi}{{\rm d}E} = \frac{\langle\sigma_{\rm ann}v\rangle}{2\,m^2}\frac{v_{\overline{p}}}{4\pi}\frac{{\rm d}N_{\overline{p}}}{{\rm d}E}\int {\rm d}^3\vec{x}_{\rm s}\,G(\vec{x}_{\rm s}, E\to\vec{x}, E)\,\rho^2(\vec{x}_{\rm s})\,. \tag{4.48}$$

Just like the gamma-ray contribution, the cosmic-ray flux can be separated into a particle-physics part and an astrophysics part. The latter is the diffusive halo integral

$$D(\vec{x}, E) = \int {\rm d}^3\vec{x}_{\rm s}\,G(\vec{x}_{\rm s}, E\to\vec{x}, E)\,\rho^2(\vec{x}_{\rm s})\,. \tag{4.49}$$

To get the contribution from substructures, one has to replace the squared-density ρ^2 by the luminosity densities defined in Eqs. (4.15),(4.16),(4.17). It is then straightforward to define a boost factor

$$\mathcal{B}_{\rm cr}(\vec{x}, E) = \frac{\int {\rm d}^3\vec{x}_{\rm s}\,G(\vec{x}_{\rm s}, E\to\vec{x}, E)\,\left[\mathcal{L}_{\rm sub}+\mathcal{L}_{\rm smooth}+\mathcal{L}_{\rm cross}\right]}{\int {\rm d}^3\vec{x}_{\rm s}\,G(\vec{x}_{\rm s}, E\to\vec{x}, E)\,\rho^2(\vec{x}_{\rm s})} \tag{4.50}$$

Since $\vec{x}$ is the position of the observer *i.e.* the Earth, the boost only depends on the energy. Since the energy-dependence comes from the Green's function which encodes the propagation, the boost factor is a priori different for each cosmic ray species.

[4] Like for gamma rays, this expression is valid for *self*-annihilating dark matter. It should be multiplied by 1/2 in alternative cases.

4.3.5 Impact of subhalos on searches with antiprotons

4.3.5.1 Propagation equation for antiprotons

The transport equation for antiprotons is given in Eq. (4.43). Antiprotons are not affected by energy losses, and reacceleration can also be neglected at high energies (neglecting reacceleration is also consistent with the latest B/C data (Kappl et al., 2015; Reinert & Winkler, 2018)), hence the equation simplifies to

$$\partial_t \Psi + V_c \, \partial_z \Psi - K(E) \Delta \Psi + S = Q \, . \tag{4.51}$$

We write the sink term as

$$S = \Gamma_{\rm spal} \Psi \, , \tag{4.52}$$

where

$$\Gamma_{\rm spal}(E) = v_{\overline{p}} \left[n_{\rm H} \, \sigma_{\overline{p}+{\rm H}}(E) + n_{\rm He} \, \sigma_{\overline{p}+{\rm He}}(E) \right] \tag{4.53}$$

is the total spallation rate. The cross-sections $\sigma_{\overline{p}+{\rm H}}$ and $\sigma_{\overline{p}+{\rm He}}$ are the total inelastic interaction cross-sections of antiprotons with H and He. The energy dependence of these cross-section is taken from Tan & Ng (1983). The gas densities in the disc are fixed to $n_{\rm H} = 0.9 \, {\rm cm}^{-3}$ and $n_{\rm He} = 0.1 \, {\rm cm}^{-3}$.

The Green's function, solution of the stationary equation

$$\left\{ -K \Delta + V_c \, \partial_z + 2h \, \Gamma_{\rm spal} \delta(z) \right\} G_{\overline{p}} = \delta^{(3)}(\vec{x}_{\rm s} - \vec{x}) \, , \tag{4.54}$$

can be explicitly written in terms of $r = |\vec{x}_{\rm s} - \vec{x}|$ and $z = z_{\rm s}$, assuming $\vec{x}$ is the position of the Sun ($x_\odot = R_\odot$, $y_\odot = 0$, $z_\odot = 0$). We have (Lavalle et al., 2008)

$$G_{\overline{p}}(r, z) = \frac{e^{-k_v z}}{2 \pi K \, L} \sum_{n=0}^{\infty} c_n^{-1} K_0 \left(r \sqrt{k_n^2 + k_v^2} \right) \sin \left[k_n L \right] \sin \left[k_n (L - z) \right] \, , \tag{4.55}$$

where K_0 is the modified Bessel function of the second kind. The quantity k_n is the solution of

$$2 k_n \cos \left[k_n L \right] = - k_d \sin \left[k_n L \right] \, , \tag{4.56}$$

and

$$c_n = 1 - \frac{\sin \left[k_n L \right] \cos \left[k_n L \right]}{k_n L} \, . \tag{4.57}$$

We also have

$$k_v \equiv \frac{V_c}{2 \, K} \tag{4.58}$$

$$k_d \equiv \frac{2h \, \Gamma_{\rm spal}}{K} + 2 \, k_v \, . \tag{4.59}$$

4.3.6 Antiproton analysis

Since the release by the AMS collaboration of new measurements of the antiproton flux (Aguilar et al., 2016) and the B/C ratio (Aguilar et al., 2016), several groups have re-evaluated the secondary backgrounds and primary contribution from dark matter annihilation (Giesen et al., 2015; Kappl et al., 2015; Cui et al., 2017; Cuoco et al., 2017; Winkler, 2017; Reinert & Winkler, 2018; Cui et al., 2018). The latest estimations show that the data at low and high energies can entirely be explained by secondary antiprotons. Between a few GeVs and a few tens of GeVs, however, the secondary background underestimates the data. The significance of this excess

depends on the analysis (Cuoco et al., 2017; Winkler, 2017; Cui et al., 2018). This excess can be interpreted has a signature of dark matter annihilation (Cui et al., 2017; Cuoco et al., 2017). It could also point toward a need to revise some of the basic assumptions of the propagation models, which may now be challenged by the very high precision of the data. In any case, it is timely to evaluate the astrophysical uncertainties associated to the dark matter signal. All the analyses done so far have focused on a smooth dark matter halo. We know that CDM predicts a clumpy structure for the Galactic halo and that this clumpiness systematically enhances the dark matter annihilation rate.

4.3.6.1 Boost factors and primary fluxes

The flux of primary antiprotons as well as the boost factor are shown, for the K15 propagation model, in Fig. 4.11. The flux and boost factor for the MED propagation model are shown in Fig. 4.12. The choice of the propagation model has a strong impact on the amplitude of the primary antiproton flux, with the K15 model leading to higher values than the MED model as expected from the value of the half-height L in each model. However, the choice of the propagation model has little impact on the amplitude of the boost factor, which is comparable in both models at a given value of $\alpha_{\rm m}$ and $m_{\rm min}$. The prediction of the boost for antiprotons is therefore robust. Nevertheless, we note that the boost in K15 is slightly higher than in MED over most of the kinetic energy range. This difference comes from the size of the diffusive region. The larger diffusive region in K15 includes a part of the outer region of the dark halo which is dominated by subhalos and therefore leads to a slightly higher boost. As for gamma rays, the flux and the boost are sensitive to the value of the disruption parameter $\epsilon_{\rm t}$, with lower $\epsilon_{\rm t}$ leading to a larger boost. The flux and the boost are also highly sensitive to the value of $\alpha_{\rm m}$ and $m_{\rm min}$. In the K15 model for instance, the flux for $m_{\rm min} = 10^{-10}\,M_\odot$ can be enhanced by 10% for $\alpha_{\rm m} = 1.9$ up to 130% for $\alpha_{\rm m} = 2$. We recall that the matter power spectrum on these scales is completely unknown and unconstrained.

We compare the primary antiproton flux to the experimental data from AMS and the secondary prediction from Winkler (2017) in Fig. 4.13. The left panel shows the prediction from the MED model, which has a half-height $L = 4$ kpc, and the right panel shows the prediction from the propagation model of Kappl et al. (2015) (K15) with $L = 13.7$ kpc. As expected from the difference in half-heights, the K15 model leads to a higher prediction than MED. In both models, subhalos lead to a sizeable enhancement of the primary flux for $\alpha_{\rm m} = 2$ and $m_{\rm min} = 10^{-6}\,{\rm M}_\odot$. The case $\alpha_{\rm m} = 2$ and $m_{\rm min} = 10^{-10}\,{\rm M}_\odot$ leads to an even stronger enhancement as shown in Fig. 4.14. However, as already shown by our analysis of the boost factor, the case $\alpha_{\rm m} = 1.9$ leads to a boost too small to be interesting, see Fig. 4.15.

4.3.6.2 Exclusion curves

We can now derive exclusion curves on the annihilation cross-section $\langle\sigma_{\rm ann}v\rangle$ and the mass m of the dark matter particle by comparing our predictions to the data. We perform a $\Delta\chi^2$ analysis and derive the 3σ exclusion curves by requiring

$$\Delta\chi^2 = \chi^2(\text{primaries} + \text{secondaries}) - \chi^2(\text{secondaries}) > 3^2 \tag{4.60}$$

for a model to be excluded. We include the experimental uncertainty (statistic and systematic) on the AMS data. We associate to the primaries and secondaries a 5% theoretical uncertainty on propagation. For secondaries, we add a 20% uncertainty on nuclear cross-sections relevant for spallation processes. For a much more detailed treatment of these uncertainties, we refer to the analysis of Winkler (2017). We show in Fig. 4.16 to 4.18 the exclusion curves corresponding to the fluxes shown in Fig. 4.13 to 4.15. Our best constraints our obtained with the K15 propagation model, with the mass function parameters $\alpha_{\rm m} = 2$ and $m_{\rm min} = 10^{-10}\,{\rm M}_\odot$, as shown in the right panel on Fig. 4.17. In that case, for a dark matter particle annihilating into $b\bar{b}$, we exclude a

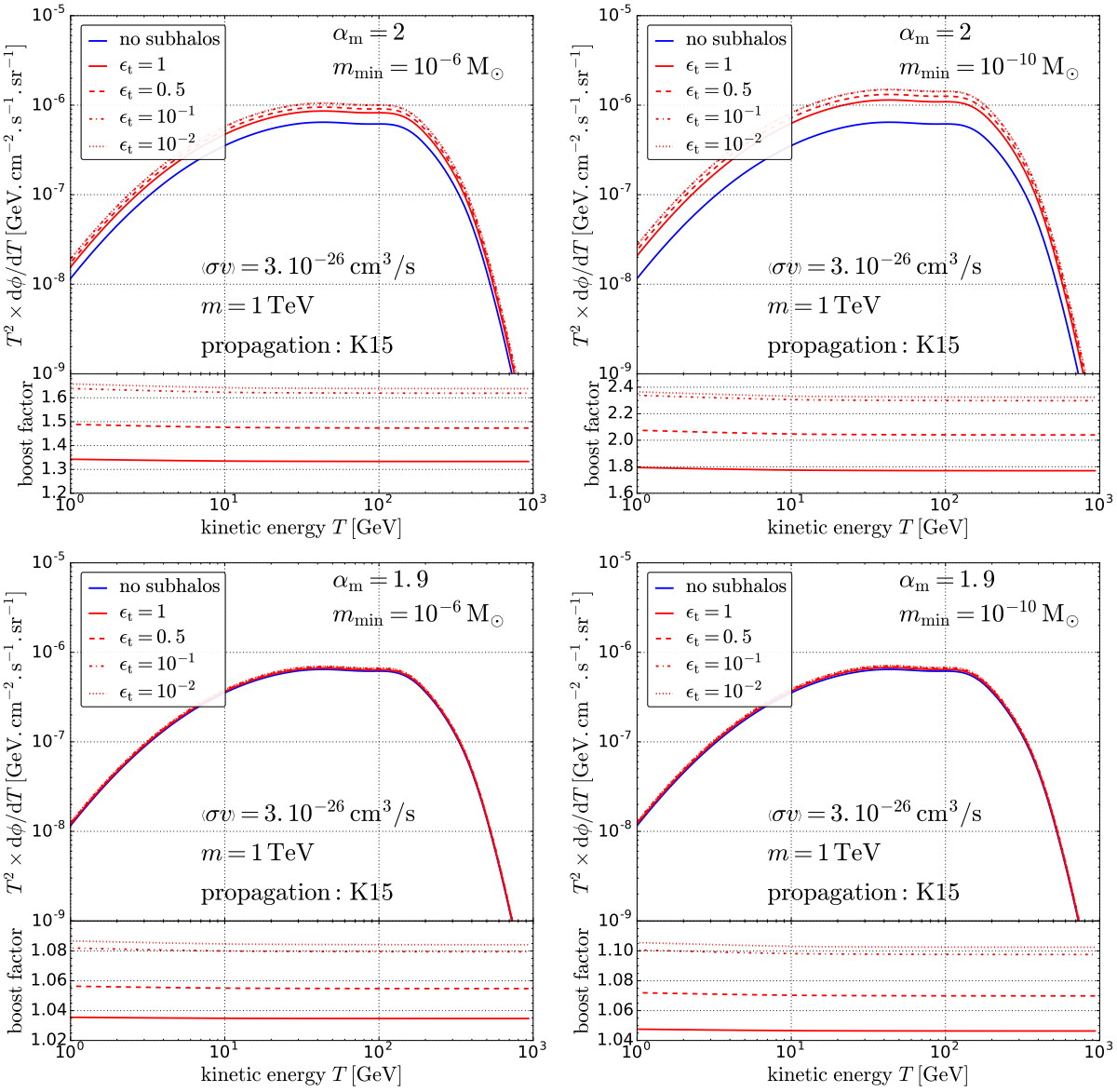

Figure 4.11 – Top panel: we show the primary antiproton flux, multiplied by T^2, for different values of the disruption parameter ϵ_t. The minimal mass is set to $m_{\rm min} = 10^{-6}\,M_\odot$ (left panel) or $m_{\rm min} = 10^{-10}\,M_\odot$ (right panel), and the mass index is $\alpha_m = 2$. The bottom panels show the corresponding boost factors. **Bottom panel:** same as the top panel, for $\alpha_m = 1.9$.

thermal relic up to $m \sim 200$ GeV. Without subhalos, the thermal relic is excluded up to $m \sim 100$ GeV. These constraints have been derived using an NFW profile for the Galactic halo. In App. C, we show the same constraints derived with a cored profile. The difference between the two profiles is rather small.

This shows that the inclusion of subhalos can have an important effect on indirect searches, in particular in the antiproton channel. Given the high precision of the data now available, this enhancement should be taken into account in searches for CDM particle candidates.

4.3.6.3 Statistical variance

So far, we have computed the average value of the primary antiproton differential flux $\langle\Phi\rangle$ where

$$\Phi \equiv \frac{d\phi}{dT}\,. \tag{4.61}$$

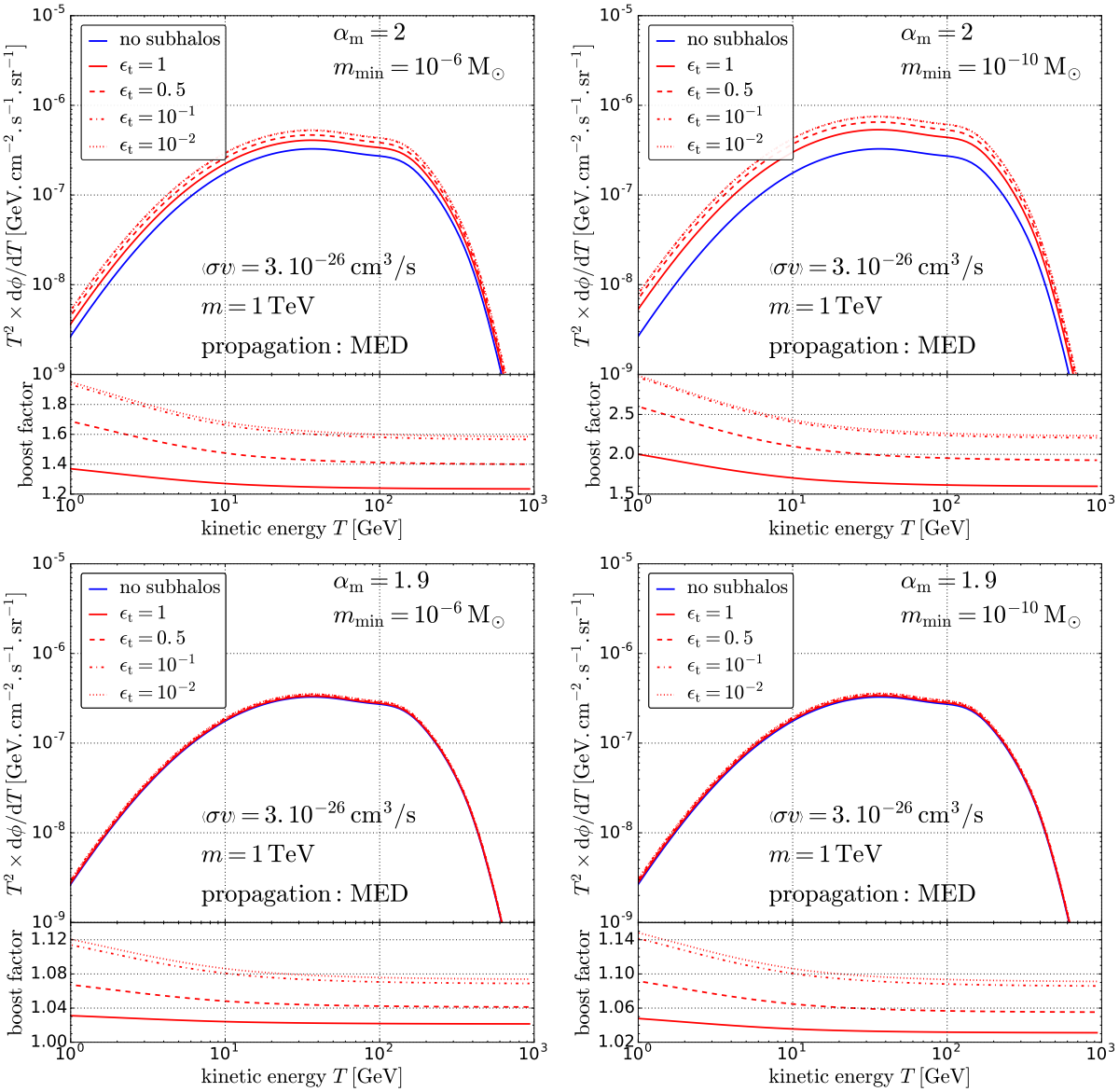

Figure 4.12 – Same as Fig. 4.11, for the MED propagation model.

The average is taken over the subhalo parameter-space distribution function. The Green's function formalism provides us with a way to compute the statistical variance associated to the average value as

$$\sigma_\Phi^2 \equiv \left\langle \Phi^2 \right\rangle - \langle \Phi \rangle^2 \,. \tag{4.62}$$

We must first compute the variance σ_1^2 in the case where the number of subhalos is $N_{\rm sub} = 1$, then we get the variance for $N_{\rm sub} > 1$ through

$$\sigma_\Phi^2 = N_{\rm sub}\, \sigma_{\Phi,1}^2 \,. \tag{4.63}$$

Let us first compute $\left\langle \Phi^2 \right\rangle$. We saw that the flux can be written as the sum of three contributions: the subhalos, the smooth halo and the cross contribution. Hence we have

$$\left\langle \Phi^2 \right\rangle = \left\langle \Phi_{\rm sub}^2 + \Phi_{\rm smooth}^2 + \Phi_{\rm cross}^2 + 2\,\Phi_{\rm sub}\Phi_{\rm smooth} + 2\,\Phi_{\rm sub}\Phi_{\rm cross} + 2\,\Phi_{\rm smooth}\Phi_{\rm cross} \right\rangle \,. \tag{4.64}$$

The smooth component is constant with respect to the statistical averaging over the subhalos parameters therefore

$$\langle \Phi_{\rm smooth}^n \rangle = \Phi_{\rm smooth}^n, \;\; \forall n > 1 \,. \tag{4.65}$$

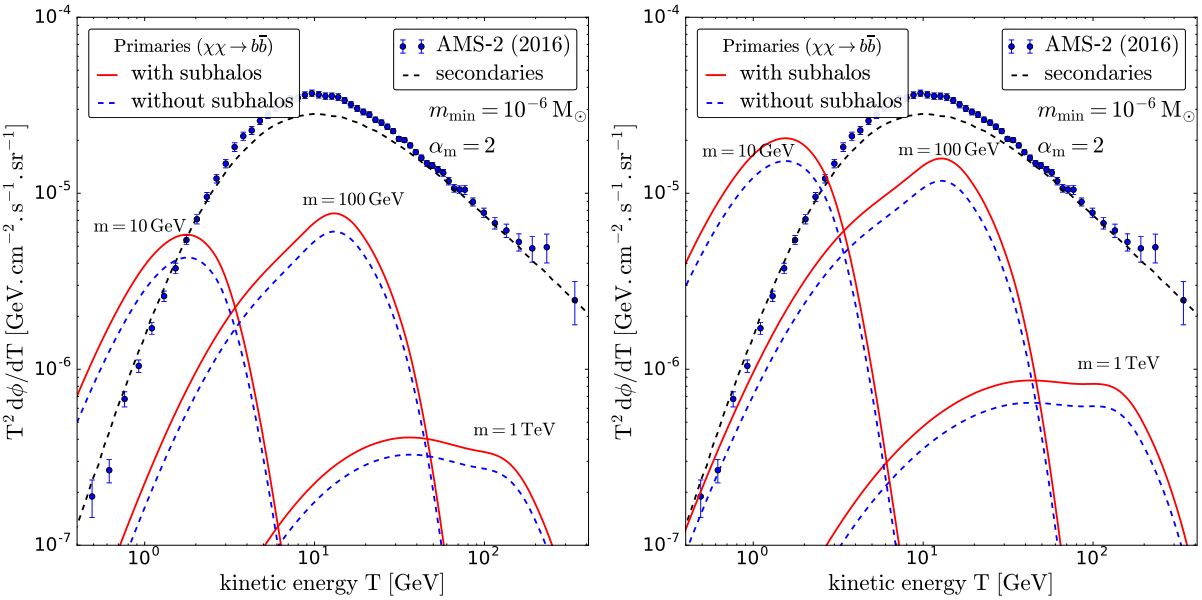

Figure 4.13 – In both panels, we assume $\langle\sigma_{\rm ann}v\rangle = 3\times10^{-26}\,{\rm cm}^3/{\rm s}$, $\alpha_{\rm m} = 2$ and $m_{\rm min} = 10^{-6}\,{\rm M}_\odot$. **Left panel:** annihilation-induced primary antiprotons flux with/without subhalos (solid red/dashed blue), for three different mass of the dark matter particle. The propagation model used is MED. The primary flux is compared to the measurement of AMS-2 (blue points) and the secondary prediction by Winkler (2017) (black dashed). **Right panel:** same as the left panel, for the K15 propagation model. For both panels, the Fisk potential is set to $\phi_{\rm F} = 0.83$ GV (max of Ghelfi et al. (2016)).

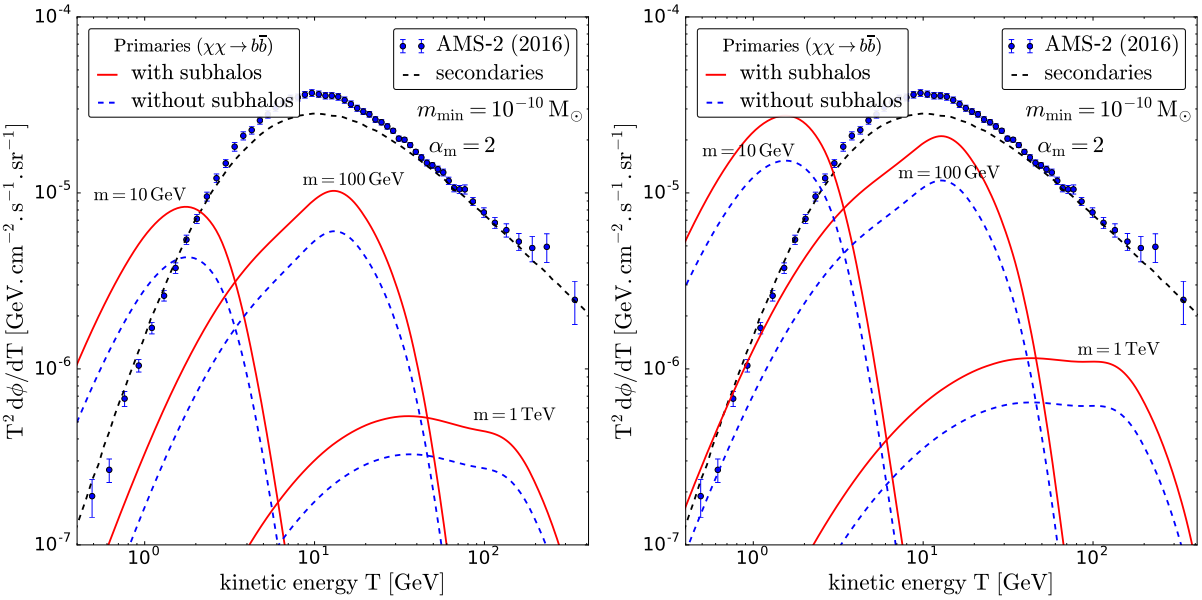

Figure 4.14 – Same as Fig. 4.13 for $\alpha_{\rm m} = 2$ and $m_{\rm min} = 10^{-10}\,{\rm M}_\odot$.

This allows us to rewrite

$$\left\langle\Phi^2\right\rangle = \left\langle\Phi^2_{\rm sub}\right\rangle + \left\langle\Phi^2_{\rm cross}\right\rangle + \Phi^2_{\rm smooth} + 2\,\Phi_{\rm smooth}\left\langle\Phi_{\rm sub} + \Phi_{\rm cross}\right\rangle + 2\left\langle\Phi_{\rm sub}\Phi_{\rm cross}\right\rangle \qquad (4.66)$$

The expressions of all the second order terms are given in the Appendix. We can express the relative flux variation due to our limited knowledge of the clump population as $\sigma_\Phi/\langle\Phi\rangle$. We computed this number and found that it is less than 10^{-3} over the entire range of energy, hence the statistical uncertainty is very small. This is because antiprotons probe a large volume containing many subhalos. Positrons, on the other hand, have their propagation dominated by

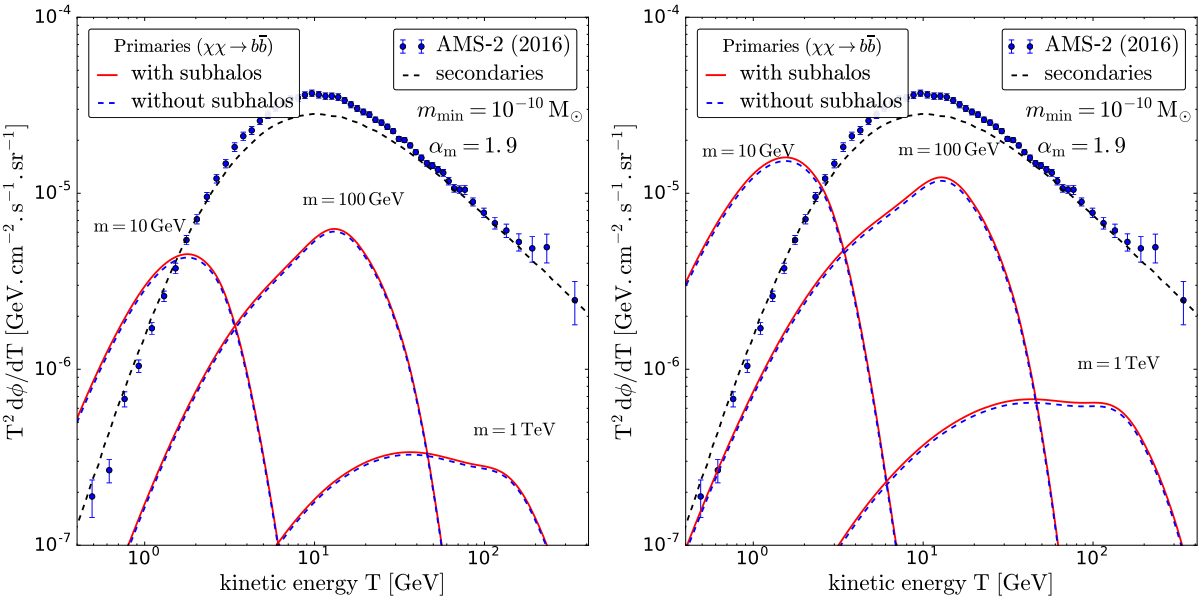

Figure 4.15 – Same as Fig. 4.13 for $\alpha_{\rm m} = 1.9$ and $m_{\rm min} = 10^{-10}\,{\rm M}_\odot$.

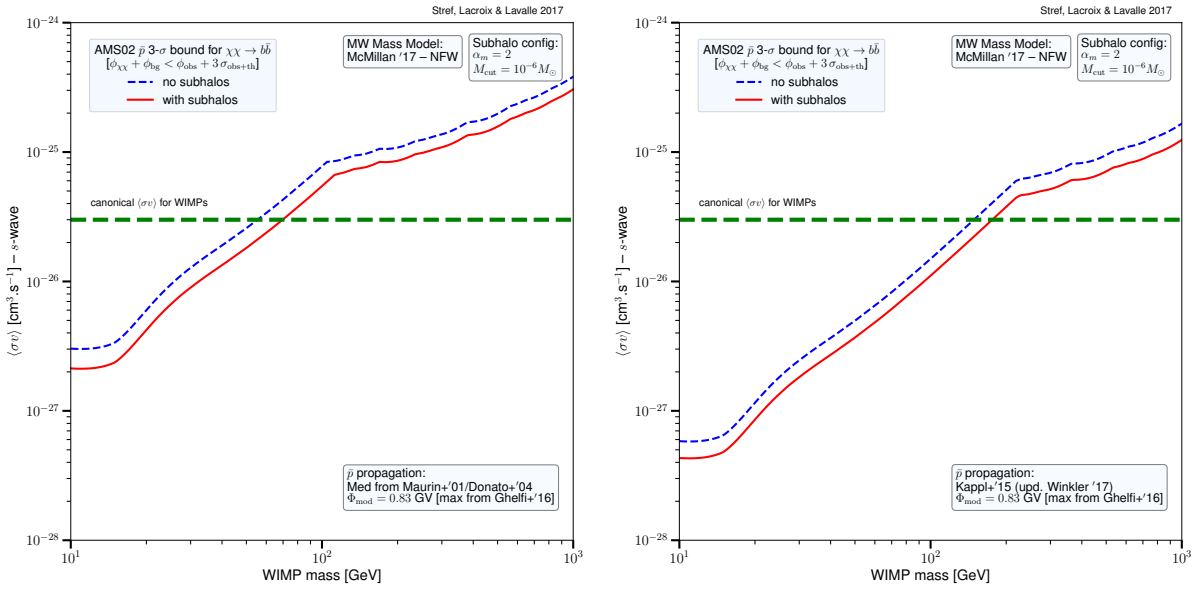

Figure 4.16 – Exclusion curves obtained using the data from Aguilar et al. (2016). **Left panel:** MED propagation model. **Right panel:** same as left panel for the K15 propagation model.

energy losses and probe a much smaller volume at high energies therefore the variance of the positron flux is in general more important (Lavalle et al., 2007; Lavalle et al., 2008).

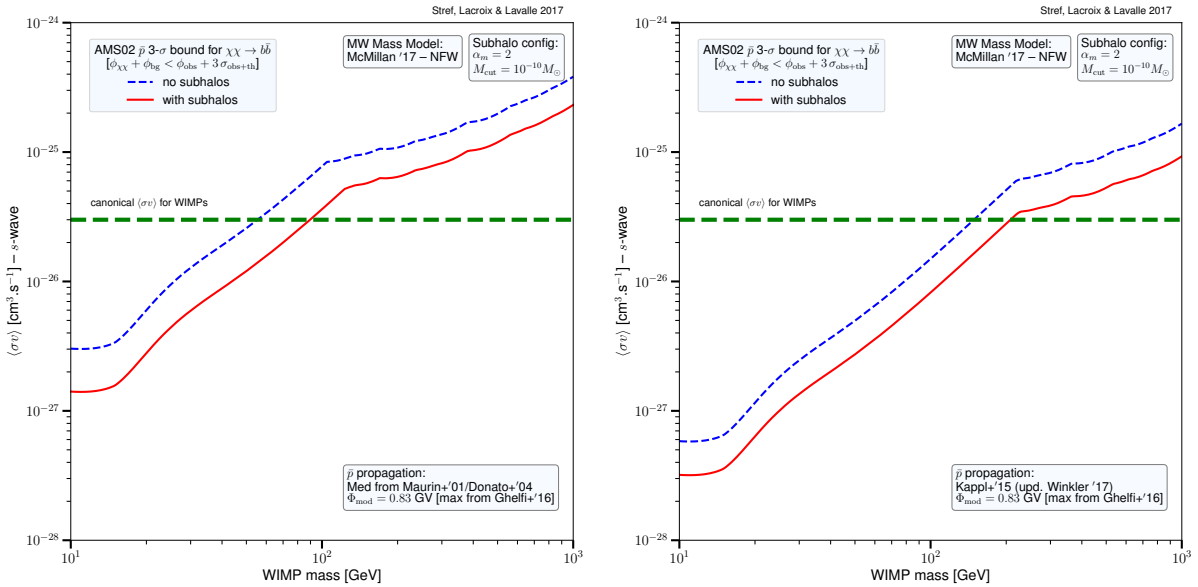

Figure 4.17 – Same as Fig. 4.16 for $\alpha_{\rm m} = 2$ and $m_{\rm min} = 10^{-10}\,{\rm M}_\odot$.

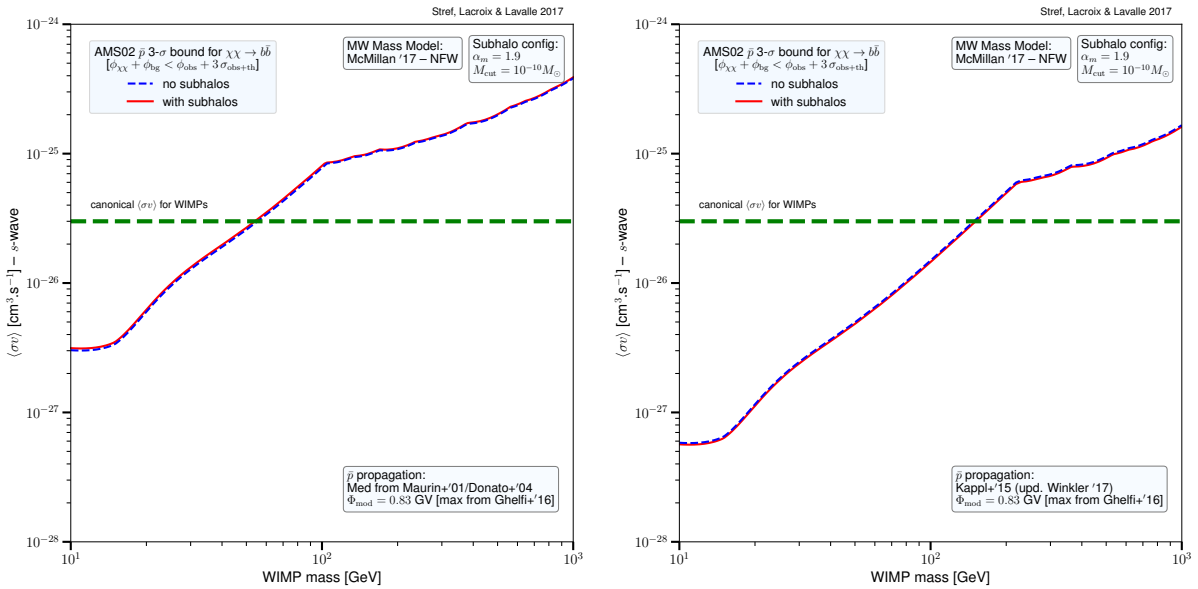

Figure 4.18 – Same as Fig. 4.16 for $\alpha_{\rm m} = 1.9$ and $m_{\rm min} = 10^{-10}\,{\rm M}_\odot$..

Chapter 5

The dark matter phase space of the Galaxy

In this chapter, we focus on the study of the dark matter phase space in our Galaxy. We first describe the structure of the Milky Way as inferred from observations then introduce some basic notions of statistical physics for gravitational systems. We then turn to our main subject of interest: the study of the Eddington inversion formalism. We present this formalism in details and then discuss its limitations and issues.

5.1 Milky Way mass models

In this section, we give a short overview on the structure of the Milky Way and review the mass models available in the literature. For detailed reviews on the structure of our Galaxy, we refer to Bland-Hawthorn & Gerhard (2016) and Binney & Tremaine (1987).

5.1.0.1 Structure of the Galaxy

A schematic view of the Milky Way galaxy, as it would be seen for an observer at latitude $b = 90°$ far from the Galactic plane, is shown in Fig. 5.1. The main structures, such as the spiral arms and the central bars, are represented. There are ample evidences that galaxies are embedded in large dark matter halos, as reviewed in the introduction. This of course includes the Milky Way where we know, using for instance the kinematics of satellite galaxies (Watkins et al., 2010), that the dark halo extends far beyond the Galactic disc.

A great number of authors tried to build consistent mass models for the Milky Way. A mass model is a description of the different components of the Galaxy in terms of density, mass or gravitational potential, in a way that agrees with a set of observational constraints. The improvements of observations over the last decades has allowed to build more and more refined models, see *e.g.*Dehnen & Binney (1998); Widrow & Dubinski (2005); Catena & Ullio (2010); McMillan (2011); Catena & Ullio (2012); Fornasa & Green (2014); Piffl et al. (2015); Binney & Piffl (2015); Pato et al. (2015); Cole & Binney (2017); McMillan (2017). The recent data release from the Gaïa collaboration is a major step forward that will help sharpen our understanding of the dynamics and history of our Galaxy.

In this work, we use the Milky Way mass models of McMillan (2017), which are detailed in App. D. The author models the bulge, two stellar discs (thin and thick), two gas discs (H and H_2) and the dark halo. The parameters of the model are constrained using kinematic data from maser observations, the solar velocity, terminal velocity curves, measurements of the vertical force and the mass within large radii.

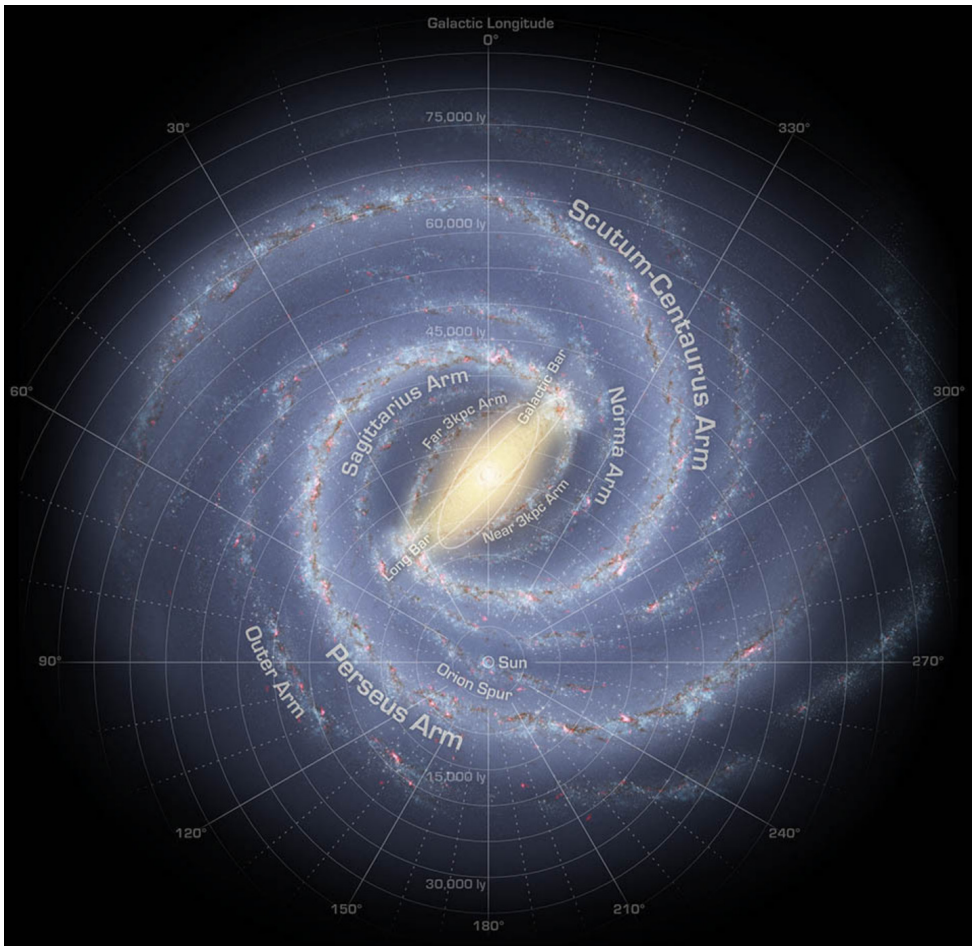

Figure 5.1 – Schematic view of the Milky Way. Source: NASA/JPL-Caltech/R. Hurt (SSC/Caltech).

5.1.0.2 Spherical approximation

In Sec. 5.3, we present the Eddington inversion method to derive the DM phase-space distribution given the dark matter density profiles and the total baryonic potential. This method only applies to spherically symmetric systems. To apply it to the Galaxy, we need to make a spherical approximation for the baryonic components. Given an axisymmetric component $\rho(R,z)$, we compute its mass within a spherical shell of radius r

$$m(r) = 2\pi \int_{-r}^{r} \mathrm{d}z \int_{0}^{\sqrt{r^2-z^2}} \mathrm{d}R\, R\, \rho(R,z)\,, \tag{5.1}$$

and defined a spherically-averaged density

$$\begin{aligned} \overline{\rho}(r) &\equiv \frac{1}{4\pi r^2}\frac{\mathrm{d}m}{\mathrm{d}r} \\ &= \frac{1}{r}\int_0^r \mathrm{d}z\, \rho\left[\sqrt{r^2-z^2}, z\right]\,. \end{aligned} \tag{5.2}$$

The spherically-averaged density profile is compared to the original profile along the R and z axis on the upper panel in Fig. 5.2. Since the bulge and the disc are significantly oblate, the spherical average overestimates the density profile along the z axis and underestimates it in the Galactic plane. The spherical density of the baryonic components is compared to the DM density on the lower panel in Fig. 5.2.

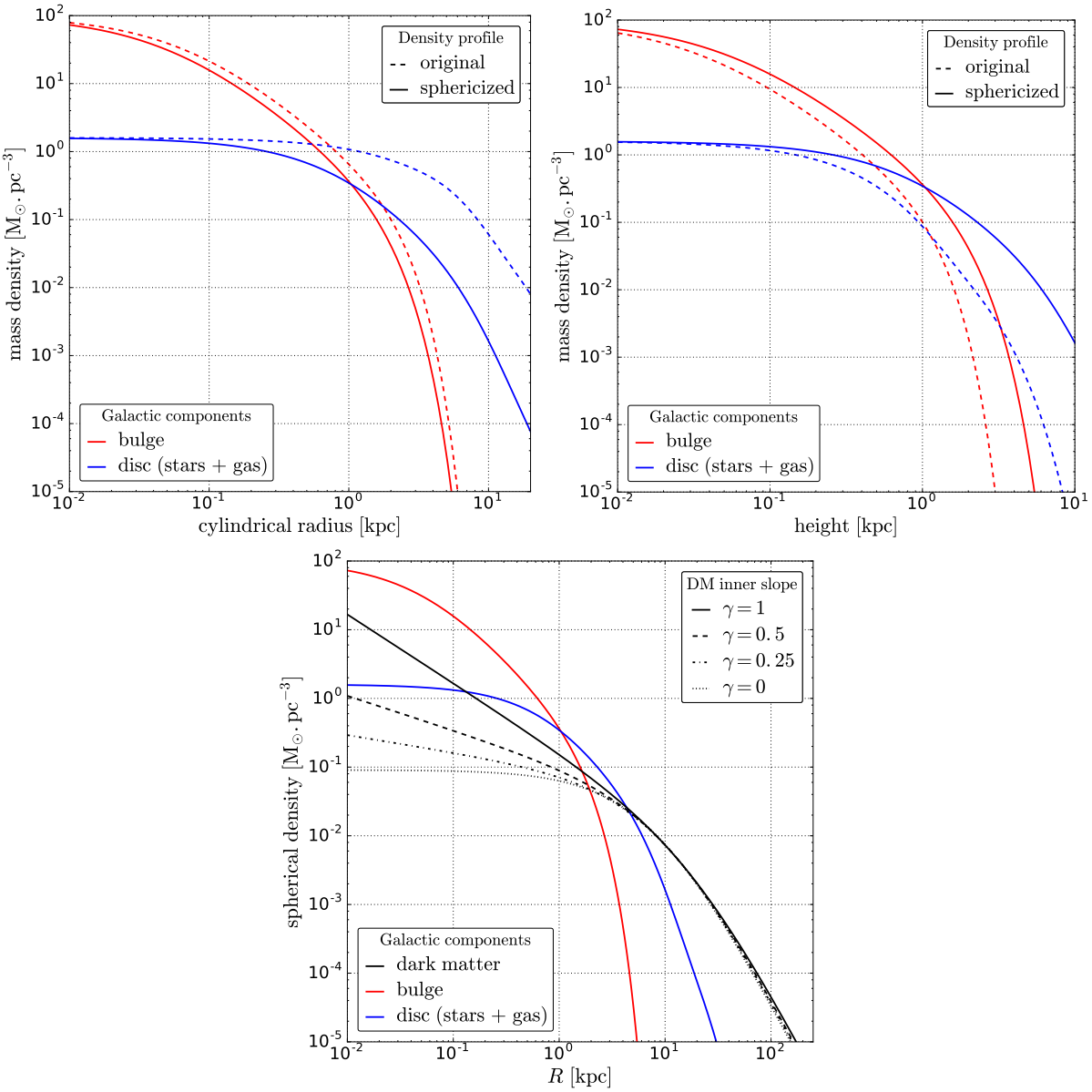

Figure 5.2 – For the mass model of McMillan (2017) **Upper left panel:** mass density and spherically-averaged density for the bulge and the disc in the Galactic plane. **Upper right panel:** mass density and spherically-averaged density for the bulge and the disc along the z-axis. **Lower panel:** Spherical mass density of the different Galactic components.

5.2 Statistical mechanics of gravitational systems

This section briefly describes some basic notions of statistical physics applied to gravitational systems.

5.2.1 The Liouville theorem and the Boltzmann equation

Let us consider a system of N interacting particles and let $f^{(N)}$ be the N-particle phase-space DF of the system. We consider for simplicity that all the particles are identical, therefore we can take as phase-space coordinates the position $\vec{r}$ and the velocity $\vec{v}$ (rather than the position and the momentum). The N-particle DF is a function of the phase-space coordinates of every particle in the system

$$f^{(N)} \equiv f^{(N)}(t; \vec{r}_1, ..., \vec{r}_N; \vec{v}_1, ..., \vec{v}_N)\,. \tag{5.3}$$

The distribution is normalised

$$\int \left(\prod_{i=1}^{N} \mathrm{d}^3\vec{r}_i \, \mathrm{d}^3\vec{v}_i \right) f^{(N)} = 1 \,. \tag{5.4}$$

If the system is isolated, $f^{(N)}$ obeys the *Liouville theorem*

$$\frac{\mathrm{d}f^{(N)}}{\mathrm{d}t} \equiv \frac{\partial f^{(N)}}{\partial t} + \sum_{i=1}^{N} \left(\dot{\vec{r}}_i . \vec{\nabla}_{\vec{r}_i} f^{(N)} + \dot{\vec{v}}_i . \vec{\nabla}_{\vec{v}_i} f^{(N)} \right) = 0 \,. \tag{5.5}$$

This equation states that the phase-space density of the system is conserved during its evolution. This theorem is valid regardless of the interactions between the particles and the state of equilibrium of the system, see Binney & Tremaine (1987). In particular, it applies in the out-of-equilibrium regime. If the only interaction between particles is gravitation, we have

$$\begin{aligned} \dot{\vec{v}}_i &= \sum_{j \neq i} \frac{G_\mathrm{N} \, m \, (\vec{r}_j - \vec{r}_i)}{|\vec{r}_j - \vec{r}_i|^3} \\ &= -\sum_{j \neq i} \vec{\nabla}_{\vec{r}_i} \Phi_{ji} \,, \end{aligned} \tag{5.6}$$

where

$$\Phi_{ji} \equiv -\frac{G_\mathrm{N} \, m}{|\vec{r}_j - \vec{r}_i|} \tag{5.7}$$

is the gravitational potential between particle i and j. The Liouville equation can then be written

$$\frac{\mathrm{d}f^{(N)}}{\mathrm{d}t} = \frac{\partial f^{(N)}}{\partial t} + \sum_{i=1}^{N} \left(\vec{v}_i . \vec{\nabla}_{\vec{r}_i} f^{(N)} - \sum_{j \neq i} \vec{\nabla}_{\vec{r}_i} \Phi_{ji} . \vec{\nabla}_{\vec{v}_i} f^{(N)} \right) = 0 \,. \tag{5.8}$$

For our purposes, it is more convenient to work with the 1-particle distribution function

$$f^{(1)}(t, \vec{r}_1, \vec{v}_1) \equiv \int \left(\prod_{k=2}^{N} \mathrm{d}^3\vec{r}_k \, \mathrm{d}^3\vec{v}_k \right) f^{(N)} \,. \tag{5.9}$$

Since all particles are identical, we simply write $f^{(1)} \equiv f$ and we call f the phase-space DF from now on. The DF is normalised

$$\int \mathrm{d}^3\vec{r} \, \mathrm{d}^3\vec{v} \, f(t, \vec{r}, \vec{v}) = 1 \,. \tag{5.10}$$

We want to derive an equation for f starting from the Liouville equation (5.5). We integrate the Liouville equation over $\prod_{k=2}^{N} \mathrm{d}^3\vec{r}_\mathrm{k} \, \mathrm{d}^3\vec{v}_\mathrm{k}$. This removes all terms in the sum except the $i = 1$ term if we assume $f^{(N)}$ decreases sufficiently fast at infinity so that

$$\int \mathrm{d}^3\vec{r}_\mathrm{i} \, \vec{\nabla}_{\vec{r}_\mathrm{i}} f^{(N)} = 0 \tag{5.11}$$

$$\int \mathrm{d}^3\vec{v}_\mathrm{i} \, \vec{\nabla}_{\vec{v}_\mathrm{i}} f^{(N)} = 0 \,. \tag{5.12}$$

We are left with

$$\frac{\partial f}{\partial t} + \vec{v}_1 . \vec{\nabla}_{\vec{r}_1} f - \int \left(\prod_{k=2}^{N} \mathrm{d}^3\vec{r}_k \, \mathrm{d}^3\vec{v}_k \right) \vec{\nabla}_{\vec{v}_1} f^{(N)} . \vec{\nabla}_{\vec{r}_1} \sum_{j=2}^{N} \Phi_{j1} = 0 \,. \tag{5.13}$$

To simplify the last term in this equation, we further assume $f^{(N)}$ is *separable* which means it can be written

$$f^{(N)} = \prod_{n=1}^{N} f(t, \vec{r}_n, \vec{v}_n)\,. \tag{5.14}$$

This implies in particular that the phase-space coordinates of the particles in the system are completely uncorrelated. This leads to

$$\frac{\partial f}{\partial t} + \vec{v}_1.\vec{\nabla}_{\vec{r}_1} f - (N-1)\vec{\nabla}_{\vec{v}_1} f(t, \vec{r}_1, \vec{v}_1).\vec{\nabla}_{\vec{r}_1} \int \mathrm{d}^3\vec{r}_2\, \mathrm{d}^3\vec{v}_2\, \Phi_{21}\, f(t, \vec{r}_2, \vec{v}_2) = 0\,, \tag{5.15}$$

where we have used the individual normalization of f and the equality of each term in the sum over j. We define the average gravitational potential at position $\vec{r}_1$ through

$$\Phi(\vec{r}_1) \equiv N \int \mathrm{d}^3\vec{r}_2\, \mathrm{d}^3\vec{v}_2\, \Phi_{12}\, f(t, \vec{r}_2, \vec{v}_2)\,, \tag{5.16}$$

and we get

$$\frac{\partial f}{\partial t} + \vec{v}_1.\vec{\nabla}_{\vec{r}_1} f - \frac{(N-1)}{N}\, \vec{\nabla}_{\vec{v}_1} f(t, \vec{r}_1, \vec{v}_1).\vec{\nabla}_{\vec{r}_1} \Phi = 0\,. \tag{5.17}$$

We now take the $N \to \infty$ limit and get the *collisionless Boltzmann equation*

$$\frac{\mathrm{d}f}{\mathrm{d}t} \equiv \frac{\partial f}{\partial t} + \vec{v}.\vec{\nabla}_{\vec{r}} f - \vec{\nabla}_{\vec{r}}\, \Phi.\vec{\nabla}_{\vec{v}} f = 0\,. \tag{5.18}$$

This equation is also often called the *Vlasov equation*, as it is identical to the equation that determines the evolution of a plasma. It is less general than the Liouville equation since it relies on the separability of $f^{(N)}$ and $N \to \infty$. Similar to the Liouville equation, it expresses the conservation of the phase-space density around a particle in the system. Note that according to this equation, particles are only sensitive to a smooth gravitational potential Φ and do not "see" the potential generated by each individual particle.

If correlation between particles cannot be neglected, then $f^{(N)}$ cannot be considered separable. In that case, it is useful to consider the 2-particle phase space DF

$$f^{(2)}(\vec{r}_1, \vec{r}_2; \vec{v}_1, \vec{v}_2) = f(\vec{r}_1, \vec{v}_1) f(\vec{r}_2, \vec{v}_2) + g(\vec{r}_1, \vec{r}_2; \vec{v}_1, \vec{v}_2)\,, \tag{5.19}$$

where g is the *correlation function* of particle 1 and 2. In that case, the Boltzmann equation is not called collisionless any more and takes the form

$$\frac{\mathrm{d}f}{\mathrm{d}t} = C[f]\,, \tag{5.20}$$

where

$$C[f] \equiv N \int \mathrm{d}^3\vec{r}_2\, \mathrm{d}^3\vec{v}_2\, \vec{\nabla}_{\vec{r}_1} \Phi_{12}.\vec{\nabla}_{\vec{v}_1} g \tag{5.21}$$

is the *collision operator* or *encounter operator*.

Which equation should we choose to study dark matter systems? We will see in the next section that most self-gravitating systems can be considered as being essentially collisionless.

5.2.2 Relaxation time

We compute the relaxation time of a self-gravitating, homogeneous system, following the derivation of Binney & Tremaine (1987). We consider a test particle moving through a medium consisting of homogeneously distributed point-mass particles. We want to estimate the difference in velocity induced by the particles distribution with respect to a case where the total mass of these particles is smoothly distributed. First, we focus on the case of a single encounter: the test particle A passes-by a particle B which we consider at rest, see 5.3. We assume the velocity is small $\delta v/v \ll 1$, in which case the trajectory of A is approximately a straight line. Consequently, the velocity change parallel to the trajectory averages to zero and we are left with a perpendicular velocity change. The perpendicular force felt by A at a given time is then

$$\begin{aligned} F_\perp &= \frac{G_\mathrm{N}\, m_\mathrm{A}\, m_\mathrm{B}}{x^2+b^2}\cos(\theta) \\ &= \frac{G_\mathrm{N}\, m_\mathrm{A}\, m_\mathrm{B}}{b^2}\left[1+\frac{x^2}{b^2}\right]^{-3/2} \\ &= \frac{G_\mathrm{N}\, m_\mathrm{A}\, m_\mathrm{B}}{b^2}\left[1+\left(\frac{vt}{b}\right)^2\right]^{-3/2}\,, \end{aligned} \tag{5.22}$$

where $t=0$ is the moment when the distance between A and B is equal to the impact parameter b. By Newton's second law, we have

$$m_\mathrm{A}\frac{\mathrm{d}\vec{v}}{\mathrm{d}t} = \vec{F}\,, \tag{5.23}$$

which projected to the direction perpendicular to the trajectory leads to

$$\begin{aligned} \delta v &= \frac{G_\mathrm{N}\, m_\mathrm{B}}{b^2}\int_{-\infty}^{+\infty}\left[1+\left(\frac{vt}{b}\right)^2\right]^{-3/2}\mathrm{d}t \\ &= \frac{2\,G_\mathrm{N}\, m_\mathrm{B}}{bv}\,. \end{aligned} \tag{5.24}$$

We recall that this expression is only valid if $\delta v \ll v$ which translates into $b \gg b_\mathrm{min}$ where

$$b_\mathrm{min} = \frac{2\,G_\mathrm{N}\, m_\mathrm{B}}{v^2}\,. \tag{5.25}$$

We now have to evaluate the number of encounter experienced by A as it orbits in the mass distribution. We assume this distribution to be a homogeneous sphere of radius R containing N particles. The number of encounters with impact parameter between b and $b+\mathrm{d}b$ after one orbit in the system is then

$$\delta n = \frac{N}{\pi R^2}2\pi b\,\mathrm{d}b\,. \tag{5.26}$$

We can now compute the velocity variance created by these encounters

$$(\delta v)^2\delta n = \left(\frac{G_\mathrm{N}\, m_\mathrm{B}}{bv}\right)^2\frac{N}{\pi R^2}2\pi b\,\mathrm{d}b\,. \tag{5.27}$$

Integrating over the impact parameter, we get

$$\Delta v^2 = 8N\left(\frac{G_\mathrm{N}\, m_\mathrm{B}}{vR}\right)^2\ln\left(\frac{b_\mathrm{max}}{b_\mathrm{min}}\right)\,. \tag{5.28}$$

The maximal impact parameter $b_{\max}$ is set by our assumption of a homogeneous distribution, which cannot be true for $b \geqslant R$. Therefore we assume $b_{\max} \simeq R$. The expression of Δv^2 can be simplified by considering A is on a circular orbit, in which case we have

$$v \simeq \sqrt{\frac{G_{\rm N} N\, m_{\rm B}}{R}}\,, \tag{5.29}$$

and

$$\frac{b_{\max}}{b_{\min}} = \frac{R\, v^2}{2\, G_{\rm N}\, m_{\rm B}} \simeq \frac{N}{2}\,. \tag{5.30}$$

We finally get the relative change in v^2 after one crossing of the system

$$\frac{\Delta v^2}{v^2} = \frac{8}{N} \ln\left(\frac{N}{2}\right)\,. \tag{5.31}$$

The number of crossing needed to have a deviation in v^2 comparable to the original value is then

$$n_{\rm cross} = \frac{N}{8 \ln\left(\frac{N}{2}\right)}\,, \tag{5.32}$$

and two body encounters become relevant after a time

$$t_{\rm relax} = \frac{N}{8 \ln\left(\frac{N}{2}\right)}\, t_{\rm cross}\,, \tag{5.33}$$

where $t_{\rm cross} = R/v = R^{3/2}/(G_{\rm N} M)^{1/2}$ is the typical crossing time. The crossing time has the more general expression $t_{\rm cross} = (G_{\rm N}\rho)^{-1/2}$ and is also called the *dynamical time*. $t_{\rm relax}$ is the (two-body) *relaxation time*. At a time $t \ll t_{\rm relax}$, the effect of two-body encounters is subdominant and the dynamics of the system should obey the collisionless Boltzmann equation (5.18). At time $t \geqslant t_{\rm relax}$, two-body encounters start to dominate the dynamics, particles have a diffusive motion and the phase-space DF is solution of the Boltzmann equation with collisions (5.20). Note that if the system is not homogeneous the dynamical time depends on the position through the density, therefore relaxation might be important at the center while remaining irrelevant at the edges.

What is the relaxation time of realistic self-gravitating systems? Some stellar systems such as globular clusters are known to be affected by relaxation. What about dark matter systems? If the DM particle has a mass around the electroweak scale $m \sim 100\,\text{GeV}$, the number of particles in a halo is gigantic and relaxation is completely irrelevant. As an illustration, we consider a DM structure of mass $M = 10^{-10}\,\text{M}_\odot$ which is near the smallest mass reachable in WIMP models, see *e.g.*Bringmann (2009). The number of particles is $M/m \simeq 10^{50}$ and the crossing time $t_{\rm cross} \simeq 1\,\text{Myr}$, so relaxation is indeed of no importance there.[1] Relaxation can only be of relevance for very heavy DM particles. For instance, we can consider the case of Primordial Black Holes DM with mass $M_{\rm PBH} \simeq 10\,\text{M}_\odot$ and a halo composed of ~ 100 PBHs. The cosmological radius of the structure is roughly $R_{200} \simeq 0.2\,\text{kpc}$ and the relaxation time is $t_{\rm relax} \sim 5\,\text{Gyr}$, so relaxation should impact structure formation is this case.

5.2.3 Thermodynamic equilibrium?

The statistical treatment exposed so far is very reminiscent of the statistical mechanics of gaseous systems developed by Maxwell, Boltzmann and Gibbs. A major difference is the nature of the force driving the evolution of the system. While gaseous systems evolve because of the numerous

[1] This does not mean the particle nature of DM is irrelevant for WIMP DM structures. In particular, the free-streaming of DM particles is what sets the minimal mass of DM halos in WIMP models.

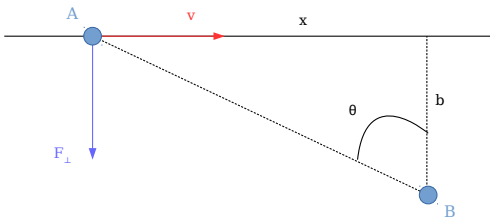

Figure 5.3 – A test particle A approaches at speed v a stationary particle B with an impact parameter b. The trajectory of A is assumed to be a straight line during the encounter.

collisions between their constituents, gravitational systems can be considered as being essentially collisionless and driven by the long-ranged gravitational interaction. One can wonder if the results of thermodynamics apply in that case. In particular, is there a thermodynamic equilibrium for gravitational systems? The answer to that question is negative: gravitational systems do not have a thermal equilibrium. A very simple way of seeing this is given by Binney & Tremaine (1987). Let us consider an N-body gravitational system and assume it is in thermal equilibrium. The N-particle phase-space DF should take the usual form

$$f^{(N)}(\vec{r}_1, ..., \vec{r}_N; \vec{v}_1, ..., \vec{v}_N) = \frac{1}{K} \exp\left[-\beta\, H(\vec{r}_1, ..., \vec{r}_N; \vec{v}_1, ..., \vec{v}_N)\right] , \tag{5.34}$$

where K is a normalization constant, $\beta = 1/(k_{\rm B}T)$, T is the system's temperature and H its Hamiltonian. The constant K should be fixed by requiring the normalization over the full phase-space

$$K = \int \left(\prod_{i=1}^{N} \mathrm{d}^3\vec{r}_i\, \mathrm{d}^3\vec{v}_i\right) \exp\left[-\beta\, H(\vec{r}_1, ..., \vec{r}_N; \vec{v}_1, ..., \vec{v}_N)\right] . \tag{5.35}$$

However, the spatial part of the integral diverges for a gravitational system. It diverges at short distances because of the singular behaviour of the gravitational potential, and it diverges at large distances because the Hamiltonian becomes independent of the position while still being velocity dependent. Consequently, the DF cannot be normalized and there is no thermal equilibrium! In fact, many results of statistical mechanics are not valid for gravitational systems: the heat capacity is negative, there is no micro-canonical ensemble, entropy cannot be maximized (and consequently there is no canonical ensemble), etc...

5.2.4 The Jeans equations

The characterization of the dynamics of self-gravitating systems involves solving the collisionless Boltzmann equation

$$\frac{\partial f}{\partial t} + v_i \frac{\partial f}{\partial x_i} - \frac{\partial \Phi}{\partial x_i}\frac{\partial f}{\partial v_i} = 0\,. \tag{5.36}$$

Summation over the indices is assumed. There is unfortunately no known classification of the solutions of this equation. It is possible however to learn about the dynamics of a system without solving the full equation. The idea is to compute the velocity moments of Eq. (5.36). The zeroth-order moment is

$$\int \frac{\partial f}{\partial t}\, \mathrm{d}^3\vec{v} + \int v_i \frac{\partial f}{\partial x_i}\, \mathrm{d}^3\vec{v} - \int \frac{\partial \Phi}{\partial x_i}\frac{\partial f}{\partial v_i}\, \mathrm{d}^3\vec{v} = 0\,. \tag{5.37}$$

Multiplying by the total mass of the system (assumed constant), this leads to

$$\frac{\partial \rho}{\partial t} + \frac{\partial(\rho \overline{v}_i)}{\partial x_i} = 0\,. \tag{5.38}$$

which is simply the continuity equation for the mass density ρ. Note that this equation involves four unknowns, ρ and the components of the mean velocity $\overline{v}_i$, and therefore cannot be solve unless further assumptions are made. Taking the first-order moment leads to

$$\frac{\partial(\rho \overline{v}_i)}{\partial t} + \frac{\partial(\rho \overline{v_i v_j})}{\partial x_j} = -\rho \frac{\partial \Phi}{\partial x_i}\,. \tag{5.39}$$

The first term can be replaced by using the continuity equation and we get

$$\frac{\partial \overline{v}_i}{\partial t} + \overline{v}_j \frac{\partial \overline{v}_i}{\partial x_j} = -\frac{\partial \Phi}{\partial x_i} - \frac{1}{\rho}\frac{\partial(\rho \sigma_{ij}^2)}{\partial x_j}\,, \tag{5.40}$$

where $\sigma_{ij}^2 = \overline{v_i v_j} - \overline{v}_i \overline{v}_j$ is the velocity variance tensor. This equation has the same form as the Euler equation in Eqs. (3.1) with a pressure tensor $p_{ij} = \rho \sigma_{ij}^2$. Hence, in collisionless systems, the velocity dispersion acts as an effective pressure. Note that Eq. (5.40) together with Eq. (5.38) have again too many unknowns to be solved. Other equations can be added to the system by considering the second-order moment of the Boltzmann equation, but this also introduces new unknowns such as $\overline{v_i v_j v_k}$. We can actually form a system of hierarchical equations by taking moments of higher and higher order. These are called the Jeans equations after Jeans (1919). Obviously the system of equations has to be truncated at some order, and closed by making assumptions on the unknown quantities. The time-independent version of Eq. (5.40) is often written is spherical coordinates

$$\frac{1}{\rho}\frac{\partial(\rho \overline{v_r^2})}{\partial r} + 2\,\frac{\beta}{r}\,\overline{v_r^2} = -\frac{\partial \Phi}{\partial r}\,, \tag{5.41}$$

where we introduced the anisotropy parameter

$$\beta(r) \equiv 1 - \frac{\overline{v_\theta^2} + \overline{v_\phi^2}}{2\,\overline{v_r^2}}\,. \tag{5.42}$$

This can be seen as a differential equation for $\rho \overline{v_r^2}$ where $\beta(r)$ is an unknown function. Usually, a specific form is assumed for $\beta(r)$ so the equation can be solved.

Unlike the Boltzmann equation, the Jeans equation gives informations about the moments of the phase-space DF rather than the DF itself. In the next section, we present the Eddington formalism which enables the determination of the full DF of a spherical system.

5.3 The Eddington formalism

5.3.1 Jeans Theorem

The starting point of the Eddington formalism is the theorem of Jeans (1915). To state this theorem, we first need to define the *integrals of motion*. An integral of motion is a function of the phase-space coordinates $I[x(t), v(t)]$ which is conserved along the trajectory of the system, *i.e.*

$$\frac{\mathrm{d}}{\mathrm{d}t} I[x(t), v(t)] = \frac{\mathrm{d}x}{\mathrm{d}t}\frac{\partial I}{\partial x} + \frac{\mathrm{d}v}{\mathrm{d}t}\frac{\partial I}{\partial v} = 0\,. \tag{5.43}$$

We see that an integral of motion is by definition a solution of the stationary collisionless Boltzmann equation, and therefore any function depending on the phase-space coordinates only

through integrals of motion is also solution of the Boltzmann equation since we have

$$\begin{aligned}\frac{\mathrm{d}}{\mathrm{d}t} f[I_1, ..., I_n] &= \sum_{i=1}^{n} \frac{\mathrm{d}I_i}{\mathrm{d}t} \frac{\partial f}{\partial I_i} \\ &= 0\,.\end{aligned} \tag{5.44}$$

Reciprocally, if f is a solution of the stationary collisionless Boltzmann equation then it is also an integral of motion, hence the Jeans theorem: any solution of the stationary collisionless Boltzmann equation depends on the phase-space coordinates only through integrals of motion. Finding phase-space DFs therefore reduces to finding quantities that are conserved along the trajectory of the system.

5.3.2 Isotropic velocity distributions

The simplest case we can consider is a phase-space DF that only depends on the energy $E/m = \Phi + v^2/2$, where m is the particle's mass and Φ the gravitational potential. This was first considered by Eddington (1916). Since for bounded particles the energy is negative, we instead consider the variable $\mathcal{E} = \Psi - v^2/2$ where $\Psi = \Phi_0 - \Phi$ up to a constant. This is simply minus the energy divided by the particle's mass (we do refer to $\mathcal{E}$ as the energy and to Ψ as the potential in the following). Since the energy only depends on the modulus of the velocity, any phase-space DF that depends only on the energy describes an isotropic velocity distribution. Consequently, we refer to a DF of the type $f(\mathcal{E})$ as *isotropic*.[2] It is conventional in statistical physics to normalize the DF to unity so that it can be interpreted as a probability density function, however it is more convenient for our purposes to normalize the DF to the mass of the system of interest:

$$\begin{aligned}\rho(r) &= \int f(\mathcal{E})\, \mathrm{d}^3\vec{v} \\ &= 4\pi \int_0^{+\infty} v^2\, f\left(\Psi(r) - \frac{v^2}{2}\right) \mathrm{d}v\,,\end{aligned} \tag{5.45}$$

where ρ is the mass density of the system. Note that the system under study (a galaxy for instance) can have several components (dark matter and baryons for instance). We are only interested in describing the phase space of the dark matter, therefore in such a case ρ refers to the *dark matter* mass density $\rho = \rho_{\mathrm{DM}}$. The potential Ψ, however, is the *total* potential $\Psi = \Psi_{\mathrm{DM}} + \Psi_{\mathrm{bar}}$. Note that the DM density and the total potential are independent variables since one cannot compute the total potential from the DM density alone.

We restrict ourselves to the study of a completely bounded system, where all the particles have positive energy $\mathcal{E}$ and therefore $f(\mathcal{E} < 0) = 0$. The normalization of f is then written as

$$\rho(r) = 4\pi \int_0^{v_{\mathrm{esc}}} v^2\, f\left(\Psi - \frac{v^2}{2}\right) \mathrm{d}v\,, \tag{5.46}$$

where $v_{\mathrm{esc}}(r) = \sqrt{2\Psi(r)}$ is the *escape speed*, that is the minimal speed needed for a particle at r to become unbounded. We can perform the change of variable $v = \sqrt{2(\Psi - \mathcal{E})}$ in Eq. (5.46) to get

$$\rho(\Psi) = 4\pi\sqrt{2} \int_0^{\Psi} \sqrt{\Psi - \mathcal{E}}\, f(\mathcal{E})\, \mathrm{d}\mathcal{E}\,. \tag{5.47}$$

Since the potential Ψ is a monotonically decreasing function of the radius, it can be used as a substitute variable for r and $\rho(\Psi)$ is well defined. We derive Eq. (5.47) with respect to Ψ

$$\frac{\mathrm{d}\rho}{\mathrm{d}\Psi} = \sqrt{8}\pi \int_0^{\Psi} \frac{f(\mathcal{E})}{\sqrt{\Psi - \mathcal{E}}}\, \mathrm{d}\mathcal{E}\,. \tag{5.48}$$

[2] The term *ergodic* is also used in the literature to describe a DF of this type, see Binney & Tremaine (1987)

This is an *Abel integral equation*. The following mathematical result helps us to go further: the equation

$$f(x) = \int_0^x \frac{g(t)}{(x-t)^\alpha}\,\mathrm{d}t,\ 0 < \alpha < 1 \tag{5.49}$$

has the solution

$$g(t) = \frac{\sin(\pi\alpha)}{\pi}\frac{\mathrm{d}}{\mathrm{d}t}\int_0^t \frac{f(x)}{(t-x)^{1-\alpha}}\,\mathrm{d}x\,. \tag{5.50}$$

Applied to Eq. (5.48) this leads to *Eddington's formula*

$$f(\mathcal{E}) = \frac{1}{\sqrt{8}\pi^2}\frac{\mathrm{d}}{\mathrm{d}\mathcal{E}}\left\{\int_0^{\mathcal{E}} \frac{1}{\sqrt{\mathcal{E}-\Psi}}\frac{\mathrm{d}\rho}{\mathrm{d}\Psi}\,\mathrm{d}\Psi\right\}. \tag{5.51}$$

Thus we have found the expression of the phase-space DF in terms of the mass density ρ and the gravitational potential Ψ. This solution is unique, there is only one possible DF that describes a spherical isotropic system. The expression of the DF can be simplified by performing an integration by parts, then apply the derivative with respect to $\mathcal{E}$. We get

$$f(\mathcal{E}) = \frac{1}{\sqrt{8}\pi^2}\left[\frac{1}{\sqrt{\mathcal{E}}}\left(\frac{\mathrm{d}\rho}{\mathrm{d}\Psi}\right)_{\Psi=0} + \int_0^{\mathcal{E}} \frac{1}{\sqrt{\mathcal{E}-\Psi}}\frac{\mathrm{d}^2\rho}{\mathrm{d}\Psi^2}\,\mathrm{d}\Psi\right]. \tag{5.52}$$

A striking feature of this expression is a term $\propto \mathcal{E}^{-1/2}$ which diverges at small energies. The meaning of this term and the theoretical issues it poses are discussed in Sec. 5.4.

5.3.2.1 Concrete examples

The singular isothermal sphere The mass density profile of the singular isothermal sphere (SIS) is

$$\rho(r) = \frac{\sigma^2}{2\pi G_\mathrm{N}\, r^2}\,, \tag{5.53}$$

where σ is a free parameter homogeneous to a velocity. This is actually the one-dimension velocity dispersion of the system, as it is shown later. This density profile strongly diverges at the center of the system. The regularization of this divergence is discussed in Sec. 5.4. The mass profile is

$$m(r) = \frac{2\sigma^2}{G_\mathrm{N}}\,r\,, \tag{5.54}$$

and therefore the total mass of the system is infinite. This is not a big problem from the point of view of Eddington's method since it accommodates with a finite boundary for the system. Using the expression of the mass, one immediately finds the circular speed

$$v_\mathrm{c}^2 = 2\,\sigma^2 \tag{5.55}$$

which is independent of the radius. The gravitational potential can be found by solving Poisson's equation

$$\frac{1}{r^2}\frac{\mathrm{d}}{\mathrm{d}r}\left(r^2\frac{\mathrm{d}\Psi}{\mathrm{d}r}\right) = -4\pi G_\mathrm{N}\,\rho = -\frac{2\sigma^2}{r^2}\,. \tag{5.56}$$

With the boundary conditions $(r^2\mathrm{d}\Psi/\mathrm{d}r)_{r=0} = 0$ and $\Psi(r_0) = 0$, we get

$$\Psi(r) = -2\sigma^2 \ln\left(\frac{r}{r_0}\right). \tag{5.57}$$

Note that the potential diverges both at large and short distances. We can express the mass density as a function of the potential

$$\begin{aligned}\rho(\Psi) &= \frac{\sigma^2}{2\pi G_{\rm N}\, r_0^2}\, \exp\left(\frac{\Psi}{\sigma^2}\right) \\ &= \rho_0\, \exp\left(\frac{\Psi}{\sigma^2}\right)\end{aligned} \tag{5.58}$$

and inject it in Eddington's formula Eq. (5.51)

$$f(\mathcal{E}) = \frac{\rho_0}{\sqrt{8}\pi^2\sigma^2}\frac{\mathrm{d}}{\mathrm{d}\mathcal{E}}\int_0^{\mathcal{E}} \frac{1}{\sqrt{\mathcal{E}-\Psi}}\exp\left(\frac{\Psi}{\sigma^2}\right)\mathrm{d}\Psi\,. \tag{5.59}$$

This leads to

$$f(\mathcal{E}) = \frac{\rho_0}{(2\pi\sigma^2)^{3/2}}\left\{\frac{1}{\sqrt{\pi}}\sqrt{\frac{\sigma^2}{\mathcal{E}}} + e^{\mathcal{E}/\sigma^2}\mathrm{erf}\left(\sqrt{\frac{\mathcal{E}}{\sigma^2}}\right)\right\}\,. \tag{5.60}$$

The DF diverges at small $\mathcal{E}$, where we have

$$f(\mathcal{E}) \simeq \frac{\rho_0}{(2\pi\sigma^2)^{3/2}}\frac{1}{\sqrt{\pi}}\sqrt{\frac{\sigma^2}{\mathcal{E}}}\,. \tag{5.61}$$

The behaviour $f(\mathcal{E}) \propto \mathcal{E}^{-1/2}$ at small energies is intrinsic to the Eddington procedure, as seen in Eq. (5.52). Since the potential diverges at the center of the system, the energy $\mathcal{E}$ takes arbitrary large values as a particle falls down the potential well. It is therefore interesting to consider the limit $\mathcal{E} \gg \sigma^2$ in Eq. (5.60). This limit considers particles whose energy is dominated by their potential energy rather than their kinetic energy. We get

$$f(\mathcal{E}) \simeq \frac{\rho_0}{(2\pi\sigma^2)^{3/2}}\, e^{\mathcal{E}/\sigma^2}\,, \tag{5.62}$$

which is the Boltzmann distribution function, and therefore f diverges at large $\mathcal{E}$. This phase-space DF predicts in particular that the velocity distribution is, at any position, the Maxwell-Boltzmann distribution

$$f_r(\vec{v}) = \frac{1}{(2\pi\sigma^2)^{3/2}}\, e^{-v^2/(2\sigma^2)} \tag{5.63}$$

The velocity dispersion at radius r is then given by

$$\sigma_{\vec{v}}^2 \equiv \left\langle \vec{v}^2 \right\rangle - \langle \vec{v} \rangle^2 = 3\,\sigma^2 \tag{5.64}$$

and is therefore independent of the radius. The velocity distribution extends to arbitrary large velocities, *i.e.* there is no escape speed to the system. This is not surprising since the escape speed is defined by $\mathcal{E} = 0$ and we took the limit $\mathcal{E} \gg \sigma^2$. Note that this approximation breaks down when the radius gets close to r_0 where we have $\Psi(r_0) = 0$, therefore we expect the velocity distribution to depart from the Maxwell-Boltzmann DF in the outskirts of the system. The DF in Eq. (5.60) and the Boltzmann DF are shown in the left panel of Fig. 5.4.

It is interesting to consider the DF of a system with the SIS profile which contains unbounded particles. We have to remove the condition $f(\mathcal{E} < 0) = 0$ in Eddington's calculation to get the correct result. This leads to a change of the lower bound of the integral in Eq. (5.60) from $\mathcal{E} = 0$ to $\mathcal{E} = -\infty$. The expression of the DF is again

$$f(\mathcal{E}) = \frac{\rho_0}{(2\pi\sigma^2)^{3/2}}\, e^{\mathcal{E}/\sigma^2}\,. \tag{5.65}$$

This expression is valid at all energies (positive or negative). The escape speed is still well-defined by $v_{\rm esc} = \sqrt{2(\Phi(r_0) - \Phi(r)}$ however, unlike the phase space described by the distribution in Eq. (5.60), this phase space contains unbound particles at all positions. In other words, at any position r, the phase-space DF includes particles with $v > v_{\rm esc}(r)$. In such a system, the radius r_0 is the position of the bound particle farthest from the center of the system.

The Plummer model The Plummer mass density profile is

$$\rho(r) = \rho_\mathrm{s} \left(1 + \frac{r^2}{r_\mathrm{s}^2}\right)^{-5/2} . \tag{5.66}$$

This profile has a core (of radius r_s), unlike the SIS. It was first introduced by Plummer (1911) who used it to describe the inner density of globular clusters. The associated mass is

$$m(r) = \frac{4}{3}\pi\rho_\mathrm{s} r_\mathrm{s}^3 \frac{(r/r_\mathrm{s})^3}{[1 + (r/r_\mathrm{s})^2]^{3/2}} , \tag{5.67}$$

which tends toward the finite value $M = 4/3\,\pi\rho_\mathrm{s} r_\mathrm{s}^3$ at infinity. The gravitational potential obtained from Poisson's equation with the boundary conditions $(r^2 \mathrm{d}\Phi/\mathrm{d}r)_{r=0} = 0$ and $\Phi(r \to \infty) = 0$ is

$$\begin{aligned} \Phi(r) &= -\frac{4}{3}\pi\, G_\mathrm{N}\rho_\mathrm{s} r_\mathrm{s}^2 \left(1 + \frac{r^2}{r_\mathrm{s}^2}\right)^{-1/2} \\ \Psi(r) &= \Phi(r_0) - \Phi(r) , \end{aligned} \tag{5.68}$$

with r_0 some arbitrary radius. Note that the potential stays finite at the center of the system. The density can be expressed as a function of the potential

$$\rho(\Psi) = \rho_\mathrm{s} \left(\overline{\Psi} - \overline{\Phi}_0\right)^5 , \tag{5.69}$$

where $\overline{X} = X/(4/3\,\pi G_\mathrm{N}\rho_\mathrm{s} r_\mathrm{s}^2)$.[3] Eddington's formula leads to

$$f(\mathcal{E}) = \frac{\rho_\mathrm{s}}{(4\pi G_\mathrm{N}\rho_\mathrm{s} r_\mathrm{s}^2)^{3/2}} \frac{1}{\pi^2\sqrt{2\overline{\mathcal{E}}}} \left(\overline{\Phi}_0^4 - 20\,\overline{\Phi}_0^3\overline{\mathcal{E}} + 40\,\overline{\Phi}_0^2\overline{\mathcal{E}}^2 - 32\,\overline{\Phi}_0\overline{\mathcal{E}}^3 + \frac{64}{7}\,\overline{\mathcal{E}}^4\right) . \tag{5.70}$$

This DF features the standard $\mathcal{E}^{-1/2}$ divergence at low energies and behaves like a power-law $\mathcal{E}^{7/2}$ at large energies. Note that there is no divergence at high energies because the potential, and therefore the energy, has a finite maximum in $r = 0$ equal to $\overline{\Psi}(0) = 1 - (1 + r_0^2/r_\mathrm{s}^2)^{-1/2}$.

Unlike in the SIS case, we cannot compute the DF if some particles are unbound because the integral in Eddington's formula does not converge if the lower bound is $\mathcal{E} = -\infty$. This means the Plummer density profile is not compatible with particles having arbitrary large velocities, though it is not clear why that is the case for this profile and not for the SIS for instance. Another difference with the SIS is that the Plummer profile offers the possibility to consider an infinite system, since both the total mass and the potential at large distances are finite quantities. The DF in that case can be very simply deducted from Eq. (5.70) by taking the limit $\overline{\Phi}_0 \to 0$, which leads

$$f(\mathcal{E}) = \frac{\rho_\mathrm{s}}{(4\pi G_\mathrm{N}\rho_\mathrm{s} r_\mathrm{s}^2)^{3/2}} \frac{64}{7\pi^2\sqrt{2}}\,\overline{\mathcal{E}}^{7/2} . \tag{5.71}$$

Hence the DF is a pure power-law. Note that the entire system is still bound as we have $f(\mathcal{E} \leqslant 0) = 0$ and the escape speed with respect to infinity is well-defined. The DF in Eq. (5.70) and the DF in Eq. (5.71) are shown in the right panel of Fig. 5.4.

5.3.3 Anisotropic extensions

A DF which is function of the energy only cannot describe an isotropic velocity distribution. To model anisotropic systems, we must include another integral of motion. The simplest choice is to consider the modulus of the angular momentum (per particle mass)

$$L = |\vec{r} \times \vec{v}| , \tag{5.72}$$

[3] Note that $\overline{\Phi}_0 \equiv \overline{\Phi}(r_0)$ is negative with our convention.

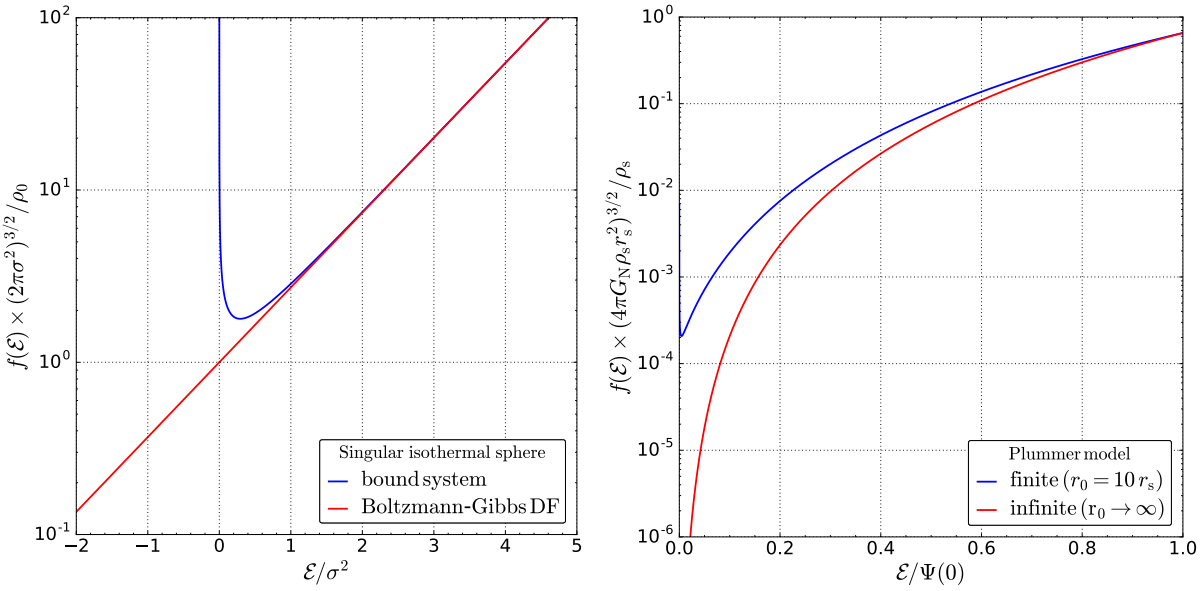

Figure 5.4 – Left panel: isotropic DF of the bound singular isothermal sphere (blue) compared to the Boltzmann-Gibbs DF (red) **Right panel:** Isotropic DF of the finite Plummer model (blue) compared to the infinite model (red).

and a DF of the form $f(\mathcal{E}, L)$. Similar to the isotropic case, we normalize the DF to the mass through

$$\rho = \int f(\mathcal{E}, L)\, \mathrm{d}^3\vec{v}\,. \tag{5.73}$$

Changing variables, we get

$$\rho(\Psi) = 4\pi \int_0^\Psi \frac{\mathrm{d}\mathcal{E}}{r\sqrt{8(\Psi-\mathcal{E})}} \int_0^{\sqrt{2r^2(\Psi-\mathcal{E})}} \frac{f(\mathcal{E}, L)}{\sqrt{2r^2(\Psi-\mathcal{E}) - L^2}}\, \mathrm{d}L\,, \tag{5.74}$$

where $r = r(\Psi)$ is a function of the potential. This integral equation cannot be inverted like in the isotropic case, and the solution is not unique for a given $\rho(\Psi)$. We must give a precise measure of the anisotropy to go any further. This is done through the anisotropy parameter as defined by Binney (1980)

$$\beta(r) \equiv 1 - \frac{\sigma_\theta^2 + \sigma_\phi^2}{2\sigma_r^2} = 1 - \frac{\sigma_\mathrm{t}^2}{2\sigma_r^2}\,. \tag{5.75}$$

In this equation, σ_i^2 is the velocity dispersion along spatial coordinate i

$$\sigma_i^2(r) \equiv \left\langle v_i^2 \right\rangle - \langle v_i \rangle^2 = \frac{1}{\rho(r)} \int v_i^2\, f(r, \vec{v})\, \mathrm{d}^3\vec{v}\,. \tag{5.76}$$

If particles at a position r are on mostly circular orbits, we have $\sigma_r^2 \ll \sigma_\mathrm{t}^2$ and $\beta \to -\infty$. If particles are on mostly radial orbits, we have $\sigma_r^2 \gg \sigma_\mathrm{t}^2$ and $\beta \simeq 1$. The system is locally isotropic if $\beta = 0$, *i.e.* $2\sigma_r^2 = \sigma_\mathrm{t}^2$. For a given system $\rho(\Psi)$ there are several anisotropy profiles possible, therefore we need to specify $\beta(r)$ to find an explicit solution to Eq. (5.74).

5.3.3.1 Constant anisotropy models

The simplest case we can consider is a system with an anisotropy parameter independent of the radius, *i.e.* $\beta(r) = \beta_0$ is a constant. It was shown by Cuddeford (1991) that the corresponding DF takes the form

$$f(\mathcal{E}, L) = G(\mathcal{E}) L^{-2\beta_0}\,. \tag{5.77}$$

That this DF effectively leads to a constant anisotropy parameter with β_0 is shown in App. D.2. The expression of G can be found by considering the normalization equation

$$\begin{aligned}\rho &= \int f(\mathcal{E}, L)\, \mathrm{d}^3\vec{v} \\ &= 2\pi \int_0^{\pi} \mathrm{d}\eta \sin(\eta) \int_0^{v_{\rm esc}} \mathrm{d}v\, v^2\, G(\mathcal{E})\, [rv\sin(\eta)]^{-2\beta_0}\ .\end{aligned} \tag{5.78}$$

Using the integral

$$\int_0^{\pi} [\sin(\eta)]^{1-2\alpha}\, \mathrm{d}\eta = \sqrt{\pi}\, \frac{\Gamma(1-\alpha)}{\Gamma\left(\frac{3}{2}-\alpha\right)}\,, \tag{5.79}$$

and performing the change of variable $v = \sqrt{2(\Psi - \mathcal{E})}$, we get

$$r^{2\beta_0}\rho = \lambda(\beta_0) \int_0^{\Psi} \frac{G(\mathcal{E})}{(\Psi-\mathcal{E})^{\beta_0-1/2}}\, \mathrm{d}\mathcal{E}\,, \tag{5.80}$$

where

$$\lambda(\beta_0) = 2^{3/2-\beta_0}\pi^{3/2}\, \frac{\Gamma(1-\beta_0)}{\Gamma\left(\frac{3}{2}-\beta_0\right)} \tag{5.81}$$

This is an Abel integral equation of the form in Eq. (5.49) only if $1/2 < \beta_0 < 1$. If $\beta_0 \leqslant 1/2$, then we derive Eq. (5.80) n times with respect to Ψ

$$\frac{\mathrm{d}^n}{\mathrm{d}\Psi^n}\left(r^{2\beta_0}\rho\right) = \lambda(\beta_0)\left(\frac{1}{2}-\beta_0\right)! \int_0^{\Psi} \frac{G(\mathcal{E})}{(\Psi-\mathcal{E})^{\beta_0-1/2+n}}\, \mathrm{d}\mathcal{E}\,, \tag{5.82}$$

where

$$n \equiv \left[\frac{3}{2} - \beta_0\right] \tag{5.83}$$

is the floor of $3/2 - \beta_0$ and

$$\left(\frac{1}{2}-\beta_0\right)! = \begin{cases} \left(\frac{1}{2}-\beta_0\right)\left(-\frac{1}{2}-\beta_0\right)\ldots\left(\frac{1}{2}-\beta_0-(n-1)\right) & \text{for } \beta_0 < \frac{1}{2} \\ 1 & \text{for } \beta_0 \geqslant \frac{1}{2} \end{cases} \tag{5.84}$$

This ensures that $0 < \beta_0 - 1/2 + n < 1$ and Eq. (5.82) is an Abel equation. This equation is actually identical to the Abel equation found in the isotropic case Eq. (5.48) with the correspondence $\rho \to r^{2\beta_0}\rho$ and $1 \to n$. The solution of Eq. (5.82) is

$$G(\mathcal{E}) = \frac{\sin([n-1/2+\beta_0]\pi)}{\pi\lambda(\beta_0)(1/2-\beta_0)!}\, \frac{\mathrm{d}}{\mathrm{d}\mathcal{E}} \int_0^{\mathcal{E}} \frac{\mathrm{d}^n}{\mathrm{d}\Psi^n}\left(r^{2\beta_0}\rho\right)(\mathcal{E}-\Psi)^{n-3/2+\beta_0}\, \mathrm{d}\Psi\,. \tag{5.85}$$

Note that in the particular case $\beta_0 = 0$, G is equal to the isotropic DF in Eq. (5.51) therefore the isotropic case is included in the constant-β models. Just like in the isotropic case, we can develop this expression to get

$$\begin{aligned} G(\mathcal{E}) =& \frac{\sin([n-1/2+\beta_0]\pi)}{\pi\lambda(\beta_0)(1/2-\beta_0)!} \\ &\times \left[\frac{1}{\mathcal{E}^{3/2-\beta_0-n}}\left(\frac{\mathrm{d}^n}{\mathrm{d}\Psi^n} r^{2\beta_0}\rho\right)_{\Psi=0} + \int_0^{\mathcal{E}} \frac{\mathrm{d}^{n+1}}{\mathrm{d}\Psi^{n+1}}\left(r^{2\beta_0}\rho\right) \frac{\mathrm{d}\Psi}{(\mathcal{E}-\Psi)^{3/2-\beta_0-n}}\right] \end{aligned} \tag{5.86}$$

5.3.3.2 Osipkov-Merritt models

An alternative anisotropic DF was found independently by Osipkov (1979) and Merritt (1985) and takes the form

$$f_{\rm om}(Q) \equiv f\left(\mathcal{E} - \frac{L^2}{2r_{\rm a}^2}\right) . \tag{5.87}$$

The corresponding anisotropy parameter is

$$\beta(r) = \frac{r^2}{r^2 + r_{\rm a}^2} , \tag{5.88}$$

as demonstrated in App. D.2. Unlike the constant-β models, the Osipkov-Merritt (OM) models lead to a radius-dependent anisotropy. The anisotropy tends to zero at the center of the system, which is therefore almost isotropic for $r \ll r_{\rm a}$, and becomes close to one when $r \gg r_{\rm a}$. The radius $r_{\rm a}$ is a free parameter called the *anisotropy radius*, it controls the transition between the isotropic center and the radial orbits at large radius. The DF is normalized so that

$$\begin{aligned} \rho &= \int f_{\rm om}(Q)\, {\rm d}^3\vec{v} \\ &= \frac{4\pi\sqrt{2}}{1+\frac{r^2}{r_{\rm a}^2}} \int_0^\Psi \sqrt{\Psi - Q}\, f_{\rm om}(Q)\, {\rm d}Q . \end{aligned} \tag{5.89}$$

This leads to the Abel integral equation

$$\frac{{\rm d}\rho_{\rm OM}}{{\rm d}\Psi} = \sqrt{8}\pi \int_0^\Psi \frac{f_{\rm om}(Q)}{\sqrt{\Psi - Q}}\, {\rm d}Q , \tag{5.90}$$

where

$$\rho_{\rm OM}(r) \equiv \left(1 + \frac{r^2}{r_{\rm a}^2}\right) \rho(r) . \tag{5.91}$$

The solution of the Abel equation is

$$\begin{aligned} f_{\rm om}(Q) &= \frac{1}{\sqrt{8}\pi^2} \frac{\rm d}{{\rm d}Q} \int_0^Q \frac{1}{\sqrt{Q-\Psi}} \frac{{\rm d}\rho_{\rm OM}}{{\rm d}\Psi}\, {\rm d}\Psi \\ &= \frac{1}{\sqrt{8}\pi^2} \left[\frac{1}{\sqrt{Q}} \left(\frac{{\rm d}\rho_{\rm OM}}{{\rm d}\Psi}\right)_{\Psi=0} + \int_0^Q \frac{1}{\sqrt{Q-\Psi}} \frac{{\rm d}^2\rho_{\rm OM}}{{\rm d}\Psi^2}\, {\rm d}\Psi \right] . \end{aligned} \tag{5.92}$$

This is the same expression as the isotropic DF with the correspondence $\rho \to \rho_{\rm OM}$. Note that the OM models include the isotropic model which is recovered in the limit $r_{\rm a} \to \infty$.

5.3.3.3 More complicated models

The two classes of models presented above (constant-β and OM) both feature one single independent parameter which completely determines the anisotropy profile. While these models are appealing because of their simplicity, they also lack flexibility and in general their anisotropy profile is different from those observed in cosmological simulations, see Wojtak et al. (2008); Ludlow et al. (2011); Lemze et al. (2012); Sparre & Hansen (2012); Wojtak et al. (2013). It is therefore useful to consider alternatives models which involve a larger number of parameters.

Cuddeford models A simple extension of the constant-β and OM models was considered by Cuddeford (1991), who looked at DFs of the form

$$f(\mathcal{E}, L) = f_{\rm om}(Q) L^{-2\beta_0} \,. \tag{5.93}$$

This class of models involves two free parameters, β_0 and $r_{\rm a}$. The constant-β models are recovered in the limit $r_{\rm a} \to 0$ and the OM models are recovered when $\beta_0 = 0$. The anisotropy parameter is

$$\beta(r) = \frac{r^2 + \beta_0 r_{\rm a}^2}{r^2 + r_{\rm a}^2} \,, \tag{5.94}$$

as demonstrated in App. D.2. Thus it has radial orbits at large distances $\beta \simeq_{r \gg r_{\rm a}} 1$ but an arbitrary central anisotropy $\beta \simeq_{r \ll r_{\rm a}} \beta_0$. The anisotropy at $r = r_{\rm a}$ is also equal to $(1 + \beta_0)/2$ instead of $1/2$ in the OM models. The anisotropy parameter in the constant-β, Osipkov-Merritt and Cuddeford models are compared in Fig. 5.5.

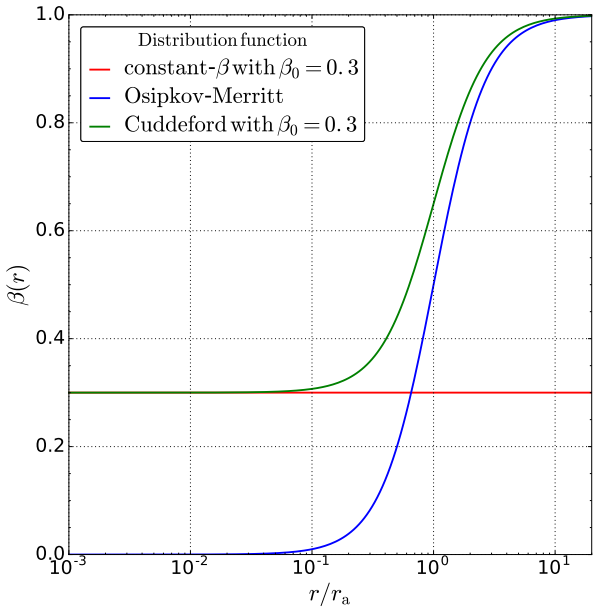

Figure 5.5 – Anisotropy parameter β as defined in Eq. (5.75) as a function of the radius, in the constant-β model with $\beta_0 = 0.3$ (red curve), in the Osipkov-Merritt model (blue curve) and in the Cuddeford model with $\beta_0 = 0.3$ (green curve).

Models of Bozorgnia et al The radial anisotropy predicted by the Cuddeford models is still too high with respect to that observed in simulations. To solve this problem, Bozorgnia et al. (2013) proposed a DF which is a linear combination of the constant-β DF and the OM DF:

$$f(\mathcal{E}, L) = w\, f_1(Q) + (1 - w)\, f_2(\mathcal{E}) L^{-2\beta_0} \,. \tag{5.95}$$

The DFs f_1 and f_2 are computed from Eq. (5.92) and Eq. (5.85), respectively. These models have three free parameters which can be tuned to fit the average anisotropy profile observed in simulated galactic halos. Unfortunately, the anisotropy parameter does not take a fully analytical expression in that case. It can be expressed as

$$\beta(r) = \frac{w\, r^2}{r^2 + r_{\rm a}^2} \frac{\sigma_r^2(f_1)}{\sigma_r^2(f)} + \beta_0 (1 - w) \frac{\sigma_r^2(f_2)}{\sigma_r^2(f)} \,. \tag{5.96}$$

This anisotropy parameter depends on the underlying mass density profile and gravitational potential, unlike all the other models we have seen so far.

Models of Wojtak et al To reproduce the anisotropy profiles observed in simulations of massive DM halos, Wojtak et al. (2008) proposed the following three-parameters models

$$f(\mathcal{E}, L) = f_{\mathcal{E}}(\mathcal{E}) \left(1 + \frac{L^2}{2L_0}\right)^{\beta_0 - \beta_\infty} L^{-2\beta_0} \,. \tag{5.97}$$

The constants β_0 and β_∞ are the asymptotical anisotropies at the center and at large radii, respectively. L_0 is an angular momentum constant that sets the radius of transition between these two asymptotical regimes. The energy-dependent part $f_{\mathcal{E}}$ is derived from the mass density as usual, though this involves an iterative procedure which makes these models slightly harder to handle numerically.

5.4 Theoretical issues and limitations

We presented in the previous section the Eddington formalism and some of its anisotropic extensions, which is a powerful method to find phase-space DFs that are solutions of the collisionless Boltzmann equation. This formalism is especially appealing for DM searches since it provides a way to built the DM phase-space DF starting from a dynamically constrained mass model. Using this method however requires the knowledge of its limitations. In particular, its range of application has to be well delimited. This section is devoted to the study of the solutions of the Eddington inversion method. We first discuss non-physical features that generically appear in the phase-space DF, and present several techniques to remove these features. Second, we discuss the positivity and stability of the solutions, and the consequences these considerations have on the applicability of Eddington's method. The content of this section is based mainly on Lacroix et al. (2018).

5.4.1 Finite-size systems instability

A generic issue with the Eddington formalism and its extensions is the presence of diverging term in the phase-space DF. We recall the expression of the isotropic DF

$$f(\mathcal{E}) = \frac{1}{\sqrt{8}\pi^2} \left[\frac{1}{\sqrt{\mathcal{E}}} \left(\frac{\mathrm{d}\rho}{\mathrm{d}\Psi}\right)_{\Psi=0} + \int_0^{\mathcal{E}} \frac{1}{\sqrt{\mathcal{E}-\Psi}} \frac{\mathrm{d}^2\rho}{\mathrm{d}\Psi^2} \,\mathrm{d}\Psi \right] , \tag{5.98}$$

which features a term $\propto \mathcal{E}^{-1/2}$ diverging in $\mathcal{E} = 0$, as illustrated in Fig. 5.4. This term is proportional to the derivative of the density with respect to the potential $(\mathrm{d}\rho/\mathrm{d}\Psi)_{\Psi=0}$ evaluated at the radial boundary of the system where the potential cancels, hence it is related to the shape of the density profile at the boundary. A divergence at $\mathcal{E} = 0$ is a sign of instability in the system. This can be seen clearly by considering the *speed distribution* $f_{\vec{r}}(v)$ at a given position $\vec{r}$ in the system

$$f_{\vec{r}}(v) \equiv \frac{v^2}{\rho(\vec{r})} \int f(\vec{r}, \vec{v}) \,\mathrm{d}\Omega \,. \tag{5.99}$$

For an isotropic DF $f(\vec{r}, \vec{v}) = f(\mathcal{E})$, this is simply

$$f_r(v) = \frac{4\pi v^2}{\rho(r)} f\left(\Psi(r) - \frac{v^2}{2}\right) , \tag{5.100}$$

hence the speed distribution is directly related to the phase-space DF in the isotropic case. From Eq. (5.100), we see that the divergence at $\mathcal{E} = 0$ translates into a divergence at $v = \sqrt{2\Psi(r)}$ in the speed distribution, as illustrated with the Plummer profile in Fig. 5.6. This speed is precisely the escape speed at r, *i.e.* the minimal speed needed for a particle at r to escape to the radius

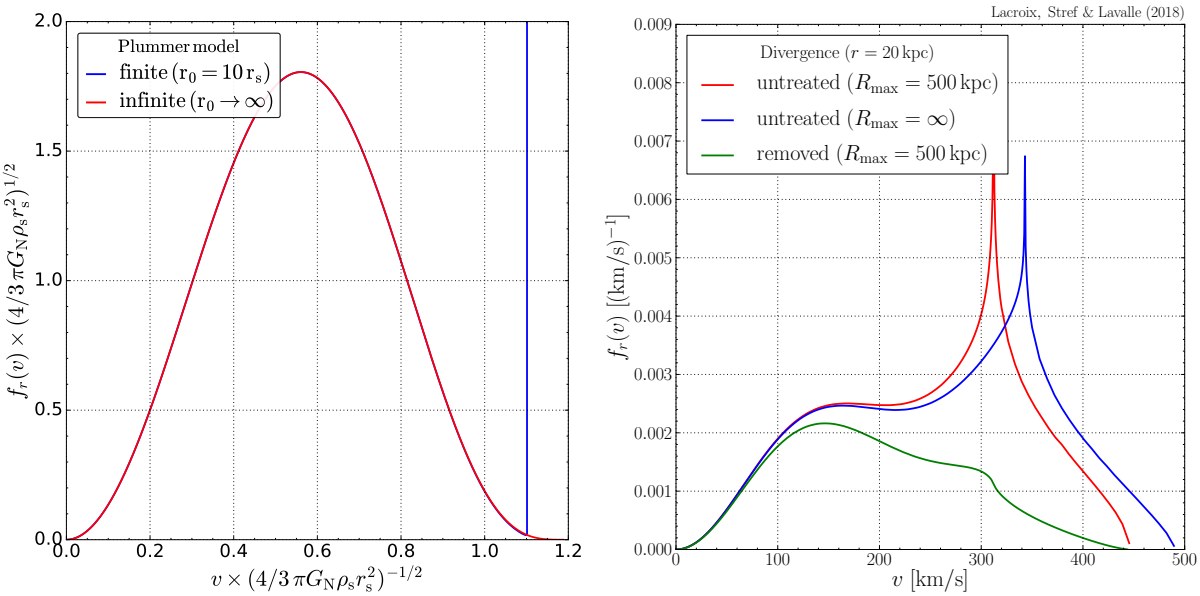

Figure 5.6 – Left panel: Speed distribution for the Plummer profile at $r = r_s$, in the finite case with extension $r_0 = 10\,r_s$ (blue curve) and the infinite case (red). The speed distribution is scaled to the halo parameters. **Right panel:** Speed distribution for the OM DF of the NFW model of McMillan (2017) for the finite case $r_{max} = 500\,\text{kpc}$ (red), the infinite case $r_{max} = \infty$ (blue) and the case where the diverging term is removed (green).

where $\Psi = 0$. In a system which has the speed distribution shown in Fig. 5.6 many particles have a speed very close to the escape speed and are therefore susceptible to leave the system if perturbed. This a clear sign of instability. To apply the Eddington formalism to a stable system like the Galactic halo, we need to remove the instability. Note that this instability issue is in no way limited to the isotropic case. The OM and constant anisotropy DF also have a diverging behaviour as one can see from Eq. (5.92) and Eq. (5.85). In the OM models, the divergence is at $Q = \mathcal{E} - L^2/(2\,r_a^2) = 0$. Integration over the angles in Eq. (5.99) moves the divergence to a speed lower than $\sqrt{2\Psi}$ and therefore the speed distribution present a non-physical peak right in the middle of the speed range as shown on the right panel in Fig. 5.6.

5.4.1.1 Radial boundary and escape speed

We recall that there is a freedom in choosing the radius r where the potential cancels. This freedom is inherent to the very definition of the gravitational potential as a solution of the Poisson equation

$$\Delta\Psi = -4\pi G_N\,\rho\,, \tag{5.101}$$

which is defined up to an arbitrary constant. Since the diverging term in the Eddington DF depends on the derivative $\mathrm{d}\rho/\mathrm{d}\Psi$ evaluated at the radius r_{max} where $\Psi(r_{max}) = 0$, we can ask if there is a particular choice of r_{max} that removes the divergence. There is actually such a choice, one simply has to assume the potential cancels at infinity

$$\Psi \xrightarrow[r\to\infty]{} 0\,, \tag{5.102}$$

i.e. $r_{max} = \infty$. For a power-law profile $\rho \propto r^{-\beta}$, which is the general behaviour of CDM halos far from the scale radius, we have $\mathrm{d}\rho/\mathrm{d}r \propto r^{-\beta-1}$ and $\mathrm{d}\Psi/\mathrm{d}r \propto m(r)/r^2 \propto r^{1-\beta}$ hence

$$\frac{\mathrm{d}\rho}{\mathrm{d}\Psi} \propto r^{-2} \xrightarrow[r\to\infty]{} 0 \tag{5.103}$$

and our phase-space DF is divergence-free while still being solution of the Boltzmann equation. The speed distribution is also regularized, as shown on the left panel in Fig. 5.6 (red curve). Though this is a mathematically sound solution, it is not entirely satisfying.

First, while setting the potential to zero at infinity removes the divergence in the constant anisotropy case (isotropic case included), in general it does not work for the OM models. This is because the troublesome derivative in that case is $(\mathrm{d}\rho_{\mathrm{OM}}/\mathrm{d}\Psi)_{\Psi=0}$ where ρ_{OM} is given in Eq. (5.91). Let us consider a pure power-law density profile $\rho \propto r^{-\beta}$. The OM pseudo-profile is then $\rho_{\mathrm{OM}} \propto r^{2-\beta}$ when $r \gg r_{\mathrm{a}}$. We then have

$$\frac{\mathrm{d}\rho_{\mathrm{OM}}}{\mathrm{d}r} \propto r^{1-\beta} \tag{5.104}$$

$$\frac{\mathrm{d}\Psi}{\mathrm{d}r} = \frac{G_{\mathrm{N}}\, m(r)}{r^2} \propto r^{1-\beta}\,, \tag{5.105}$$

and the derivative

$$\frac{\mathrm{d}\rho_{\mathrm{OM}}}{\mathrm{d}\Psi} = \frac{\mathrm{d}\rho_{\mathrm{OM}}}{\mathrm{d}r}\frac{\mathrm{d}r}{\mathrm{d}\Psi} \xrightarrow[r\to\infty]{} \text{constant} \tag{5.106}$$

therefore the derivative is non-zero at infinity and the phase-space DF is still divergent. This shows that for most DM profiles, the OM models cannot be regularized by taking the radial boundary of the system to infinity. This is illustrated by the speed distribution on the right panel in Fig. 5.6. This is the speed distribution at $r = 20\,\mathrm{kpc}$ predicted by the OM when applied to the NFW mass model of McMillan (2017), with the anisotropy radius $r_{\mathrm{a}} = r_{\mathrm{s}} = 19.6\,\mathrm{kpc}$. The distribution in the case $r_{\mathrm{max}} = \infty$ features a clear unstable behaviour due to the sharp peak at 340 km/s, very similar to the peak observed in the distribution computed for $r_{\mathrm{max}} = 500\,\mathrm{kpc}$.

A more serious problem is posed by the physical interpretation of the radius r_{max}. This radius is in some sense the true physical extension of the bound system. Indeed a particle at a radius $r > r_{\mathrm{max}}$ has a negative potential $\Psi(r) < 0$ and is therefore not bound to the system. The question is then: can we pick an arbitrary large value for that physical extension? This extension is in fact set by the neighbouring systems. In the case of the Milky Way halo, the distance to the Andromeda galaxy naturally gives a maximal extension. Since the center of Andromeda is approximately 800 kpc away from the center of the Milky Way, we do not expect our dark halo to extend much farther than 450-500 kpc. A crucial point is that the physical size of the system has consequences on observables deep within the halo, because this size determines the local escape speed. More precisely, the escape speed at radius r is

$$v_{\mathrm{esc}}(r) = \sqrt{2\Psi(r)} = \sqrt{2(\phi(r_{\mathrm{max}}) - \phi(r))}\,, \tag{5.107}$$

where $\phi(r)$ is the (negative-defined) gravitational potential cancelling at infinity. This shows that $v_{\mathrm{esc}}(r)$ explicitly depends on r_{max}. The escape speed is crucial because it is the maximal speed a particle can have at r if the system is in equilibrium. The local value of the escape speed is in principle an observable quantity. It can be inferred from the distribution of nearby high-velocity stars (Leonard & Tremaine, 1990; Piffl et al., 2014) or computed within a full Galactic mass model (see Sec. 5.1). Changing the value of r_{max} can strongly impact the escape speed This illustrated in Fig. 5.7. We show the relative change in v_{esc} induced by increasing r_{max}, starting from a reference value of $r_{\mathrm{max}} = 500\,\mathrm{kpc}$. At 8 kpc, v_{esc} is increased by more than 8%. This is a sizeable change because the experimental uncertainty on the local value of v_{esc} is of order 10%, see Piffl et al. (2014). The change in v_{esc} gets more important farther away from the center. For $r = 100\,\mathrm{kpc}$, v_{esc} can be modified by up to 24%. This shows that sending r_{max} to infinity is not a good approach to regularize the solution of Eddington's inversion, since it leads to a sizeable modification of the escape speed *everywhere in the system*.

In the following, we discuss regularization methods that remove the divergence while keeping the escape speed essentially unchanged.

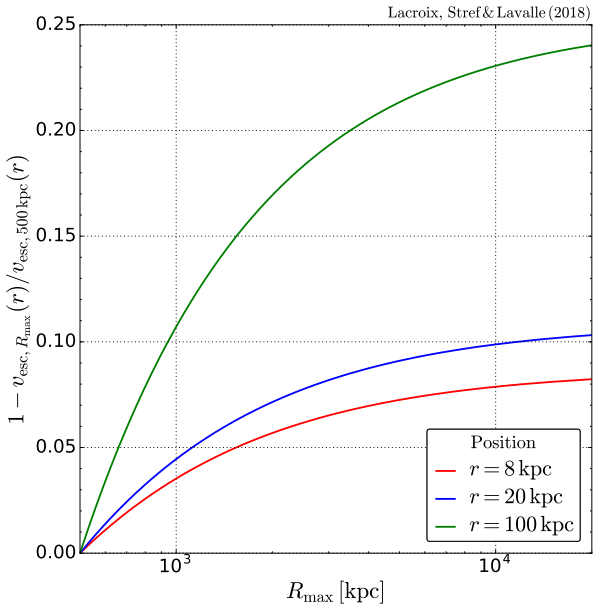

Figure 5.7 – Relative difference between the escape speed for $r_{\mathrm{max}} = 500\,\mathrm{kpc}$ and the escape speed for $r_{\mathrm{max}} > 500\,\mathrm{kpc}$, at different positions in the halo.

5.4.1.2 Modification of the density profile

The divergence in the Eddington DF when the system has a finite extension is an indication that the density profile is not realistic in the outer region. This is not surprising since most of the DM profiles used in the literature are coming from fits within the inner 200 kpc of Milky-Way-like halos found in simulations. Observational constraints are also local, mostly based on kinematic data coming from the inner 50 kpc (McMillan, 2017). The kinematics of satellite galaxies have also been used to set constraints on the MW mass within 300 kpc, though with large uncertainties (Watkins et al., 2010). Therefore the behaviour of the DM density around $r_{\mathrm{max}} \sim 500\,\mathrm{kpc}$ is completely unprobed and might depart from the typical power-law $\rho \propto r^{-3}$ of NFW-like profiles. Here we attempt to modify the initial density profile ρ so that $(\mathrm{d}\rho/\mathrm{d}\Psi)_{\Psi=0} = 0$ at finite r_{max}. Let us first consider the Eddington DF in the isotropic case Eq. (5.52) and remove "by-hand" the diverging term to get a modified DF

$$F(\mathcal{E}) = \frac{1}{\sqrt{8}\pi^2} \int_0^{\mathcal{E}} \frac{\mathrm{d}\Psi}{\sqrt{\mathcal{E} - \Psi}} \frac{\mathrm{d}^2\rho}{\mathrm{d}\Psi^2} \,. \tag{5.108}$$

Assuming the gravitational potential of the system is not modified by the removal of this term, we can reconstruct the density profile starting from the DF in Eq. (5.108) by computing the integral

$$\tilde{\rho}(\Psi) = 4\pi\sqrt{2} \int_0^{\Psi} F(\mathcal{E}) \sqrt{\Psi - \mathcal{E}}\, \mathrm{d}\mathcal{E} \,. \tag{5.109}$$

By definition of F, this is

$$\tilde{\rho}(\Psi) = 4\pi\sqrt{2} \int_0^{\Psi} \left[f(\mathcal{E}) - \frac{1}{\sqrt{8}\pi^2} \frac{1}{\sqrt{\mathcal{E}}} \left(\frac{\mathrm{d}\rho}{\mathrm{d}\Psi} \right)_{\Psi=0} \right] \sqrt{\Psi - \mathcal{E}}\, \mathrm{d}\mathcal{E} \,, \tag{5.110}$$

and the initial density profile is given by

$$\rho(\Psi) = \rho(r_{\mathrm{max}}) + 4\pi\sqrt{2} \int_0^{\Psi} f(\mathcal{E}) \sqrt{\Psi - \mathcal{E}}\, \mathrm{d}\mathcal{E} \,, \tag{5.111}$$

therefore we get the modified density

$$\begin{aligned}\tilde{\rho}(\Psi) &= \rho(\Psi) - \rho(r_{\max}) - \frac{2}{\pi}\left(\frac{\mathrm{d}\rho}{\mathrm{d}\Psi}\right)_{\Psi=0}\int_0^{\Psi}\frac{\sqrt{\Psi-\mathcal{E}}}{\sqrt{\mathcal{E}}}\,\mathrm{d}\mathcal{E} \\ &= \rho(\Psi) - \rho(r_{\max}) - \Psi\left(\frac{\mathrm{d}\rho}{\mathrm{d}\Psi}\right)_{\Psi=0}.\end{aligned} \tag{5.112}$$

This modified profile has a radial derivative

$$\begin{aligned}\frac{\mathrm{d}\tilde{\rho}}{\mathrm{d}r} &= \frac{\mathrm{d}\rho}{\mathrm{d}r} - \frac{\mathrm{d}\Psi}{\mathrm{d}r}\left(\frac{\mathrm{d}\rho}{\mathrm{d}\Psi}\right)_{\Psi=0} \\ &= \frac{\mathrm{d}\rho}{\mathrm{d}r} - \frac{\mathrm{d}\Psi}{\mathrm{d}r}\left(\frac{\mathrm{d}\rho}{\mathrm{d}r}\right)_{r=r_{\max}}\left(\frac{\mathrm{d}r}{\mathrm{d}\Psi}\right)_{r=r_{\max}},\end{aligned} \tag{5.113}$$

hence

$$\left(\frac{\mathrm{d}\tilde{\rho}}{\mathrm{d}r}\right)_{r=r_{\max}} = 0 \tag{5.114}$$

by construction. Our calculation is not fully consistent because we assumed the potential is not modified by the removal of the diverging term. Nevertheless, the Eddington formalism itself points toward a modification of the density profile that regularizes the phase-space DF. Based on this simple calculation we propose, given a density-potential pair (ρ, Ψ), the following modified profile

$$\tilde{\rho} \equiv \rho - \Psi\left(\frac{\mathrm{d}\rho}{\mathrm{d}\Psi}\right)_{\Psi=0}. \tag{5.115}$$

This definition differs from Eq. (5.112) by the constant $\rho(r_{\max})$. This ensures $\tilde{\rho}(r_{\max}) = \rho(r_{\max})$, unlike the profile in Eq. (5.112) which goes to zero in $r_{\max}$. The two modified profiles are compared on the left panel in Fig. 5.8 for a NFW profile cut at $r_{\max} = 500\,\mathrm{kpc}$. Both modified profiles significantly differ from the original one near $r_{\max}$. The biggest difference appears above the virial radius $R_{200} \simeq 230\,\mathrm{kpc}$ and the density below remains essentially unchanged. The profile in Eq. (5.115) has a 30% deficit at R_{200} while the profile in Eq. (5.112) has a 40% deficit which shows the importance of keeping the constant $\rho(r_{\max})$. The mass profiles, shown on the right panel in Fig. 5.8 have an approximate 10% deficit.

If the system has two components (DM and baryons) and its total potential is written $\Psi = \Psi_{\mathrm{dm}} + \Psi_{\mathrm{bar}}$, we define the modified profile using the DM component only

$$\tilde{\rho} \equiv \rho - \Psi_{\mathrm{dm}}\left(\frac{\mathrm{d}\rho}{\mathrm{d}\Psi_{\mathrm{dm}}}\right)_{\Psi_{\mathrm{dm}}=0}. \tag{5.116}$$

The modified potential can be computed from Poisson's equation

$$\tilde{\Psi}(r') = \int_r^{r_{\max}}\frac{\tilde{m}(r')}{r'^2}\,\mathrm{d}r', \tag{5.117}$$

and the derivative with respect to this potential vanishes in $r_{\max}$ by construction, therefore we know without even constructing the DF that it is non-singular. The radial boundary of the system is also preserved by this method. Note that the escape speed, which is the true observable, is still slightly modified because the potential is. Indeed, the original escape speed associated to the divergent DF is

$$v_{\mathrm{esc}}(r) = \sqrt{2\Psi(r)}, \tag{5.118}$$

while the modified escape speed is

$$\tilde{v}_{\mathrm{esc}}(r) = \sqrt{2\tilde{\Psi}(r)}. \tag{5.119}$$

While both these functions go to zero in $r = r_{\rm max}$, they are not identical for smaller radii as shown in Fig. 5.9. The relative difference between the escape speed in the different configurations is only of a few percent.

The discussion above is based on the isotropic case, let us now comment on the anisotropic extensions. The definition of the modified density profile has to be adapted to cancel the divergence when the density is non-zero. For the constant-β case, we need to cancel the derivative $(\mathrm{d}(r^{2\beta_0}\rho)/\mathrm{d}\Psi)_{\Psi=0}$ therefore we define the modified density as

$$\tilde{\rho}_{\beta_0} = \rho - \frac{\Psi_{\rm dm}}{r^{2\beta_0}} \left(\frac{\mathrm{d}(r^{2\beta_0}\rho)}{\mathrm{d}\Psi_{\rm dm}} \right)_{\Psi_{\rm dm}=0} . \tag{5.120}$$

Developing the derivative, this definition leads to

$$\tilde{\rho}_{\beta_0} = \rho - \Psi_{\rm dm} \left(\frac{r_{\rm max}}{r} \right)^{2\beta_0} \left(\frac{\mathrm{d}\rho}{\mathrm{d}\Psi_{\rm dm}} \right) - 2\beta_0 \Psi_{\rm dm} \left(\frac{r_{\rm max}}{r} \right)^{2\beta_0} \frac{\rho(r_{\rm max})}{r_{\rm max}} \left(\frac{\mathrm{d}r}{\mathrm{d}\Psi_{\rm dm}} \right)_{\Psi_{\rm dm}=0} . \tag{5.121}$$

Comparing this expression to the isotropic case in Eq. (5.116), we notice that this modified profile is more or less close to the original depending on the sign of β_0. If $\beta_0 > 0$, the difference is bigger than in the isotropic case while it is smaller if $\beta_0 < 0$. This illustrated in Fig. 5.10 where we show the modified density profile (left panel) and mass profile (right panel) for different anisotropy model.

For the OM models, our definition is

$$\tilde{\rho}_{\rm OM} = \rho - \frac{\Psi_{\rm dm}}{1 + r^2/r_{\rm a}^2} \left(\frac{\mathrm{d}\rho_{\rm OM}}{\mathrm{d}\Psi_{\rm dm}} \right)_{\Psi_{\rm dm}=0} . \tag{5.122}$$

Working the derivative, we get

$$\tilde{\rho}_{\rm OM} = \rho - \Psi_{\rm dm} \frac{r_{\rm a}^2 + r_{\rm max}^2}{r_{\rm a}^2 + r^2} \left(\frac{\mathrm{d}\rho}{\mathrm{d}\Psi_{\rm dm}} \right)_{\Psi_{\rm dm}=0} - \frac{\Psi_{\rm dm}}{r_{\rm a}^2 + r^2} 2 r_{\rm max} \rho(r_{\rm max}) \left(\frac{\mathrm{d}r}{\mathrm{d}\Psi_{\rm dm}} \right)_{\Psi_{\rm dm}=0} . \tag{5.123}$$

This expression shows that the difference between the modified and the original profile is larger in the OM models than in the isotropic model. The modified density and mass profiles for the OM models are shown in Fig. 5.10. Unlike the isotropic modification, this profile is vastly different from the original, especially below the virial radius where the difference goes to a maximum of 60% in density and 50% in mass.

Our regularization of the density profile works well for systems with a low or negative anisotropy parameter. It fails badly for systems that are radially biased like those following the OM phase-space DF.

5.4.1.3 Regularization of the phase-space DF

We now turn to an alternative way of getting rid of the divergence in phase-space. While the previous method relies on a modification a priori of the density profile used in Eddington's inversion method, here we modify a posteriori the phase-space DF to get a physically meaningful quantity.

Removal of the diverging term The simplest way of regularizing the DF is to simply remove the diverging term. This is what we did in the previous section to get the approximative form of the modified density profile. Our derivation was not fully consistent however since we assumed the potential was not modified by the removal of the divergence. Here we perform the same procedure but in a consistent way. We remove the diverging term to get a new DF

$$F(\tilde{\mathcal{E}}) \equiv f(\tilde{\mathcal{E}}) - \frac{1}{\sqrt{8}\pi^2} \frac{1}{\sqrt{\tilde{\mathcal{E}}}} \left(\frac{\mathrm{d}\rho}{\mathrm{d}\Psi} \right)_{\Psi=0} = \frac{1}{\sqrt{8}\pi^2} \int_0^{\tilde{\mathcal{E}}} \frac{\mathrm{d}^2\rho}{\mathrm{d}\Psi^2} \frac{\mathrm{d}\Psi}{\sqrt{\tilde{\mathcal{E}} - \Psi}} . \tag{5.124}$$

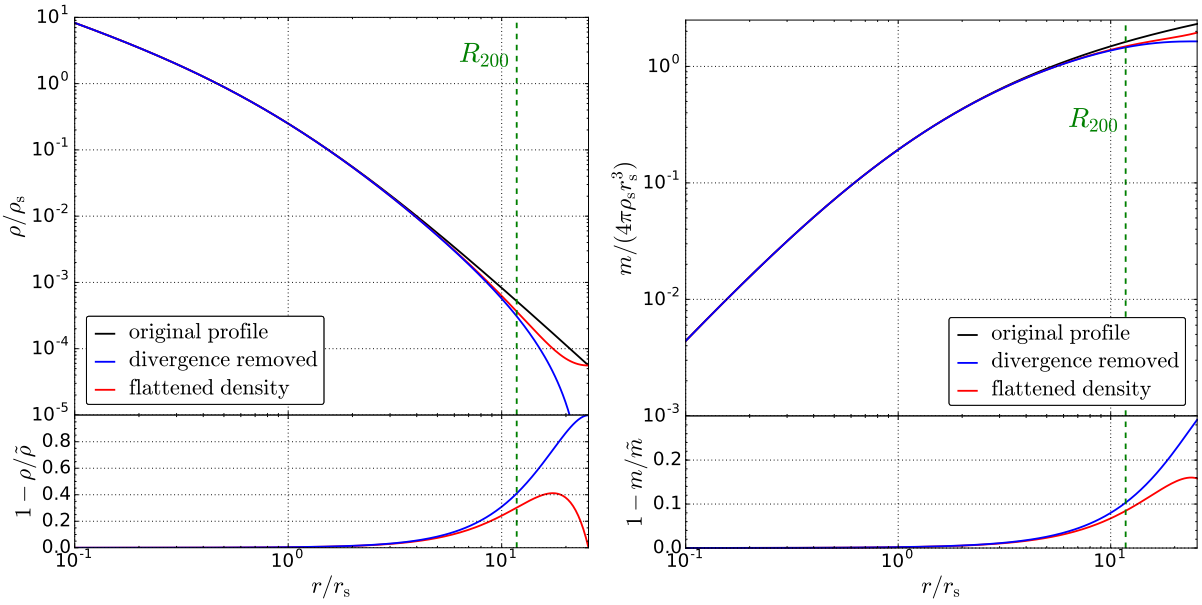

Figure 5.8 – Left panel: NFW density profile (black line) cut at $r_{\rm max} = 500\,{\rm kpc}$, with $r_{\rm s} = 19.6\,{\rm kpc}$. Are also shown the approximative density profile in Eq. (5.112) obtained when removing the divergence (blue line), and our prescription for the regularized density in Eq. (5.115) (red line). **Right panel:** same thing for the mass profile.

Note that we also defined a new energy $\tilde{\mathcal{E}}$ which is different from $\mathcal{E}$ because the potential of the system has been modified. To find the potential of the new system, we have to solve Poisson's equation

$$\begin{aligned}\Delta\tilde{\Psi}_{\rm dm} &= -4\pi G_{\rm N}\tilde{\rho} \\ &= -4\pi G_{\rm N} \times \left[\tilde{\rho}_0 + 4\pi\sqrt{2}\int_0^{\tilde{\Psi}} {\rm d}\tilde{\mathcal{E}}\, F(\tilde{\mathcal{E}})\sqrt{\tilde{\Psi}-\tilde{\mathcal{E}}}\right] .\end{aligned} \tag{5.125}$$

The constant $\tilde{\rho}_0$ is there to allow for a non-zero density where the potential cancels. This equation must be solved for the DM gravitational potential $\tilde{\Psi}_{\rm dm}$, even though the right-hand side involves the total potential $\tilde{\Psi} = \tilde{\Psi}_{\rm dm} + \tilde{\Psi}_{\rm bar}$. Since we only modify the DM phase-space DF, the baryons potential is left unchanged $\tilde{\Psi}_{\rm bar} = \Psi_{\rm bar}$. We need boundary conditions on $\tilde{\Psi}_{\rm dm}$ and ${\rm d}\Psi_{\rm dm}/{\rm d}r$ to solve this equation. The original DF is defined for $\mathcal{E} \in [0, \Psi(r=0)]$ hence our definition of F implies $\tilde{\mathcal{E}} \in [0, \tilde{\Psi}(r=0)]$ with $\tilde{\Psi}(r=0) \leqslant \Psi(r=0)$. We want our modified density profile to be as close as possible to the original one therefore we choose the following boundary conditions

$$\left\{\begin{array}{ll}\tilde{\Psi}(r=0) & = \Psi(r=0) \\ \frac{{\rm d}\tilde{\Psi}}{{\rm d}r}(r=0) & = \frac{{\rm d}\Psi}{{\rm d}r}(r=0)\,.\end{array}\right. \tag{5.126}$$

While the original potential cancels at $r_{\rm max}$, there is no reason for $\tilde{\Psi}$ to do the same. We only impose that the original and modified potential be equal at the center of the system, and do not require a cancellation of $\tilde{\Psi}$ at $r_{\rm max}$. The radius $\tilde{r}_{\rm max}$ verifying $\tilde{\Psi}(\tilde{r}_{\rm max}) = 0$ is found *after* solving the Poisson equation. Once the equation is solved for $\tilde{\Psi}_{\rm dm}$, the evaluation of the second term yields the modified density $\tilde{\rho}$ up to a factor $-4\pi G_{\rm N}$.

The density profile obtained after removal of the divergence is shown in Fig. 5.11. The calculation was performed in a consistent way by solving the Poisson equation to get the potential. However, as we saw in the previous section, removing the divergence by hand essentially leads to the modified density profile in Eq. (5.112) hence Fig. 5.8 and 5.10 also apply to this situation. In practice, we find the boundary of the system to be very close to the initial boundary $\tilde{r}_{\rm max} \simeq r_{\rm max}$.

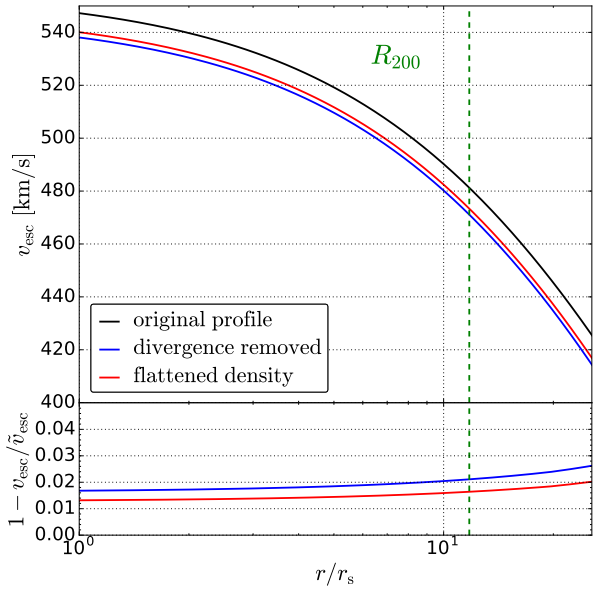

Figure 5.9 – Escape speed as a function of radius for the two modified profiles shown in Fig. 5.8.

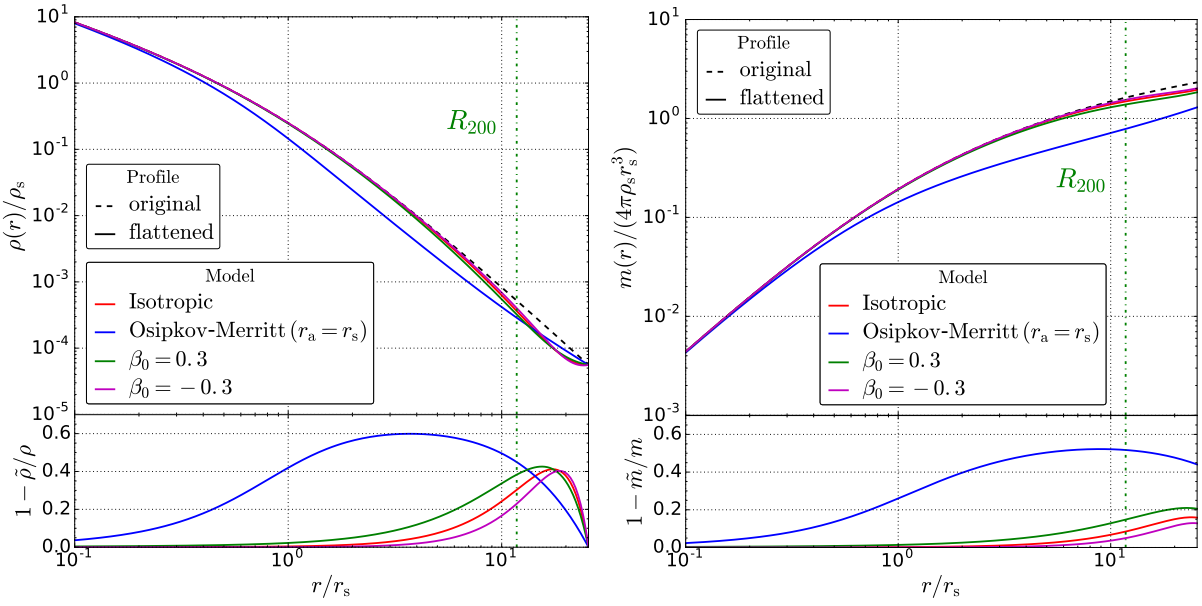

Figure 5.10 – **Left panel:** NFW density profile (black dashed line) compared to its modification in the isotropic model (red line), constant-β model with $\beta_0 = 0.3$ and $\beta_0 = -0.3$ (green and magenta) and the OM model (blue line). **Right panel:** same as in the left panel for the mass profile.

King models We now turn to a more physically motivated modification of the DF based on the so-called King model, named after King (1966) (see also Woolley (1954); Woolley & Robertson (1956); King (1962); Michie (1963); Michie & Bodenheimer (1963); King (1981)). This model was originally designed to deal with the divergences appearing in the singular isothermal sphere system, see 5.3.2.1. While this model was originally designed to study globular clusters, it has since been applied to galactic halos (Widrow & Dubinski, 2005; Strigari et al., 2017) and subhalos (Drakos et al., 2017). The general idea is to start from the DF $f(\mathcal{E})$ obtained for an infinite system $r_{\rm max} = \infty$ and defined a new DF

$$F(\tilde{\mathcal{E}}) \equiv \begin{cases} f(\tilde{\mathcal{E}} + \mathcal{E}_{\rm c}) - f(\mathcal{E}_{\rm c}) & \text{for } \tilde{\mathcal{E}} \geqslant 0 \\ 0 & \text{for } \tilde{\mathcal{E}} < 0 \end{cases} \tag{5.127}$$

Note that this is the definition used by Drakos et al. (2017), which slightly differs from the original King model. The new DF is by definition continuous in $\tilde{E} = 0$ and non-divergent. Building the density profile requires solving the Poisson equation (5.125). The definition of the DF implies $\tilde{\mathcal{E}} \in [0, \tilde{\Psi}(r=0)]$ with $\tilde{\Psi}(r=0) + \mathcal{E}_{\rm c} \leqslant \Psi(r=0)$. To minimize the difference in potential/density between the original and final profiles, we set

$$\begin{cases} \tilde{\Psi}(r=0) & = \Psi(r=0) - \mathcal{E}_{\rm c} \\ \frac{{\rm d}\tilde{\Psi}}{{\rm d}r}(r=0) & = \frac{{\rm d}\Psi}{{\rm d}r}(r=0)\,. \end{cases} \tag{5.128}$$

The definition of F guarantees the finiteness of the final density profile. The final radial extension $\tilde{r}_{\rm max}$ is set by the value of the energy cutoff $\mathcal{E}_{\rm c}$. The relation between $\tilde{r}_{\rm max}$ and $\mathcal{E}_{\rm c}$ is not clear however. One needs to solve the Poisson equation for a given $\mathcal{E}_{\rm c}$ and find the radius at which the potential goes to zero. If one wants the potential to cancel at a specific radius, one has to tune $\mathcal{E}_{\rm c}$ until agreement is reached. In practice however, we find that a good guess for the energy cutoff is $\mathcal{E}_{\rm c} = \Psi(\tilde{r}_{\rm max})$ where Ψ is the potential of the initial, infinite system.

Unlike the removal "by-hand" of the divergence, the King-like regularization has a possible physical interpretation in terms of tidal stripping. Assuming DM particles (or stars in a stellar system) are removed by tidal interactions based on their energy (rather than their angular momentum). This is supported by some numerical simulations (Choi et al., 2009). The cut in energy in the initial DF can then be interpreted as the result of tidal interactions between our Galaxy and neighbouring systems. We show the resulting density and mass profiles in Fig. 5.11.

5.4.1.4 Summary

We shortly summarize our results. We found two main ways of regularizing the DF resulting from Eddington's inversion methods. One way consists in modifying the DM density profile such that it cancels the troublesome derivative appearing in the expression of the DF. The other way is to modify directly the DF to render it finite. We investigated two possible modifications of the DF, namely the removal "by-hand" of the diverging term and the so-called King model approach. We stress that the modification of the DF is technically slightly more challenging than the modification of the density profile because it involves solving Poisson's equation to get the modified potential and density of the regularized system. In any case, we found that all methods lead to satisfactory modified profiles in the isotropic and tangentially-biased cases. When the system is radially-biased however, as in the OM models for instance, all regularization methods strongly affect the density profile even in its inner regions. This is because very radial orbits contribute to the density on a wide range of radius. Removing particles in the outer regions to get rid of the divergence inevitably decreases the density at lower radii as well.

5.4.2 Positivity

We turn to a different though complementary issue concerning the solutions of Eddington-like inversion methods: the requirement of positivity. Since we want to interpret our solution as

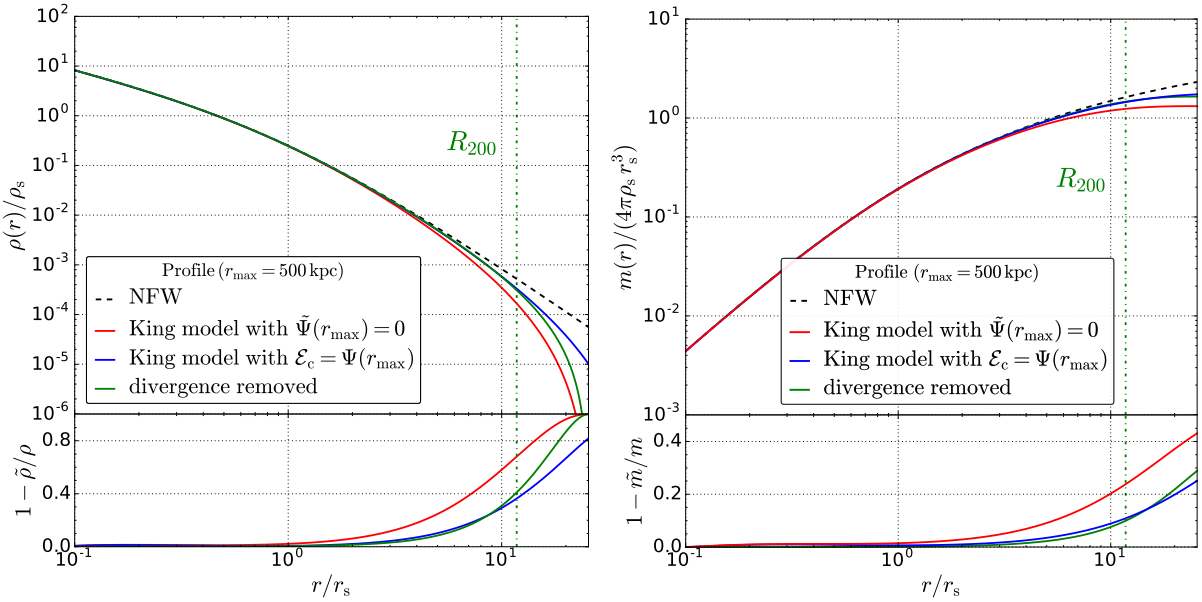

Figure 5.11 – Same as in Fig. 5.8 with the modified profiles obtained by removing the divergence in the DF (green curve) or using the King model with a tuning of the initial condition (red) or a particular choice of the cutoff energy (blue). **Left panel:** density profiles **Right panel:** mass profiles.

phase-space DF, it is obvious that it has to be positive over the entire phase space. There is no guarantee that this holds for an arbitrary density-potential pair (ρ, Ψ). In fact, necessary and sufficient conditions for the positivity of the DF in the isotropic and OM models have been identified by Ciotti & Pellegrini (1992) (see also Ciotti (1996)). We consider a multicomponent system with potential

$$Psi = \sum_k \Psi_k \tag{5.129}$$

and consider a particular component i with density profile ρ_i. The OM pseudo-density is $\rho_{\rm OM,i} = \rho_i \times (1 + r^2/r_{\rm a}^2)$ and the OM phase-space DF is f_i. A necessary condition for the positivity of f_i is then

$$\frac{{\rm d}\rho_{\rm OM,i}}{{\rm d}\Psi_i} \geqslant 0 \text{ for } 0 \leqslant \Psi_i \leqslant \Psi_i(0)\,. \tag{5.130}$$

If this necessary condition is satisfied, a strong sufficient condition is

$$\frac{\rm d}{{\rm d}\Psi_i}\left[\frac{{\rm d}\rho_{\rm OM,i}}{{\rm d}\Psi_i}\left(\frac{{\rm d}\Psi}{{\rm d}\Psi_i}\right)^{-1}\sqrt{\Psi}\right] \geqslant 0 \text{ for } 0 \leqslant \Psi_i \leqslant \Psi_i(0)\,. \tag{5.131}$$

The proof of that theorem is given in Ciotti & Pellegrini (1992). A much simpler, though weaker, sufficient condition for positivity is given by

$$\frac{{\rm d}^2\rho_{\rm OM,i}}{{\rm d}\Psi_i^2} \geqslant 0 \text{ for } 0 \leqslant \Psi_i \leqslant \Psi_i(0)\,. \tag{5.132}$$

This last condition is very easily proved using the expression of the DF in Eq. (5.92). These two theorems apply to multicomponent OM models which include the isotropic case in the $r_{\rm a} \to \infty$ limit.

We would like to stress that negativity issues are not restricted to multicomponent systems. Though many DM density profiles used in the literature lead to a positive DF (such as NFW, Einasto, Burkert), some profiles are not compatible with the isotropic assumption. These profiles

can be identified starting from the Abel equation (5.48). If the derivative $\mathrm{d}\rho/\mathrm{d}\Psi$ goes to zero at some radius r_0, then we have

$$0 = \int_0^{\Psi_0} \frac{f(\mathcal{E})}{\sqrt{\Psi_0 - \mathcal{E}}}\,\mathrm{d}\mathcal{E}\,, \tag{5.133}$$

with $\Psi_0 \equiv \Psi(r_0)$. This is only possible if f is negative for a range of potential between 0 and Ψ_0. Cored density profiles are expected to have a null derivative at their center. Let us look at a class of cored profiles parametrized as

$$\rho(r) = \rho_\mathrm{s}\left[1 + \left(\frac{r}{r_\mathrm{s}}\right)^\alpha\right]^{-\beta/\alpha}. \tag{5.134}$$

This is simply the generalized NFW profile defined in Eq. (3.73) with $\gamma = 0$. The radial derivative of the density is

$$\frac{\mathrm{d}\rho}{\mathrm{d}r} = -\beta\rho_\mathrm{s} r_\mathrm{s}\left(\frac{r}{r_\mathrm{s}}\right)^{\alpha-1}\left[1 + \left(\frac{r}{r_\mathrm{s}}\right)^\alpha\right]^{-1-\beta/\alpha} \tag{5.135}$$

$$\underset{r\to 0}{\sim} -\beta\rho_\mathrm{s} r_\mathrm{s}^{2-\alpha} r^{\alpha-1}\,, \tag{5.136}$$

and the derivative of the potential is

$$\frac{\mathrm{d}\Psi}{\mathrm{d}r} = -\frac{G_\mathrm{N}\,m(r)}{r^2} \underset{r\to 0}{\sim} -\frac{4}{3}\,\pi G_\mathrm{N}\,\rho_\mathrm{s}\,r\,, \tag{5.137}$$

therefore we get

$$\frac{\mathrm{d}\rho}{\mathrm{d}\Psi} \underset{r\to 0}{\sim} \frac{3\,\beta}{4\pi G_\mathrm{N}}\left(\frac{r}{r_\mathrm{s}}\right)^{\alpha-2}. \tag{5.138}$$

If $\alpha \leqslant 2$, the derivative goes to infinity or, if $\alpha = 2$, to a finite positive value. If $\alpha > 2$ however, the derivative goes to zero and the Abel equation imposes

$$0 = \int_0^{\Psi(0)} \frac{f(\mathcal{E})}{\sqrt{\Psi(0) - \mathcal{E}}}\,\mathrm{d}\mathcal{E}\,, \tag{5.139}$$

which implies that f is negative for some $\mathcal{E}$. To summarize, a single-component system with density given by Eq. (5.134) has a positive isotropic DF only if $\alpha \leqslant 2$. Since our proof is based on the asymptotic behaviour as $r \to 0$, it also extends to the Osipkov-Merrit models which are isotropic when $r \ll r_\mathrm{a}$. The condition $\alpha \leqslant 2$ is necessary but not sufficient to ensure positivity.

We now turn to the impact of anisotropy on the positivity of the DF. Let us reconsider the previous example but assuming now a constant anisotropy parameter $\beta_0 \neq 0$. We take $\beta_0 \leqslant 1/2$ for now and still consider a single-component system. The pseudo-density is given by $r^{2\beta_0}\rho$ with ρ in Eq. (5.134), therefore the asymptotic limits become

$$\frac{\mathrm{d}\rho}{\mathrm{d}r} \underset{r\to 0}{\sim} 2\beta_0 r^{2\beta_0-1}\,, \tag{5.140}$$

and

$$\frac{\mathrm{d}\Psi}{\mathrm{d}r} \underset{r\to 0}{\sim} -\frac{4\pi G_\mathrm{N}}{1-2\beta_0}\,r^{-1-2\beta_0}\,. \tag{5.141}$$

The derivative is now

$$\frac{\mathrm{d}\rho}{\mathrm{d}\Psi} \underset{r\to 0}{\sim} -\frac{2\beta_0(1-2\beta_0)}{4\pi G_\mathrm{N}}\,r^{4\beta_0} \underset{r\to 0}{\to} \begin{cases} +\infty & \text{if } \beta_0 < 0 \\ 0 & \text{if } \beta_0 > 0 \end{cases} \tag{5.142}$$

We can see that a negative β_0, which corresponds to tangentially-biased system, ensures the necessary condition for positivity is satisfied. Note that the asymptotic behaviour no longer depends on α, only on the sign of β_0. If $\beta_0 > 0$, *i.e.* the system is radially-biased, the DF is necessarily non-positive. There is no need to take an asymptotic limit to see that a positive β_0 generically endangers the positivity of the DF. This is because a necessary condition for positivity, in the case of constant β_0, is

$$\frac{\mathrm{d}(r^{2\beta_0}\rho)}{\mathrm{d}\Psi} > 0 \text{ for } 0 \leqslant \Psi \leqslant \Psi(0)\,. \tag{5.143}$$

Let us consider a generalized NFW profile for ρ. If we have $2\beta_0 > \gamma$ then $\mathrm{d}(r^{2\beta_0}\rho)/\mathrm{d}r$ is non-negative and condition (5.143) is violated. This is a particular case of the cusp slope-anisotropy theorem (An & Evans, 2006), which states that a necessary condition for the positivity of the DF is

$$\gamma \geqslant 2\beta \tag{5.144}$$

where γ is the cusp slope and β the central anisotropy. It has been postulated, and demonstrated for a wide class of models, that this condition holds at any radius (Ciotti & Morganti, 2010), namely

$$\gamma(r) \geqslant 2\beta(r)\,, \tag{5.145}$$

where

$$\gamma(r) \equiv -\frac{\mathrm{d}\rho}{\mathrm{d}\ln r} \tag{5.146}$$

is the logarithmic slope and $\beta(r)$ is the anisotropy parameter at radius r. This condition further restricts the domain of application of Eddington's method. We illustrate this limitation by considering again the generalized NFW profiles in Eq. (3.73) for which we have

$$\gamma(r) = \gamma + (\beta - \gamma)\,\frac{x^\alpha}{1+x^\alpha}\,. \tag{5.147}$$

This function must be compared to the anisotropy parameter in Eq. (5.88). The slope $\gamma(r)$ and $2\beta(r)$ are shown in Fig. 5.12. We see that $2\beta(r)$ can be larger than $\gamma(r)$ at some radii, if the anisotropy parameter r_a is low enough. In a given mass model, with fixed parameters (α, β, γ), this leads to a lower bound on r_a. From now on, we only consider the case $r_\mathrm{a} = r_\mathrm{s}$ which has the double advantage of leading to a positive DF and only requiring a single length scale.

5.4.3 Stability

Though positivity is a restrictive criterion on the pair (ρ, Ψ) that are compatible with Eddington's method, it is not a sufficient condition for the DF to give a good description of DM galactic halos. Another crucial condition is stability. While the Jeans theorem ensures that the Eddington DF is a solution of the collisionless Boltzmann equation, it does not say anything about the stability of this solution. Since DM halos are stable as far as we can tell, we need to discriminate between stable and unstable DFs to make reliable predictions.

5.4.3.1 Analytic criteria

Stability being a very complex issue, it is mainly studied through numerical simulations. Fortunately, a few analytic results have been derived. In particular, Antonov's second law (Antonov, 1962; Lebovitz, 1965; Lynden-Bell & Wood, 1968) states that a sufficient condition for an isotropic DF to be stable against non-radial perturbation modes is $\mathrm{d}f/\mathrm{d}\mathcal{E} > 0$. Stability against radial

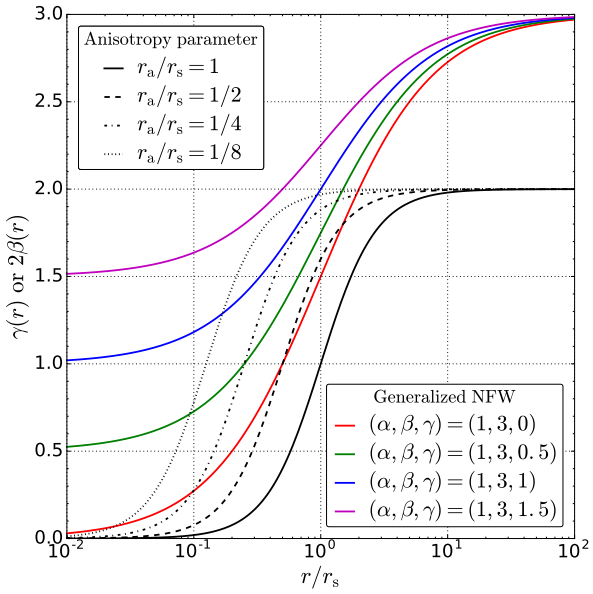

Figure 5.12 – Value of $\gamma(r)$ defined in Eq. (5.147) (coloured lines) compared to $2\beta(r)$ (black lines).

modes is also assured under the same condition according to the Doremus-Feix-Baumann theorem (Doremus et al., 1971; Kandrup & Sygnet, 1985). Putting these two results together, we get a sufficient condition for an isotropic DF to be stable:

$$\frac{\mathrm{d}f}{\mathrm{d}\mathcal{E}} > 0, \ \forall \mathcal{E} > 0\,. \tag{5.148}$$

We wish to test mass models according to this condition. First of all, let us remark the phase-space divergence discussed in Sec. 5.4.1 violates condition (5.148), which is in agreement with our interpretation of this divergence being an unstable phase-space configuration of the system. We want to know if realistic halo configurations can lead to additional instabilities. To this end, we remove the diverging term in the Eddington DF and its extensions, either by considering a modified density profile or removing the divergence by hand.

When studying stability, it is more convenient to have a criterion that does not involve the computation of the full DF. The expression of the isotropic DF without the diverging term is

$$f(\mathcal{E}) = \frac{1}{\sqrt{8}\pi^2} \int_0^{\mathcal{E}} \frac{\mathrm{d}^2\rho}{\mathrm{d}\Psi^2} \frac{\mathrm{d}\Psi}{\sqrt{\mathcal{E} - \Psi}}\,. \tag{5.149}$$

It is obvious from this expression that $\mathrm{d}f/\mathrm{d}\mathcal{E} > 0, \ \forall \mathcal{E} > 0$ only if $\mathrm{d}^2\rho/\mathrm{d}\Psi^2 > 0, \ \forall \Psi > 0$. The reverse implication is also true, as one can see by considering the Abel equation

$$\frac{\mathrm{d}\rho}{\mathrm{d}\Psi} = \sqrt{8}\pi \int_0^{\Psi} \frac{f(\mathcal{E})}{\sqrt{\Psi - \mathcal{E}}}\,\mathrm{d}\mathcal{E}\,, \tag{5.150}$$

and performing an integration by parts to get

$$\frac{\mathrm{d}\rho}{\mathrm{d}\Psi} = 2\sqrt{8}\pi \int_0^{\Psi} \sqrt{\Psi - \mathcal{E}}\,\frac{\mathrm{d}f}{\mathrm{d}\mathcal{E}}\,\mathrm{d}\mathcal{E}\,. \tag{5.151}$$

We can see from this last identity that $\mathrm{d}\rho/\mathrm{d}\Psi$ is a growing function of Ψ only if $\mathrm{d}f/\mathrm{d}\mathcal{E} > 0\ \forall \mathcal{E} > 0$. This proves the equivalence between two sufficient conditions for stability

$$\frac{\mathrm{d}f}{\mathrm{d}\mathcal{E}} > 0, \ \forall \mathcal{E} > 0 \iff \frac{\mathrm{d}^2\rho}{\mathrm{d}\Psi^2} > 0, \ \forall \Psi > 0\,. \tag{5.152}$$

The latter condition is much simpler to test in practice. We already encountered this condition in Eq. (5.132) as a sufficient condition for positivity. Unsurprisingly, a stable DF is also positive. Note that Eq. (5.152) is a sufficient condition but it is not necessary a priori, hence there might exist systems that violate Eq. (5.152) but still have a stable Eddington DF. In the following, we look at realistic mass models and disregard those that do not satisfy (5.152) as potentially unstable. Though this criterion is limited to the isotropic case, it can be partially extended to anisotropic systems. For a DF of the form $f(\mathcal{E}, L)$, Doremus et al. (1973) showed that a sufficient condition for stability against radial modes of perturbations is $\partial f/\partial \mathcal{E} > 0$ for all $(\mathcal{E}, L)$. For the constant-β and OM models in Eqs. (5.85) and (5.92), this condition translates into

$$\frac{\mathrm{d}G}{\mathrm{d}\mathcal{E}} > 0, \ \forall \mathcal{E} > 0 \qquad \text{(constant-}\beta\text{)} \tag{5.153}$$

$$\frac{\mathrm{d}f_{\mathrm{om}}}{\mathrm{d}Q} > 0, \ \forall Q > 0 \qquad \text{(Osipkov-Merritt)} \tag{5.154}$$

Anisotropic systems are sensitive to non-radial perturbations in a very complex way. The possible appearance of radial-orbit instabilities make the study of stability a very complicated issue in that case. We refer to analytical (Antonov, 1987; Perez & Aly, 1996; Guo & Rein, 2003; Maréchal & Perez, 2010) and numerical studies (Merritt & Aguilar, 1985; Barnes et al., 1986; Meza & Zamorano, 1997) on this subject. The bottom line is that there is no simple criterion ensuring stability against non-radial perturbations, therefore we only consider Eq. (5.154) when looking at anisotropic DFs but we regard the criterion as a necessary one rather than a sufficient one.

5.4.3.2 Stability of Galactic mass models

We analyse the stability of the isotropic DFs computed for the mass models of McMillan (2017). The isotropic DFs for four different mass models are shown on the upper left panel in Fig. 5.13. When baryons do not contribute to the potential, the DFs are all growing functions of the energy $\mathcal{E}$ irrespective of the central slope γ. According to the stability criterion (5.148), these DFs are stable. When the full mass models are considered, *i.e.* when baryons do contribute to the total potential, the DFs significantly flatten and in the $\gamma = 0$ case, the stability criterion is violated. This means that the $\gamma = 0$ configuration is not compatible with the assumptions of spherical symmetry and isotropy: one of these two assumptions should be relaxed to find a stable phase-space description. We check the alternative, equivalent criterion in Eq. (5.152) on the upper right panel in Fig. 5.13. We note that the presence of a dip in the DF, as for the $\gamma = 0$ case, has consequences on the shape of the speed distribution. This is shown in Fig. 5.14. While DM speed distributions usually present a single peak, the distribution in the $\gamma = 0$ case (magenta line) has two peaks: a very large and high one at $v \sim 450\,\mathrm{km/s}$, and a much smaller one at $v \sim 30\,\mathrm{km/s}$. Note that this unusual feature appears very close to the Galactic center at $r = 0.01\,\mathrm{kpc}$ while the speed distribution at larger radii takes a more common shape. It is not straightforward to interpret this puzzling feature as a mark of instability because it also appears in the speed distribution of the $\gamma = 0.25$ model (blue line) even though this model is stable according to the upper panel in Fig. 5.13. We note that the third derivative $\mathrm{d}^3\rho/\mathrm{d}\Psi^3$ takes negative values for both the $\gamma = 0$ and $\gamma = 0.25$ models, see the lower panel in Fig. 5.13. This lead us to the following conjecture:

$$\frac{\mathrm{d}^3\rho}{\mathrm{d}\Psi^3} > 0, \ \forall \Psi > 0 \tag{5.155}$$

is a sufficient criterion to get a single-peak speed distribution at any radius. As stated, this is a conjecture and we do not have a proof of that statement. In the following, we remain agnostic about the origin of the camel-back shape of speed distributions and only consider the stability criterion given in Eq. (5.152). According to this criterion, an isotropic description of the $\gamma = 0.25$ is acceptable.

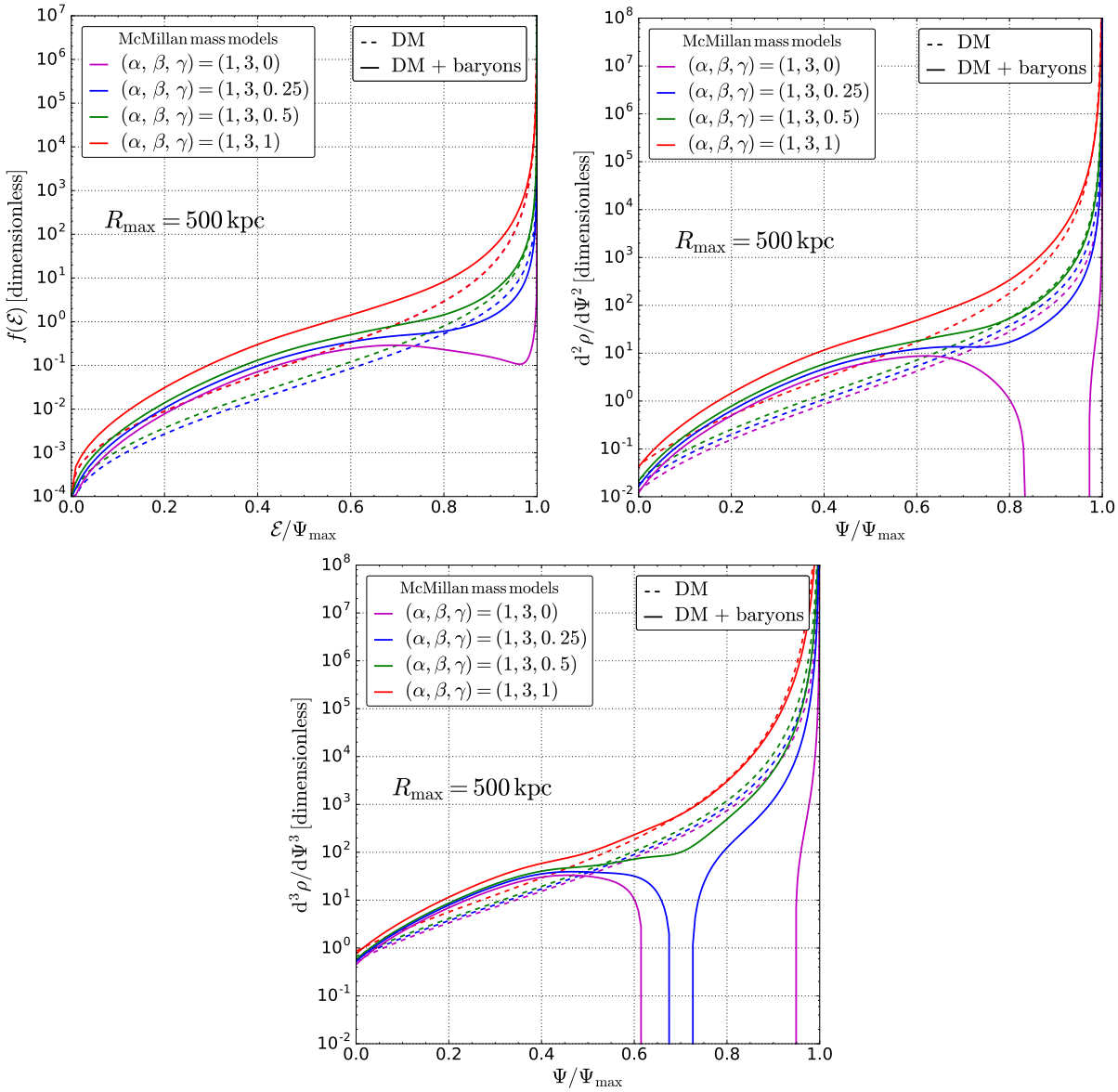

Figure 5.13 – Several quantities computed for the mass models of McMillan (2017), with or without baryons (solid or dashed lines, respectively). **Top left panel:** isotropic phase-space DF as a function of the energy. The DFs are in units of $(4\pi G_{\rm N})^{-3/2} r_{\rm s}^{-3} \rho_{\rm s}^{-1/2}$. **Top right panel:** second derivative with respect to the total potential as a function of the potential. The derivatives are in units of $(4\pi G_{\rm N} \rho_{\rm s} r_{\rm s}^2)^{-2}$. **Bottom panel:** third derivative with respect to the total potential as a function of the potential. The derivatives are in units of $(4\pi G_{\rm N} \rho_{\rm s} r_{\rm s}^2)^{-3}$.

It is clear from our analysis that baryons can destabilize a DM phase-space configuration which would have been stable otherwise. Let us try to quantify that statement. We consider a system with a DM and a baryonic component and write its total mass $m = m_{\rm dm} + m_{\rm bar}$ and potential $\Psi = \Psi_{\rm dm} + \Psi_{\rm bar}$. The stability criterion is $\mathrm{d}^2\rho/\mathrm{d}\Psi^2 > 0$ for all $\Psi > 0$. Using Poisson's equation, the radial of the potential can be written

$$\frac{\mathrm{d}\Psi_i}{\mathrm{d}r} = -\frac{G_{\rm N}\, m_i(r)}{r^2}\,. \tag{5.156}$$

Let us try to express the derivative with respect to the full potential as a function of the derivative

over the DM potential:

$$\begin{aligned}\frac{\mathrm{d}^2\rho}{\mathrm{d}\Psi^2} &= \frac{\mathrm{d}}{\mathrm{d}\Psi}\left(\frac{\mathrm{d}\rho}{\mathrm{d}\Psi}\right)\\ &= \frac{\mathrm{d}\Psi_{\rm dm}}{\mathrm{d}\Psi}\frac{\mathrm{d}}{\mathrm{d}\Psi_{\rm dm}}\left(\frac{\mathrm{d}\Psi_{\rm dm}}{\mathrm{d}\Psi}\frac{\mathrm{d}\rho}{\mathrm{d}\Psi_{\rm dm}}\right)\\ &= \frac{m_{\rm dm}}{m_{\rm dm}+m_{\rm bar}}\frac{\mathrm{d}}{\mathrm{d}\Psi_{\rm dm}}\left(\frac{m_{\rm dm}}{m_{\rm dm}+m_{\rm bar}}\frac{\mathrm{d}\rho}{\mathrm{d}\Psi_{\rm dm}}\right)\\ &= \left(\frac{m_{\rm dm}}{m_{\rm dm}+m_{\rm bar}}\right)^2\frac{\mathrm{d}^2\rho}{\mathrm{d}\Psi_{\rm dm}^2}+\frac{m_{\rm dm}}{m_{\rm dm}+m_{\rm bar}}\frac{\mathrm{d}\rho}{\mathrm{d}\Psi_{\rm dm}}\frac{\mathrm{d}}{\mathrm{d}\Psi_{\rm dm}}\left(\frac{m_{\rm dm}}{m_{\rm dm}+m_{\rm bar}}\right).\end{aligned} \tag{5.157}$$

The derivative of the mass ratio on the can be further expressed as

$$\begin{aligned}\frac{\mathrm{d}}{\mathrm{d}\Psi_{\rm dm}}\left(\frac{m_{\rm dm}}{m_{\rm dm}+m_{\rm bar}}\right) &= \frac{m_{\rm dm}}{m_{\rm dm}+m_{\rm bar}}\frac{\mathrm{d}}{\mathrm{d}\Psi_{\rm dm}}\ln\left(\frac{m_{\rm dm}}{m_{\rm dm}+m_{\rm bar}}\right)\\ &= \frac{\mathrm{d}}{\mathrm{d}\Psi}\ln\left(\frac{m_{\rm dm}}{m_{\rm dm}+m_{\rm bar}}\right)\\ &= -\frac{\mathrm{d}}{\mathrm{d}\Psi}\ln\left(\frac{m_{\rm bar}}{m_{\rm dm}}+1\right)\\ &= -\frac{\frac{\mathrm{d}}{\mathrm{d}\Psi}\left(\frac{m_{\rm bar}}{m_{\rm dm}}\right)}{\frac{m_{\rm bar}}{m_{\rm dm}}+1}\\ &= -\frac{m_{\rm dm}}{m_{\rm dm}+m_{\rm bar}}\frac{\mathrm{d}}{\mathrm{d}\Psi}\left(\frac{m_{\rm bar}}{m_{\rm dm}}\right).\end{aligned} \tag{5.158}$$

Injecting this result into the expression of $\mathrm{d}^2\rho/\mathrm{d}\Psi^2$ we finally get

$$\frac{\mathrm{d}^2\rho}{\mathrm{d}\Psi^2} = \left(\frac{m_{\rm dm}}{m_{\rm dm}+m_{\rm bar}}\right)^2\left[\frac{\mathrm{d}^2\rho}{\mathrm{d}\Psi_{\rm dm}^2}-\frac{\mathrm{d}\rho}{\mathrm{d}\Psi_{\rm dm}}\frac{\mathrm{d}}{\mathrm{d}\Psi}\left(\frac{m_{\rm bar}}{m_{\rm dm}}\right)\right]. \tag{5.159}$$

Using this expression, we find that the stability criterion translates into the inequality

$$\frac{\mathrm{d}^2\rho}{\mathrm{d}\Psi_{\rm dm}^2}\Big/\frac{\mathrm{d}\rho}{\mathrm{d}\Psi_{\rm dm}} > \frac{\mathrm{d}}{\mathrm{d}\Psi}\left(\frac{m_{\rm bar}}{m_{\rm dm}}\right), \tag{5.160}$$

where the left-hand side contains only DM-related quantities and all the baryonic contributions are on the right-hand side. The criterion shows that the impact of baryons on the stability depends on the slope of the ratio $m_{\rm bar}/m_{\rm dm}$ rather than the value of the mass $m_{\rm bar}$. This means that "adding more baryons" does not necessarily destabilizes an otherwise stable DF. The $m_{\rm bar}/m_{\rm dm}$ ratio is shown as a function of the total potential on the right panel in Fig. 5.14. We note that the ratio $(m_{\rm bulge}+m_{\rm disc}/m_{\rm dm}$ grows slower than $m_{\rm bulge}/m_{\rm dm}$, hence the disc stabilizes the DF with respect to the bulge only configuration, even though the baryonic mass is much higher when the two components are included.

We also investigated the impact of changing the bulge's scale parameters on the stability of the isotropic DF. This is illustrated in Fig. 5.15 where we show the sign of Min $\left[\mathrm{d}^2\rho/\mathrm{d}\Psi^2\right]$. If this quantity is negative, the stability criterion is violated and the system is possibly unstable. The symbols represent the mass models and the red-coloured area the (potential) instability region. One sees that the $\gamma = 0$ is inside its own instability region which means it violates the stability criterion. A significant change in the bulge parameters is required to destabilize the $\gamma > 0$ models.

5.5 Test of the Eddington formalism on hydrodynamic cosmological simulations

We discussed the Eddington formalism in the previous sections and established its validity range. So far the discussion has focused on the formalism itself and its inner limits. A crucial aspect

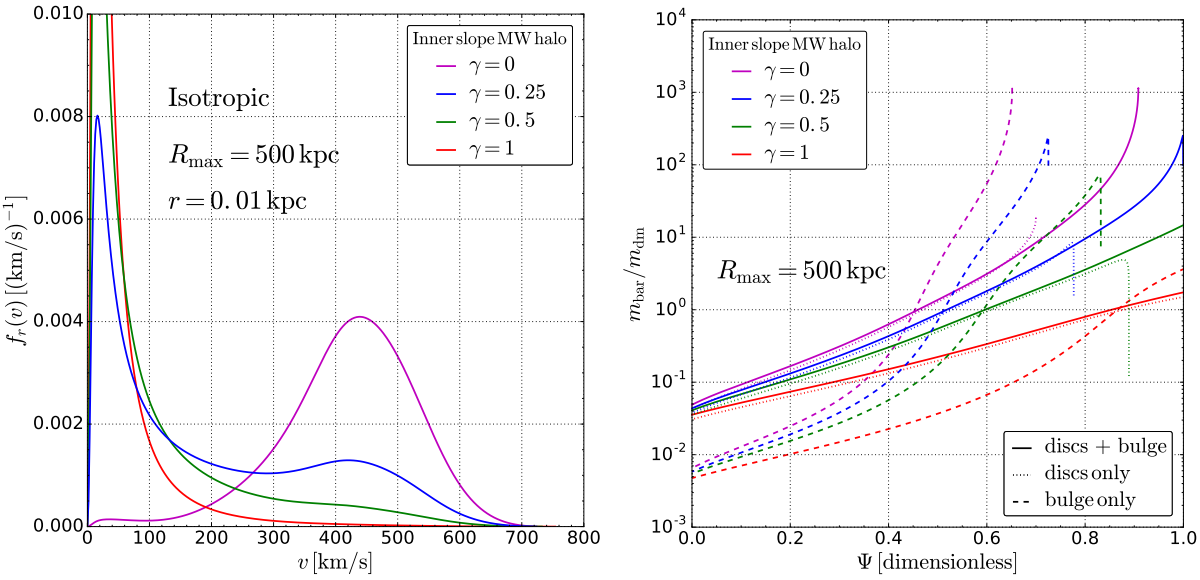

Figure 5.14 – **Left panel:** isotropic speed distribution at $r = 0.01\,{\rm kpc}$ for the mass models of McMillan (2017). **Right panel:** ratio of the baryons mass to the DM mass as a function of the total potential in units of $4\pi G_{\rm N}\rho_{\rm s}r_{\rm s}^2$.

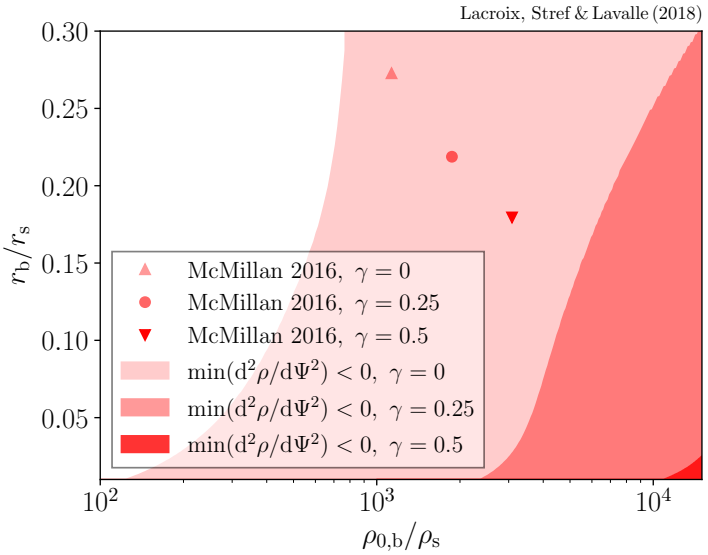

Figure 5.15 – Sign of the minimum of $d^2\rho/d\Psi^2$ in the plane $(\rho_{0,{\rm b}}/\rho_{\rm s}, r_{\rm b}/r_{\rm s})$ with $\rho_{0,{\rm b}}$ and $r_{\rm b}$ the scale parameters of the bulge and $\rho_{\rm s}$ and $r_{\rm s}$ the scale parameters of the DM halo. The disc parameters are fixed to the value of McMillan (2017).

that remains to be addressed is the performance of the Eddington method. How well does this technique capture the phase-space distribution function of dark matter halos? To answer this question, we test the Eddington method on hydrodynamic cosmological simulations. We choose a set of observables relevant for dark matter searches, such as the velocity distribution at different radii, and compare the predictions of the Eddington formalism with the observable extracted from the simulations. We systemically perform our comparison for both the Eddington model and the Standard Halo Model (SHM). A crucial point of our analysis is the study of composite systems, including both dark matter and baryons, such as Milky-Way-like disc galaxies.

This work is done in collaboration with Arturo Nũnez, Thomas Lacroix, Emmanuel Nezri and Julien Lavalle.

5.5.1 Cosmological simulations

5.5.1.1 Description of the simulations

Two sets of simulations are used in this study. The first one consists of two high-resolution simulations published in Mollitor et al. (2015), which we labelled Halo B and Halo C. These simulations were run with the RAMSES package (Teyssier, 2002) in 20 Mpc cosmological boxes and using the zoom-in technique with a carefully decomtaminated Lagrangian volume. The initial conditions were generated with the MUSIC package (Hahn & Abel, 2011). Conventional recipes were used for cooling, ultraviolet background and self-shielding. The gas dynamics, star formation scheme and supernovae (SN) feedback are all described in Mollitor et al. (2015). The star formation follows a standard Schmidt law with an adapted density threshold and efficiency (Schmidt, 1959; Kennicutt, 1998). The SN feedback is carried out through a thermal energy injection after 10 Myr with a Chabrier initial mass function (Chabrier, 2003) with a thermal energy of 10^{51} erg per SN event. A non-thermal energy injection is also implemented. We refer to Mollitor et al. (2015) for a detailed analysis of these simulations. One of their main features is to exhibit both a compression of the dark matter profile around the scale radius of the disc and a flattening of the dark matter profile below due to the SN feedback.

The second set of simulations are also two cosmological hydrodynamic zoom-in simulations performed with the RAMSES package, with a slightly lower resolution. The stellar physics (star formation and SN feedback) is the same. The corresponding high-resolution runs are part of a suite of simulations that will be soon published in a forthcoming paper (Nũnez et al., 2018) where the authors will consider different subgrid physics of star formation and SN feedback, which is far beyond the scope of the present study. Those two simulations are labelled respectively Mochima and Adicora after two Venezuelian beaches favoured by our colleague Arturo.

Regardless of their precise Milky-Way-like morphology and features, we will use these simulations as consistent frameworks with regard to gravity to study the phase-space distribution of dark matter and test the Eddington method in a numerical galaxy environment. For the four objects we consider (Halo B, Halo C, Mochima and Adicora), both dark-matter-only (DMO) and hydrodynamic runs including baryons are studied.

The mass resolution ($m_{\rm DM}$, $m_\star$) and spatial resolution (hsml), as well as the pseudo-virial mass and radius M_{200} and R_{200} and the total baryonic mass $M_\star$, are given in Tab. 5.1 for all the objects under study.

Run		M_{200} ($10^{10} M_\odot$)	R_{200} (kpc)	$M_\star$ ($10^{10} M_\odot$)	$m_{\rm DM}$ ($M_\odot$)	$m_\star$ ($M_\odot$)	hsml (pc)
Halo B	DMO	49.60	163.5		2.757×10^5		
	Hydro	50.06	177.54	7.96	2.308×10^5	2.87×10^4	151.67
Halo C	DMO	62.48	176.36		2.757×10^5		
	Hydro	55.02	182.23	9.56	2.308×10^5	2.87×10^4	151.67
Mochima	DMO	91.35	206.34		2.27×10^5		
	Hydro	82.14	213.2	10.87	1.536×10^6	1.836×10^5	281.1
Adicora	DMO	91.67	202.46		2.27×10^5		
	Hydro	81.07	212.7	11.07	1.536×10^6	1.836×10^5	281.1

Table 5.1 – Main features of the four simulations at $z = 0$. The columns are the pseudo-virial mass M_{200} and radius R_{200}, the baryonic mass $M_\star$, the mass resolution for dark matter $m_{\rm DM}$, the mass resolution for baryons $m_\star$ and the spatial resolution (hsml).

5.5.1.2 Halo shape and level of equilibrium

The Eddington method only applies to spherical systems in dynamical equilibrium. We do not expect realistic simulated galactic halos to be perfectly spherical nor in perfect equilibrium, therefore we need to measure the departure from these two regimes.

A system of N particles with mass m_k, $k = 1...N$ at position $\vec{r}_k$ can be characterized by its mass distribution tensor

$$\mathcal{M}_{ij} \equiv \sum_k m_k \, r_{ki} \, r_{kj} \,, \tag{5.161}$$

where $r_{ij} \equiv \vec{r}_i \otimes \vec{r}_j$. We denote the three square root of the eigenvalues of $\mathcal{M}$ by a, b and c with $a > b > c$. We then define the sphericity, the elongation and the triaxiality by

$$S \equiv \frac{c}{a} \tag{5.162}$$

$$e \equiv \frac{b}{a} \tag{5.163}$$

$$T \equiv \frac{a^2 - b^2}{a^2 - c^2} \,. \tag{5.164}$$

A system with spherical symmetry has $a = b = c$, and therefore $S = e = 1$ and T is ill-defined. Otherwise a low triaxiality $T \ll 1$ corresponds to an oblate system while a high triaxiality $T \simeq 1$ corresponds to a prolate system [see *e.g.*, Bryan et al. (2013)]. The sphericity and triaxiality of the dark matter halo in the hydrodynamical runs are shown as functions of the radius in Fig. 5.16. Halos are close to spherical though slightly oblate.

In cosmological simulations, there is no definitive test to assess the level of virialization of a halo. We use the criterion of Zjupa & Springel (2017) who define a virial ratio

$$q \equiv \frac{2\,E_{\rm kin}}{E_{\rm pot}} + 1 \,, \tag{5.165}$$

such that $q = 0$ for an isolated structure in equilibrium according to the virial theorem. The kinetic and potential energies are computed according to

$$E_{\rm kin} = \sum_i \frac{1}{2} \, m_i \, v_i^2 + \sum_j \frac{3}{2} \, k_{\rm B} \, T_j \tag{5.166}$$

$$E_{\rm pot} = \sum_i \sum_j \frac{G_{\rm N} \, m_i \, m_j}{|\vec{r}_i - \vec{r}_j|} \, f_{ij} \,, \tag{5.167}$$

where the second term on the right-hand side of Eq. (5.166) accounts for the kinetic energy of gas cells, and the f_{ij} factor in Eq. (5.167) accounts for the particular prescription used for the force-softening on short distances (Shapiro et al., 2004). The virial ratio q in shown on the right panel in Fig. 5.16. The Mochima galaxy in the hydrodynamical run is the only one satisfying the virial criterion, though we have $|q| < 0.2$ in all the other cases.

5.5.2 Fitting the galactic components

The dark matter halos are fitted with a generalized NFW density profile

$$\rho_{\rm DM}(r) = \rho_0 \left(\frac{r}{r_{\rm s}}\right)^{-\gamma} \left[1 + \left(\frac{r}{r_{\rm s}}\right)^{\alpha}\right]^{(\gamma-\beta)/\alpha} \,. \tag{5.168}$$

A density can be assigned to each dark matter particle in the simulation through the procedure described in Dehnen (2002). We refer to this density as the particle density $\rho_{\rm par}$. A density variance $\sigma(\rho_{\rm par})$ can also be computed. The density profile can then be fitted by minimizing

$$\chi^2_\rho = \sum_{\text{bin } i} \left(\frac{\log_{10}\left[\rho_{\rm DM}(r_i)\right] - \log_{10}\left[\rho_{\rm shell}(r_i)\right]}{\sigma\left[\log_{10}(\rho_{\rm par}(r_i))\right]} \right)^2 \,. \tag{5.169}$$

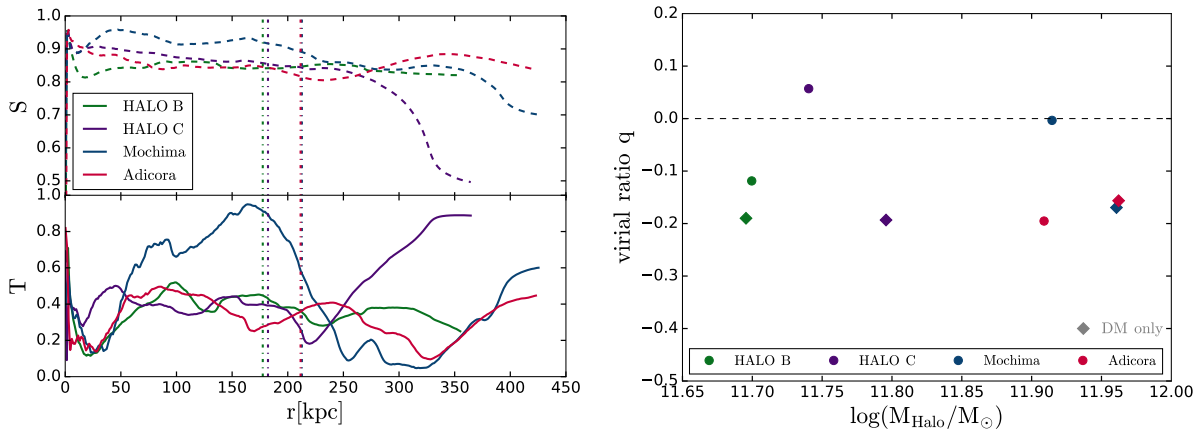

Figure 5.16 – Left panel: sphericity (upper panel) and triaxiality (lower panel) for the hydrodynamic simulations used, as functions of the distance to the galaxy centre. **Right panel:** virial ratio as defined in Eq. (5.165) for the four simulations considered here.

In this equation, $\rho_{\rm shell}(r_i)$ is the mean density within a spherical shell of radius r_i. The minimisation is performed on $\log_{10}(\rho)$ rather than ρ to get a good fit over a wide range of radius. An alternative fitting procedure makes use of the mass within a spherical shell rather than the mean density. In this case, the fit is obtained by minimizing

$$\chi^2_m = \sum_{\text{bin } i} \left(\log_{10}\left[m_{\rm DM}(r_i)\right] - \log_{10}\left[m_{\rm shell}(r_i)\right]\right)^2 . \tag{5.170}$$

We show the density measured in Halo B along with the fits in Fig. 5.17. As one can see, both fitting procedure lead to very similar results. From definiteness, we used the fits obtained with the mass fitting procedure in Eq. (5.170). The high density variance above 20-30 kpc in Fig. 5.17 is due to the presence of substructures, which start to significantly contribute to the mean dark matter density (see Chap. 3). The fitting parameters obtained for Halo B are shown in Tab. 5.2. The main differences between the DMO and hydrodynamical runs are seen on parameters $r_{\rm s}$ and γ. Adiabatic compression of the dark halo decreases the value of $r_{\rm s}$, and supernovae feedback decreases the value of γ from an NFW-like value of $\gamma \simeq 1$ to a smaller value $\gamma \ll 1$. These two effects are also observed in the other halos. The dark matter parameters for the other halos are shown in App. D.3.

Halo B	$\log_{10}(\rho_0)$ $[\mathrm{M}_\odot/\mathrm{kpc}^3]$	$r_{\rm s}$ [kpc]	α	β	γ
DMO	7.101± 0.532	10.338± 6.592	1.0± 0	2.785± 0.258	1.101± 0.182
Hydro	7.622± 0.096	4.885± 0.514	2.639± 0.858	2.621± 0.117	0.127± 0.097

Table 5.2 – Parameters of the dark matter halo in Halo B.

The same fitting procedure is applied to baryons in the hydrodynamical runs. We fit the baryon distribution using the same parametrisation as in McMillan (2017), see App. D.1. For each hydrodynamical run, we fit a bulge, a thin stellar disc, a thick stellar disc and one gas disc (for the gas disc, we use the same mass distribution as the stellar disc *i.e.* a double exponential). The mass profile and fitting parameters for the baryons in Halo B are shown in Fig. 5.18. The mass profiles for the other galaxies are shown in App. D.1.

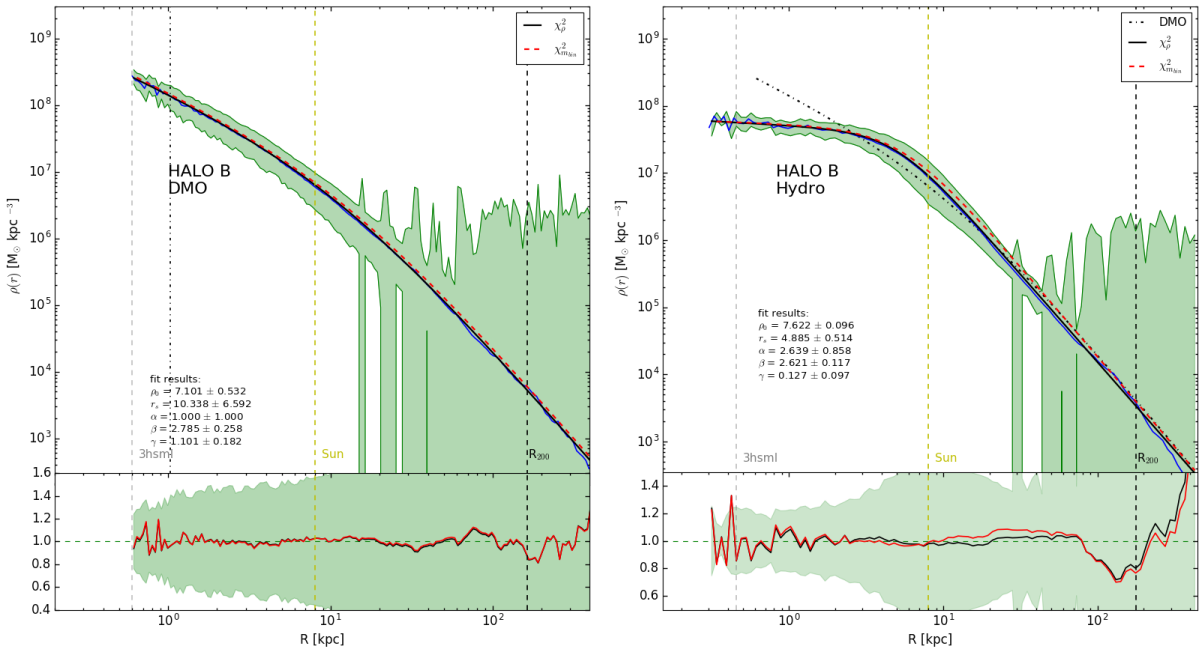

Figure 5.17 – **Left panel:** mean density in spherical shells (blue curve) with the associated 1σ band (green) for the DMO run of Halo B. We show the fit obtained using the χ^2 defined in Eq. (5.169) (black curve) and the χ^2 in Eq. (5.170) (dashed red curve). **Right panel:** same as left panel, for the hydrodynamical run.

5.5.3 Radial boundary and escape speed

As we saw when we discussed the theoretical issues associated with the Eddington formalism, the definition of a finite radial boundary is essential to correctly account for the local value of the escape speed. While the radial extension of physical systems like the Milky Way is in general difficult to infer, we can extract this information for the simulated galaxies.

The radial boundary $R_{\rm max}$ is define as the maximum of the (negative) gravitational potential averaged in spherical shells centred on the simulated galaxy. As the radius of the shells gets larger the potential increases to reach a maximum, then decreases again when entering the region of influence of the nearest neighbouring galaxy. The maximum between the two potential wells defines $R_{\rm max}$. This procedure is illustrated in Fig. 5.19 for Halo B, where a radial border of $R_{\rm max} \simeq 800\,{\rm kpc}$ is found.

Once the radial border $R_{\rm max}$ has been measured, the gravitational potential is defined so that is is zero at $R_{\rm max}$ *i.e.*

$$\Psi(r) \equiv -\left(\Phi(R_{\rm max}) - \Phi(r)\right)\,, \tag{5.171}$$

where Φ is the local potential which is computed within the simulation. The potential is positive at radii $r < R_{\rm max}$ with our definition, which is the convention we used when we discussed the Eddington formalism in the two previous sections. As we have seen before, the escape speed at a radius r is defined by

$$v_{\rm esc}(r) \equiv \sqrt{2\Psi(r)}\,. \tag{5.172}$$

An alternative measure of this speed can be obtained by looking at the maximum velocity of particles inside radial shells. We refer to this maximum speed as $v_{\rm max}$. In a spherical system in dynamical equilibrium, we should have $v_{\rm esc}(r) = v_{\rm max}(r)$ at all r. We compare $v_{\rm esc}$ and $v_{\rm max}$ for Halo B on Fig. 5.20. The two method roughly agree although we have $v_{\rm esc} > v_{\rm max}$ in the inner

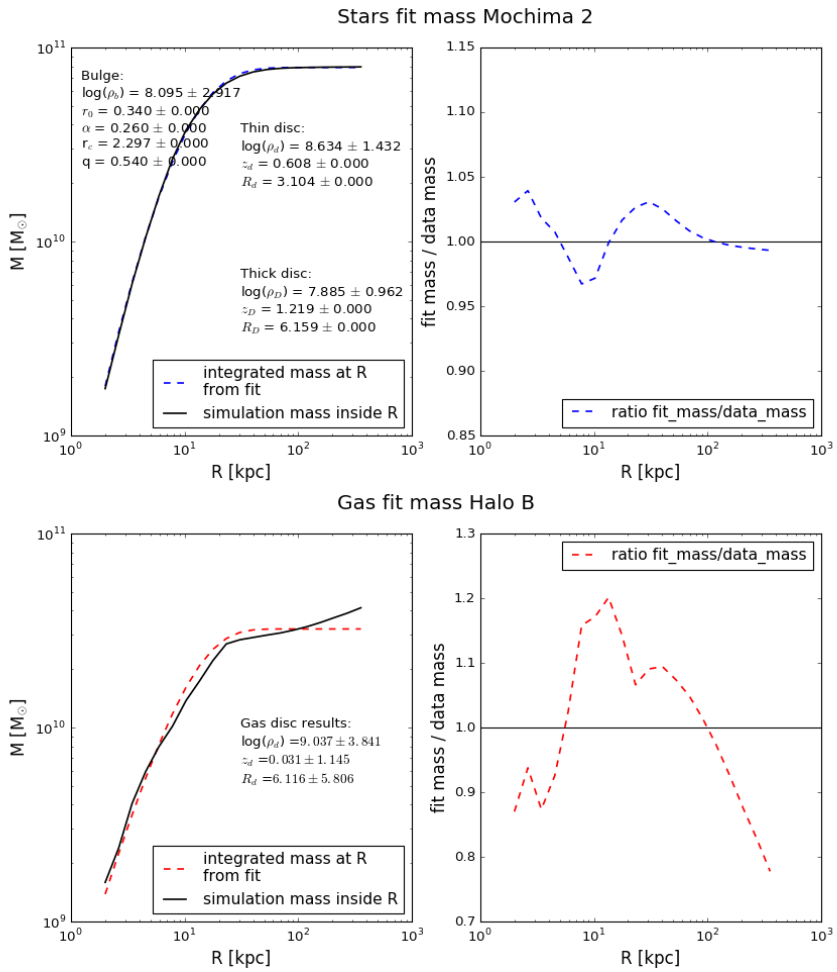

Figure 5.18 – Mass profile and fitting parameters for the stellar discs and bulge (upper panel) and the gas disc (lower panel) for the Halo B galaxy.

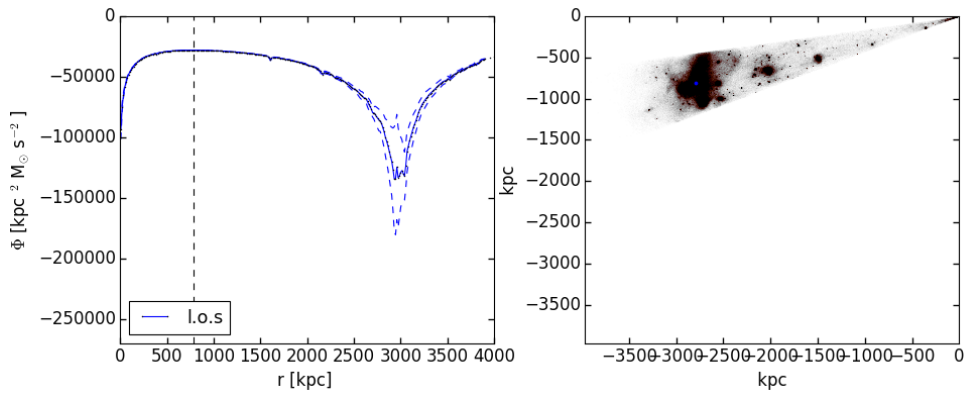

Figure 5.19 – **Left panel:** gravitational potential averaged in spherical shells centred on Halo B (gray line). The maximum of the potential, which defines $R_{\max}$, is shown by the dashed vertical line. We also show the potential along the line of sight connecting the two potential wells (blue line) and the 1σ dispersion around (dashed blue lines). **Right panel:** projected density in a cone around the line of sight. The center of the nearest "big" neighbour is marked by a blue point.

region $r < 10$ kpc. Note however that the measure of $v_{\max}$ is limited by statistics in this region

and therefore not reliable. Beyond the virial radius, we observe $v_{\rm esc} < v_{\rm max}$. The comparison of $v_{\rm esc}$ and $v_{\rm max}$ for the other galaxies is shown in App. D.3.2, where similar features are observed.

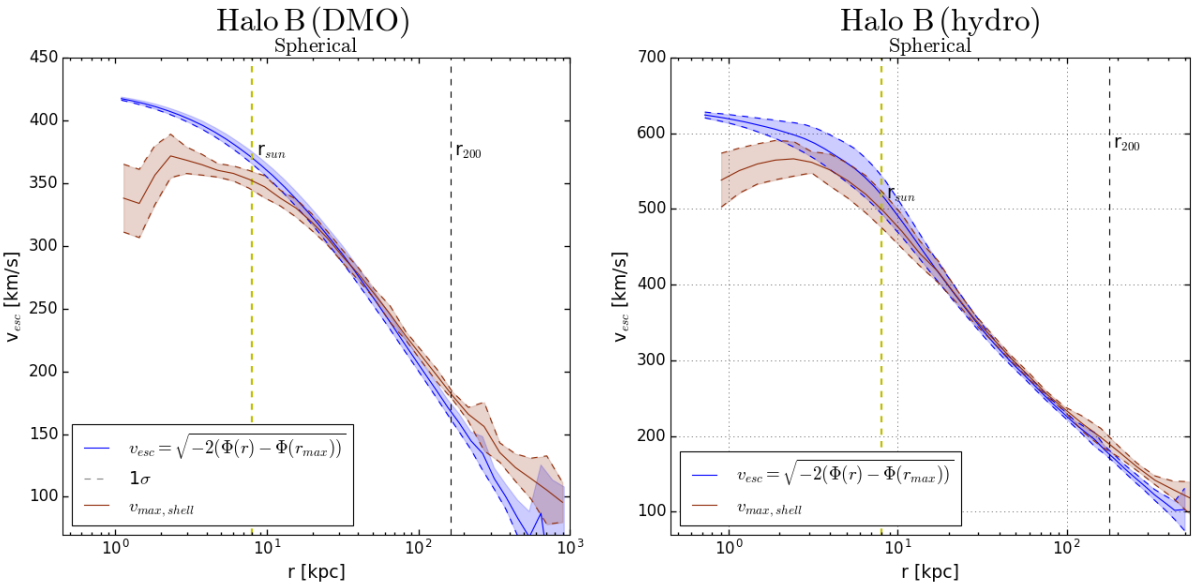

Figure 5.20 – Escape speed computed from the potential (blue) compared to maximal velocity of particles in radial shells (green). The comparison is made in the DMO run (left panel) and the hydrodynamical run (right panel).

5.5.4 Velocity distributions

We now turn to the comparison between the Eddington formalism and the simulations. The fitting procedure provides us with the dark matter density profile as well as the total gravitational potential for each galaxy in our sample. Thus we have all we need to compute the phase-space DF following the inversion procedure described in Sec. 5.3.2. From the phase-space DF, we can compute the velocity distribution at any radius r. Here we only show results regarding the isotropic Eddington inversion, where the velocity distribution is simply related to phase-space DF through

$$f_{\vec{v}}(\vec{v}) = \frac{1}{\rho_{\rm DM}(r)} f\left(\Psi(r) - \frac{v^2}{2}\right) . \tag{5.173}$$

Our full analysis will include study of anisotropic cases. We also compare the velocity distribution measured in the simulations to the prediction of the SHM. In this model, it is assumed that the velocity distribution follows the Maxwell-Boltzmann distribution

$$f_{\rm mb}(\vec{v}) \equiv \left(\pi v_0^2\right)^{-3/2} \exp\left[-\frac{v^2}{v_0^2}\right] , \tag{5.174}$$

where the speed v_0 is chosen to be the circular speed at radius r: $v_{\rm circ}(r)$. This model is *not* dynamically consistent since this distribution is not a solution of the collisionless Boltzmann equation consistent with the dark matter distribution under study. Indeed, the only density profile compatible with a Maxwell-Boltzmann velocity distribution is the singular isothermal sphere (see Sec. 5.3.2.1), which does not give a good description of galactic halos. In particular, the Maxwell-Boltzmann extends to arbitrary large velocities *i.e.* it does not account for a local

escape speed. It can be truncated at the escape speed for a more realistic modelling, for a instance with a smooth truncations

$$f_{\text{smooth}}(\vec{v}) \equiv \frac{1}{N_{\text{smooth}}} \left\{ \exp\left[-\frac{v^2}{v_0^2}\right] - \exp\left[-\frac{v_{\text{esc}}^2}{v_0^2}\right] \right\} , \tag{5.175}$$

with a normalisation factor

$$N_{\text{smooth}} \equiv \left(\pi v_0^2\right)^{3/2} \left[\text{erf}(z) - \frac{2\,z}{\sqrt{\pi}} \left(1 + \frac{2\,z^2}{3}\right) e^{-z^2} \right] , \tag{5.176}$$

with $z = v_0/v_{\text{esc}}$.

The velocity distributions in Eq. (5.173), Eq. (5.174) and Eq. (5.175) are compared to the simulation data from Halo B in Fig. 5.21. We show the comparison for the DMO and the hydrodynamical runs. The escape velocity v_{esc} computed from the gravitational potential is shown with its 1σ uncertainty band.

To make a quantitative comparison between the three models, we perform a χ^2 test. The value of χ^2 is shown on the plots. Regardless of the radius and the model used, the value of χ^2 is very high. This means that none of the models give a satisfactory description of the observed velocity distribution. This is valid for all the objects we considered, see App. D.3.3. This is hardly a surprising fact however, given the crudity of the Maxwell-Boltzmann description or even the Eddington method, which assumes spherical symmetry, isotropy and perfect equilibrium. More interesting is the relative performance of the models. We note that the Eddington velocity distribution performs better, in most cases, than the Maxwell-Boltzmann distribution in Eq. (5.174). This is especially true at low radii, for $2\,\text{kpc} < r < 4\,\text{kpc}$ and $7\,\text{kpc} < r < 9\,\text{kpc}$, and it is true for both the DMO and hydrodynamical runs. The reason for the lack of performance of the Maxwellian approximation is the difference in the peak velocity. Simulations show a peak velocity higher than the circular velocity in the central regions. This is compatible with the observation that simulated halos are in general isotropic at the center, see *e.g.*, Bozorgnia et al. (2013). Since by construction, the Maxwell-Boltzmann distribution has its peak velocity at the circular velocity, it fails at reproducing the simulations in their central region. This lack of performance is also observed for the truncated Maxwell-Boltzmann distribution in Eq. (5.175). However, this distribution performs just as well, if not better, than the Eddington distribution at most radii and in most of our simulated objects. We should recall that this distribution is ad hoc and not motivated by first principles, unlike the Eddington formalism. The shape of the cut at v_{esc} is in particular completely arbitrary, which is a limitation of this method since the presence of this cut is precisely what improves the fit at large radii.

5.5.5 Moments of the velocity distributions

Although all the information is contained in the velocity distribution, dark matter searches are only sensitive to some of its moments. For instance, direct detection is essentially sensitive to $\langle 1/v \rangle$. The exact moments relevant for dark matter searches will be listed and studied in the next chapter. For now, we limit ourselves to the quantity $\langle v^n \rangle (r)$. We directly compare its predicted value from the distributions in Eq. (5.173), Eq. (5.174) and Eq. (5.175) to the same quantity measured in the simulation. The results for Halo B are shown in Fig. 5.22 while the results for the other halos are shown in App. D.3.4. The Eddington prediction is compared to the (uncut) Maxwell-Boltzmann prediction. In agreement with the observations made on the velocity distribution, we see that the Eddington prediction follows the general trend of the moments as functions of the radius much better the SHM. Quantitative comparisons and the inclusion of the smoothly-cut Maxwell-Boltzmann distribution will be featured in the final work.

To conclude on these very preliminary results, we see that the Eddington formalism not only provides a consistent framework to compute the phase-space DF of dark matter halos but also

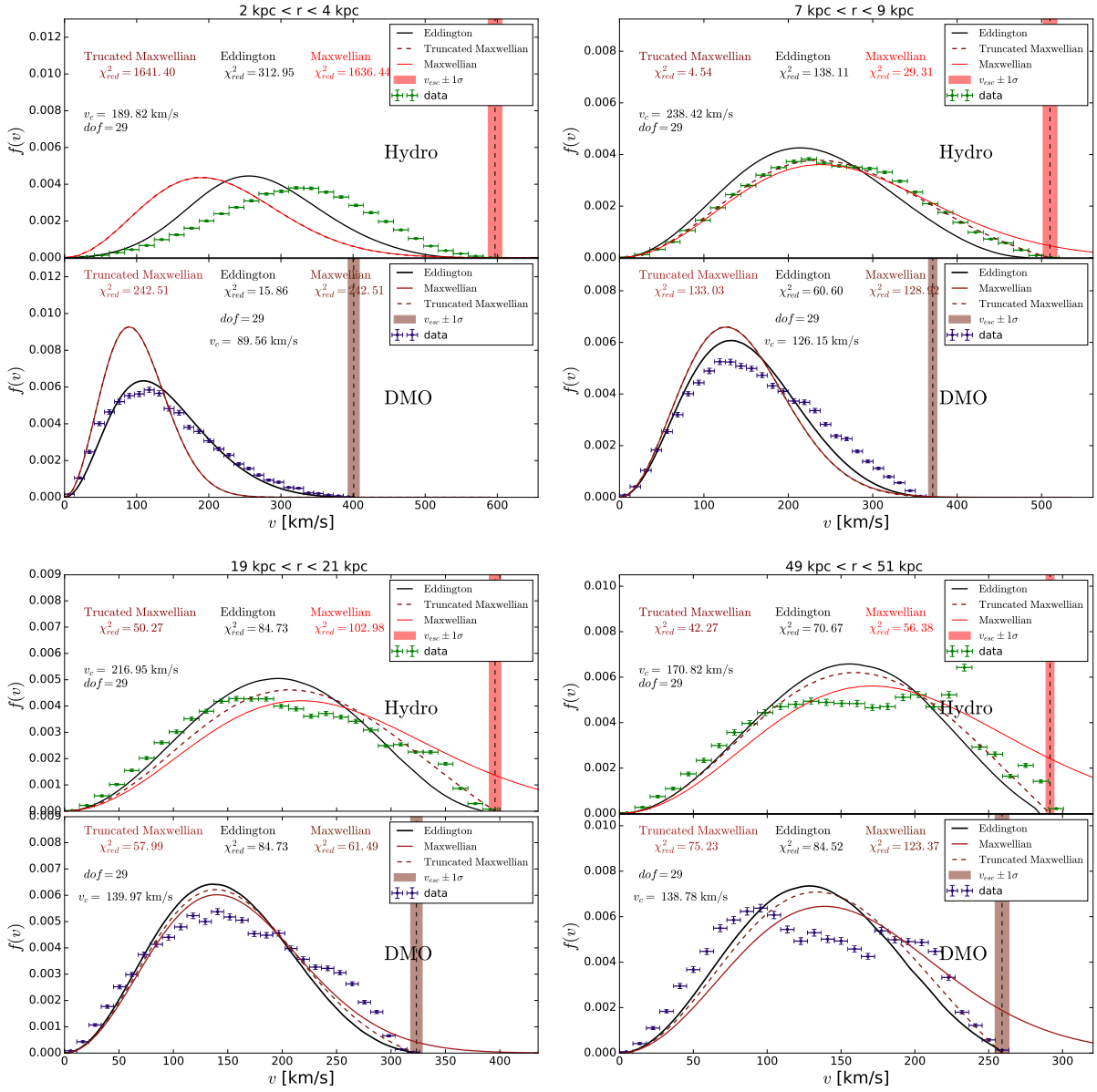

Figure 5.21 – Velocity distributions measured in Halo B, at $2\,\mathrm{kpc} < r < 4\,\mathrm{kpc}$ (upper left panel), $7\,\mathrm{kpc} < r < 9\,\mathrm{kpc}$ (upper right panel), $19\,\mathrm{kpc} < r < 21\,\mathrm{kpc}$ (lower left panel), and $49\,\mathrm{kpc} < r < 51\,\mathrm{kpc}$. We also show the distribution predicted by the Eddington method, the Maxwell-Boltzmann distribution and the smoothly-truncated Maxwell-Boltzmann distribution.

seems to roughly capture the main features observed in the simulations. In particular, it seems to perform better than the Maxwell-Boltzmann approximation, which is widely used in dark matter studies. When completed, our study will include direct comparison of the phase-space distributions from the Eddington method and the simulations, as well as the study of anisotropic cases. This will allow us to have a quantitative estimate of the astrophysical uncertainties in dark matter studies based on Eddington-like methods, and a good idea of the global performance of this framework in dark-matter-related searches.

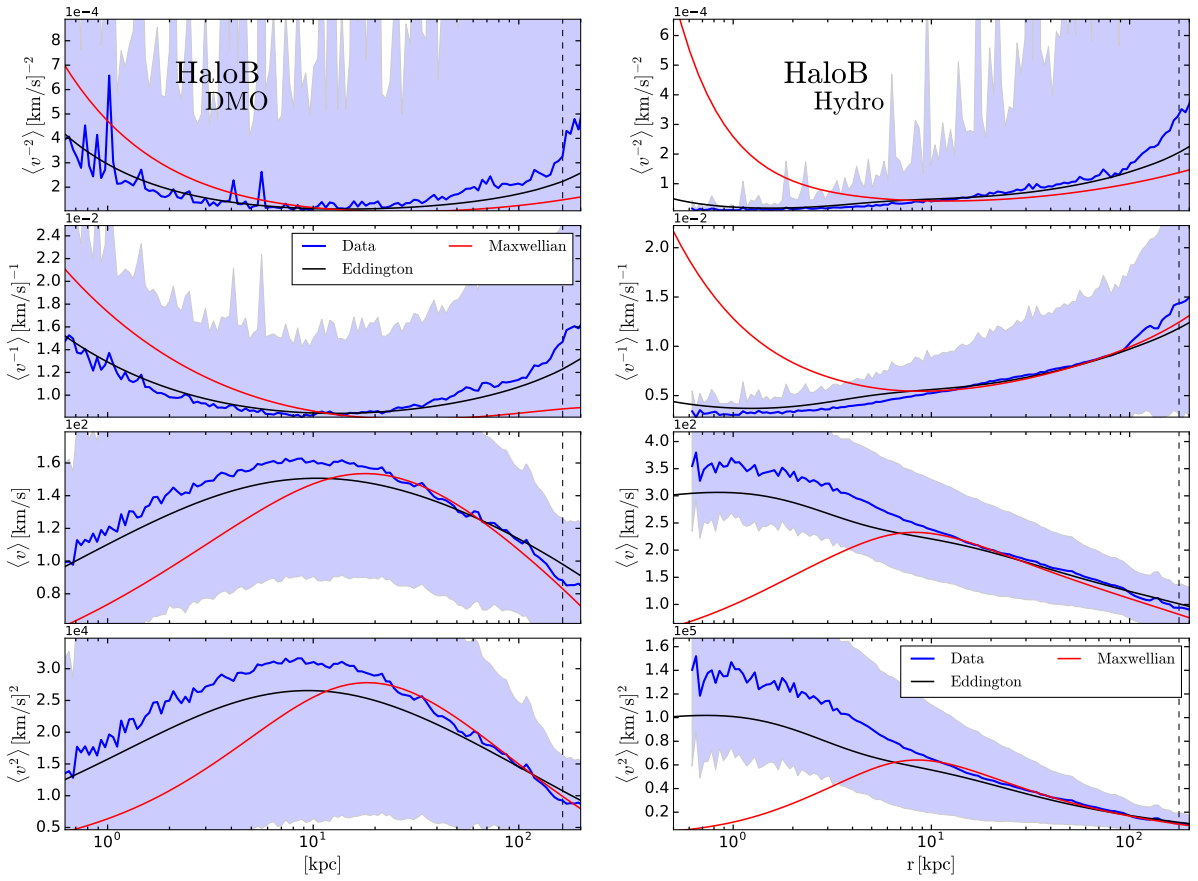

Figure 5.22 – Left panel: moments of the velocity distributions as functions of the radius (blue curves) in the DMO run of Halo B, compared to the moments of the Maxwell-Boltzmann velocity distribution (red curves) and the Eddington velocity distribution (black curves). **Right panel:** same as left panel, for the hydro run of Halo B.

Chapter 6

Impact of the phase space on dark matter searches

In this section, we study the impact of the Eddington inversion formalism on predictions for DM searches. The DM phase-space DF is an important quantity which enters a number of different searches for DM, such as direct searches, indirect searches for p-wave annihilating DM and Sommerfeld-enhanced annihilation, microlensing searches for compact objects and capture of DM by stars. We present general results relevant for all these approaches. We investigate the impact of the regularization methods discussed in the previous chapter on some key observables. Finally, we apply the Eddington formalism to indirect searches for p-wave annihilating DM through cosmic-ray positrons.

6.1 Direct-searches-like observables

6.1.1 Direct searches

The impact of the velocity distribution on the direct detection event rate in Eq. (1.9) has been extensively studied in the literature through numerical (Hansen et al., 2006; Fairbairn & Schwetz, 2009; Vogelsberger et al., 2009; Kuhlen et al., 2010; Mao et al., 2013) and analytical calculations (Evans et al., 2000; Green, 2001, 2017b). The Eddington method, including its anisotropic extensions, has also been used to make predictions (Ullio & Kamionkowski, 2001; Vergados & Owen, 2003; Catena & Ullio, 2012; Pato et al., 2013; Bhattacharjee et al., 2013; Bozorgnia et al., 2013; Fornasa & Green, 2014; Lavalle & Magni, 2015). In particular, differences between the predictions of the Eddington formalism and those of the Standard Halo Model (SHM) have been shown to be important. In the SHM, the velocity distribution in the rest frame of the Galactic halo is assumed to follow the Maxwell-Boltzmann law

$$f_{\rm mb}(\vec{v}) = \left(\pi v_0^2\right)^{-3/2} \exp\left[-\frac{v^2}{v_0^2}\right] . \tag{6.1}$$

The peak velocity v_0 is usually chosen to be the local circular velocity $v_0 = v_{\rm circ}(R_\odot)$. The distribution in Eq. (6.1) extends to arbitrary large velocities while in a collisionless system in equilibrium we do not expect particles to have a speed exceeding the local escape speed $v_{\rm esc}(R_\odot)$. The Maxwell-Boltzmann distribution is often truncated to account for $v_{\rm esc}$. A sharp cut is sometimes implemented

$$f_{\rm sharp}(\vec{v}) = \frac{1}{N_{\rm sharp}} \left[-\frac{v^2}{v_0^2}\right] \Theta(v_{\rm esc} - v) , \tag{6.2}$$

with a normalization

$$N_{\rm sharp} = \left(\pi v_0^2\right)^{3/2} \left[{\rm erf}(z) - \frac{2\,z}{\sqrt{\pi}}\, e^{-z^2}\right] , \tag{6.3}$$

and $z = v_0/v_{\rm esc}$. A sharp truncation is obviously not physical hence a smooth cut is also found in the literature

$$f_{\rm smooth}(\vec{v}) = \frac{1}{N_{\rm smooth}} \left\{ \exp\left[-\frac{v^2}{v_0^2}\right] - \exp\left[-\frac{v_{\rm esc}^2}{v_0^2}\right] \right\} \Theta(v_{\rm esc} - v)\,, \tag{6.4}$$

with

$$N_{\rm smooth} = \left(\pi v_0^2\right)^{3/2} \left[{\rm erf}(z) - \frac{2\,z}{\sqrt{\pi}} \left(1 + \frac{2\,z^2}{3}\right) e^{-z^2} \right]. \tag{6.5}$$

Note that the Maxwell-Boltzmann velocity distribution gives a dynamically consistent description of a collisionless system *only* if the density profile is that of the (infinite) singular isothermal sphere, see Sec. 5.3.2.1. This is not in agreement with observations hence the Maxwell-Boltzmann approximation has little theoretical motivation. Nevertheless, it is often assumed to give a reasonable description of the DM velocity distribution. Speed distributions with the different conventions found in the literature are shown on the left panel in Fig. 6.1. These distributions are computed at the position of the Sun. One sees small differences in the high velocity tail and in the height of the peak.

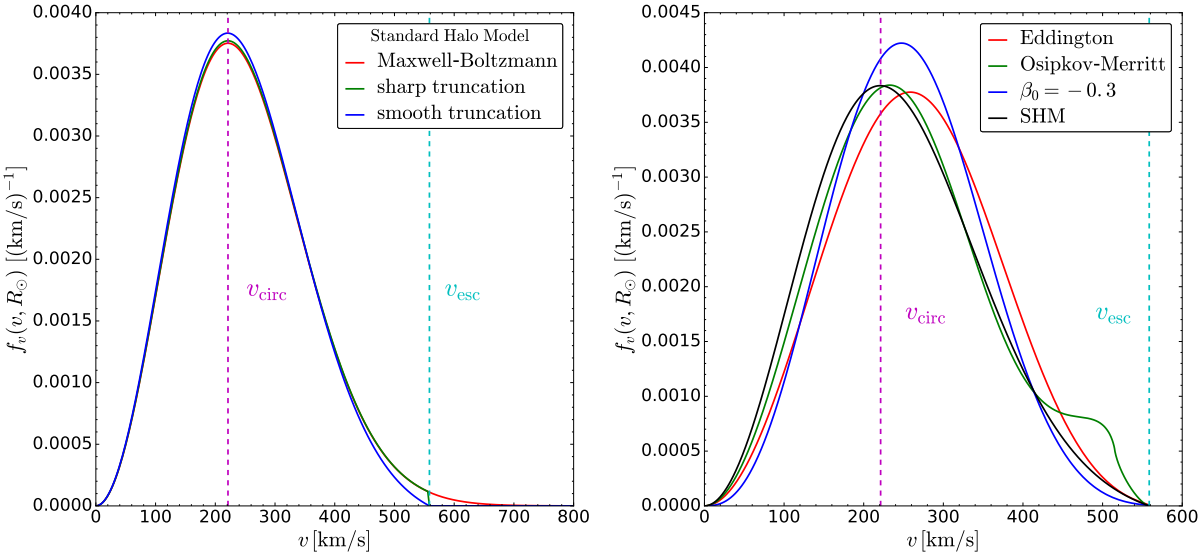

Figure 6.1 – At the position of the Sun $R_\odot = 8.21\,$kpc in the NFW mass model of McMillan (2017). **Left panel:** Speed distribution in the SHM . Are shown the Maxwell-Boltzmann (red curve), sharply cut (green curve) and smoothly cut (blue curve) speed distributions. **Right panel:** Smoothly cut SHM speed DF compared to the Eddington theory for the isotropic (red), Osipkov-Merritt (green) and $\beta_0 = -0.3$ (blue) cases.

We want to compare the Eddington formalism to the SHM with a particular emphasis on the regularization methods we discussed in the previous chapter. We first show the speed distributions predicted by the isotropic (red), OM (green) and constant-β with $\beta_0 = -0.3$ (blue) at $R = R_\odot$ together with the smoothly-cut SHM on the right panel in Fig. 6.1. The phase-space divergence has been removed by hand and the speed distribution artificially renormalized to one. Significant differences between the SHM and the Eddington formalism are visible by eye. Irrespective of the model, the peak of the distribution is at $v > v_{\rm circ}$ rather than $v_{\rm circ}$. The peak is also higher in the constant-β model. This is not surprising since $\beta_0 < 0$ leads to more circular orbits hence a higher peak close to $v_{\rm circ}$. Large differences also appear in the tail: the OM model in particular presents a bump where the divergence was present. The isotropic prediction also has more power in the tail. These features have already been pointed out in the literature (see

*e.g.*Ullio & Kamionkowski (2001); Vergados & Owen (2003); Fornasa & Green (2014)). Several regularization methods are introduced in the previous chapter to deal with the phase-space divergence and these methods lead to different speed distributions for a given mass model. We define a general function to investigate the impact of these regularizations on direct-searches-like observables:

$$\begin{aligned} \Xi_n(v_{\rm min}, v_{\rm max}, r) &\equiv \omega^{-1}(r) \int_{v_{\rm min}\leqslant v\leqslant v_{\rm max}} \mathrm{d}^3\vec{v}\, v^n\, f_{\vec{v}}(\vec{v}, r) \\ \omega(r) &\equiv \int_{v_{\rm min}\leqslant v\leqslant v_{\rm max}} \mathrm{d}^3\vec{v}\, f_{\vec{v}}(\vec{v}, r)\,. \end{aligned} \tag{6.6}$$

This function Ξ allows to investigate moments of the velocity distribution relevant for different DM searches including direct searches and capture by stars ($n = -1$) and microlensing ($n = 1$). A normalization ω is explicitly introduced to get a well-defined average even when the Eddington DF is modified by hand and thus not consistently normalized. We compute the velocity distribution and its moments in the rest frame of the halo and neglect the effects induced by the Galilean transformation to the rest frame of the Earth. This is justified because we essentially try to quantify the differences between the Eddington approach and the SHM, and we do not expect these differences to depend much on the frame of reference. For direct searches, the relevant moment is η given in Eq. (1.14). Ignoring the change of frame, this is

$$\eta(v_{\rm min}) \simeq \Xi_{-1}(v_{\rm min}, v_{\rm esc}, R_\odot)\,. \tag{6.7}$$

We show η as a function of $v_{\rm min}$ in Fig. 6.2. The isotropic prediction is shown in the left panel and the Osipkov-Merritt one is shown in the right panel. The lower panel show the relative difference between the Eddington prediction and the SHM. The largest differences are observed at high values of $v_{\rm min}$, when the contribution of the tail of the speed distribution is most important. This is also where the different regularization methods give the most different results. Neither the sharply-cut nor smoothly-cut SHM are in good agreement with Eddington, though the smoothly-cut SHM is doing significantly better. Comparison with the OM model is shown in the right panel. The differences there are much larger than in the isotropic case. This is not surprising given we have not found any satisfactory way of regularizing the divergence in the OM models, see Sec. 5.4.1. Either the divergence is not removed or the DM density profile is significantly modified.

In conclusion, the prediction of the Eddington theory departs from the SHM in a significant way. The choice of the regularization method is also important, particularly at high $v_{\rm min}$. This could have implication for direct searches of low mass WIMPs, since these DM candidates typically need a large velocity to give a detectable recoil and are therefore sensitive to the high velocity tail of the speed distribution.

6.1.2 Capture by compact objects, microlensing

The function Ξ is related to observables relevant for other types DM searches. In particular, the quantity

$$\overline{\eta}(v_{\rm max}, r) = \Xi_{-1}(0, v_{\rm max}, r) \tag{6.8}$$

appears when computing the number of DM particles captured by stars or planets. This is important since dark matter particles can have an effect on stellar evolution or annihilate at the core into detectable particles like neutrinos (Press & Spergel, 1985; Silk et al., 1985; Gould, 1987; Salati & Silk, 1989; Bouquet & Salati, 1989b,a; Kouvaris, 2008; Bertone & Fairbairn, 2008; Scott et al., 2009). The varying value of $v_{\rm max}$ accounts for the escape speed from the particular object under consideration (star, planet, etc..). The quantity $\overline{\eta}$ at the position of the Sun is shown in Fig. 6.3. Again, differences are observable between Eddington's theory and the SHM. For the

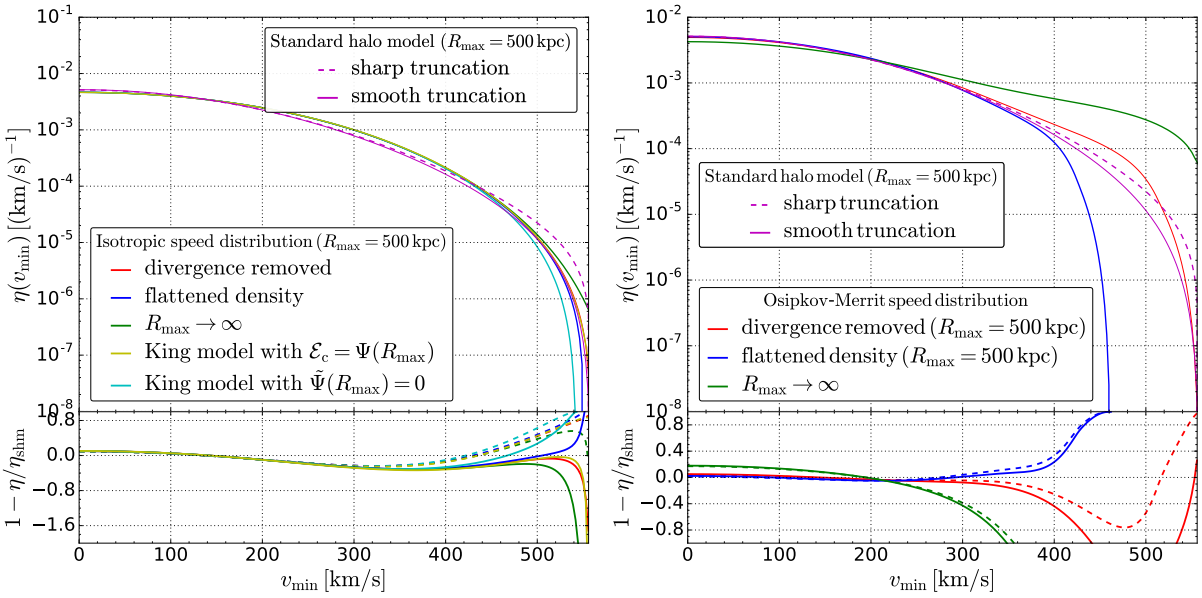

Figure 6.2 – **Left panel:** η integral as a function of $v_{\rm min}$. The various curves shown are the sharply-cut SHM (solid magenta), the smoothly-cut SHM (dashed magenta), and the predictions of the Eddington formalism for an isotropic system, with the regularizations of the phase-space divergence discussed in Sec. 5.4.1, namely setting $R_{\rm max}$ to infinity (green), removing the diverging term (red), modifying the density profile (blue), regularizing à la King with $\mathcal{E}_{\rm c} = \Psi(R_{\rm max})$ (yellow) or with $\tilde{\Psi}(R_{\rm max}) = 0$ (cyan). **Right panel:** Same as left panel, for Osipkov-Merritt.

isotropic case (left panel), the regularization method has little impact on the final prediction. This is because most of the difference resides in the tail of the speed distribution while $\overline{\eta}$ is only sensitive to speeds below $v_{\rm max}$. Differences between the methods are still important in the OM models (right panel).

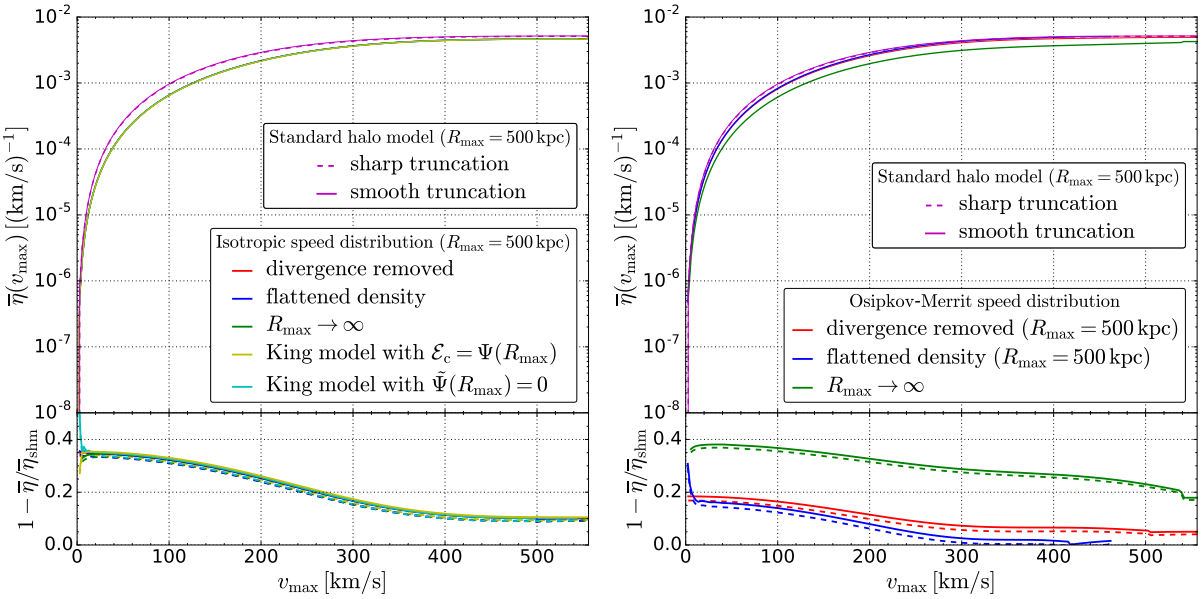

Figure 6.3 – Same as Fig. 6.2 for $\overline{\eta} = \Xi_{-1}(0, v_{\rm max}, R_\odot)$.

Finally, for the sake of completeness we look the mean speed

$$\langle v \rangle\,(r) \equiv \Xi_1(0, v_{\rm esc}, r)\,, \tag{6.9}$$

which is important for computing expected microlensing event rates (Griest, 1991; Green, 2017a).

Microlensing is an interesting probe if DM is made of compact objects. It is relevant for primordial black holes DM (García-Bellido & Clesse, 2018) and axion DM if it forms miniclusters (Fairbairn et al., 2018). The mean speed is shown as a function of the radius in Fig. 6.4 in the isotropic (top left panel), Osipkov-Merritt (top right panel) and $\beta_0 = -0.3$ model (bottom panel). Again, we observe important difference between the Eddington technique and the SHM. While the two methods agree in the outer parts, there prediction significantly differ at the center of the Galaxy, by up to an order of magnitude.

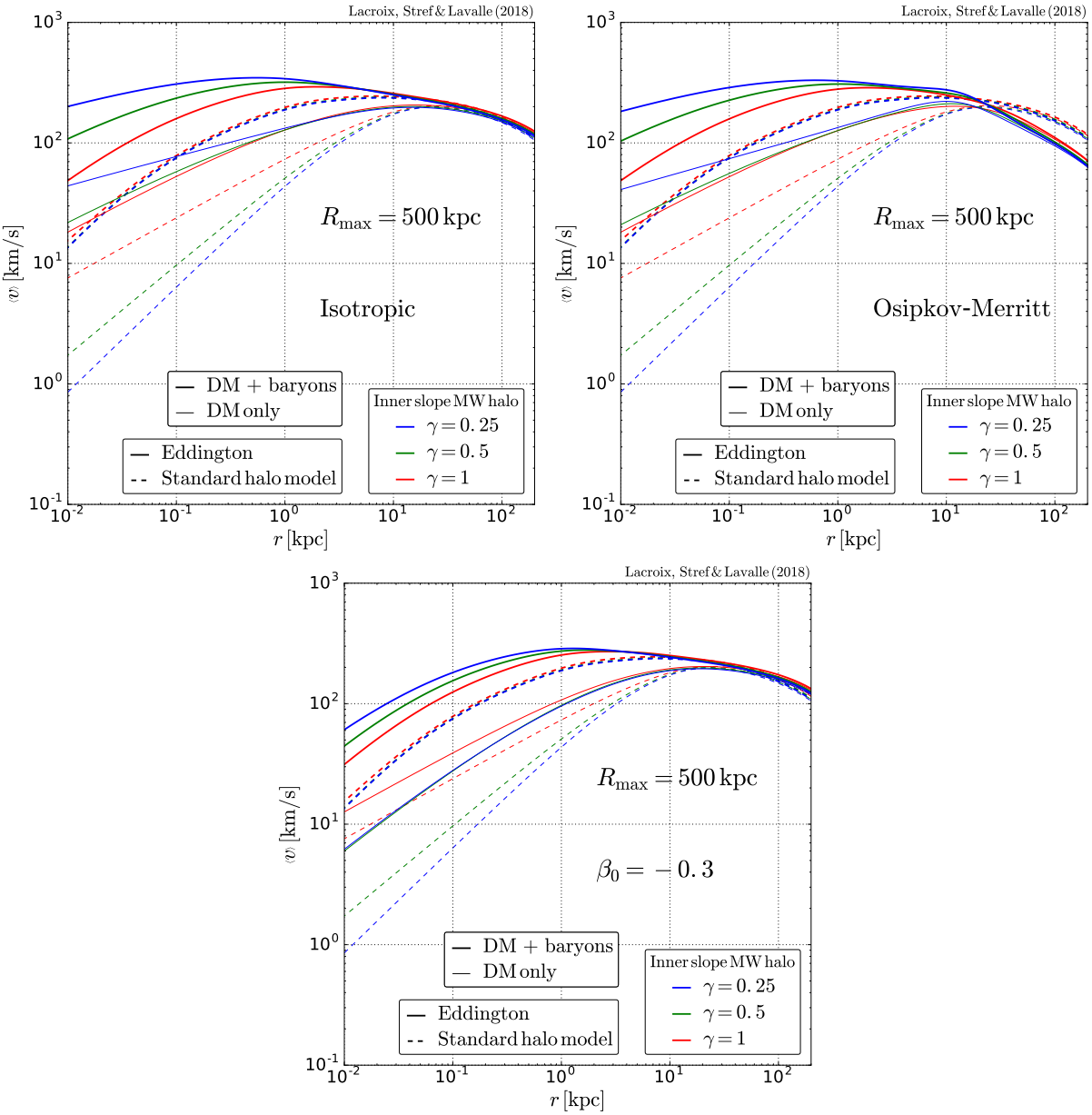

Figure 6.4 – Mean speed profiles for the Standard Halo Model and the Eddington formalism for the isotropic (top left panel), Osipkov-Merritt (top right panel) and $\beta_0 = -0.3$ (bottom panel) cases. Here we show the DM-only (thin line) and DM+baryons (thick line) cases, for the McMillan (2017) mass models providing well-behaved Eddington-inverted DFs.

6.2 Indirect-searches-like observables

In this section, we investigate the impact on indirect searches for annihilating DM. The Eddington method has been used in a few studies to constrain p-wave annihilating DM, see Ferrer & Hunter (2013); Boddy et al. (2017); Petac et al. (2018). Relevant for annihilation is the relative velocity distribution rather than the speed distribution, therefore we introduce a new function

$$\begin{aligned} \langle v_{\rm r}^n \rangle &\equiv \kappa^{-1}(r) \int \mathrm{d}^3\vec{v}_1 \int \mathrm{d}^3\vec{v}_2 \; |\vec{v}_{\rm r}|^n \; f_{\vec{v}}(\vec{v}_1, r)\, f_{\vec{v}}(\vec{v}_2, r) \\ \kappa(r) &\equiv \int \mathrm{d}^3\vec{v}_1 \int \mathrm{d}^3\vec{v}_2 \, f_{\vec{v}}(\vec{v}_1, r)\, f_{\vec{v}}(\vec{v}_2, r)\,, \end{aligned} \tag{6.10}$$

where $\vec{v}_{\rm r} = v\vec{v}_2 - \vec{v}_1$ is the relative velocity. Searches for p-wave annihilating DM typically probe the $n = 2$ moment *i.e.* the relative velocity dispersion. In some cases, the annihilation cross-section can be strongly impacted by non-perturbative effects that lead to the so-called Sommerfeld enhancement (Sommerfeld, 1931; Hisano et al., 2003, 2004, 2005; Profumo, 2005; Cirelli et al., 2007; March-Russell et al., 2008; Arkani-Hamed et al., 2009; Pospelov & Ritz, 2009; Lattanzi & Silk, 2009). In that particular case, the relevant moment is $n = -1$, or $n = -2$ near the resonance features appearing in the cross-section. It is more convenient for computations to perform a change of variables $(\vec{v}_1, \vec{v}_2) \to (\vec{v}_{\rm c}, \vec{v}_{\rm r})$ in Eq. (6.10) with

$$\left\{ \begin{array}{ll} \vec{v}_{\rm c} & = (\vec{v}_1 + \vec{v}_2)/2 \\ \vec{v}_{\rm r} & = \vec{v}_2 - \vec{v}_1 \end{array} \right. \iff \left\{ \begin{array}{ll} \vec{v}_1 & = \vec{v}_{\rm c} - \vec{v}_{\rm r}/2 \\ \vec{v}_2 & = \vec{v}_{\rm c} + \vec{v}_{\rm r}/2 \end{array} \right. \tag{6.11}$$

as it is usually done when computing the DM annihilation rate in the early Universe (Gondolo & Gelmini, 1991). Details on the computation are given in App. E. The computation of the moments in the general anisotropic case is an original result. We show the moments $n = -2, -1, 1, 2$ in Fig. 6.5 for the isotropic case, in Fig. 6.6 for the Osipkov-Merritt models and Fig. 6.7 for the constant-β model. Following our discussion regarding the stability of the DFs in the previous chapter, we only consider here mass models leading to stable solutions of the Boltzmann equation. The velocity distribution in the Eddington case have been computed *without* the diverging term. We recall that this is in practice similar to assuming a flattened density profile at the outskirts of the halo. One see in Fig. 6.5 that, for both the SHM and the Eddington model, the moments with and without baryons converge at large radii. This is because the total mass, and therefore the gravitational dynamics, is then fully dominated by dark matter, and baryons become irrelevant. Though similar in shape, predictions from the two models are numerically quite different. For the $n > 0$ moments, the Eddington model's predictions typically exceed the SHM's. At the center of the Galaxy, the two models differ by at least an order of magnitude, up to three orders of magnitude. The hierarchy of the moments with respect to the value of the dark matter inner slope is also reverted. While the cuspiest mass model ($\gamma = 1$) leads to the largest prediction for the SHM, it is the model the closest to the core ($\gamma = 0.25$) that dominates the Eddington result. We stress that even locally at $r = R_\odot \sim 8$ kpc, and for all n, there are sizeable differences between the Eddington formalism and the Maxwell-Boltzmann approximation. Therefore, since the Eddington formalism turns out to better capture the dynamical properties of the dark matter halo than the SHM, the latter should only be used to make very rough estimates of p-wave annihilating dark matter signals, even when isotropy is assumed.

We also compared the (isotropic) SHM with some of the anisotropic extensions of the Eddington formalism. The prediction of the Osipkov-Merritt model is shown in Fig. 6.6 for a particular choice of the anisotropy radius $r_{\rm a} = r_{\rm s}$. Note that the value of $r_{\rm s}$ depends on the underlying mass model. The result is close to the isotropic case at radii $r \ll r_{\rm a}$, as expected from the behaviour of the anisotropy parameter. At large radii however, the slope of the moments steepens significantly. The steepening starts roughly where $r \simeq r_{\rm a}$ which is where the system begins to be strongly anisotropic. We stress again that the regularization of the diverging term

changes considerably the underlying profile density profile in the Osipkov-Merritt case (see the previous chapter). The behaviour of $\langle v_r^n \rangle$ beyond $r = r_a$ should therefore be treated with caution. We also studied the constant-β case, focusing on $\beta_0 = -0.3$. We considered a negative anisotropy to get a well-defined DF for all the mass models of relevance here. The corresponding relative speed moments are shown in Fig. 6.7. They differ from the isotropic ones at all radii, unlike the Osipkov-Merritt ones, which is not surprising since the constant anisotropy is non-zero everywhere.

Regardless of the assumption made on the anisotropy, the Eddington formalism generically predicts huge differences with respect to the SHM. The various anisotropic models used allow us to bracket the theoretical uncertainty on the Eddington method.

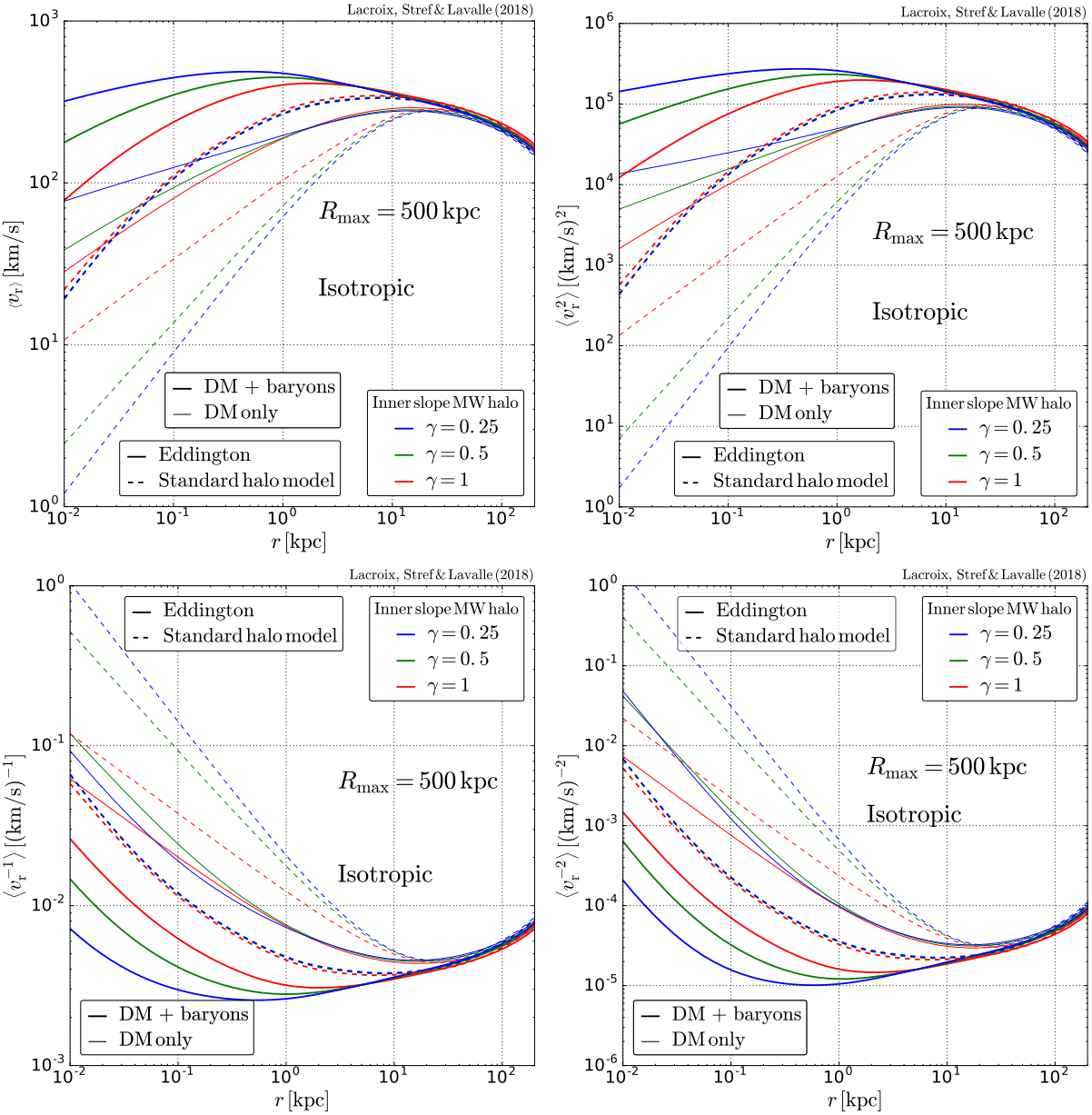

Figure 6.5 – Moments of the relative velocity distribution, for the Standard Halo Model and the Eddington formalism (isotropic case). Here we show the DM-only (thin line) and DM+baryons (thick line) cases, for several mass models from McMillan (2017).

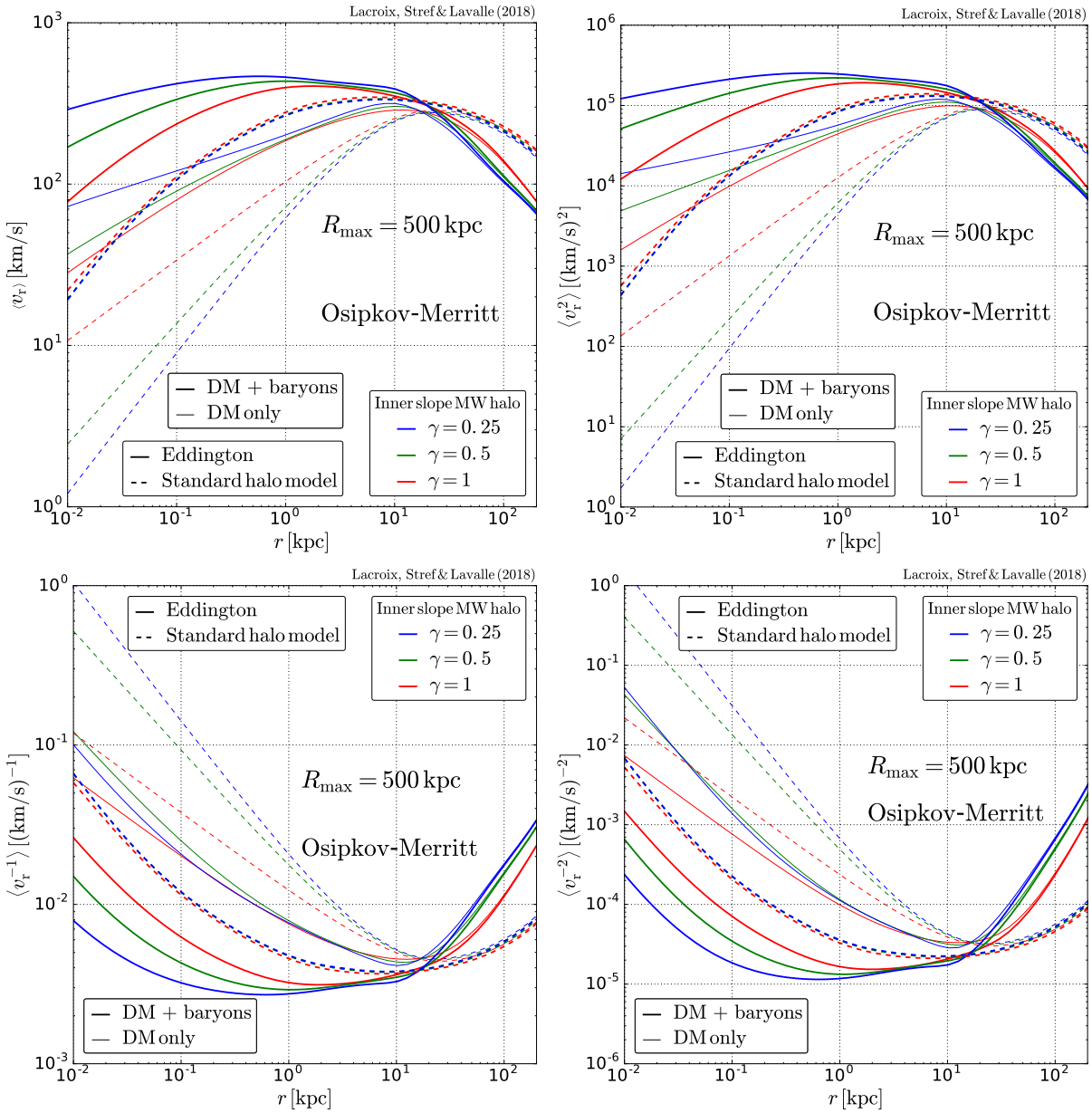

Figure 6.6 – Same as Fig. 6.5, for the Osipkov-Merritt model with $r_{\rm a} = r_{\rm s}$.

6.3 New bounds on p-wave annihilating dark matter

We turn to a direct application of the Eddington formalism: the constraint of p-wave annihilating dark matter using cosmic-ray positrons. This work is an extension of the study done by Boudaud et al. (2017) (hereafter B16). We first review the analysis and results of B16, then use the same idea to derive new bounds on p-annihilating dark matter. This work was done in collaboration with Mathieu Boudaud, Thomas Lacroix, Julien Lavalle and Pierre Salati.

The authors of B16 derived new constraints on the s-wave annihilation cross-section for dark matter masses in the MeV to TeV range. They studied the contribution of dark matter annihilation, as well as decay, into electrons and positrons and use measurements of the cosmic-ray fluxes of these species to derive new limits. These limits are especially important in the MeV mass range. WIMPs with MeV masses are not light enough to differ significantly from CDM on observable scales, however a variety of scenarios involve dark matter particles in this range and provide potential solutions to the small-scale issues (we refer to Sec. 1.4 for a discussion

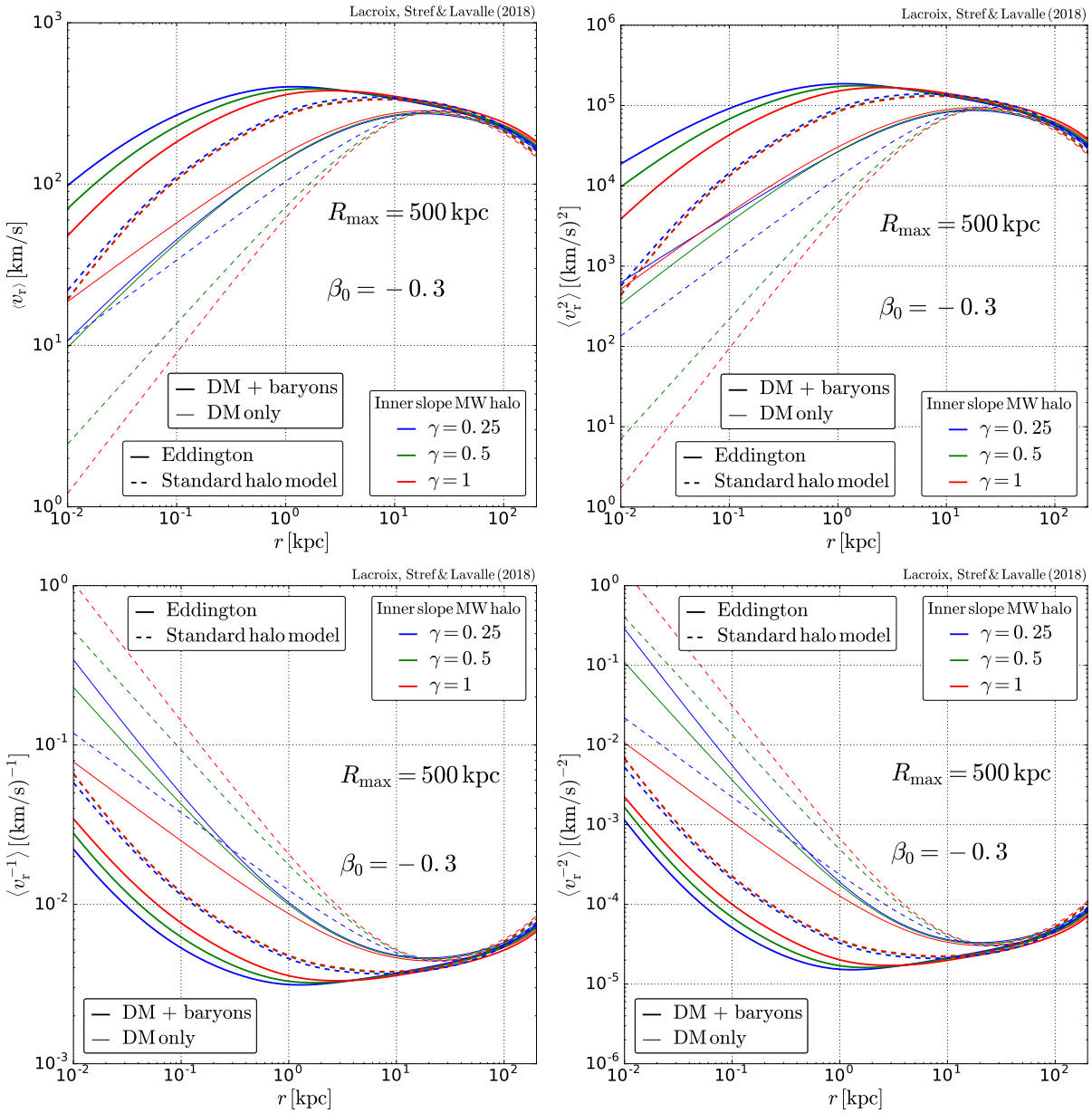

Figure 6.7 – Same as Fig. 6.5, for the constant-β model with $\beta_0 = -0.3$.

on these small-scale problems). For instance, self-interacting dark matter (Chu et al., 2016) and strongly-interacting dark matter (Hochberg et al., 2014) can both be produced thermally if the dark matter particle has a mass in the MeV range. Alternatively, if dark matter is coupled to radiation long enough, an oscillatory pattern appears in the power spectrum which can help resolve the small-scale tensions (Boehm et al., 2004, 2014). MeV dark matter is already constrained by a number of observables, including indirect searches with gamma rays (Beacom et al., 2005; Essig et al., 2013). The most stringent bounds currently available are coming from the CMB which is very sensitive to energy injection by annihilation or decay at the time of recombination (Chen & Kamionkowski, 2004; Slatyer, 2016a; Liu et al., 2016; Poulin et al., 2016).

Dark matter annihilation in the MeV mass range is difficult to probe with cosmic radiation because sub-GeV cosmic rays are affected by Solar modulation (see Sec. 4.3). The Solar magnetic field forbid charged particles with sub-GeV energies to reach the Earth. This Solar shielding extends up to a region called the heliopause. Fortunately, the *Voyager 1* spacecraft (Krimigis et al., 1977) crossed the heliopause during the summer of 2012 (Stone et al., 2013). The spacecraft

carries a "golden record", destined to advanced extra-terrestrial civilizations, containing among other things music from such luminaries as Johann Sebastian Bach and Chuck Berry. Of more direct interest to us is the presence on-board of a cosmic-ray detector sensitive to electrons and positrons (without discrimination between the two). High-statistics measurements of the $e^+ + e^-$ flux *unaffected by Solar modulation* is therefore available in Stone et al. (2013); Cummings et al. (2016).

6.3.1 Bounds on s-wave annihilation

The authors of B16 used two propagation models for $e^\pm$. The first model, dubbed A in their analysis, is the MAX model whose propagation parameters are shown in Tab. 4.1. The second model, dubbed B, is the model of Kappl et al. (2015) (K15), whose parameters are also shown in Tab. 4.1. Both propagation models have comparable values for all parameters except the Alfven speed V_a. This speed controls the efficiency of reacceleration processes in the magnetic halo. Cosmic rays injected at a given energy E and subject to a strong reacceleration can be detected at energies $E' > E$. In this case, model A has an efficient reacceleration ($V_\mathrm{a} = 117.6\,\mathrm{km/s}$) while reacceleration in model B is much less efficient ($V_\mathrm{a} = 31.9\,\mathrm{km/s}$). This has strong consequences on the $e^\pm$ flux, as shown in the right panel in Fig. 6.8. For a dark matter particle with mass $m = 10\,\mathrm{MeV}$ annihilating into e^+e^-, the $e^+ + e^-$ flux is shown for model A (green) and model B (blue). While the flux in the B model sharply falls at $E = 10$ MeV, it extends up to more than 1 GeV in the A model. This also implies that at a given mass, the A propagation model is more sensitive to the data points of AMS than the B model.

Solving the propagation equation for electrons and positrons is technically very involved because energy losses and reacceleration are not confined to the disc, as is the case for nuclei, but extend to the whole diffusive halo. A semi-analytic framework to consistently solve the propagation equation was successfully built by Boudaud et al. (2017). This "pinching" method was used in B16 and is also used in our new p-wave analysis.

The bounds on the s-wave annihilation cross-sections obtained by B16 are shown in the right panel on Fig. 6.8, for different annihilation channels. The most stringent bound is obtained, unsurprisingly, for dark matter annihilating directly to electrons and positrons. These bounds are conservative: the B propagation model, with low reacceleration, is used and the Fisk potential accounting for solar modulation is fixed to $\phi_\mathrm{F} = 0.83$ GV (which the maximum value found in Ghelfi et al. (2016)). We note the presence of a "gap" in the exclusion curve *i.e.* the curve increases then sharply decreases again. This is due to the energy range 0.4 MeV to 2 GeV left unexplored by both *Voyager 1* and AMS. These bounds are about an order of magnitude less stringent than those found with the CMB (Liu et al., 2016) and slightly better than those inferred from gamma rays (Essig et al., 2013).

6.3.2 Bounds on p-wave annihilation

We now turn to the computation of the p-wave bounds. The best p-wave bounds currently available at low masses are coming from the CMB (Liu et al., 2016). A rough order-of-magnitude estimate tells us that our bounds should be much better than the CMB's. The CMB bounds are derived assuming a velocity dispersion $\sigma_\mathrm{v} = 100\,\mathrm{km/s}$ for WIMPs at the time of recombination. In the Solar neighbourhood, the WIMP velocity dispersion should be comparable to the local circular velocity $\sigma_v^\mathrm{MW}/\sqrt{2} \sim v_\mathrm{c}(R_\odot) \simeq 240\,\mathrm{km/s}$. To obtain the "CMB-like" p-wave bound from the s-wave bound shown in Fig. 6.8, one can rescale the curves by a factor $(\sigma_v/\sigma_v^\mathrm{CMB})^2$ 0.1. This leads to an exclusion curve which is about five orders of magnitude better than the CMB's. This motivates us to investigate the p-wave calculation in a more detailed fashion.

Let us write the annihilation cross-section as

$$\langle \sigma_\mathrm{ann} v \rangle = \langle \sigma_\mathrm{ann} v \rangle_0 + \sigma_1 c \frac{\langle v_\mathrm{r}^2 \rangle}{c^2} + ... \tag{6.12}$$

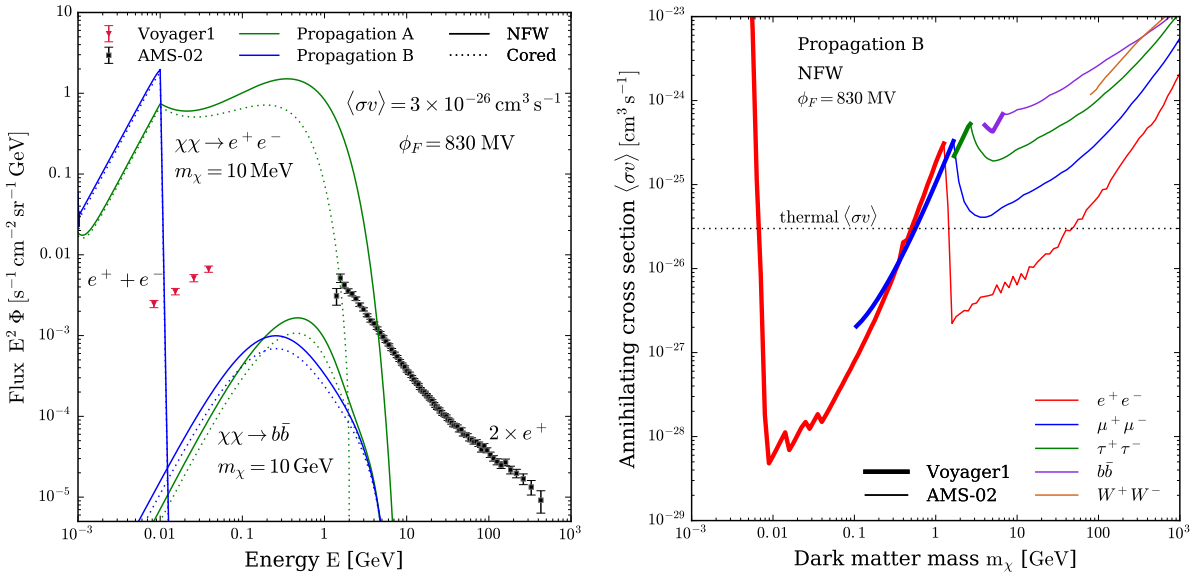

Figure 6.8 – Left panel: predictions ($e^{\pm}$) for two template cases: a 10 MeV WIMP annihilating into e^+e^- (plus final-state radiation), and a 10 GeV WIMP annihilating into $b\bar{b}$. We show the $e^+ + e^-$ data from *Voyager* (red trianges) and the $2e^+$ data from AMS-2 (black squares). The AMS-2 e^+ data is multiplied by two to compare with the $e^+ + e^-$ data from *Voyager*. The AMS-2 data are demodulated with a Fisk potential $\phi_{\rm F} = 0.83$ GV. Propagation models *A* and *B*, and the NFW and cored profiles were used. **Right panel:** limits from different annihilation channels, assuming model *B*, an NFW profile and $\phi_{\rm F} = 0.83$. Both plots are taken from Boudaud et al. (2017).

where $\langle\sigma_{\rm ann}v\rangle_0$ is the *s*-wave contribution, $\sigma_1 c$ is the amplitude of the *p*-wave contribution and $\langle v_{\rm r}^2\rangle$ is the relative velocity dispersion. Here we assume $\langle\sigma_{\rm ann}v\rangle_0 = 0$ and put constraints on $\sigma_1 c$. All higher-order terms are neglected.

The electron/positron flux can be written in the Green's function formalism

$$\frac{{\rm d}\phi}{{\rm d}\Omega\,{\rm d}E} = \frac{\sigma_1 c}{2\,m^2}\int {\rm d}E_{\rm s}\int {\rm d}^3\vec{x}_{\rm s}\,G_e(E_{\rm s},\vec{x}_{\rm s}\to E,\vec{x})\,\frac{{\rm d}N_e}{{\rm d}E}(E_{\rm s})\,\rho(\vec{x}_{\rm s})\,\frac{\langle v_{\rm r}^2\rangle}{c^2}\,. \tag{6.13}$$

The injection spectrum ${\rm d}N_e/{\rm d}E$ is generated with the *MicrOMEGAs* code (Bélanger et al., 2015). The function G_e is a Green's function of the propagation equation Eq. (4.43). It is convenient to define an effective annihilation profile

$$\rho^2_{\rm eff}(r) \equiv \rho^2(r)\,\frac{\langle v_{\rm r}^2\rangle}{c^2}\,, \tag{6.14}$$

which contains all the relevant information on the dark matter phase-space distribution. We compute the relative velocity dispersion using the Eddington formalism. We considered three cases: the isotropic DF, the Osipkov-Merritt model, and the constant anisotropy model with $\beta_0 = -0.3$. We also compare with the prediction of the Standard Halo model given in Eq. (6.4). Two dark matter profiles are considered: the $\gamma = 1$ and $\gamma = 0.25$ profiles of McMillan (2017). We do not consider the cored profile ($\gamma = 0$) because the Eddington method leads to an unstable DF in that case (see Sec. 5.4). The effective annihilation profiles are shown in Fig. 6.9. As we have already seen in the previous section, the prediction of the Eddington model and its extensions lead to a larger velocity dispersion than the SHM over a wide range of radii.

We show the resulting bounds in Fig. 6.10. Our bounds are derived for the same propagation models *A* and *B* as B16. The left panel shows the bounds assuming an NFW dark matter profile and the right panel shows the bounds for $\gamma = 0.25$. We note that the central slope of the dark matter profile has very impact on the bound obtained with *B* propagation model, while the *A* model is more sensitive to the shape of the dark halo. This difference in sensitivity is due to

reacceleration: in model A, electrons and positrons being injected near the center of the halo are subject to efficient enough reacceleration to reach the Earth. In model B, however, e^+ and e^- have a more local origin. The uncertainty due to our lack of knowledge of the anisotropy in the dark halo is represented with a coloured band around each exclusion curve. This uncertainty is estimated thanks to our three models for anisotropy (isotropic, Osipkov-Merrit, constant-β). It is found to be very small regardless of the propagation model or the shape of the dark matter halo. The uncertainty associated with propagations, however, is very important especially at low mass and in the "gap" corresponding to the unexplored energy range. We compare our bounds to those obtained from the CMB by Liu et al. (2016) and the bound from dwarf spheroidal galaxies computed by Zhao et al. (2016).

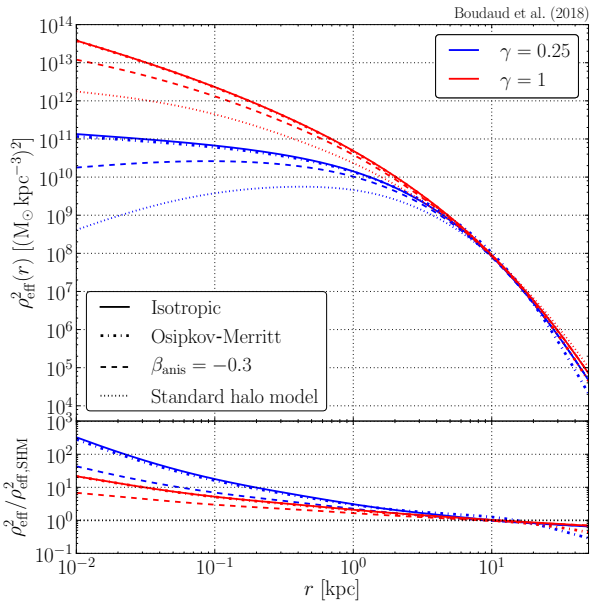

Figure 6.9 – Effective annihilation profiles as defined in Eq. (6.14). We show the prediction of Eddington's method in the isotropic case (solid line), the Osipkov-Merrit model (dotted-dashed), the constant-β model with $\beta_0 = -0.3$ (dashed) and SHM (dotted). Effective profiles are shown for the $\gamma = 1$ (red) and $\gamma = 0.25$ (blue) mass models.

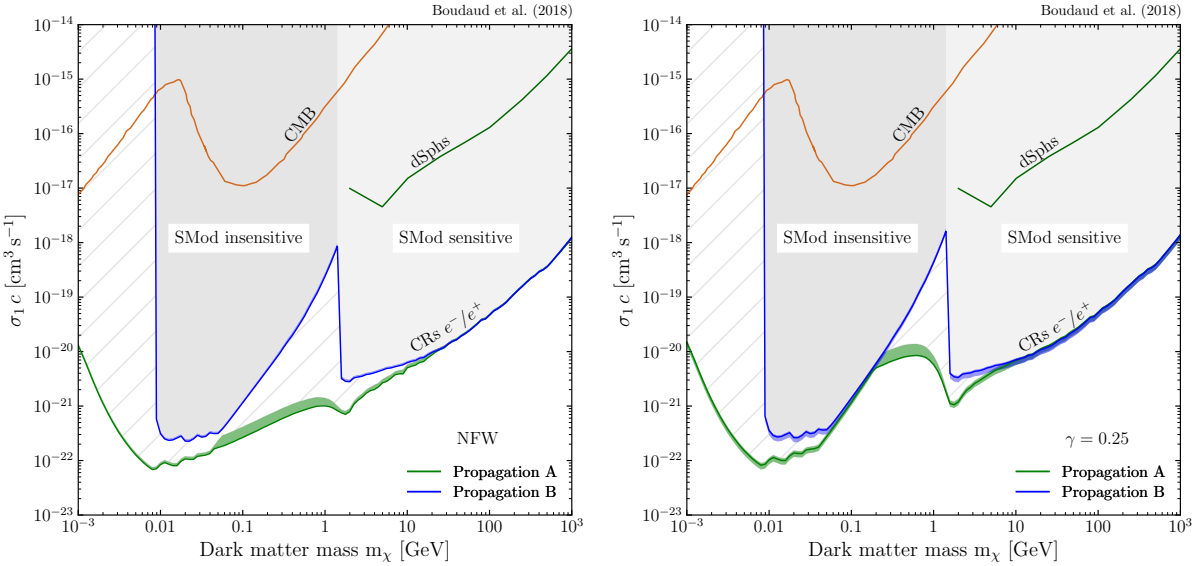

Figure 6.10 – Left panel: p-wave exclusion curves for the propagation model A (green) and B (blue). We highlight the region unaffected by Solar modulation, corresponding to the data points from *Voyager 1*. The dark matter halo is the NFW profile of McMillan (2017). **Right panel:** same as the left panel for the $\gamma = 0.25$ mass model.

Conclusion

In this work, we have focused on several aspects of particle dark matter on the Galactic scale. Several general guidelines were followed. We focused on building models and developing tools which allow to capture the structuring of dark matter while remaining consistent with observational constraints. This is of importance since Galactic dynamics is now entering an era of very high precision with the recent data release from the Gaïa satellite. A precise evaluation of the astrophysical uncertainties affecting dark matter searches was one of our main objective. Another was to develop techniques applicable to a wide range of dark matter models.

Our main achievement is the construction of the first model of Galactic subhalos consistent with dynamical constraints. We recall the main ingredients of this model. First, we start from a dynamically constrained mass model of the Galaxy (or any other galaxy, since our model is not specific to the Milky Way). We assume subhalos are spatially distributed along the constrained dark matter density profile. The mass and concentration distributions of subhalos are those of *field* halos, which can be safely extracted from N-body simulations or derived from analytic computations (following the Press-Schechter theory for the mass function and the Bullock et al. model for the concentration, for instance). We then account for the interactions between subhalos and the host galaxy by computing a tidal for each subhalo. This computation is done in performed using the mass distributions given by the mass model *i.e.* it is also consistent with observational constraints. We take into account the effect of the tidal stripping by the gravitational potential of the galaxy, as well as the effect of shocking induced by the stellar disc. For this last effect, we propose our own simple definition of the tidal radius and shown that tidal shocking is very efficient at stripping subhalos from their mass, a result in agreement with simulations. From this computations, we built a distribution function describing the Galactic subhalo population. The post-tides mass and concentration distributions, as well as the subhalo number and mass densities are evaluated. We show that all these quantities strongly depart from their initial, cosmological value.

Our model of subhalos can be applied to a number of dark-matter-related studies. Perhaps the most obvious application is indirect searches, where subhalos have been known to play an important role. The systematic enhancement of the annihilation signal, the "boost", is estimated thanks to our model. Theoretical uncertainties associated to the small-scale power spectrum, the dark matter free-streaming scale and the disruption of subhalos by tidal effects are estimated. We first apply our model to gamma-ray searches and show that the boost can very easily be of more than 100%, which we should dramatically improve exclusion bounds set with the diffuse gamma ray background. We investigated another complementary channel with cosmic-ray antiprotons. There again, the boost is shown to be significant. Using several propagation models, we compute exclusion bounds by exploiting the latest data from AMS-2. This shows in particular how important it is to incorporate subhalos when trying to interpret an excess in terms of dark matter annihilation.

A complementary work was done on the Eddington inversion method, a tool devised to infer the phase-space distribution function of collisionless system starting from its density and gravitational potential. This method is of great interest for dark matter searches because it allows to make prediction which are both theoretically consistent (we are using solutions of the collisionless Boltzmann equation) and in agreement with the observed dynamics (which gives the

density profile and potential). While the appealing character of this method was already pointed before, its limitations have been overlooked when applied to dark matter searches. A serious problem appears when this technique is applied to finite systems. In this case, the Eddington solution present an unphysical divergence, which must be removed to get acceptable results. We propose a number of possible solutions to this issue. Another problem is related to the stability of Eddington's solution. We show that stability considerations restrict the domain of applicability of Eddington's method and that some realistic halo configurations actually outside of this domain.

We investigate in a rather general way the impact of these considerations on observables relevant for direct and indirect searches. We show that these theoretical issues are of importance if one wants to make reliable prediction using Eddington's theory. To illustrate the potential of this method for dark matter searches, we use cosmic-ray electrons and positrons measured by *Voyager 1* to get new stringent bounds on p-wave annihilating dark matter. The use of Eddington's method allows to bracket the uncertainties due to our lack of knowledge of the velocity anisotropy in the dark halo.

A number of projects related to these topics are currently being worked out. We are currently working on the application of our subhalo model to gamma-ray searches with the aim of deriving stringent bounds using the data from Fermi and making prospects for CTA. I am also working together with J. Silk and T. Nakama on deriving new constraints on ultracompact minihalos, a natural extension of CDM subhalos. The clustering of CDM is also relevant for primordial black holes and axion miniclusters. The impact of clustering on microlensing constraints on the fraction of these objects in the halo is currently largely unexplored. We are currently investigating this problem with Sébastien Clesse. Finally, I would like to mention projects related to Galactic dynamics. I am working together with Raphaël Errani and Thomas Lacroix on the use of the Eddington method to model the effect of tides on subhalos. We are also investigating potential signatures of the collective effect of a large population of subhalos on stellar objects such as binaries and stellar streams.

Appendices

Appendix A

Mathematical functions and identities

A.1 Error function

The error function is defined as

$$\operatorname{erf}(x) \equiv \frac{2}{\sqrt{\pi}} \int_0^x e^{-t^2} \mathrm{d}t \,. \tag{A.1}$$

It is normalized so that

$$\operatorname{erf}(x) \underset{x\to\infty}{\to} 1 \,. \tag{A.2}$$

Also useful is the complementary error function

$$\begin{aligned} \operatorname{erfc}(x) &\equiv 1 - \operatorname{erf}(x) \\ &= \frac{2}{\sqrt{\pi}} \int_x^\infty e^{-t^2} \mathrm{d}t \,. \end{aligned} \tag{A.3}$$

A.2 Gamma and beta functions

The gamma function is defined for all complex numbers except non-positive integers as

$$\Gamma(x) \equiv \int_0^\infty t^{x-1} e^{-t} \mathrm{d}t \,. \tag{A.4}$$

It has the following remarkable property

$$\Gamma(x+1) = x\,\Gamma(x) \,, \tag{A.5}$$

which immediatly leads

$$\Gamma(n) = (n-1)! \text{ if } n \geqslant 1 \text{ is an integer} \,. \tag{A.6}$$

It has the following particular values

$$\begin{aligned} \Gamma\left(\frac{1}{2}\right) &= \sqrt{\pi} \\ \Gamma\left(\frac{3}{2}\right) &= \frac{\sqrt{\pi}}{2} \\ \Gamma\left(\frac{5}{2}\right) &= \frac{3\sqrt{\pi}}{4} \,. \end{aligned}$$

A closely-related function is the beta function

$$B(x,y) \equiv \int_0^1 t^{x-1}(1-t)^{y-1}\,\mathrm{d}t\,, \tag{A.7}$$

which is related to Γ through

$$B(x,y) = \frac{\Gamma(x)\Gamma(y)}{\Gamma(x+y)}\,. \tag{A.8}$$

A.3 Riemann zeta function

The Riemann zeta function is defined for all complex number s with $\mathrm{Re}(s) < 1$ as the analytic continuation of the series

$$\zeta(s) \equiv \sum_{n=1}^{\infty} \frac{1}{n^s}\,. \tag{A.9}$$

It is related to the gamma function through the identity

$$\zeta(x)\,\Gamma(x) = \int_0^\infty \frac{t^{x-1}}{e^t-1}\,\mathrm{d}t\,. \tag{A.10}$$

It has the particular values

$$\begin{aligned} \zeta(-1) &= -\frac{1}{12} \\ \zeta(0) &= -\frac{1}{2} \\ \zeta(2) &= \frac{\pi^2}{6} \\ \zeta(4) &= \frac{\pi^4}{90} \end{aligned}$$

The motivated reader can try to prove that all the non-trivial zeros s of ζ have $\mathrm{Re}(s) = 1/2$.

A.4 Bessel functions

A.4.1 Bessel function of the first kind

The Bessel function of the first kind J_α is defined as the solution of the ordinary differential equation

$$x^2\frac{\mathrm{d}^2 J_\alpha}{\mathrm{d}x^2} + x\,\frac{\mathrm{d}J_\alpha}{\mathrm{d}x} + (x^2-\alpha^2)\,J_\alpha = 0\,. \tag{A.11}$$

The solution has the expression

$$J_\alpha(x) = \sum_{n=0}^{\infty} \frac{(-1)^n}{n!\,\Gamma(n+\alpha+1)}\left(\frac{x}{2}\right)^{2n+\alpha}\,. \tag{A.12}$$

If α is an integer, it has an integral representation

$$J_\alpha(x) = \frac{1}{\pi}\int_0^\pi \cos(\alpha\pi - x\sin(\tau))\,\mathrm{d}\tau\,. \tag{A.13}$$

A.4.2 Modified Bessel functions of the second kind

The modified Bessel function of the second kind K_α is defined as the decaying solution of the differential equation

$$x^2 \frac{\mathrm{d}^2 y}{\mathrm{d}x^2} + x \frac{\mathrm{d}y}{\mathrm{d}x} - (x^2 + \alpha^2) y = 0\,. \tag{A.14}$$

If $\alpha > -1/2$, this solution can be expressed as an integral

$$K_\alpha(x) = \frac{\sqrt{\pi}}{\Gamma(\alpha + 1/2)} \left(\frac{x}{2}\right)^\alpha \int_1^\infty e^{-tx} (t^2 - 1)^{\alpha - 1/2} \mathrm{d}t\,. \tag{A.15}$$

The following recurrence relation is useful

$$C_{\alpha-1}(x) - C_{\alpha+1}(x) = \frac{2\alpha}{x} C_\alpha(x)\,, \tag{A.16}$$

where $C_\alpha \equiv e^{i\alpha\pi} K_\alpha$.

A.5 Fourier transform

The Fourier transform of a function f is defined as

$$\hat{f}(\vec{k}) \equiv \int f(\vec{x})\, e^{-i\vec{x}.\vec{k}}\, \mathrm{d}^n\vec{x}\,, \tag{A.17}$$

where n is the number of space dimensions. The function f can be expressed with the inverse Fourier transform

$$f(\vec{x}) \equiv \int \hat{f}(\vec{k})\, e^{i\vec{x}.\vec{k}}\, \frac{\mathrm{d}^n\vec{k}}{(2\pi)^n}\,. \tag{A.18}$$

In physics, the Fourier transform is often used to go from real space to momentum space. If $\vec{r}$ is a position vector and $\vec{p}$ a momentum vector, we have in n dimensions

$$\hat{f}(\vec{p}) \equiv \int f(\vec{r})\, e^{-i\vec{r}.\vec{p}/\hbar}\, \mathrm{d}^n\vec{r}, \tag{A.19}$$

and

$$f(\vec{r}) \equiv \int \hat{f}(\vec{p})\, e^{i\vec{r}.\vec{p}/\hbar}\, \frac{\mathrm{d}^n\vec{p}}{(2\pi\hbar)^n}\,. \tag{A.20}$$

These definitions are used to define the Dirac delta distribution on momentum space.

$$(2\pi\hbar)^n \delta^{(n)}(\vec{p}) \equiv \int e^{-i\vec{r}.\vec{p}/\hbar}\, \mathrm{d}^n\vec{r}. \tag{A.21}$$

Appendix B

The WIMP template

B.1 Thermodynamics

The number of effective degrees of freedom in energy is given by

$$g_{\rm eff}(T) = g\,\frac{15}{\pi^4}\int_0^\infty \frac{u^2}{e^{\sqrt{u^2+x^2}}+\epsilon}\,\sqrt{u^2+x^2}\,{\rm d}u\,. \tag{B.1}$$

We introduce $y^2 \equiv u^2 + x^2$ and $y \geqslant 0$ such that

$$\begin{aligned} g_{\rm eff}(T) &= g\,\frac{15}{\pi^4}\int_x^\infty \frac{\sqrt{y^2-x^2}\,y^2}{e^y+\epsilon}\,{\rm d}y & \text{(B.2)}\\ &= g\,\frac{15}{\pi^4}\int_x^\infty e^{-y}\,\frac{\sqrt{y^2-x^2}\,y^2}{1+\epsilon\,e^{-y}}\,{\rm d}y\,. & \text{(B.3)} \end{aligned}$$

We expand the denominator into a power series

$$g_{\rm eff}(T) = g\,\frac{15}{\pi^4}\sum_{n=1}^\infty(-\epsilon)^{n+1}\int_x^\infty \sqrt{y^2-x^2}\,y^2\,e^{-ny}\,{\rm d}y\,, \tag{B.4}$$

and separate the integral into

$$g_{\rm eff}(T) = g\,\frac{15}{\pi^4}\sum_{n=1}^\infty(-\epsilon)^{n+1}\left\{\int_x^\infty \left(y^2-x^2\right)^{3/2}\,y^2\,e^{-ny}\,{\rm d}y + x^2\int_x^\infty \sqrt{y^2-x^2}\,y^2\,e^{-ny}\,{\rm d}y\right\}. \tag{B.5}$$

Using Eq. (A.15), we get

$$g_{\rm eff}(T) = g\,\frac{15}{\pi^4}\sum_{n=1}^\infty(-\epsilon)^{n+1}\left\{\frac{3\,x^2}{n^2}\,K_2(nx) + \frac{x^3}{n}\,K_1(nx)\right\}. \tag{B.6}$$

Finally, we use the recursion relation (A.16) to get

$$g_{\rm eff}(T) = g\,\frac{15}{\pi^4}\sum_{n=1}^\infty(-\epsilon)^{n+1}\left\{\left(\frac{6\,x}{n^3}+\frac{x^3}{n}\right)\,K_1(nx) + \frac{3\,x^2}{n^2}\,K_0(nx)\right\}. \tag{B.7}$$

A similar calculation leads to the number of effective degrees of freedom in entropy

$$h_{\rm eff}(T) = g\,\frac{45}{4\pi^4}\sum_{n=1}^\infty(-\epsilon)^{n+1}\left\{\left(\frac{8x}{n^3}+\frac{x^3}{n}\right)\,K_1(nx) + \frac{4x^2}{n^2}\,K_0(nx)\right\}. \tag{B.8}$$

B.2 Particle physics

B.2.1 Conventions and Diracology

We use the following conventions for our calcutions. The Minkowski metric has signature $(+---)$. The Dirac gamma matrices are written in the Dirac basis where they take the form

$$\gamma^0 = \begin{bmatrix} 1 & 0 & 0 & 0 \\ 0 & 1 & 0 & 0 \\ 0 & 0 & -1 & 0 \\ 0 & 0 & 0 & -1 \end{bmatrix} \quad \gamma^1 = \begin{bmatrix} 0 & 0 & 0 & 1 \\ 0 & 0 & 1 & 0 \\ 0 & -1 & 0 & 0 \\ -1 & 0 & 0 & 0 \end{bmatrix}$$
$$\gamma^2 = \begin{bmatrix} 0 & 0 & 0 & -i \\ 0 & 0 & i & 0 \\ 0 & i & 0 & 0 \\ -i & 0 & 0 & 0 \end{bmatrix} \quad \gamma^1 = \begin{bmatrix} 0 & 0 & 1 & 0 \\ 0 & 0 & 0 & -1 \\ -1 & 0 & 0 & 0 \\ 0 & 1 & 0 & 0 \end{bmatrix} \tag{B.9}$$

These matrices are defined through there anticommutation relations

$$\{\gamma^\mu, \gamma^\nu\} = 2\eta^{\mu\nu} I_4 \,. \tag{B.10}$$

In particular, we $(\gamma^0)^2 = I_4$ and $(\gamma^i)^2 = -I_4$ for $i = 1, 2, 3$. This immediately leads to $(\gamma^\mu)^\dagger = \gamma^0\gamma^\mu\gamma^0$.

The fifth gamma matrix γ^5 is defined as $\gamma^5 \equiv i\gamma^0\gamma^1\gamma^2\gamma^3$, which leads to

$$\gamma^5 = \begin{bmatrix} 0 & 0 & 1 & 0 \\ 0 & 0 & 0 & 1 \\ 1 & 0 & 0 & 0 \\ 0 & 1 & 0 & 0 \end{bmatrix} \tag{B.11}$$

It verifies

$$\left(\gamma^5\right)^2 = I_4 \,, \tag{B.12}$$

and

$$\left\{\gamma^5, \gamma^\mu\right\} = 0 \,. \tag{B.13}$$

We recall the expression of the Dirac spinors for particles

$$u(\vec{p}, \uparrow) = \sqrt{E+m} \begin{bmatrix} 1 \\ 0 \\ \frac{p_3}{E+m} \\ \frac{p_1+ip_2}{E+m} \end{bmatrix} \quad u(\vec{p}, \downarrow) = \sqrt{E+m} \begin{bmatrix} 0 \\ 1 \\ \frac{p_1-ip_2}{E+m} \\ \frac{-p_3}{E+m} \end{bmatrix} \tag{B.14}$$

and for antiparticles

$$v(\vec{p}, \uparrow) = \sqrt{E+m} \begin{bmatrix} \frac{p_1-ip_2}{E+m} \\ \frac{-p_3}{E+m} \\ 0 \\ 1 \end{bmatrix} \quad v(\vec{p}, \downarrow) = \sqrt{E+m} \begin{bmatrix} \frac{p_3}{E+m} \\ \frac{p_1+ip_2}{E+m} \\ 1 \\ 0 \end{bmatrix} \tag{B.15}$$

where $\uparrow\downarrow$ refers to the direction of the spin (up or down). These spinors are by definition solutions of the Dirac equation

$$(\not{p} + m\, I_4) u(\vec{p}) = 0 \tag{B.16}$$
$$(-\not{p} + m\, I_4) v(\vec{p}) = 0 \,, \tag{B.17}$$

with the Feynman notation $\not{p} \equiv \gamma_\mu p^\mu$. The completeness relations are

$$\sum_{s=\uparrow\downarrow} u(\vec{p},s)\,\overline{u}(\vec{p},s) = \not{p} + m\,I_4 \tag{B.18}$$

$$\sum_{s=\uparrow\downarrow} v(\vec{p},s)\,\overline{v}(\vec{p},s) = \not{p} - m\,I_4\,, \tag{B.19}$$

where

$$\overline{u} \equiv u^\dagger \gamma^0\,. \tag{B.20}$$

When computing a spin-averaged amplitude, it is very convenient to use the Casimir trick: let Γ_1 and Γ_2 be two 4×4 matrices, then

$$\sum_{\text{spins}} [\overline{u}_1\Gamma_1 u_2]\,[\overline{u}_1\Gamma_2 u_2]^* = \text{Tr}\left[\overline{\Gamma}_2(\not{p}_1 + m)\Gamma_1(\not{p}_2 + m)\right] \tag{B.21}$$

$$\sum_{\text{spins}} [\overline{u}_1\Gamma_1 v_2]\,[\overline{u}_1\Gamma_2 v_2]^* = \text{Tr}\left[\overline{\Gamma}_2(\not{p}_1 + m)\Gamma_1(\not{p}_2 - m)\right] \tag{B.22}$$

$$\sum_{\text{spins}} [\overline{v}_1\Gamma_1 u_2]\,[\overline{v}_1\Gamma_2 u_2]^* = \text{Tr}\left[\overline{\Gamma}_2(\not{p}_1 - m)\Gamma_1(\not{p}_2 + m)\right] \tag{B.23}$$

$$\sum_{\text{spins}} [\overline{v}_1\Gamma_1 v_2]\,[\overline{v}_1\Gamma_2 v_2]^* = \text{Tr}\left[\overline{\Gamma}_2(\not{p}_1 - m)\Gamma_1(\not{p}_2 - m)\right]\,, \tag{B.24}$$

where $\overline{\Gamma}_i \equiv \gamma^0\Gamma_i^\dagger\gamma^0$. The following trace identities are useful

$$\text{Tr}\left[\gamma^{\mu_1}...\gamma^{\mu_{2n+1}}\right] = 0 \tag{B.25}$$

$$\text{Tr}\left[\gamma^5\gamma^{\mu_1}...\gamma^{\mu_{2n+1}}\right] = 0 \tag{B.26}$$

$$\text{Tr}\left[\gamma^\mu\gamma^\nu\right] = 4\,\eta^{\mu\nu} \tag{B.27}$$

$$\text{Tr}\left[\gamma^\mu\gamma^\nu\gamma^\rho\gamma^\sigma\right] = 4\,(\eta^\mu\eta^{nu} - \eta^{\mu\rho}\eta^{\nu\sigma} + \eta^{\mu\sigma}\eta^{\nu\rho}) \tag{B.28}$$

$$\text{Tr}\left[\gamma^5\right] = \text{Tr}\left[\gamma^5\gamma^\mu\gamma^\nu\right] = 0 \tag{B.29}$$

$$\tag{B.30}$$

B.2.2 Amplitudes

B.2.2.1 Tree-level Annihilation

We compute the amplitudes shown on Fig. 2.3. Impulsion along each line of the diagram are going *from the left to the right*. We compute the amplitude for both the scalar and pseudo-scalar case by using the Feynman rules for the vertices $-i\lambda(\alpha + \beta\gamma^5)$ (we drop the identity I_4 in front of α to lighten the notation). The case $(\alpha,\beta) = (1,0)$ is the scalar channel and $(\alpha,\beta) = (0,1)$ is the pseudo-scalar channel. The amplitude is

$$-i\mathcal{M} = \overline{v}(\vec{p_2}) \times -i\lambda_{\text{med}}(\alpha + \beta\gamma^5) \times u(\vec{p_1}) \times \frac{i}{s - m_{\text{med}}^2 + im_{\text{med}}\Gamma_{\text{med}}} \times \overline{u}(\vec{k_3}) \times -i\lambda'_{\text{med}}(\alpha + \beta\gamma^5) \times v(\vec{k_4})\,,$$

where p^1 and p^2 are the 4-momenta of the incoming DM particle and anti-particle respectively, and k_3 and k_4 are the 4-momenta of the outgoing SM fermion and anti-fermion respectively. We introduced a decay constant Γ_{med} for the mediator in the propagator (Breit-Wigner form). We perform our calculation in the case where the DM particle is a Dirac fermion, one can check that the final result is the same if its a Majorana fermion (though the calculation is different). The squared amplitude is

$$|\mathcal{M}|^2 = \frac{(\lambda_{\text{med}}\lambda'_{\text{med}})^2}{(s - m_{\text{med}}^2)^2 + m_{\text{med}}^2\Gamma_{\text{med}}^2} \left[\overline{v}_2(\alpha + \beta\gamma^5)u_1\right]\left[\overline{u}_3(\alpha + \beta\gamma^5)v_4\right] \times \left[\overline{v}_2(\alpha + \beta\gamma^5)u_1\right]^*\left[\overline{u}_3(\alpha + \beta\gamma^5)v_4\right]^* \tag{B.31}$$

We average over initial spins, sum over final spins and use the Casimir trick to get

$$\overline{|\mathcal{M}|^2} \equiv \frac{1}{4}\sum_{\text{spins}}|\mathcal{M}|^2 = \frac{1}{4}\frac{\left(\lambda_{\text{med}}\lambda'_{\text{med}}\right)^2}{\left(s-m_{\text{med}}^2\right)^2+m_{\text{med}}^2\Gamma_{\text{med}}^2}\text{Tr}\left[(\alpha-\beta\gamma^5)(\not{p}_2-m_\chi)(\alpha+\beta\gamma^5)(\not{p}_1+m_\chi)\right] \times \text{Tr}\left[(\alpha-\beta\gamma^5)(\not{k}_3+m_\text{f})(\alpha+\beta\gamma^5)(\not{k}_4-m_\text{f})\right] \tag{B.32}$$

Developping the traces, we get

$$\overline{|\mathcal{M}|^2} = \frac{\left(\lambda_{\text{med}}\lambda'_{\text{med}}\right)^2}{\left(s-m_{\text{med}}^2\right)^2+m_{\text{med}}^2\Gamma_{\text{med}}^2}\left[\alpha^2(s-4\,m_\chi^2)+\beta^2\,s\right]\left[\alpha^2(s-4\,m_\text{f}^2)+\beta^2\,s\right], \tag{B.33}$$

which leads to Eq. (2.65) in the scalar and pseudo-scalar limits.

B.2.2.2 Tree-level scattering

The amplitudes for tree-level scattering are shown on Fig. 2.4. We call p_1 the 4-momentum of the incoming DM particle and p_2 the 4-momentum of the outgoing DM particle, while k_3 and k_3 refer to the incoming and outgoing 4-momenta of the SM fermion. We compute the amplitude with the same trick as for the annihilation by writing $\alpha+\beta\gamma^5$, we get

$$-i\mathcal{M} = \overline{u}(\vec{p}_2)\times -i\lambda_{\text{med}}(\alpha+\beta\gamma^5)\times u(\vec{p}_1)\times\frac{i}{t-m_{\text{med}}^2+im_{\text{med}}\Gamma_{\text{med}}}\times\overline{u}(\vec{k}_4)\times -i\lambda'_{\text{med}}(\alpha+\beta\gamma^5)\times u(\vec{k}_3)\,,$$

and the spin-averaged squared amplitude is

$$\overline{|\mathcal{M}|^2} = \frac{\left(\lambda_{\text{med}}\lambda'_{\text{med}}\right)^2}{\left(t-m_{\text{med}}^2\right)^2+m_{\text{med}}^2\Gamma_{\text{med}}^2}\left[\alpha^2(t-4\,m_\chi^2)+\beta^2\,t\right]\left[\alpha^2(t-4\,m_\text{f}^2)+\beta^2\,t\right]. \tag{B.34}$$

This can be obtain immediately by taking the annihilation amplitude and substituting $s\to t$.

B.2.3 Invariant phase space and cross-sections

B.2.3.1 Lorentz-invariant phase-space

Let us consider a process $1+2\to 3+4+\ldots+n$. The elementary cross-section for this process is

$$\text{d}\sigma \equiv \frac{1}{4F}\overline{|\mathcal{M}|^2}(2\pi)^4\delta^4\left(p_1+p_2-\sum_{i=3}^n p_i\right)\text{d}^4\text{LIPS}\,, \tag{B.35}$$

where $\mathcal{M}$ is the amplitude of the process, F is the flux factor

$$F \equiv \sqrt{\left(p_1.p_2\right)^2-m_1^2m_2^2}\,, \tag{B.36}$$

and we introduced the Lorentz-invariant phase-space element of volume

$$\text{d}^4\text{LIPS} \equiv \prod_{i=3}^n\frac{\text{d}^4p_i}{(2\pi)^4}\Theta(p_{i,0})(2\pi)\delta\left(p_i^\mu p_{i,\mu}-m_i^2\right). \tag{B.37}$$

The Lorentz invariance is manifest in the definition of d^4LIPS however it is more convenient for computations to move to another form. We introduce the energy $E^2\equiv|\vec{p}|^2+m_2$, rewrite the phase-space element

$$\text{d}^4\text{LIPS} \equiv \prod_{i=3}^n\frac{\text{d}^4p_i}{(2\pi)^4}\Theta(p_{i,0})(2\pi)\delta\left(p_{i,0}^2-E_i^2\right), \tag{B.38}$$

and integrate over $p_{i,0}$ to get

$$\mathrm{d}^3\mathrm{LIPS} = \prod_{i=3}^{n} \frac{\mathrm{d}^3\vec{p}}{(2\pi)^3 2E_i(\vec{p}_i)}\,. \tag{B.39}$$

This form is also Lorentz-invariant since we started from d^4LIPS, though it is not manifest. Note that the integration over $p_{i,0}$ can be performed regardless of the amplitude since the components of the 4-momentum are not independent. One just has to keep in mind the relation $E = \sqrt{|\vec{p}|^2 + m^2}$ when performing the integral over $\vec{p}$.

B.2.3.2 Cross-sections

Annihilation cross-sections The elementary cross-section for the annihilation process $1{+}2 \to 3 + 4$, where 1 and 2 are DM particles and 3 and 4 SM fermions, is given by

$$\begin{aligned}\mathrm{d}\sigma_{\mathrm{ann}} &= \frac{1}{4\,F}\overline{|\mathcal{M}|^2}(2\pi)^4\delta^4\left(p_1 + p_2 - k_3 - k_4\right)\,\frac{\mathrm{d}^3\vec{k}_3}{(2\pi)^3 2E_3}\frac{\mathrm{d}^3\vec{k}_4}{(2\pi)^3 2E_4} \\ &= \frac{1}{4\,F}\overline{|\mathcal{M}|^2}(2\pi)^4\delta\left(E_1 + E_2 - E_3 - E_4\right)\delta^3\left(\vec{p}_1 + \vec{p}_2 - \vec{k}_3 - k_4\right)\,\frac{\mathrm{d}^3\vec{k}_3}{(2\pi)^3 2E_3}\frac{\mathrm{d}^3\vec{k}_4}{(2\pi)^3 2E_4}\,.\end{aligned} \tag{B.40}$$

We perform our calculation in the center-of-mass frame

$$\begin{aligned}E_1 + E_2 &= \sqrt{s} \\ \vec{p}_1 + \vec{p}_2 &= \vec{k}_3 + \vec{k}_4 = 0\,.\end{aligned} \tag{B.41}$$

Since both SM fermions have the same mass m_{f}, the integration over $\vec{k}_4$ leads $E_3 = E_4 = E$ and we get

$$\begin{aligned}\mathrm{d}\sigma_{\mathrm{ann}} &= \frac{1}{4\,F}\overline{|\mathcal{M}|^2}(2\pi)^4\delta\left(\sqrt{s} - 2E\right)\,\frac{\mathrm{d}^3\vec{k}}{(2\pi)^6 4\,E^2} \\ &= \frac{1}{4\,F}\overline{|\mathcal{M}|^2}(2\pi)^4\delta\left(\sqrt{s} - 2E\right)\,\frac{k\,\mathrm{d}E\mathrm{d}\Omega}{(2\pi)^6 4\,E} \\ &= \frac{1}{4\,F}\overline{|\mathcal{M}|^2}(2\pi)^4\frac{1}{2}\delta\left(\frac{\sqrt{s}}{2} - E\right)\,\frac{k\,\mathrm{d}E\mathrm{d}\Omega}{(2\pi)^6 4\,E}\,.\end{aligned} \tag{B.42}$$

Since the amplitude depends on s only, integration of the solid angle Ω leads a factor of 4π. Since for the case of annihilation, the flux factor can be expressed as

$$F = \frac{\sqrt{s}}{2}\sqrt{s - 4\,m^2}\,, \tag{B.43}$$

integration of the elementary cross-section over E finally leads

$$\sigma_{\mathrm{ann}} = \frac{1}{16\pi}\frac{1}{s}\sqrt{\frac{s - 4\,m_{\mathrm{f}}^2}{s - 4\,m^2}}\,\overline{|\mathcal{M}|^2}\,. \tag{B.44}$$

For the two annihilation channels we considered, the expression of the cross-section is

$$\sigma_{\mathrm{ann}} = \frac{1}{16\pi}\frac{\left(\lambda_{\mathrm{med}}\lambda'_{\mathrm{med}}\right)^2}{\left(s - m_{\mathrm{med}}^2\right)^2 + m_{\mathrm{med}}^2\Gamma_{\mathrm{med}}^2}\begin{cases}(s - 4\,m^2)^{1/2}(s - 4\,m_{\mathrm{f}}^2)^{3/2}\,s^{-1} & \text{scalar} \\ \left(\frac{s-4\,m_{\mathrm{f}}^2}{s-4\,m^2}\right)^{1/2}\,s & \text{pseudoscalar}\end{cases} \tag{B.45}$$

Since the cross-sections are manifestely Lorentz-invariant, these expressions are valid in any frame even though we made the computation in the rest frame.

B.2.4 Thermally-averaged cross-section

Here we compute the temperature expansion of the thermally-averaged cross-section as done by Srednicki et al. (1988). Let $x = m/T$ where T is the temperature of DM particles, then the annihilation cross-section can be developped as

$$\langle \sigma_{\rm ann} v \rangle = a + \frac{b}{x} + \frac{c}{x^2} + ... \tag{B.46}$$

The expressions for a and b are given by Srednicki et al. (1988) in terms of the function

$$w(s) \equiv \sigma_{\rm ann}(s)\, F = \sigma_{\rm ann}\, \frac{\sqrt{s}}{2} \sqrt{s - 4\,m^2}\,, \tag{B.47}$$

and its derivative with respect to s, both evaluated at $s = 4\,m^2$. The general expressions for the first two coefficient are

$$a = \frac{w(4\,m^2)}{m^2} \tag{B.48}$$

$$b = -\frac{3}{2\,m^2} \left[2\,w(4\,m^2) - 4\,m^2\, \frac{{\rm d}w}{{\rm d}s}\bigg|_{4\,m^2} \right]. \tag{B.49}$$

For the scalar channel, this leads to

$$a = 0 \tag{B.50}$$

$$b = \frac{3}{4\pi} \frac{(\lambda_{\rm med} \lambda'_{\rm med})^2}{\left(4\,m^2 - m^2_{\rm med}\right)^2 + m^2_{\rm med} \Gamma^2_{\rm med}} \frac{(m^2 - m_{\rm f}^2)^{3/2}}{m}\,. \tag{B.51}$$

For the pseudo-scalar channel, we have

$$a = \frac{1}{2\pi} \frac{(\lambda_{\rm med} \lambda'_{\rm med})^2}{\left(4\,m^2 - m^2_{\rm med}\right)^2 + m^2_{\rm med} \Gamma^2_{\rm med}} (m^2 - m_{\rm f}^2)^{1/2} m \tag{B.52}$$

$$b = w(4\,m^2) \left[-\frac{2(4\,m^2 - m^2_{\rm med})}{\left(4\,m^2 - m^2_{\rm med}\right)^2 + m^2_{\rm med} \Gamma^2_{\rm med}} + \frac{1}{2(4\,m^2 - 4\,m_{\rm f}^2)} + \frac{3}{8\,m^2} \right] \tag{B.53}$$

B.3 The Boltzmann equation in an expanding Universe

In this section, we work out the form of the Boltzmann equation in General Relativity, following the treatment given by Bernstein (1988). The general-covariant Liouville operator for the one-particle phase-space distribution function takes the form

$$\hat{L}[f] \equiv \frac{\rm d}{{\rm d}\lambda} f[x(\lambda), p(\lambda)] = \frac{{\rm d}x^\mu}{{\rm d}\lambda} \frac{\partial f}{\partial x^\mu} + \frac{{\rm d}p^\mu}{{\rm d}\lambda} \frac{\partial f}{\partial p^\mu}\,, \tag{B.54}$$

where λ is a scalar parameter of motion (for instance the proper time). The momentum is defined through $p^\mu \equiv {\rm d}x^\mu/{\rm d}\lambda$ and, if the particles are free-falling, it obeys the geodesic equation

$$\frac{{\rm d}p^\mu}{{\rm d}\lambda} + \Gamma^\mu_{\alpha\beta} p^\alpha p^\beta = 0\,, \tag{B.55}$$

where $\Gamma^\mu_{\alpha\beta}$ are the Christoffel symbols of the second kind. Casting this equation into the Liouville operator, we get

$$\hat{L}[f] = p^\mu \frac{\partial f}{\partial x^\mu} - \Gamma^\mu_{\alpha\beta} p^\alpha p^\beta \frac{\partial f}{\partial p^\mu}\,. \tag{B.56}$$

B.3.1 Liouville operator in the flat FLRW metric

The Liouville operator simplifies in a particular metric with the expression of the Christoffel symbols

$$\Gamma^{\mu}_{\alpha\beta} = \frac{1}{2}\, g^{\mu\nu} \left[\frac{\partial g_{\alpha\nu}}{\partial x^{\beta}} + \frac{\partial g_{\beta\nu}}{\partial x^{\alpha}} - \frac{\partial g_{\alpha\beta}}{\partial x^{\nu}} \right] . \tag{B.57}$$

We restrict our calculations to the flat Friedmann-Lemaitre-Robertson-Walker (FLRW) metric, which has the simple form

$$\mathrm{d}s^2 = \mathrm{d}t^2 - a^2(t)\, \delta_{ij} \mathrm{d}x^i \mathrm{d}x^j \,, \tag{B.58}$$

It is straightforward to compute

$$\begin{aligned} \Gamma^{i}_{0j} &= \frac{\dot{a}}{a}\, \delta^{i}_{j} \\ \Gamma^{0}_{ij} &= a\dot{a}\, \delta_{ij} \,. \end{aligned} \tag{B.59}$$

Note that the FLRW metric is homogeneous and isotropic by definition. Since it is related to the mass distribution f through Einstein's equations, we expect f to only depend on the time t, the energy p^0 and the modulus of the momentum $|\vec{p}| = \sqrt{-a^2 \delta_{ij} p^i p^j}$. Injecting the expression of $\Gamma^{\mu}_{\alpha\beta}$ into Eq. (B.56), we get

$$\hat{L}[f] = p^0\, \frac{\partial f}{\partial x^0} + p^i\, \frac{\partial f}{\partial x^i} - a\dot{a}\, \delta_{ij} p^i p^j\, \frac{\partial f}{\partial p^0} - 2\, \frac{\dot{a}}{a}\, p^0 p^i\, \frac{\partial f}{\partial p^i} \,. \tag{B.60}$$

The factor of 2 in the last term accounts for the components $0i$ and $i0$. The energy is related to the momentum through Einstein's relation $p^0 = \sqrt{m^2 + |\vec{p}|^2} = E$ which we implement through a mass-shell integral

$$\hat{L}_0[f] \equiv \int \mathrm{d}p^0\, \delta\left(p^0 - \sqrt{m^2 + |\vec{p}|^2}\right)\, \hat{L}[f]\, \frac{1}{p^0} \,. \tag{B.61}$$

This defines a mass-shell Liouville operator $\hat{L}_0$. With the mass-shell condition, we get the following simplification

$$\begin{aligned} \frac{\partial}{\partial x^i} &= \frac{\mathrm{d}p^0}{\mathrm{d}x^i} \frac{\partial}{\partial p^0} \\ &= \frac{\mathrm{d}}{\mathrm{d}x^i} \left(\sqrt{-a^2 \delta_{jk} p^j p^k + m^2} \right) \frac{\partial}{\partial p^0} \\ &= 0 \\ \frac{\partial}{\partial p^i} &= -a^2\, \frac{p_i}{p^0} \frac{\partial}{\partial p^0} \end{aligned} \tag{B.62}$$

which leads to the final expression

$$\hat{L}_0[f] = \frac{\partial f}{\partial t} - \frac{H|\vec{p}|^2}{E} \frac{\partial f}{\partial E} \tag{B.63}$$

B.3.2 Liouville operator for the number density

Integrating Eq. (B.63) over the 3-momentum leads to the Liouville operator for the number density. We recall the definion of the number density n as

$$n(t) \equiv g \int \frac{\mathrm{d}^3 \vec{p}}{(2\pi)^3}\, f(\vec{p}, t) \,, \tag{B.64}$$

where g is the number of internal degrees of freedom. By integration by parts, we get the identity

$$\int \frac{\mathrm{d}^3\vec{p}}{(2\pi)^3}\frac{p^2}{E}\frac{\partial f}{\partial E} = -3\int \frac{\mathrm{d}^3\vec{p}}{(2\pi)^3}\frac{\partial f}{\partial p}\,, \tag{B.65}$$

and the integrated Liouville operator simplifies to

$$\int \frac{\mathrm{d}^3\vec{p}}{(2\pi)^3}\,\hat{L}_0[f] = \frac{\mathrm{d}n}{\mathrm{d}t} + 3\,H\,n\,. \tag{B.66}$$

B.3.3 Collision operator for two-body annihilation processes

Here we simplify the collision operator appearing in the Boltzmann equation for a process $1+2\to 3+4$, closely following the pedagogical treatment given by Gondolo & Gelmini (1991). The full collision operator is quite complicated since it involves all the processes that modify the phase-space distribution of 1. Following Bernstein (1988), we split the operator into two terms, one for the elastic collisions and one for the inelastic ones

$$\hat{C}[f_1] = \hat{C}_{\mathrm{E}}[f_1] + \hat{C}_{\mathrm{I}}[f_1]\,. \tag{B.67}$$

The inelastic collision operator can be written

$$\begin{aligned}\hat{C}_{\mathrm{I}}[f_1] \equiv -\frac{1}{2}\sum_{\text{spins}}\int &\left[f_1 f_2(1\pm f_3)(1\pm f_4)\left|\mathcal{M}_{12\to 34}\right|^2 - f_3 f_4(1\pm f_1)(1\pm f_2)\left|\mathcal{M}_{34\to 12}\right|^2\right]\\ &\times (2\pi)^4\delta^{(4)}\left(p_1+p_2-p_3-p_4\right)\\ &\times \frac{\mathrm{d}^3\vec{p}_2}{(2\pi)^3 2E_2}\frac{\mathrm{d}^3\vec{p}_3}{(2\pi)^3 2E_3}\frac{\mathrm{d}^3\vec{p}_4}{(2\pi)^3 2E_4}\,,\end{aligned} \tag{B.68}$$

where the sum is over initial and final spins, the $\pm$ sign is $+/-$ for bosons/fermions and $\mathcal{M}$ is a probability amplitude. We want to derive the evolution equation for the number density therefore we integrate over the momenta $\vec{p}_1$ as in Eq. (B.64). This integration suppress all processes that do not change the number density n_1, which include elastic collisions. Hence we have

$$\int \frac{\mathrm{d}^3\vec{p}_1}{(2\pi)^3}\,\hat{C}_{\mathrm{E}}[f_1] = 0\,, \tag{B.69}$$

and the only relevant operator is the one accounting for inelastic collisions. We implement the mass-shell condition Eq. (B.61) and integrate over the momenta as in Eq. (B.64) to get a "number-density collision operator"

$$\begin{aligned}\hat{C}_0[n_1] &\equiv g_1\int \frac{\mathrm{d}^3\vec{p}_1}{(2\pi)^3 E_1}\,\hat{C}_{\mathrm{I}}[f_1]\\ &= -\sum_{\text{spins}}\int \left[f_1 f_2(1\pm f_3)(1\pm f_4)\left|\mathcal{M}_{12\to 34}\right|^2 - f_3 f_4(1\pm f_1)(1\pm f_2)\left|\mathcal{M}_{34\to 12}\right|^2\right]\\ &\times (2\pi)^4\delta^{(4)}\left(p_1+p_2-p_3-p_4\right)\\ &\times \frac{\mathrm{d}^3\vec{p}_1}{(2\pi)^3 2E_1}\frac{\mathrm{d}^3\vec{p}_2}{(2\pi)^3 2E_2}\frac{\mathrm{d}^3\vec{p}_3}{(2\pi)^3 2E_3}\frac{\mathrm{d}^3\vec{p}_4}{(2\pi)^3 2E_4}\,.\end{aligned} \tag{B.70}$$

We neglect the quantum mechanical factors *i.e.* $1\pm f_i \simeq 1$. Particles 3 and 4 are assumed in chemical and thermal equilibrium with the bath, hence $f_3 = f_{3,\mathrm{eq}}$ and $f_4 = f_{4,\mathrm{eq}}$. The DM particle is assumed to be in thermal equilibrium during chemical decoupling, so we can write

$$f_{\mathrm{DM}}(\vec{p}) = \frac{n_{\mathrm{DM}}(T)}{n_{\mathrm{DM,eq}}(T)}\,f_{\mathrm{DM,eq}}(\vec{p})\,, \tag{B.71}$$

i.e. the DM phase-space density is proportional to the full chemical and thermal equilibrium density, with a temperature-dependent proportionality factor. This assumption of thermal equilibrium of the DM can be relaxed, see Binder et al. (2017) for details. The detailed balance on $1+2 \to 3+4$ implies

$$f_{3,\mathrm{eq}}\, f_{4,\mathrm{eq}} = f_{1,\mathrm{eq}}\, f_{2,\mathrm{eq}}\,. \tag{B.72}$$

and unitarity leads

$$\begin{aligned} &\sum_{\text{spins}} \int |\mathcal{M}_{34\to 12}|^2\, (2\pi)^4 \delta^{(4)}\left(p_1+p_2-p_3-p_4\right) \frac{\mathrm{d}^3\vec{p}_3}{(2\pi)^3 2E_3} \frac{\mathrm{d}^3\vec{p}_4}{(2\pi)^3 2E_4} \\ &= \sum_{\text{spins}} \int |\mathcal{M}_{12\to 34}|^2\, (2\pi)^4 \delta^{(4)}\left(p_1+p_2-p_3-p_4\right) \frac{\mathrm{d}^3\vec{p}_3}{(2\pi)^3 2E_3} \frac{\mathrm{d}^3\vec{p}_4}{(2\pi)^3 2E_4} \end{aligned} \tag{B.73}$$

We introduce the unpolarized cross-section (averaged over incoming spins and summed over outgoing spins)

$$4F_{12}\,\sigma_{12\to 34} \equiv \frac{1}{g_1 g_2} \sum_{\text{spins}} \int |\mathcal{M}_{12\to 34}|^2\, (2\pi)^4 \delta^{(4)}\left(p_1+p_2-p_3-p_4\right) \frac{\mathrm{d}^3\vec{p}_3}{(2\pi)^3 2E_3} \frac{\mathrm{d}^3\vec{p}_4}{(2\pi)^3 2E_4}\,, \tag{B.74}$$

where $F_{12} \equiv \sqrt{(p_1.p_2)^2 - m_1^2 m_2^2}$ is the flux factor. With the introduction of the Moller velocity

$$v_{\mathrm{m}} \equiv \frac{F_{12}}{E_1 E_2}\,, \tag{B.75}$$

and the definition of the thermally-averaged cross-section

$$\langle \sigma v \rangle \equiv \frac{\int \mathrm{d}^3\vec{p}_1 \mathrm{d}^3\vec{p}_2\, \sigma v_{\mathrm{m}}\, f_1 f_2}{\int \mathrm{d}^3\vec{p}_1 \mathrm{d}^3\vec{p}_2\, f_1 f_2}\,, \tag{B.76}$$

the collision operator finally simplifies into

$$\hat{C}_0[n_1] = -\left\langle \sigma v \right\rangle \left(n_1 n_2 - n_{1,\mathrm{eq}} n_{2,\mathrm{eq}}\right)\,. \tag{B.77}$$

B.3.4 Liouville operator for the temperature

Here we derive the form of the Liouville operator when taking the second-moment of Eq. (B.63). With the definition

$$T_{\mathrm{dm}} \equiv \frac{2}{3}\frac{1}{n} \int \frac{\mathrm{d}^3\vec{p}}{(2\pi)^3}\, \frac{\vec{p}^2}{2\,m}\, f(\vec{p})\,, \tag{B.78}$$

and the identity

$$\int \frac{\mathrm{d}^3\vec{p}}{(2\pi)^3}\, \vec{p}^2\, \frac{H\,\vec{p}^2}{E} \frac{\partial f}{\partial E} = -5\,H\,3\,n\,m\,T_{\mathrm{dm}} \tag{B.79}$$

obtained by integration by parts, we immediately get

$$\frac{2}{3}\frac{1}{n} \int \frac{\mathrm{d}^3\vec{p}}{(2\pi)^3}\, \frac{\vec{p}^2}{2\,m}\, L[f] = \frac{\partial T_{\mathrm{dm}}}{\partial t} + 5\,H\,T_{\mathrm{dm}}\,. \tag{B.80}$$

We can use the photon temperature T as an alternate time variable. We have

$$\dot{T}_{\mathrm{dm}} = \dot{a}\, \frac{\mathrm{d}T_{\mathrm{dm}}}{\mathrm{d}a} = a\,H\, \frac{\mathrm{d}T}{\mathrm{d}a} \frac{\mathrm{d}T_{\mathrm{dm}}}{\mathrm{d}T}\,. \tag{B.81}$$

Using the constancy of the entropy $sa^3 = \mathrm{cst}$ and its expression in terms of the effective degrees of freedom Eq. (2.54), we get

$$\frac{\mathrm{d}T}{\mathrm{d}a} = \frac{\mathrm{d}s}{\mathrm{d}a}\frac{\mathrm{d}T}{\mathrm{d}s} = -\frac{s}{a}\frac{45}{2\pi^2}\frac{1}{h_{\rm eff}T^2}\left(1+\frac{1}{3}\frac{\mathrm{d}\ln h_{\rm eff}}{\mathrm{d}\ln T}\right)^{-1}, \tag{B.82}$$

i.e.

$$\dot{T}_{\rm dm} = -\frac{s\, g_*^{-1/2}}{2\pi m_{\rm p}}\frac{\mathrm{d}T_{\rm dm}}{\mathrm{d}T}, \tag{B.83}$$

where g_* is defined in Eq. (2.80) and $m_{\rm p}$ is the reduced Planck mass.

B.3.5 Kinetic decoupling temperature

The expression of the kinetic decoupling temperature is given in Bringmann & Hofmann (2007)

$$\frac{m}{T_{\rm kd}} = \left(\frac{a}{n+2}\right)^{1/(n+2)}\Gamma\left[\frac{n+1}{n+2}\right]. \tag{B.84}$$

The index n is defined through an expansion of the scattering cross-section

$$\overline{|\mathcal{M}|^2}_{t=0,\ s=m^2+2m\omega} = c_n\left(\frac{\omega}{m}\right)^n + \mathcal{O}\left(\left(\frac{\omega}{m}\right)^{n+1}\right), \tag{B.85}$$

and

$$a = \sum_f \left(\frac{5}{2(2\pi)^9 g_{\rm eff}}\right)^{1/2} g_{\rm SM}\, c_n\, N_{n+3}\,\frac{M_{\rm Pl}}{m}, \tag{B.86}$$

where the sum is over SM scattering partners, $g_{\rm SM}$ is their number of internal degrees of freedom, $M_{\rm Pl}$ is the Planck mass and

$$N_j^+ = (1-2^{-j})(j+1)!\zeta(j+1) \tag{B.87}$$

$$N_j^- = (j+1)!\zeta(j+1). \tag{B.88}$$

The $+$ sign applies to fermions while the $-$ sign applies to bosons.

Appendix C

Impact of subhalos on indirect dark matter searches

C.1 Indirect searches with gamma rays

The Galactic latitude b and longitude l are defined in Fig. C.1. The relations between these coordinates and Cartesian coordinates are:

$$\begin{aligned} x &= d_{\rm obs} - s\,\cos(b)\,\cos(l) \\ y &= -s\,\cos(b)\,\sin(l) \\ z &= s\,\sin(b) \end{aligned} \tag{C.1}$$

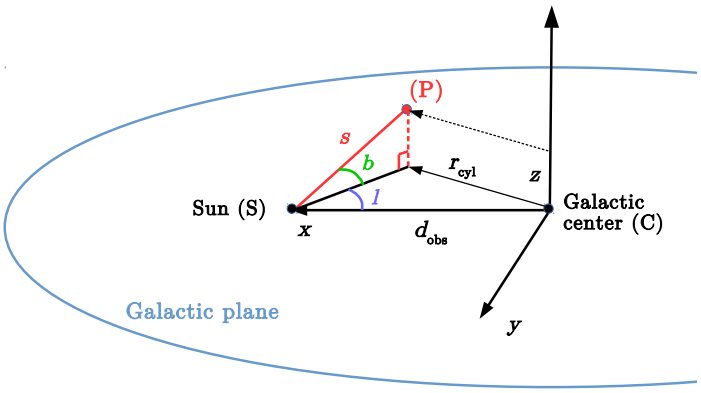

Figure C.1 – Galactic coordinates (s, b, l) used for the integral along the line of sight.

C.2 Indirect searches with cosmic rays

C.2.1 Effect of propagation parameters

C.2.2 Moving clumps

Here we derive the solution of the transport equation

$$\partial_{\rm t}\Psi + \vec{\nabla}.(\vec{v}\,\Psi) - K\Delta\Psi = Q(\vec{x}, t)\,, \tag{C.2}$$

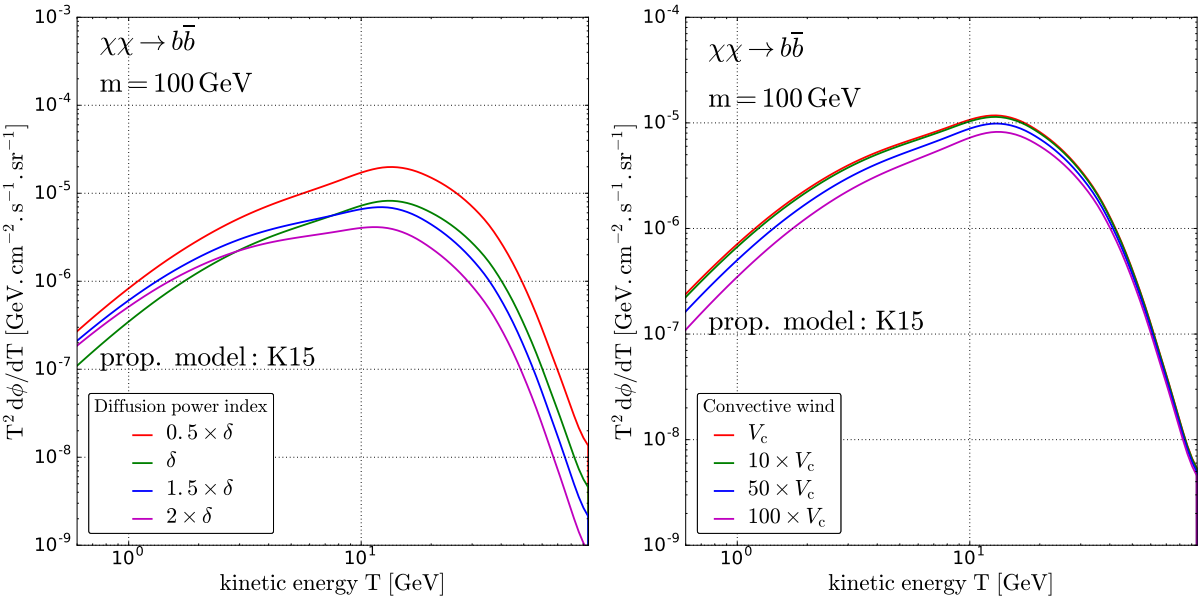

Figure C.2 – Same as Fig. 4.10 but varying the diffusion index δ (left panel) or the convective wind V_c (right panel).

We look for a Green's function $G(t_0, \vec{x}_0 \to t, \vec{x})$ of this equation

$$\partial_t G + \vec{\nabla}.(\vec{v}\,G) - K\Delta G = \delta(t - t_0)\,\delta^{(3)}(\vec{x} - \vec{x}_0)\,. \tag{C.3}$$

The spatial Fourier transform of the Green's function $\hat{G}$ is solution of

$$\partial_t \hat{G} + (i\,\vec{k}.\vec{v} + K\,k^2)\,\hat{G} = e^{-i\,\vec{k}.\vec{x}_0}\,\delta(t - t_0) \tag{C.4}$$

We choose the solution

$$\hat{G}(t_0, t; \vec{k}) = \Theta(t - t_0)\,e^{-i\,\vec{k}.\vec{x}_0}\,e^{-(i\,\vec{k}.\vec{v} + K\,k^2)(t - t_0)} \tag{C.5}$$

Taking the inverse Fourier transform, this leads to

$$G(t_0, \vec{x}_0 \to t, \vec{x}) = \frac{\Theta(t - t_0)}{(2\pi)^3} \int \mathrm{d}^3\vec{k}\,e^{i\,\vec{k}.(\vec{x} - \vec{x}_0)}\,e^{-(i\,\vec{k}.\vec{v} + K\,k^2)(t - t_0)}\,, \tag{C.6}$$

which can be straightforwardly integrated to get

$$G(t_0, \vec{x}_0 \to t, \vec{x}) = \Theta(t - t_0)\left\{\frac{1}{4\pi K\,(t - t_0)}\right\}^{3/2} \exp\left[-\frac{\{\vec{x} - \vec{x}_0 - \vec{v}(t - t_0)\}^2}{4\,K\,(t - t_0)}\right]. \tag{C.7}$$

C.2.3 Fluxes and exclusion curves

C.2.4 Variance

The primary antiproton flux *from subhalos only* can be written as

$$\langle \Phi_{\rm sub} \rangle = \frac{\mathrm{d}\phi}{\mathrm{d}E\,\mathrm{d}\Omega} = \mathcal{S} \int \mathrm{d}^3\vec{x}_{\rm s}\,G(\vec{x}_{\rm s} \to \vec{x})\,\mathcal{L}_{\rm sub}\,, \tag{C.8}$$

where $\mathcal{L}_{\rm sub}$ is the subhalo luminosity density given in Eq. (4.17). The factor $\mathcal{S}$ depends on particle-physics-related quantities (mass, cross-section, spectrum). Using the expression of the

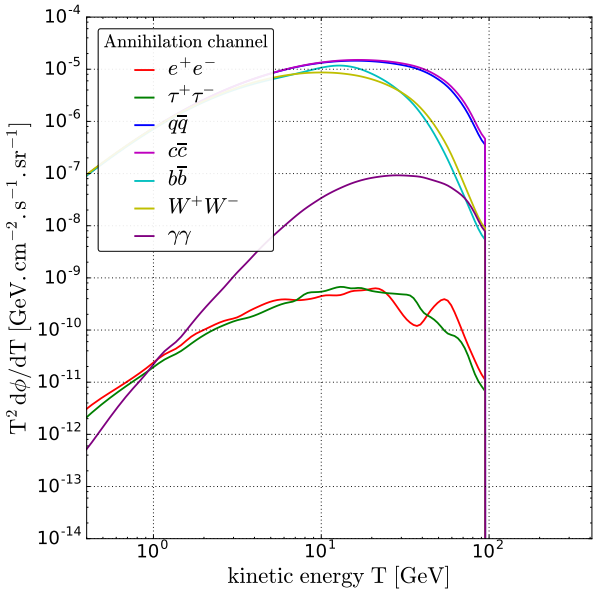

Figure C.3 – Contribution from a few annihilation channels. We used the NFW profile of McMillan 2017.

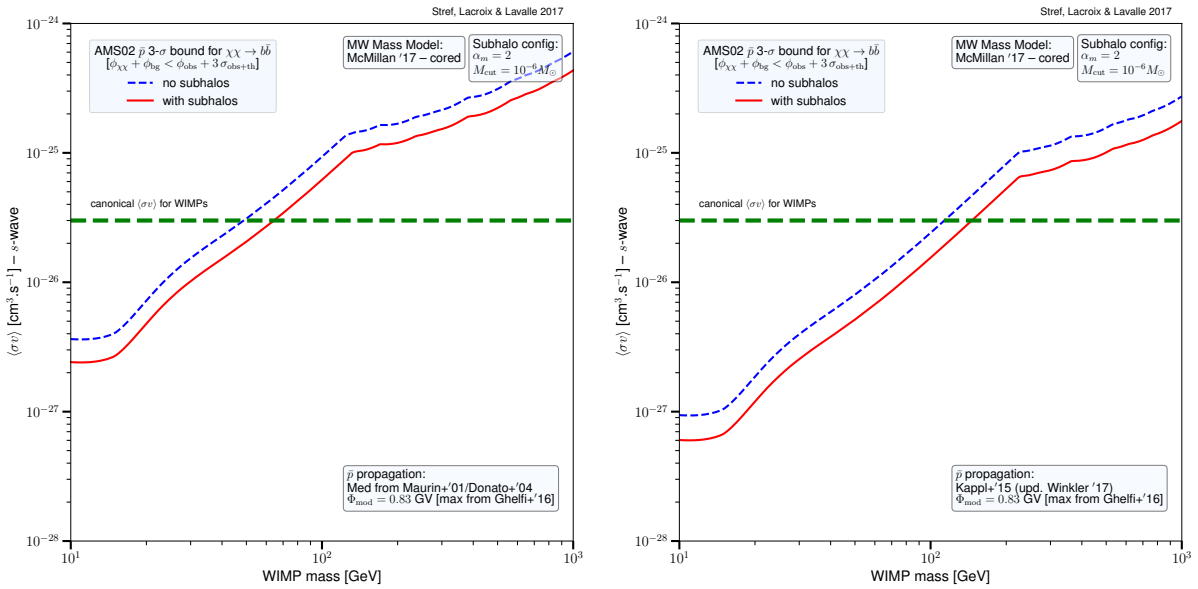

Figure C.4 – Same as Fig. 4.16 for cored Galactic dark matter profile.

luminosity, we have

$$\langle\Phi_{\rm sub}\rangle = \mathcal{S}\int {\rm d}V\, G \int {\rm d}m \int {\rm d}c\, \mathcal{F}_{\rm t}\, \xi_{\rm t} \tag{C.9}$$

$$= \mathcal{S}\frac{N_{\rm sub}}{K_{\rm t}}\int {\rm d}V \int {\rm d}m \int {\rm d}c\, \frac{{\rm d}P}{{\rm d}V}\frac{{\rm d}P}{{\rm d}m}\frac{{\rm d}P}{{\rm d}c}\, G\, \xi_{\rm t} \tag{C.10}$$

$$= \mathcal{S}\frac{N_{\rm sub}}{K_{\rm t}}\int {\rm d}V\, \frac{{\rm d}P}{{\rm d}V}\, G\, \langle\xi_{\rm t}\rangle_{m,c}\,. \tag{C.11}$$

This is the average contribution for the whole subhalo population. For a single subhalo, the average contribution is simply $\langle\Phi_{\rm sub}\rangle/N_{\rm sub}$. From this, it is quite clear that we have

$$\left\langle\Phi^2_{\rm sub,1}\right\rangle = \frac{\mathcal{S}^2}{K_{\rm t}}\int {\rm d}V\, \frac{{\rm d}P}{{\rm d}V}\, G^2\, \left\langle\xi^2_{\rm t}\right\rangle_{m,c}\,. \tag{C.12}$$

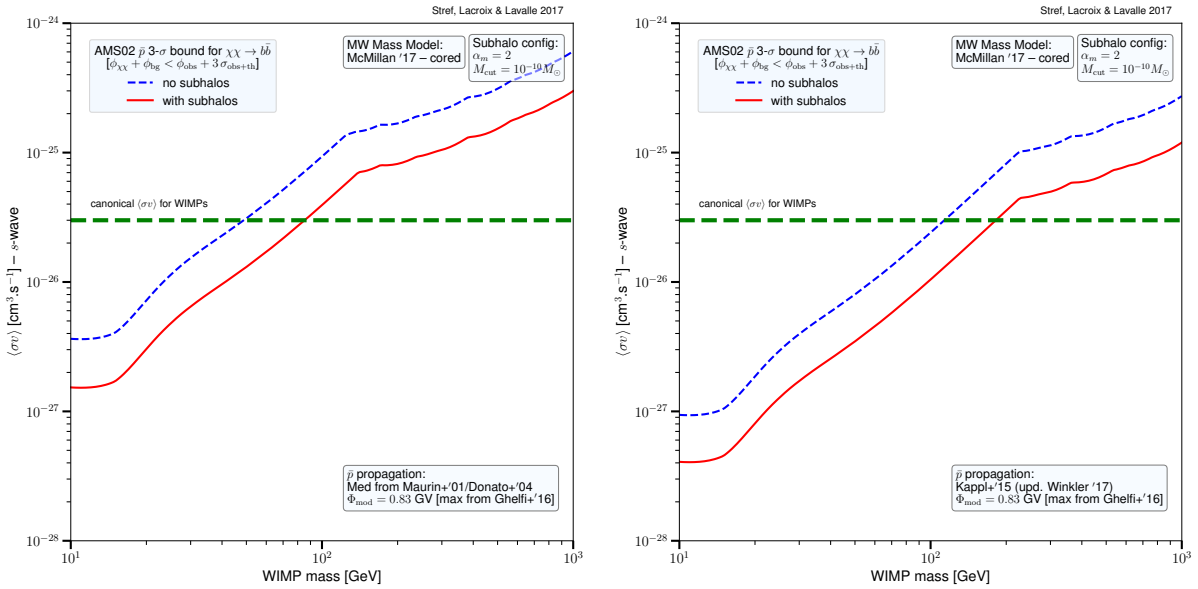

Figure C.5 – Same as Fig. 4.17 for cored Galactic dark matter profile.

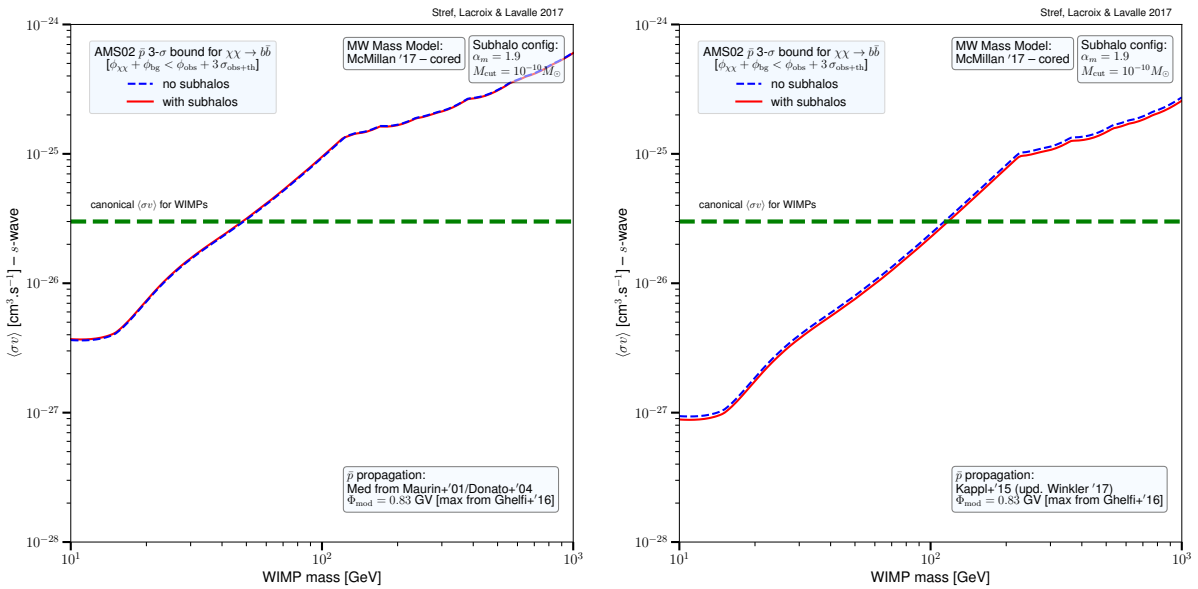

Figure C.6 – Same as Fig. 4.18 for cored Galactic dark matter profile.

In the same way, we find the following expressions

$$\left\langle \Phi^2_{\rm cross} \right\rangle = \frac{4\,\mathcal{S}^2}{K_{\rm t}} \int {\rm d}V \, \frac{{\rm d}P}{{\rm d}V} \, G^2 \, \rho^2_{\rm smooth} \left\langle m^2_{\rm t} \right\rangle_{m,c} \tag{C.13}$$

$$\langle \Phi_{\rm sub} \Phi_{\rm cross} \rangle = \frac{2\,\mathcal{S}^2}{K_{\rm t}} \int {\rm d}V \, \frac{{\rm d}P}{{\rm d}V} \, G^2 \, \rho_{\rm smooth} \, \langle \xi_{\rm t} \, m_{\rm t} \rangle_{m,c} \, . \tag{C.14}$$

These are all the expressions needed to compute the flux variance $\sigma^2_{\Phi,1}$ for a single clump. We can then compute the full variance

$$\sigma^2_\Phi = N_{\rm sub} \, \sigma_{\Phi,1} \, . \tag{C.15}$$

Appendix D

The dark matter phase space of the Galaxy

D.1 Mass models of McMillan (2017)

In this work, we make extensive use of the mass models built by McMillan (2017). In these models, the bulge mass density is described by

$$\rho_{\rm b}(R,z) = \frac{\rho_{0,\rm b}}{(1+r'/r_0)^{\alpha_{\rm b}}} \exp\left[-(r'/r_{\rm b})^2\right] , \tag{D.1}$$

with

$$r' = \sqrt{R^2 + (z/q)^2} \, . \tag{D.2}$$

The author fixed $\alpha_{\rm b} = 1.8$, $r_0 = 0.075$ kpc, $r_{\rm b} = 2.1$ kpc and $q = 0.5$. The best fitting model has $\rho_{0,\rm b} = 98.4\,{\rm M}_\odot.{\rm pc}^{-3}$.

The stellar discs have a density

$$\rho_{\rm d}(R,z) = \frac{\Sigma_0}{2\,z_{\rm d}} \exp\left[-\frac{|z|}{z_{\rm d}} - \frac{R}{R_{\rm d}}\right] . \tag{D.3}$$

The scale heights are fixed to $z_{\rm d} = 300$ pc for the thin disc and $z_{\rm d} = 900$ pc for the thick disc. The best fit parameters for the thin and thick discs are given in Tab. D.1.

The gas discs (H and H_2) have the density profile

$$\rho_{\rm g}(R,z) = \frac{\Sigma_0}{4\,z_{\rm d}} \exp\left[-\frac{R_{\rm m}}{R} - \frac{R}{R_{\rm d}}\right] {\rm sech}^2\left(\frac{z}{2\,z_{\rm d}}\right) , \tag{D.4}$$

where

$${\rm sech}(x) = \frac{1}{\cosh(x)} = \frac{2}{e^x + e^{-x}} \tag{D.5}$$

is the hyperbolic secant. The parameters of the gas discs are fixed and their value is given in Tab. D.1.

The dark matter halo has a density profile parametrized with

$$\rho(r) = \frac{\rho_{\rm s}}{x^\gamma} \frac{1}{(1+x)^3} \, . \tag{D.6}$$

The best fitting values of $\rho_{\rm s}$ and $r_{\rm s}$ for different γ are given in Tab. D.2.

	Σ_0 [$M_\odot.pc^{-2}$]	R_d [kpc]
thin	896	2.50
thick	183	3.02

	Σ_0 [$M_\odot.pc^{-2}$]	R_d [kpc]	R_d [kpc]	z_d [kpc]
H	53.1	7	4	0.085
H_2	2180	1.5	12	0.045

Table D.1 – Left panel: best fitting parameters for the stellar discs. **Right panel:** fixed parameters for the gas discs.

γ	0	0.25	0.5	1
ρ_s [$M_\odot.pc^{-3}$]	0.09086	0.05261	0.03190	0.00852
r_s [kpc]	7.7	9.6	11.7	19.6

Table D.2 – Best fitting parameters of the dark matter halo.

D.2 Anisotropy in the Cuddeford models

This section focuses on the models of Cuddeford (1991) with DF

$$f(\mathcal{E}, L) = G(Q) L^{-2\beta_0} \,. \tag{D.7}$$

We prove that the anisotropy parameter for these models takes the form

$$\begin{aligned} \beta(r) &\equiv 1 - \frac{\sigma_t^2}{2\sigma_r^2} \\ &= \frac{r^2 + \beta_0 r_a^2}{r^2 + r_a^2} \,. \end{aligned} \tag{D.8}$$

Since this is a generalization of the constant-β and Osipkov-Merritt models, this also demonstrates the form of the anisotropy profile in these two cases. We start by computing the radial velocity variance $\sigma_r^2 \equiv \langle \vec{v}_r^2 \rangle - \langle \vec{v}_r \rangle^2 = \langle v^2 \cos^2(\eta) \rangle$:

$$\begin{aligned} \rho\, \sigma_r^2 &= \int v_r^2 \, f(\mathcal{E}, L) \, \mathrm{d}^3 \vec{v} \\ &= 2\pi \int\int v^2 \cos^2(\eta) \, G(Q) \, L^{-2\beta_0} v^2 \, \sin(\eta) \, \mathrm{d}\eta \, \mathrm{d}v \\ &= 4\pi \int\int v^2 \mu^2 G(Q) \, L^{-2\beta_0} v^2 \, \mathrm{d}\mu \, \mathrm{d}v \,, \end{aligned} \tag{D.9}$$

where we used the change of variable $\cos(\eta) \to \mu$ and μ-parity of the integrand to get the last identity. We now make the following change of variable $(v, \mu) \to (Q, L^2)$. One can compute the Jacobian and finds

$$v^2 \mathrm{d}v \, \mathrm{d}\mu = -\frac{1}{2r^2} \left[2(\Psi - Q) - \frac{L^2}{r^2} \left(1 + \frac{r^2}{r_a^2} \right) \right]^{-1/2} \mathrm{d}Q \, \mathrm{d}L^2 \,. \tag{D.10}$$

What are the bounds on Q and L^2 ? As for the Osipkov-Merritt models, we have $Q \geqslant 0$ and since $Q = \Psi - v^2/2 - L^2/(2r_a^2)$, we have $Q \leqslant \Psi$. To find the upper bound on L^2, we notice that

$$Q = \Psi - \frac{v^2}{2} \cos^2(\eta) - \frac{L^2}{2r^2} \left(1 + \frac{r^2}{r_a^2} \right) \,, \tag{D.11}$$

and therefore

$$L^2 \leqslant L^2_{\max} \equiv \frac{2r^2(\Psi - Q)}{1 + r^2/r_a^2} \,. \tag{D.12}$$

We now have

$$\rho\,\sigma_r^2 = \frac{2\pi}{r^2}\int_0^{\Psi} \mathrm{d}Q\, G(Q) \int_0^{L^2_{\max}} \mathrm{d}L^2 \sqrt{2(\Psi - Q) - \frac{L^2}{r^2}\left(1 + \frac{r^2}{r_\mathrm{a}^2}\right)}\, L^{-2\beta_0}\,, \tag{D.13}$$

where we replace $v^2\mu^2$ in Eq. (D.9) using Eq. (D.11). We rescale L^2 by $L^2_{\max}$ to finally obtain

$$\rho\,\sigma_r^2 = 2\pi \frac{r^{-2\beta_0}}{(1 + r^2/r_\mathrm{a}^2)^{1-\beta_0}} \int_0^{\Psi} \mathrm{d}Q\, G(Q)[2(\Psi - Q)]^{3/2-\beta_0} \int_0^1 \mathrm{d}x\, \sqrt{1-x}\, x^{-\beta_0}\,. \tag{D.14}$$

The integral over x is a particular value of the *beta function*, see Sec. A.2. Its relation to the gamma function leads

$$\rho\,\sigma_r^2 = \pi^{3/2} \frac{r^{-2\beta_0}}{(1 + r^2/r_\mathrm{a}^2)^{1-\beta_0}} \frac{\Gamma(1-\beta_0)}{\Gamma(5/2-\beta_0)} \int_0^{\Psi} \mathrm{d}Q\, G(Q)[2(\Psi - Q)]^{3/2-\beta_0}\,. \tag{D.15}$$

Let us now compute the tangential velocity dispersion

$$\begin{aligned} \rho\,\sigma_\mathrm{t}^2 &= 2\pi \int\int v^2 \sin^2(\eta)\, G(Q)\, L^{-2\beta_0} v^2\, \sin(\eta)\, \mathrm{d}\eta\, \mathrm{d}v \\ &= \frac{4\pi}{r^2} \int\int G(Q)\, L^{2-2\beta_0} v^2\, \mathrm{d}\mu\, \mathrm{d}v\,, \end{aligned} \tag{D.16}$$

where we used $v^2 \sin(\eta) = L^2/r^2$. Performing the same change of variables as before, we obtain

$$\rho\,\sigma_\mathrm{t}^2 = 2\pi \frac{r^{-2\beta_0}}{(1 + r^2/r_\mathrm{a}^2)^{2-\beta_0}} \int_0^{\Psi} \mathrm{d}Q\, G(Q)[2(\Psi - Q)]^{3/2-\beta_0} \int_0^1 \mathrm{d}x\, (1-x)^{-1/2}\, x^{1-\beta_0}\,. \tag{D.17}$$

Using again the properties of the beta and gamma functions, we finally get

$$\rho\,\sigma_\mathrm{t}^2 = 2\pi^{3/2} \frac{r^{-2\beta_0}}{(1 + r^2/r_\mathrm{a}^2)^{2-\beta_0}} \frac{\Gamma(2-\beta_0)}{\Gamma(5/2-\beta_0)} \int_0^{\Psi} \mathrm{d}Q\, G(Q)[2(\Psi - Q)]^{3/2-\beta_0}\,. \tag{D.18}$$

We can now compute the ratio

$$\begin{aligned} \frac{\sigma_\mathrm{t}^2}{2\sigma_r^2} &= \frac{1}{1 + r^2/r_\mathrm{a}^2} \frac{\Gamma(2-\beta_0)}{\Gamma(1-\beta_0)} \\ &= \frac{1-\beta_0}{1 + r^2/r_\mathrm{a}^2}\,, \end{aligned} \tag{D.19}$$

and the anisotropy parameter

$$\beta(r) = \frac{r^2 + \beta_0 r_\mathrm{a}^2}{r^2 + r_\mathrm{a}^2}\,. \tag{D.20}$$

D.3 Numerical simulations

D.3.1 Fitting the simulated galaxies

D.3.2 Escape speed

D.3.3 Velocity distributions

D.3.4 Moments of the velocity distributions

Halo C	$\log_{10}(\rho_0)$ [$M_\odot$/kpc^3]	r_s [kpc]	α	β	γ
DMO	6.848± 0.472	14.291± 8.514	1.0± 0	2.805± 0.297	1.065± 0.142
Hydro	7.746± 0.126	4.210± 0.441	2.165± 0.627	2.504± 0.104	0.189± 0.122

Table D.3 – Parameters of the dark matter halo in Halo C.

Adicora	$\log_{10}(\rho_0)$ [$M_\odot$/kpc^3]	r_s [kpc]	α	β	γ
DMO	7.181± 0.5	11.288± 6.955	1.0± 0	2.744± 0.257	0.975± 0.195
Hydro	7.667± 0.033	6.671± 0.860	1.407± 0.191	2.756± 0.146	0.090± 0.038

Table D.4 – Parameters of the dark matter halo in Adicora.

Mochima	$\log_{10}(\rho_0)$ [$M_\odot$/kpc^3]	r_s [kpc]	α	β	γ
DMO	6.963± 0.442	13.786± 7.744	1.0± 0	2.721± 0.251	1.066± 0.134
Hydro	7.414± 0.185	7.364± 1.115	1.768± 0.573	2.633± 0.165	0.468± 0.171

Table D.5 – Parameters of the dark matter halo in Mochima.

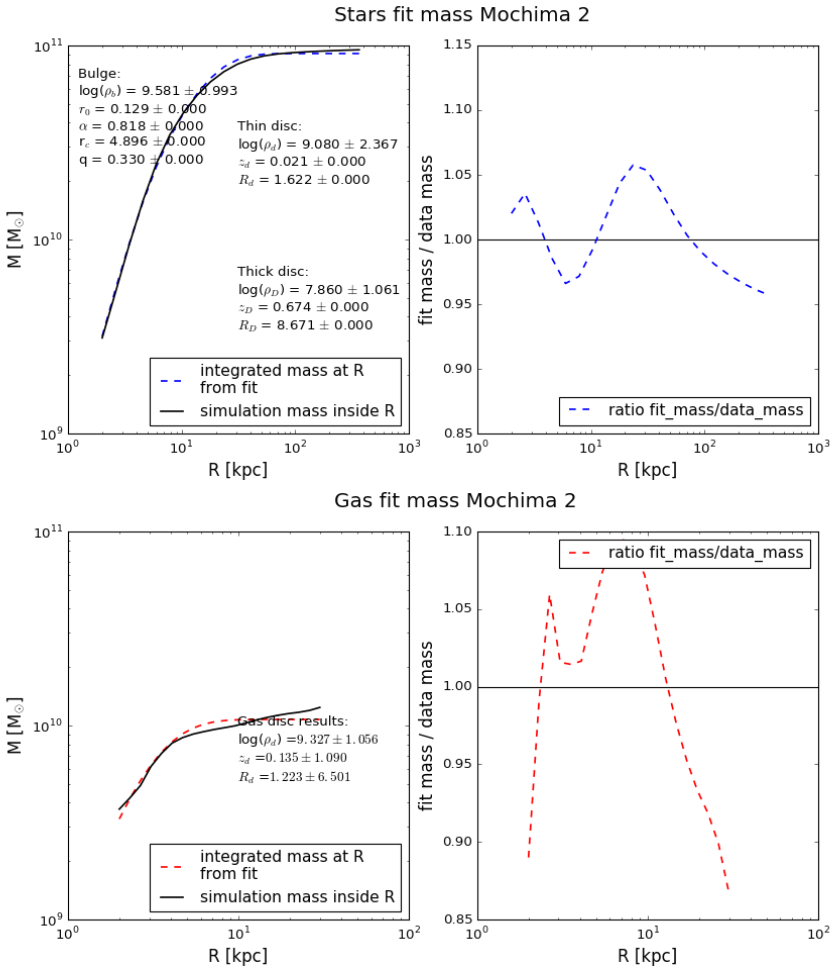

Figure D.1 – Same as Fig. 5.18, for Halo C.

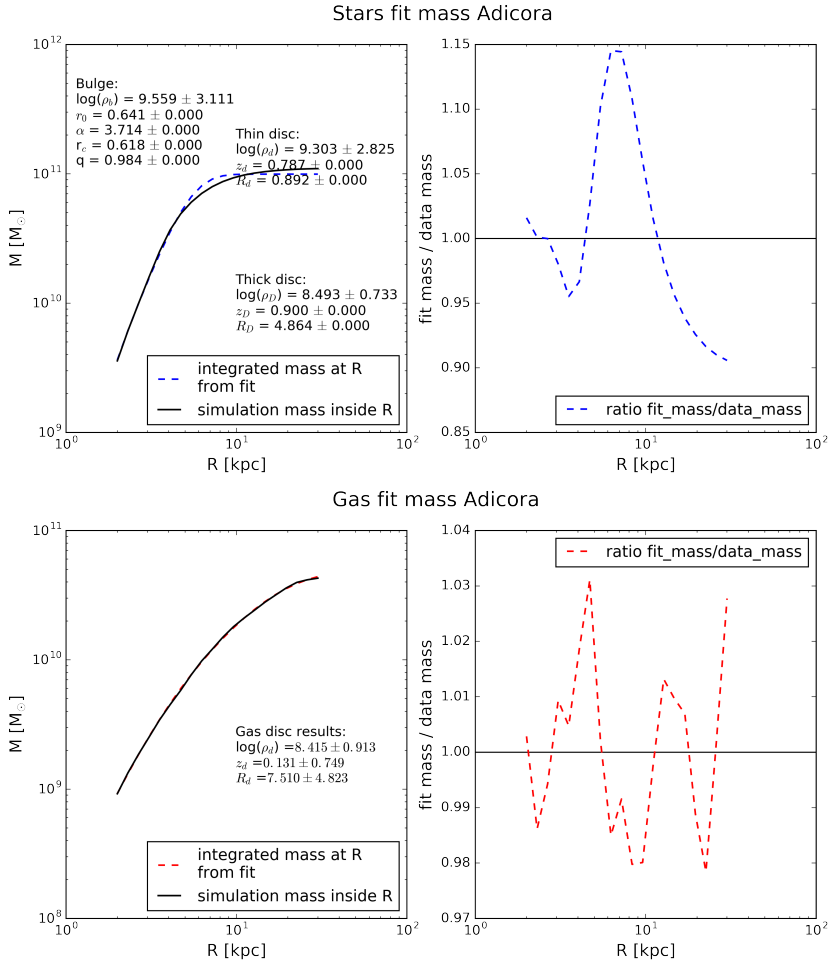

Figure D.2 – Same as Fig. 5.18, for Adicora.

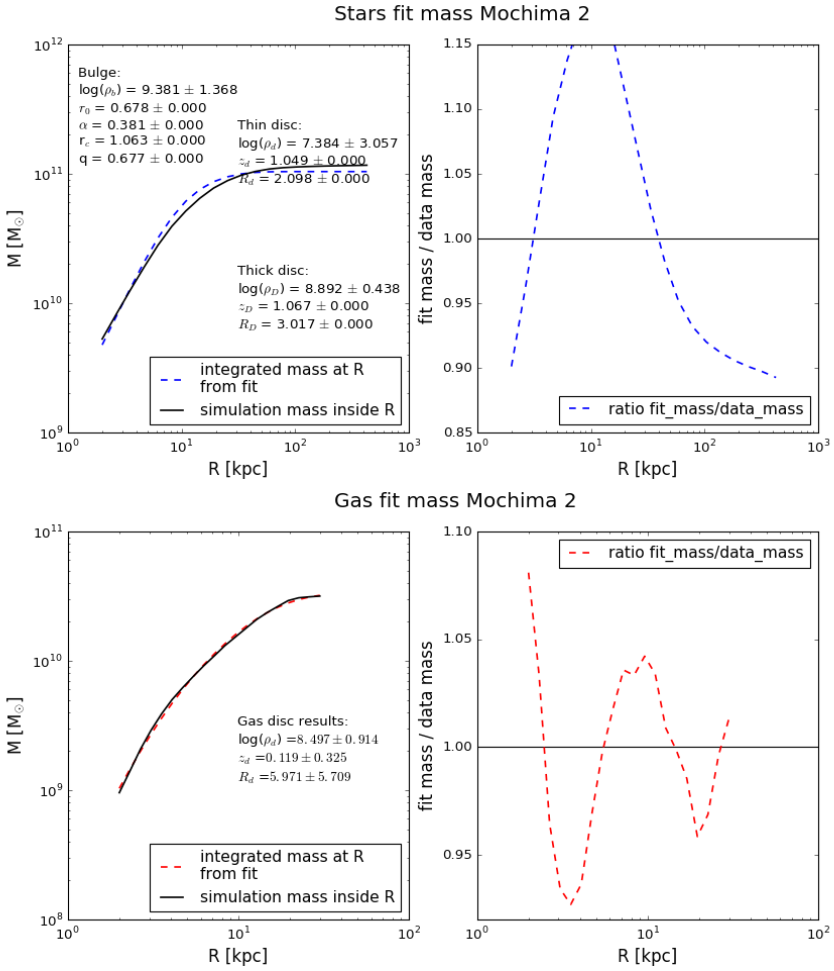

Figure D.3 – Same as Fig. 5.18, for Mochima.

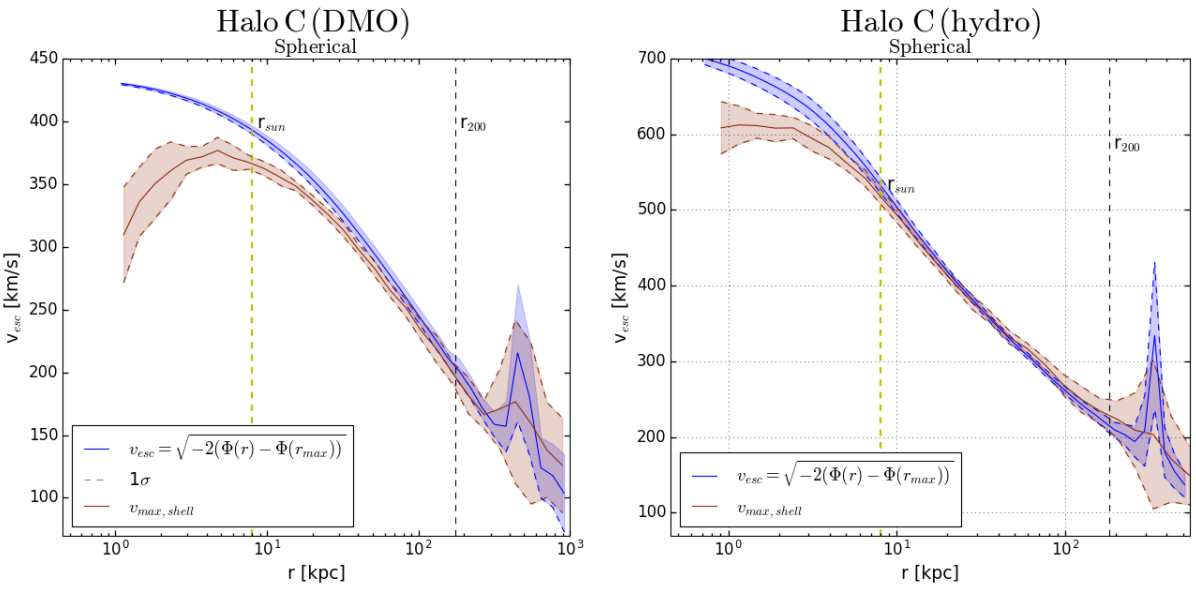

Figure D.4 – Same as Fig. 5.20, for Halo C.

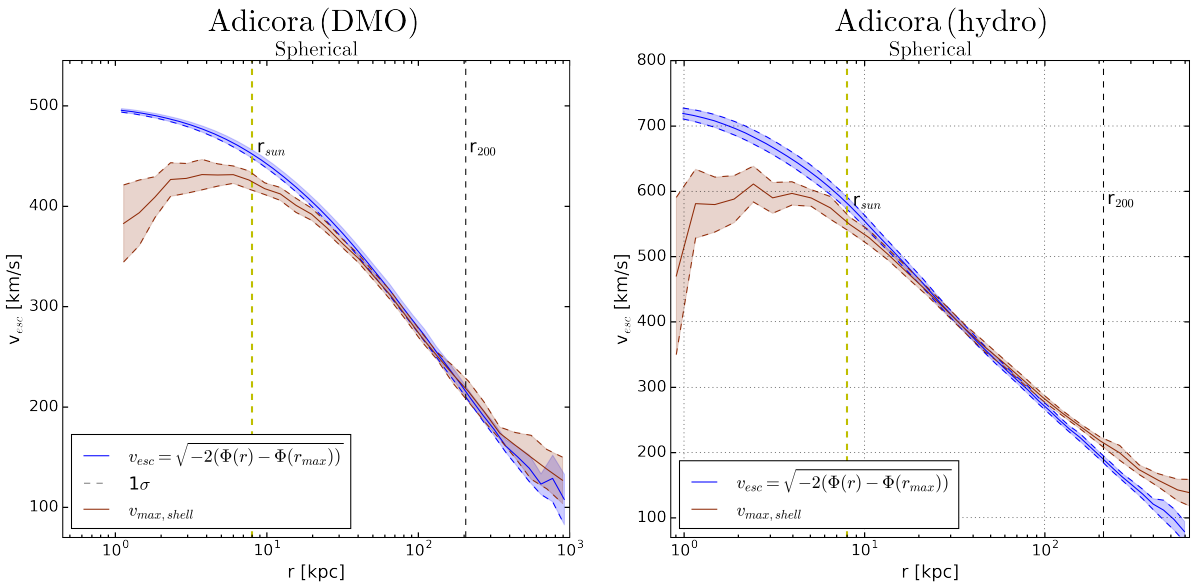

Figure D.5 – Same as Fig. 5.20, for Adicora.

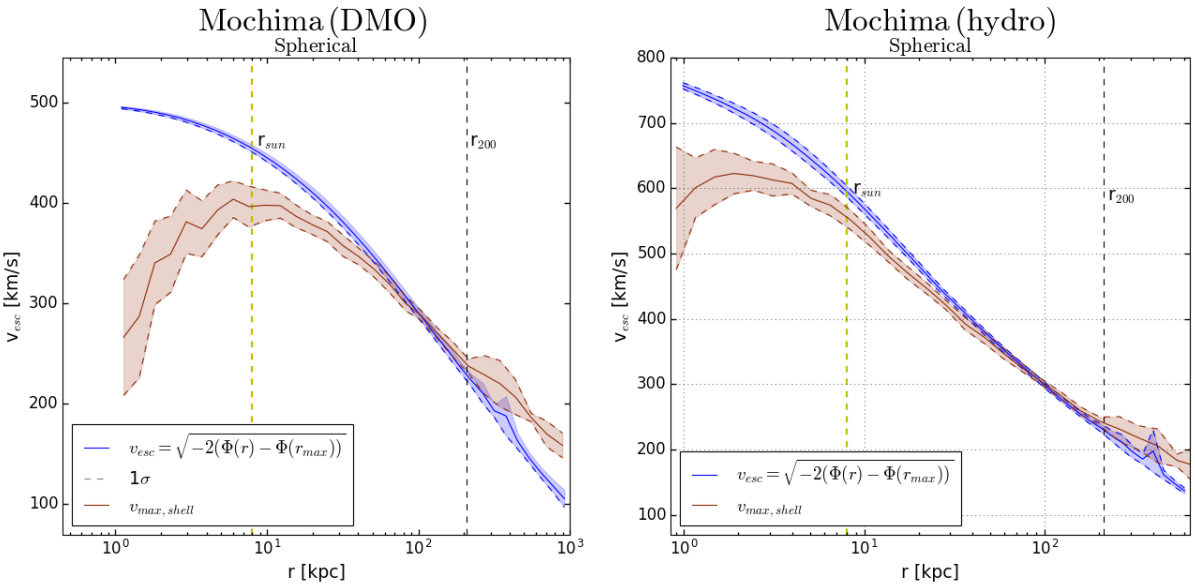

Figure D.6 – Same as Fig. 5.20, for Mochima.

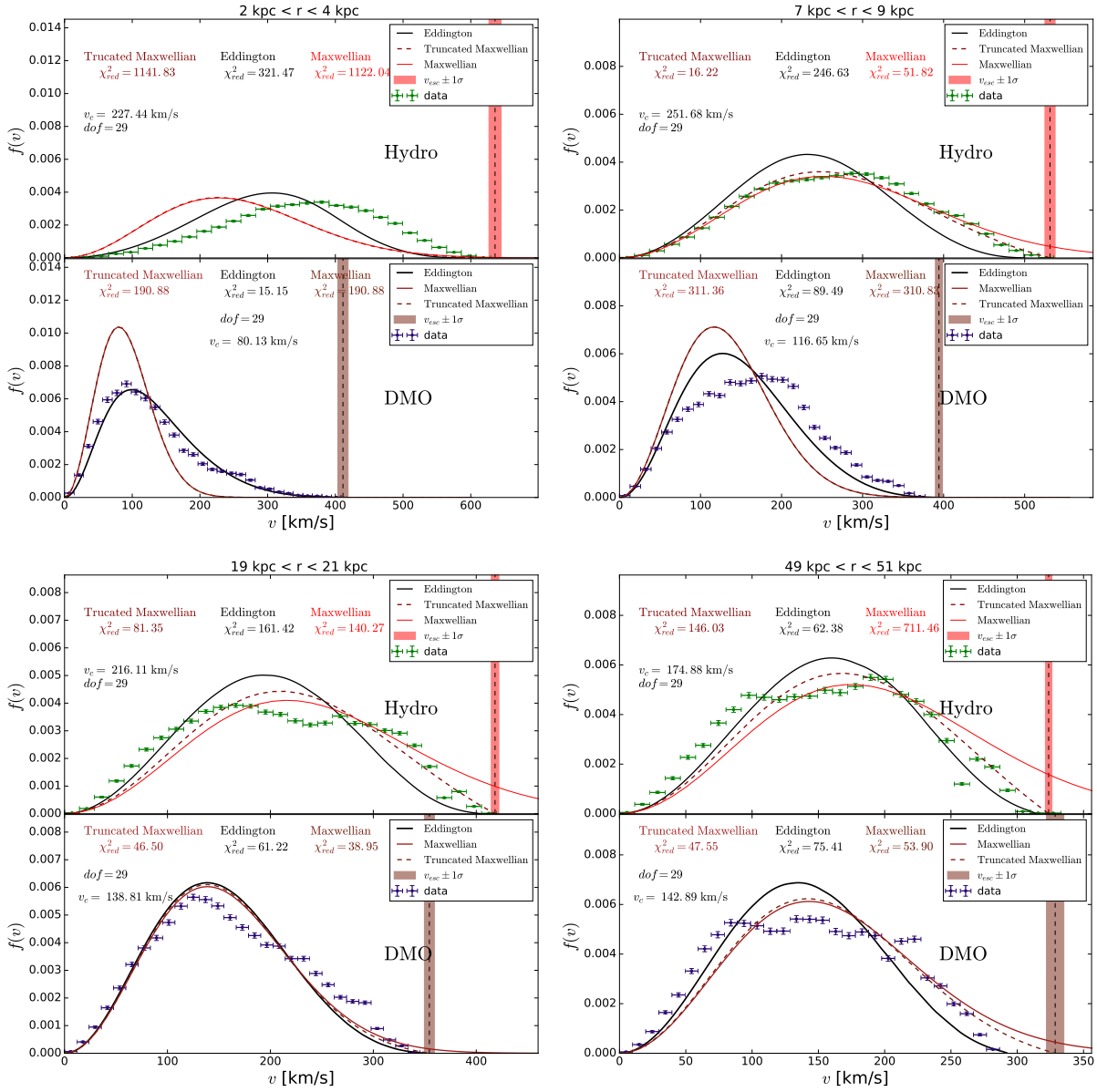

Figure D.7 – Same as Fig. 5.21, for Halo C.

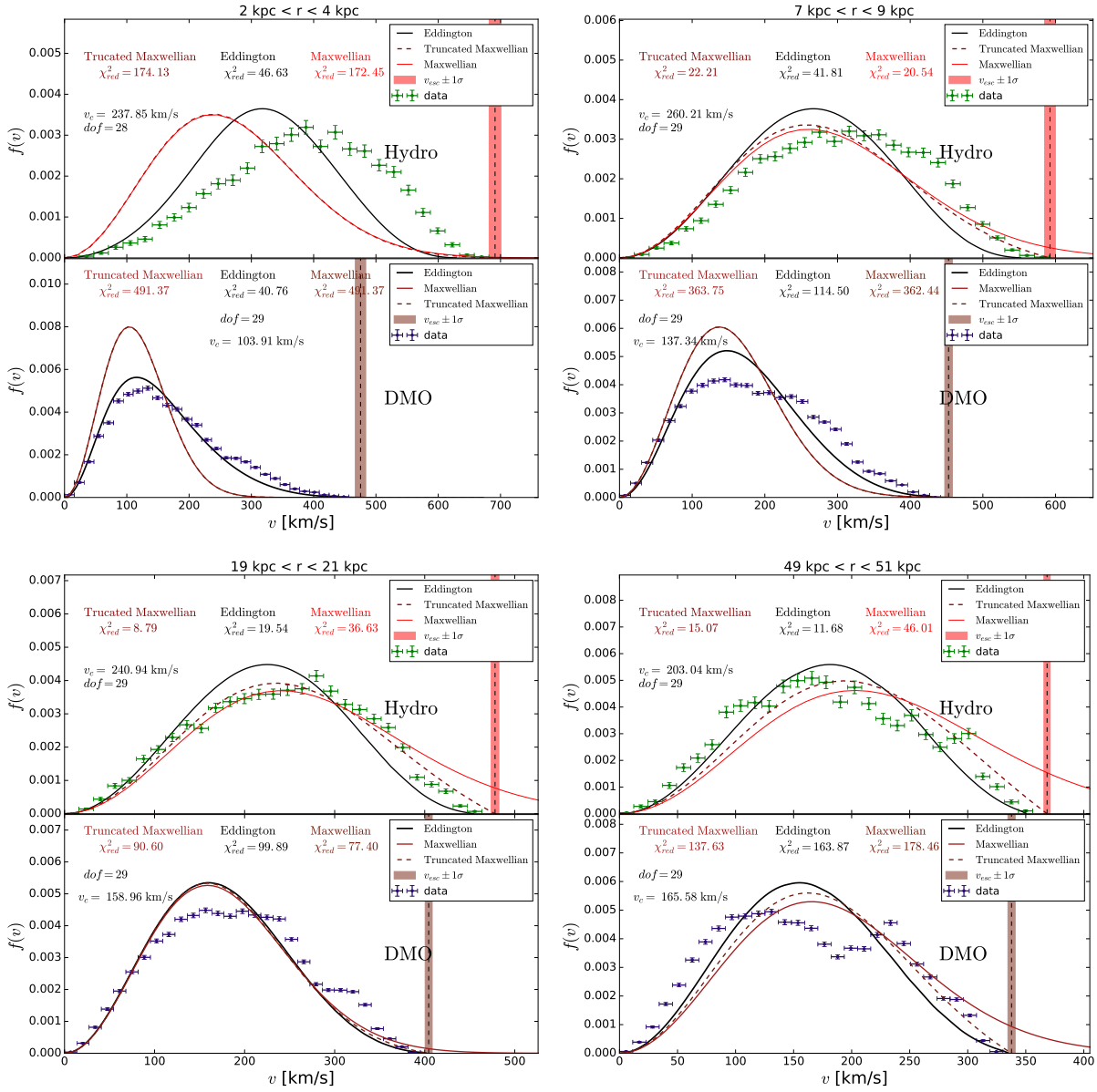

Figure D.8 – Same as Fig. 5.21, for Adicora.

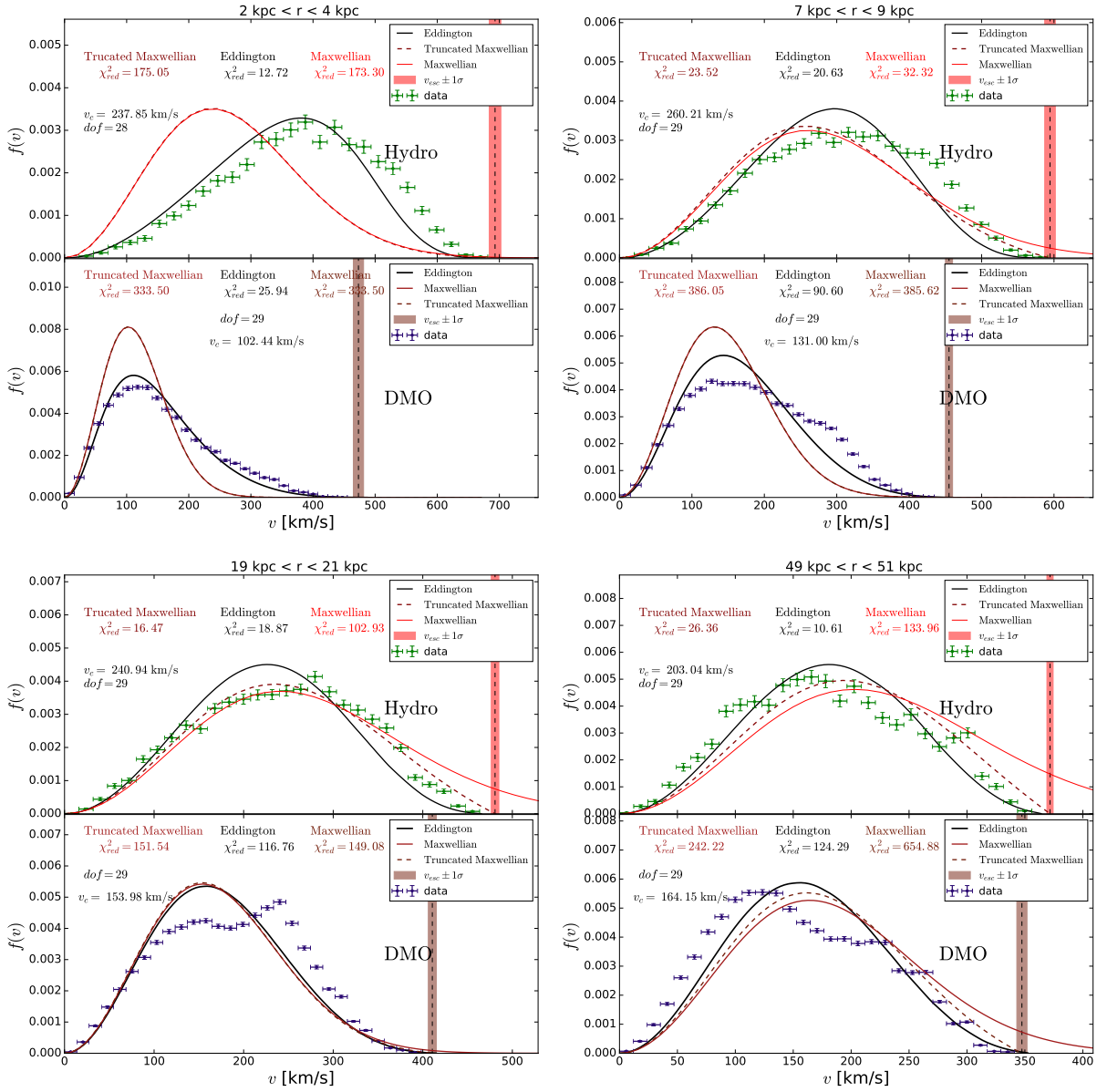

Figure D.9 – Same as Fig. 5.21, for Mochima.

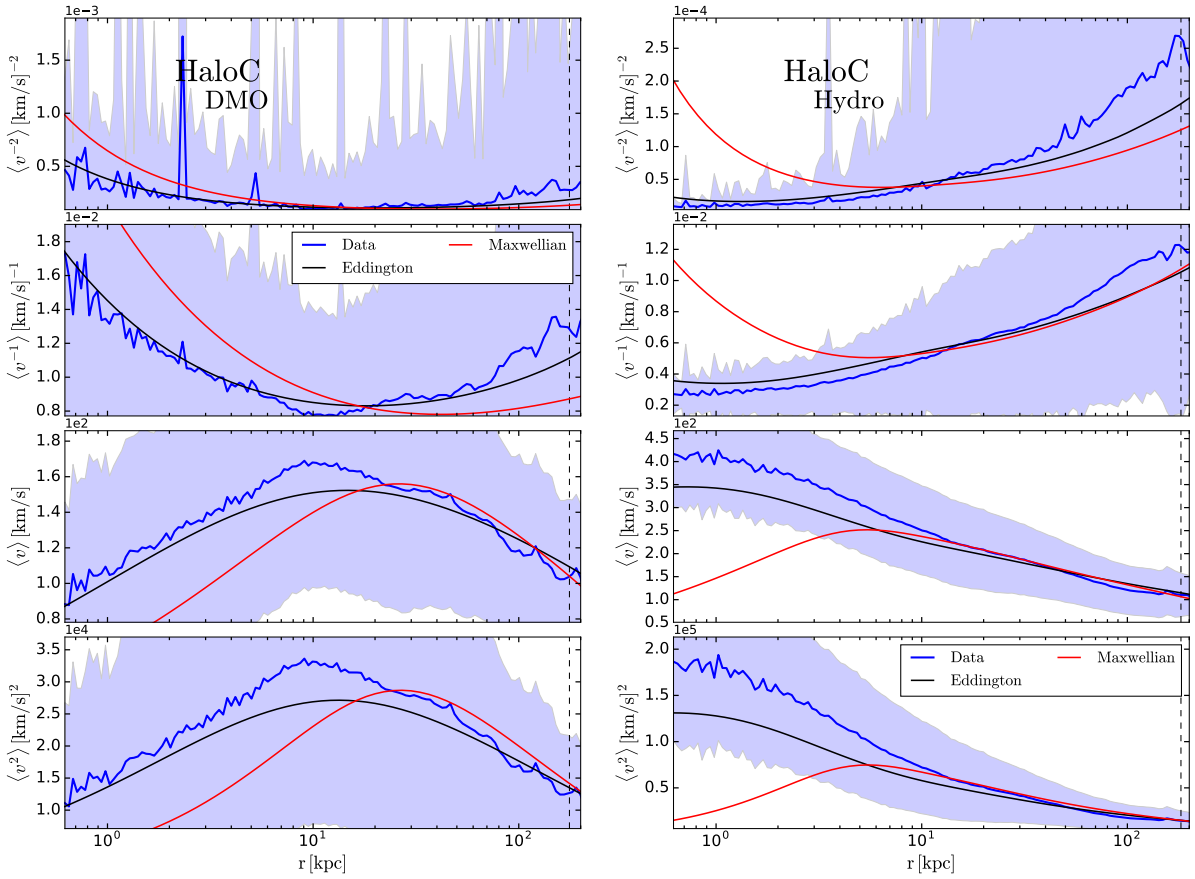

Figure D.10 – Same as Fig. 5.22, for Halo C.

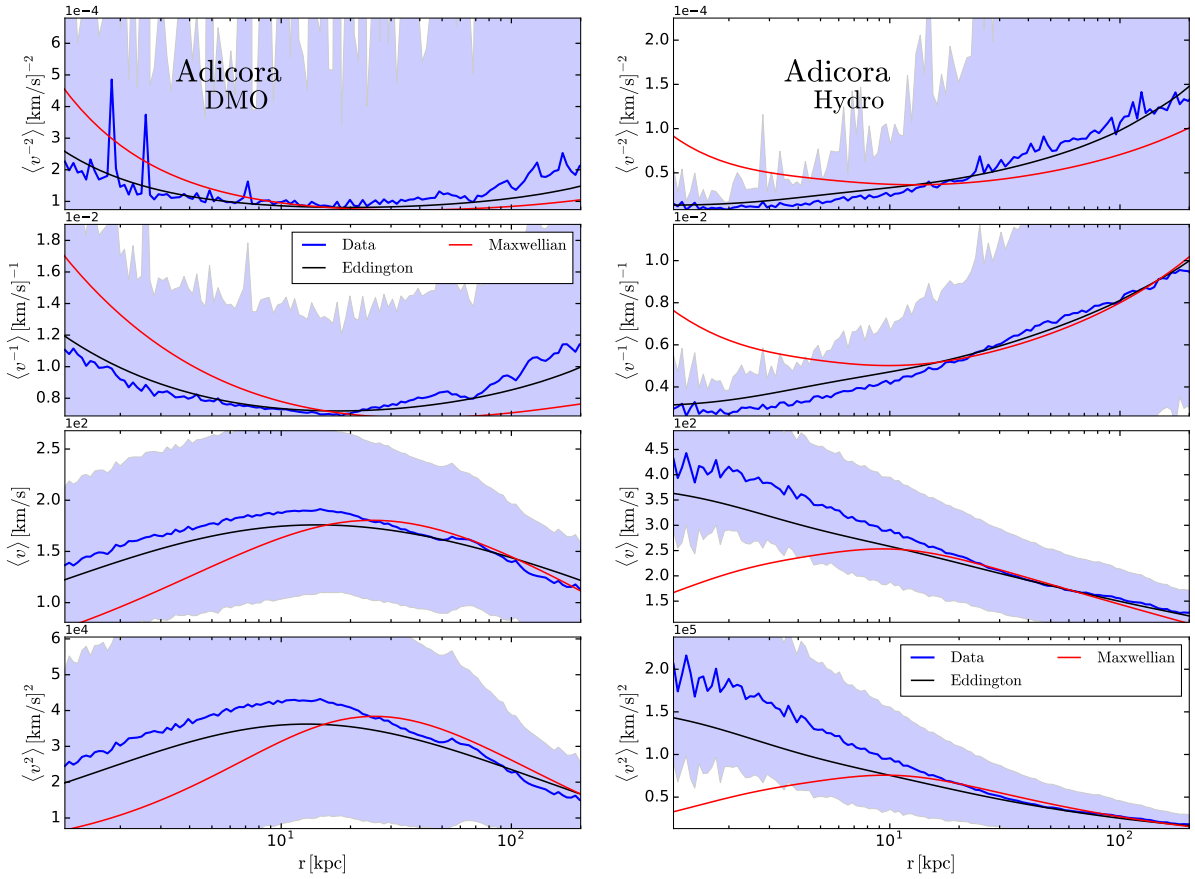

Figure D.11 – Same as Fig. 5.22, for Adicora.

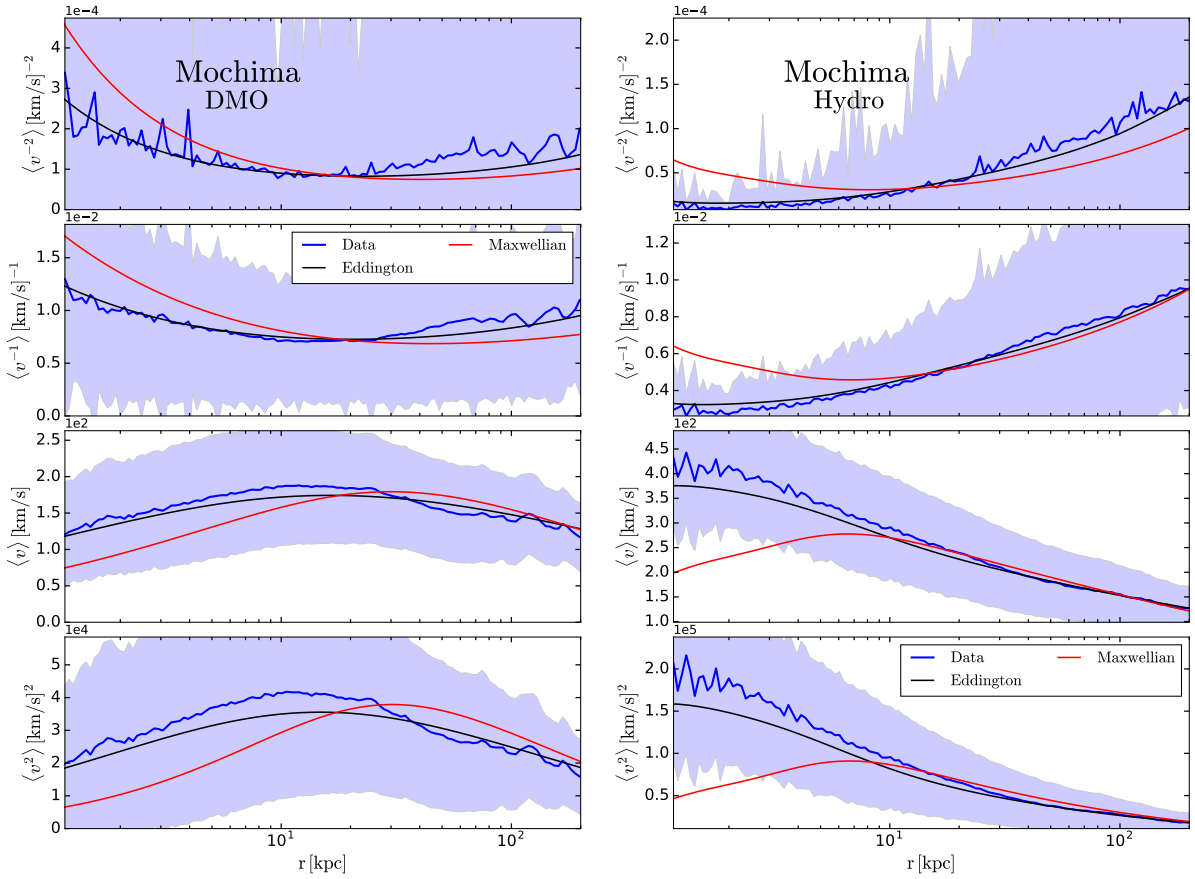

Figure D.12 – Same as Fig. 5.22, for Mochima.

Appendix E

Impact of the phase space on dark matter searches

E.1 Relative velocity distribution

Here we detail the computation of the moments of the relative velocity distribution

$$\langle v_{\rm r}^n \rangle = \int {\rm d}^3\vec{v}_{\rm r}\, v_{\rm r}^n\, F_{\vec{v}_r}(\vec{v}_r, r)\,, \tag{E.1}$$

with the relative velocity distribution defined as

$$F_{\vec{v}_r}(\vec{v}_r, r) = \kappa^{-1}(r) \int {\rm d}^3\vec{v}_{\rm c}\, f_{\vec{v}}(\vec{v}_1, r)\, f_{\vec{v}}(\vec{v}_2, r)\,, \tag{E.2}$$

with the normalization

$$\kappa(r) = \int {\rm d}^3\vec{v}_1 \int {\rm d}^3\vec{v}_2\, f_{\vec{v}}(\vec{v}_1, r)\, f_{\vec{v}}(\vec{v}_2, r)\,. \tag{E.3}$$

We performed the change of variables

$$\left\{ \begin{array}{ll} \vec{v}_{\rm c} & = (\vec{v}_1 + \vec{v}_2)/2 \\ \vec{v}_{\rm r} & = \vec{v}_2 - \vec{v}_1 \end{array} \right. \iff \left\{ \begin{array}{ll} \vec{v}_1 & = \vec{v}_{\rm c} - \vec{v}_{\rm r}/2 \\ \vec{v}_2 & = \vec{v}_{\rm c} + \vec{v}_{\rm r}/2\,. \end{array} \right. \tag{E.4}$$

E.1.1 Isotropic case

If the velocity distribution is isotropic, we have $f_{\vec{v}}(\vec{v}, r) = f_{\vec{v}}(|\vec{v}|, r)$ and the relative velocity distribution is also isotropic therefore

$$\langle v_{\rm r}^n \rangle = 4\pi \int_{v_r^{\rm min}}^{v_r^{\rm max}} {\rm d}v_{\rm r}\, v_{\rm r}^2\, F_{\vec{v}_{\rm r}}(|\vec{v}_{\rm r}|, r)\, v_{\rm r}^n\,. \tag{E.5}$$

We introduce θ as the angle between $\vec{v}_{\rm c}$ and $\vec{v}_{\rm r}$, and define $\mu \equiv \cos(\theta)$. The speed of particles 1 and 2 can then be expressed as

$$\begin{aligned} v_1 &= \sqrt{v_{\rm c}^2 + \frac{v_{\rm r}^2}{4} - v_{\rm c} v_{\rm r}\, \mu} \\ v_2 &= \sqrt{v_{\rm c}^2 + \frac{v_{\rm r}^2}{4} + v_{\rm c} v_{\rm r}\, \mu}\,. \end{aligned} \tag{E.6}$$

In the Galactic frame, we have $v_1 \leqslant v_{\rm esc}(r)$ and $v_2 \leqslant v_{\rm esc}(r)$ which leads

$$|\mu| \leqslant \mu_0\,, \tag{E.7}$$

with

$$\mu_0 = \frac{v_{\rm esc}(r) - v_{\rm c}^2 - v_{\rm r}^2/4}{v_{\rm c}\, v_{\rm r}} \,. \tag{E.8}$$

Eq. (E.4) also leads to $v_{\rm c} \leqslant v_{\rm esc}(r)$ and $v_{\rm r} \leqslant 2\, v_{\rm esc}(r)$. Note that the quantity $f_{\vec{v}}(\vec{v}_1, r)\, f_{\vec{v}}(\vec{v}_2, r)$ is invariant under the transformation $\mu \to -\mu$. The relative velocity distribution can then be written

$$F_{\vec{v}_{\rm r}}(\vec{v}_{\rm r}, r) = 4\pi\kappa^{-1}(r) \int_0^{v_{\rm esc}(r)} {\rm d}v_{\rm c}\, v_{\rm c}^2 \int_0^{\mu_0} {\rm d}\mu\, f_{\vec{v}}(\vec{v}_1, r)\, f_{\vec{v}}(\vec{v}_2, r) \,, \tag{E.9}$$

and the n-order moment

$$\langle v_{\rm r}^n \rangle = 4\pi \int_0^{2\, v_{\rm esc}} {\rm d}v_{\rm r}\, v_{\rm r}^2\, F_{\vec{v}_{\rm r}}(\vec{v}_{\rm r}, r)\, v_{\rm r}^n \,. \tag{E.10}$$

E.1.2 Anisotropic case

In the anisotropic models, the velocity distribution also depends also depends on the modulus of the angular momentum L through

$$f_{\vec{v}}(\vec{v}, r) = \frac{f(\mathcal{E}, L)}{\rho(r)} \,. \tag{E.11}$$

In this case, it is still convenient to perform a change of variables from $\vec{v}_1, \vec{v}_2$ to $\vec{v}_{\rm c}, \vec{v}_{\rm r}$, provided one uses the appropriate coordinate systems to describe the quantities of interest. We introduce the radial unit vector $\vec{e}_r$: the system is invariant under rotation around $\vec{e}_r$ hence the integral over $\vec{v}_{\rm c}$ leads a factor of 2π, see the left panel in Fig. E.1. There is also an integration over the modulus $v_{\rm cm}$ and the angle $\alpha_{\rm cm}$ between $\vec{v}_{\rm cm}$ and $\vec{e}_r$. To perform the integration over $\vec{v}_{\rm r}$, we move to a frame with the z-axis defined by $\vec{v}_{\rm cm}$ and the y-axis chosen orthogonal to $\vec{e}_r$, see the right panel in Fig. E.1. In that frame, we have

$$\begin{aligned} \vec{v}_{\rm cm} &= v_{\rm cm}\, \vec{e}_z \\ \vec{e}_r &= \cos(\alpha_{\rm cm})\, \vec{e}_z + \sin(\alpha_{\rm cm})\, \vec{e}_x \\ \vec{v}_{\rm r} &= v_{\rm r}\, [\cos(\theta)\, \vec{e}_z + \sin(\theta)\cos(\phi)\, \vec{e}_x + \sin(\theta)\sin(\phi)\, \vec{e}_y] \end{aligned} \tag{E.12}$$

with θ the angle between $\vec{v}_{\rm r}$ and $\vec{v}_{\rm cm}$ (already introduced in the isotropic case) and ϕ the complemetary spherical angle. This allows us to write the relative *speed* distribution as

$$F_{v_{\rm r}}(v_{\rm r}, r) = 2\pi\kappa^{-1}(r)\, v_{\rm r}^2 \int_0^{v_{\rm esc}(r)} {\rm d}v_{\rm c}\, v_{\rm c}^2 \int_{-1}^{1} {\rm d}\mu_{\rm cm} \int_0^{2\pi} {\rm d}\phi \int_{-\mu_0}^{\mu_0} {\rm d}\mu\, f_{\vec{v}}(\vec{v}_1, r)\, f_{\vec{v}}(\vec{v}_2, r) \,. \tag{E.13}$$

We used $\mu_{\rm cm} \equiv \cos(\alpha_{\rm cm})$ in the equation above. We give the expressions of the angular momentum for each particle

$$\begin{aligned} L_1^2 &= \left| \vec{r} \times \left(\vec{v}_{\rm cm} - \frac{v_{\rm r}}{2} \right) \right|^2 \\ &= r^2 \left[\frac{v_{\rm r}^2}{4} (1-\mu^2) \sin^2(\phi) + \left\{ -\frac{v_{\rm r}}{2}\, \mu_{\rm cm} \sqrt{1-\mu^2} \cos(\phi) - \sqrt{1-\mu_{\rm cm}^2} \left(v_{\rm cm} - \frac{v_{\rm r}}{2}\, \mu \right) \right\} \right] \\ L_2^2 &= \left| \vec{r} \times \left(\vec{v}_{\rm cm} + \frac{v_{\rm r}}{2} \right) \right|^2 \\ &= r^2 \left[\frac{v_{\rm r}^2}{4} (1-\mu^2) \sin^2(\phi) + \left\{ +\frac{v_{\rm r}}{2}\, \mu_{\rm cm} \sqrt{1-\mu^2} \cos(\phi) - \sqrt{1-\mu_{\rm cm}^2} \left(v_{\rm cm} + \frac{v_{\rm r}}{2}\, \mu \right) \right\} \right] . \end{aligned} \tag{E.14}$$

E.2 Bounds on p-wave annihilating dark matter

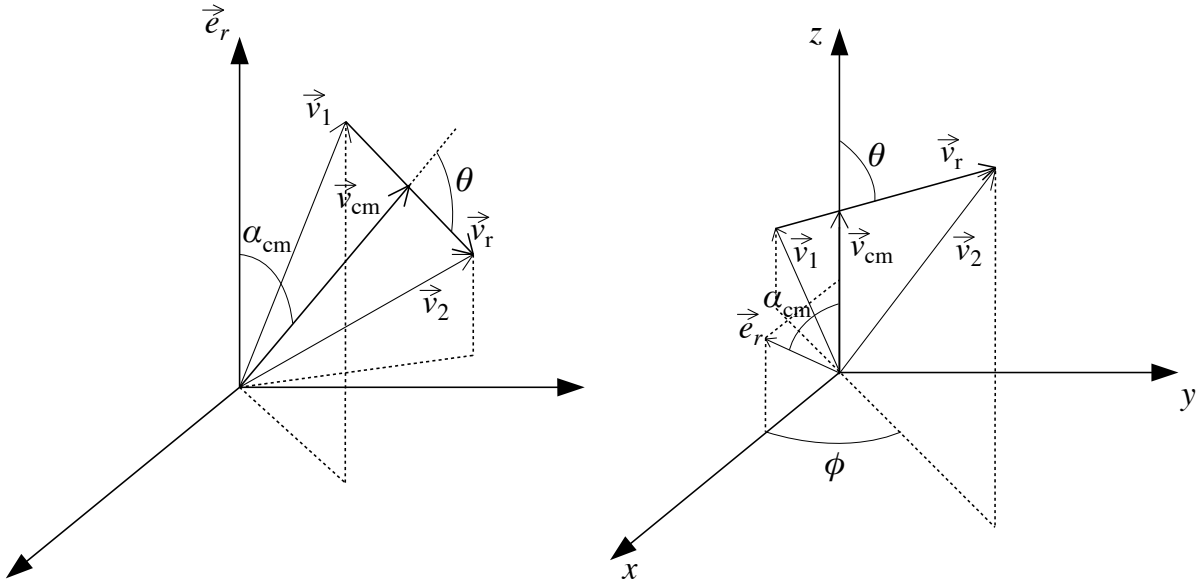

Figure E.1 – Coordinate systems for the derivation of the relative velocity DF for an anisotropic system. **Left panel:** frame associated with $\vec{r}$, in which we define $\vec{v}_c$. **Right panel:** coordinate system associated with $\vec{v}_c$.

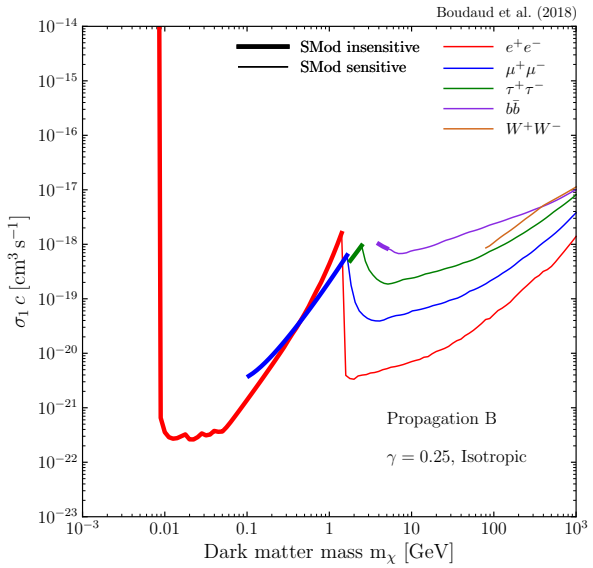

Figure E.2 – p-wave constraints for different annihilation channels, for the $\gamma = 0.25$ mass model.

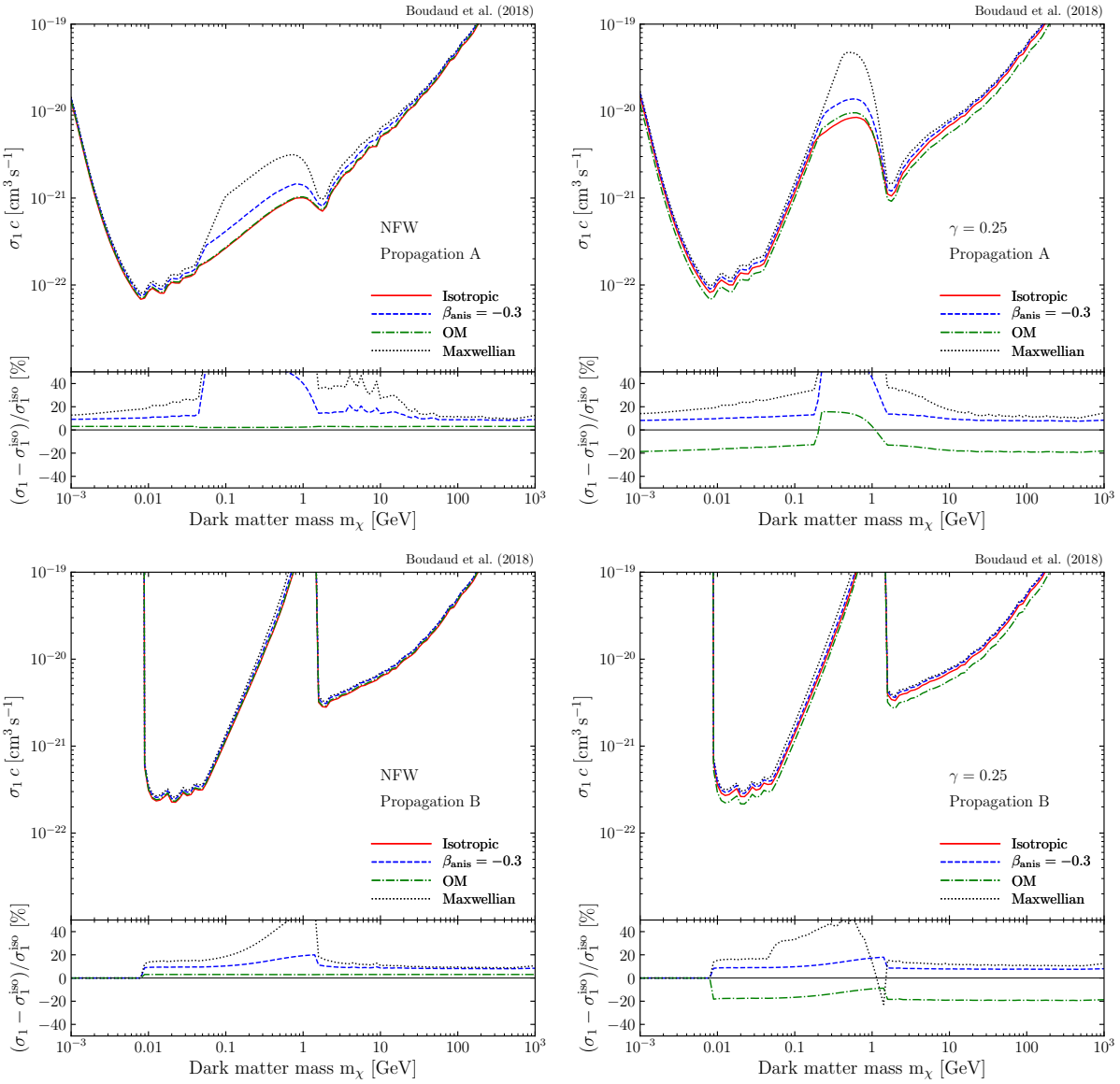

Figure E.3 – Top panel:. Uncertainties related to the anistropy in the propagation model A, for the NFW profile (left) and the $\gamma = 0.25$ profile (right) **Bottom panel:** same as the top panel, for the propagation model B.

Appendix F

Résumé en français

F.1 Introduction

F.1.1 Le problème de la masse manquante: preuves observationnelles

Les physiciens et astronomes sont aujourd'hui confrontés à une multitude de données observationnelles pointant vers un déficit de masse dans notre Univers.

La manifestation la plus frappante de ce déficit est à l'échelle des galaxies, notamment les galaxies spirales. La mesure des courbes de rotation de ces galaxies permet d'estimer leur masse, et l'on constate que celle-ci diffère fortement de la masse extrapolée à partir de la luminosité. Un problème similaire est présent à l'échelle des amas de galaxies, où des méthodes telles que le lentillage graviationnel permettent d'estimer la masse indépendamment de la luminosité. Là encore, une différence considérable est constatée entre la masse totale et la masse lumineuse.

Un problème de masse manquante est également présent aux échelles cosmologiques. L'analyse des anisotropies de température du fond diffus micro-ondes a permis l'établissement du modèle ΛCDM qui est aujourd'hui le modèle standard de la cosmologie. Ce modèle stipule que le budget énergétique de l'Univers est composé à 70% d'une constante cosmologique Λ, à 25% d'une matière "froide" (non-relativiste) et sans interactions, et à 5% de matière baryonique, c'est-à-dire de matière ordinaire. Cela qu'environ 80% de la matière dans l'Univers est d'origine et de composition inconnue. Il est naturel d'identifier cette matière étrange avec la masse manquante mesurée dans les galaxies et les amas de galaxies.

F.1.2 Le modèle ΛCDM aux petites échelles

Le modèle ΛCDM rencontre un succés phénoménale lorqu'on le confronte aux observations liées à des échelles super-galactiques. A l'échelle des galaxies, en revanche, des points de désaccord entre la théorie et les observations apparaissent.

Ces problèmes aux petites échelles se manifestent de différentes manières. Tout d'abord, le profile de densité aux centres de galaxies semblent être, dans la plupart des cas, assez plat alors que ΛCDM prédit un profile très piqué pour les halos de matière sombre. D'autre part, ΛCDM prédit une multitude de petites galaxies satellites associée à notre Voie Lactée, hors seule une poignée de ces satellites est observée. Finalement, les satellites qui sont effectivement observés sont moins massifs que ce que la théorie prédit.

Plusieurs solutions ont été proposées pour résoudre ces problèmes. Deux grandes classes de solutions peuvent êtres distinguées. On peut tout d'abord supposé que ces tensions montrent un échec du modèle ΛCDM, qui doit donc être modifié. Parmis ces solutions, on peut citer les modèles de matière sombre "tiède" ou la matière sombre auto-intéragissante. Une autre approche consiste à supposer que le modèle ΛCDM est correct et les problèmes aux petites échelles sont en fait dues aux effets de la matière ordinaire qui sont encore mal compris à l'échelle galactique.

F.1.3 Approches théoriques du problèmes de la matière sombre

Deux approches théoriques radicalement différentes sont aujourd'hui envisagées pour résoudre le problème de la matière sombre.

Une première approche consiste à interpreter la masse manquante comme un échec de la théorie de la gravitation actuellement admise. Selon cette approche, la gravitation Newtonienne et la relativité générale doivent être modifiées pour expliquer les observations sans faire intervenir une nouvelle forme de matière. Parmis les théories proposées, on peut citer la Gravité Newtonienne Modifiée et ses extensions relativistes.

La seconde approche consiste à supposer que la masse manquante est bien constituée d'une forme de matière exotique. Il a été établit que la matière ordinaire ne peut pas être la matière sombre, cette matière doit donc être constituée de particules encore inconnues. De très nombreux modèles de physique des particules incorporent des candidats au titre de particule de matière sombre. On peut citer, entres autres, la supersymétrie, les théories à dimensions supplémentaires, les axions et les neutrinos stériles.

F.1.4 Recherches expérimentales des particules de matière sombre

Si la matière sombre est constituée de particules exotiques et que ces particules ont des interactions autres que gravitationnelles avec la matière ordinaires, on peut espérer identifiée ces particules en suivant plusieurs démarches expérimentales.

On peut tout d'abord espérer produire les particules de matière sombre dans des accélerateurs de particules comme le LHC au Cern. Si la matière sombre peut intéragir avec les noyaux atomiques, on peut également espérer détecter une collision entre une particule de matière sombre cosmique et un noyau terrestre. C'est ce que l'on nomme la détection directe. Enfin, si la matière sombre peut s'annihilaler ou est instable, on peut espérer détecter les produits de son annihilation (ou de sa désingration) dans le rayonnement cosmique. On parle alors de détection indirecte.

F.2 Histoire thermique des particules massives intéragissant faiblement

On suppose dans cette section que la particule de matière sombre est stable, qu'elle a une masse très élevée (typiquement entre quelques GeV et quelques TeV) et des interactions faibles avec les particules standards. On suppose de plus que cette particule peut s'auto-annihiler. Des particules de ce type sont appelées WIMPs pour Weakly Interacting Massive Particles.

F.2.1 Découplage chimique

Lorsque la température du plasma primordial T est supérieure à la masse m de la matière sombre la réaction $\chi + \chi \rightleftharpoons f + \overline{f}$, où χ est la matière sombre et f une particule standard (un lepton ou un quark, par exemple), est à l'équilibre. L'univers étant en expansion, la température décroit et le taux d'annihilation Γ_{ann} de la matière sombre chute. Lorsque $T < m$ la réaction $f + \overline{f} \rightarrow \chi + \chi$ ne se produit plus. Enfin arrive un instant où $\Gamma_{\text{ann}} < H$ où H est le paramètre de Hubble et l'annihilation de χ devient hautement improbable. On parle de découple chimique de la matière sombre. Le nombre de particules de matière sombre est alors fixé et la densité de matière sombre aujourd'hui peut être prédite. On peut exprimer l'abondance de χ en fonction de la section efficace d'annihilation $\langle \sigma_{\text{ann}} v \rangle$ et on trouve

$$\Omega_\chi h^2 \simeq 0.1 \left(\frac{\langle \sigma_{\text{ann}} v \rangle}{3 \times 10^{-26}\,\text{cm}^3/\text{s}} \right)^{-1} . \tag{F.1}$$

La coïncidence de la valeur observée de $\Omega_{\text{cdm}} h^2$ avec une section efficace électrofaible est appelée le "miracle du WIMP".

F.2.2 Découplage cinétique

Aprés le découplage chimique, la matière sombre reste en équilibre thermique avec le plasma à travers les réactions de diffusion $\chi + f \leftrightharpoons \chi + f$. Au bout d'une certain temps, on a $\Gamma_{\rm diff} < H$ où $\Gamma_{\rm diff}$ est le taux de diffusion, et la diffusion devient inefficace. On parle de découplage cinétique de la matière sombre. Ce découplage est très important car il fixe la taille des toutes premières structures de matière sombre qui se forment dans l'Univers. Un calcul détaillé montre que la masse de ces structures est très faible

$$M_{\rm min} \sim 10^{-10} - 10^{-4}\,{\rm M}_\odot. \tag{F.2}$$

F.3 Halos et sous-halos de matière sombre dans l'Univers

F.3.1 Formation des structures

Après l'égalité matière-radiation, les perturbations de matière sombre croissent efficacement jusqu'à s'effondrer et former des halos. Le formalisme de Press-Schechter permet de calculer la fonction de masse de ces objets, et l'on trouve pour le modèle ΛCDM

$$\frac{{\rm d}n}{{\rm d}m} \propto m^{-2}\,. \tag{F.3}$$

Le profile de densité ρ des halos est mesuré dans les simulations cosmologiques et on trouve une forme universelle, identique pour tous les halos. La densité est fortement piquée au centre du halo $\rho(r) \propto r^{-1}$ et se comporte comme $\rho(r) \propto r^{-3}$ dans les parties externes. La taille de la région centrale rapportée à la taille totale de la structure définit sa concentration. Cette quantité est corrélée à la masse de sorte que les plus petits halos sont aussi les plus concentrés.

F.3.2 Évolution des sous-halos

Les halos galactiques comme celui de la Voie Lactée sont formés par l'accrétion de halos plus petits. La majeure partie de ces petits halos survit en fait à l'accrétion et sont toujours présents dans les galaxies aujourd'hui. On parle alors de sous-halos. L'intéraction de ces sous-halos avec le potentiel gravitationnel de la galaxie hôte, que l'on nomme effets de marée, épluche ces structures, qui perdent ainsi une grande partie de leur masse. Ces intéractions, en particulier l'effet de choc du disque stellaire, sont modélisées en détails et la forme finale des sous-halos est précisement calculée.

F.3.3 Modèle contraint des sous-halos Galactiques

Avec tous éléments en main, nous construisons un modèle de la population Galactique de sous-halos. Ce modèle a l'originalité de reposer sur des contraintes observationnelles, c'est-à-dire qu'il est cohérent *par construction* avec la dynamique de notre Galaxie telle qu'elle est observée. Nous démontrons que la distribution des sous-halos dans la Galaxies est fortement affectée par les effets de marée. En particulier, les sous-halos sont épluchés bien plus efficacement au centre de la Galaxie qu'au bord. De plus, une sélection des structures s'opère en fonction de leur concentration. Les moins concentrées sont détruites alors que les plus concentrées résistent davantages aux marées. Ceci augmente la concentration moyenne des structures au centre de la Galaxies. La fonction de masse est elle aussi affectée du fait de la corrélation entre masse et concentration.

F.4 Impact des sous-halos sur les recherches indirectes de matière sombre

La présence de sous-halos, qui sont des régions de surdensité de matière sombre au sein de la Galaxie, augmente la taux d'annihilation de ces particules. On s'attend donc à ce que les prédictions pour les recherches indirectes soient affectées par la structuration de la matière sombre aux petites échelles. En utilisant notre modèle de sous-halos, nous calculons précisement le "boost" attendus sur les signaux indirectes. Deux canaux complémentaires sont ensuite considérés: les rayons gamma et les antiprotons cosmiques.

F.4.1 Impact sur les recherches avec les rayons gamma

Les rayons gamma permettent d'explorer le halo de matière sombre le long d'une ligne de visée. Nous calculons le facteur de "boost" en fonction de la ligne de visée et montrons comment ce facteur dépend des paramètres de la distribution des sous-halos, en particulier les paramètres de la fonction de masse. Nous trouvons un boost important au dessus d'une latitude de 30°, ce qui doit fortement impacter les contraintes sur les modèles microscopiques dérivées à partir des données sur les rayons gamma.

F.4.2 Impact sur les recherches avec les antiprotons

Les antiprotons cosmiques forment un canal complémentaire des rayons gamma du fait de leur propagation dans la Galaxie. Contrairement aux photons, les antiprotons sont des particules chargés qui diffusent sur les inhomogénéités du champ magnétique turbulent de la Galaxie. Leur trajectoire est donc aléatoire. Les antiprotons reçus sur Terre ont donc exploré un volume moyen contenue dans une sphère autour de la Terre, sphère dont le rayon dépend par ailleurs de l'énergie des antiprotons. Nous calculons le boost pour le signal d'antiprotons et montrons sa dépendance dans les paramètres des sous-halos. Nous montrons enfin comment l'inclusion des sous-halos modifie les contraintes sur la section efficaces d'annihilation obtenues à partir des données de l'expérience AMS-2.

F.5 L'espace des phases de la matière sombre Galactique

F.5.1 Le formalisme d'Eddington

La dynamique des particules de matière sombre dans la Galaxie est gouvernée par l'équation de Boltzmann sans collisions. La méthode d'Eddington permet d'obtenir une fonction de distribution dans l'espace des phases $f(\vec{r}, \vec{v})$ solution stationnaire de cette équation. Dans l'hypothèse où la distribution de vitesse des particules de matière sombre est isotrope, f est simplement une fonction de l'énergie et peut s'exprimer directement en fonction du profile de densité du halo de matière sombre et du potentiel gravitationnel total du système.

L'hypothèse d'isotropie peut-être levée, auquel cas f dépend à la fois de l'énergie et de la norme du moment angulaire. Plusieurs extensions du modèle d'Eddington incorporant de l'anisotropie ont été découvertes. Nous en discutons deux en détails: les modèles à anisotropie constante, et les modèles de Osipkov-Merrit.

F.5.2 Problèmes et limitations du formalisme d'Eddington

Bien que la méthode d'Eddington soit connue depuis longtemps, relativement peu d'attention à été portée sur ses limites d'applicabilité. Ces deux aspects sont étudiés en détail.

Une première limite du formalisme d'Eddington apparaît lorqu'on l'applique à un système de taille finie. La présence d'un bord induit une divergence dans la distribution f. Cette divergence

n'a pas d'origine physique et doit être régularisée. Nous proposons plusieurs méthodes permettant de traiter cette divergence et quantifions précisement l'impact de ces méthodes sur f.

Une autre limit concerne le problème de la stabilité. Rien ne garantit que la solution d'Eddington soit stable, il faut donc s'en assurer. Il se trouve que de nombreuses configurations [profile de densité, potentiel gravitationnel] amènent à des solutions qui sont instables. Nous développons des critères analytiques permettant de déterminer la stabilité a priori, et classifions les systèmes problématiques où le formalisme ne peut pas être appliqué.

F.6 Impact de l'espace des phases sur les recherches de matières sombre

F.6.1 Impact générique sur les observables

Les conséquences de notre étude sur l'applicabilité du formalisme d'Eddington sont étudiées en détail dans le contexte des recherches de matière sombre. Nous considérons plusieurs observables intervenant dans les recherches directes et indirectes, et évaluons l'impact des méthodes de régularisations discutées dans le chapitre précédent. Nous comparons systématiquement les prédictions de la méthode d'Eddington avec celles du "Modèle Standard du Halo" qui est très souvent utilisé dans ce cadre, et montrons que la différence entre ces deux approches est en générale très importante.

F.6.2 Application aux positrons cosmiques

La méthode d'Eddington est appliquée de manière concrète à l'étude des électrons et positrons cosmiques. L'exploitation des données de la sonde *Voyager 1* nous permet de dériver des contraintes très fortes sur la section efficace d'annihilation des particules de matière sombre.

F.7 Conclusion

Plusieurs aspects de la recherche de la matière sombre ont été abordés au cours de ce travail. En partant autant que possible de principes élémentaires issus de la physique des particules et de la cosmologie, nous avons construit et développé un ensemble de modèles et d'outils permettant d'attaquer le problème de l'identification de la matière sombre dans la Galaxie. Nous tenons à souligner que les outils que nous avons développé sont suffisament généraux pour s'appliquer à de nombreux modèles de matière sombre, comme les WIMPs, les axions et les trous noirs primordiaux. Un grand nombre de pistes de recherches sont ouvertes à l'issue de ce travail. Nous allons continuer à exploiter notre connaissance de la structuration aux petites échelles et de l'espace des phase pour explorer l'espace des modèles de matière sombre. L'application aux recherches directes et indirectes, déjà en parti réalisé, sera complété par une étude des effets gravitationnels des petites structures sur la matière observables.

Bibliography

Aad G. et al. (ATLAS Collaboration), *The ATLAS Experiment at the CERN Large Hadron Collider,* JINST **3**, S08003 (2008). 14

Abazajian K. N., *The Consistency of Fermi-LAT Observations of the Galactic Center with a Millisecond Pulsar Population in the Central Stellar Cluster,* JCAP **1103**, 010 (2011). 17

Abazajian K. N., Canac N., Horiuchi S., Kaplinghat M., *Astrophysical and Dark Matter Interpretations of Extended Gamma-Ray Emission from the Galactic Center,* Phys. Rev. **D90**, 023526 (2014). 17

Abazajian K. N., Kaplinghat M., *Detection of a Gamma-Ray Source in the Galactic Center Consistent with Extended Emission from Dark Matter Annihilation and Concentrated Astrophysical Emission,* Phys. Rev. **D86**, 083511 (2012). 17

Abbott L. F., Sikivie P., *A Cosmological Bound on the Invisible Axion,* Phys. Lett. **B120**, 133-136 (1983). 11

Abdallah J., Araujo H., Arbey A., Ashkenazi A., Belyaev A., Berger J., Boehm C., Boveia A., Brennan A., Brooke J., Buchmueller O., Buckley M., Busoni G., Calibbi L., Chauhan S., Daci N., Davies G., De Bruyn I., De Jong P., De Roeck A., de Vries K., Del Re D., De Simone A., Di Simone A., Doglioni C., Dolan M., Dreiner H., Ellis J., Eno S., Etzion E., Fairbairn M., Feldstein B., Flaecher H., Eric F., Genest M.-H., Gouskos L., Gramling J., Haisch U., Harnik R., Hibbs A., Hoh S., Hopkins W., Ippolito V., Jacques T., Kahlhoefer F., Khoze V. V., Kirk R., Korn A., Kotov K., Kunori S., Landsberg G., Liem S., Lin T., Lowette S., Lucas R., Malgeri L., Malik S., McCabe C., Serhan Mete A., Morgante E., Mrenna S., Nakahama Y., Newbold D., Nordstrom K., Pani P., Papucci M., Pataraia S., Penning B., Pinna D., Polesello G., Racco D., Re E., Riotto A. W., Rizzo T., Salek D., Sarkar S., Schramm S., Skubic P., Slone O., Smirnov J., Soreq Y., Sumner T., Tait T. M. P., Thomas M., Tomalin I., Tunnell C., Vichi A., Volansky T., Weiner N., West S. M., Wielers M., Worm S., Yavin I., Zaldivar B., Zhou N., Zurek K., *Simplified Models for Dark Matter Searches at the LHC,* ArXiv e-prints (2015). 10, 28

Abercrombie D. et al., *Dark Matter Benchmark Models for Early LHC Run-2 Searches: Report of the ATLAS/CMS Dark Matter Forum,* (2015). 14

Abeysekara A. U. et al. (HAWC Collaboration), *Extended gamma-ray sources around pulsars constrain the origin of the positron flux at Earth,* Science **358**, 911-914 (2017). 19

Ackermann M., Ajello M., Allafort A., Atwood W. B., Baldini L., Barbiellini G., Bastieri D., Bechtol K., Bellazzini R., Berenji B., Blandford R. D., Bloom E. D., Bonamente E., Borgland A. W., Bouvier A., Bregeon J., Brigida M., Bruel P., Buehler R., Buson S., Caliandro G. A., Cameron R. A., Caraveo P. A., Casandjian J. M., Cecchi C., Charles E., Chekhtman A., Cheung C. C., Chiang J., Ciprini S., Claus R., Cohen-Tanugi J., Conrad J., Cutini S., de Angelis A., de Palma F., Dermer C. D., Digel S. W., Do Couto E Silva E., Drell P. S., Drlica-Wagner A., Favuzzi C., Fegan S. J., Ferrara E. C., Focke W. B., Fortin P., Fukazawa Y., Funk S., Fusco

P., Gargano F., Gasparrini D., Germani S., Giglietto N., Giommi P., Giordano F., Giroletti M., Glanzman T., Godfrey G., Grenier I. A., Grove J. E., Guiriec S., Gustafsson M., Hadasch D., Harding A. K., Hayashida M., Hughes R. E., Jóhannesson G., Johnson A. S., Kamae T., Katagiri H., Kataoka J., Knödlseder J., Kuss M., Lande J., Latronico L., Lemoine-Goumard M., Llena Garde M., Longo F., Loparco F., Lovellette M. N., Lubrano P., Madejski G. M., Mazziotta M. N., McEnery J. E., Michelson P. F., Mitthumsiri W., Mizuno T., Moiseev A. A., Monte C., Monzani M. E., Morselli A., Moskalenko I. V., Murgia S., Nakamori T., Nolan P. L., Norris J. P., Nuss E., Ohno M., Ohsugi T., Okumura A., Omodei N., Orlando E., Ormes J. F., Ozaki M., Paneque D., Parent D., Pesce-Rollins M., Pierbattista M., Piron F., Pivato G., Porter T. A., Rainò S., Rando R., Razzano M., Razzaque S., Reimer A., Reimer O., Reposeur T., Ritz S., Romani R. W., Roth M., Sadrozinski H. F.-W., Sbarra C., Schalk T. L., Sgrò C., Siskind E. J., Spandre G., Spinelli P., Strong A. W., Takahashi H., Takahashi T., Tanaka T., Thayer J. G., Thayer J. B., Tibaldo L., Tinivella M., Torres D. F., Tosti G., Troja E., Uchiyama Y., Usher T. L., Vandenbroucke J., Vasileiou V., Vianello G., Vitale V., Waite A. P., Winer B. L., Wood K. S., Wood M., Yang Z., Zimmer S., *Measurement of Separate Cosmic-Ray Electron and Positron Spectra with the Fermi Large Area Telescope,* Physical Review Letters **108**, 011103 (2012)a. 19

Ackermann M., Ajello M., Atwood W. B., Baldini L., Ballet J., Barbiellini G., Bastieri D., Bechtol K., Bellazzini R., Berenji B., Blandford R. D., Bloom E. D., Bonamente E., Borgland A. W., Brandt T. J., Bregeon J., Brigida M., Bruel P., Buehler R., Buson S., Caliandro G. A., Cameron R. A., Caraveo P. A., Cavazzuti E., Cecchi C., Charles E., Chekhtman A., Chiang J., Ciprini S., Claus R., Cohen-Tanugi J., Conrad J., Cutini S., de Angelis A., de Palma F., Dermer C. D., Digel S. W., Silva E. d. C. e., Drell P. S., Drlica-Wagner A., Falletti L., Favuzzi C., Fegan S. J., Ferrara E. C., Focke W. B., Fortin P., Fukazawa Y., Funk S., Fusco P., Gaggero D., Gargano F., Germani S., Giglietto N., Giordano F., Giroletti M., Glanzman T., Godfrey G., Grove J. E., Guiriec S., Gustafsson M., Hadasch D., Hanabata Y., Harding A. K., Hayashida M., Hays E., Horan D., Hou X., Hughes R. E., Jóhannesson G., Johnson A. S., Johnson R. P., Kamae T., Katagiri H., Kataoka J., Knödlseder J., Kuss M., Lande J., Latronico L., Lee S.-H., Lemoine-Goumard M., Longo F., Loparco F., Lott B., Lovellette M. N., Lubrano P., Mazziotta M. N., McEnery J. E., Michelson P. F., Mitthumsiri W., Mizuno T., Monte C., Monzani M. E., Morselli A., Moskalenko I. V., Murgia S., Naumann-Godo M., Norris J. P., Nuss E., Ohsugi T., Okumura A., Omodei N., Orlando E., Ormes J. F., Paneque D., Panetta J. H., Parent D., Pesce-Rollins M., Pierbattista M., Piron F., Pivato G., Porter T. A., Rainò S., Rando R., Razzano M., Razzaque S., Reimer A., Reimer O., Sadrozinski H. F.-W., Sgrò C., Siskind E. J., Spandre G., Spinelli P., Strong A. W., Suson D. J., Takahashi H., Tanaka T., Thayer J. G., Thayer J. B., Thompson D. J., Tibaldo L., Tinivella M., Torres D. F., Tosti G., Troja E., Usher T. L., Vandenbroucke J., Vasileiou V., Vianello G., Vitale V., Waite A. P., Wang P., Winer B. L., Wood K. S., Wood M., Yang Z., Ziegler M., Zimmer S., *Fermi-LAT Observations of the Diffuse γ-Ray Emission: Implications for Cosmic Rays and the Interstellar Medium,* Astrophys. J. **750**, 3 (2012)b. 17, 95

Ackermann M. et al. (Fermi-LAT Collaboration), *Searching for Dark Matter Annihilation from Milky Way Dwarf Spheroidal Galaxies with Six Years of Fermi Large Area Telescope Data,* Phys. Rev. Lett. **115**, 231301 (2015). 17, 94

Ade P. A. R. et al. (Planck Collaboration), *Planck 2013 results. XVI. Cosmological parameters,* Astron. Astrophys. **571**, A16 (2014). 62

Ade P. A. R. et al. (Planck Collaboration), *Planck 2015 results. XIII. Cosmological parameters,* Astron. Astrophys. **594**, A13 (2016). 5, 6, 9, 23, 24, 36, 49, 53, 54, 57, 61, 81

Adriani O., Barbarino G. C., Bazilevskaya G. A., Bellotti R., Boezio M., Bogomolov E. A., Bonechi L., Bongi M., Bonvicini V., Borisov S., Bottai S., Bruno A., Cafagna F., Campana D.,

Carbone R., Carlson P., Casolino M., Castellini G., Consiglio L., De Pascale M. P., De Santis C., De Simone N., Di Felice V., Galper A. M., Gillard W., Grishantseva L., Jerse G., Karelin A. V., Koldashov S. V., Krutkov S. Y., Kvashnin A. N., Leonov A., Malakhov V., Malvezzi V., Marcelli L., Mayorov A. G., Menn W., Mikhailov V. V., Mocchiutti E., Monaco A., Mori N., Nikonov N., Osteria G., Palma F., Papini P., Pearce M., Picozza P., Pizzolotto C., Ricci M., Ricciarini S. B., Rossetto L., Sarkar R., Simon M., Sparvoli R., Spillantini P., Stozhkov Y. I., Vacchi A., Vannuccini E., Vasilyev G., Voronov S. A., Yurkin Y. T., Wu J., Zampa G., Zampa N., Zverev V. G., *PAMELA Measurements of Cosmic-Ray Proton and Helium Spectra,* Science **332**, 69 (2011). 104

Adriani O. et al. (PAMELA Collaboration), *An anomalous positron abundance in cosmic rays with energies 1.5-100 GeV,* Nature **458**, 607-609 (2009). 19

Adriani O. et al. (PAMELA Collaboration), *Cosmic-Ray Positron Energy Spectrum Measured by PAMELA,* Phys. Rev. Lett. **111**, 081102 (2013). 19

Agashe K., Servant G., *Warped Unification, Proton Stability, and Dark Matter,* Physical Review Letters **93**, 231805 (2004). 10

Aghanim N. et al. (Planck Collaboration), *Planck 2018 results. VI. Cosmological parameters,* (2018). 5, 6

Aguilar M., Aisa D., Alpat B., Alvino A., Ambrosi G., Andeen K., Arruda L., Attig N., Azzarello P., Bachlechner A., et al., *Precision Measurement of the Helium Flux in Primary Cosmic Rays of Rigidities 1.9 GV to 3 TV with the Alpha Magnetic Spectrometer on the International Space Station,* Physical Review Letters **115**, 211101 (2015)a. 104

Aguilar M., Aisa D., Alpat B., Alvino A., Ambrosi G., Andeen K., Arruda L., Attig N., Azzarello P., Bachlechner A., et al., *Precision Measurement of the Proton Flux in Primary Cosmic Rays from Rigidity 1 GV to 1.8 TV with the Alpha Magnetic Spectrometer on the International Space Station,* Physical Review Letters **114**, 171103 (2015)b. 104

Aguilar M., Alberti G., Alpat B., Alvino A., Ambrosi G., Andeen K., Anderhub H., Arruda L., Azzarello P., Bachlechner A., Barao F., Baret B., Barrau A., Barrin L., Bartoloni A., Basara L., Basili A., Batalha L., Bates J., Battiston R., Bazo J., Becker R., Becker U., Behlmann M., Beischer B., Berdugo J., Berges P., Bertucci B., Bigongiari G., Biland A., Bindi V., Bizzaglia S., Boella G., de Boer W., Bollweg K., Bolmont J., Borgia B., Borsini S., Boschini M. J., Boudoul G., Bourquin M., Brun P., Buénerd M., Burger J., Burger W., Cadoux F., Cai X. D., Capell M., Casadei D., Casaus J., Cascioli V., Castellini G., Cernuda I., Cervelli F., Chae M. J., Chang Y. H., Chen A. I., Chen C. R., Chen H., Cheng G. M., Chen H. S., Cheng L., Chernoplyiokov N., Chikanian A., Choumilov E., Choutko V., Chung C. H., Clark C., Clavero R., Coignet G., Commichau V., Consolandi C., Contin A., Corti C., Costado Dios M. T., Coste B., Crespo D., Cui Z., Dai M., Delgado C., Della Torre S., Demirkoz B., Dennett P., Derome L., Di Falco S., Diao X. H., Diago A., Djambazov L., Díaz C., von Doetinchem P., Du W. J., Dubois J. M., Duperay R., Duranti M., D'Urso D., Egorov A., Eline A., Eppling F. J., Eronen T., van Es J., Esser H., Falvard A., Fiandrini E., Fiasson A., Finch E., Fisher P., Flood K., Foglio R., Fohey M., Fopp S., Fouque N., Galaktionov Y., Gallilee M., Gallin-Martel L., Gallucci G., García B., García J., García-López R., García-Tabares L., Gargiulo C., Gast H., Gebauer I., Gentile S., Gervasi M., Gillard W., Giovacchini F., Girard L., Goglov P., Gong J., Goy- Henningsen C., Grandi D., Graziani M., Grechko A., Gross A., Guerri I., de la Guía C., Guo K. H., Habiby M., Haino S., Hauler F., He Z. H., Heil M., Heilig J., Hermel R., Hofer H., Huang Z. C., Hungerford W., Incagli M., Ionica M., Jacholkowska A., Jang W. Y., Jinchi H., Jongmanns M., Journet L., Jungermann L., Karpinski W., Kim G. N., Kim K. S., Kirn T., Kossakowski R., Koulemzine A., Kounina O., Kounine A., Koutsenko V., Krafczyk M. S.,

Laudi E., Laurenti G., Lauritzen C., Lebedev A., Lee M. W., Lee S. C., Leluc C., León Vargas H., Lepareur V., Li J. Q., Li Q., Li T. X., Li W., Li Z. H., Lipari P., Lin C. H., Liu D., Liu H., Lomtadze T., Lu Y. S., Lucidi S., Lübelsmeyer K., Luo J. Z., Lustermann W., Lv S., Madsen J., Majka R., Malinin A., Mañá C., Marín J., Martin T., Martínez G., Masciocchi F., Masi N., Maurin D., McInturff A., McIntyre P., Menchaca-Rocha A., Meng Q., Menichelli M., Mereu I., Millinger M., Mo D. C., Molina M., Mott P., Mujunen A., Natale S., Nemeth P., Ni J. Q., Nikonov N., Nozzoli F., Nunes P., Obermeier A., Oh S., Oliva A., Palmonari F., Palomares C., Paniccia M., Papi A., Park W. H., Pauluzzi M., Pauss F., Pauw A., Pedreschi E., Pensotti S., Pereira R., Perrin E., Pessina G., Pierschel G., Pilo F., Piluso A., Pizzolotto C., Plyaskin V., Pochon J., Pohl M., Poireau V., Porter S., Pouxe J., Putze A., Quadrani L., Qi X. N., Rancoita P. G., Rapin D., Ren Z. L., Ricol J. S., Riihonen E., Rodríguez I., Roeser U., Rosier-Lees S., Rossi L., Rozhkov A., Rozza D., Sabellek A., Sagdeev R., Sandweiss J., Santos B., Saouter P., Sarchioni M., Schael S., Schinzel D., Schmanau M., Schwering G., Schulz von Dratzig A., Scolieri G., Seo E. S., Shan B. S., Shi J. Y., Shi Y. M., Siedenburg T., Siedling R., Son D., Spada F., Spinella F., Steuer M., Stiff K., Sun W., Sun W. H., Sun X. H., Tacconi M., Tang C. P., Tang X. W., Tang Z. C., Tao L., Tassan-Viol J., Ting S. C. C., Ting S. M., Titus C., Tomassetti N., Toral F., Torsti J., Tsai J. R., Tutt J. C., Ulbricht J., Urban T., Vagelli V., Valente E., Vannini C., Valtonen E., Vargas Trevino M., Vaurynovich S., Vecchi M., Vergain M., Verlaat B., Vescovi C., Vialle J. P., Viertel G., Volpini G., Wang D., Wang N. H., Wang Q. L., Wang R. S., Wang X., Wang Z. X., Wallraff W., Weng Z. L., Willenbrock M., Wlochal M., Wu H., Wu K. Y., Wu Z. S., Xiao W. J., Xie S., Xiong R. Q., Xin G. M., Xu N. S., Xu W., Yan Q., Yang J., Yang M., Ye Q. H., Yi H., Yu Y. J., Yu Z. Q., Zeissler S., Zhang J. G., Zhang Z., Zhang M. M., Zheng Z. M., Zhuang H. L., Zhukov V., Zichichi A., Zuccon P., Zurbach C., *First Result from the Alpha Magnetic Spectrometer on the International Space Station: Precision Measurement of the Positron Fraction in Primary Cosmic Rays of 0.5-350 GeV,* Phys. Rev. Let. **110**, 141102 (2013). 19

Aguilar M., Ali Cavasonza L., Alpat B., Ambrosi G., Arruda L., Attig N., Aupetit S., Azzarello P., Bachlechner A., Barao F., et al., *Antiproton Flux, Antiproton-to-Proton Flux Ratio, and Properties of Elementary Particle Fluxes in Primary Cosmic Rays Measured with the Alpha Magnetic Spectrometer on the International Space Station,* Physical Review Letters **117**, 091103 (2016). 18, 108, 113

Aguilar M. et al. (AMS 01 Collaboration), *Cosmic-ray positron fraction measurement from 1 to 30-GeV with AMS-01,* Phys. Lett. **B646**, 145-154 (2007). 19

Aguilar M. et al. (AMS Collaboration), *Precision Measurement of the Boron to Carbon Flux Ratio in Cosmic Rays from 1.9 GV to 2.6 TV with the Alpha Magnetic Spectrometer on the International Space Station,* Phys. Rev. Lett. **117**, 231102 (2016). 104, 106, 108

Ahn H. S., Allison P., Bagliesi M. G., Beatty J. J., Bigongiari G., Childers J. T., Conklin N. B., Coutu S., DuVernois M. A., Ganel O., Han J. H., Jeon J. A., Kim K. C., Lee M. H., Lutz L., Maestro P., Malinin A., Marrocchesi P. S., Minnick S., Mognet S. I., Nam J., Nam S., Nutter S. L., Park I. H., Park N. H., Seo E. S., Sina R., Wu J., Yang J., Yoon Y. S., Zei R., Zinn S. Y., *Discrepant Hardening Observed in Cosmic-ray Elemental Spectra,* Astrophys. J. Lett. **714**, L89-L93 (2010). 104

Ahrens J. et al. (IceCube Collaboration), *Icecube - the next generation neutrino telescope at the south pole,* Nucl. Phys. Proc. Suppl. **118**, 388-395 (2003). 18

Ajello M. et al. (Fermi-LAT Collaboration), *Fermi-LAT Observations of High-Energy γ-Ray Emission Toward the Galactic Center,* Astrophys. J. **819**, 44 (2016). 17

Albert A. et al. (DES, Fermi-LAT Collaboration), *Searching for Dark Matter Annihilation in Recently Discovered Milky Way Satellites with Fermi-LAT,* Astrophys. J. **834**, 110 (2017). 17, 94

Aloisio R., Blasi P., De Mitri I., Petrera S., *Selected Topics in Cosmic Ray Physics* (2018), p. 1. 97

Alpher R. A., Bethe H., Gamow G., *The origin of chemical elements,* Phys. Rev. **73**, 803–804 (1948). 6

Alpher R. A., Follin J. W., Herman R. C., *Physical conditions in the initial stages of the expanding universe,* Phys. Rev. **92**, 1347–1361 (1953). 6

Alpher R. A., Herman R., *Evolution of the Universe,* Nature **162**, 774-775 (1948)a. 3

Alpher R. A., Herman R. C., *On the Relative Abundance of the Elements,* Physical Review **74**, 1737-1742 (1948)b. 3

An J. H., Evans N. W., *A cusp slope-central anisotropy theorem,* Astrophys. J. **642**, 752-758 (2006). 143

Anderhalden D., Diemand J., *Density Profiles of CDM Microhalos and their Implications for Annihilation Boost Factors,* JCAP **1304**, 009 (2013). 58, 63

Anderson G. W., Castaño D. J., *Measures of fine tuning,* Physics Letters B **347**, 300-308 (1995). 10

Anderson L. et al. (BOSS Collaboration), *The clustering of galaxies in the SDSS-III Baryon Oscillation Spectroscopic Survey: baryon acoustic oscillations in the Data Releases 10 and 11 Galaxy samples,* Mon. Not. Roy. Astron. Soc. **441**, 24-62 (2014). 6

Ando S., Kamionkowski M., Lee S. K., Koushiappas S. M., *Can proper motions of dark-matter subhalos be detected?,* Phys. Rev. **D78**, 101301 (2008). 94

Angulo R. E., Hahn O., Ludlow A., Bonoli S., *Earth-mass haloes and the emergence of NFW density profiles,* (2016). 57

Angus G. W., Shan H. Y., Zhao H. S., Famaey B., *On the Proof of Dark Matter, the Law of Gravity, and the Mass of Neutrinos,* Astrophys. J. Lett. **654**, L13-L16 (2007). 8

Angus G. W., Zhao H., *Analysis of galactic tides and stars on CDM microhalos,* Mon. Not. Roy. Astron. Soc. **375**, 1146-1156 (2007). 72

Antoniadis I., Arkani-Hamed N., Dimopoulos S., Dvali G. R., *New dimensions at a millimeter to a Fermi and superstrings at a TeV,* Phys. Lett. **B436**, 257-263 (1998). 10

Antonov V. A., *Solution of the problem of stability of stellar system Emden's density law and the spherical distribution of velocities* (1962). 143

Antonov V. A., *Solution of the Problem of Stability of a Stellar System with Emden's Density Law and a Spherical Distribution of Velocities,* in Structure and Dynamics of Elliptical Galaxies, Vol. 127 (1987). 145

Arbey A., Lesgourgues J., Salati P., *Quintessential halos around galaxies,* Phys. Rev. D **64**, 123528 (2001). 13

Arkani-Hamed N., Dimopoulos S., Dvali G. R., *The Hierarchy problem and new dimensions at a millimeter,* Phys. Lett. **B429**, 263-272 (1998). 10

Arkani-Hamed N., Dimopoulos S., Dvali G. R., *Phenomenology, astrophysics and cosmology of theories with submillimeter dimensions and TeV scale quantum gravity,* Phys. Rev. **D59**, 086004 (1999). 10

Arkani-Hamed N., Finkbeiner D. P., Slatyer T. R., Weiner N., *A Theory of Dark Matter,* Phys. Rev. **D79**, 015014 (2009). 164

Armengaud E., Palanque-Delabrouille N., Yèche C., Marsh D. J. E., Baur J., *Constraining the mass of light bosonic dark matter using SDSS Lyman-α forest,* Mon. Not. Roy. Astron. Soc. **471**, 4606-4614 (2017). 11, 14

Askew A., Chauhan S., Penning B., Shepherd W., Tripathi M., *Searching for Dark Matter at Hadron Colliders,* Int. J. Mod. Phys. **A29**, 1430041 (2014). 14

Aslanides E. et al. (ANTARES Collaboration), *A deep sea telescope for high-energy neutrinos,* (1999). 18

Aslanyan G., Price L. C., Adams J., Bringmann T., Clark H. A., Easther R., Lewis G. F., Scott P., *Ultracompact minihalos as probes of inflationary cosmology,* (2015). 83

Atwood W. B. et al. (Fermi-LAT Collaboration), *The Large Area Telescope on the Fermi Gamma-ray Space Telescope Mission,* Astrophys. J. **697**, 1071-1102 (2009). 17

Axford W. I., Leer E., Skadron G., *The Acceleration of Cosmic Rays by Shock Waves,* International Cosmic Ray Conference **11**, 132 (1977). 100

Baade W., Zwicky F., *Remarks on Super-Novae and Cosmic Rays,* Physical Review **46**, 76-77 (1934). 101

Bardeen J. M., *Gauge-invariant cosmological perturbations,* Phys. Rev. D **22**, 1882-1905 (1980). 46

Bardeen J. M., Steinhardt P. J., Turner M. S., *Spontaneous creation of almost scale-free density perturbations in an inflationary universe,* Phys. Rev. D **28**, 679-693 (1983). 52

Barnes J., Goodman J., Hut P., *Dynamical instabilities in spherical stellar systems,* Astrophys. J. **300**, 112-131 (1986). 145

Barrau A., Salati P., Servant G., Donato F., Grain J., Maurin D., Taillet R., *Kaluza-Klein dark matter and Galactic antiprotons,* Phys. Rev. **D72**, 063507 (2005). 18

Bartels R., Ando S., *Boosting the annihilation boost: Tidal effects on dark matter subhalos and consistent luminosity modeling,* Phys. Rev. **D92**, 123508 (2015). 64, 76, 94

Bartels R., Krishnamurthy S., Weniger C., *Strong support for the millisecond pulsar origin of the Galactic center GeV excess,* Phys. Rev. Lett. **116**, 051102 (2016). 17

Barwick S. W. et al. (HEAT Collaboration), *Measurements of the cosmic ray positron fraction from 1-GeV to 50-GeV,* Astrophys. J. **482**, L191-L194 (1997). 19

Baudis L., *Direct dark matter detection: the next decade,* Phys. Dark Univ. **1**, 94-108 (2012). 14

Beacom J. F., Bell N. F., Bertone G., *Gamma-ray constraint on Galactic positron production by MeV dark matter,* Phys. Rev. Lett. **94**, 171301 (2005). 167

Bekenstein J., Milgrom M., *Does the missing mass problem signal the breakdown of Newtonian gravity?,* Astrophys. J. **286**, 7-14 (1984). 8

Bekenstein J. D., *Relativistic gravitation theory for the modified Newtonian dynamics paradigm,* Phys. Rev. D **70**, 083509 (2004). 8

Bell A. R., *The acceleration of cosmic rays in shock fronts - I.,* Mon. Not. Roy. Astron. Soc. **182**, 147-156 (1978)a. 100

Bell A. R., *The acceleration of cosmic rays in shock fronts - II.,* Mon. Not. Roy. Astron. Soc. **182**, 443-455 (1978)b. 100

Berezhko E. G., Ksenofontov L. T., Ptuskin V. S., Zirakashvili V. N., Völk H. J., *Cosmic ray production in supernova remnants including reacceleration: The secondary to primary ratio,* Astron. Astroph. **410**, 189-198 (2003). 102

Berezinsky V., Bottino A., Mignola G., *High-energy gamma radiation from the galactic center due to neutralino annihilation,* Phys. Lett. **B325**, 136-142 (1994). 17

Berezinsky V., Dokuchaev V., Eroshenko Y., *Small - scale clumps in the galactic halo and dark matter annihilation,* Phys. Rev. **D68**, 103003 (2003). 40, 42, 64, 76, 94

Berezinsky V., Dokuchaev V., Eroshenko Y., *Destruction of small-scale dark matter clumps in the hierarchical structures and galaxies,* Phys. Rev. **D73**, 063504 (2006). 72

Berezinsky V., Dokuchaev V., Eroshenko Y., *Remnants of dark matter clumps,* Phys. Rev. **D77**, 083519 (2008). 74

Berezinsky V., Dokuchaev V., Eroshenko Y., Kachelrieß M., Solberg M. A., *Superdense cosmological dark matter clumps,* Phys. Rev. D **81**, 103529 (2010). 73

Berezinsky V. S., Bulanov S. V., Dogiel V. A., Ptuskin V. S., *Astrophysics of cosmic rays* (1990). 102

Berezinsky V. S., Dokuchaev V. I., Eroshenko Y. N., *Small-scale clumps of dark matter,* Phys. Usp. **57**, 1-36 (2014). 64, 73, 80

Berezinsky V. S., Gurevich A. V., Zybin K. P., *Distribution of dark matter in the galaxy and the lower limits for the masses of supersymmetric particles,* Physics Letters B **294**, 221-228 (1992). 17

Bergstrom L., *Dark Matter Candidates,* New J. Phys. **11**, 105006 (2009). 9

Bergstrom L., Bringmann T., Edsjo J., *New Positron Spectral Features from Supersymmetric Dark Matter - a Way to Explain the PAMELA Data?,* Phys. Rev. **D78**, 103520 (2008). 19

Bergstrom L., Edsjo J., Gondolo P., Ullio P., *Clumpy neutralino dark matter,* Phys. Rev. **D59**, 043506 (1999). 94

Bergström L., Edsjö J., Ullio P., *Cosmic Antiprotons as a Probe for Supersymmetric Dark Matter?,* Astrophys. J. **526**, 215-235 (1999). 18

Bergstrom L., Snellman H., *Observable Monochromatic Photons From Cosmic Photino Annihilation,* Phys. Rev. **D37**, 3737-3741 (1988). 16

Bergstrom L., Ullio P., Buckley J. H., *Observability of gamma-rays from dark matter neutralino annihilations in the Milky Way halo,* Astropart. Phys. **9**, 137-162 (1998). 16, 17

Bernabei R. et al., *First model independent results from DAMA/LIBRA-phase2,* (2018). 14

Bernal J. L., Verde L., Riess A. G., *The trouble with H_0,* JCAP **1610**, 019 (2016). 6

Bernstein J., *Kinetic Theory in the Expanding Universe* (1988). 186, 188

Bernstein J., Brown L. S., Feinberg G., *The Cosmological Heavy Neutrino Problem Revisited,* Phys. Rev. **D32**, 3261 (1985). 31

Bertone G., Fairbairn M., *Compact Stars as Dark Matter Probes,* Phys. Rev. **D77**, 043515 (2008). 161

Bertone G., Hooper D., *A History of Dark Matter,* Submitted to: Rev. Mod. Phys. (2016). 1

Bertone G., Hooper D., Silk J., *Particle dark matter: Evidence, candidates and constraints,* Phys. Rept. **405**, 279-390 (2005). 9

Bertschinger E., *The Effects of Cold Dark Matter Decoupling and Pair Annihilation on Cosmological Perturbations,* Phys. Rev. **D74**, 063509 (2006). 40, 41, 46

Bhattacharjee P., Chaudhury S., Kundu S., Majumdar S., *Sizing-up the WIMPs of Milky Way : Deriving the velocity distribution of Galactic Dark Matter particles from the rotation curve data,* Phys. Rev. **D87**, 083525 (2013). 159

Binder T., Bringmann T., Gustafsson M., Hryczuk A., *Early kinetic decoupling of dark matter: when the standard way of calculating the thermal relic density fails,* Phys. Rev. **D96**, 115010 (2017). 32, 39, 189

Binétruy P., Girardi G., Salati P., *Constraints on a system of two neutral fermions from cosmology,* Nuclear Physics B **237**, 285-306 (1984). 36

Binney J., *The radius-dependence of velocity dispersion in elliptical galaxies,* Mon. Not. Roy. Astron. Soc. **190**, 873-880 (1980). 128

Binney J., Piffl T., *The distribution function of the Galaxy's dark halo,* Mon. Not. Roy. Astron. Soc. **454**, 3653-3663 (2015). 2, 115

Binney J., Tremaine S., *Galactic dynamics* (1987). 50, 57, 64, 66, 72, 115, 118, 120, 122, 124

Bird S., Cholis I., Muñoz J. B., Ali-Haïmoud Y., Kamionkowski M., Kovetz E. D., Raccanelli A., Riess A. G., *Did LIGO detect dark matter?,* Phys. Rev. Lett. **116**, 201301 (2016). 9

Blanchet L., *Dipolar particles in general relativity,* Classical and Quantum Gravity **24**, 3541-3570 (2007). 8

Blanchet S., Lavalle J., *Diffuse gamma-ray constraints on dark matter revisited. I: the impact of subhalos,* JCAP **1211**, 021 (2012). 94

Bland-Hawthorn J., Gerhard O., *The Galaxy in Context: Structural, Kinematic, and Integrated Properties,* Ann. Rev. Astron. Astrophys. **54**, 529-596 (2016). 115

Blandford R., Eichler D., *Particle acceleration at astrophysical shocks: A theory of cosmic ray origin,* Phys. Rept. **154**, 1-75 (1987). 99, 103

Blasi P., *The origin of galactic cosmic rays,* Astron. Astroph. Rev. **21**, 70 (2013). 97

Blumenthal G. R., Faber S. M., Primack J. R., Rees M. J., *Formation of galaxies and large-scale structure with cold dark matter.,* Nature **311**, 517-525 (1984). 6

Boddy K. K., Kumar J., Strigari L. E., Wang M.-Y., *Sommerfeld-Enhanced J-Factors For Dwarf Spheroidal Galaxies,* Phys. Rev. **D95**, 123008 (2017). 164

Bode P., Ostriker J. P., Turok N., *Halo formation in warm dark matter models,* Astrophys. J. **556**, 93-107 (2001). 13

Boehm C., Ensslin T. A., Silk J., *Can Annihilating dark matter be lighter than a few GeVs?,* J. Phys. **G30**, 279-286 (2004). 167

Boehm C., Fayet P., *Scalar dark matter candidates,* Nucl. Phys. **B683**, 219-263 (2004). 9

Boehm C., Fayet P., Schaeffer R., *Constraining dark matter candidates from structure formation,* Phys. Lett. **B518**, 8-14 (2001). 39, 40

Boehm C., Schaeffer R., *Constraints on dark matter interactions from structure formation: Damping lengths,* Astron. Astrophys. **438**, 419-442 (2005). 40, 43

Boehm C., Schewtschenko J. A., Wilkinson R. J., Baugh C. M., Pascoli S., *Using the Milky Way satellites to study interactions between cold dark matter and radiation,* Mon. Not. Roy. Astron. Soc. **445**, L31-L35 (2014). 167

Bond J. R., Cole S., Efstathiou G., Kaiser N., *Excursion set mass functions for hierarchical Gaussian fluctuations,* Astrophys. J. **379**, 440-460 (1991). 56

Bond J. R., Szalay A. S., Turner M. S., *Formation of galaxies in a gravitino-dominated universe,* Physical Review Letters **48**, 1636-1639 (1982). 13

Borsanyi S. et al., *Calculation of the axion mass based on high-temperature lattice quantum chromodynamics,* Nature **539**, 69-71 (2016). 28

Bosma A., PhD thesis, - (1978). 2

Boudaud M., Bueno E. F., Caroff S., Genolini Y., Poulin V., Poireau V., Putze A., Rosier S., Salati P., Vecchi M., *The pinching method for Galactic cosmic ray positrons: implications in the light of precision measurements,* Astron. Astrophys. **605**, A17 (2017). 106, 168

Boudaud M., Cirelli M., Giesen G., Salati P., *A fussy revisitation of antiprotons as a tool for Dark Matter searches,* JCAP **5**, 13 (2015). 18

Boudaud M., Lavalle J., Salati P., *Novel cosmic-ray electron and positron constraints on MeV dark matter particles,* Phys. Rev. Lett. **119**, 021103 (2017). 19, 166, 169

Bouquet A., Casse M., Prantzos N., Salati P., *Weakly Interacting Massive Particles and Solar Neutrinos,* International Cosmic Ray Conference **4**, 365 (1987). 18

Bouquet A., Salati P., *Dark Matter and the Suppression of Stellar Core Convection,* Astrophys. J. **346**, 284 (1989)a. 161

Bouquet A., Salati P., *Life and death of cosmions in stars,* Astron. Astroph. **217**, 270-282 (1989)b. 161

Bouquet A., Salati P., Silk J., *Gamma-ray Lines as a Probe for a Cold Dark Matter Halo,* Phys. Rev. **D40**, 3168 (1989). 16, 17

Boyarsky A., Ruchayskiy O., Shaposhnikov M., *The Role of sterile neutrinos in cosmology and astrophysics,* Ann. Rev. Nucl. Part. Sci. **59**, 191-214 (2009). 11, 13

Boylan-Kolchin M., Bullock J. S., Kaplinghat M., *Too big to fail? The puzzling darkness of massive Milky Way subhaloes,* Mon. Not. Roy. Astron. Soc. **415**, L40-L44 (2011). 12

Boylan-Kolchin M., Bullock J. S., Kaplinghat M., *The Milky Way's bright satellites as an apparent failure of ΛCDM,* Mon. Not. Roy. Astron. Soc. **422**, 1203-1218 (2012). 12

Bozorgnia N., Catena R., Schwetz T., *Anisotropic dark matter distribution functions and impact on WIMP direct detection,* JCAP **1312**, 050 (2013). 131, 155, 159

Brans C., Dicke R. H., *Mach's Principle and a Relativistic Theory of Gravitation,* Physical Review **124**, 925-935 (1961). 7

Bringmann T., *Particle Models and the Small-Scale Structure of Dark Matter,* New J. Phys. **11**, 105027 (2009). 40, 41, 43, 77, 83, 121

Bringmann T., Hofmann S., *Thermal decoupling of WIMPs from first principles,* JCAP **0704**, 016 (2007). 39, 40, 41, 77, 83, 190

Bringmann T., Salati P., *The galactic antiproton spectrum at high energies: Background expectation vs. exotic contributions,* Phys. Rev. **D75**, 083006 (2007). 18

Bringmann T., Scott P., Akrami Y., *Improved constraints on the primordial power spectrum at small scales from ultracompact minihalos,* Phys. Rev. **D85**, 125027 (2012). 83

Bringmann T., Weniger C., *Gamma Ray Signals from Dark Matter: Concepts, Status and Prospects,* Phys. Dark Univ. **1**, 194-217 (2012). 17

Bryan G. L., Norman M. L., *Statistical properties of x-ray clusters: Analytic and numerical comparisons,* Astrophys. J. **495**, 80 (1998). 59

Bryan S. E., Kay S. T., Duffy A. R., Schaye J., Dalla Vecchia C., Booth C. M., *The impact of baryons on the spins and shapes of dark matter haloes,* Mon. Not. Roy. Astron. Soc. **429**, 3316-3329 (2013). 150

Bullock J. S., Boylan-Kolchin M., *Small-Scale Challenges to the ΛCDM Paradigm,* Ann. Rev. Astron. Astrophys. **55**, 343-387 (2017). 11, 12, 81

Bullock J. S., Kolatt T. S., Sigad Y., Somerville R. S., Kravtsov A. V., Klypin A. A., Primack J. R., Dekel A., *Profiles of dark haloes: evolution, scatter and environment,* Mon. Not. Roy. Astron. Soc. **321**, 559-575 (2001). 61, 62, 63

Bélanger G., Boudjema F., Pukhov A., Semenov A., *micrOMEGAs4.1: two dark matter candidates,* Comput. Phys. Commun. **192**, 322-329 (2015). 169

Calore F., Cholis I., McCabe C., Weniger C., *A Tale of Tails: Dark Matter Interpretations of the Fermi GeV Excess in Light of Background Model Systematics,* Phys. Rev. **D91**, 063003 (2015). 17

Calore F., Cholis I., Weniger C., *Background Model Systematics for the Fermi GeV Excess,* JCAP **1503**, 038 (2015). 17

Calore F., De Romeri V., Di Mauro M., Donato F., Marinacci F., *Realistic estimation for the detectability of dark matter sub-halos with Fermi-LAT,* Phys. Rev. **D96**, 063009 (2017). 94

Carlson E., Profumo S., *Cosmic Ray Protons in the Inner Galaxy and the Galactic Center Gamma-Ray Excess,* Phys. Rev. **D90**, 023015 (2014). 17

Carlson E. D., Machacek M. E., Hall L. J., *Self-interacting dark matter,* Astrophys. J. **398**, 43-52 (1992). 13

Carr B., Kuhnel F., Sandstad M., *Primordial Black Holes as Dark Matter,* Phys. Rev. **D94**, 083504 (2016). 9

Carroll S. M., Press W. H., Turner E. L., *The cosmological constant,* Ann. Rev. Astron. Astrophys. **30**, 499-542 (1992). 48

Casse F., Lemoine M., Pelletier G., *Transport of cosmic rays in chaotic magnetic fields,* Phys. Rev. **D65**, 023002 (2002). 103

Catena R., Ullio P., *A novel determination of the local dark matter density,* JCAP **1008**, 004 (2010). 2, 115

Catena R., Ullio P., *The local dark matter phase-space density and impact on WIMP direct detection,* JCAP **1205**, 005 (2012). 115, 159

Cerdeño D. G., Delahaye T., Lavalle J., *Cosmic-ray antiproton constraints on light singlino-like dark matter candidates,* Nuclear Physics B **854**, 738-779 (2012). 18

Cerdeno D. G., Green A. M., *Direct detection of WIMPs,* pp 347–369 (2010). 14

Chabrier G., *Galactic stellar and substellar initial mass function,* Publ. Astron. Soc. Pac. **115**, 763-796 (2003). 149

Chang L. J., Lisanti M., Mishra-Sharma S., *Search for dark matter annihilation in the Milky Way halo,* Phys. Rev. **D98**, 123004 (2018). 17, 97

Charbonnier A., Combet C., Maurin D., *CLUMPY: A code for γ-ray signals from dark matter structures,* Computer Physics Communications **183**, 656-668 (2012). 79

Chardonnet P., Fayet P., Salati P., *Heavy triplet neutrinos as a new dark-matter option,* Nuclear Physics B **394**, 35-72 (1993). 10

Chatrchyan S. et al. (CMS Collaboration), *The CMS Experiment at the CERN LHC,* JINST **3**, S08004 (2008). 14

Chen X.-L., Kamionkowski M., *Particle decays during the cosmic dark ages,* Phys. Rev. **D70**, 043502 (2004). 19, 167

Chen X.-l., Kamionkowski M., Zhang X.-m., *Kinetic decoupling of neutralino dark matter,* Phys. Rev. **D64**, 021302 (2001). 39

Choi J.-H., Weinberg M. D., Katz N., *The dynamics of satellite disruption in cold dark matter haloes,* Mon. Not. Roy. Astron. Soc. **400**, 1247 (2009). 140

Chu X., Garcia-Cely C., Hambye T., *Can the relic density of self-interacting dark matter be due to annihilations into Standard Model particles?,* JHEP **11**, 048 (2016). 167

Ciotti L., *The analytical distribution function of anisotropic hernquist+hernquist models,* Astrophys. J. **471**, 68 (1996). 141

Ciotti L., Morganti L., *How general is the global density slope-anisotropy inequality?,* Mon. Not. Roy. Astron. Soc. **408**, 1070-1074 (2010). 143

Ciotti L., Pellegrini S., *Self-consistent two-component models of elliptical galaxies,* Mon. Not. Roy. Astron. Soc. **255**, 561-571 (1992). 141

Cirelli M., *Status of Indirect (and Direct) Dark Matter searches,* (2015). 16

Cirelli M., Corcella G., Hektor A., Hutsi G., Kadastik M., Panci P., Raidal M., Sala F., Strumia A., *PPPC 4 DM ID: A Poor Particle Physicist Cookbook for Dark Matter Indirect Detection,* JCAP **1103**, 051 (2011). 96, 107

Cirelli M., Fornengo N., Strumia A., *Minimal dark matter,* Nucl. Phys. **B753**, 178-194 (2006). 10

Cirelli M., Hambye T., Panci P., Sala F., Taoso M., *Gamma ray tests of Minimal Dark Matter,* JCAP **1510**, 026 (2015). 10

Cirelli M., Moulin E., Panci P., Serpico P. D., Viana A., *Gamma ray constraints on decaying dark matter,* Phys. Rev. D **86**, 083506 (2012). 17

Cirelli M., Strumia A., Tamburini M., *Cosmology and Astrophysics of Minimal Dark Matter,* Nucl. Phys. **B787**, 152-175 (2007). 10, 164

Clark H. A., Scott P., Trotta R., Lewis G. F., *Substructure considerations rule out dark matter interpretation of Fermi Galactic Center excess,* (2016). 17

Clesse S., García-Bellido J., *Seven Hints for Primordial Black Hole Dark Matter,* (2017). 9

Clowe D., Bradac M., Gonzalez A. H., Markevitch M., Randall S. W., Jones C., Zaritsky D., *A direct empirical proof of the existence of dark matter,* Astrophys. J. **648**, L109-L113 (2006). 8

Cole D. R., Binney J., *A centrally heated dark halo for our Galaxy,* Mon. Not. Roy. Astron. Soc. **465**, 798-810 (2017). 115

Colless M. et al. (2DFGRS Collaboration), *The 2dF Galaxy Redshift Survey: Spectra and redshifts,* Mon. Not. Roy. Astron. Soc. **328**, 1039 (2001). 6

Colombi S., Dodelson S., Widrow L. M., *Large scale structure tests of warm dark matter,* Astrophys. J. **458**, 1 (1996). 13

Cooley J., *Overview of Non-Liquid Noble Direct Detection Dark Matter Experiments,* Phys. Dark Univ. **4**, 92-97 (2014). 15

Corbelli E., Salucci P., *The Extended Rotation Curve and the Dark Matter Halo of M33,* Mon. Not. Roy. Astron. Soc. **311**, 441-447 (2000). 2

Cox D. P., *The Three-Phase Interstellar Medium Revisited,* Annual Review of Astronomy and Astrophysics **43**, 337-385 (2005). 103

Cuddeford P., *An analytic inversion for anisotropic spherical galaxies,* Mon. Not. Roy. Astron. Soc. **253**, 414-426 (1991). 128, 131, 196

Cui M.-Y., Pan X., Yuan Q., Fan Y.-Z., Zong H.-S., *Revisit of cosmic ray antiprotons from dark matter annihilation with updated constraints on the background model from AMS-02 and collider data,* JCAP **1806**, 024 (2018). 18, 108, 109

Cui M.-Y., Yuan Q., Tsai Y.-L. S., Fan Y.-Z., *Possible dark matter annihilation signal in the AMS-02 antiproton data,* Phys. Rev. Lett. **118**, 191101 (2017). 18, 108, 109

Cummings A. C., Stone E. C., Heikkila B. C., Lal N., Webber W. R., Jóhannesson G., Moskalenko I. V., Orlando E., Porter T. A., *Galactic Cosmic Rays in the Local Interstellar Medium: Voyager 1 Observations and Model Results,* Astrophys. J. **831**, 18 (2016). 168

Cuoco A., Krämer M., Korsmeier M., *Novel Dark Matter Constraints from Antiprotons in Light of AMS-02,* Phys. Rev. Lett. **118**, 191102 (2017). 18, 108, 109

Cyr-Racine F.-Y., Sigurdson K., Zavala J., Bringmann T., Vogelsberger M., Pfrommer C., *ETHOS—an effective theory of structure formation: From dark particle physics to the matter distribution of the Universe,* Phys. Rev. **D93**, 123527 (2016). 43

Daylan T., Finkbeiner D. P., Hooper D., Linden T., Portillo S. K. N., Rodd N. L., Slatyer T. R., *The characterization of the gamma-ray signal from the central Milky Way: A case for annihilating dark matter,* Phys. Dark Univ. **12**, 1-23 (2016). 17

de Blok W. J. G., McGaugh S. S., Rubin V. C., *High-Resolution Rotation Curves of Low Surface Brightness Galaxies. II. Mass Models,* Astron. J. **122**, 2396-2427 (2001). 12

de Lapparent V., Geller M. J., Huchra J. P., *A Slice of the Universe,* Astrophys. J. **302**, L1 (1986). 6

Dehnen W., *A Hierarchical <E10>O</E10>(N) Force Calculation Algorithm,* Journal of Computational Physics **179**, 27-42 (2002). 150

Dehnen W., Binney J., *Mass models of the Milky Way,* Mon. Not. Roy. Astron. Soc. **294**, 429 (1998). 2, 115

Dekel A., Devor J., Hetzroni G., *Galactic halo cusp-core: tidal compression in mergers,* Monthly Notices of the Royal Astronomical Society **341**, 326-342 (2003). 66

Delahaye T., Lavalle J., Lineros R., Donato F., Fornengo N., *Galactic electrons and positrons at the Earth: new estimate of the primary and secondary fluxes,* Astron. Astroph. **524**, A51 (2010). 19

Dicke R. H., Peebles P. J. E., Roll P. G., Wilkinson D. T., *Cosmic Black-Body Radiation.,* Astrophys. J. **142**, 414-419 (1965). 3

Dicus D. A., Kolb E. W., Teplitz V. L., *Cosmological Upper Bound on Heavy Neutrino Lifetimes,* Phys. Rev. Lett. **39**, 168 (1977). 30

Diemand J., Kuhlen M., Madau P., Zemp M., Moore B., Potter D., Stadel J., *Clumps and streams in the local dark matter distribution,* Nature **454**, 735-738 (2008). 12, 63, 74, 80, 81

Diemand J., Moore B., Stadel J., *Velocity and spatial biases in cold dark matter subhalo distributions,* Monthly Notices of the Royal Astronomical Society **352**, 535-546 (2004). 74

Diemand J., Moore B., Stadel J., *Earth-mass dark-matter haloes as the first structures in the early Universe,* Nature **433**, 389-391 (2005). 61, 62, 63

Diemer B., Joyce M., *An accurate physical model for halo concentrations,* (2018). 61

Diemer B., Kravtsov A. V., *A universal model for halo concentrations,* Astrophys. J. **799**, 108 (2015). 61

Dine M., Fischler W., Srednicki M., *A Simple Solution to the Strong CP Problem with a Harmless Axion,* Phys. Lett. **104B**, 199-202 (1981). 10

Dodelson S., Widrow L. M., *Sterile-neutrinos as dark matter,* Phys. Rev. Lett. **72**, 17-20 (1994). 11, 13

Donato F., Fornengo N., Maurin D., Salati P., *Antiprotons in cosmic rays from neutralino annihilation,* Phys. Rev. **D69**, 063501 (2004). 18, 106

D'Onghia E., Springel V., Hernquist L., Keres D., *Substructure Depletion in the Milky Way Halo by the Disk,* Astrophys. J. **709**, 1138-1147 (2010). 68, 72

Doremus J. P., Baumann G., Feix M. R., *Stability of a Self Gravitating System with Phase Space Density Function of Energy and Angular Momentum,* Astron. Astroph. **29**, 401 (1973). 145

Doremus J.-P., Feix M. R., Baumann G., *Stability of Encounterless Spherical Stellar Systems,* Physical Review Letters **26**, 725-728 (1971). 144

Drakos N. E., Taylor J. E., Benson A. J., *The phase-space structure of tidally stripped haloes,* Mon. Not. Roy. Astron. Soc. **468**, 2345-2358 (2017). 87, 140

Drewes M. et al., *A White Paper on keV Sterile Neutrino Dark Matter,* JCAP **1701**, 025 (2017). 11, 13

Drlica-Wagner A., Bechtol K., Rykoff E. S., Luque E., Queiroz A., Mao Y. Y., Wechsler R. H., Simon J. D., Santiago B., Yanny B., Balbinot E., Dodelson S., Fausti Neto A., James D. J., Li T. S., Maia M. A. G., Marshall J. L., Pieres A., Stringer K., Walker A. R., Abbott T. M. C., Abdalla F. B., Allam S., Benoit-Lévy A., Bernstein G. M., Bertin E., Brooks D., Buckley-Geer E., Burke D. L., Carnero Rosell A., Carrasco Kind M., Carretero J., Crocce M., da Costa L. N., Desai S., Diehl H. T., Dietrich J. P., Doel P., Eifler T. F., Evrard A. E., Finley D. A., Flaugher B., Fosalba P., Frieman J., Gaztanaga E., Gerdes D. W., Gruen D., Gruendl R. A., Gutierrez G., Honscheid K., Kuehn K., Kuropatkin N., Lahav O., Martini P., Miquel R., Nord B., Ogando R., Plazas A. A., Reil K., Roodman A., Sako M., Sanchez E., Scarpine V., Schubnell M., Sevilla-Noarbe I., Smith R. C., Soares-Santos M., Sobreira F., Suchyta E., Swanson M. E. C., Tarle G., Tucker D., Vikram V., Wester W., Zhang Y., Zuntz J., DES Collaboration, *Eight Ultra-faint Galaxy Candidates Discovered in Year Two of the Dark Energy Survey,* Astrophys. J. **813**, 109 (2015). 12

Drukier A., Stodolsky L., *Principles and Applications of a Neutral Current Detector for Neutrino Physics and Astronomy,* Phys. Rev. **D30**, 2295 (1984). 14

Drukier A. K., Freese K., Spergel D. N., *Detecting Cold Dark Matter Candidates,* Phys. Rev. **D33**, 3495-3508 (1986). 14

Drury L. O., *An introduction to the theory of diffusive shock acceleration of energetic particles in tenuous plasmas,* Reports on Progress in Physics **46**, 973-1027 (1983). 99

Du N. et al. (ADMX Collaboration), *A Search for Invisible Axion Dark Matter with the Axion Dark Matter Experiment,* Phys. Rev. Lett. **120**, 151301 (2018). 16

Durrer R., *The theory of CMB anisotropies,* J. Phys. Stud. **5**, 177-215 (2001). 4

Dutton A. A., Macciò A. V., *Cold dark matter haloes in the Planck era: evolution of structural parameters for Einasto and NFW profiles,* Mon. Not. Roy. Astron. Soc. **441**, 3359-3374 (2014). 61, 62, 63, 77

Dyson F. W., Eddington A. S., Davidson C., *A Determination of the Deflection of Light by the Sun's Gravitational Field, from Observations Made at the Total Eclipse of May 29, 1919,* Philosophical Transactions of the Royal Society of London Series A **220**, 291-333 (1920). 7

Eddington A. S., *The distribution of stars in globular clusters,* Mon. Not. Roy. Astron. Soc. **76**, 572-585 (1916). 124

Edsjo J., Gondolo P., *Neutralino relic density including coannihilations,* Phys. Rev. **D56**, 1879-1894 (1997). 31, 36

Einasto J., *On the Construction of a Composite Model for the Galaxy and on the Determination of the System of Galactic Parameters,* Trudy Astrofizicheskogo Instituta Alma-Ata **5**, 87-100 (1965). 58

Einasto J., *On constructing models of stellar systems. II. The descriptive functions and parameters.,* Publications of the Tartu Astrofizica Observatory **36**, 357-378 (1968). 58

Einasto J., Kaasik A., Saar E., *Dynamic evidence on massive coronas of galaxies,* Nature **250**, 309-310 (1974). 2

Eisenstein D. J., Hu W., *Baryonic features in the matter transfer function,* Astrophys. J. **496**, 605 (1998). 53, 54

Eisenstein D. J., Hu W., *Power Spectra for Cold Dark Matter and Its Variants,* Astrophys. J. **511**, 5-15 (1999). 53

Ellis J. R., Hagelin J. S., Nanopoulos D. V., Olive K. A., Srednicki M., *Supersymmetric Relics from the Big Bang,* Nucl. Phys. **B238**, 453-476 (1984). 10

Errani R., Peñarrubia J., Laporte C. F. P., Gómez F. A., *The effect of a disc on the population of cuspy and cored dark matter substructures in Milky Way-like galaxies,* Mon. Not. Roy. Astron. Soc. **465**, L59-L63 (2017). 68

Errani R., Peñarrubia J., Walker M. G., *Systematics in virial mass estimators for pressure-supported systems,* ArXiv e-prints (2018). 87

Essig R., Kuflik E., McDermott S. D., Volansky T., Zurek K. M., *Constraining Light Dark Matter with Diffuse X-Ray and Gamma-Ray Observations,* JHEP **11**, 193 (2013). 167, 168

Evans N. W., Carollo C. M., de Zeeuw P. T., *Triaxial haloes and particle dark matter detection,* Mon. Not. Roy. Astron. Soc. **318**, 1131 (2000). 159

Evoli C., Blasi P., Morlino G., Aloisio R., *Origin of the Cosmic Ray Galactic Halo Driven by Advected Turbulence and Self-Generated Waves,* Physical Review Letters **121**, 021102 (2018). 104

Ewen H. I., Purcell E. M., *Observation of a Line in the Galactic Radio Spectrum: Radiation from Galactic Hydrogen at 1,420 Mc./sec.,* Nature **168**, 356 (1951). 2

F. Hess V., *Über Beobachtungen der durchdringenden Strahlung bei sieben Freiballonfahrten,* Physikalische Zeitschrift **13**, 1084–1091 (1912). 97

Fairbairn M., Kraan A. C., Milstead D. A., Sjöstrand T., Skands P., Sloan T., *Stable massive particles at colliders,* Phys. Rept. **438**, 1-63 (2007). 14

Fairbairn M., Marsh D. J. E., Quevillon J., Rozier S., *Structure formation and microlensing with axion miniclusters,* Phys. Rev. **D97**, 083502 (2018). 163

Fairbairn M., Schwetz T., *Spin-independent elastic WIMP scattering and the DAMA annual modulation signal,* JCAP **0901**, 037 (2009). 159

Famaey B., McGaugh S. S., *Modified Newtonian Dynamics (MOND): Observational Phenomenology and Relativistic Extensions,* Living Reviews in Relativity **15**, 10 (2012). 7

Fermi E., *On the Origin of the Cosmic Radiation,* Physical Review **75**, 1169-1174 (1949). 99

Ferrer F., Hunter D. R., *The impact of the phase-space density on the indirect detection of dark matter,* JCAP **1309**, 005 (2013). 164

Fich M., Blitz L., Stark A. A., *The rotation curve of the Milky Way to 2 R(0),* Astrophys. J. **342**, 272-284 (1989). 2

Fitzpatrick A. L., Haxton W., Katz E., Lubbers N., Xu Y., *The effective field theory of dark matter direct detection,* Journal of Cosmology and Astro-Particle Physics **2013**, 004 (2013). 14, 16

Flores R. A., Primack J. R., *Observational and theoretical constraints on singular dark matter halos,* Astrophys. J. **427**, L1-4 (1994). 12

Fornasa M., Green A. M., *Self-consistent phase-space distribution function for the anisotropic dark matter halo of the Milky Way,* Phys. Rev. **D89**, 063531 (2014). 115, 159, 161

Fox P. J., Harnik R., Kopp J., Tsai Y., *LEP Shines Light on Dark Matter,* Phys. Rev. **D84**, 014028 (2011). 14

Freedman D. Z., van Nieuwenhuizen P., Ferrara S., *Progress toward a theory of supergravity,* Phys. Rev. D **13**, 3214-3218 (1976). 10

Freeman K. C., *On the Disks of Spiral and S0 Galaxies,* Astrophys. J. **160**, 811 (1970). 2

Freese K., Lisanti M., Savage C., *Colloquium: Annual modulation of dark matter,* Rev. Mod. Phys. **85**, 1561-1581 (2013). 14

Friedmann A., *Über die Krümmung des Raumes,* Zeitschrift fur Physik **10**, 377-386 (1922). 21

Fukuda S., Fukuda Y., Hayakawa T., Ichihara E., Ishitsuka M., Itow Y., Kajita T., Kameda J., Kaneyuki K., Kasuga S., Kobayashi K., Kobayashi Y., Koshio Y., Miura M., Moriyama S., Nakahata M., Nakayama S., Namba T., Obayashi Y., Okada A., Oketa M., Okumura K., Oyabu T., Sakurai N., Shiozawa M., Suzuki Y., Takeuchi Y., Toshito T., Totsuka Y., Yamada S., Desai S., Earl M., Hong J. T., Kearns E., Masuzawa M., Messier M. D., Stone J. L., Sulak L. R., Walter C. W., Wang W., Scholberg K., Barszczak T., Casper D., Liu D. W., Gajewski W., Halverson P. G., Hsu J., Kropp W. R., Mine S., Price L. R., Reines F., Smy M., Sobel H. W., Vagins M. R., Ganezer K. S., Keig W. E., Ellsworth R. W., Tasaka S., Flanagan J. W., Kibayashi A., Learned J. G., Matsuno S., Stenger V. J., Hayato Y., Ishii T., Ichikawa A., Kanzaki J., Kobayashi T., Maruyama T., Nakamura K., Oyama Y., Sakai A., Sakuda M., Sasaki O., Echigo S., Iwashita T., Kohama M., Suzuki A. T., Hasegawa M., Inagaki T., Kato I., Maesaka H., Nakaya T., Nishikawa K., Yamamoto S., Haines T. J., Kim B. K., Sanford R., Svoboda R., Blaufuss E., Chen M. L., Conner Z., Goodman J. A., Guillian E., Sullivan G. W., Turcan D., Habig A., Ackerman M., Goebel F., Hill J., Jung C. K., Kato T., Kerr D., Malek M., Martens K., Mauger C., McGrew C., Sharkey E., Viren B., Yanagisawa C., Doki W., Inaba S., Ito K., Kirisawa M., Kitaguchi M., Mitsuda C., Miyano K., Saji C., Takahata M., Takahashi M., Higuchi K., Kajiyama Y., Kusano A., Nagashima Y., Nitta K., Takita M., Yamaguchi T., Yoshida M., Kim H. I., Kim S. B., Yoo J., Okazawa H., Etoh M., Fujita K., Gando Y., Hasegawa A., Hasegawa T., Hatakeyama S., Inoue K., Ishihara K., Iwamoto T., Koga M., Nishiyama I., Ogawa H., Shirai J., Suzuki A., Takayama T., Tsushima F., Koshiba M., Ichikawa Y., Hashimoto T., Hatakeyama Y., Koike M., Horiuchi T., Nemoto M., Nishijima K., Takeda H., Fujiyasu H., Futagami T., Ishino H., Kanaya Y., Morii M., Nishihama H., Nishimura H., Suzuki T., Watanabe Y., Kielczewska D., Golebiewska U., Berns H. G., Boyd S. B., Doyle R. A., George J. S., Stachyra A. L., Wai L. L., Wilkes R. J., Young K. K., Kobayashi H., Super-Kamiokande Collaboration, *The Super-Kamiokande detector,* Nuclear Instruments and Methods in Physics Research A **501**, 418-462 (2003). 18

Gaensler B. M., Slane P. O., *The Evolution and Structure of Pulsar Wind Nebulae,* Ann. Rev. Astron. Astrophys. **44**, 17-47 (2006). 19

Gaggero D., Taoso M., Urbano A., Valli M., Ullio P., *Towards a realistic astrophysical interpretation of the gamma-ray Galactic center excess,* JCAP **1512**, 056 (2015). 17

Gaia Collaboration, Brown A. G. A., Vallenari A., Prusti T., de Bruijne J. H. J., Babusiaux C., Bailer-Jones C. A. L., *Gaia Data Release 2. Summary of the contents and survey properties,* ArXiv e-prints (2018). 76

Gamow G., *Expanding Universe and the Origin of Elements,* Physical Review **70**, 572-573 (1946). 6

Gamow G., *The Evolution of the Universe,* Nature **162**, 680-682 (1948)a. 3

Gamow G., *The Origin of Elements and the Separation of Galaxies,* Physical Review **74**, 505-506 (1948)b. 3

Gan J., Kang X., van den Bosch F. C., Hou J., *An improved model for the dynamical evolution of dark matter subhaloes,* Mon. Not. Roy. Astron. Soc. **408**, 2201-2212 (2010). 64, 75

Gao L., Navarro J. F., Cole S., Frenk C., White S. D. M., Springel V., Jenkins A., Neto A. F., *The redshift dependence of the structure of massive LCDM halos,* Mon. Not. Roy. Astron. Soc. **387**, 536 (2008). 58

García-Bellido J., Clesse S., *Constraints from microlensing experiments on clustered primordial black holes,* Phys. Dark Univ. **19**, 144-148 (2018). 163

Garrison-Kimmel S., Wetzel A., Bullock J. S., Hopkins P. F., Boylan-Kolchin M., Faucher-Giguère C.-A., Kereš D., Quataert E., Sanderson R. E., Graus A. S., Kelley T., *Not so lumpy after all: modelling the depletion of dark matter subhaloes by Milky Way-like galaxies,* Mon. Not. Roy. Astron. Soc. **471**, 1709-1727 (2017). 63

Geller M. J., Huchra J. P., *Mapping the Universe,* Science **246**, 897-903 (1989). 6

Génolini Y., Serpico P. D., Boudaud M., Caroff S., Poulin V., Derome L., Lavalle J., Maurin D., Poireau V., Rosier S., Salati P., Vecchi M., *Indications for a High-Rigidity Break in the Cosmic-Ray Diffusion Coefficient,* Physical Review Letters **119**, 241101 (2017). 104, 106

Gervais J.-L., Sakita B., *Field Theory Interpretation of Supergauges in Dual Models,* Nucl. Phys. **B34**, 632-639 (1971). 9

Ghelfi A., Barao F., Derome L., Maurin D., *Non-parametric determination of H and He interstellar fluxes from cosmic-ray data,* Astron. Astrophys. **591**, A94 (2016). 112, 168

Giesen G., Boudaud M., Génolini Y., Poulin V., Cirelli M., Salati P., Serpico P. D., *AMS-02 antiprotons, at last! Secondary astrophysical component and immediate implications for Dark Matter,* JCAP **1509**, 023 (2015). 18, 108

Gildener E., *Gauge Symmetry Hierarchies,* Phys. Rev. **D14**, 1667 (1976). 9

Ginzburg V. L., Syrovatskii S. I., *The Origin of Cosmic Rays* (1964). 102

Gleeson L. J., Axford W. I., *Solar Modulation of Galactic Cosmic Rays,* Astrophys. J. **154**, 1011 (1968). 102

Gnedin O. Y., Hernquist L., Ostriker J. P., *Tidal shocking by extended mass distributions,* Astrophys. J. **514**, 109-118 (1999). 68, 69

Gnedin O. Y., Ostriker J. P., *On the selfconsistent response of stellar systems to gravitational shocks,* Astrophys. J. **513**, 626 (1999). 68, 69

Golfand Yu. A., Likhtman E. P., *Extension of the Algebra of Poincare Group Generators and Violation of p Invariance,* JETP Lett. **13**, 323-326 (1971). 9

Gondolo P., Gelmini G., *Cosmic abundances of stable particles: improved analysis.,* Nuclear Physics B **360**, 145-179 (1991). 31, 33, 34, 164, 188

Gondolo P., Hisano J., Kadota K., *The Effect of quark interactions on dark matter kinetic decoupling and the mass of the smallest dark halos,* Phys. Rev. **D86**, 083523 (2012). 40

Goodenough L., Hooper D., *Possible Evidence For Dark Matter Annihilation In The Inner Milky Way From The Fermi Gamma Ray Space Telescope,* (2009). 17

Goodman J., Ibe M., Rajaraman A., Shepherd W., Tait T. M. P., Yu H.-B., *Constraints on Dark Matter from Colliders,* Phys. Rev. **D82**, 116010 (2010). 14

Goodman J., Ibe M., Rajaraman A., Shepherd W., Tait T. M. P., Yu H.-B., *Constraints on Light Majorana dark Matter from Colliders,* Phys. Lett. **B695**, 185-188 (2011). 14

Goodman M. W., Witten E., *Detectability of Certain Dark Matter Candidates,* Phys. Rev. **D31**, 3059 (1985). 14

Gould A., *WIMP Distribution in and Evaporation From the Sun,* Astrophys. J. **321**, 560 (1987). 161

Graham A. W., Merritt D., Moore B., Diemand J., Terzic B., *Empirical models for Dark Matter Halos. I. Nonparametric Construction of Density Profiles and Comparison with Parametric Models,* Astron. J. **132**, 2685-2700 (2006). 58

Graham P. W., Irastorza I. G., Lamoreaux S. K., Lindner A., van Bibber K. A., *Experimental Searches for the Axion and Axion-Like Particles,* Ann. Rev. Nucl. Part. Sci. **65**, 485-514 (2015). 16

Green A. M., *The WIMP annual modulation signal and nonstandard halo models,* Phys. Rev. **D63**, 043005 (2001). 159

Green A. M., *Astrophysical uncertainties on stellar microlensing constraints on multi-Solar mass primordial black hole dark matter,* Phys. Rev. **D96**, 043020 (2017)a. 162

Green A. M., *Astrophysical uncertainties on the local dark matter distribution and direct detection experiments,* J. Phys. **G44**, 084001 (2017)b. 159

Green A. M., Goodwin S. P., *On mini-halo encounters with stars,* Mon. Not. Roy. Astron. Soc. **375**, 1111-1120 (2007). 64, 73

Green A. M., Hofmann S., Schwarz D. J., *The power spectrum of SUSY - CDM on sub-galactic scales,* Mon. Not. Roy. Astron. Soc. **353**, L23 (2004). 40, 77

Green A. M., Hofmann S., Schwarz D. J., *The First wimpy halos,* JCAP **0508**, 003 (2005). 40, 54, 61, 77, 83

Greisen K., *End to the Cosmic-Ray Spectrum?,* Physical Review Letters **16**, 748-750 (1966). 98

Griest K., *Galactic microlensing as a method of detecting massive compact halo objects,* Astrophys. J. **366**, 412-421 (1991). 162

Griest K., Seckel D., *Three exceptions in the calculation of relic abundances,* Phys. Rev. D **43**, 3191-3203 (1991). 31

Gu P.-H., Lindner M., Sarkar U., Zhang X., *WIMP Dark Matter and Baryogenesis,* Phys. Rev. **D83**, 055008 (2011). 11

Gunn J. E., Lee B. W., Lerche I., Schramm D. N., Steigman G., *Some astrophysical consequences of the existence of a heavy stable neutral lepton,* Astrophys. J. **223**, 1015-1031 (1978). 16, 31

Guo Q., White S., Angulo R. E., Henriques B., Lemson G., Boylan-Kolchin M., Thomas P., Short C., *Galaxy formation in WMAP1 and WMAP7 cosmologies,* Mon. Not. Roy. Astron. Soc. **428**, 1351-1365 (2013). 81

Guo Y., Rein G., *Stable models of elliptical galaxies,* Mon. Not. Roy. Astron. Soc. **344**, 1296-1306 (2003). 145

Guth A. H., Pi S.-Y., *Fluctuations in the new inflationary universe,* Physical Review Letters **49**, 1110-1113 (1982). 52

Hagelin J. S., Kane G. L., *Cosmic ray antimatter from supersymmetric dark matter,* Nuclear Physics B **263**, 399-412 (1986). 18

Hagelin J. S., Ng K. W., Olive K. A., *A high-energy neutrino signature from supersymmetric relics,* Physics Letters B **180**, 375-380 (1986). 18

Hahn O., Abel T., *Multi-scale initial conditions for cosmological simulations,* Mon. Not. Roy. Astron. Soc. **415**, 2101-2121 (2011). 149

Hall L. J., Jedamzik K., March-Russell J., West S. M., *Freeze-In Production of FIMP Dark Matter,* JHEP **03**, 080 (2010). 37

Hamilton A. J. S., *Formulae for growth factors in expanding universes containing matter and a cosmological constant,* Mon. Not. Roy. Astron. Soc. **322**, 419-425 (2001). 48

Han J., Cole S., Frenk C. S., Jing Y., *A unified model for the spatial and mass distribution of subhaloes,* Mon. Not. Roy. Astron. Soc. **457**, 1208-1223 (2016). 64, 75

Hansen S. H., Moore B., Zemp M., Stadel J., *A Universal velocity distribution of relaxed collisionless structures,* JCAP **0601**, 014 (2006). 159

Harrison E. R., *Fluctuations at the threshold of classical cosmology,* Phys. Rev. **D1**, 2726-2730 (1970). 53

Hawking S., *Gravitationally collapsed objects of very low mass,* Mon. Not. Roy. Astron. Soc. **152**, 75 (1971). 9

Hawking S. W., *The Development of Irregularities in a Single Bubble Inflationary Universe,* Phys. Lett. **115B**, 295 (1982). 52

Hayashi E., Navarro J. F., Taylor J. E., Stadel J., Quinn T. R., *The Structural evolution of substructure,* Astrophys. J. **584**, 541-558 (2003). 74, 82

Heath D. J., *The growth of density perturbations in zero pressure Friedmann-Lemaitre universes,* Mon. Not. Roy. Astron. Soc. **179**, 351-358 (1977). 48

Hillas A. M., *Cosmic Rays: Recent Progress and some Current Questions,* ArXiv e-printspp astro–ph/0607109 (2006). 99

Hillas A. M., *Evolution of ground-based gamma-ray astronomy from the early days to the Cherenkov Telescope Arrays,* Astroparticle Physics **43**, 19-43 (2013). 17

Hiroshima N., Ando S., Ishiyama T., *Modeling evolution of dark matter substructure and annihilation boost,* Phys. Rev. **D97**, 123002 (2018). 64, 76, 94

Hisano J., Matsumoto S., Nojiri M. M., *Unitarity and higher order corrections in neutralino dark matter annihilation into two photons,* Phys. Rev. **D67**, 075014 (2003). 164

Hisano J., Matsumoto S., Nojiri M. M., *Explosive dark matter annihilation,* Phys. Rev. Lett. **92**, 031303 (2004). 164

Hisano J., Matsumoto S., Nojiri M. M., Saito O., *Non-perturbative effect on dark matter annihilation and gamma ray signature from galactic center,* Phys. Rev. **D71**, 063528 (2005). 164

Hochberg Y., Kuflik E., Volansky T., Wacker J. G., *Mechanism for Thermal Relic Dark Matter of Strongly Interacting Massive Particles,* Phys. Rev. Lett. **113**, 171301 (2014). 167

Hoekstra H., Bartelmann M., Dahle H., Israel H., Limousin M., Meneghetti M., *Masses of galaxy clusters from gravitational lensing,* Space Sci. Rev. **177**, 75-118 (2013). 3

Hofmann S., Schwarz D. J., Stoecker H., *Damping scales of neutralino cold dark matter,* Phys. Rev. **D64**, 083507 (2001). 39, 40

Hooper D., Blasi P., Serpico P. D., *Pulsars as the Sources of High Energy Cosmic Ray Positrons,* JCAP **0901**, 025 (2009). 19

Hooper D., Goodenough L., *Dark Matter Annihilation in The Galactic Center As Seen by the Fermi Gamma Ray Space Telescope,* Phys. Lett. **B697**, 412-428 (2011). 17

Hooper D., Linden T., *On The Origin Of The Gamma Rays From The Galactic Center,* Phys. Rev. **D84**, 123005 (2011). 17

Hooper D., Linden T., *Measuring the Local Diffusion Coefficient with H.E.S.S. Observations of Very High-Energy Electrons,* (2017). 19

Hooper D., Profumo S., *Dark matter and collider phenomenology of universal extra dimensions,* Phys. Rept. **453**, 29-115 (2007). 10

Hu W., Barkana R., Gruzinov A., *Cold and fuzzy dark matter,* Phys. Rev. Lett. **85**, 1158-1161 (2000). 11, 13

Hu W., Silk J., *Thermalization constraints and spectral distortions for massive unstable relic particles,* Phys. Rev. Lett. **70**, 2661-2664 (1993). 19

Hu W. T., PhD thesis, UC, Berkeley (1995). 4

Hui L., Ostriker J. P., Tremaine S., Witten E., *Ultralight scalars as cosmological dark matter,* Phys. Rev. **D95**, 043541 (2017). 11, 14

Hulse R. A., Taylor J. H., *Discovery of a pulsar in a binary system.,* Astrophys. J. **195**, L51-L53 (1975). 7

Hut P., *Limits on Masses and Number of Neutral Weakly Interacting Particles,* Phys. Lett. **B69**, 85 (1977). 30

Hütten M., Combet C., Maier G., Maurin D., *Dark matter substructure modelling and sensitivity of the Cherenkov Telescope Array to Galactic dark halos,* JCAP **9**, 047 (2016). 94

Hütten M., Combet C., Maurin D., *Extragalactic diffuse γ-rays from dark matter annihilation: revised prediction and full modelling uncertainties,* JCAP **1802**, 005 (2018). 17

Iršič V., Viel M., Haehnelt M. G., Bolton J. S., Becker G. D., *First constraints on fuzzy dark matter from Lyman-α forest data and hydrodynamical simulations,* Phys. Rev. Lett. **119**, 031302 (2017). 11, 14

Ishiyama T., *Hierarchical Formation of Dark Matter Halos and the Free Streaming Scale,* Astrophys. J. **788**, 27 (2014). 58, 63

Ishiyama T., Makino J., Ebisuzaki T., *Gamma-ray Signal from Earth-mass Dark Matter Microhalos,* Astrophys. J. Lett. **723**, L195-L200 (2010). 58, 62, 63

Jeans J. H., *On the theory of star-streaming and the structure of the universe,* Mon. Not. Roy. Astron. Soc. **76**, 70-84 (1915). 123

Jeans J. H., *Bakerian Lecture, 1917: The Configurations of Rotating Compressible Masses,* Philosophical Transactions of the Royal Society of London Series A **218**, 157-210 (1919). 123

Jedamzik K., *Did something decay, evaporate, or annihilate during Big Bang nucleosynthesis?,* Phys. Rev. **D70**, 063524 (2004). 19

Jedamzik K., *Big bang nucleosynthesis constraints on hadronically and electromagnetically decaying relic neutral particles,* Phys. Rev. **D74**, 103509 (2006). 19

Jungman G., Kamionkowski M., *Cosmic ray anti-protons from neutralino annihilation into gluons,* Phys. Rev. **D49**, 2316-2321 (1994). 18

Jungman G., Kamionkowski M., *Gamma-rays from neutralino annihilation,* Phys. Rev. **D51**, 3121-3124 (1995). 16

Jungman G., Kamionkowski M., Griest K., *Supersymmetric dark matter,* Phys. Rept. **267**, 195-373 (1996). 10, 14

Kahlhoefer F., *Review of LHC Dark Matter Searches,* Int. J. Mod. Phys. **A32**, 1730006 (2017). 14

Kahlhoefer F., Schmidt-Hoberg K., Schwetz T., Vogl S., *Implications of unitarity and gauge invariance for simplified dark matter models,* JHEP **02**, 016 (2016). 10

Kaluza T., *Zum Unitätsproblem der Physik,* Sitzungsber. Preuss. Akad. Wiss. Berlin (Math. Phys.) **1921**, 966-972 (1921). 10

Kamionkowski M., Koushiappas S. M., Kuhlen M., *Galactic substructure and dark-matter annihilation in the Milky Way halo,* Phys. Rev. D **81**, 043532 (2010). 64, 76, 94

Kandrup H. E., Sygnet J. F., *A simple proof of dynamical stability for a class of spherical clusters,* Astrophys. J. **298**, 27-33 (1985). 144

Kappl R., Reinert A., Winkler M. W., *AMS-02 Antiprotons Reloaded,* JCAP **1510**, 034 (2015). 103, 106, 108, 109, 168

Kennicutt Jr. R. C., *The Global Schmidt law in star forming galaxies,* Astrophys. J. **498**, 541 (1998). 149

Kim J. E., *Weak Interaction Singlet and Strong CP Invariance,* Phys. Rev. Lett. **43**, 103 (1979). 10

King I., *The structure of star clusters. I. an empirical density law,* Astron. J. **67**, 471 (1962). 64, 140

King I. R., *The structure of star clusters. III. Some simple dynamical models,* Astron. J. **71**, 64 (1966). 140

King I. R., *The Dynamics of Globular Clusters,* Quarterly Journal of the Royal Astronomical Society **22**, 227 (1981). 140

Kissmann R., *PICARD: A novel code for the Galactic Cosmic Ray propagation problem,* Astropart. Phys. **55**, 37-50 (2014). 105

Kissmann R., Werner M., Reimer O., Strong A. W., *Propagation in 3D spiral-arm cosmic-ray source distribution models and secondary particle production using PICARD,* Astropart. Phys. **70**, 39-53 (2015). 105

Klein O., *Quantum Theory and Five-Dimensional Theory of Relativity. (In German and English),* Z. Phys. **37**, 895-906 (1926). 10

Klypin A. A., Trujillo-Gomez S., Primack J., *Dark Matter Halos in the Standard Cosmological Model: Results from the Bolshoi Simulation,* Astrophys. J. **740**, 102 (2011). 6

Knobel C., *An Introduction into the Theory of Cosmological Structure Formation,* ArXiv e-prints (2012). 45, 49

Kofman L., Linde A. D., Starobinsky A. A., *Towards the theory of reheating after inflation,* Phys. Rev. **D56**, 3258-3295 (1997). 37

Kolb E. W., Olive K. A., *The Lee-Weinberg Bound Revisited,* Phys. Rev. **D33**, 1202 (1986). 31

Kolmogorov A., *The Local Structure of Turbulence in Incompressible Viscous Fluid for Very Large Reynolds' Numbers,* Akademiia Nauk SSSR Doklady **30**, 301-305 (1941). 103

Koushiappas S. M., *Proper motion of gamma-rays from microhalo sources,* Phys. Rev. Lett. **97**, 191301 (2006). 94

Kouvaris C., *WIMP Annihilation and Cooling of Neutron Stars,* Phys. Rev. **D77**, 023006 (2008). 161

Kraljic D., Sarkar S., *How rare is the Bullet Cluster (in a ΛCDM universe)?,* JCAP **4**, 050 (2015). 8

Krauss L. M., Srednicki M., Wilczek F., *Solar System Constraints and Signatures for Dark Matter Candidates,* Phys. Rev. **D33**, 2079-2083 (1986). 18

Krimigis S. M., Armstrong T. P., Axford W. I., Bostrom C. O., Fan C. Y., Gloeckler G., Lanzerotti L. J., *The Low Energy Charged Particle (LECP) Experiment on the Voyager Spacecraft,* SSR **21**, 329-354 (1977). 167

Kuhlen M., Diemand J., Madau P., *The Dark Matter Annihilation Signal from Galactic Substructure: Predictions for GLAST,* Astrophys. J. **686**, 262 (2008). 94

Kuhlen M., Weiner N., Diemand J., Madau P., Moore B., Potter D., Stadel J., Zemp M., *Dark Matter Direct Detection with Non-Maxwellian Velocity Structure,* JCAP **1002**, 030 (2010). 159

Lacey C., Cole S., *Merger rates in hierarchical models of galaxy formation,* Mon. Not. Roy. Astron. Soc. **262**, 627-649 (1993). 56

Lacroix T., Stref M., Lavalle J., *Anatomy of Eddington-like inversion methods in the context of dark matter searches,* JCAP **1809**, 040 (2018). 87, 132

Lattanzi M., Silk J. I., *Can the WIMP annihilation boost factor be boosted by the Sommerfeld enhancement?,* Phys. Rev. **D79**, 083523 (2009). 164

Lavalle J., *10 GeV dark matter candidates and cosmic-ray antiprotons,* Phys. Rev. D **82**, 081302 (2010). 18

Lavalle J., Magni S., *Making sense of the local Galactic escape speed estimates in direct dark matter searches,* Phys. Rev. **D91**, 023510 (2015). 159

Lavalle J., Maurin D., Putze A., *Direct constraints on diffusion models from cosmic-ray positron data: Excluding the minimal model for dark matter searches,* Phys. Rev. **D90**, 081301 (2014). 106

Lavalle J., Pochon J., Salati P., Taillet R., *Clumpiness of dark matter and positron annihilation signal: computing the odds of the galactic lottery,* Astron. Astrophys. **462**, 827-848 (2007). 19, 76, 106, 113

Lavalle J., Salati P., *Dark matter indirect signatures,* Comptes Rendus Physique **13**, 740-782 (2012). 16

Lavalle J., Yuan Q., Maurin D., Bi X.-J., *Full calculation of clumpiness boost factors for antimatter cosmic rays in the light of ΛCDM N-body simulation results. Abandoning hope in clumpiness enhancement?,* Astron. Astroph. **479**, 427-452 (2008). 18, 19, 76, 106, 108, 113

Lebovitz N. R., *On Schwarzschild's Criterion for the Stability of Gaseous Masses.,* Astrophys. J. **142**, 229 (1965). 143

Lee B. W., Weinberg S., *Cosmological lower bound on heavy-neutrino masses,* Physical Review Letters **39**, 165-168 (1977). 9, 30

Lee S. K., Lisanti M., Safdi B. R., Slatyer T. R., Xue W., *Evidence for Unresolved γ-Ray Point Sources in the Inner Galaxy,* Phys. Rev. Lett. **116**, 051103 (2016). 17

Lemaître G., *Un Univers homogène de masse constante et de rayon croissant rendant compte de la vitesse radiale des nébuleuses extra-galactiques,* Annales de la Société Scientifique de Bruxelles **47**, 49-59 (1927). 21

Lemze D., Wagner R., Rephaeli Y., Sadeh S., Norman M. L., Barkana R., Broadhurst T., Ford H., Postman M., *Profiles of Dark Matter Velocity Anisotropy in Simulated Clusters,* Astrophys. J. **752**, 141 (2012). 130

Leonard P. J. T., Tremaine S., *The local Galactic escape speed,* Astrophys. J. **353**, 486-493 (1990). 134

Lewin J. D., Smith P. F., *Review of mathematics, numerical factors, and corrections for dark matter experiments based on elastic nuclear recoil,* Astropart. Phys. **6**, 87-112 (1996). 14

LIGO Scientific Collaboration, Virgo Collaboration, *Observation of Gravitational Waves from a Binary Black Hole Merger,* Phys. Rev. Let. **116**, 061102 (2016). 7, 9

Linden T., Profumo S., *Probing the Pulsar Origin of the Anomalous Positron Fraction with AMS-02 and Atmospheric Cherenkov Telescopes,* Astrophys. J. **772**, 18 (2013). 19

Liu H., Slatyer T. R., Zavala J., *Contributions to cosmic reionization from dark matter annihilation and decay,* Phys. Rev. **D94**, 063507 (2016). 167, 168, 170

Loeb A., Zaldarriaga M., *Measuring the Small-Scale Power Spectrum of Cosmic Density Fluctuations through 21cm Tomography Prior to the Epoch of Structure Formation,* Physical Review Letters **92**, 211301 (2004). 19

Loeb A., Zaldarriaga M., *The Small-scale power spectrum of cold dark matter,* Phys. Rev. **D71**, 103520 (2005). 40, 54

Lopez-Honorez L., Mena O., Moliné Á., Palomares-Ruiz S., Vincent A. C., *The 21 cm signal and the interplay between dark matter annihilations and astrophysical processes,* JCAP **8**, 004 (2016). 19

Lovell M. R., Frenk C. S., Eke V. R., Jenkins A., Gao L., Theuns T., *The properties of warm dark matter haloes,* Mon. Not. Roy. Astron. Soc. **439**, 300-317 (2014). 13

Ludlow A. D., Bose S., Angulo R. E., Wang L., Hellwing W. A., Navarro J. F., Cole S., Frenk C. S., *The mass–concentration–redshift relation of cold and warm dark matter haloes,* Mon. Not. Roy. Astron. Soc. **460**, 1214-1232 (2016). 61

Ludlow A. D., Navarro J. F., Angulo R. E., Boylan-Kolchin M., Springel V., Frenk C., White S. D. M., *The mass-concentration-redshift relation of cold dark matter haloes,* Mon. Not. Roy. Astron. Soc. **441**, 378-388 (2014). 61

Ludlow A. D., Navarro J. F., White S. D. M., Boylan-Kolchin M., Springel V., Jenkins A., Frenk C. S., *The density and pseudo-phase-space density profiles of cold dark matter haloes,* Mon. Not. Roy. Astron. Soc. **415**, 3895-3902 (2011). 130

Lynden-Bell D., *Statistical mechanics of violent relaxation in stellar systems,* Mon. Not. Roy. Astron. Soc. **136**, 101 (1967). 57

Lynden-Bell D., Wood R., *The gravo-thermal catastrophe in isothermal spheres and the onset of red-giant structure for stellar systems,* Mon. Not. Roy. Astron. Soc. **138**, 495 (1968). 143

Macciò A. V., Dutton A. A., van den Bosch F. C., *Concentration, spin and shape of dark matter haloes as a function of the cosmological model: WMAP1, WMAP3 and WMAP5 results,* Mon. Not. Roy. Astron. Soc. **391**, 1940-1954 (2008). 61, 62, 63, 77

Maccio A. V., Paduroiu S., Anderhalden D., Schneider A., Moore B., *Cores in warm dark matter haloes: a Catch 22 problem,* Mon. Not. Roy. Astron. Soc. **424**, 1105-1112 (2012). 13

Maccione L., Evoli C., Gaggero D., Grasso D., 2011, *DRAGON: Galactic Cosmic Ray Diffusion Code*, Astrophysics Source Code Library. 105

Macias O., Gordon C., *Contribution of cosmic rays interacting with molecular clouds to the Galactic Center gamma-ray excess,* Phys. Rev. **D89**, 063515 (2014). 17

Malkov M. A., Drury L. O., *Nonlinear theory of diffusive acceleration of particles by shock waves,* Reports on Progress in Physics **64**, 429-481 (2001). 99

Mao Y.-Y., Strigari L. E., Wechsler R. H., Wu H.-Y., Hahn O., *Halo-to-halo Similarity and Scatter in the Velocity Distribution of Dark Matter,* Astrophys. J. **764**, 35 (2013). 159

March-Russell J., West S. M., Cumberbatch D., Hooper D., *Heavy Dark Matter Through the Higgs Portal,* JHEP **07**, 058 (2008). 164

Marciano W. J., Senjanovic G., *Predictions of Supersymmetric Grand Unified Theories,* Phys. Rev. **D25**, 3092 (1982). 10

Maréchal L., Perez J., *Radial orbit instability as a dissipation-induced phenomenon,* Mon. Not. Roy. Astron. Soc. **405**, 2785-2790 (2010). 145

Markevitch M., Gonzalez A. H., Clowe D., Vikhlinin A., David L., Forman W., Jones C., Murray S., Tucker W., *Direct constraints on the dark matter self-interaction cross-section from the merging galaxy cluster 1E0657-56,* Astrophys. J. **606**, 819-824 (2004). 13

Marsh D. J. E., *Axion Cosmology,* Phys. Rept. **643**, 1-79 (2016). 11, 14

Martin J., *Everything you always wanted to know about the cosmological constant problem (but were afraid to ask),* Comptes Rendus Physique **13**, 566-665 (2012). 23

Martin J., Ringeval C., Vennin V., *Encyclopædia Inflationaris,* Phys. Dark Univ. **5-6**, 75-235 (2014). 53

Martin S. P., *A Supersymmetry primer,* (1997). 10

Mashchenko S., Wadsley J., Couchman H. M. P., *Stellar Feedback in Dwarf Galaxy Formation,* Science **319**, 174 (2008). 12

Massey R., Kitching T., Richard J., *The dark matter of gravitational lensing,* Rept. Prog. Phys. **73**, 086901 (2010). 3

Maurin D., *USINE propagation code and associated tools,* PoS **ICRC2015**, 484 (2016). 105

Maurin D., Donato F., Taillet R., Salati P., *Cosmic rays below z=30 in a diffusion model: new constraints on propagation parameters,* Astrophys. J. **555**, 585-596 (2001). 104

Maurin D., Taillet R., Donato F., Salati P., Barrau A., Boudoul G., *Galactic cosmic ray nuclei as a tool for astroparticle physics,* (2002). 18, 105, 106

McGaugh S. S., *Distinguishing between Cold Dark Matter and Modified Newtonian Dynamics: Predictions for the Microwave Background,* Astrophys. J. Lett. **523**, L99-L102 (1999). 8

McGaugh S. S., Lelli F., Schombert J. M., *Radial Acceleration Relation in Rotationally Supported Galaxies,* Physical Review Letters **117**, 201101 (2016). 8

McMillan P. J., *Mass models of the Milky Way,* Mon. Not. Roy. Astron. Soc. **414**, 2446-2457 (2011). 2, 115

McMillan P. J., *The mass distribution and gravitational potential of the Milky Way,* Mon. Not. Roy. Astron. Soc. **465**, 76-94 (2017). 66, 67, 76, 78, 83, 84, 85, 86, 87, 97, 115, 117, 133, 134, 135, 145, 146, 148, 151, 160, 163, 165, 169, 171, 195

Merritt D., *Spherical stellar systems with spheroidal velocity distributions,* Astron. J. **90**, 1027-1037 (1985). 130

Merritt D., Aguilar L. A., *A numerical study of the stability of spherical galaxies,* Mon. Not. Roy. Astron. Soc. **217**, 787-804 (1985). 145

Merritt D., Navarro J. F., Ludlow A., Jenkins A., *A Universal Density Profile for Dark and Luminous Matter?,* Astrophys. J. Lett. **624**, L85-L88 (2005). 58

Meszaros P., *The behaviour of point masses in an expanding cosmological substratum,* Astron. Astrophys. **37**, 225-228 (1974). 42, 53

Meza A., Zamorano N., *Numerical Stability of a Family of Osipkov-Merritt Models,* Astrophys. J. **490**, 136-142 (1997). 145

Michie R. W., *On the distribution of high energy stars in spherical stellar systems,* Mon. Not. Roy. Astron. Soc. **125**, 127 (1963). 140

Michie R. W., Bodenheimer P. H., *The dynamics of spherical stellar systems, II,* Mon. Not. Roy. Astron. Soc. **126**, 269 (1963). 140

Milgrom M., *A Modification of the Newtonian dynamics as a possible alternative to the hidden mass hypothesis,* Astrophys. J. **270**, 365-370 (1983). 7

Milgrom M., *Bimetric MOND gravity,* Phys. Rev. D **80**, 123536 (2009). 8

Mirabal N., *Dark matter vs. Pulsars: Catching the impostor,* Mon. Not. Roy. Astron. Soc. **436**, 2461 (2013). 17

Mo H., van den Bosch F. C., White S., *Galaxy Formation and Evolution* (2010). 45, 48

Moliné A., Sánchez-Conde M. A., Palomares-Ruiz S., Prada F., *Characterization of subhalo structural properties and implications for dark matter annihilation signals,* Mon. Not. Roy. Astron. Soc. **466**, 4974-4990 (2017). 61

Mollitor P., Nezri E., Teyssier R., *Baryonic and dark matter distribution in cosmological simulations of spiral galaxies,* Mon. Not. Roy. Astron. Soc. **447**, 1353-1369 (2015). 12, 149

Moore B., *Evidence against dissipationless dark matter from observations of galaxy haloes,* Nature **370**, 629 (1994). 12

Moore B., Diemand J., Stadel J., Quinn T. R., *On the survival and disruption of Earth mass CDM micro-haloes,* (2005). 94

Moore B., Ghigna S., Governato F., Lake G., Quinn T. R., Stadel J., Tozzi P., *Dark matter substructure within galactic halos,* Astrophys. J. **524**, L19-L22 (1999). 12

Nath P., Arnowitt R., *Generalized super-gauge symmetry as a new framework for unified gauge theories,* Physics Letters B **56**, 177-180 (1975). 10

Navarro J. F., Eke V. R., Frenk C. S., *The cores of dwarf galaxy halos,* Mon. Not. Roy. Astron. Soc. **283**, L72-L78 (1996). 12

Navarro J. F., Frenk C. S., White S. D. M., *The Structure of cold dark matter halos,* Astrophys. J. **462**, 563-575 (1996). 12, 57, 61

Navarro J. F., Frenk C. S., White S. D. M., *A Universal Density Profile from Hierarchical Clustering,* Astrophys. J. **490**, 493-508 (1997). 12, 57

Navarro J. F., Hayashi E., Power C., Jenkins A. R., Frenk C. S., White S. D. M., Springel V., Stadel J., Quinn T. R., *The inner structure of ΛCDM haloes - III. Universality and asymptotic slopes,* Mon. Not. Roy. Astron. Soc. **349**, 1039-1051 (2004). 58

Neveu A., Schwarz J. H., *Factorizable dual model of pions,* Nucl. Phys. **B31**, 86-112 (1971). 9

Ogiya G., Hahn O., *What sets the central structure of dark matter haloes?,* Mon. Not. Roy. Astron. Soc. **473**, 4339-4359 (2018). 57, 58

Oh S.-H., de Blok W. J. G., Brinks E., Walter F., Kennicutt Jr. R. C., *Dark and Luminous Matter in THINGS Dwarf Galaxies,* Astron. J. **141**, 193 (2011). 12

Olive K. A., Steigman G., Walker T. P., *Primordial nucleosynthesis: Theory and observations,* Phys. Rept. **333**, 389-407 (2000). 6

Oman K. A., Navarro J. F., Fattahi A., Frenk C. S., Sawala T., White S. D. M., Bower R., Crain R. A., Furlong M., Schaller M., Schaye J., Theuns T., *The unexpected diversity of dwarf galaxy rotation curves,* Mon. Not. Roy. Astron. Soc. **452**, 3650-3665 (2015). 12

Oort J. H., *The force exerted by the stellar system in the direction perpendicular to the galactic plane and some related problems,* Bulletin of the Astronomical Institutes of the Netherlands **6**, 249 (1932). 2

Osipkov L. P., *Spherical systems of gravitating bodies with an ellipsoidal velocity distribution,* Pisma v Astronomicheskii Zhurnal **5**, 77-80 (1979). 130

Ostriker J. P., Peebles P. J. E., Yahil A., *The size and mass of galaxies, and the mass of the universe,* Astrophys. J. Lett. **193**, L1-L4 (1974). 2

Ostriker J. P., Spitzer Jr. L., Chevalier R. A., *On the Evolution of Globular Clusters,* Astrophys. J. Lett. **176**, L51 (1972). 68

Oñorbe J., Boylan-Kolchin M., Bullock J. S., Hopkins P. F., Kerěs D., Faucher-Giguère C.-A., Quataert E., Murray N., *Forged in FIRE: cusps, cores, and baryons in low-mass dwarf galaxies,* Mon. Not. Roy. Astron. Soc. **454**, 2092-2106 (2015). 12

Paczynski B., *Gravitational microlensing by the galactic halo,* Astrophys. J. **304**, 1-5 (1986). 9

Padmanabhan N., Finkbeiner D. P., *Detecting dark matter annihilation with CMB polarization: Signatures and experimental prospects,* Phys. Rev. **D72**, 023508 (2005). 19

Panov A. D., Adams J. H., Ahn H. S., Bashinzhagyan G. L., Watts J. W., Wefel J. P., Wu J., Ganel O., Guzik T. G., Zatsepin V. I., Isbert I., Kim K. C., Christl M., Kouznetsov E. N., Panasyuk M. I., Seo E. S., Sokolskaya N. V., Chang J., Schmidt W. K. H., Fazely A. R., *Energy spectra of abundant nuclei of primary cosmic rays from the data of ATIC-2 experiment: Final results,* Bulletin of the Russian Academy of Sciences, Physics **73**, 564-567 (2009). 104

Pato M., Iocco F., Bertone G., *Dynamical constraints on the dark matter distribution in the Milky Way,* Journal of Cosmology and Astro-Particle Physics **2015**, 001 (2015). 115

Pato M., Strigari L. E., Trotta R., Bertone G., *Taming astrophysical bias in direct dark matter searches,* JCAP **1302**, 041 (2013). 159

Peccei R. D., Quinn H. R., *CP Conservation in the Presence of Instantons,* Phys. Rev. Lett. **38**, 1440-1443 (1977). 10

Peebles P. J. E., *The Black-Body Radiation Content of the Universe and the Formation of Galaxies.,* Astrophys. J. **142**, 1317 (1965). 4

Peebles P. J. E., *Primordial Helium Abundance and the Primordial Fireball. II,* Astrophys. J. **146**, 542 (1966). 6

Peebles P. J. E., *Large-scale background temperature and mass fluctuations due to scale-invariant primeval perturbations,* Astrophys. J. Lett. **263**, L1-L5 (1982)a. 3, 13

Peebles P. J. E., *Primeval adiabatic perturbations - Effect of massive neutrinos,* Astrophys. J. **258**, 415-424 (1982)b. 3

Peebles P. J. E., Dicke R. H., *Origin of the Microwave Radio Background,* Nature **211**, 574-575 (1966). 4

Peebles P. J. E., Schramm D. N., Turner E. L., Kron R. G., *The case for the relativistic hot Big Bang cosmology,* Nature **352**, 769-776 (1991). 4

Peebles P. J. E., Yu J. T., *Primeval adiabatic perturbation in an expanding universe,* Astrophys. J. **162**, 815-836 (1970). 4, 53

Penarrubia J., Benson A. J., *Effects of dynamical evolution on the distribution of substructures,* Mon. Not. Roy. Astron. Soc. **364**, 977-989 (2005). 75

Penarrubia J., Navarro J. F., McConnachie A. W., *The Tidal Evolution of Local Group Dwarf Spheroidals,* Astrophys. J. **673**, 226 (2008). 87

Penning B., *The pursuit of dark matter at colliders—an overview,* J. Phys. **G45**, 063001 (2018). 14

Penzias A. A., Wilson R. W., *A Measurement of Excess Antenna Temperature at 4080 Mc/s.,* Astrophys. J. **142**, 419-421 (1965). 3

Percival W. J. et al. (SDSS Collaboration), *Baryon Acoustic Oscillations in the Sloan Digital Sky Survey Data Release 7 Galaxy Sample,* Mon. Not. Roy. Astron. Soc. **401**, 2148-2168 (2010). 6

Perez J., Aly J. J., *Stability of spherical stellar systems. 1: Analytical results,* Mon. Not. Roy. Astron. Soc. **280**, 689 (1996). 145

Perlmutter S., Aldering G., Goldhaber G., Knop R. A., Nugent P., Castro P. G., Deustua S., Fabbro S., Goobar A., Groom D. E., Hook I. M., Kim A. G., Kim M. Y., Lee J. C., Nunes N. J., Pain R., Pennypacker C. R., Quimby R., Lidman C., Ellis R. S., Irwin M., McMahon R. G., Ruiz-Lapuente P., Walton N., Schaefer B., Boyle B. J., Filippenko A. V., Matheson T., Fruchter A. S., Panagia N., Newberg H. J. M., Couch W. J., Project T. S. C., *Measurements of* Ω *and* Λ *from 42 High-Redshift Supernovae,* Astrophys. J. **517**, 565-586 (1999). 7

Petac M., Ullio P., Valli M., *On velocity-dependent dark matter annihilations in dwarf satellites,* (2018). 164

Petraki K., Volkas R. R., *Review of asymmetric dark matter,* Int. J. Mod. Phys. **A28**, 1330028 (2013). 11

Petrou M., PhD thesis, - (1981). 9

Petrović J., Serpico P. D., Zaharijaš G., *Galactic Center gamma-ray "excess" from an active past of the Galactic Centre?,* JCAP **1410**, 052 (2014). 17

Pieri L., Bertone G., Branchini E., *Dark Matter Annihilation in Substructures Revised,* Mon. Not. Roy. Astron. Soc. **384**, 1627 (2008). 94

Pieri L., Lavalle J., Bertone G., Branchini E., *Implications of high-resolution simulations on indirect dark matter searches,* Phys. Rev. D **83**, 023518 (2011). 19, 76, 81, 94, 106

Piffl T. et al., *The RAVE survey: the Galactic escape speed and the mass of the Milky Way,* Astron. Astrophys. **562**, A91 (2014). 134

Piffl T., Penoyre Z., Binney J., *Bringing the Galaxy's dark halo to life,* Mon. Not. Roy. Astron. Soc. **451**, 639-650 (2015). 115

Pillepich A., Springel V., Nelson D., Genel S., Naiman J., Pakmor R., Hernquist L., Torrey P., Vogelsberger M., Weinberger R., Marinacci F., *Simulating galaxy formation with the IllustrisTNG model,* Mon. Not. Roy. Astron. Soc. **473**, 4077-4106 (2018). 13

Plummer H. C., *On the problem of distribution in globular star clusters,* Mon. Not. Roy. Astron. Soc. **71**, 460-470 (1911). 127

Pointecouteau E., Silk J., *New Constraints on MOND from galaxy clusters,* Mon. Not. Roy. Astron. Soc. **364**, 654-658 (2005). 8

Polisensky E., Ricotti M., *Constraints on the Dark Matter Particle Mass from the Number of Milky Way Satellites,* Phys. Rev. **D83**, 043506 (2011). 13

Pontzen A., Governato F., *How supernova feedback turns dark matter cusps into cores,* Mon. Not. Roy. Astron. Soc. **421**, 3464 (2012). 12

Pospelov M., Ritz A., *Astrophysical Signatures of Secluded Dark Matter,* Phys. Lett. **B671**, 391-397 (2009). 164

Potgieter M. S., *Solar Modulation of Cosmic Rays,* Living Reviews in Solar Physics **10**, 3 (2013). 102

Poulin V., Serpico P. D., Lesgourgues J., *A fresh look at linear cosmological constraints on a decaying dark matter component,* JCAP **1608**, 036 (2016). 19, 167

Prada F., Klypin A. A., Cuesta A. J., Betancort-Rijo J. E., Primack J., *Halo concentrations in the standard Λ cold dark matter cosmology,* Mon. Not. Roy. Astron. Soc. **423**, 3018-3030 (2012). 61, 62, 63

Preskill J., Wise M. B., Wilczek F., *Cosmology of the Invisible Axion,* Phys. Lett. **B120**, 127-132 (1983). 10

Press W. H., Schechter P., *Formation of Galaxies and Clusters of Galaxies by Self-Similar Gravitational Condensation,* Astrophys. J. **187**, 425-438 (1974). 55

Press W. H., Spergel D. N., *Capture by the sun of a galactic population of weakly interacting, massive particles,* Astrophys. J. **296**, 679-684 (1985). 18, 161

Primakoff H., *Photoproduction of neutral mesons in nuclear electric fields and the mean life of the neutral meson,* Phys. Rev. **81**, 899 (1951). 16

Profumo S., *TeV gamma-rays and the largest masses and annihilation cross sections of neutralino dark matter,* Phys. Rev. **D72**, 103521 (2005). 164

Profumo S., *Dissecting cosmic-ray electron-positron data with Occam's Razor: the role of known Pulsars,* Central Eur. J. Phys. **10**, 1-31 (2011). 19

Profumo S., Sigurdson K., Kamionkowski M., *What mass are the smallest protohalos?,* Phys. Rev. Lett. **97**, 031301 (2006). 41

Profumo S., Ullio P., *Multi-wavelength Searches for Particle Dark Matter,* ArXiv e-prints (2010). 16

Pullen A. R., Benson A. J., Moustakas L. A., *Nonlinear evolution of dark matter subhalos and applications to warm dark matter,* Astrophys. J. **792**, 24 (2014). 75

Ramond P., *Dual Theory for Free Fermions,* Phys. Rev. **D3**, 2415-2418 (1971). 9

Randall L., Sundrum R., *A Large mass hierarchy from a small extra dimension,* Phys. Rev. Lett. **83**, 3370-3373 (1999). 10

Read J. I., *The Local Dark Matter Density,* J. Phys. **G41**, 063101 (2014). 2

Read J. I., Agertz O., Collins M. L. M., *Dark matter cores all the way down,* Mon. Not. Roy. Astron. Soc. **459**, 2573-2590 (2016). 12

Read J. I., Walker M. G., Steger P., *The case for a cold dark matter cusp in Draco,* (2018). 77

Rees M. J., Gunn J. E., *The origin of the magnetic field and relativistic particles in the Crab Nebula,* Mon. Not. Roy. Astron. Soc. **167**, 1-12 (1974). 19

Reeves H., Audouze J., Fowler W. A., Schramm D. N., *On the Origin of Light Elements,* Astrophys. J. **179**, 909-930 (1973). 6

Reinert A., Winkler M. W., *A Precision Search for WIMPs with Charged Cosmic Rays,* JCAP **1801**, 055 (2018). 18, 106, 108

Renaud F., Bournaud F., Emsellem E., Elmegreen B., Teyssier R., Alves J., Chapon D., Combes F., Dekel A., Gabor J., Hennebelle P., Kraljic K., *A sub-parsec resolution simulation of the Milky Way: global structure of the interstellar medium and properties of molecular clouds,* Mon. Not. Roy. Astron. Soc. **436**, 1836-1851 (2013). 13

Riess A. G., Casertano S., Yuan W., Macri L., Anderson J., MacKenty J. W., Bowers J. B., Clubb K. I., Filippenko A. V., Jones D. O., Tucker B. E., *New Parallaxes of Galactic Cepheids from Spatially Scanning the Hubble Space Telescope: Implications for the Hubble Constant,* Astrophys. J. **855**, 136 (2018). 6

Riess A. G. et al., *A 2.4% Determination of the Local Value of the Hubble Constant,* Astrophys. J. **826**, 56 (2016). 6

Riess A. G. et al., *Milky Way Cepheid Standards for Measuring Cosmic Distances and Application to Gaia DR2: Implications for the Hubble Constant,* Astrophys. J. **861**, 126 (2018). 6

Riess A. G., Filippenko A. V., Challis P., Clocchiatti A., Diercks A., Garnavich P. M., Gilliland R. L., Hogan C. J., Jha S., Kirshner R. P., Leibundgut B., Phillips M. M., Reiss D., Schmidt B. P., Schommer R. A., Smith R. C., Spyromilio J., Stubbs C., Suntzeff N. B., Tonry J., *Observational Evidence from Supernovae for an Accelerating Universe and a Cosmological Constant,* Astron. J. **116**, 1009-1038 (1998). 7

Rigault M. et al., *Confirmation of a Star Formation Bias in Type Ia Supernova Distances and its Effect on Measurement of the Hubble Constant,* Astrophys. J. **802**, 20 (2015). 7

Roberts M. S., Rots A. H., *Comparison of Rotation Curves of Different Galaxy Types,* Astron. Astroph. **26**, 483-485 (1973). 2

Robertson H. P., *Kinematics and World-Structure,* Astrophys. J. **82**, 284 (1935). 21

Rodriguez-Puebla A., Behroozi P., Primack J., Klypin A., Lee C., Hellinger D., *Halo and subhalo demographics with Planck cosmological parameters: Bolshoi–Planck and MultiDark–Planck simulations,* Mon. Not. Roy. Astron. Soc. **462**, 893-916 (2016). 63

Rogstad D. H., Shostak G. S., *Gross Properties of Five Scd Galaxies as Determined from 21-CENTIMETER Observations,* Astrophys. J. **176**, 315 (1972). 2

Rosdahl J., Schaye J., Dubois Y., Kimm T., Teyssier R., *Snap, crackle, pop: sub-grid supernova feedback in AMR simulations of disc galaxies,* Mon. Not. Roy. Astron. Soc. **466**, 11-33 (2017). 13

Rovelli C., *Loop quantum gravity,* Living Rev. Rel. **1**, 1 (1998). 7

Rubin V. C., Ford Jr. W. K., Thonnard N., *Extended rotation curves of high-luminosity spiral galaxies. IV - Systematic dynamical properties, SA through SC,* Astrophys. J. Lett. **225**, L107-L111 (1978). 2

Sachs R. K., Wolfe A. M., *Perturbations of a Cosmological Model and Angular Variations of the Microwave Background,* Astrophys. J. **147**, 73 (1967). 4

Salati P., *The distortions of the microwave background radiation, heavy neutral decaying leptons and decaying gravitinos,* Physics Letters B **163**, 236-242 (1985). 19

Salati P., Silk J., *A STELLAR PROBE OF DARK MATTER ANNIHILATION IN GALACTIC NUCLEI,* Astrophys. J. **338**, 24-31 (1989). 161

Sánchez-Conde M. A., Prada F., *The flattening of the concentration mass relation towards low halo masses and its implications for the annihilation signal boost,* Mon. Not. Roy. Astron. Soc. **442**, 2271-2277 (2014). 61, 62, 63, 77

Sanders R. H., *Resolving the virial discrepancy in clusters of galaxies with modified newtonian dynamics,* Astrophys. J. **512**, L23 (1999). 8

Sanders R. H., *Clusters of galaxies with modified Newtonian dynamics (MOND),* Mon. Not. Roy. Astron. Soc. **342**, 901 (2003). 8

Sarkar S., *Big bang nucleosynthesis and physics beyond the standard model,* Rept. Prog. Phys. **59**, 1493-1610 (1996). 6

Sato K., Kobayashi M., *Cosmological Constraints on the Mass and the Number of Heavy Lepton Neutrinos,* Prog. Theor. Phys. **58**, 1775 (1977). 30

Schmid C., Schwarz D. J., Widerin P., *Amplification of cosmological inhomogeneities from the QCD transition,* Phys. Rev. **D59**, 043517 (1999). 39

Schmidt M., *The Rate of Star Formation,* Astrophys. J. **129**, 243 (1959). 149

Schneider A., *Structure formation with suppressed small-scale perturbations,* Mon. Not. Roy. Astron. Soc. **451**, 3117-3130 (2015). 13

Schneider A., Krauss L., Moore B., *Impact of Dark Matter Microhalos on Signatures for Direct and Indirect Detection,* Phys. Rev. **D82**, 063525 (2010). 73

Schneider A., Smith R. E., Reed D., *Halo Mass Function and the Free Streaming Scale,* Mon. Not. Roy. Astron. Soc. **433**, 1573 (2013). 77

Schwetz T., Zupan J., *Dark matter attempts for CoGeNT and DAMA,* JCAP **8**, 008 (2011). 16

Scott P., Fairbairn M., Edsjo J., *Dark stars at the Galactic centre - the main sequence,* Mon. Not. Roy. Astron. Soc. **394**, 82 (2009). 161

Sefusatti E., Zaharijas G., Serpico P. D., Theurel D., Gustafsson M., *Extragalactic gamma-ray signal from dark matter annihilation: an appraisal,* Mon. Not. Roy. Astron. Soc. **441**, 1861-1878 (2014). 17

Sekido Y., Masuda T., Yoshida S., Wada M., *The Crab Nebula as an Observed Point Source of Cosmic Rays,* Physical Review **83**, 658-659 (1951). 101

Serpico P. D., Sefusatti E., Gustafsson M., Zaharijas G., *Extragalactic gamma-ray signal from dark matter annihilation: a power spectrum based computation,* Mon. Not. Roy. Astron. Soc. **421**, L87-L91 (2012). 17, 94

Servant G., Tait T. M. P., *Is the lightest Kaluza-Klein particle a viable dark matter candidate?,* Nuclear Physics B **650**, 391-419 (2003). 10

Shalchi A., ed. 2009, *Nonlinear Cosmic Ray Diffusion Theories* Vol. 362 of Astrophysics and Space Science Library. 103

Shapiro P. R., Iliev I. T., Martel H., Ahn K., Alvarez M. A., *The Equilibrium structure of CDM halos,* (2004). 150

Sheth R. K., Mo H. J., Tormen G., *Ellipsoidal collapse and an improved model for the number and spatial distribution of dark matter haloes,* Mon. Not. Roy. Astron. Soc. **323**, 1 (2001). 56

Sheth R. K., Tormen G., *Large-scale bias and the peak background split,* Mon. Not. Roy. Astron. Soc. **308**, 119-126 (1999). 56

Shifman M. A., Vainshtein A. I., Zakharov V. I., *Can Confinement Ensure Natural CP Invariance of Strong Interactions?,* Nucl. Phys. **B166**, 493-506 (1980). 10

Shokair T. M. et al., *Future Directions in the Microwave Cavity Search for Dark Matter Axions,* Int. J. Mod. Phys. **A29**, 1443004 (2014). 16

Sikivie P., *Experimental Tests of the Invisible Axion,* Phys. Rev. Lett. **51**, 1415-1417 (1983). 11

Silk J., *Cosmic black body radiation and galaxy formation,* Astrophys. J. **151**, 459-471 (1968). 4

Silk J., Bloemen H., *A gamma-ray constraint on the nature of dark matter,* Astrophys. J. Lett. **313**, L47-L51 (1987). 16, 17

Silk J., Olive K. A., Srednicki M., *The Photino, the Sun and High-Energy Neutrinos,* Phys. Rev. Lett. **55**, 257-259 (1985). 18, 161

Silk J., Srednicki M., *Cosmic-ray antiprotons as a probe of a photino-dominated universe,* Physical Review Letters **53**, 624-627 (1984). 18

Silk J., Stebbins A., *Clumpy cold dark matter,* Astrophys. J. **411**, 439-449 (1993). 91, 94

Sin S.-J., *Late time cosmological phase transition and galactic halo as Bose liquid,* Phys. Rev. **D50**, 3650-3654 (1994). 13

Sivertsson S., Edsjö J., *Publisher's Note: WIMP diffusion in the solar system including solar WIMP-nucleon scattering [Phys. Rev. D 85, 123514 (2012)],* Phys. Rev. D **85**, 129905 (2012). 18

Skordis C., *Generalizing tensor-vector-scalar cosmology,* Phys. Rev. D **77**, 123502 (2008). 8

Slatyer T. R., *Indirect dark matter signatures in the cosmic dark ages. I. Generalizing the bound on s-wave dark matter annihilation from Planck results,* Phys. Rev. **D93**, 023527 (2016)a. 19, 167

Slatyer T. R., *Indirect Dark Matter Signatures in the Cosmic Dark Ages II. Ionization, Heating and Photon Production from Arbitrary Energy Injections,* Phys. Rev. **D93**, 023521 (2016)b. 19

Slatyer T. R., Padmanabhan N., Finkbeiner D. P., *CMB Constraints on WIMP Annihilation: Energy Absorption During the Recombination Epoch,* Phys. Rev. **D80**, 043526 (2009). 19

Slatyer T. R., Wu C.-L., *General Constraints on Dark Matter Decay from the Cosmic Microwave Background,* Phys. Rev. **D95**, 023010 (2017). 19

Slosar A., Melchiorri A., Silk J. I., *Test of modified Newtonian dynamics with recent Boomerang data,* Phys. Rev. D **72**, 101301 (2005). 8

Smoot G. F., Bennett C. L., Kogut A., Wright E. L., Aymon J., Boggess N. W., Cheng E. S., de Amici G., Gulkis S., Hauser M. G., Hinshaw G., Jackson P. D., Janssen M., Kaita E., Kelsall T., Keegstra P., Lineweaver C., Loewenstein K., Lubin P., Mather J., Meyer S. S., Moseley S. H., Murdock T., Rokke L., Silverberg R. F., Tenorio L., Weiss R., Wilkinson D. T., *Structure in the COBE Differential Microwave Radiometer First-Year Maps,* Astrophys. J. **396**, L1 (1992). 4

Sommerfeld A., *Über die Beugung und Bremsung der Elektronen,* Annalen der Physik **403**, 257-330 (1931). 164

Sparre M., Hansen S. H., *The behaviour of shape and velocity anisotropy in dark matter haloes,* JCAP **10**, 049 (2012). 130

Spergel D. N. et al. (WMAP Collaboration), *Wilkinson Microwave Anisotropy Probe (WMAP) three year results: implications for cosmology,* Astrophys. J. Suppl. **170**, 377 (2007). 81

Spergel D. N., Steinhardt P. J., *Observational evidence for selfinteracting cold dark matter,* Phys. Rev. Lett. **84**, 3760-3763 (2000). 13

Spitzer L., *Dynamical evolution of globular clusters* (1987). 64

Spitzer Jr. L., *Disruption of Galactic Clusters.,* Astrophys. J. **127**, 17 (1958). 67, 74

Springel V., Pakmor R., Pillepich A., Weinberger R., Nelson D., Hernquist L., Vogelsberger M., Genel S., Torrey P., Marinacci F., Naiman J., *First results from the IllustrisTNG simulations: matter and galaxy clustering,* Mon. Not. Roy. Astron. Soc. **475**, 676-698 (2018). 13, 81

Springel V., Wang J., Vogelsberger M., Ludlow A., Jenkins A., Helmi A., Navarro J. F., Frenk C. S., White S. D. M., *The Aquarius Project: the subhalos of galactic halos,* Mon. Not. Roy. Astron. Soc. **391**, 1685-1711 (2008). 12, 58, 63, 64, 66, 74, 80, 81, 97

Springel V., White S. D. M., Jenkins A., Frenk C. S., Yoshida N., Gao L., Navarro J., Thacker R., Croton D., Helly J., Peacock J. A., Cole S., Thomas P., Couchman H., Evrard A., Colberg J., Pearce F., *Simulations of the formation, evolution and clustering of galaxies and quasars,* Nature **435**, 629-636 (2005). 6

Srednicki M., Olive K. A., Silk J., *High-energy neutrinos from the sun and cold dark matter,* Nuclear Physics B **279**, 804-823 (1987). 18

Srednicki M., Watkins R., Olive K. A., *Calculations of relic densities in the early universe,* Nuclear Physics B **310**, 693-713 (1988). 31, 33, 186

Starobinsky A. A., *Dynamics of phase transition in the new inflationary universe scenario and generation of perturbations,* Physics Letters B **117**, 175-178 (1982). 52

Stecker F. W., *The cosmic gamma-ray background from the annihilation of primordial stable neutral heavy leptons,* Astrophys. J. **223**, 1032-1036 (1978). 16

Stecker F. W., *GAMMA-RAY CONSTRAINTS ON DARK MATTER RECONSIDERED,* Phys. Lett. **B201**, 529-532 (1988). 17

Stecker F. W., Rudaz S., Walsh T. F., *Galactic Anti-protons From Photinos,* Phys. Rev. Lett. **55**, 2622-2625 (1985). 18

Steigman G., Dasgupta B., Beacom J. F., *Precise Relic WIMP Abundance and its Impact on Searches for Dark Matter Annihilation,* Phys. Rev. **D86**, 023506 (2012). 31, 36

Stone E. C., Cummings A. C., McDonald F. B., Heikkila B. C., Lal N., Webber W. R., *Voyager 1 Observes Low-Energy Galactic Cosmic Rays in a Region Depleted of Heliospheric Ions,* Science **341**, 150-153 (2013). 167, 168

Stref M., Lavalle J., *Modeling dark matter subhalos in a constrained galaxy: Global mass and boosted annihilation profiles,* Phys. Rev. **D95**, 063003 (2017). 64, 65, 67, 74

Strigari L. E., Frenk C. S., White S. D. M., *Dynamical Models for the Sculptor Dwarf Spheroidal in a ΛCDM Universe,* Astrophys. J. **838**, 123 (2017). 140

Strong A. W., Moskalenko I. V., *Propagation of cosmic-ray nucleons in the galaxy,* Astrophys. J. **509**, 212-228 (1998). 104, 105

Strong A. W., Moskalenko I. V., Ptuskin V. S., *Cosmic-ray propagation and interactions in the Galaxy,* Ann. Rev. Nucl. Part. Sci. **57**, 285-327 (2007). 103

Sunyaev R. A., Zeldovich Y. B., *Small-Scale Fluctuations of Relic Radiation,* Astrophysics and Space Science **7**, 3-19 (1970). 4

't Hooft G., *Naturalness, chiral symmetry, and spontaneous chiral symmetry breaking,* NATO Sci. Ser. B **59**, 135-157 (1980). 9, 10

Tan L. C., Ng L. K., *Calculation of the equilibrium antiproton spectrum,* Journal of Physics G Nuclear Physics **9**, 227-242 (1983). 108

Tasitsiomi A., Olinto A. V., *Detectability of neutralino clumps via atmospheric Cherenkov telescopes,* Phys. Rev. D **66**, 083006 (2002). 94

Taylor J. E., Babul A., *The Evolution of substructure in galaxy, group and cluster haloes. 1. Basic dynamics,* Mon. Not. Roy. Astron. Soc. **348**, 811 (2004). 75

Teyssier R., *Cosmological hydrodynamics with adaptive mesh refinement: a new high resolution code called ramses,* Astron. Astrophys. **385**, 337-364 (2002). 149

The L. S., White S. D. M., *Modified Newtonian dynamics and the Coma cluster,* Astron. J. **95**, 1642-1646 (1988). 8

Tisserand P. et al. (EROS-2 Collaboration), *Limits on the Macho Content of the Galactic Halo from the EROS-2 Survey of the Magellanic Clouds,* Astron. Astrophys. **469**, 387-404 (2007). 9

Tollet É., Cattaneo A., Mamon G. A., Moutard T., van den Bosch F. C., *On stellar mass loss from galaxies in groups and clusters,* Mon. Not. Roy. Astron. Soc. **471**, 4170-4193 (2017). 66

Tormen G., Diaferio A., Syer D., *Survival of substructure within dark matter haloes,* Mon. Not. Roy. Astron. Soc. **299**, 728 (1998). 74

Traschen J. H., Brandenberger R. H., *Particle Production During Out-of-equilibrium Phase Transitions,* Phys. Rev. **D42**, 2491-2504 (1990). 37

Tremaine S., Gunn J. E., *Dynamical role of light neutral leptons in cosmology,* Physical Review Letters **42**, 407-410 (1979). 31

Tulin S., Yu H.-B., *Dark Matter Self-interactions and Small Scale Structure,* Phys. Rept. **730**, 1-57 (2018). 13

Tully R. B., Fisher J. R., *A new method of determining distances to galaxies,* Astron. Astroph. **54**, 661-673 (1977). 8

Turner M. S., *Coherent Scalar Field Oscillations in an Expanding Universe,* Phys. Rev. **D28**, 1243 (1983). 37

Ullio P., Bergström L., Edsjö J., Lacey C., *Cosmological dark matter annihilations into γ rays: A closer look,* Phys. Rev. D **66**, 123502 (2002). 17, 94

Ullio P., Kamionkowski M., *Velocity distributions and annual modulation signatures of weakly interacting massive particles,* JHEP **03**, 049 (2001). 159, 161

van de Hulst H. C., *Observations of the interstellar hydrogen line of wave length 21 cm made at Kootwijk, Netherlands.,* Astron. J. **56**, 144-144 (1951). 2

van den Aarssen L. G., Bringmann T., Pfrommer C., *Is dark matter with long-range interactions a solution to all small-scale problems of Λ CDM cosmology?,* Phys. Rev. Lett. **109**, 231301 (2012). 13

van den Bosch F. C., *Dissecting the Evolution of Dark Matter Subhaloes in the Bolshoi Simulation,* Mon. Not. Roy. Astron. Soc. **468**, 885-909 (2017). 74

van den Bosch F. C., Ogiya G., *Dark Matter Substructure in Numerical Simulations: A Tale of Discreteness Noise, Runaway Instabilities, and Artificial Disruption,* Mon. Not. Roy. Astron. Soc. **475**, 4066-4087 (2018). 64, 72, 74

van den Bosch F. C., Ogiya G., Hahn O., Burkert A., *Disruption of Dark Matter Substructure: Fact or Fiction?,* Mon. Not. Roy. Astron. Soc. **474**, 3043-3066 (2018). 64, 72, 74, 82, 97

van den Bosch F. C., Tormen G., Giocoli C., *The Mass function and average mass loss rate of dark matter subhaloes,* Mon. Not. Roy. Astron. Soc. **359**, 1029-1040 (2005). 75

Vergados J. D., Owen D., *New velocity distribution for cold dark matter in the context of the Eddington theory,* Astrophys. J. **589**, 17-28 (2003). 159, 161

Viel M., Lesgourgues J., Haehnelt M. G., Matarrese S., Riotto A., *Constraining warm dark matter candidates including sterile neutrinos and light gravitinos with WMAP and the Lyman-alpha forest,* Phys. Rev. **D71**, 063534 (2005). 13

Visinelli L., Gondolo P., *Kinetic decoupling of WIMPs: analytic expressions,* Phys. Rev. **D91**, 083526 (2015). 40

Vitale V., Morselli A., for the Fermi/LAT Collaboration, *Indirect Search for Dark Matter from the center of the Milky Way with the Fermi-Large Area Telescope,* ArXiv e-prints (2009). 17

Vogelsberger M., Helmi A., Springel V., White S. D. M., Wang J., Frenk C. S., Jenkins A., Ludlow A. D., Navarro J. F., *Phase-space structure in the local dark matter distribution and its signature in direct detection experiments,* Mon. Not. Roy. Astron. Soc. **395**, 797-811 (2009). 159

Vogelsberger M., Zavala J., Cyr-Racine F.-Y., Pfrommer C., Bringmann T., Sigurdson K., *ETHOS – an effective theory of structure formation: dark matter physics as a possible explanation of the small-scale CDM problems,* Mon. Not. Roy. Astron. Soc. **460**, 1399-1416 (2016). 13

Volkov D. V., Akulov V. P., *Is the Neutrino a Goldstone Particle?,* Phys. Lett. **46B**, 109-110 (1973). 9

Vysotsky M. I., Dolgov A. D., Zeldovich Ya. B., *Cosmological Restriction on Neutral Lepton Masses,* JETP Lett. **26**, 188-190 (1977). 30

Wagoner R. V., Fowler W. A., Hoyle F., *On the Synthesis of Elements at Very High Temperatures,* Astrophys. J. **148**, 3 (1967). 6

Walker A. G., *On the formal comparison of Milne's kinematical system with the systems of general relativity,* Mon. Not. Roy. Astron. Soc. **95**, 263-269 (1935). 21

Watkins L. L., Evans N. W., An J. H., *The masses of the Milky Way and Andromeda galaxies,* Mon. Not. Roy. Astron. Soc. **406**, 264-278 (2010). 115, 135

Weinberg M. D., *Adiabatic invariants in stellar dynamics. 2. Gravitational shocking,* Astron. J. **108**, 1403 (1994)a. 68, 69

Weinberg M. D., *Adiabatic Invariants in Stellar Dynamics: I. Basic concepts,* Astron. J. **108**, 1398 (1994)b. 68, 69

Weinberg S., *Gravitation and Cosmology: Principles and Applications of the General Theory of Relativity* (1972). 1, 22, 23, 49

Weinberg S., *A New Light Boson?,* Phys. Rev. Lett. **40**, 223-226 (1978). 10

Weinberg S., *The cosmological constant problem,* Reviews of Modern Physics **61**, 1-23 (1989). 23

Wells J. D., *Naturalness, Extra-Empirical Theory Assessments, and the Implications of Skepticism,* ArXiv e-prints (2018). 10

Weniger C., *A tentative gamma-ray line from Dark Matter annihilation at the Fermi Large Area Telescope,* JCAP **8**, 007 (2012). 18

Wess J., Zumino B., *Supergauge Transformations in Four-Dimensions,* Nucl. Phys. **B70**, 39-50 (1974). 9

Widrow L. M., Dubinski J., *Equilibrium disk-bulge-halo models for the Milky Way and Andromeda galaxies,* Astrophys. J. **631**, 838-855 (2005). 115, 140

Wilczek F., *Problem of Strong p and t Invariance in the Presence of Instantons,* Phys. Rev. Lett. **40**, 279-282 (1978). 10

Will C. M., *The Confrontation between General Relativity and Experiment,* Living Reviews in Relativity **17**, 4 (2014). 7

Winkler M. W., *Cosmic Ray Antiprotons at High Energies,* JCAP **1702**, 048 (2017). 18, 108, 109, 112

Wojtak R., Gottlöber S., Klypin A., *Orbital anisotropy in cosmological haloes revisited,* Mon. Not. Roy. Astron. Soc. **434**, 1576-1585 (2013). 130

Wojtak R., Lokas E. L., Mamon G. A., Gottloeber S., Klypin A., Hoffman Y., *The distribution function of dark matter in massive haloes,* Mon. Not. Roy. Astron. Soc. **388**, 815 (2008). 130, 132

Woolley R. V. D. R., *A study of the equilibrium of globular clusters,* Mon. Not. Roy. Astron. Soc. **114**, 191 (1954). 140

Woolley R. V. D. R., Robertson D. A., *Studies in the equilibrium of globular clusters (II),* Mon. Not. Roy. Astron. Soc. **116**, 288 (1956). 140

York D. G. et al. (SDSS Collaboration), *The Sloan Digital Sky Survey: Technical Summary,* Astron. J. **120**, 1579-1587 (2000). 6

Yurin D., Springel V., *The stability of stellar discs in Milky Way-sized dark matter haloes,* Mon. Not. Roy. Astron. Soc. **452**, 2367-2387 (2015). 68

Zatsepin G. T., Kuz'min V. A., *Upper Limit of the Spectrum of Cosmic Rays,* Soviet Journal of Experimental and Theoretical Physics Letters **4**, 78 (1966). 98

Zel'dovich Y. B., Novikov I. D., *A Hypothesis for the Initial Spectrum of Perturbations in the Metric of the Friedmann Model Universe.,* Soviet Ast. **13**, 754 (1970). 53

Zeldovich Y. B., Sunyaev R. A., *The Interaction of Matter and Radiation in a Hot-Model Universe,* Astrophysics and Space Science **4**, 301-316 (1969). 3

Zentner A. R., *The Excursion Set Theory of Halo Mass Functions, Halo Clustering, and Halo Growth,* International Journal of Modern Physics D **16**, 763-815 (2007). 55

Zentner A. R., Berlind A. A., Bullock J. S., Kravtsov A. V., Wechsler R. H., *The Physics of galaxy clustering. 1. A Model for subhalo populations,* Astrophys. J. **624**, 505-525 (2005). 75

Zhao H., Taylor J. E., Silk J., Hooper D., *Tidal Disruption of the First Dark Microhalos,* Astrophys. J. **654**, 697-701 (2007). 73

Zhao Y., Bi X.-J., Jia H.-Y., Yin P.-F., Zhu F.-R., *Constraint on the velocity dependent dark matter annihilation cross section from Fermi-LAT observations of dwarf galaxies,* Phys. Rev. **D93**, 083513 (2016). 170

Zhitnitsky A. R., *On Possible Suppression of the Axion Hadron Interactions. (In Russian),* Sov. J. Nucl. Phys. **31**, 260 (1980). 10

Zhu Q., Marinacci F., Maji M., Li Y., Springel V., Hernquist L., *Baryonic impact on the dark matter distribution in Milky Way-size galaxies and their satellites,* (2015). 63

Zjupa J., Springel V., *Angular momentum properties of haloes and their baryon content in the Illustris simulation,* Mon. Not. Roy. Astron. Soc. **466**, 1625-1647 (2017). 150

Zlosnik T. G., Ferreira P. G., Starkman G. D., *Modifying gravity with the Aether: An alternative to Dark Matter,* Phys. Rev. **D75**, 044017 (2007). 8

Zwicky F., *Die Rotverschiebung von extragalaktischen Nebeln,* Helv. Phys. Acta **6**, 110-127 (1933). 3

Zwicky F., *On the Masses of Nebulae and of Clusters of Nebulae,* Astrophys. J. **86**, 217 (1937). 3

Understanding the nature of dark matter is one of the greatest challenges of modern physics. If dark matter is made of particles, we can hope to detect it, directly or indirectly, using Earth-based or spatial experiments. Make predictions for the outcome of these experiments, or interpret the results in case of a detection, requires a deep understanding of the structuring of dark matter in our Galaxy. Starting from particle physics and cosmological considerations, I built a dynamically constrained model of the Galactic dark halo including a detailed description of its inhomogeneities. The impact of these inhomogeneities on searches with cosmic rays is then analysed in details. I also study a method allowing to predict the phase-space distribution of dark matter particles, and discuss its possible application to dark matter searches. This method is then applied to searches with cosmic-ray electrons and positrons, and new very stringent constraints are obtained on microscopic models of dark matter.